Measurements of X-ray Selected AGN and Novel Superconducting X-ray Detectors

Thesis by

Megan E. Eckart

In Partial Fulfillment of the Requirements

for the Degree of

Doctor of Philosophy

California Institute of Technology

Pasadena, California

2007

(Defended May 22, 2007)

Acknowledgements

First and foremost, I would like to thank my parents, Mark and Judy Eckart, and my sister, Janet; their importance in my life is immeasurable. I would also like to warmly thank my extended family for their love and support.

The SEXSI survey not only provided opportunities to use a variety of world class telescopes, but allowed me to learn from and collaborate with a great group of people. My advisor, Fiona Harrison, led the project and took a lead role in the X-ray data reduction and analysis. I thank Fiona for her work on SEXSI as well as for her unwavering support and advice; she was extremely helpful and generous with her time, especially as I prepared my thesis. David Helfand offered guidance and support throughout my graduate career, for which I am deeply grateful. His input from across the country as well as his frequent visits to Caltech made the project what it is today. I should mention here, for the record, that it was David and Fiona who crafted our project name (with the lovely acronym). Daniel Stern has played a key role as an expert in the optical and mid-infrared observing and analyses, and I thank him for teaching me about spectral reductions and classifications, among many other things. I also especially thank Dan for his support during the final stages of my thesis writing. As the first graduate student on SEXSI, Peter Mao was instrumental both in starting the project and in much of the optical followup effort. I thank Pedro for his many contributions to the survey and for showing me the ropes. I am so glad that we remained good friends after he graduated and left Caltech. Also, I thank James Chakan, who assisted in the X-ray data analysis, Elise Laird, who was crucial to the optical imaging effort, Sarah Yost, who was responsible for the DEIMOS spectral reductions, and Luke Kotredes, who contributed greatly to the *Spitzer* data analysis. Without the contributions from these colleagues, the first part of my thesis would not have been possible. Finally, I would like to thank the scientists, engineers, and staff who built and operate the telescopes and instruments employed by the SEXSI program. I especially thank the teams responsible

for the *Chandra*, Keck, Palomar, and *Spitzer* observatories.

I'm grateful to have had the opportunity to work with the Caltech/JPL microwave kinetic inductance detector group for the final few years of my time at Caltech. First I thank Jonas Zmuidzinas for introducing me to MKIDs and for his patient and inspiring discussions. Bruce Bumble, Sunil Golwala, and Benjamin Mazin were my primary colleagues on the strip detector work that is described in the second part of this thesis. I thank Bruce for his skilled and persistent fabrication efforts that produced the majority of the devices presented in this thesis. Ben and I spent countless hours in the lab together, and I thank him for both his companionship and for introducing me to many aspects of the laboratory work and data analysis. Sunil played a valuable advisory role and I thank him for teaching me a great deal about data analysis and device physics. I thank Peter Mason for teaching me about cryogenics involved in the project, Peter Day for his efforts in helping me to understand the operating principles of the detectors, and Rick LeDuc for sharing his vast knowledge of device fabrication. Last but definitely not least, I thank my fellow graduate students: Jiansong Gao, Tasos Vayonakis, and Shwetank Kumar, who have helped me to understand numerous aspects of the lab work and detector physics.

Another important group that I would like to thank consists of Fiona, Sunil, Re'em Sari, and Chuck Steidel, who served as both my candidacy and thesis defense committees. They showed interest in my work and provided crucial feedback.

I would also like to recognize the entire Space Radiation Laboratory staff for their friendly support and scientific guidance; in particular, a handful of SRLers have been especially significant in my time at Caltech. My long-time officemate, Brad Cenko, has been a fantastic presence in my life for the past 5 years, and I thank him for his friendship. My days were always interesting during the period when Dae-Sik Moon was a postdoc down the hall – each morning I never knew whether Dae-Sik would taunt me with his signature "Watch your back!," or provide me with his warm support and advice. SRL has not been the same since he left. Another long-time officemate during earlier years was fellow graduate student Hubert Chen. I thank Hubert for many interesting discussions and for always lending a helping hand when needed. Postdocs Wayne Baumgartner and Mike Muno have provided me with numerous amusing lunchtime discussions as well as valuable guidance.

I am grateful that my time at Caltech has allowed me to become friends with many of my fellow physics students: I have enjoyed the many hours spent with Mike Armen,

Parsa Bonderson, Nathan Lundblad, Dave Sand, John Stockton, and Ian Swanson. Parsa Bonderson deserves special mention, as he has been a wonderful friend for every day of my tenure at Caltech, from orientation through our defenses, which commenced a mere 29 hours apart. I thank Donna Driscoll, the Physics Graduate Coordinator, who has been extremely helpful and has always had an open door when I've needed assistance. I also appreciate the friendship of fellow Caltech graduate students Serena Guarnaschelli, Tobias Kippenberg, Julie Liu, Melissa Enoch, Cecily Ryan, and Mary Laura Lind. Kevin McHale has been a true friend and a superb companion over the past couple of years, and I cannot thank him enough. I am especially grateful for his extremely generous help during the writing of this thesis; I guarantee that without him my thesis would not have been completed on time or in good health.

Friendships cultivated off campus have also been crucial to my time at Caltech. Tara Klassen, Talia Starkey and I came together through unlikely connections to become Pasadena running buddies and great friends; I owe them so much for their ceaseless encouragement and for being an inspiration to me. I especially thank Talia for her support during my thesis crunch through her frequent calls and emails, home cooking, beautiful home-grown flowers and stress-relieving trail runs. I also greatly appreciate the friendship of Jim Chonko, Erin (Kelley) Holford, and Deirdre Scripture-Adams.

I'm pleased to have stayed close to friends from Livermore and Cal, and I thank them for their support from afar and especially for their visits to Pasadena. In particular I'd like to thank Livermorons Alison Anastasio, Marisa (Daniel) Beck, Christina Coll, Jodi Denton, Jason Dietrich, Cameron Fortner, and Wendy (Robson) Westcamp, and Berkeley comrades Lea Boyd, Antara Basu-Zych, Blake (Likins) Bullock, Steve Dawson, Jenny (Michel) Dixon, Brenda Fletcher, Laura (Zmijewski) Grant, Nicole Izant, Dale Li, Brian Medeiros, Jessica Wellner, and Victor Bigvic Wong.

Finally, I would like to thank Bruce Macintosh and the scientists at the Institute of Geophysics and Planetary Physics at LLNL for mentoring me through undergraduate summers spent as a research assistant, as well as my professors at Berkeley and Caltech.

The research presented here was supported in part by a NASA Graduate Student Research Program Fellowship.

Abstract

Major astrophysical advances typically come through combining new observational approaches with new technologies. This thesis involves work on both fronts, combining observational work using data from the *Chandra* X-ray Observatory and Keck Observatory, two of the premier telescopes of the current generation, with novel superconducting detector development to further technology for future observatories.

The subject of the first part of this thesis is the Serendipitous Extragalactic X-ray Source Identification (SEXSI) program, a survey using *Chandra* data specifically selected to probe the dominant contributors to the 2 – 10 keV cosmic X-ray background. To accomplish this, SEXSI covers more than 2 deg^2 of sky and employs optical photometric and spectroscopic followup of sources discovered in archival *Chandra* fields. The resulting source sample consists of 1034 hard X-ray-selected sources with R-band optical-followup imaging, and optical spectroscopy for 477 of the sources, primarily from Keck Observatory, filling the gap between wide-area, shallow surveys and the deep, pencil-beam surveys such as the *Chandra* Deep Fields. The vast majority of the 2 – 10 keV-selected sample are AGN with redshifts between 0.1 and 3. In this thesis we discuss results from our survey, including the spectroscopic properties of hard X-ray sources, the relationship between X-ray and optical properties of our sources, and our sample of spectroscopically-confirmed, narrow-lined, obscured type II quasar candidates. In addition, we present infrared data from the *Spitzer* Space Telescope that cover a subset of the *Chandra* fields, which allows us to explore the relative strengths of *Chandra* and *Spitzer* as black-hole finders.

The second part of this thesis focuses on microwave kinetic inductance detectors (MKIDs), which are an exciting new superconducting detector technology that has breakthrough potential for providing megapixel imagers with several eV energy resolution for use in future X-ray missions. These detectors utilize simple, thin-film lithographed microwave resonators as photon detectors in a multiplexed readout approach. X-ray absorption in a superconduc-

tor creates quasiparticle excitations, with number proportional to the X-ray energy. The surface impedance of a superconductor changes with the quasiparticle density, and if operated at $T \ll T_c$ where the quasiparticle generation-recombination noise is low, extremely small changes in the surface impedance can be measured using the thin-film resonant circuit and microwave readout techniques. This provides a sensitive detector with excellent energy resolution.

MKIDs offer the advantage over many other cryogenic detector technologies that they can be easily multiplexed by coupling many resonators to a single microwave transmission line, so that arrays with many thousand pixels are readily achievable. In addition, the readout electronics can be operated at room temperature, a significant advantage for space applications. The practical application of MKIDs for photon detection requires a method of efficiently coupling the photon energy to the MKID. To this end we have been studying MKIDs in a strip detector architecture. The second part of this thesis presents our results using strip detectors with tantalum absorbers coupled to aluminum MKIDs.

Contents

Acknowledgements iii

Abstract vi

1 Introduction and Overview 1

1.1 X-ray Surveys of Active Galaxies 1

1.2 Detector Technologies for Future X-ray Surveys 4

1.3 Thesis Organization 6

1.3.1 Part 1: SEXSI-Focused Chapters 6

1.3.2 Part 2: MKIDs-Focused Chapters 7

I The Serendipitous Extragalactic X-ray Source Identification Program 9

2 Introduction to the SEXSI Program 10

2.1 The Extragalactic X-Ray Background 10

2.1.1 The Shape of the XRB 10

2.1.2 Resolving the XRB 12

2.1.3 The Advanced Satellite for Cosmology and Astrophysics (ASCA) . . 15

2.2 A New Era in X-ray Astrophysics 15

2.2.1 The *Chandra* Telescope Design 17

2.2.1.1 The Advanced CCD Imaging Spectrometer (ACIS) 17

2.3 XRB Surveys with *Chandra* 20

2.4 The SEXSI Program 21

3 SEXSI X-Ray Analysis and Characteristics of the Hard X-Ray Sample 22

3.1 Introduction . . . 23

3.2 Selection of *Chandra* Fields . . . 27

3.3 Data Reduction and Analysis . . . 28

3.3.1 Basic X-ray Reduction . . . 28

3.3.2 Source Deletions . . . 30

3.3.3 Hardness Ratio Calculation . . . 31

3.3.4 Calculation of the Effective Area Function . . . 34

3.4 The Source Catalog . . . 35

3.4.1 Comparison of Methodology with Previous Work . . . 37

3.5 The 2 – 10 keV log N – log S Relation . . . 38

3.6 X-ray Properties of the Sample . . . 42

3.6.1 Distribution of Hardness Ratios . . . 45

3.6.2 X-ray Spectral Comparison to Previous Work . . . 47

3.7 Summary . . . 49

3.8 Appendix . . . 50

4 SEXSI Optical Imaging 53

4.1 Introduction . . . 53

4.2 Optical Imaging and Reduction . . . 55

4.2.1 Photometric Calibration . . . 57

4.2.2 Source Extraction and Limiting Magnitudes . . . 57

4.3 Optical Counterparts to X-Ray Sources . . . 61

4.4 The Catalog . . . 65

4.5 Discussion . . . 67

4.6 Summary . . . 76

5 SEXSI Optical Spectroscopy 78

5.1 Introduction . . . 79

5.2 Survey Design . . . 82

5.3 Optical Spectroscopy: Data Collection and Reduction . . . 85

5.3.1 LRIS Data . . . 85

5.3.2 DEIMOS Data . . . 86

5.3.3 Doublespec Data . . . 87
5.4 Redshift Determination and Source Classification . . . 87
5.5 The Catalog . . . 93
5.6 Hard X-ray Source Population Statistics . . . 110
5.6.1 Redshift Distribution . . . 110
5.6.2 X-ray Flux and X-ray-to-Optical Flux Ratio Distributions . . . 112
5.6.3 X-ray Luminosity Distribution . . . 112
5.6.4 Absorbing Column Density Distribution . . . 116
5.7 Source Classes . . . 119
5.7.1 Broad-Lined AGN . . . 119
5.7.2 Narrow-Lined AGN . . . 124
5.7.3 Emission-Line Galaxies . . . 125
5.7.4 Absorption-Line Galaxies . . . 126
5.7.5 Line-Free Spectra . . . 126
5.7.5.1 BL Lac Contribution . . . 127
5.7.5.2 ELGs in the Redshift Desert? . . . 128
5.7.6 Stars . . . 130
5.8 Selection Effects and Sample Completion . . . 131
5.9 Global Characteristics of the Sample and Comparison with Other Surveys . . . 137
5.9.1 Redshift Distribution . . . 137
5.9.2 Obscured Sources . . . 139
5.9.3 Obscured Sources with Quasar Luminosities . . . 144
5.10 The Nature of the Emission-Line Galaxies . . . 146
5.10.1 Low-Luminosity ELG; Powered by Star Formation? . . . 147
5.10.2 Non-Stellar Emission . . . 148
5.10.3 Search for Faint High-Ionization Lines . . . 149
5.11 Sources Associated with Target and Non-Target Galaxy Clusters . . . 154
5.11.1 Target Clusters . . . 155
5.11.2 Non-Target Clusters Identified in Holden et al. (2002) . . . 156
5.12 Summary . . . 157

6 Obscured AGN: Comparing X-ray and Mid-Infrared Selection 160

6.1 Introduction . . . 160

6.1.1 *Spitzer* "Wedge" Selection of AGN . . . 161

6.2 *Spitzer* Imaging with IRAC and MIPS . . . 162

6.3 Source Catalog . . . 164

6.4 X-ray Selected SEXSI Sources Viewed in the Infrared . . . 164

6.4.1 X-ray Luminosity Dependence . . . 166

6.4.2 Dependence on R-band Magnitude . . . 169

6.5 Mean X-ray Properties of Infrared Selected Active Galaxies . . . 172

6.5.1 X-ray Stacking Methodology . . . 172

6.5.2 Stacking Results . . . 173

6.6 Conclusions and Future Work . . . 175

II Microwave Kinetic Inductance Detectors for X-ray Astrophysics 177

7 Focal-Plane Arrays for Next-Generation Missions 178

7.1 Scientific Motivation for Next-Generation X-ray Survey Missions . . . 178

7.1.1 Overview . . . 178

7.1.2 Next-Generation AGN Surveys . . . 178

7.2 Basic Design Requirements for Future X-ray Survey Missions . . . 179

7.3 Superconducting Detectors for X-ray Astrophysics . . . 180

7.3.1 Pair-Breaking Detectors: Analogy to Photoconductors . . . 181

7.3.2 Superconducting Tunnel Junctions . . . 182

7.3.3 Microcalorimeters . . . 183

7.4 The Push for Large Arrays . . . 185

7.4.1 Brute Force: Scaling Up Current Detector Arrays . . . 185

7.4.2 TES Multiplexing Approaches . . . 185

7.4.2.1 Time-Division and Frequency-Division Multiplexing . . . 186

7.4.2.2 Microwave Frequency-Domain Multiplexing . . . 189

7.4.3 Distributed Pixel Approaches . . . 190

7.4.3.1 Position Sensitive TES (PoST) Microcalorimeter Arrays . . . 190

7.4.3.2 STJ-Based Strip Detectors . . . 191

7.5 Motivation for MKIDs Development 191

8 Microwave Kinetic Inductance Detectors and the Strip Detector Architecture 193

8.1 Basic Electrodynamics of Superconductors 193

8.2 MKIDs with Quarter-Wave Resonators 196

8.2.1 Response to Quasiparticles 196

8.2.2 Practical Implementation and Design 201

8.2.2.1 Resonator Fabrication 202

8.3 Basic Quasiparticle Generation and Decay in MKIDs 203

8.4 Noise Processes in MKIDs 204

8.4.1 Generation-Recombination Noise 204

8.4.2 Excess Phase Noise 205

8.5 Coupling to X-ray Photons 205

8.5.1 The Strip Detector Architecture 207

8.5.1.1 Quasiparticle Generation and Dynamics in the Absorber . 207

8.5.1.2 Quasiparticle Trapping 211

8.5.1.3 Energy Resolution 213

8.5.1.4 Materials Choices 214

9 Experimental Setup and Strip Detector Device Fabrication 216

9.1 Cryogenics: Achieving $T \lesssim 100$ mK 216

9.1.1 The Oxford 25 MKIDs Testbed 217

9.2 Testbed and Wiring Upgrades 217

9.3 Electronics 222

9.4 Strip Detector Fabrication 223

9.4.1 Masks for Strip Detector Testing 224

9.4.1.1 Original Optical Mask (2003) 224

9.4.1.2 X-Ray Test Mask (2005) 225

9.4.1.3 Lateral Trapping Mask (2006) 225

9.4.2 Fabrication parameters of selected wafers 226

10 Detector Testing: From Working Resonators to Working Strip Detectors 227

10.1 Questions Addressed During Strip-Detector Testing . . . 227

10.2 Record of Testing . . . 229

10.2.1 Calibration Sources for Detector Testing . . . 229

10.2.2 Stainless-Steel Masking Experiment . . . 232

10.3 Observations . . . 235

10.3.1 Quasiparticle Connection Between Absorber and MKID . . . 235

10.3.1.1 Thinner Absorber to Reduce the Step . . . 237

10.3.1.2 Physical Barrier . . . 237

10.3.1.3 Bad Tantalum . . . 239

10.3.1.4 Sloped Edge of Absorber . . . 239

10.3.1.5 Liftoff Plug . . . 239

10.3.2 Quasiparticle Trapping: Vertical versus Lateral . . . 243

10.3.3 Diffusion Parameters of Ta Absorber . . . 244

10.3.3.1 Higher RRR or Thicker Tantalum . . . 244

10.3.3.2 Protect Ta During Al Etch . . . 245

10.3.3.3 Absorber–Substrate Acoustic Match . . . 245

10.3.3.4 Straight-Walled Strips versus Sloped-Wall Stri . . . 246

10.3.4 Noise Properties in Strip-Detector MKIDs . . . 246

10.3.4.1 Single-Layer Resonator Noise versus Strip-Detector Resonator Noise . . . 247

10.3.4.2 One Sapphire is Better than Another . . . 247

10.3.4.3 Chlorine in Etch . . . 247

10.4 Testing Conclusions . . . 249

11 Experimental Results 250

11.1 Data Analysis Procedures . . . 250

11.1.1 Fitting the Resonance Data . . . 250

11.1.2 Optimal Pulse-Height Estimator . . . 251

11.1.3 Energy Resolution Limit Set By Resonators . . . 252

11.1.4 Fitting for Absorber Diffusion Parameters . . . 253

11.1.5 Energy Resolution of a Strip Detector . . . 254

11.2 Data Analysis of Device Tested During Runs 79 and 82 255
11.2.1 Brief Comparison to Run 86 261
11.2.2 Comparison to Run 87 262

12 MKIDs Conclusion **265**

A Dilution Refrigerators **266**
A.1 ^{3}He-^{4}He Mixtures 266
A.2 Design of a Dilution Refrigerator 268

B Phonon Loss to Substrate During Initial Energy Downconversion **272**

Bibliography **277**

List of Figures

2.1 Photon spectrum of the extragalactic X-ray background. 11

2.2 Transmission as a function of incident X-ray energy through various column densities. 13

2.3 R-band optical image of CXOSEXSI_J084905.0+445714, also detected with *ASCA*, illustrating the difficulting in optically identifying 2 – 10 keV sources in the pre-*Chandra* era. 16

2.4 The effective area of *Chandra*. 18

2.5 Focal plane of the CCD chips that combine to form the ACIS-I and ACIS-S arrays. 19

3.1 Area of sky surveyed as a function of hard (2 – 10 keV) X-ray flux for several hard X-ray surveys. 26

3.2 Histogram of exposure times for the 27 *Chandra* fields. 28

3.3 Comparison of hardness ratio $HR \equiv (H-S)/(H+S)$ as a function of hard X-ray flux (H; 2 – 10 keV), with soft-band flux (S; 0.5 – 2 keV) measured in two ways. 32

3.4 Hardness ratio $HR_H \equiv (H-S)/(H+S)$ as a function of hard X-ray flux for sources lacking a counterpart in the soft X-ray catalog. 33

3.5 Comparison of the SEXSI and SPICES catalogs of hard-band 2 – 10 keV sources from the 185 ks *Chandra*/ACIS observation of the CL0848+4454 field in Lynx. 39

3.6 Differential $\log N - \log S$ for the SEXSI survey and *Chandra* Deep Field South. 41

3.7 Differential $\log N - \log S$ residuals, defined as (data – fit)/data, for SEXSI, CDF-S, and Hawaii SSA22 and CDF-N. 43

3.8 Hardness ratio $HR \equiv (H-S)/(H+S)$ of SEXSI sources as a function of hard X-ray (2 – 10 keV) flux. 44

3.9 Histogram of hardness ratio values for the SEXSI 2−10 keV selected sample of X-ray sources. 46
3.10 Differential $\log N - \log S$ for the SEXSI sources split at $HR = 0$. 48

4.1 Example of R-band number counts for a typical SEXSI image with the Capak et al. (2004) fit and our 80% completeness limit. 59
4.2 Histogram of limiting optical magnitudes for SEXSI sources with optical coverage. 61
4.3 Example of the R-band postage stamp cutout images. 64
4.4 Optical magnitude of SEXSI sources, plotted as a function of their hard-band (2 – 10 keV) X-ray flux. 69
4.5 Histogram of 2 – 10 keV fluxes, split by optical counterpart R-band magnitude from SEXSI and the CDF-N. 71
4.6 Histogram of X-ray hardness ratios (HR), split by optical counterpart R-band magnitude. 72
4.7 Mean hardness ratio (HR) of sources split by optical counterpart R-band magnitude, as a function of 2 – 10 keV flux. 74
4.8 Hardness ratio as a function of X-ray-to-optical flux ratio. The right panel shows HR as a function of redshift for an intrinsic $\Gamma = 1.9$ spectrum with several intrinsic obscuring column densities, for reference. 75

5.1 Redshift versus luminosity for SEXSI sources, with optical spectral classification indicated. The approximate phase space covered by the ASCA Medium Sensitivity Survey and the *Chandra* Deep Fields is illustrated with text. . . . 81
5.2 Example optical spectrum of one of the 212 SEXSI BLAGN. 89
5.3 Example spectra of NLAGN at $z = 0.5$, $z = 1.2$, and $z = 2.4$. 90
5.4 Example spectra for two of the 168 SEXSI ELG. 91
5.5 Example of one of the eight SEXSI ALG. 92
5.6 Redshift histogram for the 419 sources with spectroscopic redshifts presented in Table 5.2, excluding the stars (at $z = 0$). 111
5.7 R-magnitude versus redshift for spectroscopically identified sources. The distinct regions in $R - z$ parameter space covered by each class type is illustrated. 113

5.8 The 2 – 10 keV flux histogram of spectroscopically identified sources split at $R = 22$. . . . 114
5.9 Histogram of $\log(f_x/f_o)$ distribution of spectroscopically-identified sources. . 115
5.10 X-ray luminosity histograms, uncorrected for intrinsic absorption at the source. 117
5.11 2 – 10 keV luminosity versus HR. . . . 118
5.12 N_H histogram for BLAGN, ELG, and NLAGN. . . . 120
5.13 Hardness ratio histogram of spectroscopically identified sources split at $R = 22$. 121
5.14 HR versus R-magnitude for five redshift ranges. The bottom right panel shows HR versus z for three typical values of intrinsic obscuring column density given a source power-law index $\Gamma = 1.9$, for reference. . . . 123
5.15 The ELG population compared to sources that have spectra with a continuum lacking detected emission or absoprtion features. . . . 129
5.16 A cataclysmic variable (CV) that shows a blueshift of 274 km s^{-1}. The measured velocity indicates either that the star is at an extremum in its orbit or that it is a rare halo CV. . . . 131
5.17 N_H versus redshift. . . . 132
5.18 Histograms of $f_{2-10\ \mathrm{keV}}$, R, $\log(f_x/f_o)$, and HR from seventeen fields where we have extensive spectral coverage, to illustrate spectroscopic completeness. 136
5.19 Redshift distribution of SEXSI, HELLAS2XMM, ChaMP, CLASXS, and CYDER. . . . 138
5.20 Fraction of obscured ($\log N_H > 22$) sources as a function of *unobscured* 2 – 10 keV flux for the spectroscopically identified samples from SEXSI, GOODS CDFN and ChaMP. . . . 141
5.21 Comparison of N_H calculation methods: X-ray spectral fitting verses HR derived. . . . 142
5.22 Fraction of obscured sources as a function of *unobscured* luminosity for spectroscopically identified sources. . . . 145
5.23 These plots show the relationship between $\log(f_x/f_o)$ versus $\log(L_{2-10\ \mathrm{keV}})$ for SEXSI BLAGN (top panel) and sources that lack broad emission lines in their optical spectrum including SEXSI NLAGN, ELG, and ALG as well as the HELLAS2XMM 1-degree field and the CDFN 2 Ms sample. . . . 150

5.24 Here we again plot the relationship between $\log(f_{\rm x}/f_{\rm o})$ and $\log(L_{2-10\ \rm keV})$ for the NLAGN and ELG separately. 151
5.25 Stacked spectrum of 21 ELG all obtained with LRIS on the Keck I Telescope. 154

6.1 Color-color diagram of sources with IR-detections in all four IRAC bands. . . 167
6.2 IRAC color-color diagram of SEXSI 2 – 10 keV sources, split by absorption-corrected intrinsic X-ray luminosity. 168
6.3 IRAC color-color diagram of sources with optical counterparts brighter than $R = 22$. 170
6.4 IRAC color-color diagram of sources with optical counterparts fainter than $R = 22$. 170

7.1 Photon absorption in a superconductor. 181
7.2 I-V curve of a superconducting tunnel junction. 183
7.3 Ideal microcalorimeter. 184
7.4 Resistance as a function of temperature for a superconductor with a critical temperature of $T_c \sim 100$ mK, illustrating the operational regime of TESs. . . 185
7.5 TES time-division multiplexing scheme. 187
7.6 TES resolution as a function of number of multiplexed pixels using a time-division multiplexer. 188

8.1 Illustration of MKID detection scheme. 197
8.2 Cross section of a coplanar-waveguide resonator. 200
8.3 Illustration of an elbow coupler. 202
8.4 Power and material dependence of the excess phase noise in MKIDs. 206
8.5 Cartoon of a strip detector. 207
8.6 Quasiparticle dynamics and trapping in a strip detector. 212

9.1 The homodyne detection scheme employed for MKID readout 223

10.1 Spectrum of K3670 NIST-glass X-ray reflection source for detector testing. . 233
10.2 Spectrum of silicon reflection source for detector testing. 234
10.3 Optical microscope image of the stainless-steel mask placed on top of an LT-A Ta-Al strip detector. 236

10.4 SEM of device from B060306. The absorber Ta is thinner than the Al film to avoid step coverage problems but shows a 'flag' at the edge of the Ta that may hinder quasiparticle flow. Vertical trapping bars are also shown in this image. 238
10.5 SEM of device from wafer B060530.1, showing the lateral-trapping bar design, sloped Ta edges, and an Al liftoff patch at the Ta edge. 240
10.6 SEM of device from wafer B070207, illustrating a device with straight Ta walls and an Al-liftoff patch. 242
10.7 Ta T_c and RRR as a function of film thickness 245
10.8 SEM image of device from wafer B061002, with a grainy Ta surface. 246
10.9 Frequency noise as a function of internal power of Al MKIDs in the strip-detector architecture as compared to that of single-layer Al MKIDs on several different substrates. 248

11.1 Resonance data of a $Q \approx 47000$ resonator with $f_o \approx 7.7$ GHz at 60 mK with fitting models overlaid. 251
11.2 X-ray pulses in each MKID attached to a 200 μm-long Ta strip absorber. . . 256
11.3 Noise power spectra, pulse templates, and NEPs derived from Run 82, 200 μm-long strip detector. 258
11.4 X-ray pulses with diffusion-recombination model fits overlaid. 259
11.5 Optimally filtered maximum phase height 'banana' plot from the 200 μm-long Ta strip from Run 82. 261
11.6 Comparison of frequency noise from strip detectors tested in Runs 82 and 87, respectively; the devices are fabricated on different brands of sapphire. 263
11.7 Banana plot comparison of 200 μm-long strips tested during Runs 82 and 87, respectively. 264

A.1 Phase diagram of liquid ^{3}He -^{4}He mixtures. 267
A.2 Cartoon of dilution cooling. 269
A.3 Diagram of the main components of a dilution refrigerator. 270

B.1 Average probability of phonon energy loss to the substrate as a function of $E_{\rm lost}$. 276

List of Tables

3.1 Comparison of sources detected in 2 – 10 keV hard X-ray surveys 25

3.2 *Chandra* observations of the 27 SEXSI fields 27

3.3 Percentage of PSF half-width as a function of off-axis angle used to extract hard counts (the value for soft count extraction is obtained by adding 0.6% to the hard counts % of PSF half-width value). These values optimize the signal-to-noise of each detection (see §3.3.1) 30

3.4 SEXSI 2 – 10 keV source catalog (SEXSI I catalog) 36

3.5 HR_H averages for sources with $HR_H < 0$ and $HR_H > 0$ (see §3.6.1) 45

3.6 SEXSI soft-band only source catalog 52

4.1 Optical imaging instruments employed in the SEXSI survey 56

4.2 Summary of optical imaging for each of the 27 SEXSI fields 60

4.3 SEXSI optical counterpart catalog (SEXSI II catalog) 66

5.1 Summary of spectroscopic follow-up of each of the SEXSI Fields 84

5.2 SEXSI optical spectroscopy catalog (SEXSI III catalog) 94

5.2 SEXSI optical spectroscopy catalog (SEXSI III catalog) 95

5.2 SEXSI optical spectroscopy catalog (SEXSI III catalog) 96

5.2 SEXSI optical spectroscopy catalog (SEXSI III catalog) 97

5.2 SEXSI optical spectroscopy catalog (SEXSI III catalog) 98

5.2 SEXSI optical spectroscopy catalog (SEXSI III catalog) 99

5.2 SEXSI optical spectroscopy catalog (SEXSI III catalog) 100

5.2 SEXSI optical spectroscopy catalog (SEXSI III catalog) 101

5.2 SEXSI optical spectroscopy catalog (SEXSI III catalog) 102

5.2 SEXSI optical spectroscopy catalog (SEXSI III catalog) 103

5.3 Photometry for sources with spectral ID outside the formal match area . . . 108

5.4 Optical spectroscopic line detections 122
5.5 Cluster fields: SEXSI sources associated with known clusters 155

6.1 *Spitzer* data 163
6.2 SEXSI-*Spitzer* Catalog 165
6.3 Wedge selection of SEXSI X-ray sources for several luminosity ranges 169
6.4 Wedge selection of IRAC sources and SEXSI X-ray sources split at $R_{\rm cut} = 22$ 171
6.5 Average properties of X-ray undetected IRAC sources 174
6.6 Wedge stack: implied N_H 175

9.1 Fabrication Parameters of Selected Wafers 226

10.1 Log of strip detector tests 230
10.2 Strip detector test notes 231

B.1 Important Ta parameters 274

Chapter 1

Introduction and Overview

Major astrophysical advances typically come through combining new observational approaches with new technologies. This thesis invovles work on both fronts, combining observational work using data from the *Chandra* X-ray Observatory and Keck Observatory, two of the premier telescopes of the current generation, with novel superconducting detector development to further technology for future observatories.

1.1 X-ray Surveys of Active Galaxies

Since the confirmation of the cosmological distance of the first active galaxy, a $z = 0.158$ quasar (Schmidt 1963), there has been intense interest in understanding these sources and their role in the growth and evolution of structures in the Universe. It became increasingly clear that these sources are not uncommon; rather, that there are millions of active galactic nuclei (AGN) in the Universe, radiating significant energy through accretion of gas onto supermassive black holes. The energy density radiated by AGN accretion in the X-ray is almost as much as that produced by starlight in the optical and UV. The discovery of the $M - \sigma$ relationship (e.g., Magorrian et al. 1998; Tremaine et al. 2002), which indicates that a galaxy's growth and evolution is closely linked to that of the supermassive black hole residing at its center, has led to even greater interest in mapping the accretion history of the Universe as a means to understand this unexpected relationship. Understanding the nature and evolution of supermassive black holes and their role in galaxy formation and evolution is a major question of modern astrophysics.

An important observational tool for understanding the population of AGN is to resolve the X-ray background (XRB). Discovered by early X-ray rocket experiments (Giacconi et al.

1962), this seemingly diffuse, isotropic radiation with large energy density (from 0.5 to $\sim$ 300 keV), has since been shown to be primarily produced by the integrated emission from AGN, at least at low energies. However, a complete understanding of the X-ray background is far from realized; discovering the populations of AGN that can reproduce the XRB is important to ensure that a large population of sources is not missed. At energies above a few keV the X-ray-detected sources fail to reproduce the magnitude and spectral shape of the XRB. Much of the black-hole growth in the Universe is obscured by significant column densities of gas and dust, which makes detecting these sources challenging.

A complete, unbiased census of black-hole growth is thus of great interest. Much information about AGN populations has been gained from optical spectroscopic surveys (e.g., Richards et al. 2006) and soft X-ray surveys at $E \lesssim 2.4$ keV (e.g., Hasinger et al. 1998; Schmidt et al. 1998); however, these methods are highly susceptible to the effects of dusty, obscuring material, and leave many dust-shrouded sources unidentified. Recently the *Spitzer* Space Telescope has been surveying AGN in the mid-IR, detecting thermal emission from reprocessed AGN light, and constructing samples that include bright, highly obscured sources. *Spitzer* selection will be discussed in more detail in Chapter 6.

Through the XRB we know that the hard X-ray wave band is well suited for this census of black-hole growth through cosmic time. The *Chandra X-ray Observatory* (Weisskopf et al. 1996) provides a large collecting area, a large field of view (FOV), and exquisite angular resolution ($< 1''$) from 0.5 to 8 keV. These capabilities have allowed *Chandra* extragalactic surveys to efficiently select and optically identify large samples of AGN in the 2 – 8 keV range; observing in this hard X-ray energy band means that even sources shrouded by considerable ($\lesssim 10^{24}$ cm^{-2}) obscuring column densities can be detected at low redshift, and sources with even higher column densities can be detected at $z \approx 2$. Previous X-ray telescopes with comparable angular-imaging performance were only sensitive at energies below ~ 2 keV and thus missed many of the obscured AGN, a source population that has been long-theorized to explain the mismatch in spectral shapes between the 2 – 10 keV X-ray background ($\Gamma \approx 1.4$) and unobscured active galaxies ($\Gamma \approx 1.9$; Nandra & Pounds 1994).

Accreting massive black holes are observed over more than five orders of magnitude in luminosity, and exhibit a broad range of intrinsic X-ray absorption (from negligible levels to Compton-thick obscuration with $N_H \gtrsim 10^{24}$ cm^{-2}). Additionally, cosmic X-ray sources

undergo significant evolution between the current epoch and redshifts of $z \approx 3$. Measuring this enormous phase space requires broadband X-ray surveys extending from essentially the whole sky (to constrain the bright end) to the deepest surveys carried out with the most sensitive telescopes available over sky regions comparable to the telescope field of view.

Enormous progress has been made at the faintest end over the last five years with megasecond surveys performed by *Chandra* and *XMM-Newton* (see review by Brandt & Hasinger 2005). Together, these surveys have covered more than a thousand square arcminutes to depths of $f_{2-10\ \mathrm{keV}} \lesssim 10^{-15}\,\mathrm{erg\ cm^{-2}\ s^{-1}}$. These projects have resolved a significant fraction of the diffuse extragalactic X-ray background (at least in the lower half of the accessible energy band — Worsley et al. 2005). Spectroscopic optical followup has been successful in classifying and measuring redshifts for a large fraction (over half) of the resolved sources.

Also very important in covering the interesting phase space are surveys with depths of $f_{2-10\ \mathrm{keV}} \sim 10^{-14} - 10^{-15}\ \mathrm{erg\ cm^{-2}\ s^{-1}}$ and with large areas. The slope of the extragalactic X-ray $\log N - \log S$ relation breaks at $f_{2-10\ \mathrm{keV}} = 1 - 2 \times 10^{-14}\,\mathrm{erg\ cm^{-2}\ s^{-1}}$ (Cowie et al. 2002; Harrison et al. 2003), so that sources in this flux range dominate the integrated light from accretion. In this brightness range, source densities on the sky are a few hundred per square degree, requiring surveys covering on the order of a square degree or more to obtain statistically useful samples for the study of source properties and the evolution of the population.

The subject of the first part of this thesis is the Serendipitous Extragalactic X-ray Source Identification (SEXSI) program, a survey using *Chandra* fields specifically selected to obtain a significant sample of spectroscopically identified objects in the flux range from a few times 10^{-13} to $10^{-15}\,\mathrm{erg\ cm^{-2}\ s^{-1}}$. To accomplish this, SEXSI covers more than 2 deg^2 of sky and employs optical photometric and spectroscopic followup of sources discoverd in archival *Chandra* guaranteed-time-observer (GTO) and general-observer (GO) fields. The resulting source sample consists of 1034 hard X-ray-selected sources with R-band optical-followup imaging, and optical spectroscopy for 477 of the sources, filling the gap between wide-area, shallow surveys (e.g., HELLAS – La Franca et al. 2002; ASCA Large Sky Survey – Akiyama et al. 2000; ASCA Medium Sensitivity Survey – Akiyama et al. 2003) and the deep, pencil-beam surveys (e.g., CDF-N – Alexander et al. 2003; Barger et al. 2003; CDF-S – Rosati et al. 2002; Szokoly et al. 2004).

Chapter 2 gives a more detailed introduction to the SEXSI survey, putting SEXSI into the context of both astronomical studies and the capabilities of X-ray telescopes.

1.2 Detector Technologies for Future X-ray Surveys

Many square degrees of sky have been surveyed with the current generation *Chandra* and *XMM-Newton* X-ray telescopes, studying the intermediate-redshift $0.5-10$ keV X-ray Universe with unprecedented depths. However, these are (CCD-grade) low spectral resolution surveys with limited X-ray photon counts. There is great scientific potential if these surveys can extend a decade in sensitivity and sample tens of square degrees with a factor of ~ 30 improvement in X-ray spectroscopic resolution. For example, large-FOV imagers with high spectral resolution will enable unprecedented studies of suppermassive black hole growth and evolution over cosmic time through X-ray surveys of active galactic nuclei. These next-generation AGN surveys will provide high quality spectra of sources that are faint detections in current X-ray surveys. These faint sources, like many in the SEXSI survey, have only a handful of counts in the *Chandra* images, and thus we gain little spectral information about the sources beyond rough spectral-shape estimates from broad band hardness ratios. High quality spectra of each source in the SEXSI survey would dramatically increase the scientific value of the survey—providing these data is one goal for future X-ray missions.

There has already been a large investment and tremendous progress in developing sensitive, nondispersive imaging spectrometers for X-ray astrophysics in the form of transition-edge-sensor (TES)-based microcalorimeters. While excellent spectral resolution has been realized, current microcalorimeters will prove extremely difficult to build into large arrays. The most pressing technical challenge in the field lies in achieving large arrays of these devices to enable the field of views necessary for future X-ray astrophysics missions.

A significant effort is underway to push current X-ray microcalorimeter arrays toward 1000-pixel arrays, as required for the proposed $2.5' \times 2.5'$-FOV of *Constellation-X,* for example. For future spectroscopic survey applications that require a truly large FOV, such as *Generation-X,* the next wide-FOV X-ray survey mission, using current schemes to achieve larger pixel count will not be practical. Heat load requirements alone will limit the size of arrays to a few thousand pixels. To increase the pixel count to the 100×100 level and eventually 1000×1000 level, a leap in technology is required. While several groups are

pursuing advanced multiplexing technologies for TES-based microcalorimeters in efforts to overcome current pixel-count limitations, we are pursuing an altogether different detector technology: microwave kinetic inductance detectors (MKIDs).

MKIDs are an exciting new superconducting detector technology that has breakthrough potential for providing megapixel imagers with excellent energy resolution. These detectors utilize simple, thin-film lithographed microwave resonators as photon detectors in a multiplexed readout approach (Day et al. 2003). X-ray absorption in a superconductor creates quasiparticle excitations, with number proportional to the X-ray energy. The surface impedance of a superconductor changes with the quasiparticle density, and if operated at $T \ll T_c$ where the quasiparticle generation-recombination noise is low, extremely small changes in the kinetic inductance can be measured using a thin-film resonant circuit and microwave readout techniques. This provides a sensitive detector with excellent energy resolution. The frequency-domain multiplexing scheme for these detectors is simple yet powerful: by coupling multiple resonators to a single transmission line, thousands of pixels can be simultaneously monitored with only a couple of coaxial cables fed to the cryostat. Unlike other cryogenic detectors which require complicated wiring for each pixel at low temperature, MKIDs are easily multiplexed to large arrays. This is a key advantage over other cryogenic detectors.

Although MKIDs are in an early stage of development, they hold promise to revolutionize observations from the submillimeter to X-ray, and even dark matter (WIMP) detection. A first step is to demonstrate a strip detector—a design architecture that enables efficient coupling of photon energy to the MKID for optical, UV, and X-ray applications. This approach employs a long strip of superconducting material as the photon absorber with MKIDs attached at either end as quasiparticle sensors, allowing not only high absorption efficiency and precise energy determination, but large numbers of distributed pixels, as is required to meet next-generation mission design requirements. Experimental efforts leading to the first demonstration of a MKID-based strip detector are detailed in the second part of this thesis.

1.3 Thesis Organization

The first part of this thesis, found in Chapters 2 – 6, details the background, design, datasets, analysis, and survey synthesis of the SEXSI program. The second part, contained in Chapters 7 – 12, relates to the superconducting detector development effort that focuses on MKIDs-based strip detectors for future large-FOV X-ray astrophysics missions. Specifically, the chapters of this thesis are summarized as follows.

1.3.1 Part 1: SEXSI-Focused Chapters

Introductions to active galactic nuclei, the X-ray background, and relevant X-ray surveys are presented in Chapter 2, along with an overview of the specific observatories and instruments used in the SEXSI program. The following three chapters address the core datasets and analysis of the SEXSI survey, including the X-ray, optical imaging, and optical spectroscopic data and analyses, respectively. These chapters are taken verbatim from our series of published journal articles: Harrison et al. (2003), Eckart et al. (2005), and Eckart et al. (2006). Chapter 3 presents the X-ray observations and data analysis techniques and the resulting 2 – 10 keV source catalog. A sample page of the X-ray catalog is presented in this chapter, with the full catalog available in the online version of the *Astrophysical Journal* The 2 – 10 keV $\log N - \log S$ and other general characteristics of the X-ray sample are presented in this chapter. The R-band optical imaging of the SEXSI *Chandra* fields is presented in Chapter 4 as is the methodology used to derive X-ray counterpart source identifications and a catalog of R-band counterpart magnitudes. The online edition of the published journal article carries the full source catalog and a full sample of 'postage-stamp' images for each SEXSI source; examples of these materials are presented in this chapter. In addition, Chapter 4 explores the relationship between the X-ray flux, hardness ratio, and R-band magnitude. The final chapter in the three-part core of the SEXSI program is presented in Chapter 5. The most extensive of the SEXSI sections, this chapter presents the optical-spectroscopic followup sample: because these data allow the determination of spectroscopic redshifts and source classifications they are key to many of the project goals and facilitate the main SEXSI survey synthesis. We present the methodology for determining source redshifts and classifications as well as the full catalog of $\sim$ 500 spectroscopic followup obserservations of the SEXSI optical counterparts. The statistical characteristics of each

source-class population are presented, as are the global characteristics of the sample and a comparison to other surveys. A discussion of the issues of sample completeness and selection effects is included in this chapter. Also, the final section (§5.11) provides a discussion of spectroscopically identified AGN associated with target galaxy clusters in our sample. Followup of the cluster members was not a primary science goal for the SEXSI program, but because many of the targets of the *Chandra* GO observations that comprise the SEXSI fields include high-redshift galaxy clusters our spectroscopic followup of X-ray sources includes $\sim$ 17 sources associated with clusters, a relatively large sample of spectroscopically confirmed cluster-member AGN, as compared to the previously publised work on this topic. The final SEXSI-focused chapter (Chapter 6) concludes the series and highlights future work. We present preliminary analyses of mid-infrared data for six of the SEXSI fields, highlighting the powerful synergistic approach of studying AGN radiation using both *Chandra* and the *Spitzer Space Telescope* and motivating future research goals.

1.3.2 Part 2: MKIDs-Focused Chapters

Chapter 7 presents an introduction to low-temperature detectors with a focus on current non-dispersive imaging spectrometers that have X-ray astrophysics applications. We discuss the science goals that motivate proposed next-generation mission requirements as well as the major technical challenges faced in the development of large-FOV cryogenic detectors that are needed to meet these goals. We introduce the basic operational principles of MKIDs in Chapter 8. We also present the strip-detector architecture concept and the corresponding theoretical considerations, and a discussion of strip-detector materials and design choices. Chapter 9 documents the strip-detector testing setup and device fabrication. This chapter includes a brief introduction to dilution refrigerators, with more detail provided in Appendix A, as well as an explaination of the upgrades we have completed to our dilution-refrigerator testbed during my tenure. Chapter 9 also covers the readout electronics. Finally, Chapter 9 ends with an introduction to the fabrication techniques for MKIDs with a focus on the fabrication of strip detectors, including a summary of the mask sets and fabrication runs that are important to the work presented in Chapters 10 and 11. Chapter 10 details the series of fabrication and testing cycles that allowed us to shift from working *resonators* to working *strip detectors*, where quasiparticles created by X-ray absorption can easily diffuse from the absorbing element to the sensing element. The analysis techniques and results of

the 'working' strip detectors are presented in Chapter 11. Chapter 12 presents a conclusion of our MKIDs strip detector work and highlights areas for future improvements.

Part I

The Serendipitous Extragalactic X-ray Source Identification Program

Chapter 2

Introduction to the SEXSI Program

2.1 The Extragalactic X-Ray Background

The cosmic X-ray background (XRB), discovered over forty years ago by X-ray instruments aboard a rocket experiment (Giacconi et al. 1962), has been the topic of intense study for the past decades, reinvigorated with the launch of each X-ray astrophysics mission. The observations of this isotropic background with large energy density led researchers to posit that the origin of the background was extragalactic. Figure 2.1 shows the spectrum of the XRB from $\sim$ 3 to 300 keV measured primarily by instruments aboard the *High Energy Astronomical Observatory 1 (HEAO 1;* Gruber et al. 1999).

2.1.1 The Shape of the XRB

The total diffuse XRB photon spectrum in Figure 2.1 shows that the peak of the curve is at $\sim$ 30 keV with most of the energy density emitted from 20 to 40 keV. The intensity spectrum (Figure 3 of Gruber et al. 1999) is well fit by a simple exponential at energies of 3– $\sim$ 60 keV and three summed power-law functions above 60 keV (e.g., Gruber et al. 1999):

$$3-60 \text{ keV}: \ 7.877 \left(\frac{E}{\text{keV}}\right)^{-0.29} \exp\left(-\frac{E}{41.13 \text{ keV}}\right) \frac{\text{keV}}{\text{keV cm}^2 \text{ s sr}}, \qquad (2.1)$$

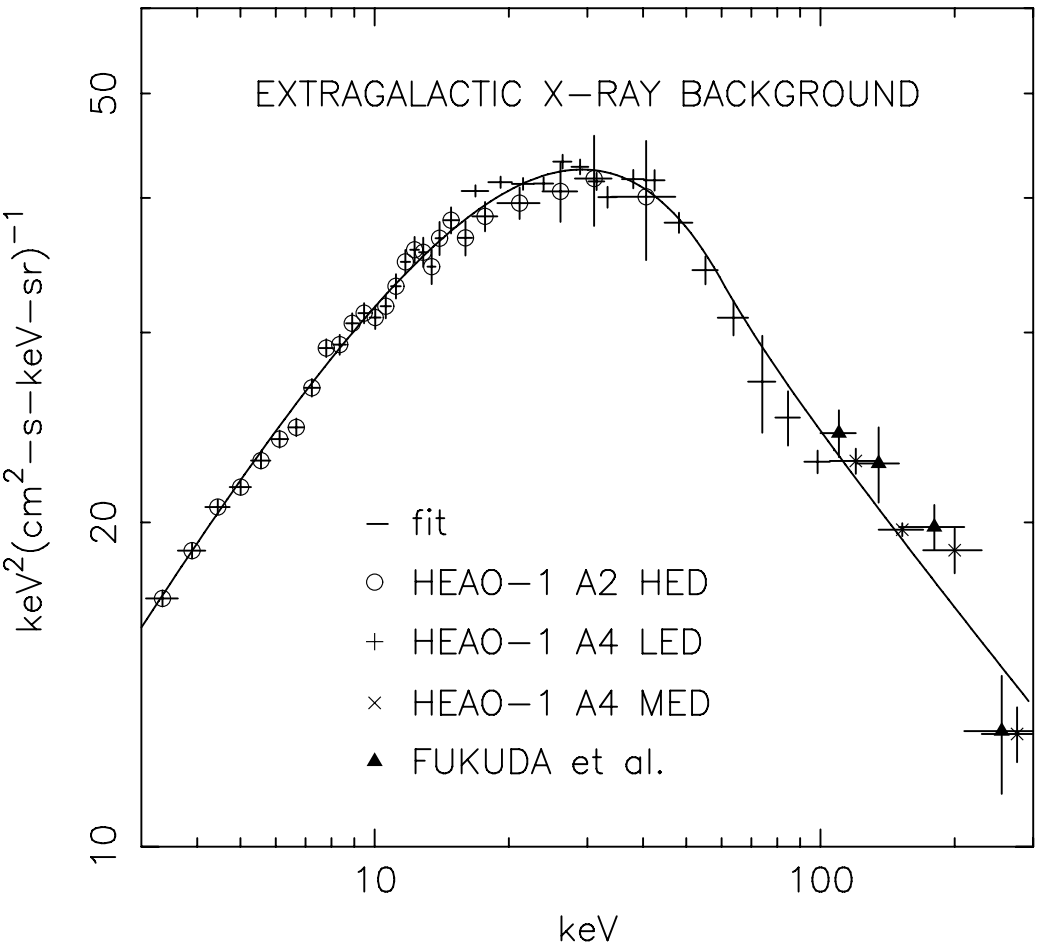

Figure 2.1 This plot, from Gruber et al. (1999) illustrates the photon spectrum of the diffuse isotropic component of the extragalactic X-ray background. The data was taken with several detectors on *HEAO 1*

$$> 60 \text{ keV}: \ 0.0259 \left(\frac{E}{60 \text{ keV}}\right)^{-5.5} + 0.504 \left(\frac{E}{60 \text{ keV}}\right)^{-1.58} + 0.0288 \left(\frac{E}{60 \text{ keV}}\right)^{-1.05} \frac{\text{keV}}{\text{keV cm}^2 \text{ s sr}}. \quad (2.2)$$

The XRB spectrum in the 2 – 10 keV range is well described by a simple power law spectrum with photon index Γ of 1.4: $N(E) \propto E^{-1.4}$. About 20 percent of the total energy of the X-ray background is emitted from $\sim 3 - 10$ keV, whereas, at energies below 3 keV only a few percent of the extragalactic XRB energy is emitted.

The XRB spectrum from ~ 3 to 45 keV is well matched to the spectrum of $T \sim 40$ keV thermal bremsstrahlung radiation, or radiation due to free-free interactions. This led some researchers in the late 1970ss and 1980s to suggest that the cosmic X-ray background was produced by thermal bremsstrahlung radiation from an exploding galaxy-heated hot smooth intergalactic medium (IGM) (e.g., Field & Perrenod 1977; Guilbert & Fabian 1986; Taylor & Wright 1989). This suggestion was ruled out by the subsequent measurements of the cosmic microwave background (CMB) radiation by the *Cosmic Background Explorer (COBE)* satellite (Mather et al. 1990). The *COBE* analysis showed that the CMB-spectrum intensity deviates less that 1 percent from a perfect blackbody spectrum with $T = 2.735 \pm 0.006$ K, while an IGM-produced XRB would cause a distortion of the CMB away from a pure blackbody spectrum due to Compton scattering of the CMB photons off of the hot, dense IGM. Mather et al. (1990) found that the XRB would be constrained to a magnitude of less than 1/36 of its observed value if produced by the IGM. Researchers have dubbed the XRB's similarity to a ~ 40 keV bremsstrahlung spectrum a 'cosmic conspiracy.'

2.1.2 Resolving the XRB

It is now clear that this "diffuse" background is, in fact, largely produced by the integrated light from many discrete sources. The constituent sources are primarily active galactic nuclei: galaxies with central supermassive black holes that are undergoing active accretion.

Several missions from 1978 to 1999 imaged the low-energy (< 3.5 keV) X-ray sky with increasing sensitivity and angular resolution. These observatories included the *Einstein Observatory, EXOSAT,* and *ROSAT* Results from deep surveys performed by *ROSAT*, a mission with $3''$ angular-imaging performance at $E \lesssim 2.5$ keV, found that 70%−80% of

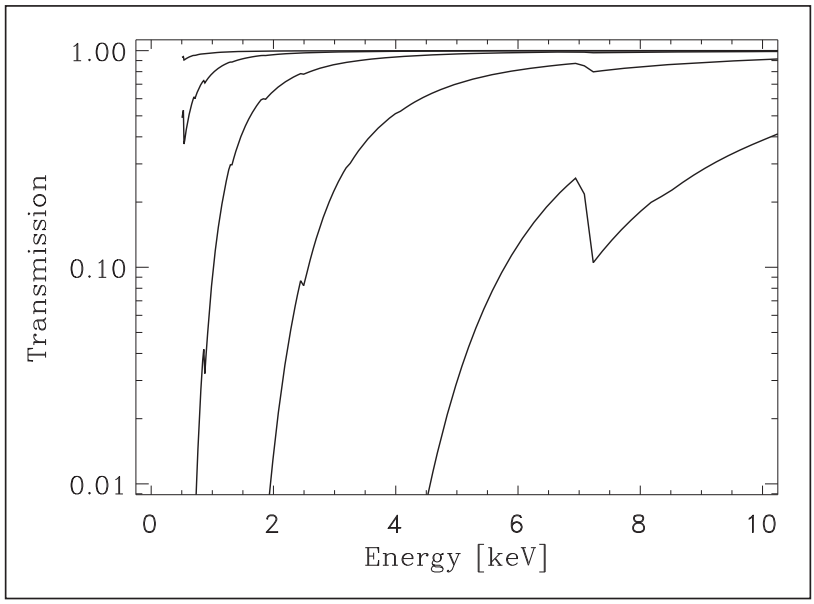

Figure 2.2 Transmission as a function of incident X-ray energy through column densities of 10^{20}, 10^{21}, 10^{22}, 10^{23}, and 10^{24} cm^{-2} (increasing column density from left to right). At column densities above $\sim 5 \times 10^{23}$ cm^{-2} there is little transmission at energies below 7 keV

the 0.5 – 2 keV background can be resolved into discrete sources (Hasinger et al. 1998). Corresponding optical identifications were also performed, revealing that the majority of the extragalactic sources were unobscured quasars and Seyfert galaxies (Schmidt et al. 1998).

Although these detected sources resolved a large fraction of the low-energy background, the spectrum of these sources, if extrapolated to higher energies, does not match the shape of the X-ray background. Typical unobscured AGN have power-law spectral indices of ~ 1.9 (Nandra & Pounds 1994), while the spectrum of the X-ray background from 2 to 10 keV is fit with $\Gamma = 1.4$, a much flatter slope. This spectral mismatch was explained by invoking a large population of obscured active galaxies.

Photoelectric absorption by dusty material either in the galaxy or surrounding the nucleus of an active galaxy will absorb incident X-rays, preferentially so at low energies. Figure 2.2 provides an illustration of the transmission of X-rays through column densities ranging from $N_H = 10^{20}$ cm^{-2} to $N_H = 10^{24}$ cm^{-2}. For the lowest column density the transmission is nearly unity throughout the entire range (0.5 – 10 keV); as the column density increases the low energy photons are not able to penetrate the material. An active galaxy with intrinsic power-law index Γ of 1.9 but surrounded by obscuring material along the line of sight will appear to have a lower power-law index (if still fit with a single power law).

In the unified model (e.g., Antonucci 1993), the central engine of each active galaxy is surrounded by a torus of obscuring material. Thus, the same object viewed from different angles will present different observational properties depending on what fraction of the torus column is within the observer's line of sight. In unified-model terms, type-1 AGN (including type-1 quasars and type-1 Seyfert galaxies) are AGN viewed face on, with an unobscured view to the central engine, while type-2 AGN are viewed edge on, such that the soft X-ray emission and doppler-broadened optical emission lines are extinguished. The development of this model was strongly motivated by polarization observations of nearby type-2 Seyfert galaxies (Antonucci 1982; Antonucci & Miller 1985). While the optical spectra of the galaxies were devoid of broad, permitted emission lines, the polarized-light spectra showed these broad lines at equivalent widths typical of type-1 AGN, implying that a hidden Seyfert 1 nucleus was reflecting light into the line of sight (Antonucci & Miller 1985). An example of a nearby active galaxy with the theorized torus-like obscuring material was studied by Jaffe et al. (1993). The authors imaged the nucleus of the galaxy with the *Hubble Space Telescope* (HST). The image showed an unresolved point source, attributed to a hot, inner accretion disk which is feeding the central SMBH, surrounded by a cooler outer accretion disk (torus) extending $\sim$ 100 pc from the point source — this observation was another striking piece of evidence for an extended dusty torus as hypothesized in the unified model.

It is this absorptive effect that was invoked when reconciling the results of the *ROSAT* survey with the shape of the 2 – 10 keV XRB. For example, Comastri et al. (1995) models the XRB over a broad range, from a few keV to $\sim$ 100 keV, by employing a large population of obscured AGN at various redshifts with intrinsic absorbing column densities ranging from 10^{21} cm^{-2} to 10^{25} cm^{-2}. The Comastri et al. (1995) model is consistent with the fraction of the soft-band XRB resolved by *ROSAT*, reproduces the $E \gtrsim 30$ keV decline in the XRB (assuming that each individual AGN has a spectral break above 70 keV), and is consistent with the luminosity function of optically selected AGN (Boyle et al. 1993).

While the model of Comastri et al. (1995) and other similar models are able to reproduce the XRB by combining the emission of populations of obscured and unobscured AGN, the existence of this large population of obscured sources that rivals or outnumbers the unobscured sources was speculative. The missing observational tool was a high-spatial-resolution X-ray telescope with survey capabilities and sensitivity to the obscured sources. In the X-ray, this requires extending surveys above $E \simeq 2$ keV. It was not until 1999 that

capabilities at 2 – 10 keV rivaled the good angular-resolution of *ROSAT*.

2.1.3 The Advanced Satellite for Cosmology and Astrophysics (ASCA)

The Advanced Satellite for Cosmology and Astrophysics (*ASCA*) was the first X-ray astronomy mission to combine imaging capability and a large effective area with a band pass that extended to higher energies ($\sim$ 10 keV). However, the $\sim$ 3 arcminute half-power diameter (HPD) made secure optical-counterpart identifications challenging or impossible for all but the brightest sources. Sources with faint optical counterparts are difficult to identify at all since there can be of order tens or hundreds of optical sources within the error circle of the X-ray source position. For example, Figure 2.3 displays an R-band image near the position where a 2 – 10 keV source was detected by both *Chandra* and *ASCA*. Optical-counterpart search areas typical of *ASCA* (0.5′) and *Chandra* (1.5″) are overlaid in black and red, respectively. To securely identify an optical counterpart to a faint ASCA AGN candidate, one must take optical spectra of many of the sources that lie within the X-ray error circle and then determine the correct counterpart based upon the optical spectral features. Not only is this inefficient, it also requires a reliance on assumptions of what AGN optical-counterpart spectral features should be (see further discussion of this in §5.10).

2.2 A New Era in X-ray Astrophysics

The 1999 launch of the *Chandra X-Ray Observatory* (Weisskopf et al. 1996) opened a new era in X-ray astronomy. *Chandra's* unprecedented angular resolution and sensitivity at energies above 2 keV allows surveys of 2 – 10 keV X-ray sources at depths approaching studies in other wave bands such as the optical, infrared, etc. The subarcsecond imaging capabilities provide the possibility of identifying optical counterparts to these faint X-ray sources with ease. While previous missions such as *ASCA* performed surveys at similar energies, the surveys were of much brighter sources and the optical identifications were challenging (sometimes prohibitively so).

XMM-Newton (Jansen et al. 2001), another powerful X-ray satellite, was also launched in 1999. This telescope has a larger collecting area and better sensitivity at high energies ($\gtrsim$ 10 keV) than *Chandra*, but poorer imaging performance: the *XMM-Newton* angular resolution is of order 6″ FWHM. While *XMM-Newton* has advantages over *Chandra*, par-

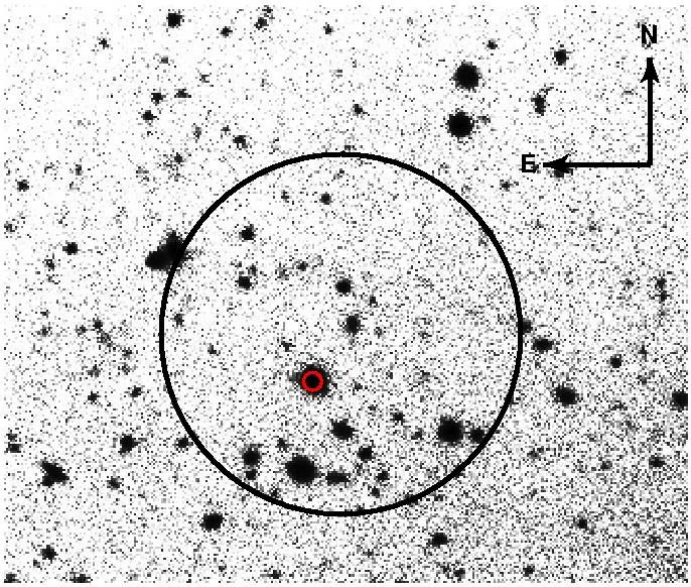

Figure 2.3 R-band optical image of CXOSEXSI_J084905.0+445714 (Eckart et al. 2005), an X-ray source detected in the SEXSI survey by *Chandra*. The source was previously detected by *ASCA*, and is reported as Source 9 in Ohta et al. (2003). The $0.5'$ error circle used by Ohta et al. (2003) is drawn in black, centered at the position of the *ASCA* source. The $1.5''$ SEXSI search area centered at the *Chandra* 2 – 10 keV source position (corrected for average X-ray-to-optical pointing error) is shown in red, clearly indicating the correct $R = 19.5$ optical counterpart. Ohta et al. (2003) determined the same optical counterpart to the *ASCA* source, but only after obtaining spectra of many of the optical sources within the *ASCA* search area. For sources that do not show obvious AGN signatures in the optical the *ASCA* identification would have been further hindered

ticularly for spectroscopic applications, for imaging surveys there are obvious advantages to using a telescope such as *Chandra* with sub-arcsecond angular resolution. For the work detailed in this thesis we have employed only *Chandra*, so we restrict our discussion in this introduction accordingly.

2.2.1 The *Chandra* Telescope Design

Chandra, the third mission to be launched by NASA's Great Observatories program, has sub-arcsecond angular imaging performance made possible by exquisite mirrors that rely on grazing-incidence total external reflection. At X-ray energies the vacuum refractive index is slightly higher than the refractive indices of materials, creating a condition for total external reflection.

The *Chandra* mirrors are composed of four pairs of thin-walled, grazing incidence Wolter Type-I mirrors with 33 nm iridium (Ir) coating. Each mirror pair consists of a 0.85 meter-long parabolic-shaped mirror and a similarly 0.85 m-long hyperbolic-shaped mirror. The four pairs have outerdiameters between 0.65 m and 1.23 m and are concentrically nested. The *Chandra* focal length is 10 m, providing a 49 μm arcsec^{-1} plate scale. Surveying the Universe to higher energies was a primary science goal for *Chandra* so mission design requirements specified a large field of view combined with a large effective area. The effective area of the telescope optics for both imaging detector arrays are shown in Figure 2.4.

2.2.1.1 The Advanced CCD Imaging Spectrometer (ACIS)

The imaging detector aboard *Chandra* is the Advanced CCD Imaging Spectrometer (ACIS; Bautz et al. 1998). The camera consists of ten 1024×1024–pixel CCDs, each subtending $8.4' \times 8.4'$. Figure 2.5 provides a detailed diagram of the ACIS flight focal plane. Four of the CCDs (chips 0–3) are arranged in a square; these are called the ACIS-I array. When the ACIS-I array is in use the optical axis is on chip 3 and the FOV of is $16.9' \times 16.9'$. The other six CCDs are arranged linearly and make up the ACIS-S array, so-called because it is this array that serves as the grating readout for spectroscopic observations with the High-Energy Transmission Grating (HETG, Canizares et al. 2005). The ACIS-S array can also be used for imaging observations, which can be desirable owing to the increased low-energy quantum efficiency provided by the inclusion of backilluminated chips (#s 5 and 7). The on-axis aimpoint for ACIS-S imaging observations is chip 7. When imaging in either ACIS-

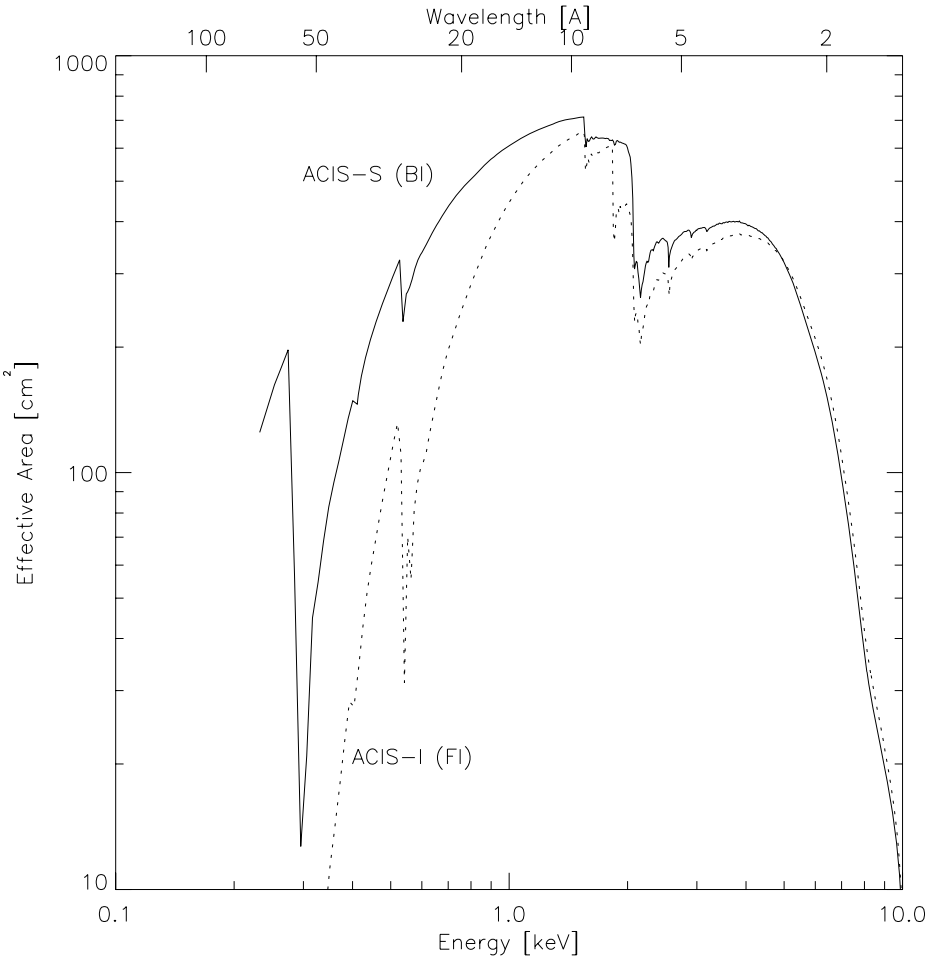

Figure 2.4 The effective area of *Chandra* using the front-illuminated (FI) ACIS-I chips and the back-illuminated (BI) ACIS-S array. The telescope has unprecedented sensitivity to high energy X-rays. The dip in effective area at $E \sim 2.1$ keV is due to the Ir M-edge of the thin Ir that coats each mirror. Credit: *Chandra* Science Center

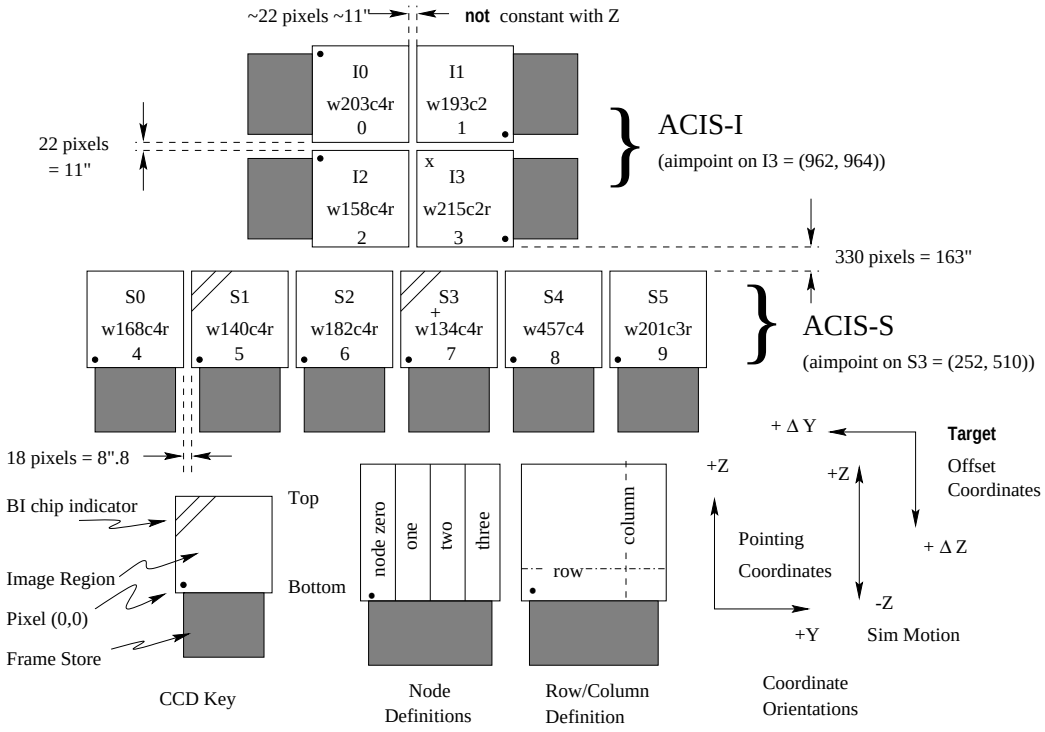

Figure 2.5 The focal plane of the CCD chips that combine to form the ACIS-I and ACIS-S arrays. SEXSI uses pointings from both configurations; our naming convention (e.g., see Table 3.2) uses the numbering system marked at the bottom of each chip, with 'I' or 'S' prepended to indicate the location of the aimpoint. Diagram credit: *Chandra* Science Center

I or ACIS-S mode a couple of off-axis chips are also illuminated (the PSF is considerably larger). For example, in the ACIS-I configuration chips 6 and 7 from the ACIS-S array also provide imaging information, extending the FOV beyond the central $16.9' \times 16.9'$.

The ACIS CCDs act as photon counters, as opposed to, for example, optical CCDs that measure the integrated flux that has been detected. With the ACIS detectors, each individual photon is time and energy stamped upon arrival. The energy resolution of the ACIS CCDs is ~ 120 eV at 6 keV.

2.3 XRB Surveys with *Chandra*

The capabilities of *Chandra* described in the last section (plus those of *XMM-Newton*), have opened new possibilities for studying active galaxies over a large range in redshifts, luminosities, and obscuring column densities. Accreting massive black holes are observed over more than five orders of magnitude in luminosity, and exhibit a broad range of intrinsic X-ray absorption (from negligible levels to Compton-thick obscuration with $N_H \gtrsim 10^{25}$ cm^{-2}). Additionally, cosmic X-ray sources undergo significant evolution between the current epoch and redshifts of $z \sim 3$. Measuring this enormous phase space requires broadband X-ray surveys extending from essentially the whole sky (to constrain the bright end) to the deepest surveys carried out with the most sensitive telescopes available over sky regions comparable to the telescope field of view.

Enormous progress has been made at the faintest end over the last five years with megasecond surveys performed by *Chandra* and *XMM-Newton* (see review by Brandt & Hasinger 2005). Together, these surveys have covered more than a thousand square arcminutes to depths of $f_{2-10\ \mathrm{keV}} \lesssim 10^{-15}$ erg cm^{-2} s^{-1}. These projects have resolved a significant fraction of the diffuse extragalactic X-ray background (at least in the lower half of the accessible energy band – Worsley et al. 2005). Spectroscopic optical followup has been successful in classifying and measuring redshifts for a large fraction (over half) of the resolved sources.

Also very important in covering the interesting phase space are surveys with depths $f_{2-10\ \mathrm{keV}} \sim 10^{-14} - 10^{-15}$ erg cm^{-2} s^{-1}. The slope of the extragalactic X-ray $\log N - \log S$ relation breaks at $f_{2-10\ \mathrm{keV}} = 1 - 2 \times 10^{-14}$ erg cm^{-2} s^{-1} (Cowie et al. 2002; Harrison et al. 2003), so that sources in this flux range dominate the integrated light from accretion.

In this brightness range, source densities on the sky are a few hundred per square degree, requiring surveys covering on the order of a square degree or more to obtain statistically useful samples for the study of source properties and the evolution of the population.

It is covering this part of the phase space that is the goal of the SEXSI survey. There are other groups with complementary surveys using both *Chandra* and *XMM-Newton* The details of many of these surveys are presented and compared to SEXSI throughout Chapters 3 – 5, and in particular in Sections 5.9.1 and 5.9.2.

2.4 The SEXSI Program

The *Serendipitous Extragalactic X-ray Source Identification (SEXSI)* program began shortly after the launch of *Chandra,* at first using GO and GTO fields with the permission of individual observing teams, and later relying on data available in the *Chandra* public archive. The survey is designed to obtain a significant sample of objects in the flux range from a few times 10^{-13} to 10^{-15} erg cm^{-2} s^{-1} and to optically identify the sources spectroscopically, using Palomar, MDM, and Keck Observatories. The details of the X-ray imaging program and survey sample are presented in the following chapter. Chapter 4 presents the optical imaging catalog and analysis; the observatories and instruments used for optical imaging follow-up are detailed in Section 4.2. Chapter 5 presents the results of the optical spectroscopic program and includes the main survey synthesis; Section 5.3 gives an overview of the observational facilities used for spectroscopy. The current push of the SEXSI project is to incorporate data from the *Spitzer Space Telescope*. Chapter 6 presents the background, observations, and preliminary results from combining six well-studied SEXSI fields with mid-infrared imaging.

Chapter 3

SEXSI X-Ray Analysis and Characteristics of the Hard X-Ray Sample[1]

The Serendipitous Extragalactic X-ray Source Identification (SEXSI) Program is designed to extend greatly the sample of identified extragalactic hard X-ray (2 – 10 keV) sources at intermediate fluxes ($\sim 10^{-13} - 10^{-15}$ erg cm^{-2} s^{-1}). SEXSI, which studies sources selected from more than 2 deg^2, provides an essential complement to the *Chandra* Deep Fields, which reach depths of 5×10^{-16} erg cm^{-2} s^{-1} (2 – 10 keV) but over a total area of < 0.2 deg^2. In this paper we describe the characteristics of the survey and our X-ray data analysis methodology. We present the cumulative flux distribution for the X-ray sample of 1034 hard sources, and discuss the distribution of spectral hardness ratios. Our $\log N - \log S$ in this intermediate flux range connects to those found in the deep fields, and by combining the data sets, we constrain the hard X-ray population over the flux range where the differential number counts change slope, and from which the bulk of the 2 – 10 keV X-ray background arises. We further investigate the $\log N - \log S$ distribution separately for soft and hard sources in our sample, finding that while a clear change in slope is seen for the softer sample, the hardest sources are well described by a single power law down to the faintest fluxes, consistent with the notion that they lie at lower average redshift.

[1]Much of this chapter has been previously published as Harrison et al. (2003)

3.1 Introduction

A primary scientific motivation for developing the *Chandra X-ray Observatory* was to perform surveys of the extragalactic sky up to 10 keV. The combination of *Chandra's* superb angular resolving power and high-energy response is enabling the detection and optical identification of hard X-ray source populations at much fainter fluxes than previously possible (Weisskopf et al. 1996). Exposure times of 1 Ms in each of two deep fields, the *Chandra* Deep Field-North (CDF-N; Brandt et al. 2001) and the *Chandra* Deep Field-South (CDF-S; Giacconi et al. 2002) reach depths of 5×10^{-16} erg cm^{-2} s^{-1} (2 – 10 keV), and have resolved most of the X-ray background up to 7 keV. Optical spectroscopic followup of a sample of the Deep-Field sources has revealed a diverse counterpart population (Rosati et al. 2002; Barger et al. 2002). Attention is now concentrated on understanding the physical nature of the counterparts, as well as their evolution over cosmic time.

Wider field-of-view surveys provide an essential complement to the Deep Fields – which in total cover < 0.2 deg^2 – particularly for this latter objective. Large-area coverage is essential for providing statistically significant source samples at intermediate to bright fluxes ($f_{2-10\ \mathrm{keV}} \sim 10^{-13} - 10^{-15}$ erg cm^{-2} s^{-1}). At the bright end of this flux range there are only ~ 20 sources deg^{-2}, so that several square degrees must be covered to obtain significant samples. Spectroscopic identification of a large fraction of these is necessary to sample broad redshift and luminosity ranges, and to determine space densities of seemingly rare populations such as high-redshift QSO IIs, which appear about once per 100 ksec *Chandra* field (Stern et al. 2002a).

Wide-field hard X-ray surveys undertaken with instruments prior to *Chandra* and *XMM-Newton* made preliminary investigations of the bright end of the hard source populations, although the positional accuracy achievable with these experiments was insufficient to securely identify a large number of counterparts. The *BeppoSAX* HELLAS survey (La Franca et al. 2002) identified 61 sources either spectroscopically or from existing catalogs in 62 deg^2 to a flux limit of $f_{2-10\ \mathrm{keV}} = 5.0 \times 10^{-14}$ erg cm^{-2} s^{-1}. The *ASCA* Large Sky Survey identified 31 extragalactic sources in 20 deg^2 (Akiyama et al. 2000), with the recent addition of 85 more spectroscopically identified sources from the *ASCA* Medium Sensitivity Survey (Akiyama et al. 2002) to a flux threshold of $f_{2-10\ \mathrm{keV}} = 1 \times 10^{-13}$ erg cm^{-2} s^{-1}.

Chandra and *XMM* offer the potential to expand significantly this initial work to hun-

dreds of sources detected over many square degrees. A number of programs are now underway to identify serendipitous sources in extragalactic pointings. Besides the *Chandra* Deep Fields, several other individual fields have been studied, and optical spectroscopic followup completed and reported. These include the Lynx cluster field (Stern et al. 2002b), the field surrounding Abell 370 (Barger et al. 2001a), and the Hawaii Survey Field (Barger et al. 2001b), each of which covers ~ 0.08 deg^2. Ambitious efforts to extend coverage to several deg^2 include the HELLAS2XMM survey (Baldi et al. 2002), and ChaMP (Hooper & ChaMP Collaboration 2002), although followup results from these surveys have not yet been published.

We present here the Serendipitous Extragalactic X-ray Source Identification (SEXSI) program, a new hard X-ray survey designed to fill the gap between wide-area, shallow surveys and the *Chandra* Deep Fields. The survey has accumulated data from 27 *Chandra* fields selected from GTO and GO observations, covering more than 2 deg^2. We have cataloged more than 1000 sources in the 2 – 10 keV band, have completed deep optical imaging over most of the survey area, and have obtained spectroscopic data on ~ 350 objects.

Table 3.1 summarizes the published 2 – 10 keV X-ray surveys and demonstrates the contribution of the SEXSI program. Tabulated flux values have been corrected to the energy band 2 – 10 keV and to the spectral assumptions adopted here (see §3.3.1), as detailed in the footnotes to the table. In the flux range 10^{-11} to 10^{-15} erg cm^{-2} s^{-1}, the seven existing surveys have discovered a total of 789 sources, several hundred fewer than the total presented here. In the flux range 10^{-13} to 3×10^{-15} erg cm^{-2} s^{-1} which lies between the *ASCA* and *BeppoSAX* sensitivity limits and the *Chandra* Deep Survey capability – where the $\log N - \log S$ relation changes slope and from which the bulk of the 2 – 10 keV X-ray background arises (Cowie et al. 2002) – we more than triple the number of known sources. Figure 3.1 illustrates our areal coverage in comparison with that of previous work, emphasizing how SEXSI complements previous surveys.

In this paper, we present the survey methodology and X-ray data analysis techniques adopted, the X-ray source catalog, and the general characteristics of the X-ray source sample. In companion papers (Eckart et al. 2005; Eckart et al. 2006), we provide summaries of our optical followup work, including a catalog of R magnitudes (and upper limits thereto) for over 1000 serendipitous X-rays sources as well as redshifts and spectral classifications for ~ 450 of these objects, and discuss the luminosity distribution, redshift distribution,

Table 3.1. Comparison of sources detected in 2 – 10 keV hard X-ray surveys

log Flux Range	PUBLISHED SURVEYS							SEXSI
	ASCA[a]	*SAX*[b]	SSA13[c]	CDF-N[d]	CDF-S[e]	Lynx[f]	TOTAL	
–14.5 – –15.0	0	0	8	106	92	49	255	55
–14.0 – –14.5	0	0	18	56	66	45	185	400
–13.5 – –14.0	0	0	6	23	21	12	62	399
–13.0 – –13.5	2	17	1	5	4	4	33	145
–12.5 – –13.0	51	89	0	1	0	1	142	24
–12.0 – –12.5	35	61	0	0	0	0	96	9
–11.5 – –12.0	5	9	0	0	0	0	14	2
–11.0 – –11.5	1	1	0	0	0	0	2	0
TOTALS	94	177	33	191	183	111	789	1034

[a]For each survey, we provide the primary reference(s), the satellite and X-ray instrument used, the spectral assumptions adopted, and the factor by which we multiplied the tabulated fluxes to bring them into conformity with the energy band and spectral parameters adopted in our study. For *ASCA*, see Cagnoni et al. (1998); GIS2-selected; $\Gamma = 1.7$, actual N_H ($N_H \sim 3 \times 10^{20}$ cm^{-2}); factor = $\times 1.06$. In addition, see Akiyama et al. (2000); SIS-selected; best PL model and $N_H (N_H \sim 3 \times 10^{20})$ from SIS + GIS fit; factor based on individual spectral indices ($= \times 0.52 - 1.36$)

[b]For *SAX*, see Giommi et al. (2000); MECS-selected; $\Gamma = 1.7$, actual $N_H (\sim 3 \times 10^{20}$ cm$^{-2})$; factor = $\times 0.959$

[c]For SSA13, see Mushotzky et al. (2000); ACIS-S-selected; $\Gamma = 1.2$, actual $N_H = 1.4 \times 10^{20}$ cm^{-2}; factor = $\times 0.986$ and, for chip 3 only, = $\times 0.948$

[d]For the CDF-N, see Brandt et al. (2001); ACIS-I-selected; hardness-ratio-derived spectral slopes, $N_H = 1.6 \times 10^{20}$ cm^{-2} *not* included; Cowie et al. (2002) claim the mean flux is increased by 13% from assuming $\Gamma = 1.2$, so factor = $\times 1.293$ (to get 2 – 10 keV intrinsic flux) $\times 0.885$ to get all sources to $\Gamma = 1.2$ $\times 0.9345$ to get $\Gamma = 1.5$, so final factor = $\times 1.069$

[e]For the CDF-S, see Giacconi et al. (2002); ACIS-I-selected; $\Gamma = 1.375, N_H = 0.8 \times 10^{20}$ cm^{-2}; factor = $\times 0.932$

[f]For the Lynx field, see Stern et al. (2002b); ACIS-I-selected; $\Gamma = 1.4, N_H = 2 \times 10^{20}$ cm^{-2}; factor = $\times 1.004$

Note. — Ueda et al. (2001) have recently published a catalog of 2 – 10 keV X-ray sources from the *ASCA* database that contains 1343 sources. Of these, 4 have a detection significance in the 2 – 10 keV band of $\gtrsim 3.0\sigma$ and 1×10^{-14} erg cm^{-2} s^{-1} $< f_{2-10\ \mathrm{keV}} < 3 \times 10^{-14}$ erg cm^{-2} s^{-1}, while 112 entries lie in the range 3×10^{-14} erg cm^{-2} s^{-1} $< f_{2-10\ \mathrm{keV}} < 1 \times 10^{-13}$ erg cm^{-2} s^{-1}. However, the effective area covered by this survey as a function of flux and the $\log N - \log S$ curves have not been presented, so we have not included these sources in the above table

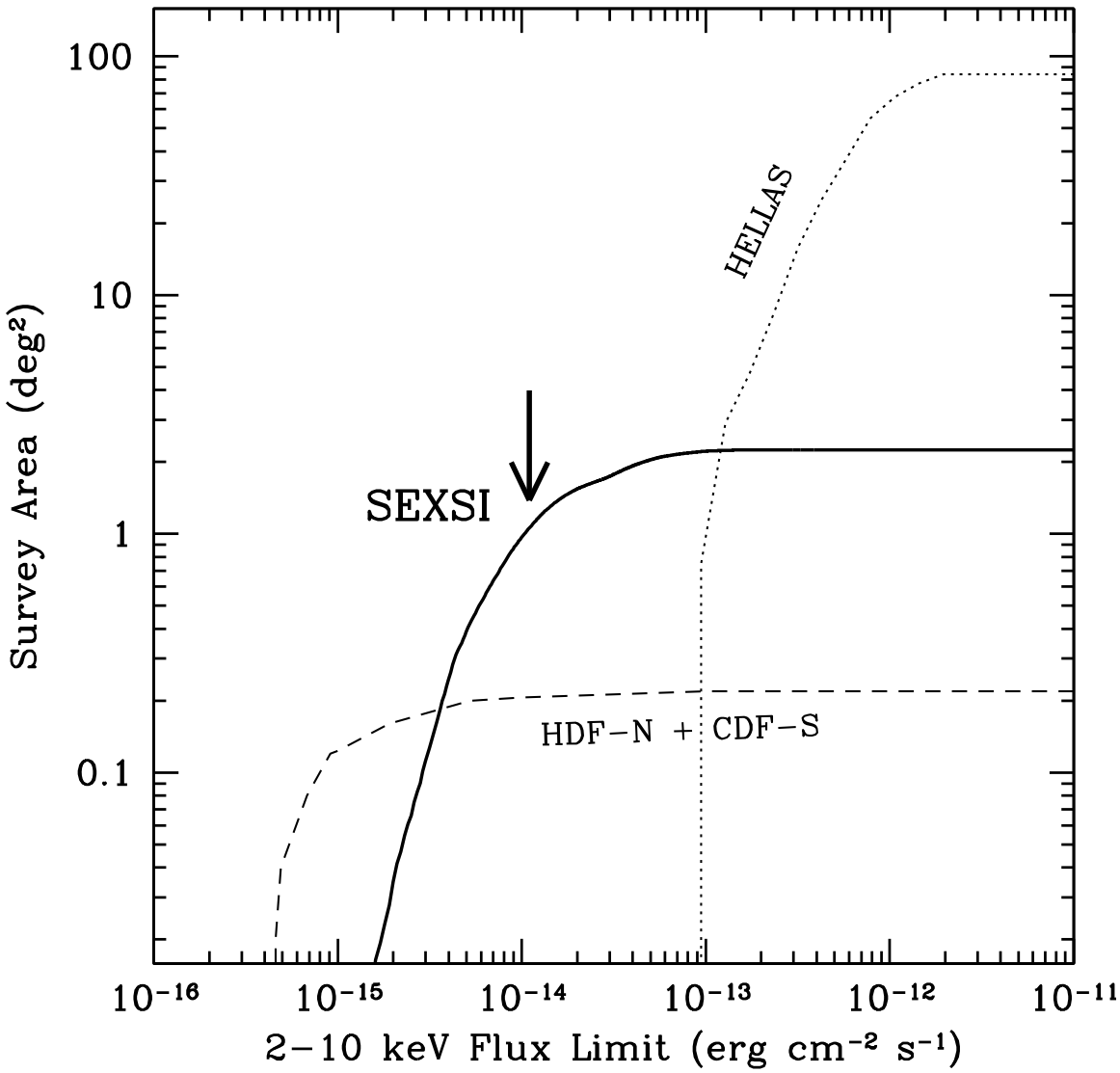

Figure 3.1 Area of sky surveyed as a function of hard (2 – 10 keV) X-ray flux for several hard X-ray surveys. SEXSI (solid line) samples the parameter space between the extremely deep, small area *Chandra* Ms surveys in the Hubble Deep Field-North (HDF-N; Brandt et al. 2001) and the Chandra Deep Field-South (CDF-S; Giacconi et al. 2002), and the shallow, wide-area *BeppoSAX* High Energy Large Area Survey (HELLAS; Fiore et al. 2001, – dotted line). Deep field coverage (dashed line) corresponds to the 1 Ms depths, combining both fields. HELLAS hard X-ray fluxes have been extrapolated from their published 5 – 10 keV depths to 2 – 10 keV by multiplying by a factor of 1.96, appropriate for the average $\alpha_E = 0.6$ they find in their survey. The large arrow indicates the break in the $\log N - \log S$ plot (Figure 3.6), corresponding to the flux level which dominates the hard X-ray source counts. The SEXSI survey is better suited to exploring this flux level than either the ultradeep Ms *Chandra* surveys or the shallow *BeppoSAX* HELLAS survey.

Table 3.2. *Chandra* observations of the 27 SEXSI fields

Target							
Name	Type	z or cz	RA (J2000)	DEC (J2000)	N_H [10^{20} cm^{-2}]	exp [ks]	ACIS chi
NGC 891	edge-on spiral	528 km s^{-1}	02 22 33	+42 20 57	6.7	51	S 235-8
AWM 7	galaxy cluster	0.017	02 54 28	+41 34 47	9.2	48	I:0-367
XRF 011130	X-ray flash afterglow	···	03 05 28	+03 49 59	9.3	30	I:0-3
NGC 1569	spiral galaxy	−104 km s^{-1}	04 30 49	+64 50 54	23.8	97	S:2357
3C 123	galaxy cluster	0.218	04 37 55	+29 40 14	19.0	47	S:235-8
CL 0442+2200	galaxy cluster	1.11	04 42 26	+02 00 07	9.5	44	I:0-3
CL 0848+4454	galaxy cluster	1.27	08 48 32	+44 53 56	2.8	186	I:0-367
RX J0910	galaxy cluster	1.11	09 10 39	+54 19 57	1.9	171	I:0-36
1156+295	blazar	0.729	11 59 32	+29 14 44	1.7	49	I:0-3
NGC 4244	edge-on spiral	244 km s^{-1}	12 17 30	+37 48 32	1.8	49	S:235-8
NGC 4631	edge-on disk galaxy	606 km s^{-1}	12 42 07	+32 32 30	1.2	59	S:235-8
HCG 62	compact group	4200 km s^{-1}	12 53 08	−09 13 27	2.9	49	S:6-8
RX J1317	galaxy cluster	0.805	13 17 12	+29 11 17	1.1	111	I:0-36
BD 1338	galaxy cluster	0.640	13 38 25	+29 31 05	1.1	38	I:0-36
RX J1350	galaxy cluster	0.804	13 50 55	+60 05 09	1.8	58	I:0-36
3C 295	galaxy cluster	0.46	14 11 20	+52 12 21	1.3	23	S:236-8
GRB 010222	GRB afterglow	1.477	14 52 12	+43 01 44	1.7	18	S:236-8
QSO 1508	quasar	4.301	15 09 58	+57 02 32	1.4	89	S:2367
MKW 3S	galaxy cluster	0.045	15 21 52	+07 42 32	2.9	57	I:0-368
MS 1621	galaxy cluster	0.4281	16 23 36	+26 33 50	3.6	30	I:0-36
GRB 000926	GRB afterglow	2.038	17 04 10	+51 47 11	2.7	32	S:236-8
RX J1716	galaxy cluster	0.81	17 16 52	+67 08 31	3.8	52	I:0-36
NGC 6543	planetary nebula	0	17 58 29	+66 38 29	4.3	46	S:5-9
XRF 011030	X-ray flash afterglow	···	20 43 32	+77 16 43	9.5	47	S:2367
MS 2053	galaxy cluster	0.583	20 56 22	−04 37 44	5.0	44	I:0-36
RX J2247	galaxy cluster	0.18	22 47 29	+03 37 13	5.0	49	I:0-36
Q2345	quasar pair	2.15	23 48 20	+00 57 21	3.6	74	S:2678
TOTAL						1648	134

and composition of the sample. Future papers will address detailed analyses of the different source populations as well as field-to-field variations.

3.2 Selection of *Chandra* Fields

We selected fields with high Galactic latitude ($|b| > 20°$) and with declinations accessible to the optical facilities available to us ($\delta > -20°$). We use observations taken with the Advanced Camera for Imaging Spectroscopy (ACIS I- and S-modes; Bautz et al. 1998) only (for sensitivity in the hard band). All the fields presented in this paper have data which are currently in the *Chandra* public archive, although in many cases we made arrangements with the target PI for advanced access in order to begin spectroscopic observations prior to public release of the data. Table 3.2 lists the 27 survey fields by target, and includes the target type and redshift if known, the coordinates of the field center, the Galactic neutral hydrogen column density in this direction (Dickey & Lockman 1990), the X-ray exposure time, and the ACIS chips reduced and included in this work. The observations included in our survey represent a total of 1.65 Msec of on-source integration time and include data from 134 $8' \times 8'$ ACIS chips.

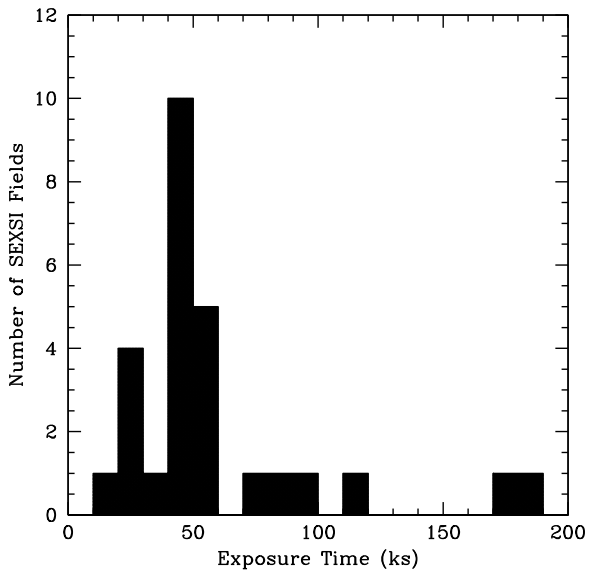

Figure 3.2 Histogram of exposure times for the 27 *Chandra* fields listed in Table 3.2.

Net exposure times range from 18 ks to 186 ks; a histogram of exposure times is given in Figure 3.2. Targets include a Galactic planetary nebula, various types of AGN, transient afterglow followup observations, NGC galaxies, and clusters of galaxies, particularly those at relatively high redshifts. For the cases in which the target is an extended X-ray source, we have taken care to exclude those sources potentially associated with the target from our $\log N - \log S$ analysis (see §3.3.2).

3.3 Data Reduction and Analysis

3.3.1 Basic X-ray Reduction

The X-ray data reduction includes filtering raw event data to reject contaminating particle events, binning the event data into images with specific energy ranges, searching the images for sources, and extracting source fluxes.

For the initial processing steps, through source identification, we use standard tools supplied by the *Chandra X-ray Observatory* Science Center (CXC). We employ *ASCA* event grades 0, 2, 3, 4, 6, and we eliminate flickering pixels and events at the chip node boundaries. For each chip we bin events into soft- (0.3 – 2.1 keV) and hard- (2.1 – 7 keV) band images. The 2.1 keV energy boundary is chosen to coincide with the abrupt mirror reflectance change caused by the Ir M-shell edge, and the upper and lower limits optimize signal to noise in

the images. We use `wavdetect` for initial source identification. In a subsequent step we test the significance of each source individually and eliminate sources with a nominal chance occurrence probability greater than 10^{-6}.

For the remainder of the processing, we use primarily our own routines to filter the `wavdetect` source list to reject spurious detections, to extract source fluxes, and to correct `wavdetect` positions when required. In some cases, particularly at large off-axis angles where the point spread function (PSF) is relatively broad, the `wavdetect` positions become unreliable, with some positions differing significantly from the centroid of the photon distribution. The differences are not uniformly distributed, and most are within the expected statistical tolerance. However, in typically one or two cases per field the `wavdetect` position will differ unacceptably, a discrepancy that has also been noted by others (Brandt et al. 2001). We use the `wavdetect` positions, the standard used by most other authors, unless the PSF-normalized radial shift $\Delta r^2/\mathrm{PSF} > 0.8$ arcsec, in which case we use the centroid position.

After correcting source positions, we extract photons from the image to determine source fluxes. The PSF width is a strong function of off-axis angle. To determine extraction radii, we use the encircled energy fractions tabulated by the CXC at eight off-axis angles and at five different energies. We use the 1.5 keV and 4.5 keV values for the soft and hard bands, respectively, and interpolate linearly between tabulated values in off-axis angle. For the extraction radius we use an encircled energy fraction ranging from 80% – 90%, depending on the band and off-axis angle (see Table 3.3). This optimizes the signal-to-noise ratio, since the optimal fraction depends on signal-to-background ratio. To determine the background level for subtraction, we identify a number of circular, source-free regions on each chip, and for each source, use the closest region to determine the background. We define a sufficient number of regions distributed over the chip to ensure that systematic background variations are small compared to statistical uncertainties.

For each `wavdetect` source, we use the background level in the extraction aperture to calculate a lower limit to the number of total counts for which the probability[1] that the detection is a random fluctuation is less than 10^{-6}. If the total extracted counts fall below this limit, we deem the candidate `wavdetect` source to have failed our significance criterion,

[1]The probability is calculated using the Poisson distribution for low-count (< 33) sources and the Gaussian limit for high-count (> 33) sources

Table 3.3. Percentage of PSF half-width as a function of off-axis angle used to extract hard counts (the value for soft count extraction is obtained by adding 0.6% to the hard counts % of PSF half-width value). These values optimize the signal-to-noise of each detection (see §3.3.1)

OAA [′]	% of PSF HW
$0-3$	90.0
$3-5$	87.5
$5-10$	85.0
>10	80.0

and remove the source from the catalog. In on-axis chips, there are about 5×10^5 detection cells, so we expect ~ 0.5 false detections per chip. Off-axis chips have $4-8$ times fewer detection cells, as we bin them before searching. Thus, on average we expect ≤ 1 false detection per field, depending on the number and configuration of chips read out.

To convert extracted source counts to flux, we use standard *CXO* software to compute energy-weighted exposure maps using a power-law spectral model with photon spectral index $\Gamma = 1.5$. Using these, we convert soft band counts to a $0.5-2$ keV flux, and hard band counts to a $2-10$ keV flux again adopting $\Gamma = 1.5$, and apply an aperture correction to account for the varying encircled energy fraction used in source extraction (see Table 3.3). We use the Galactic column density for each field listed in Table 3.2 to calculate source fluxes arriving at the Galaxy in the hard and soft bands. For an on-axis source, the conversion factor in the hard band is $f_{2-10\ \mathrm{keV}} \sim 3.0\times10^{-11}$ erg cm^{-2} s^{-1} ct^{-1}, although this value varies by 5%-10% from field to field owing to the differences in location of the aim point relative to node and chip boundaries. We note that $\Gamma = 1.5$ represents a softer spectrum than the $\Gamma = 1.2-1.4$ typically used for counts to flux conversion for the deep fields; our choice was motivated by the brighter average flux of our sample.

3.3.2 Source Deletions

In order to calculate the $\log N - \log S$ relation and to characterize the serendipitous source populations in an unbiased manner, we remove sources associated with the observation targets. In the case of point source targets such as AGN, transient afterglows, and the planetary nebula, this excision is trivial: the target object is simply excluded from the

catalog. For the nearby galaxies in which the target covers a significant area of the field, we have excised all sources within an elliptical region defined where, in our optical image of the galaxy, the galactic light is $> 11\sigma$ above the average background level. This led to the removal of 68 sources from the catalog. Finally, in the case of galaxy clusters, *Chandra's* high angular resolution allows one to easily 'see through' the diffuse emission from the hot intracluster gas to the universe beyond, and it is not necessary to exclude all discrete sources for optical followup studies. Some such sources are, however, associated with the target cluster, and should not be included in our $\log N - \log S$ analysis. Thus, apart from a few sources detected in the hard band which represent the diffuse cluster emission (and have thus been removed from the catalog), we have included all discrete sources detected in the cluster fields, but have flagged all those within ~ 1 Mpc of the cluster centroid as potentially associated with the target. We exclude these flagged sources (and the associated effective area) from the $\log N - \log S$ analysis (a total of 190 sources). Only a small fraction of these are actually optical spectroscopically identified cluster members.

3.3.3 Hardness Ratio Calculation

We define the hardness ratios as $(H - S)/(H + S)$, where H and S are the corrected counts in the 2 – 10 keV and 0.5 – 2 keV bands respectively. We extract the counts from our hard- (2.1–7 keV) and soft- (0.3–2.1 keV) band images using the centroids obtained by running `wavdetect` on the images separately (and subsequently correct the rates to the standard bands). We do this, rather than extracting counts from the soft-band image using the hard-band positions in order to minimize bias, as described below.

In a small number of cases, `wavdetect` failed to find a soft source both clearly present in the image and with a hard-source counterpart (typically as a result of a second source very nearby). In order to correct these discrepancies, and to test for any systematic differences in soft and hard source positions, we also derived a soft flux for each source using the hard source centroid. We calculated hardness ratios using both sets of soft counts (those derived by `wavdetect` and those extracted using hard-source positions). Figures 3.3 and 3.4 show a comparison of the two techniques.

Using the optimal centroid position for a fixed aperture to extract source counts systematically overestimates source fluxes since the centroid selected will be influenced by positive background fluctuations to maximize the number of counts included – a form of Eddington

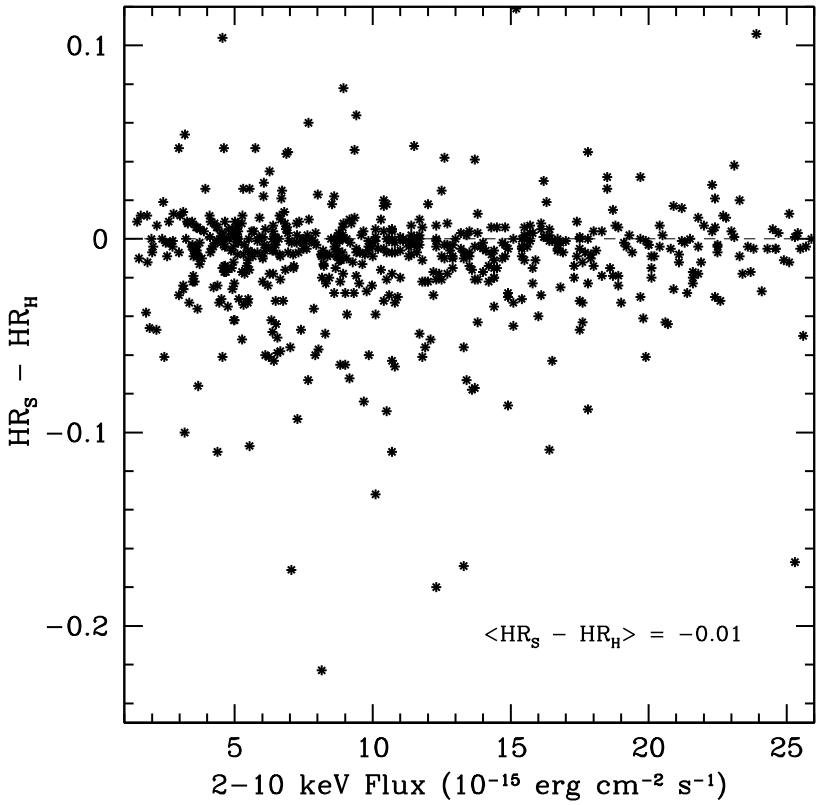

Figure 3.3 Comparison of hardness ratio $HR \equiv (H - S)/(H + S)$ as a function of hard X-ray flux (H; 2 – 10 keV), with soft-band flux (S; 0.5 – 2 keV) measured in two ways. We exclude hard-band only sources; they are plotted separately in Figure 3.4. Our primary methodology (see §3.3.3) is to produce soft-band catalogs directly from the soft-band images using `wavdetect`. The matched soft-band and hard-band catalogs were then used to produce *soft-band registered* hardness ratios HR_S; these are the hardness ratios presented as HR in Table 3.4 and Figures 3.8 and 3.9. Alternatively, hardness ratios were derived by extracting the soft-band flux using the aperture defined by the hard-band detection; the resultant *hard-band registered* hardness ratios are indicated here as HR_H. This figure shows that the difference between the techniques is typically less than a 0.1 in HR for any given source, with only a very slight systematic for HR_H producing more positive hardness ratios.

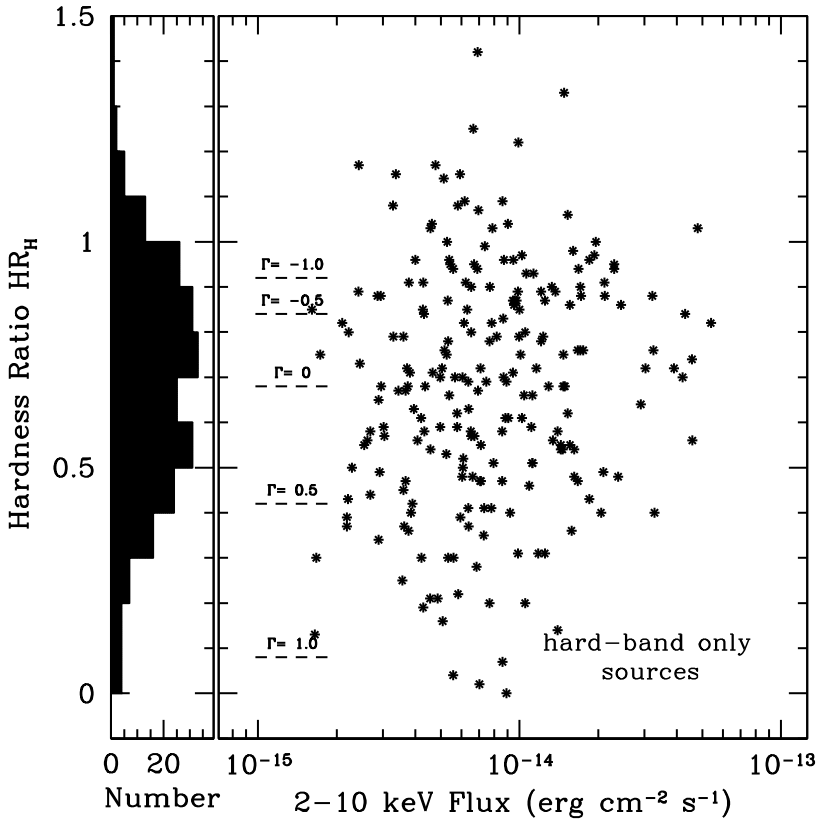

Figure 3.4 Hardness ratio $HR_H \equiv (H - S)/(H + S)$ as a function of hard X-ray flux for sources lacking a counterpart in the soft X-ray catalog. The left-hand panel collapses the scatter plot, showing the histogram of hard-band registered hardness ratios. The dashed horizontal lines indicate the photon index Γ which different hardness ratios correspond to. In Figure 3.8 these sources are all plotted along the horizontal line corresponding to $HR = 1$. Here we extract soft-band counts using the aperture defined by the hard-band detection; when the extracted soft-band counts are negative, the resultant *hard-band registered* hardness ratio HR_H is greater than unity. Visual inspection of the soft-band images of all sources with $f_{2-10\ \mathrm{keV}} \geq 2.5 \times 10^{-14}$ erg cm^{-2} s^{-1} verifies the lack of soft-band detections.

bias; see Cowie et al. (2002). Thus, calculating hardness ratios by using soft counts extracted from a region with the hard source centroid will produce a systematic bias toward greater hardness ratios. This is illustrated in Figure 3.3, where we show the difference in the two methods for calculating the hardness ratio as a function of soft source flux; while only 9 sources have a difference of $> +0.05$, 48 sources have a difference of < -0.05. The mean bias is -0.01. To avoid this, we use the hardness ratios derived from the independent soft and hard source catalogs.

3.3.4 Calculation of the Effective Area Function

In order to construct the hard X-ray source $\log N - \log S$ curve, we must determine the effective area of our survey as a function of source flux (shown in Figure 3.1). We do this by using the same algorithms we employ for the actual source extraction and flux conversion, calculated on a fine grid which samples the entire field of view. Our detailed calculation assures that, independent of the methodology used for background subtraction and source significance testing, our calculation of the effective area will be accurate. Also, since we employ significant off-axis area in the survey, calculating the response with fine sampling across the field of view is required, given the rapid PSF changes with off-axis angle and telescope vignetting.

We divide the images from each chip, with the detected sources 'blanked out,' into a fine grid sampled at a pitch of 8 pixels. At each location, we repeat the steps associated with source detection: we determine the aperture from the off-axis angle, background from the closest circular background region, and effective area from the spectrally weighted exposure map at that location. Using these, we determine the minimum detectable flux at that location corresponding to a spurious detection probability of 10^{-6}. We step across the grid in this manner, so that we determine accurately the sky area as a function of minimum detectable flux even for chips where the response changes significantly over the image. This procedure results in an effective area function which optimally matches the source detection procedure and supports the construction of a $\log N - \log S$ curve free of any biases which might be introduced by the approximate techniques adopted by some other surveys.

3.4 The Source Catalog

In Table 3.4 we present the SEXSI source catalog of 1034 hard-band discrete serendipitous X-ray sources detected as described above. Sources are designated CXOSEXSI (our IAU-registered name) followed by standard truncated source coordinates. The source positions (equinox J2000.0) are those derived from the hard-band X-ray images; in Paper II we use optical astrometry to derive mean offsets for each X-ray image and provide improved positions (although offsets are typically less than $1''$). We include only sources detected with a chance coincidence probability of $< 10^{-6}$ in the hard band. The angular distance of the source position from the telescope axis is given in column 4. Columns 5 and 6 list the background-subtracted counts for each source within the specified aperture derived from the 2.1 – 7 keV image, followed by the estimated background counts in that same aperture. Column 7 gives an estimate of the signal-to-noise ratio (SNR) of the detection. The SNR is calculated using the approximate formula for the Poisson distribution with small numbers of counts given in Gehrels (1986):

$$\mathrm{SNR} = \frac{\text{source counts}}{1 + \sqrt{0.75 + \text{source counts} + \text{background counts}}} \; ; \tag{3.1}$$

for high-count sources Equation 3.1 converges to the Gaussian limit. Owing to the relatively large background regions we have employed, the background error is negligible in the SNR calculation. It should be emphasized that these values are *not* a measure of source significance (which is $P < 10^{-6}$ in all cases) but is a measure of the uncertainty in the source flux estimates. Column 8 shows the unabsorbed hard band flux (in units of 10^{-15} erg cm^{-2} s^{-1}), corrected for source counts falling outside the aperture and translated to the standard 2 – 10 keV band assuming a power law photon spectral index of $\Gamma = 1.5$ and a Galactic absorbing column density appropriate to the field (see Table 3.2). Columns 9 – 12 provide the analogous values for the soft band. We derived soft-band fluxes by employing the same procedures on the `wavdetect` output from the 0.3 – 2.1 keV images, and then matching sources in the two bands. The soft fluxes are presented in the 0.5 – 2 keV. There are a large number of soft sources which lack a statistically significant hard counterpart; however, as we are interested in the 2 – 10 keV source populations, these sources are not included in the Table or considered further here. We do include a catalog of the soft band only sources in the Appendix.

Table 3.4. SEXSI 2 – 10 keV source catalog (SEXSI I catalog)

CXOSEXSI_	RA	DEC	OAA	Hard Band				Soft Band				HR
	(J2000)	(J2000)	[′]	Cts	Bkg	SNR	Flux[a]	Cts	Bkg	SNR	Flux[a]	
(1)	(2)	(3)	(4)	(5)	(6)	(7)	(8)	(9)	(10)	(11)	(12)	(13)
J022142.6+422654	02 21 42.67	42 26 54.1	9.49	16.30	5.70	2.83	23.10	48.50	6.50	5.73	10.30	-0.33
J022143.6+421631	02 21 43.64	42 16 31.6	8.33	98.53	4.47	8.81	74.80	244.27	3.73	14.56	29.70	-0.28
J022151.6+422319	02 21 51.68	42 23 19.3	6.17	9.13	1.87	2.06	6.55	17.67	1.33	3.25	2.02	-0.16
J022205.0+422338	02 22 05.00	42 23 38.3	4.24	13.24	0.76	2.74	8.73	0.00	0.00	0.00	0.00	1.00
J022205.1+422213	02 22 05.13	42 22 13.3	3.45	10.55	0.45	2.38	6.82	12.61	0.39	2.68	1.33	0.07
J022207.1+422918	02 22 07.11	42 29 18.8	8.93	25.10	4.90	3.84	18.90	64.86	4.14	6.94	8.46	-0.33
J022210.0+422956	02 22 10.00	42 29 56.3	9.38	22.38	5.62	3.52	17.30	127.12	4.88	10.15	16.70	-0.62
J022210.8+422016	02 22 10.85	42 20 16.7	2.17	5.52	0.48	1.53	3.63	19.42	0.58	3.50	2.17	-0.46
J022211.7+421910	02 22 11.71	42 19 10.7	2.55	10.46	0.54	2.36	6.87	10.40	0.60	2.35	1.15	0.14
J022215.0+422341	02 22 15.04	42 23 41.6	3.15	23.60	1.40	3.88	15.40	122.76	1.24	10.09	8.13	-0.40
J022215.1+422045	02 22 15.11	42 20 45.1	1.32	72.69	2.31	7.49	42.90	378.26	3.74	18.39	23.70	-0.42
J022215.5+421842	02 22 15.55	42 18 42.3	2.46	11.33	2.67	2.34	6.79	13.18	3.82	2.53	0.85	0.28
J022219.3+422052	02 22 19.32	42 20 52.2	0.54	10.89	2.11	2.31	6.38	0.00	0.00	0.00	0.00	1.00
J022224.3+422139	02 22 24.37	42 21 39.0	0.91	98.89	2.11	8.92	64.60	529.79	4.21	21.96	37.20	-0.44
J022225.2+422451	02 22 25.25	42 24 51.5	4.07	196.06	1.94	12.99	128.00	852.89	3.11	28.18	57.80	-0.34
J022226.5+422155	02 22 26.55	42 21 55.0	1.35	10.90	2.10	2.32	6.48	47.75	4.25	5.78	3.03	-0.35
J022232.5+423015	02 22 32.53	42 30 15.2	9.61	59.97	7.03	6.50	53.60	61.20	4.80	6.67	9.47	0.12
J022236.3+421730	02 22 36.37	42 17 30.8	4.23	19.39	3.61	3.30	12.00	40.32	2.68	5.30	2.64	0.01
J022236.8+422858	02 22 36.80	42 28 58.3	8.57	17.32	4.68	3.00	12.90	115.64	3.36	9.68	15.10	-0.68
J022259.1+422434	02 22 59.10	42 24 34.2	7.77	42.98	4.02	5.43	32.50	17.51	4.49	3.03	2.49	0.49
J022334.0+422212	02 23 34.05	42 22 12.2	13.34	40.98	25.02	4.47	37.50	37.78	26.22	4.18	6.21	0.15
J025325.9+413941 [b]	02 53 25.98	41 39 41.2	13.76	48.27	52.73	4.35	50.30	836.51	120.5	26.18	141.00	-0.85
J025333.7+413928 [b]	02 53 33.74	41 39 28.0	12.31	62.72	45.28	5.49	62.50	180.10	122.9	9.77	29.30	-0.35
J025340.4+413019 [b]	02 53 40.44	41 30 19.8	14.60	87.55	158.4	5.24	89.60	647.21	524.7	18.36	69.40	-0.55
J025400.3+414006 [b]	02 54 00.32	41 40 06.4	7.34	286.41	9.59	15.71	230.00	804.34	19.66	27.07	122.00	-0.41

[a]Fluxes are presented in units of 10^{-15} erg cm^{-2} s^{-1}

[b]Source falls within excluded area less than 1 Mpc from cluster center. Source not used for $\log N - \log S$ calculation

3.4.1 Comparison of Methodology with Previous Work

As Cowie et al. (2002) have recently discussed, the details of source detection and flux extraction can have non-trivial effects on the final source catalog derived from an X-ray image, as well as on conclusions drawn from the $\log N - \log S$ relation. As a test of our methodology, we have compared our results on one of the deeper fields in our sample, CL0848+4454, with the analysis published by Stern et al. (2002b; the SPICES survey) which uses the same technique as Giacconi et al. (2002) apply to the CDF-S. The source detection algorithm, the flux estimation method, and the effective area calculations all differ from ours, so a comparison is instructive.

Stern et al. (2002b) use the SExtractor source detection algorithm (Bertin & Arnouts 1996) applied to a version of the 0.5 – 7 keV image with a smoothed background and a signal-to-noise cut of 2.1. They measure source fluxes using a source aperture of $R_S = 2.4 \times$ the PSF full width at half maximum, with the background derived from an annulus $R_S + 2''$ to $R_S + 12''$. Their simulations predict five false sources using this procedure. In contrast, we employ the `wavdetect` algorithm to generate a list of source candidates from the 2.1 – 7 keV image, use hand-selected, source-free background regions with larger average areas to minimize statistical uncertainties, and require each source to have a probability of chance occurrence $< 10^{-6}$, yielding < 1 false source in this field. As noted above, we also calculate a fine-scale effective area function using exactly the same significance criterion for each PSF area on the image.

Figure 3.5 summarizes the result of comparing the two source catalogs. Apart from three bright sources in the off-axis S-6 chip which was not analyzed by Stern et al., our catalogs are identical down to a flux threshold of 10^{-14} erg cm^{-2} s^{-1}. At fainter fluxes, there is a large number of SPICES sources – 33 hard band detections – which fail to appear in our catalog (see Figure 3.5, upper panel). We examined the hard-band images at each of these locations. In seven cases, our `wavdetect` algorithm indicated source candidates were present, but each failed the $P < 10^{-6}$ significance test in the hard band. In most of the other cases, no source was apparent in the hard band, although quite a number had soft-band counterparts. In some cases, fortuitous background fluctuations in the annulus surrounding the source may have accounted for the reported SPICES hard-band detection. In nearly a third of the cases, a plausible optical identification has been found, so it is clear that

some of these sources are real X-ray emitters. However, in no case did our algorithm suite miss a source which would pass our specified threshold. Since our effective area function is calculated in a manner fully consistent with our threshold calculation, our $\log N - \log S$ will be unaffected by the absence of these faint, low-significance sources from our catalog.

The lower panel of Figure 3.5 indicates a systematic offset between the flux scale of the two catalogs of 15% – 20%, with our SEXSI fluxes being systematically higher. Most of this effect is explained by the count-to-flux conversion factors adopted in the two studies (3.24 and 2.79×10^{-11} erg cm^{-2} s^{-1} ct^{-1} respectively for SEXSI and SPICES), which in turn derives from the use of slightly different spectral index assumptions and a different generation of response function for the instrument. Individual fluxes for weaker sources have discrepancies of up to 40%, which can be accounted for by different flux extraction and background subtraction algorithms applied to low-count-rate sources.

In summary, the differences between the two analyses of this field, while producing catalogs differing at the $\sim$ 20% level in both source existence and source flux, are well understood. In particular we are confident that the self-consistent method we have adopted for calculating the source detection threshold and the effective area function will yield an unbiased estimate of the true $\log N - \log S$ relation for hard-band X-ray sources.

3.5 The 2 – 10 keV log N – log S Relation

The CDF-N and -S have provided good measurements of the 2 – 10 keV $\log N - \log S$ relationship at fluxes below $\sim 10^{-14}$ erg cm^{-2} s^{-1} . In comparison, the SEXSI sample includes 478 sources with fluxes between 10^{-12} and 10^{-14} erg cm^{-2} s^{-1}. By combining our measurements with the deep field results, we can constrain the $\log N - \log S$ over a broad range, which includes the break from Euclidean behavior.

We use the CDF-S fluxes from Giacconi et al. (2002) along with the SEXSI sample to construct the $\log N - \log S$ between 10^{-12} and 10^{-15} erg cm^{-2} s^{-1}. For the same reasons given by Cowie et al. (2002), we choose to work with the differential curve: the differential measurement provides statistically independent bins, and comparison does not rely on the bright-end normalization, which must be taken from other instruments. To calculate the SEXSI $\log N - \log S$, we use the effective area curve (Figure 3.1) to correct for incompleteness at the faint end of the sample. We have not corrected for Eddington bias which is, by

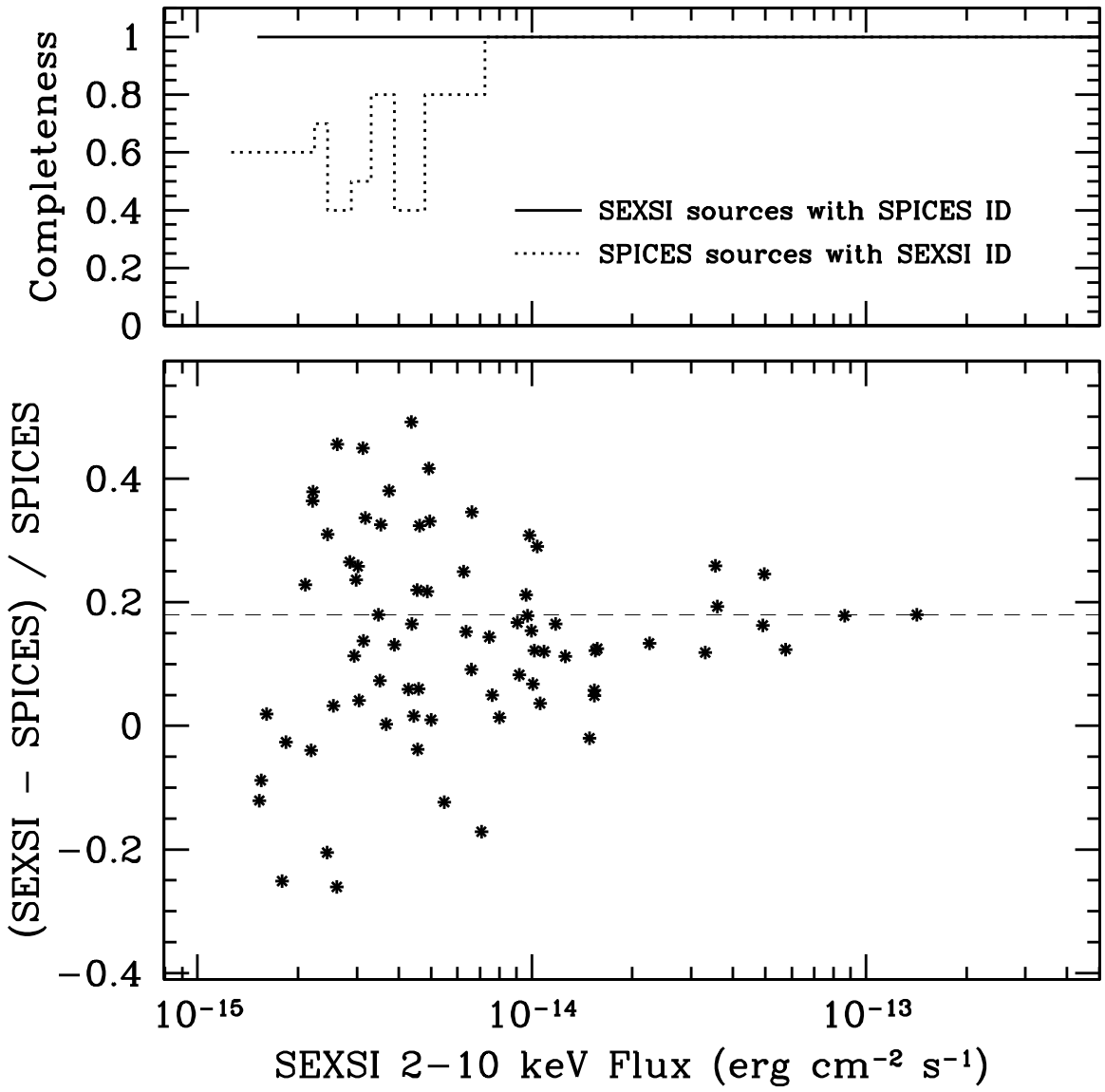

Figure 3.5 Comparison of the SEXSI and SPICES (Stern et al. 2002b) catalogs of hard-band 2 – 10 keV sources from the 185 ks *Chandra*/ACIS observation of the CL0848+4454 field in Lynx. The top panel shows the fraction of sources in each catalog which are identified in the other catalog, plotted with 10 sources per histogram bin. At bright fluxes, the source catalogs are identical. At lower fluxes, SPICES includes 33 sources that SEXSI does not, likely due to the different detection algorithms and detection passbands. The bottom panel compares photometry for the 78 sources which appear in both catalogs: SEXSI hard-band fluxes are systematically $\approx 18\%$ higher (dashed horizontal line).

comparison, a small effect. We employ the CDF-S fluxes with a correction (of about 5%) to account for the different spectral index assumption ($\Gamma = 1.375$ for CDF-S compared to $\Gamma = 1.5$ for SEXSI). To correct for incompleteness in the CDF-S sample, we use the effective area curve provided to us by P. Tozzi. We calculate the differential counts by binning ($N(S)$), the number of sources with flux S, into flux ranges, ΔS_i, then computing the average effective area, A_i for that range, and forming the differential curve by

$$n(S)_i = \sum_{S_{jmin}}^{S_{jmax}} (N(S_j))/(\Delta S_i A_i). \tag{3.2}$$

We normalize to a unit flux of 10^{-14} erg cm^{-2} s^{-1}.

Figure 3.6 shows the differential $\log N - \log S$ curve from the combined SEXSI and CDF-S catalogs, where the indicated errors are 1σ. The normalizations between the two agree well in the region of overlap, especially considering the different source extraction techniques and methodologies for calculating the effective area function. The combined data cannot be fit with a single power law, but require a break in slope between $1 - 2 \times 10^{-14}$ erg cm^{-2} s^{-1}. We fit the SEXSI data with a single power law at fluxes above 1.25×10^{-14} erg cm^{-2} s^{-1}, and the CDF-S data to a separate power law below this. The fits are shown as solid and dashed lines in Figure 3.6. The two intersect at a flux of 1.1×10^{-14} erg cm^{-2} s^{-1}. We note that the exact position of the intersection depends on where we divide the data, but for reasonable choices yielding good fits, the break always lies in the range $1 - 2 \times 10^{-14}$ erg cm^{-2} s^{-1} which contains the break point first predicted on the basis of a fluctuation analysis of the *Einstein* Deep Survey fields nearly two decades ago (Hamilton & Helfand 1987).

The best-fit curves are parameterized by

$$n(S) = (46.8 \pm 2.1)(S/10^{-14})^{-2.46 \pm 0.08} \ , \tag{3.3}$$

for $S > 1.25 \times 10^{-14}$ erg cm^{-2} s^{-1}, and

$$n(S) = (43.65 \pm^{2.1}_{2.0})(S/10^{-14})^{-1.41 \pm 0.17} \ , \tag{3.4}$$

below 1×10^{-14} erg cm^{-2} s^{-1}. The quoted errors are 1σ formal errors on the fits. The errors on the data points are statistical errors only, and do not include an estimate of the

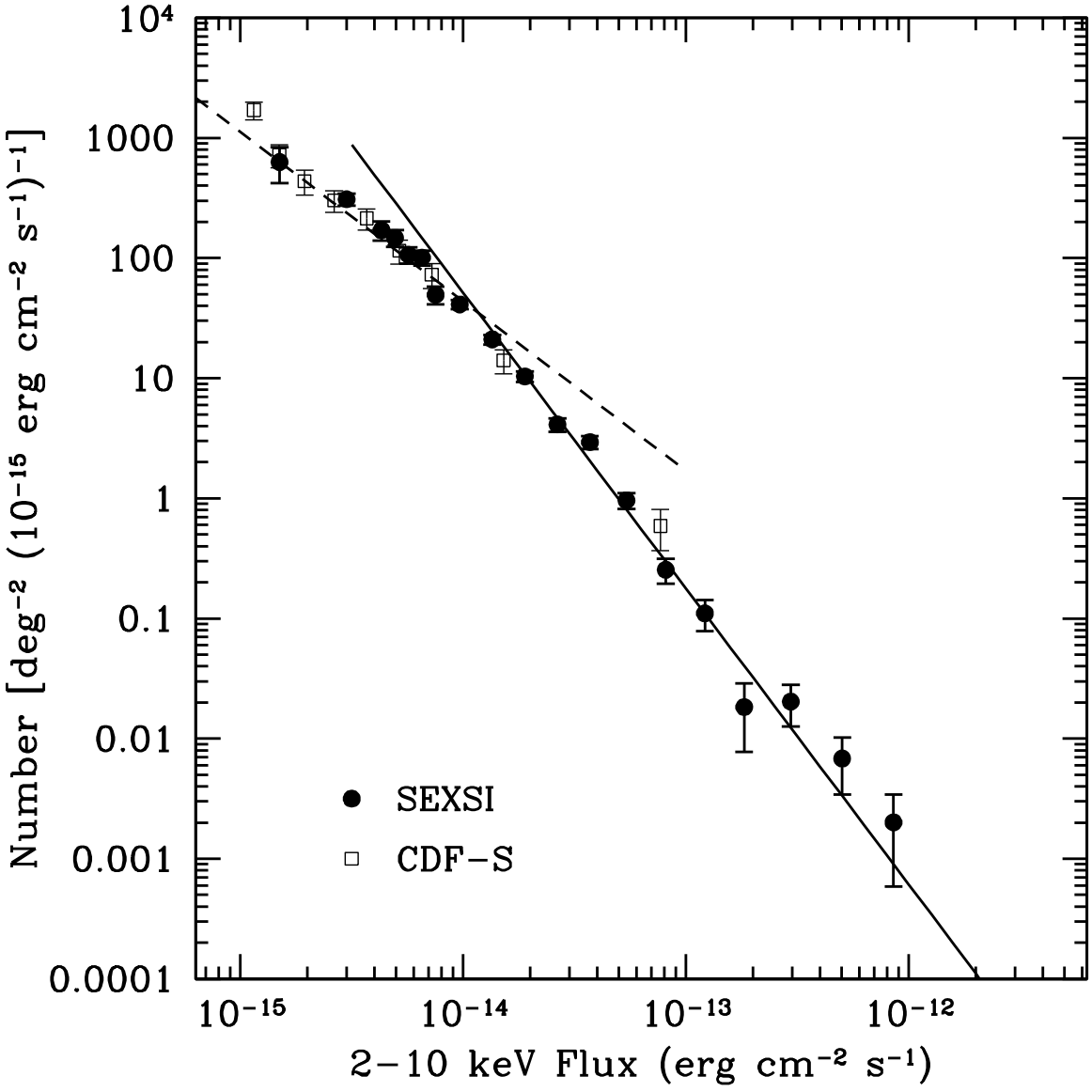

Figure 3.6 Differential $\log N - \log S$ for the SEXSI survey (circles) and *Chandra* Deep Field South (squares). The data are plotted in units of number deg^{-2} per unit flux, where the flux has been divided by 1×10^{-15} erg cm^{-2} s^{-1}. The solid lines shows a linear fit to the SEXSI data between 1×10^{-12} erg cm^{-2} s^{-1} and 1×10^{-14} erg cm^{-2} s^{-1}, and the dashed line shows a fit to the CDF-S data between 1×10^{-14} erg cm^{-2} s^{-1} and 1×10^{-15} erg cm^{-2} s^{-1}. The combined curve clearly changes slope at $1 - 2 \times 10^{-14}$ erg cm^{-2} s^{-1}. Note that the agreement of the normalization between the SEXSI and CDF-S data is good.

systematic uncertainties, such as biases on approximations in correcting for incompleteness. Based on the good agreement of the overall normalization with other surveys (see below), the systematic errors do not exceed the statistical uncertainty. The faint-end slope is dependent on where we divide the fit ranges; cutting the data at 2.5×10^{-14} erg cm^{-2} s^{-1} yields an acceptable faint-end fit, but with a steeper slope of -1.7.

Figure 3.7 shows the fractional residuals from the best-fit curves for the SEXSI survey (top panel), the CDF-S (middle), and combined Hawaii SSA22 and CDF-N sample (Cowie et al. 2002). For the Hawaii/CDF-N data, we use the binned points (provided in digital form by L. Cowie), corrected for the different spectral slope assumed for counts to flux conversion. At the faint end, the overall normalizations agree reasonably well, with the CDF-N data systematically slightly (1σ) above the mean fit to the SEXSI and CDF-S data. The faint-end slope of -1.41 ± 0.17 found here is marginally steeper than the best-fit values of -1.63 ± 0.054 found by Cowie et al. (2002) and -1.61 ± 0.10 found by Rosati et al. (2002). This difference is largely due to the somewhat different normalization; in addition, as noted above, the placement of the power-law break and the binning affects the best-fit slope, so this discrepancy is not significant. Above 2×10^{-14} erg cm^{-2} s^{-1}, the deep fields contain only 2 – 3 bins, and so the shape is much better constrained by the SEXSI data. Our best-fit slope at the bright end is -2.46 ± 0.08, consistent both with a Euclidean source distribution, and with the value of -2.57 ± 0.22 found for the Hawaii+CDF-N data.

3.6 X-ray Properties of the Sample

Most SEXSI sources have too few X-ray counts to warrant spectral fitting, so we rely on hardness ratios (HR) to characterize the spectral slope. As discussed in §3.3.3, we calculate the hardness ratio for each source, listed in column 13 of Table 3.4, using positions determined by independently searching the hard and soft images. We assign hard-band sources that have no soft-band `wavdetect` counterpart at our significance level a HR of 1.0. We have also determined a hardness ratio derived by extracting flux from the soft-band images at the position determined by searching the hard-band images, which we designate by HR_H. Note this does not require a significant independent detection in the soft band, so that for many sources with $HR = 1$, $HR_H < 1$ (see Figure 3.4). For reference, the slope of the X-ray background in this energy range, $\Gamma \sim 1.4$, corresponds to a HR of -0.22.

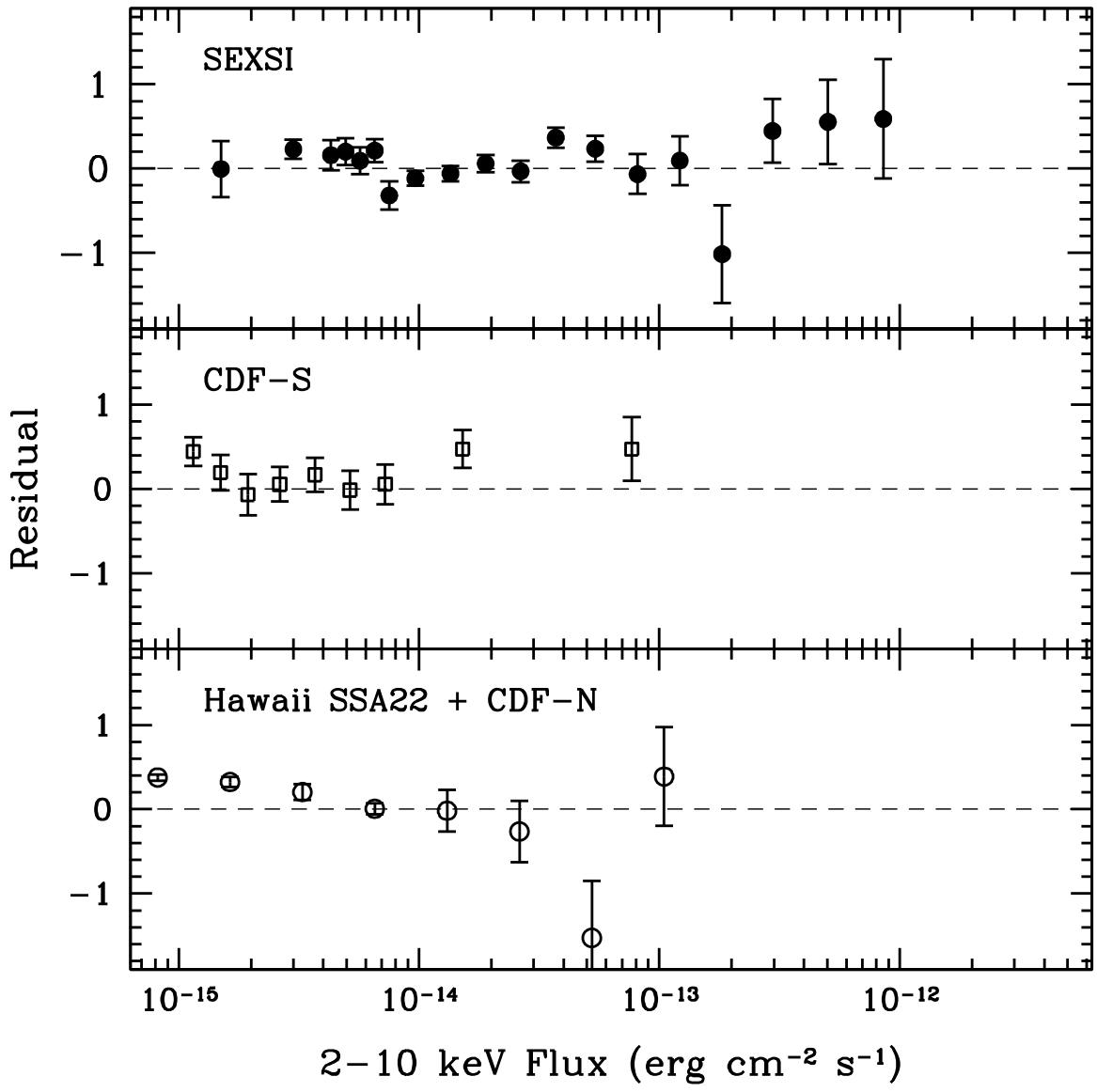

Figure 3.7 The residuals, defined as (data – fit)/data, for SEXSI, CDF-S, and Hawaii SSA22 and CDF-N. The fit is our best fit to the SEXSI data at the bright end, and the CDF-S data at the faint end.

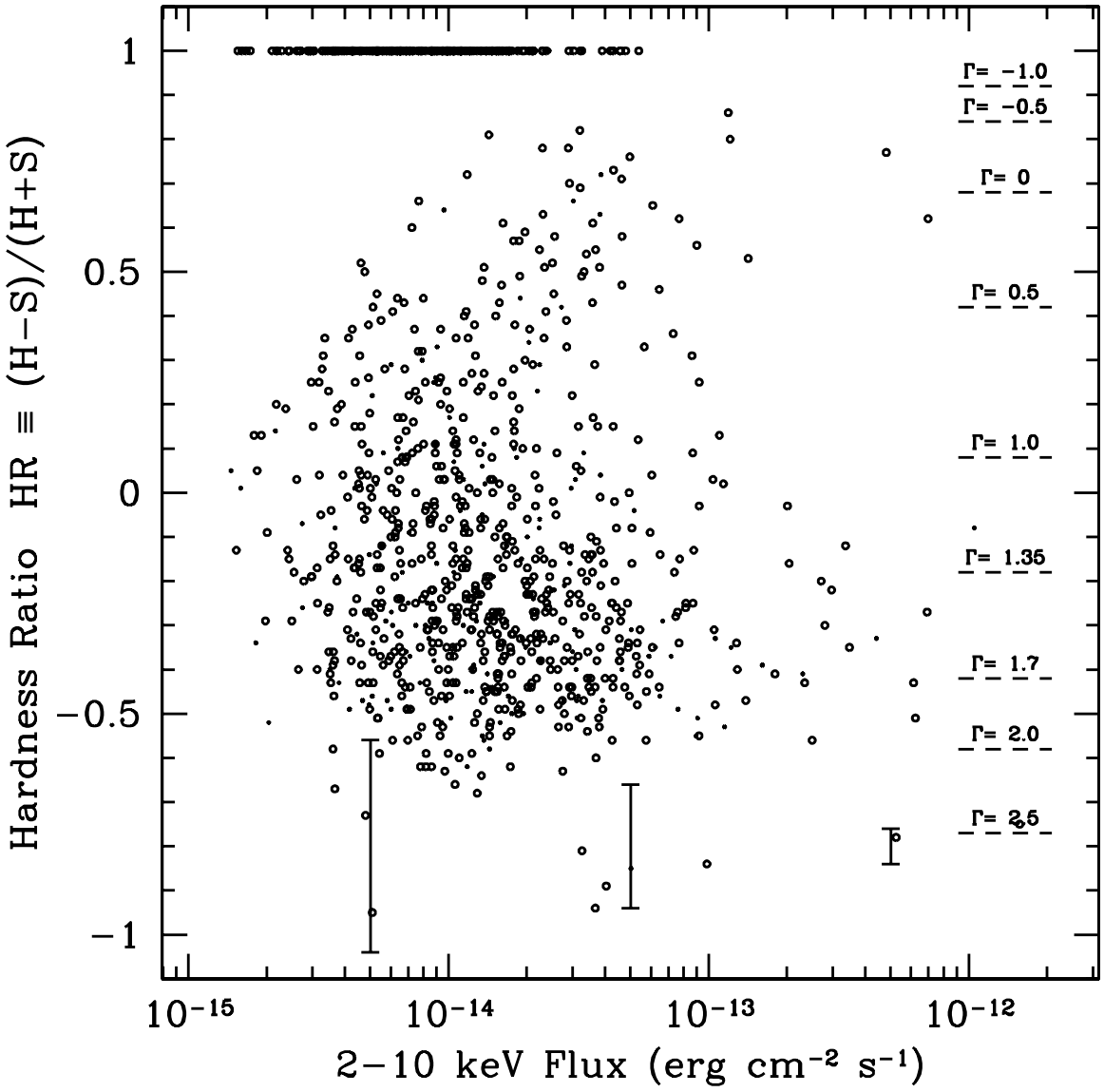

Figure 3.8 Hardness ratio $HR \equiv (H - S)/(H + S)$ of SEXSI sources as a function of hard X-ray (2 – 10 keV) flux. Sources detected only in the hard X-ray band are shown at a hardness ratio of 1, while sources detected only in the soft X-ray band are not shown. Dashed horizontal lines are power-law models with different photon indices. The 190 sources flagged as potentially being associated with *Chandra* cluster targets ($R < 1$ Mpc; §3.2) are marked as dots. The remaining 844 sources are marked as small, open circles. Error bars at bottom of figure show the typical uncertainties in hardness ratio measurements at three flux levels.

Table 3.5. HR_H averages for sources with $HR_H < 0$ and $HR_H > 0$ (see §3.6.1)

Flux Range erg cm^{-2} s^{-1}	$HR_H < 0.0$		$HR_H > 0.0$		
	$\langle HR_H \rangle$	# Srcs	$\langle HR_H \rangle$	# Srcs	% of Srcs
$10^{-12} - 10^{-13}$	-0.38 ± 0.01	26	0.42 ± 0.02	9	26
$10^{-13} - 10^{-14}$	-0.31 ± 0.01	344	0.49 ± 0.01	201	37
$10^{-14} - 10^{-15}$	-0.29 ± 0.02	201	0.50 ± 0.02	253	56

Figure 3.8 presents the HR for SEXSI's 1034 sources as a function of hard-band flux. The top panel of Figure 3.9 shows these same sources in an HR histogram. The lower three panels of Figure 3.9 show the hardness ratio histogram broken into three flux ranges. The upper right corner of each panel indicates the number of sources and average HR for each subsample. The entire sample has an average HR of 0.108 ± 0.006, corresponding to $\Gamma = 0.96$. The histograms clearly illustrate the trend, previously noted by the Ms surveys, for higher hardness ratios at lower fluxes.

3.6.1 Distribution of Hardness Ratios

The highest flux (second from the top) panel in Figure 3.9 appears to show a bimodal distribution in hardness ratio, with a peak centered around $HR \sim -0.4$ ($\Gamma \sim 1.7$), and a harder, smaller peak centered around $HR \sim 0.7$ ($\Gamma \sim -0.1$). As the flux decreases, many of the harder sources move into the $HR = 1$ bin, while the center of the softer distribution shifts only slightly to the right. This motivates us to split the hardness distribution at $HR = 0$, and investigate the distribution of the two sub-populations separately.

Table 3.5 shows the result of splitting the three flux-selected histograms at $HR = 0$, where we present the average value of HR_H for the six populations. Note we use HR_H to minimize the skew imposed by the sudden shift of sources to $HR = 1$ imposed by the requirement of separate detection in the soft image. The Table shows that the means for the two populations are relatively stable as one considers fainter fluxes, but the fraction of sources in the $HR_H < 0$ population grows (see the last column in Table 3.5).

Figure 3.10 shows the 2 – 10 keV $\log N - \log S$ relations for the SEXSI sources split at $HR = 0$. We have excluded the cluster fields from this analysis to avoid bias. For the $HR < 0$ plot (top panel) we fit the data with a single power law at fluxes above

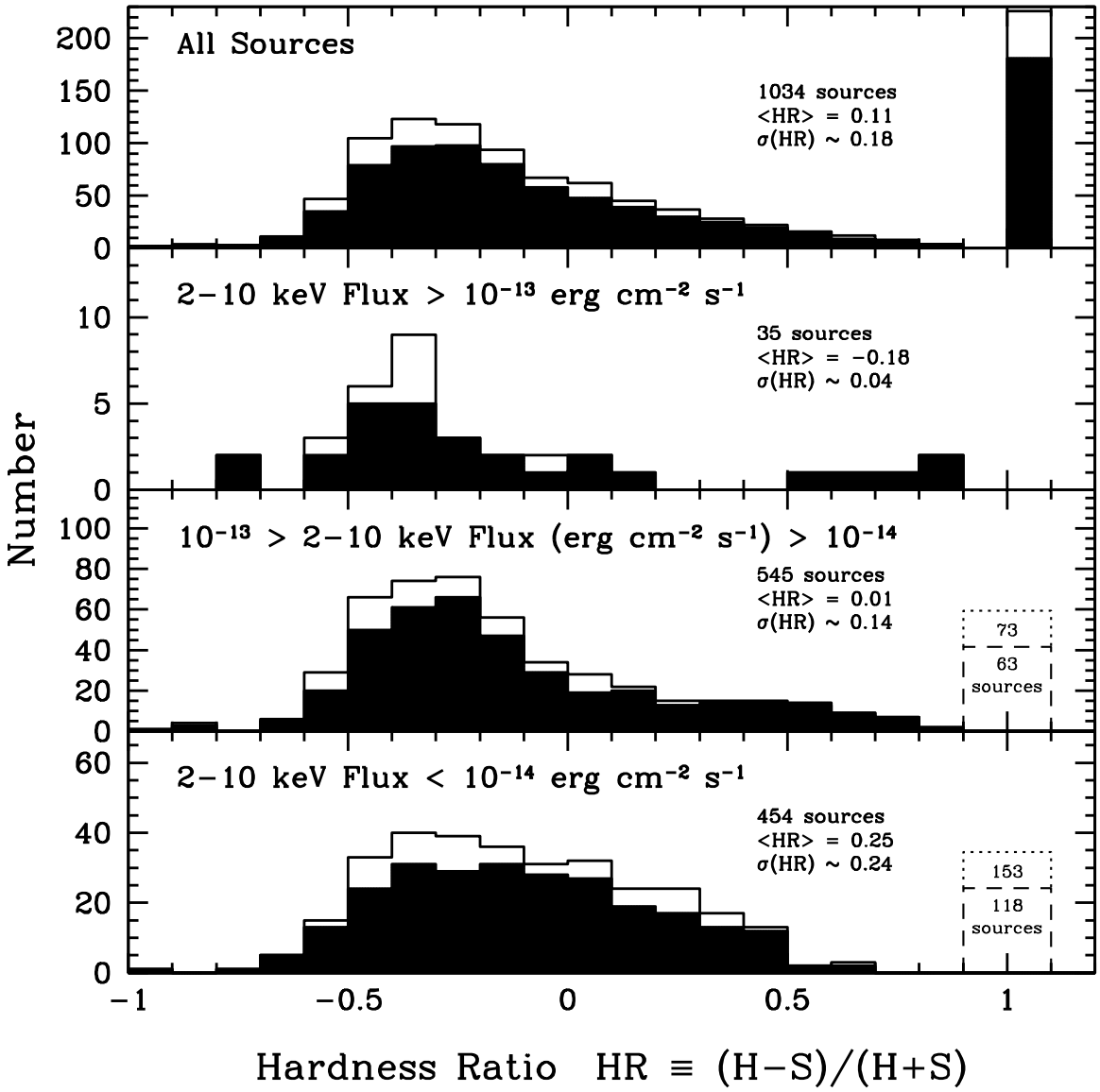

Figure 3.9 Histogram of hardness ratio values for the SEXSI 2−10 keV selected sample of X-ray sources. In the top panel, the open histogram shows all 1034 sources from our survey, and the solid histogram shows the subset of 844 sources which were not flagged as being potentially associated with the *Chandra* cluster targets ($R < 1$ Mpc). Note that when statistical uncertainties are considered, the sources in the $HR = 1$ peak will partially fill in the high HR end of the histogram (see Figure 3.4). The lower three panels show the data from the top panel split into three flux ranges. Sources undetected in the soft band are indicated in text for the bottom two panels. Typical uncertainties in hardness ratio measurements for individual sources in each flux bin are indicated as $\sigma(HR)$.

2.5×10^{-14} erg cm^{-2} s^{-1}. The best-fit curve is parameterized by

$$n(S)_{HR<0.0} = (33.9\pm^{1.6}_{1.5})(S_{2-10\mathrm{keV}}/10^{-14})^{-2.38\pm0.13}. \quad (3.5)$$

The population clearly turns over at $\sim 1\times10^{-14}$ erg cm^{-2} s^{-1}. Conversely, the $HR > 0.0$ population (bottom panel) shows no break. We fit the hard data with a single power law at fluxes all the way down to 2.5×10^{-15} erg cm^{-2} s^{-1}. The best-fit curve is parameterized by

$$n(S)_{HR>0.0} = (14.8\pm^{1.8}_{1.6})(S_{2-10\mathrm{keV}}/10^{-14})^{-2.24\pm0.05}. \quad (3.6)$$

This curve is an excellent fit all the way down to the faint end of our sample. Presumably the hard sources are on average at lower redshift and thus do not exhibit the evolutionary effects likely to be responsible for the slope break until even fainter flux levels are reached.

3.6.2 X-ray Spectral Comparison to Previous Work

The SEXSI catalog includes only sources independently identified in the hard band images, and so excludes those sources detected only in the soft band. Thus, we expect our average hardness ratio to be significantly larger than that reported for the deep fields, which include a large fraction of soft-only sources. Indeed, Rosati et al. (2002) analyze a stacked spectrum of the CDF-S total sample and report an average power law index of $\Gamma = 1.375$ ($HR = -0.2$), much softer than our average $HR = 0.108$. Even the faintest subsample, $f_{2-10\ \mathrm{keV}} < 2 \times 10^{-15}$ erg cm^{-2} s^{-1}, with an average $\Gamma = 1.05$ ($HR = 0.04$), appears softer than our entire sample.

To make a better comparison to the CDF-S, we eliminated the soft-band only sources from their source catalog (Giacconi et al. 2002). In addition, we translated their fluxes, which had been converted from counts using $\Gamma = 1.4$, to match ours, which assumed $\Gamma = 1.5$ (a correction of about 5% for the hard band). We also correct for the different spectral ranges assumed for their hard count rate measurement (2 – 7 keV for CDF-S compared to 2 – 10 keV for SEXSI). Using these converted HRs with the soft-band only sources ignored, we find that the average HR for the CDF-S sample is 0.14 ± 0.01, comparable to the SEXSI HR of 0.108 ± 0.006. Since CDF-S samples the fainter section of the $\log N - \log S$, their slightly higher average HR is not surprising.

To further compare the surveys, we break the CDF-S sample into three flux ranges, as we

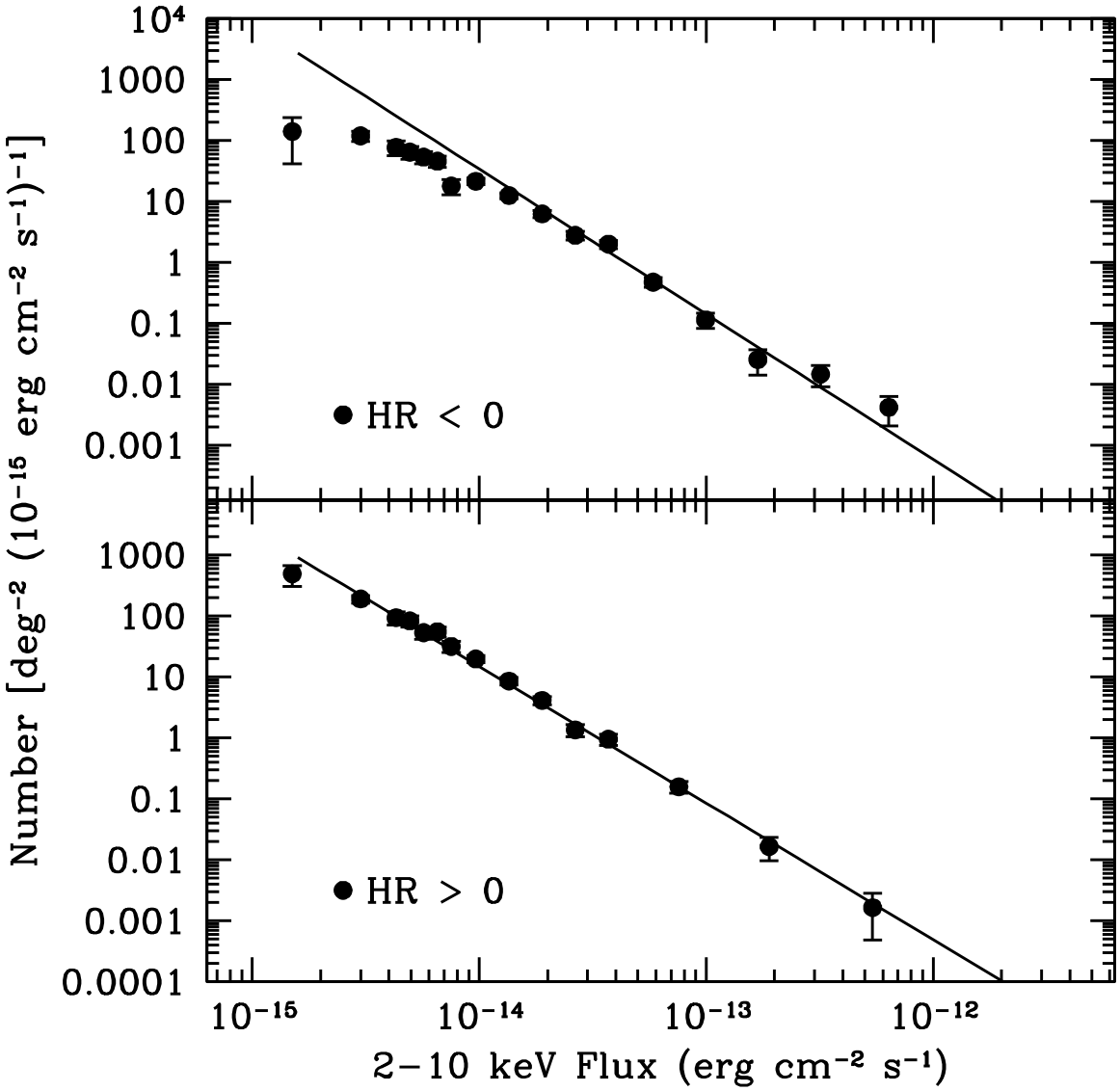

Figure 3.10 Differential $\log N - \log S$ for the SEXSI sources split at $HR = 0$. The data are plotted in units of number deg^{-2} per unit flux, where the flux has been divided by 1×10^{-15} erg cm^{-2} s^{-1}. The top panel shows the $HR < 0$ sources fit from 1×10^{-12} to 2.5×10^{-14} erg cm^{-2} s^{-1}. The bottom panel shows the $HR > 0$ sources fit from 1×10^{-12} to 2.5×10^{-15} erg cm^{-2} s^{-1}. The soft ($HR < 0$) sources clearly turn over at $\sim 1 \times 10^{-14}$ erg cm^{-2} s^{-1} while the hard ($HR > 0$) sources do not and are well fit by a single power law to faint fluxes.

did for our sample in Figure 3.9. The CDF-S has no sources in the bright range ($f_{2-10\ \mathrm{keV}} > 10^{-13}$ erg cm^{-2} s^{-1}). In the medium flux range (10^{-13} erg cm^{-2} s^{-1} $> f_{2-10\ \mathrm{keV}} >$ 10^{-14} erg cm^{-2} s^{-1}), we calculate the CDF-S average HR to be -0.09 ± 0.01, as compared to SEXSI's average HR of 0.008 ± 0.007. For the low flux range (10^{-14} erg cm^{-2} s^{-1} $> f_{2-10\ \mathrm{keV}} >$ 10^{-15} erg cm^{-2} s^{-1}), the SEXSI's average HR is 0.25 ± 0.01 as compared to 0.13 ± 0.02 for CDF-S.

For each of these flux ranges we find the average HRs of SEXSI and CDF-S to be comparable, but slightly higher for SEXSI. This is likely explained by the different survey depths and source detection processes. As with the SPICES reduction of the CL0848+0454 field, CDF-S detects sources in full band (0.5 – 7 keV) images and then extracts fluxes from the soft and hard band images regardless of detection significance in the individual bands. For a source that is below our threshold in the soft band we will report a flux of zero, while CDF-S may detect positive flux. If we compare the CDF-S HR's to our HR_H values of -0.014 ± 0.007 and 0.15 ± 0.01 for the mid- and low-flux ranges, we are consistent with the CDF-S values of -0.09 and 0.16.

3.7 Summary

We have completed the first "large"-area (> 1 deg^2) hard X-ray source survey with the *Chandra* Observatory, and report here the X-ray characteristics of 1034 serendipitous sources from 27 fields detected in the 2 – 10 keV band. This work represents a sample size in the critical flux interval 1×10^{-13} to 3×10^{-15} erg cm^{-2} s^{-1} that exceeds the sum of all previous surveys by a factor of three. We present a technique for calculating the effective area of our survey which is fully consistent with our source detection algorithm; combined with the large source sample, this allows us to derive the most accurate $\log N - \log S$ relation yet produced for hard X-ray sources at fluxes fainter than 10^{-13} erg cm^{-2} s^{-1}. We find that the slope of the relation is Euclidean at fluxes above 10^{-14} erg cm^{-2} s^{-1}. Combining the complete source sample with the CDF-S deep survey data indicates a break in the $\log N - \log S$ slope at 1.1×10^{-14} erg cm^{-2} s^{-1}. Calculation of separate $\log N - \log S$ relations for the hard and soft portions of our sample shows that it is the softer hard-band sources which are responsible for this break; sources with $HR > 0.0$ show no slope change down to a flux an order of magnitude fainter, suggesting (as our spectroscopic followup and that of the

deep surveys of Hornschemeier et al. (2001) and Tozzi et al. (2001) have confirmed) that the hardest sources are predominantly a lower redshift sample. Future papers in this series will describe our optical observations of this sample, providing further insight into the populations of X-ray luminous objects that comprise the X-ray background.

Acknowledgments

We are deeply indebted to the following *Chandra* Guest Investigators for their willingness to allow us immediate access to their data for the purposes of this statistical investigation of serendipitous sources: Jan Vrtilek, Crystal Martin, and Q. Daniel Wang. We also thank Adam Stanford and his collaborators for their enlightened approach to the deepest pointing included in our survey that waived all proprietary rights to these data and Leon van Speybroeck for contributing three of his GTO cluster fields. Elise Laird and Alan Diercks assisted greatly in the construction of our optical data reduction pipeline with useful code and helpful advice. James Chakan assisted with the X-ray data reduction. This work has been supported by NASA NAG5-6035(DJH), as well as by a small *Chandra* archival grant. The work of DS was carried out at the Jet Propulsion Laboratory, California Institute of Technology, under a contract with NASA.

3.8 Appendix

In Table 3.6 we present a source catalog of 879 soft-band serendipitous X-ray sources which lack a statistically significant hard-band counterpart. These sources are excluded from the main SEXSI catalog (Table 3.4) since the strength of SEXSI, and thus our primary scientific interest, lies in the study of 2 – 10 keV source populations.

These soft sources, detected and analyzed as described in Section 3.3.1, are designated CXOSEXSI (our IAU-registered name) followed by standard truncated source coordinates. The source positions (equinox J2000.0) are those derived from the soft-band X-ray images. We include only sources detected with a chance coincidence probability of $< 10^{-6}$ in the soft band. The angular distance of the source position from the telescope axis is given in column 4. Columns 5 and 6 list the background-subtracted counts for each source within the specified aperture derived from the 0.5 – 2.1 keV image, followed by the estimated background counts in that same aperture. Column 7 gives an estimate of the signal-to-noise ratio (SNR) of the detection (see Section 3.4 for details). Again, it should be emphasized

that these values are *not* a measure of source significance (which is $P < 10^{-6}$ in all cases) but is a measure of the uncertainty in the source flux estimates. Column 8 shows the unabsorbed soft band flux (with units of 10^{-15} erg cm^{-2} s^{-1}), corrected for source counts falling outside the aperture and translated to the standard 0.5 – 2 keV band assuming a power law photon spectral index of $\Gamma = 1.5$ and a Galactic absorbing column density appropriate to the field (see Table 3.2).

This soft-band-only catalog does have the target sources carefully eliminated for point sources and nearby galaxies, as described for the main SEXSI catalog in Section 3.3.2. This led to the removal of 86 sources from this catalog. However, the sources within ~ 1 Mpc of target galaxy cluster centroids are not flagged, as was done with the hard sources in Table 3.4. In addition, there has been no attempt to search for extended sources.

Table 3.6. SEXSI soft-band only source catalog

CXOSEXSI_	RA	DEC	OAA	Soft Band			
	(J2000)	(J2000)	[′]	Cts	Bkg	SNR	Flux[a]
(1)	(2)	(3)	(4)	(5)	(6)	(7)	(8)
J022045.8+421954	02 20 45.80	42 19 54.2	17.84	387.68	449.3	12.95	37.90
J022054.2+421724	02 20 54.22	42 17 24.3	16.62	421.68	482.3	13.57	40.60
J022101.0+422042	02 21 01.08	42 20 42.4	14.99	123.61	199.3	6.51	11.20
J022108.5+422008	02 21 08.52	42 20 08.2	13.64	109.91	206.0	5.85	9.88
J022111.1+421704	02 21 11.11	42 17 04.1	13.67	98.28	199.7	5.38	8.69
J022113.3+421842	02 21 13.35	42 18 42.3	12.90	197.24	163.7	9.85	17.40
J022122.8+421725	02 21 22.84	42 17 25.1	11.49	190.08	87.92	10.74	16.10
J022128.4+421826	02 21 28.41	42 18 26.2	10.23	54.50	7.50	6.11	8.94
J022131.1+422146	02 21 31.15	42 21 46.5	9.48	1800.8	8.19	41.36	222.00
J022131.2+422144	02 21 31.24	42 21 44.0	9.46	1659.9	8.10	39.66	204.00
J022131.5+423103	02 21 31.52	42 31 03.3	13.86	45.62	28.38	4.73	6.99
J022131.5+422148	02 21 31.58	42 21 48.3	9.41	1649.00	7.92	39.53	203.00
J022131.6+422144	02 21 31.61	42 21 44.1	9.39	1574.00	7.94	38.60	194.00
J022136.1+422730	02 21 36.11	42 27 30.7	10.82	19.42	9.58	3.01	3.00
J022140.9+422050	02 21 40.95	42 20 50.2	7.62	20.86	3.14	3.49	2.48
J022142.1+421947	02 21 42.18	42 19 47.4	7.47	26.10	2.90	4.04	3.10
J022144.2+423019	02 21 44.29	42 30 19.4	11.79	25.28	13.72	3.46	3.70
J022153.5+423026	02 21 53.50	42 30 26.1	10.97	25.00	8.00	3.67	3.59
J022155.1+421804	02 21 55.13	42 18 04.3	5.72	7.90	1.10	1.92	0.91
J022155.5+421749	02 21 55.56	42 17 49.8	5.77	7.84	1.16	1.90	0.90
J022202.6+421637	02 22 02.69	42 16 37.7	5.54	14.00	1.00	2.82	1.79
J022205.9+421652	02 22 05.90	42 16 52.3	4.98	27.05	0.95	4.25	2.99
J022221.6+422348	02 22 21.60	42 23 48.3	2.98	11.96	3.04	2.41	0.82
J022225.6+423526	02 22 25.61	42 35 26.7	14.63	115.19	32.81	8.73	18.10
J022225.7+422847	02 22 25.72	42 28 47.1	7.98	16.38	2.62	3.01	2.13
J022227.1+422336	02 22 27.18	42 23 36.6	2.93	34.28	3.72	4.75	2.21
J022227.5+422108	02 22 27.59	42 21 08.9	1.04	168.54	5.46	11.85	10.80
J022229.3+422852	02 22 29.30	42 28 52.7	8.15	16.07	2.93	2.95	2.09

[a]Fluxes are presented in units of 10^{-15} erg cm^{-2} s^{-1}

Chapter 4

SEXSI Optical Imaging[1]

The Serendipitous Extragalactic X-ray Source Identification (SEXSI) Program is designed to expand significantly the sample of identified extragalactic hard X-ray sources at intermediate fluxes, 10^{-13} erg cm^{-2} s^{-1} $\lesssim S_{2-10\ \mathrm{keV}} < 10^{-15}$ erg cm^{-2} s^{-1}. SEXSI, which includes sources derived from more than 2 deg^2 of *Chandra* images, provides the largest hard X-ray-selected sample yet studied, offering an essential complement to the *Chandra* Deep Fields (total area ~ 0.2 deg^2). In this paper we describe R-band optical imaging of the SEXSI fields from the Palomar, MDM, and Keck observatories. We have identified counterparts, or derived flux limits for nearly 1000 hard X-ray sources. Using the optical images, we derive accurate source positions. We investigate correlations between optical and X-ray flux, and optical flux and X-ray hardness ratio. We also study the density of optical sources surrounding X-ray counterparts, as well as the properties of optically-faint, hard X-ray sources.

4.1 Introduction

With the successful launch in 1999 of the *Chandra X-Ray Observatory* (Weisskopf et al. 1996) came the opportunity to explore the X-ray universe with greater angular resolution and sensitivity in the 2 – 10 keV energy range than ever before. One of the primary goals of the mission is to perform surveys of the extragalactic sky at these higher energies.

The longest *Chandra* pointings thus far are the *Chandra* Deep Field-North (Alexander et al. 2003) and the *Chandra* Deep Field-South (Giacconi et al. 2002), with 2 Ms and 1 Ms exposure times, respectively. These fields have explored faint sources, with many objects

[1]Much of this chapter has been previously published as Eckart et al. (2005)

reaching below the luminosity range of active galactic nuclei (AGN) to include "normal" galaxies. Though the Deep Fields are pushing to lower fluxes than previously attainable, they cover only a small area (~ 0.1 deg^2 each), and do not have good statistics for the flux range in which the dominant contribution to the 2 – 10 keV X-ray background arises. To get such statistics, a larger area of the sky must be covered by combining multiple *Chandra* pointings.

The *Chandra* archive provides the opportunity to explore multiple, mid-depth ($\sim 50 - 100$ ks) exposures. In Harrison et al. (2003, Paper I) we presented the Serendipitous Extragalactic X-ray Source Identification (SEXSI) program design, our X-ray analysis techniques and a catalog of over one thousand 2 – 10 keV sources, as well as some initial X-ray results and comparisons with previous work. With data from 27 archival *Chandra* fields, SEXSI is designed to focus on a large-area (~ 2 deg^2) sample of X-ray sources in the intermediate flux range ($\sim 10^{-13} - 10^{-15}$ erg cm^{-2} s^{-1}). Our goal is to determine spectroscopically the redshift distributions and nature of hard (2 – 10 keV) X-ray source populations from which the bulk of the X-ray background arises. The campaign of single-color photometry presented here attempts a minimum depth for every field of $R \sim 22 - 23$, consistent with identifying counterparts for which classifiable spectra can be obtained with a 10-m telescope in a ~ 1 hour integration. This strategy maximizes the number of hard sources identified spectroscopically in our fields for our fixed observing campaign.

Other programs are also aiming to understand the X-ray source population at medium depth with degree-scale *Chandra* and *XMM-Newton* surveys. Examples of such surveys include HELLAS2XMM (e.g., Baldi et al. 2002; Brusa et al. 2003) and the *Chandra* Multiwavelength Project (ChaMP; e.g., Kim et al. 2004; Green et al. 2004). Brandt et al. (2004) presents a comprehensive list of the many ongoing X-ray background surveys.

The SEXSI program is unique among the *Chandra* Serendipitous surveys in concentrating on obtaining a uniform spectroscopic survey restricted to the hard source population. The ChaMP, in contrast, is a comprehensive program of imaging and spectroscopy to follow-up both soft and hard sources in a large number of publicly accessible extragalactic *Chandra* pointings. The SEXSI spectroscopic catalog will therefore contain a larger fraction of obscured AGN than ChaMP. Eight of the fields are common to both surveys, and for one of these ChaMP has published some spectroscopic followup (Green et al. 2004). Even for the common fields, SEXSI plans deeper spectroscopy and should identify a greater number

of hard X-ray sources. Between the large number of distinct fields and the different focus for ground-based followup, the SEXSI survey provides an essential complement to current surveys of the sources responsible for the X-ray background.

In this paper, we present optical R-band imaging of the SEXSI *Chandra* fields, as well as the methodology used to derive X-ray source identifications and a catalog of R-band counterpart magnitudes. In addition, we explore relationships between the X-ray flux, hardness ratio, and R-band magnitude. A third paper in this series (see Chapter 5) will include our optical spectroscopic results, with redshifts and classifications for $\sim$ 450 of these objects, and a discussion of the luminosity distribution, redshift distribution, and composition of the sample.

4.2 Optical Imaging and Reduction

We have imaged the SEXSI fields using the Palomar 60-inch (P60) and 200-inch (P200) telescopes, the MDM 2.4-meter (MDM-2.4) and 1.3-meter (MDM-1.3) telescopes, and the Keck I telescope. Much of the early optical imaging for this program was done with small field-of-view, single-CCD array cameras. For example, the P60 CCD13 camera has a $12.6' \times 12.6'$ field of view. This requires several pointings to map a typical $17' \times 17'$ *Chandra* field, making multicolor imaging very time consuming. Since spring 2000, both the P200 and MDM-2.4 have had large-format ($\gtrsim 24' \times 24'$) CCD cameras available, allowing us to cover nearly all of a *Chandra* field in a single pointing. The P200 Large Format Camera (LFC; Simcoe et al. 2000) uses the Sloan digital sky survey (SDSS) filter set (g', r', i', and z'; Fukugita et al. 1996), while, for our MDM-2.4 8K camera (Crotts 2001) imaging, we used Johnson-Cousins filters (B, V, R, and I). In each filter band, our goal has been to obtain images with a limiting Vega magnitude of $\sim$ 24, the practical limit for obtaining counterpart spectra at the Keck telescope in reasonable integration times. Because the large-format cameras were not available for the first 1.5 years of the SEXSI project, some fields are imaged only in R band (due to observing time constraints), while the fields observed later in the program generally have multicolor data. For the purposes of this paper, we use only the R-band data. Table 4.1 summarizes the characteristics of the telescopes and imaging instruments used in this program.

We reduced the optical images using standard techniques, relying upon IRAF tasks for

Table 4.1. Optical imaging instruments employed in the SEXSI survey

Camera	Telescope	Plate Scale [″/pix]	FOV	Reference
8K	MDM 2.4m	0.18	$24.6' \times 24.6'$	Crotts (2001)
CCD13	Palomar 60”	0.37	$12.6' \times 12.6'$	···
Cosmic	Palomar 200”	0.29	$9.9' \times 9.9'$	Kells et al. (1998)
Echelle	MDM 1.3m	0.50	$17.1' \times 17.1'$	···
Echelle	MDM 2.4m	0.28	$9.6' \times 9.6'$	···
LFC	Palomar 200”	0.18	$\sim \pi(12.3')^2$	Simcoe et al. (2000)
LRIS	Keck I	0.22	$7.5' \times 7.5'$	Oke et al. (1995)
Templeton	MDM 1.3m	0.50	$8.5' \times 8.5'$	···

the preliminary steps. Median-combined bias frames, taken the same night as the science data, were subtracted from the images. For flatfielding, we used either dome flats or sky flats generated by combining all the images from a night, including twilight flats, with min/max rejection to remove stars. We used standard techniques to mask out cosmic rays and bad pixels prior to combining data.

For astrometric calibration of most of the data, we used the `DOPHOT` software package to locate all nonsaturated, pointlike objects in individual exposures. Comparing with the USNO-A2.0 catalog (Monet 1998), we then used the object-matching program `starmatch` (by Doug Reynolds) to both align the images before stacking and to obtain an astrometric solution for the final, combined image. The standard deviations of the astrometric solutions are generally $\leq 0.3''$ in each axis.

We reduced images using the same methodology for both the LFC data from the P200 telescope and the 8K data from the MDM-2.4 telescope, although slightly different suites of software were required. We relied upon the `MSCRED` package within IRAF, designed for reduction of large-format, multi-array optical data from the Kitt Peak/Cerra Tololo MOSAIC cameras, following the informative reduction pipeline outlined by B. Jannuzi.[1] For the LFC images this necessitated first changing the data into the requisite format using the `LFCRED` package created by M. Hunt.[2]

[1] See `http://www.noao.edu/noao/noaodeep/ReductionOpt/frames.html`
[2] See `http://wopr.caltech.edu/~mph/lfcred`

4.2.1 Photometric Calibration

We relied on a variety of methods to provide photometric calibration of the data, depending upon the conditions under which data for a SEXSI field were taken. Throughout, unless otherwise noted, we refer our magnitudes to the Vega-based system. If conditions were photometric, we determined magnitude zeropoints from Landolt (1992) fields observed the same night, at an airmass close to that of the field in question. In cases where a non-photometric image overlaps a photometric image from another night, we determined the zeropoint magnitude by matching the photometry of overlapping regions.

In cases where we obtained no photometric images of a field, we relied on shallow sky surveys to provide magnitude zeropoints. Where available, we used r' photometry from the SDSS first data release (Abazajian et al. 2003), converting from AB magnitudes to Vega magnitudes with

$$r'(\mathrm{Vega}) = r'(\mathrm{AB}) - 0.17. \tag{4.1}$$

Alternatively, we used the USNO-B1.0 catalog (Monet et al. 2003) to establish the zeropoint. Typical photometric calibration errors for this technique were 0.2 mag.

For the purposes of this paper, we make the assumption that the SDSS r' and Johnson-Cousins R filters are similar. Convolving the respective filter transmission curves with the Vanden Berk et al. (2001) composite SDSS quasar spectrum redshifted from $z = 0$ to $z = 3$, we find that this assumption provides a $\lesssim 0.1$ mag systematic uncertainty in our photometry. Performing the same exercise on the Kinney et al. (1996) composite galaxy templates, we find systematic offsets $\lesssim 0.2$ mag for $z = 0$, with larger systematic offsets at higher redshifts. For example, the S0 composite template at $z = 1$ has a 0.39 mag difference between the r' and R Vega magnitudes due to the 4000 Å break redshifting out of the r' filter. Though imprecise, our assumption that the r' and R filters are similar is adequate to establish the faint source limit of each image, and to plan spectroscopic observing runs.

4.2.2 Source Extraction and Limiting Magnitudes

For extraction of sources from our combined, calibrated optical images, we used the SExtractor code of Bertin & Arnouts (1996) to generate catalogs for both the full optical images and for the smaller, central portions of each image. Because they avoid the CCD edges where the increased noise leads to spurious sources, these latter catalogs are used to derive

photometric depths. Quoted magnitudes refer to the SExtractor MAGBEST, which usually reports photometry within elliptical apertures (Kron 1980), but reverts to a corrected isophotal magnitude if a source is strongly contaminated by nearby sources.

To determine limiting magnitudes for each image, we made histograms of the R-band source density in 0.5 magnitude bins. Figure 4.1 shows an example histogram from SEXSI field Q2345. For each SEXSI field image, we compare the measured number counts N to that derived by Capak et al. (2004) from deep Subaru imaging of the *Hubble* Deep Field-North:

$$N = B\ 10^{A*(\text{AB Magnitude})}, \tag{4.2}$$

where N has units of number degree^{-2} 0.5 mag^{-1}. For R-band magnitudes in the range $20.0 - 25.0$, Capak et al. (2004) finds $A = 0.361$ and $\log B = -4.36$. Converting our R-band photometry into the AB system with Equation 4.1, we plot our measured number counts for each image with the published, deep-field fit (see Figure 4.1). In order to derive a crude depth for our images, we compare our number counts in each 0.5 mag bin to Equation 4.2 (at bin center). Limiting magnitudes are defined by the inter-bin flux where our number counts go from greater than 80% to less than 80% of the Capak et al. (2004) value: this provides an $\sim$ 80% completeness depth for each image. By the nature of our algorithm, then, these limits are good to ~ 0.5 mag.

Table 4.2 summarizes the R-band optical imaging we have obtained for the SEXSI fields. The average X-ray to optical offsets, $\langle \Delta\alpha_{\rm xo} \rangle$ and $\langle \Delta\delta_{\rm xo} \rangle$, are discussed in § 4.3 below. We derived R-band Galactic extinction for the central position of each X-ray image using the NED Galactic extinction calculator.[3] Checking the variance of the NED extinction values across the *Chandra* field of view, we find that the typical error on the extinction is ≈ 0.02 mag. Three of our fields, however, have significantly higher extinctions than the other fields, and thus have an uncertainty of ± 0.2 mag in their extinction values for individual sources. These fields are flagged in Table 4.2.

Approximately half of the SEXSI fields were observed with a single, uniform depth image; the other half rely on imaging from multiple cameras and telescopes over several observing runs. Of the fifteen fields with a single optical image, six reach R-band depths of ≥ 24.0, and ten reach R-band depths of ≥ 23.2. The shallowest field, CL 0442+0202, only

[3] See `http://ned.ipac.caltech.edu/forms/calculator.html`

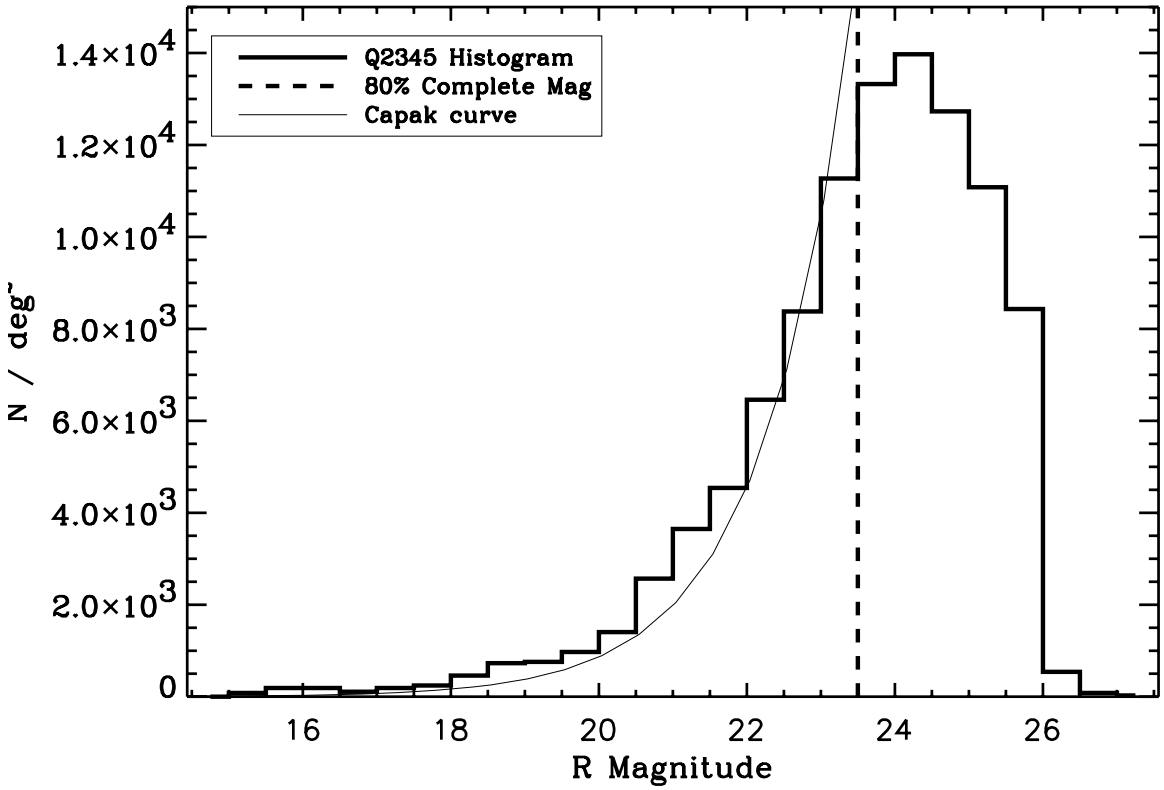

Figure 4.1 Example of R-band number counts for a typical SEXSI image: the Q2345 number counts from our MDM 2.4-meter/8K image is shown as a thick, solid histogram. The Capak et al. (2004) fit to deep imaging number counts is shown as a thin, solid line. Our 80% completeness limit (vertical dashed line) determination is described in § 4.2.2

Table 4.2. Summary of optical imaging for each of the 27 SEXSI fields

Target	X-ray Exp [ks]	$\langle\Delta\alpha_{xo}\rangle$ [″]	$\langle\Delta\delta_{xo}\rangle$ [″]	extinction[a] [R Mag]	Optical Images RA (J2000)	DEC (J2000)	Camera	R limit[b] [Mag]	Seeing [″]
NGC 891	51	-0.9 ± 0.3	0.6 ± 0.2	0.17	02 22 40	+42 26 16	8K	24.3	1.6
AWM 7	48	0.5 ± 0.3	0.2 ± 0.1	0.30	02 54 45	+41 40 10	8K	24.2[c]	1.7
XRF 011130	30	0.4 ± 0.2	-0.5 ± 0.2	0.26	03 05 28	+03 48 52	LFC	23.2[d]	1.2
NGC 1569	97	-0.3 ± 0.2	0.6 ± 0.3	2.00[e]	04 29 08	+64 45 42	Echelle (1.3)	21.5	1.7
					04 29 42	+64 42 35	LRIS	21.5	0.9
					04 29 53	+64 39 47	CCD13	21.0	1.4
					04 30 36	+64 51 06	LRIS	23.0	1.2
					04 31 15	+64 51 06	LRIS	22.5	0.9
3C 123	47	-0.1 ± 0.1	0.0 ± 0.0	2.61[e]	04 36 52	+29 40 08	8K	21.9	1.4
CL 0442+0202[f]	44	-0.2 ± 0.2	-1.2 ± 0.3	0.41	04 42 17	+02 03 35	LFC	21.1[d]	1.2
CL 0848+4454	186	-0.3 ± 0.1	-1.2 ± 0.1	0.08	04 48 49	+44 54 09	LFC	24.4[d]	1.1
RX J0910	171	-0.3 ± 0.1	-2.3 ± 0.2	0.05	09 10 33	+54 19 38	8K	24.0	1.6
1156+295	49	-0.5 ± 0.2	-1.1 ± 0.3	0.05	11 59 32	+29 16 19	8K	24.5	1.5
NGC 4244	49	-0.2 ± 0.2	0.0 ± 0.1	0.06	12 16 46	+37 51 46	CCD13	22.9[d]	1.8
					12 17 34	+37 46 54	Echelle (1.3)	23.4[d]	1.8
					12 17 54	+37 55 15	CCD13	23.4[d]	1.5
NGC 4631	59	0.4 ± 0.3	-0.3 ± 0.2	0.05	12 41 29	+32 36 46	CCD13	23.0[d]	1.6
					12 41 39	+32 30 44	CCD13	23.0[d]	2.5
					12 42 03	+32 40 53	Echelle (2.4)	23.0[d]	1.2
					12 42 21	+32 37 09	CCD13	23.0[d]	1.7
					12 42 59	+32 32 49	Templeton	23.0[d]	1.4
HCG 62	49	0.1 ± 0.1	-0.1 ± 0.1	0.13	12 53 04	−09 14 20	Echelle (2.4)	22.4[d]	1.2
					12 53 06	−09 05 48	Echelle (2.4)	23.4[d]	1.0
					12 53 04	−09 14 20	CCD13	22.4[d]	1.6
RX J1317	111	-1.6 ± 0.2	-1.6 ± 0.2	0.03	13 17 13	+29 11 32	LFC	23.5[d]	1.5
BD 1338	38	-1.3 ± 0.2	-1.1 ± 0.1	0.04	13 37 44	+29 25 24	CCD13	22.5	1.3
					13 37 53	+29 29 44	CCD13	22.5	1.7
					13 38 15	+29 36 51	CCD13	22.5	2.0
					13 38 26	+29 24 53	CCD13	22.5	1.5
RX J1350	58	0.7 ± 0.3	-2.5 ± 0.5	0.03	13 50 39	+60 04 11	LFC	22.5[g]	0.9
3C 295	23	0.2 ± 0.2	-0.3 ± 0.3	0.05	14 11 01	+52 21 18	CCD13	22.5[d]	2.2
					14 11 24	+52 13 36	CCD13	21.5[d]	2.8
					14 11 46	+52 05 42	CCD13	22.0[d]	2.3
GRB 010222	18	-0.6 ± 0.2	0.1 ± 0.1	0.06	14 51 59	+43 08 54	CCD13	21.9	2.1
					14 52 13	+43 01 06	CCD13	22.9	1.4
					14 52 43	+42 55 12	CCD13	22.4	1.6
					14 52 59	+43 06 07	CCD13	22.9	1.3
QSO 1508	89	-0.6 ± 0.2	-0.2 ± 0.1	0.03	15 09 50	+57 04 16	LFC	24.0[g]	1.2
MKW 3S	57	-0.8 ± 0.1	0.1 ± 0.1	0.09	15 21 30	+07 47 43	CCD13	23.4	1.2
					15 21 37	+07 39 08	CCD13	22.9	1.1
					15 22 12	+07 48 36	CCD13	22.9	1.3
					15 22 13	+07 47 21	CCD13	22.9	1.6
MS 1621	30	-1.2 ± 0.1	0.3 ± 0.2	0.09	16 23 06	+26 36 33	CCD13	22.4	2.3
					16 23 13	+26 30 22	Cosmic	24.4	1.4
					16 23 26	+26 38 28	Cosmic	23.9	1.6
					16 23 42	+26 43 49	CCD13	22.9	2.3
					16 24 03	+26 35 32	Cosmic	23.9	1.2
GRB 000926	32	-0.7 ± 0.2	-0.6 ± 0.3	0.08	17 03 19	+51 47 58	8K	22.9	1.2
RX J1716	52	-0.5 ± 0.1	1.2 ± 0.1	0.09	17 15 36	+67 19 45	CCD13	22.4	1.7
					17 15 55	+67 05 59	Cosmic	24.4	1.3
					17 16 39	+67 13 27	Cosmic	23.9	1.4
					17 17 11	+67 01 40	Cosmic	24.4	1.2
					17 17 42	+67 12 36	CCD13	22.9	1.3
					17 17 56	+67 09 08	Cosmic	23.9	1.6
					17 18 04	+67 12 01	CCD13	22.4	2.2
NGC 6543	46	-0.5 ± 0.2	-0.2 ± 0.1	0.12	17 57 44	+66 44 40	CCD13	22.9	1.3
					17 58 31	+66 34 02	CCD13	22.9	1.4
					18 00 25	+66 30 52	CCD13	22.9	1.2
XRF 011030	47	-0.2 ± 0.2	-0.4 ± 0.2	1.09[e]	20 44 02	+77 21 06	LFC	21.4[d]	2.2
MS 2053	44	-1.1 ± 0.1	0.4 ± 0.1	0.22	20 55 48	−04 31 10	CCD13	22.8	1.7
					20 55 59	−04 35 47	Cosmic	23.8	1.4
					20 56 09	−04 44 01	Cosmic	23.8	1.4
					20 56 30	−04 38 17	LRIS	23.8	1.0
					20 56 33	−04 30 53	CCD13	22.3	2.1
					20 56 42	−04 41 28	Cosmic	23.8	1.2
RX J2247	49	-0.8 ± 0.1	1.0 ± 0.1	0.15	22 47 21	+03 39 25	8K	23.4	1.7
Q2345	74	0.0 ± 0.1	-0.3 ± 0.2	0.07	23 48 25	+01 01 12	8K	23.4[d]	1.5

[a] Error on Galactic R-band extinction is ~ 0.02, with exceptions noted. This error is generally an order of magnitude smaller than the error on the zeropoint magnitude

[b] Image R-band limits are Galactic extinction subtracted and correct to within 0.5 mag

[c] Limiting magnitude estimated from visual inspection; the nearby cluster sources skew the R-band number counts distribution and gave an unreasonable limiting magnitude from our automated algorithm

[d] Zeropoint derived using USNO-B1.0 catalog. No SDSS coverage available

[e] Error on Galactic R-band extinction is ~ 0.2

[f] In Paper I, Table 2, CL 0442+0202 was erroneously referred to as "CL 0442+2200"

[g] Zeropoint derived using SDSS 1st data release

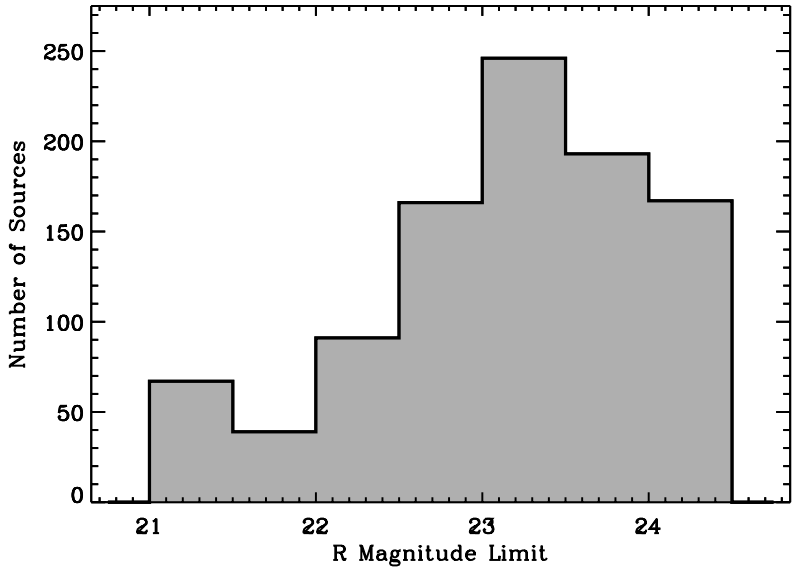

Figure 4.2 Histogram of limiting optical magnitudes for all SEXSI sources with optical coverage, excluding sources with non-detections where the background is contaminated by a nearby bright source (optflag = 6, see § 4.4). Most sources have limiting magnitudes of at least $R = 23$

reaches $R = 21.1$, while the deepest field, CL 0848+4454, reaches $R = 24.4$. Of the twelve fields with imaging from multiple pointings, eight have sections reaching depths of at least $R = 23.0$. A histogram of imaging depth for each source is shown in Figure 4.2.

4.3 Optical Counterparts to X-Ray Sources

We match X-ray and optical sources in several steps. The procedure is slightly different depending on whether there is one optical image or multiple optical images per *Chandra* field.

For fields with a single optical image, we first identify the closest optical source within $4''$ of each *Chandra* source position. Excluding sources displaced by more than 1.5σ from the mean offset, we use these identifications to calculate a first estimate of the average offset between the *Chandra* and USNO astrometry. For the following iterations, the search radius used to identify optical counterparts depends upon the off-axis angle (OAA) of the X-ray source: we use the larger of $1.5''$ and PSF/3, where PSF is the full width, half maximum of the *Chandra* point spread function at each OAA. Again, we exclude sources displaced by more than 1.5σ from the mean as we iteratively correct the X-ray source positions. We continue iterating until the corrections to the offsets are less than the corresponding

standard deviation. Two to three iterations are typically required, with the biggest shift applied after the initial matching. As shown in Table 2, the typical standard deviation on this astrometric correction is $\lesssim 0.3''$, comparable to the accuracy of the optical astrometry.

For fields with multiple optical images we modify this algorithm slightly. Some images cover an area with few (or one) X-ray sources, which, if we were to follow the procedure described above, could lead to incorrect offsets and matches. Instead, for a given *Chandra* field, we first take each optical image and find the closest match within a $4''$ radius of all *Chandra* source positions that fall within the image. We record these astrometric differences. For X-ray sources falling on multiple optical images, we use the data from the image with the deepest limiting magnitude. As before, we use this list of multi-image astrometric differences to calculate an average *Chandra* to USNO offset, again eliminating sources greater than 1.5σ from the mean offset. This astrometric correction is then applied to all *Chandra* positions for the SEXSI field considered. A second pass at optical identifications is then made with the OAA-dependent matching radius, using the larger of $1.5''$ and PSF/3. Of the 998 SEXSI sources with optical coverage, 655 used a $1.5''$ search radius, while 343 used the PSF/3 search radius.

We expect few false matches due to an optical source randomly overlapping the matching search area. The number of false matches per field depends upon both the number of X-ray sources detected in the *Chandra* field, and the depth of the optical image. We tested several fields from Table 4.2 for false matches by finding the total area covered by the $1.5''$ radius search circles and multiplying that area by the optical source density. We find that for medium-depth X-ray and optical images, the number of false sources detected per field is generally less than one. For example, we predict 0.6 false matches for Q2345, 0.7 false matches for CL 0442+0202, and 1.3 false matches for 1156+295, where these numbers are for the $1.5''$ search radius sources only. For the 34% of the sources with larger OAAs and thus larger search areas we expect a larger fraction of false matches, though still fewer than 3 per field for most fields. For example, we predict 1.3 false matches from the $> 1.5''$ match radius sources in Q2345, 1.4 false matches in CL 0442+0202, and 2.4 false matches in 1156+295. For several of the fields, including the three example fields just mentioned, we shifted all X-ray source positions by $1'$, producing a "fake" X-ray catalog, and ran the matching routine again with the average X-ray-to-optical offset forced to zero. This process, repeated with several different shifts of the X-ray source positions, gives a check

on the number of false detections predicted above. For all of the fields tested the number of false detections are consistent with the values we calculate. Our spectroscopic results are also consistent with this matching scheme and will be discussed further in Chapter 5.

Once matching is complete, we produce first-draft optical postage stamp cutouts for our entire hard X-ray catalog (see Figure 4.3). Each stamp is centered on the astrometrically corrected X-ray source position, and the size of the *Chandra* PSF-dependent search radius is shown by the (centered) solid circle. A dashed circle, located at the uncorrected *Chandra* position, illustrates the need for this offset correction. Arrows point to identified optical counterparts, while the absence of an arrow signals a non-detection. If the magnitude found by SExtractor is fainter than the limiting optical image, we annotate the photometry with an asterisk. As in Chapter 3, a "CL" flag is added if a source is potentially within 1 Mpc of a target cluster center.

Next we visually inspect postage stamps for each X-ray source, flagging sources with potentially inaccurate photometry as required. These flags, detailed in § 4.4, identify sources which either (1) have multiple optical identifications within the PSF-dependent search area, or (2) are, or are near, a saturated source in our optical image. A final matching iteration is then done, excluding the newly flagged sources. We produce new optical catalogs and postage stamp cutouts, omitting stamps for the handful of saturated sources where counterpart magnitudes are drawn from the literature and the 65 SEXSI sources that either lack optical coverage in our data or have an unknown limiting magnitude due to nearby bright-source contamination (optical flag = 6, see § 4.4). An example of six postage stamp cutouts is included as Figure 4.3; the entire catalog of postage stamps is provided in the online version of the manuscript.

For the 262 sources with $22 < R_{\rm limit} \leq 23$, 160 (61%) have identified counterparts, while for the 434 sources with $23 < R_{\rm limit} \leq 24$, 291 (67%) have identified counterparts, and for the 167 sources with $R_{\rm limit} > 24$, 124 (74%) have identified counterparts. Our total sample of 947 sources with unambiguous photometry (no contamination) identifies 603 counterparts (64%).

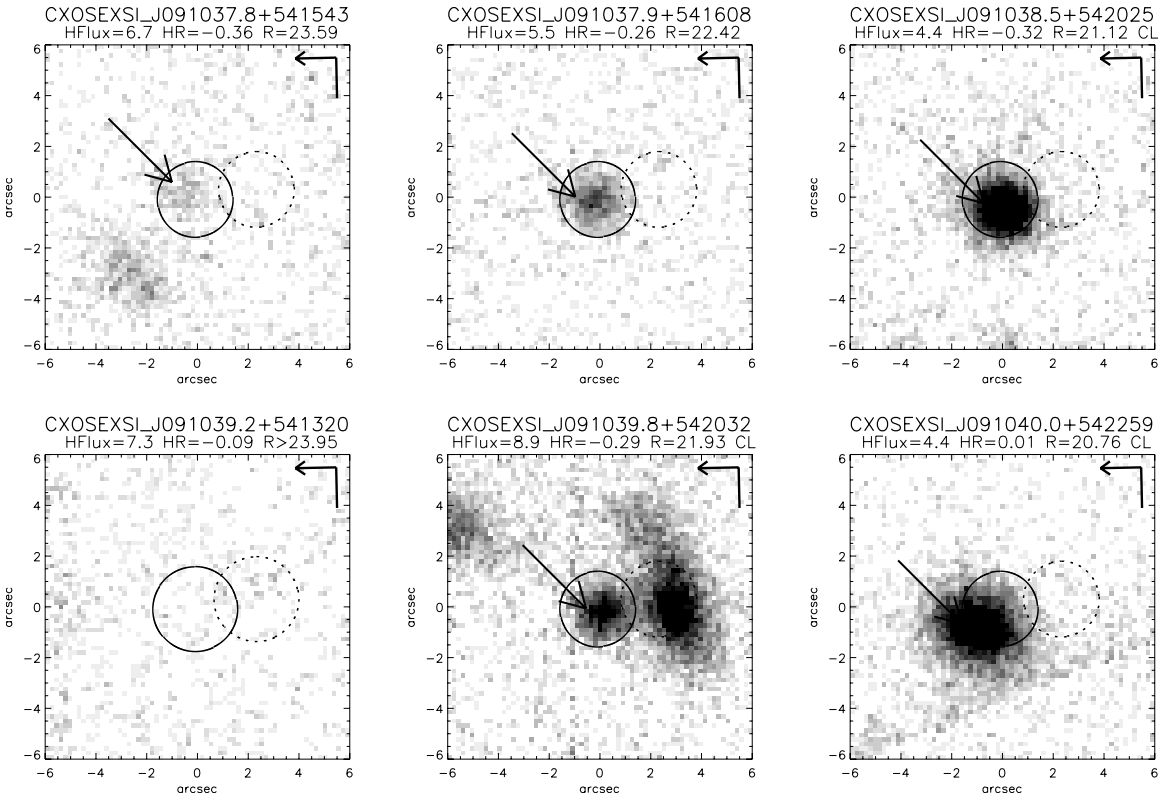

Figure 4.3 Example of the R-band postage stamp cutout images. Cutouts for the full catalog of hard-band SEXSI sources with optical follow-up are presented in the online version of Eckart et al. (2005) in Figures 3b – 3do; we show representative images from the RX J0910 field here. Images are centered at the astrometrically-corrected *Chandra* source positions, and the image orientation is shown in the upper right corners (North has the arrowhead, East lacks an arrowhead). The dashed circles are centered on the original X-ray-derived source positions, while the solid circles show X-ray source positions corrected for the *Chandra* pointing error; circle radii are a function of X-ray off-axis angle as described in the text. Arrows point to the optical counterpart if one is present. Text above each cutout identifies the source and labels its 2 – 10 keV flux (in units of 10^{-15} erg cm^{-2} s^{-1}), hardness ratio HR (defined in § 4.4), and R-band magnitude or the limit thereto. Flags on the R-band photometry are also presented, though no flagged sources are shown in the example figure. A dagger (†) indicates that the counterpart is near a bright source, affecting the R-magnitude, a double-dagger (‡) flags cases where there is more than one optical source within the search area, and an asterisk ($*$) indicates that the R-band magnitude is higher than the limiting magnitude of the image. Additionally, CL denotes a source potentially falling within 1 Mpc of a target cluster center (see § 4.3)

4.4 The Catalog

In Table 4.3 we present the catalog of 1034 hard-band SEXSI sources – the table is published in its entirety in the electronic version of the *Astrophysical Journal*. Columns 1 – 7 present X-ray source information for easy reference, while the optical photometric data are presented in columns 8 – 15. Complete X-ray source information is presented in Chapter 3, Table 4. The X-ray source positions in Table 4.3 are corrected for mean optical to X-ray offsets. Note that since the source names (column 1), identical to the source names in Chapter 3, are derived from the hard-band X-ray images, the refined positions of columns 2 – 3 will not exactly match those of column 1 (though mean offsets are typically less than $1''$). Column 4 lists the off-axis angle (OAA, i.e., the angular distance, in arcmin, of the source position from the telescope aim point). The 2 – 10 keV flux (in units of 10^{-15} erg cm^{-2} s^{-1}) and detection SNR are shown in columns 5 – 6, while column 7 gives the hardness ratio, $HR = (H - S)/(H + S)$, where H and S are the counts cm^{-2} in the 2 – 10 keV and 0.5 – 2 keV bands, respectively. Here, as distinct from Paper I, we record the hardness ratio derived from the net soft X-ray counts recorded at the hard-band source position when there was not a significant soft-band source detected (in Paper I these cases are reported as $HR = 1.0$). In addition, for a subset of these cases, when the soft-band counts recorded at the hard-band source position were less than twice the soft-band background counts, the HR is considered a lower limit, flagged as such in the catalog, and set to $HR = (H - S_{\rm limit})/(H + S_{\rm limit})$, where $S_{\rm limit} = 2 \times$ soft-band background counts.

Column 8 contains an optical flag code essential to interpretation of the optical data: 0 = no optical coverage, 1 = a solid optical ID, 2 = no optical counterpart (the magnitude listed is then a lower limit), 3 = saturated in the SEXSI optical image (R-band magnitude taken from the Guide Star Catalog II (McLean et al. 2000) or a secondary source in VIZIER database), 4 = a solid ID but R-band magnitude affected by nearby bright source, 5 = more than one optical source in X-ray error circle (the source with the smallest positional offset is recorded in the table), and 6 = lower limit (no optical counterpart) but area contaminated by nearby bright source so limiting magnitude is unknown. Column 9 is the R-band magnitude of the optical counterpart, with its error shown in column 10. Column 11 gives the limiting magnitude for the image from which the optical counterpart, or a lower limit thereto, was derived. Column 12 lists $\Delta\alpha \equiv \alpha_{\rm x} - \alpha_{\rm o}$ in arcsec, where $\alpha_{\rm x}$ is the astrometrically corrected

Table 4.3. SEXSI optical counterpart catalog (SEXSI II catalog)

CXOSEXSI_	X-ray Data							Optical Counterpart Data							
				2 – 10 keV											
	α_x (J2000)	δ_x (J2000)	OAA	Flux	SNR	HR	Flag	R	σ_R	R_{limit}	$\Delta\alpha$	$\Delta\delta$	Δr	$\log \frac{f_x}{f_o}$	Stel.
(1)	(2)[a]	(3)[a]	(4)	(5)	(6)	(7)[b]	(8)[c]	(9)	(10)	(11)	(12)	(13)	(14)	(15)	(16)
J022142.6+422654	02 21 42.75	+42 26 53.5	9.49	23.10	2.83	-0.33	1	18.73	0.16	24.3	1.0	1.8	2.1	-0.64	0.66
J022143.6+421631	02 21 43.72	+42 16 31.0	8.33	74.80	8.81	-0.28	6	...	...	...	...	...	...	...	...
J022151.6+422319	02 21 51.76	+42 23 18.7	6.17	6.55	2.06	-0.16	2	24.3	...	24.3	...	...	...	1.04	...
J022204.9+422338	02 22 05.08	+42 23 37.7	4.24	8.73	2.74	0.84[d]	1	20.37	0.16	24.3	-0.2	0.5	0.5	-0.41	0.02
J022205.1+422213	02 22 05.21	+42 22 12.7	3.45	6.82	2.38	0.07	2	24.3	...	24.3	...	...	...	1.07	...
J022207.1+422918	02 22 07.19	+42 29 18.2	8.93	18.90	3.84	-0.33	1	21.56	0.16	24.3	2.3	-0.8	2.4	0.40	0.96
J022210.0+422956	02 22 10.08	+42 29 55.7	9.38	17.30	3.52	-0.62	1	18.88	0.16	24.3	0.2	-0.6	0.6	-0.71	0.03
J022210.8+422016	02 22 10.93	+42 20 16.1	2.17	3.63	1.53	-0.46	1	21.57	0.17	24.3	0.6	-0.4	0.8	-0.31	0.95
J022211.7+421910	02 22 11.79	+42 19 10.1	2.55	6.87	2.36	0.14	6	...	...	...	...	...	...	...	...
J022215.0+422341	02 22 15.12	+42 23 41.0	3.15	15.40	3.88	-0.41	1	22.52	0.18	24.3	0.1	0.0	0.1	0.70	0.64
J022215.1+422045	02 22 15.19	+42 20 44.5	1.32	42.90	7.49	-0.42	1	17.33	0.16	24.3	-0.3	0.1	0.3	-0.94	0.03
J022215.5+421842	02 22 15.63	+42 18 41.7	2.46	6.79	2.34	0.28	1	20.33	0.16	24.3	-0.4	0.1	0.4	-0.54	0.03
J022219.3+422052	02 22 19.40	+42 20 51.6	0.54	6.38	2.31	0.37	1	23.82	0.22	24.3	-0.9	0.6	1.1	0.83	0.38
J022224.3+422138	02 22 24.45	+42 21 38.4	0.91	64.60	8.92	-0.44	1	17.41	0.16	24.3	0.0	0.0	0.0	-0.73	0.98
J022225.2+422451	02 22 25.33	+42 24 50.9	4.07	128.00	12.99	-0.34	1	19.31	0.16	24.3	0.1	0.2	0.2	0.33	0.98
J022226.5+422154	02 22 26.63	+42 21 54.4	1.35	6.48	2.32	-0.35	2	24.3	...	24.3	...	...	...	1.04	...
J022232.5+423015	02 22 32.61	+42 30 14.6	9.61	53.60	6.50	0.12	1	20.88	0.16	24.3	0.4	0.4	0.5	0.58	0.77
J022236.3+421730	02 22 36.45	+42 17 30.2	4.23	12.00	3.30	0.01	1	22.38	0.18	24.3	0.3	-0.9	1.0	0.53	0.42
J022236.7+422858	02 22 36.88	+42 28 57.7	8.57	12.90	3.00	-0.68	1	22.05	0.17	24.3	-1.5	2.1	2.6	0.43	0.81
J022259.1+422434	02 22 59.18	+42 24 33.6	7.77	32.50	5.43	0.49	2	24.3	...	24.3	...	...	...	1.74	...
J022334.0+422212	02 23 34.13	+42 22 11.6	13.34	37.50	4.47	0.15	2	24.3	...	24.3	...	...	...	1.81	...

Note. — Table 4.3 is published in its entirety in the electronic version of the *Astrophysical Journal*. A portion is shown here for guidance regarding its form and content

[a] X-ray positions are corrected for average X-ray to optical offset (to correct *Chandra* astrometry)

[b] Note that the HRs presented here for sources with soft-band counts that did not meet our detection criteria are calculated differently than they were in Paper I. Please see §4.4 for detail

[c] See §4.4 for details of the flag code. Briefly: 0 = no optical coverage, 1 = solid optical ID, 2 = upper limit, 3 = saturated in SEXSI optical image; R-band magnitude taken from the Guide Star Catalog II (McLean et al. 2000), 4 = solid ID but R-band magnitude affected by nearby bright source, 5 = more than one optical source consistent with the X-ray source position, 6 = upper limit (no optical counterpart) but area contaminated by nearby bright source so limiting magnitude is unknown

[d] HR is lower limit

[e] Source falls within an area potentially less than 1 Mpc from a target cluster center. Source was not used for 2 – 10 keV $\log N - \log S$ calculation in Paper 1

X-ray source RA (from column 2) and α_o is the optical counterpart RA; column 13 is the corresponding value for declination. Column 14, Δr ($\equiv \sqrt{\Delta\alpha^2 + \Delta\delta^2}$), is the X-ray to optical position difference, also in arcsec. Following Hornschemeier et al. (2001) and Stern et al. (2002b), the logarithmic X-ray-to-optical flux ratio (column 15) is given by the relation

$$\log (f_x/f_o) = \log f_x + (R/2.5) + 5.50, \tag{4.3}$$

derived from the Kron-Cousins R-band filter transmission function.

Column 16 presents the SExtractor CLASS_STAR parameter (Bertin & Arnouts 1996) for basic star-galaxy separation, with values ranging from 0.0 for significantly extended sources to 1.0 for sources consistent with perfectly stellar PSFs. The stellarity value of the 8 bright sources with optflag = 3 (from the literature) is set to 1.00. We present the stellarity data with the caveat that the values should only be used for broad separation, for example, of sources near 0 verses 1, but not for detailed quantitative analysis.

Note that for all of the optical counterpart data columns, special attention must be paid to the optical flag. For example, if the code is a 2 (optical counterpart is not detected), column 9 describes a lower limit, columns 10, 12 – 14, and 16 have no data, and the X-ray-to-optical flux ratio in column 15 is a lower limit.

4.5 Discussion

We now discuss the results of the optical identifications of the hard X-ray source counterparts and how the counterpart properties relate to the X-ray properties. Throughout this section, only sources with a solid optical counterpart or upper limit thereto are plotted and analyzed; we exclude sources with R-band magnitudes or limits contaminated by a nearby bright source and sources with more than one optical source within the identification radius. This provides a sample of 947 hard X-ray sources with unambiguous counterpart photometry, of which 603 are identifications and 344 have limits to the counterpart optical magnitude.

Figure 4.4 presents the R-band magnitudes, or limits thereto, plotted as a function of 2 – 10 keV X-ray flux. Dashed lines show constant X-ray-to-optical flux ratios. The bulk of the SEXSI sources have $-1 < \log(f_x/f_o) < 1$ and are fainter than $R = 20$. Shallow, wide-area X-ray surveys, such as the *ASCA* hard X-ray survey reported by Akiyama et al. (2000), find

that the majority of extremely bright X-ray sources ($S_{2-10\ \mathrm{keV}} \gtrsim 10^{-13}\,\mathrm{erg\ cm^{-2}\ s^{-1}}$) are AGN and have $-1 < \log(f_\mathrm{x}/f_\mathrm{o}) < 1$. Many of the SEXSI sources are likely fainter and/or more distant analogs.

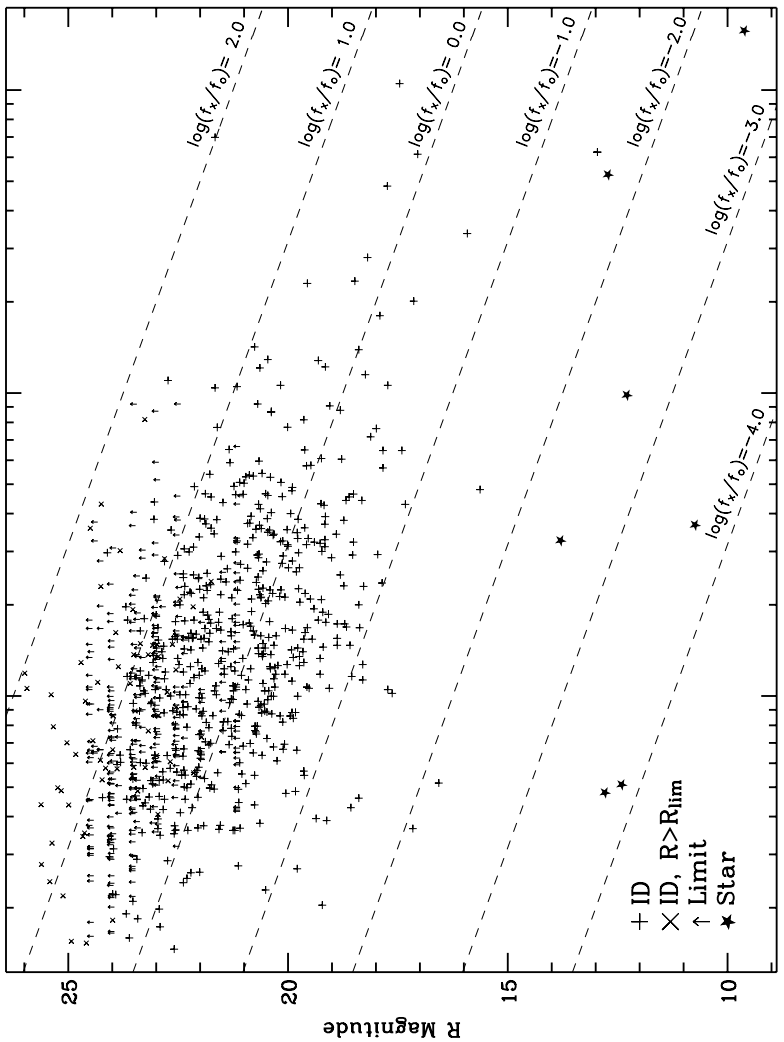

Figure 4.4 Optical magnitude of SEXSI sources, plotted as a function of their hard-band (2 – 10 keV) X-ray flux. Dashed, angled lines show constant $\log(f_x/f_o)$. Plus signs show sources with optical counterparts, crosses are sources with a SExtractor ID but where $R > R_{\rm limit}$, while arrows denote sources lacking counterparts to the image R-band limit. Star symbols show SEXSI sources identified as stars in the literature (only sources with $\log(f_x/f_o) < -1$ were checked)

As has been found in other surveys (e.g., Hornschemeier et al. 2001; Stern et al. 2002b), SEXSI detects a population of sources overluminous in the X-ray for their optical magnitudes. This population is found over the entire X-ray flux range sampled. Two explanations have been commonly discussed to explain large values of $\log(f_{\rm x}/f_{\rm o})$: (i) extremely high-redshift AGNs that might have bright X-ray fluxes but faint R-band fluxes due to absorption from the Lyman transitions of hydrogen along our line of sight, or (ii) heavy obscuration by material in the host galaxy. The latter interpretation for the majority of sources is supported by near-IR studies, which find a large fraction to be very red early-type galaxies at $z \sim 1$ (Mignoli et al. 2004). In addition, a number of *Type II quasars*, which would have similar properties, have been identified in the deepest *Chandra* surveys (e.g., Norman et al. 2002; Stern et al. 2002a; Dawson et al. 2003).

By virtue of the large area surveyed, SEXSI contains numerous sources with $\log(f_{\rm x}/f_{\rm o}) > 1.0$ at moderate X-ray fluxes, $S_{2-10\ {\rm keV}} \gtrsim 10^{-14}$ erg cm^{-2} s^{-1}. Many of these sources have $R \lesssim 24$, well within the reach of 8- to 10-meter class telescopes for spectroscopic follow-up. These are brighter examples of the new X-ray overluminous population. Deep Survey versions of these sources are typically extremely faint — as an example, Koekemoer et al. (2004) report on seven "extreme X-ray/optical" (EXO) sources in the 2 Msec *Chandra* Deep Field-North (CDF-N) which, despite having extremely robust detections in the *Chandra* data (25−89 counts), remain undetected ($z_{850} > 27.9, 3\sigma$) in the Great Observatories Origins Deep Survey imaging of the CDF-N (Giavalisco et al. 2004). Fiore et al. (2003) report on the spectra of 13 sources with $\log(f_{\rm x}/f_{\rm o}) > 1$ from the HELLAS2XMM survey. They find 8 narrow-lined sources, with $L_{\rm x} > 10^{44}$ erg s^{-1}. Our survey contains 109 such sources with $\log(f_{\rm x}/f_{\rm o}) > 1$ of which 64 have an optical limiting magnitude and $\gtrsim 20$ have spectral data. These high $f_{\rm x}/f_{\rm o}$ sources provide a useful catalog for future infrared surveys.

We also find a number of sources with very bright ($R < 14$) optical counterparts. The bulk of these sources (7 out of 8) are identified as stars in the literature.

Figure 4.5 presents a histogram of the number of sources in SEXSI and in the CDF-N (Alexander et al. 2003; Barger et al. 2003) as a function of hard X-ray flux and split by R-band magnitude at $R = 22$. This magnitude was chosen to separate our sources approximately in half. The small number of sources from images with $R_{\rm limit} < 22$ were not included in this plot or in Figures 4.6, 4.7, and 4.8. The majority of the SEXSI sources have $S_{2-10\ {\rm keV}} \approx 10^{-14}$ erg cm^{-2} s^{-1}, a flux level that lies between the *ASCA* and

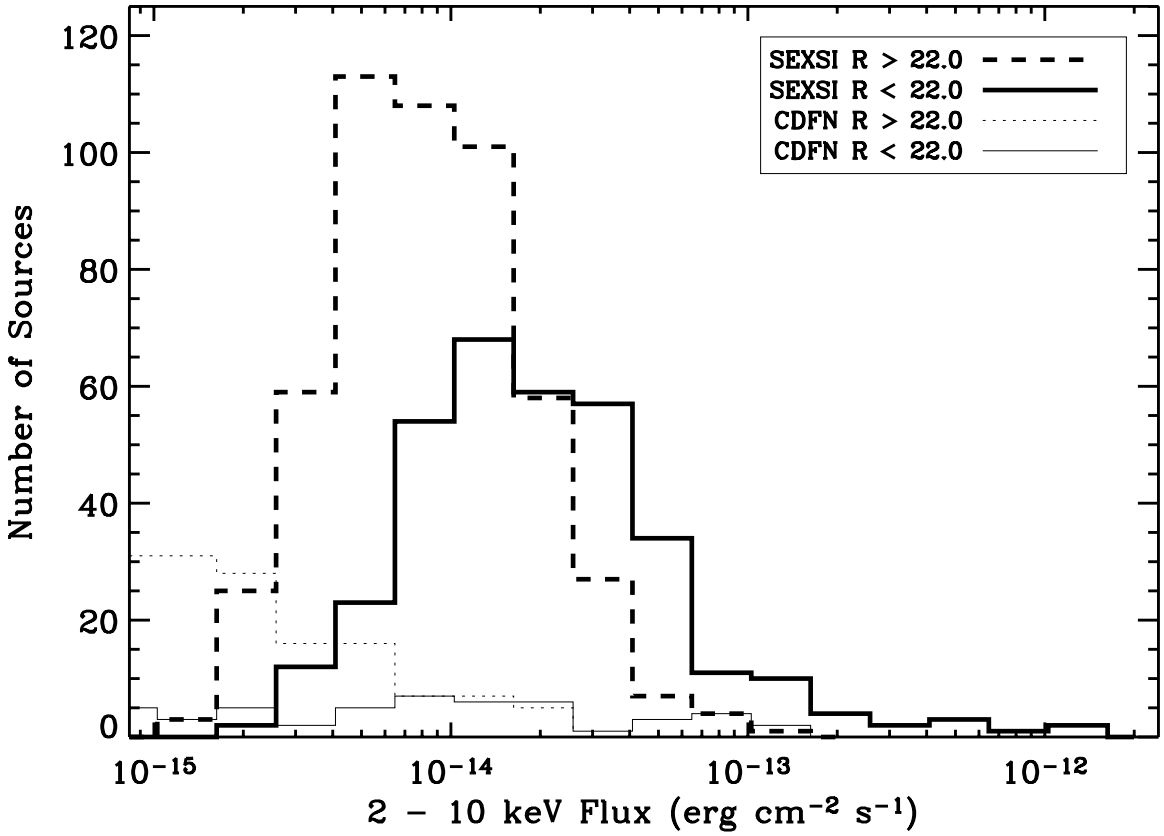

Figure 4.5 Histogram of 2 – 10 keV fluxes, split by optical counterpart R-band magnitude. Heavy lines show SEXSI sources; lighter lines show sources from the CDF-N (Alexander et al. 2003; Barger et al. 2003). For both, solid lines refer to optically brighter sources ($R < 22.0$), while dashed lines refer to optically fainter sources ($R > 22.0$). CDF-N X-ray fluxes have been converted from the published 2 – 8 keV values to the 2 – 10 keV fluxes plotted here. This involved converting X-ray photon indices Γ from the individually-derived indices used in the CDF-N X-ray catalog (Alexander et al. 2003) to the average $\Gamma = 1.5$ adopted by the SEXSI project. In addition, the sources with $R_{\rm limit} < 22.0$ were excluded from the plot

BeppoSAX sensitivity limits and the *Chandra* Deep Survey capability. This important flux range corresponds to the regime in which the $\log N - \log S$ relation changes slope and from which the bulk of the 2 – 10 keV X-ray background arises (Cowie et al. 2002; Harrison et al. 2003). Compared to the Deep Surveys, SEXSI has nearly an order of magnitude more sources at this X-ray depth, approximately half of which have $R < 22$, making them easy spectroscopic targets for 8- to 10-meter class telescopes.

Figure 4.6 shows the hardness ratio histogram of the SEXSI sources, again split at $R = 22$. The optically brighter sources are peaked at a low hardness ratio, while the fainter sources have a much harder, and broader, distribution, showing that the optically fainter

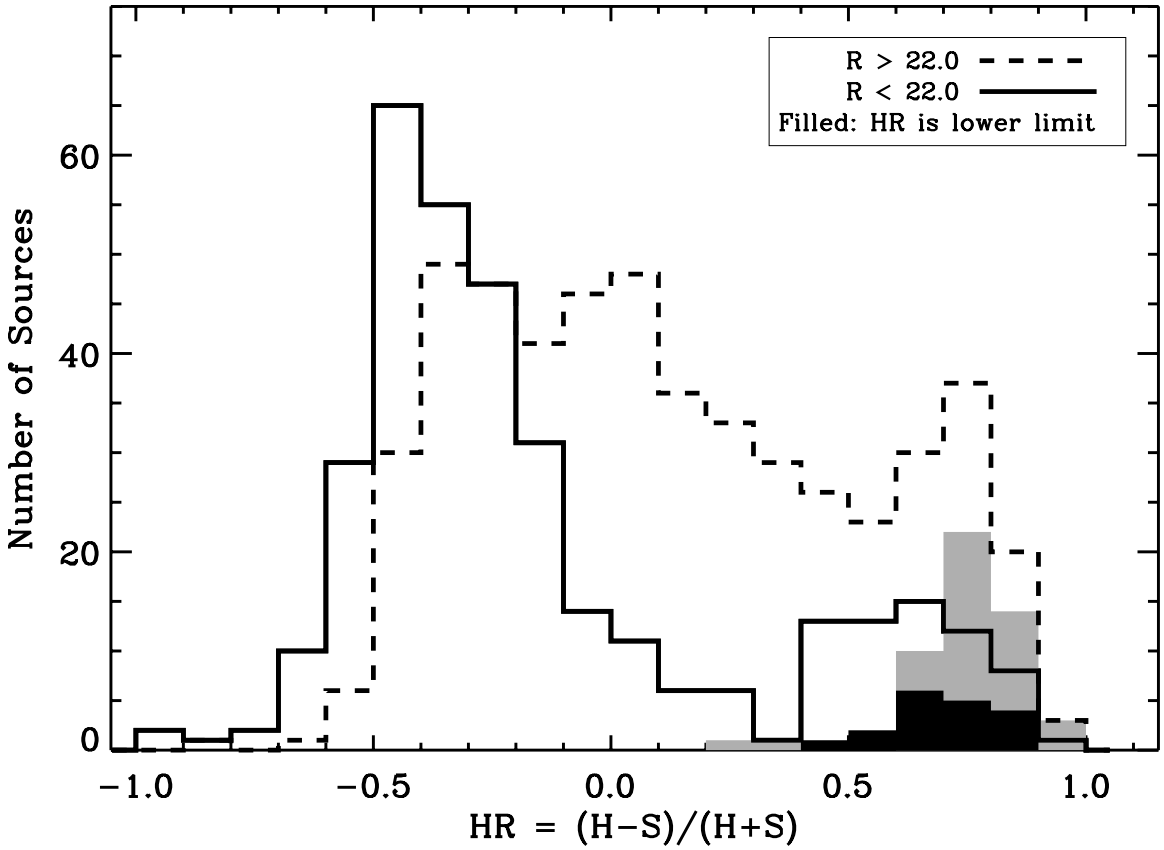

Figure 4.6 Histogram of X-ray hardness ratios (HR), split by optical counterpart R-band magnitude. The solid line shows optically-brighter ($R < 22.0$) sources, while the dashed line shows optically-fainter ($R > 22.0$) sources; objects with limiting HRs are included in these histograms, plotted at the limiting HR. The filled histograms present only the sources with limiting HR for $R > 22$ (gray) and $R < 22$ (black)

portion of the sample has a higher fraction of sources with a flat X-ray spectral slope. The large peak of the $R < 22$ sources is near $HR \sim -0.5$, which corresponds to a power-law photon index (Γ) between 1.8 and 1.9, a typical value for unobscured broad-lined AGN. This suggests that the majority of the optically brighter sources are broad-lined AGN. Spectroscopic followup (Chapter 5) will be able to specifically address this hypothesis. The harder and broader distribution of the $R > 22$ sources indicates that obscuration at the source is likely involved. Alexander et al. (2001) show a similar trend in the 1 Ms CDF-N data.

Figure 4.7, which displays the mean hardness ratio as a function of hard-band flux separately for bright and faint counterpart magnitudes, again emphasizes that distinct populations are contributing to the overall source counts. The mean values for this figure are

calculated using source HRs regardless of if they are flagged as lower limits. Setting all such flagged sources to the upper extreme, $HR = 1$, shifts the points only slightly, if at all. For reference, the HR of a $\Gamma = 1.9$ spectrum with varying intrinsic absorbing column density and redshift is presented in the adjacent panel. This shows that modest-redshift, heavily obscured sources produce the highest HRs. For sources fainter than $R = 22$, the mean hardness ratio is essentially constant at $HR = +0.15$ over two orders of magnitude in X-ray flux. For those sources with brighter magnitudes, however, there is a significant decline in mean hardness ratio, from $HR \sim -0.25$ at $f_{2-10\ \mathrm{keV}} \sim 10^{-13}$ erg cm^{-2} s^{-1} to $HR \sim -0.1$ at $f_{2-10\ \mathrm{keV}} \sim 10^{-15}$ erg cm^{-2} s^{-1}. In a simple-minded two-component model with median hardness ratios of -0.35 and $+0.2$ for the two source classes, the faint sources are dominated by the hard population with perhaps an admixture of 10% soft sources at all flux levels, while for the brighter sources, the ratio of hard to soft sources changes from 20:80 at $f_{2-10\ \mathrm{keV}} \sim 10^{-13}$ erg cm^{-2} s^{-1} to 80:20 at $f_{2-10\ \mathrm{keV}} \sim 10^{-15}$ erg cm^{-2} s^{-1}. This is qualitatively consistent with the $\log N - \log S$ relations derived in Chapter **??**, where we showed that hard sources follow a constant power law over three orders of magnitude in hard-band flux, while softer sources show a distinct break at $f_{2-10\ \mathrm{keV}} \sim 10^{-14}$ erg cm^{-2} s^{-1}. In this picture, the soft sources are the standard, largely unobscured AGN at all redshifts, while the harder component represents the lower mean-redshift, lower-luminosity populations revealed in the Deep Surveys (e.g., Tozzi et al. 2001; Barger et al. 2002).

Figure 4.8 shows the hardness ratio as a function of X-ray to optical flux ratio for the SEXSI sample, again with the HR of a $\Gamma = 1.9$ spectrum with varying intrinsic absorbing column density as a function of redshift presented in the adjacent panel. The main plot shows a trend toward larger hardness ratios as $f_{\mathrm{x}}/f_{\mathrm{o}}$ increases. This is in general consistent with the notion that the increasing $f_{\mathrm{x}}/f_{\mathrm{o}}$ results from larger absorbing columns which attenuate the R-band flux much more severely than the hard X-ray flux (e.g., Mainieri et al. 2002). It is interesting, however, that the most extreme sources with $\log(f_{\mathrm{x}}/f_{\mathrm{o}}) > 1$ are not all hard, but exhibit a wide range of HRs, implying that obscuration may not be the sole explanation for the dim optical counterparts. Fiore et al. (2003) find that for non-broad-lined sources (e.g., sources with optical spectra showing narrow AGN emission lines or early-type galaxy absorption lines) there is a linear correlation between $\log(f_{\mathrm{x}}/f_{\mathrm{o}})$ and $\log(L_{2-10\ \mathrm{keV}})$. This relationship implies that some of the high $f_{\mathrm{x}}/f_{\mathrm{o}}$ sources with low HRs are high luminosity, high redshift, narrow-lined AGN.

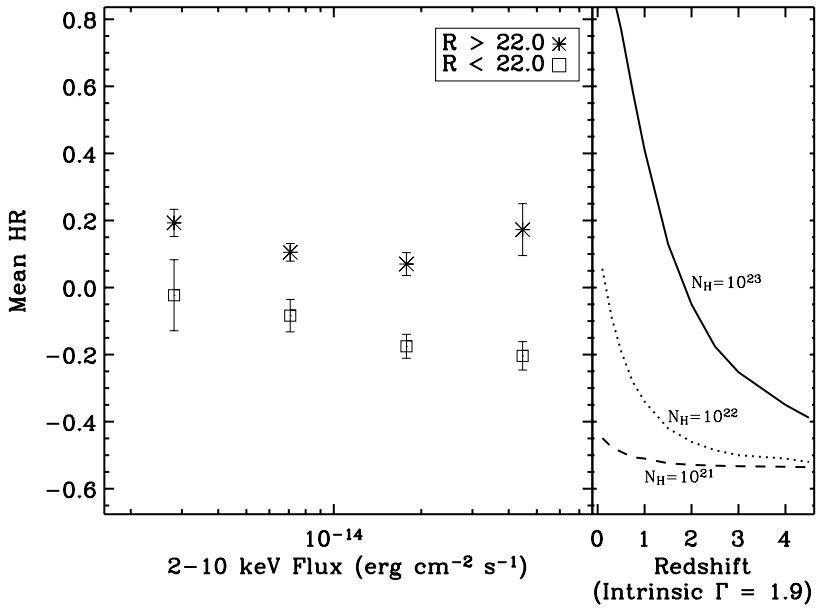

Figure 4.7 Mean hardness ratio (HR) of sources split by optical counterpart R-band magnitude, as a function of 2 – 10 keV flux. Sources were split at $R = 22.0$ and then binned into four equally spaced logarithmic X-ray flux bins. Note that at each X-ray flux, the optically faint sources (asterisks) are significantly harder than the brighter optical sources (squares). The right panel shows HR as a function of redshift for an intrinsic $\Gamma = 1.9$ spectrum with several intrinsic obscuring column densities, for reference

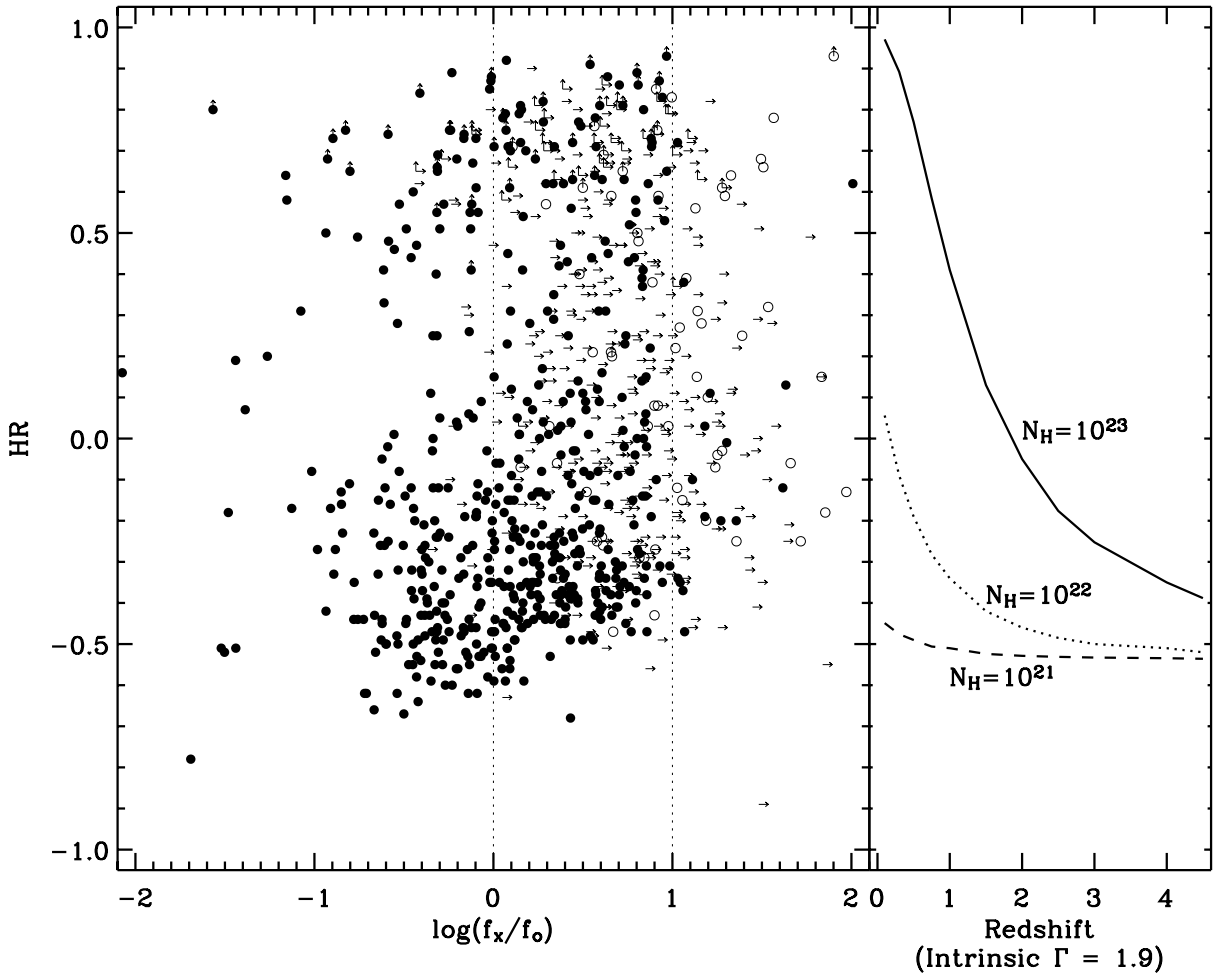

Figure 4.8 Hardness ratio as a function of X-ray-to-optical flux ratio. Sources with identified optical counterparts are shown with filled ($R < R_{\rm limit}$) and open ($R > R_{\rm limit}$) circles; sources with an optical limit are shown as right-pointing arrows – the $f_{\rm x}/f_{\rm o}$ value is a lower limit. Vertical arrows indicate a lower limit to the HR. The right panel shows HR as a function of redshift for an intrinsic $\Gamma = 1.9$ spectrum with several intrinsic obscuring column densities, for reference

We also explored the optical source densities in the vicinity of the X-ray sources. For each optical counterpart, we counted the number of sources in the surrounding region and compared the source density to the overall field density to calculate overdensities. We employed $20''$, $30''$, $40''$, and $60''$ radius circles around each optical counterpart and counted sources with R-magnitude of $|R - R_{\rm counterpart}| < 1$ and $|R - R_{\rm counterpart}| < 2$ for each of the sources. We found no significant overdensities around the X-ray sources.

4.6 Summary

We present R-band imaging of $\sim 95\%$ of the 2 – 10 keV X-ray sources in the SEXSI survey. We describe our optical data reduction and the X-ray to optical source matching algorithms employed, and present a catalog of R-band counterpart photometry and astrometry. While the power of the SEXSI sample is fully realized only with the addition of our collection of optical counterpart spectra, the photometric identification of the sources is an important step that provides clues to the composition of the source population. We find that by splitting the sources at $R = 22$ and analyzing each group's X-ray properties, we begin to see the emergence of what appear to be physically distinct populations. For example we find that the hardness ratio distribution of the optically brighter sources is sharply peaked near $HR \sim -0.5$, typical of unobscured AGN, while the fainter, $R > 22$ sources have a much broader and harder spectral distribution. The findings of this paper suggest that the analysis of optical spectral data from counterparts fainter than $R = 22$ (attainable with 10-meter-class telescopes), will be an essential part of exploring the X-ray background composition.

Acknowledgments

This research has made use of the NASA/IPAC Extragalactic Database (NED) which is operated by the Jet Propulsion Laboratory, California Institute of Technology, under contract with the National Aeronautics and Space Administration (NASA). Some of the data presented herein were obtained at the W. M. Keck Observatory, which is operated as a scientific partnership among the California Institute of Technology, the University of California and NASA. The Observatory was made possible by the generous financial support of the W. M. Keck Foundation. The authors wish to recognize and acknowledge the very significant cultural role and reverence that the summit of Mauna Kea has always had within

the indigenous Hawaiian community. We are most fortunate to have the opportunity to conduct observations from this mountain. This work has made use of the USNOFS Image and Catalog Archive operated by the United States Naval Observatory, Flagstaff Station. The Guide Star Catalog was produced at the Space Telescope Science Institute under U.S. Government grant with data based on photographic data obtained using the Oschin Schmidt Telescope on Palomar Mountain and the UK Schmidt Telescope. This research has made use of NASA's Astrophysics Data System. This work has been supported by NASA NAG5-6035 (DJH), as well as by a small *Chandra* archival grant. The work of DS was carried out at the Jet Propulsion Laboratory, California Institute of Technology, under a contract with NASA.

Chapter 5

SEXSI Optical Spectroscopy[1]

We present the catalog of 477 spectra from the *Serendipitous Extragalactic X-ray Source Identification (SEXSI)* program, a survey designed to probe the dominant contributors to the 2 – 10 keV cosmic X-ray background. Our survey covers 1 deg^2 of sky to 2 – 10 keV fluxes of 1×10^{-14} erg cm^{-2} s^{-1}, and 2 deg^2 for fluxes of 3×10^{-14} erg cm^{-2} s^{-1}. Our spectra reach to R-band magnitudes of $\lesssim 24$ and have produced identifications and redshifts for 438 hard X-ray sources. Typical completeness levels in the 27 *Chandra* fields studied are 40% – 70%. The vast majority of the 2 – 10 keV selected sample are active galactic nuclei (AGN) with redshifts between 0.1 and 3; our highest-redshift source lies at $z = 4.33$. We find that few sources at $z < 1$ have high X-ray luminosities, reflecting a dearth of high-mass, high-accretion-rate sources at low redshift, a result consistent with other recent wide-area surveys. We find that half of our sources show significant obscuration, with $N_H > 10^{22}$ cm^{-2}, independent of unobscured luminosity. We classify 168 sources as emission-line galaxies; all are X-ray luminous ($L_{\rm x} > 10^{41}$ erg s^{-1}) objects with optical spectra lacking both high-ionization lines and evidence of a non-stellar continuum. The redshift distribution of these emission-line galaxies peaks at a significantly lower redshift than does that of the sources we spectroscopically identify as AGN. We conclude that few of these sources, even at the low-luminosity end, can be powered by starburst activity. Stacking spectra for a subset of these sources in a similar redshift range, we detect [Ne V] λ3426 emission, a clear signature of AGN activity, confirming that the majority of these objects are Seyfert 2 galaxies in which the high-ionization lines are diluted by stellar emission. We find a total of 33 objects lacking broad lines in their optical spectra which have quasar X-ray luminosities ($L_x > 10^{44}$ erg s^{-1}), the largest sample of such objects identified to date. In addition, we explore seventeen

[1]Much of this chapter has been previously published as Eckart et al. (2006)

AGN associated with galaxy clusters and find that the cluster-member AGN sample has a lower fraction of broad-line AGN than does the background sample.

5.1 Introduction

A primary goal of extragalactic X-ray surveys is to determine the nature and evolution of accretion power in the Universe. Accreting massive black holes are observed over more than five orders of magnitude in luminosity, and exhibit a broad range of intrinsic X-ray absorption (from negligible levels to Compton-thick obscuration with $N_H \gtrsim 10^{24}$ cm^{-2}). Additionally, cosmic X-ray sources undergo significant evolution between the current epoch and redshifts of $z \sim 3$. Measuring this enormous phase space requires broadband X-ray surveys extending from essentially the whole sky (to constrain the bright end) to the deepest surveys carried out with the most sensitive telescopes available over sky regions comparable to the telescope field of view.

Enormous progress has been made at the faintest end over the last five years with megasecond surveys performed by *Chandra* and *XMM* (see review by Brandt & Hasinger 2005). Together, these surveys have covered more than a thousand square arcminutes to depths of $f_{2-10\ \mathrm{keV}} \lesssim 10^{-15}$ erg cm^{-2} s^{-1}. These projects have resolved a significant fraction of the diffuse extragalactic X-ray background (at least in the lower half of the accessible energy band – Worsley et al. 2005). Spectroscopic optical followup has been successful in classifying and measuring redshifts for a large fraction (over half) of the resolved sources.

Also very important in covering the interesting phase space are surveys with depths $f_{2-10\ \mathrm{keV}} \lesssim 10^{-14}$ erg cm^{-2} s^{-1}. The slope of the extragalactic X-ray $\log N - \log S$ relation breaks at $f_{2-10\ \mathrm{keV}} = 1 - 2 \times 10^{-14}$ erg cm^{-2} s^{-1} (Cowie et al. 2002; Harrison et al. 2003), so that sources in this flux range dominate the integrated light from accretion. In this brightness range, source densities on the sky are a few hundred per square degree, requiring surveys covering on the order of a square degree or more to obtain statistically useful samples for the study of source properties and the evolution of the population.

A number of programs are surveying regions of this size and depth, accompanied by significant optical followup efforts. The CLASXS survey (Yang et al. 2004) obtained data in a 0.4 deg^2 contiguous region in the Lockman Hole; optical spectroscopy has identified about half of the sample of 525 objects (Steffen et al. 2004). The ChaMP (Kim et al.

2004) survey utilizes extragalactic *Chandra* pointings largely from the guest observer (GO) program to identify sources that are not associated with the primary target. ChaMP, which ultimately aims to cover several square degrees over a range of depths, is also accompanied by an optical source identification effort (Green et al. 2004; Silverman et al. 2005). The HELLAS2XMM survey (e.g, Baldi et al. 2002; Fiore et al. 2003; Perola et al. 2004) is taking a similar approach with fields from *XMM-Newton*.

The subject of this paper is the *Serendipitous Extragalactic X-ray Source Identification (SEXSI)* program, a survey using *Chandra* GO and GTO fields specifically selected to obtain a significant sample of identified objects in the flux range from a few times 10^{-13} to 10^{-15} erg cm^{-2} s^{-1}. To accomplish this, SEXSI covers more than 2 deg^2 of sky. Harrison et al. (2003, hereafter Paper I) describes the X-ray source sample, Eckart et al. (2005, hereafter Paper II) describes the optical imaging followup, and this paper presents results of the optical spectroscopy. We have 477 spectra, of which 438 are of sufficient quality to provide redshifts and optical classifications. The $L_{\rm x} - z$ phase space covered by our survey is shown in Figure 5.1.

In our sample of 438 spectroscopically identified sources (which have counterpart magnitudes $R \lesssim 24$) we confirm with high significance a number of results found in other surveys. We find that few AGN at $z < 1$ have high rest-frame X-ray luminosities, reflecting a dearth of high-mass, high-accretion-rate sources at low redshift. In addition, our sample of broad-lined AGN peaks at a significantly higher redshift ($z > 1$) than do sources identified as emission-line galaxies. We find that 50% of our sources show significant obscuration, with $N_H > 10^{22}$ cm^{-2}, independent of intrinsic luminosity. We have identified nine narrow-lined AGN at $z > 2$ having quasar luminosities ($L_{\rm x} > 10^{44}$ erg s^{-1}). This is consistent with predictions based on unified AGN models.

We investigate in some detail the nature of the large sample of 168 sources classified as emission-line galaxies. These X-ray luminous ($10^{41} - 10^{44}$ erg s^{-1}) galaxies have optical spectra lacking both high-ionization lines and evidence for a non-stellar continuum. We conclude that few of these galaxies, even at the low-luminosity end, can be powered by starburst activity. By stacking 21 spectra for sources in a similar redshift range in order to increase the signal to noise, we detect [Ne V] λ3426 emission, an unambiguous signature of AGN activity. This suggests that the majority of these sources are Seyfert 2 galaxies, where the high-ionization lines are diluted by stellar emission and reduced in intensity by

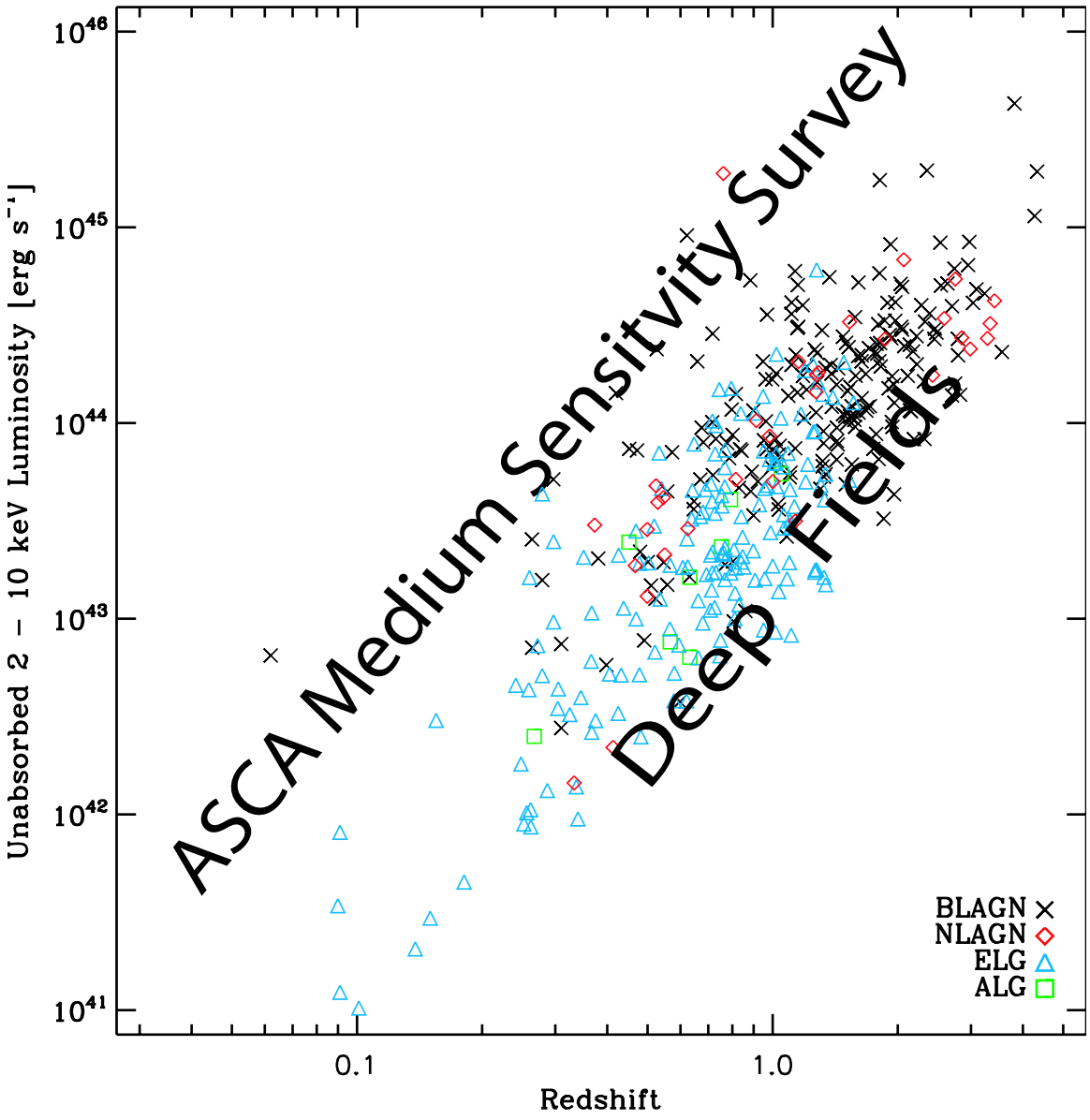

Figure 5.1 Redshift versus luminosity for SEXSI sources, with optical spectral classification indicated. The approximate phase space covered by the ASCA Medium Sensitivity Survey (Akiyama et al. 2003) and the *Chandra* Deep Fields (e.g., CDF-N – Alexander et al. 2003; Barger et al. 2003; CDF-S – Rosati et al. 2002; Szokoly et al. 2004) is illustrated with text. The luminosity plotted is the instrinsic, unobscured luminosity in the rest-frame 2 – 10 keV band. See § 5.5 for a description of the unobscured luminosity calculation

nuclear extinction.

We organize the paper as follows: § 5.2 discusses the overall design of the spectroscopic followup program; § 5.3 describes the data collection and reduction; § 5.4 details how we determine redshifts and source classifications; § 5.5 presents the catalog; § 5.6 discusses the population statistics of the sample; § 5.7 provides details on the characteristics of each source class as well as the line-free spectra; § 5.8 discusses the sample completeness and selection effects; § 5.9 presents the global characteristics of the sample and provides a comparison to other surveys; § 5.10 explores the nature of emission-line galaxies; § 5.11 provides a discussion of spectroscopically identified AGN associated with galaxy clusters; and § 5.12 provides a summary. We adopt the standard cosmology throughout: $\Omega_{\rm m} = 0.3$, $\Omega_\lambda = 0.7$, and $H_0 = 65$ km s^{-1} Mpc^{-1}. Unless otherwise mentioned, error estimates and error bars refer to 1 σ errors calculated with Poissonian counting statistics.

5.2 Survey Design

The SEXSI survey is designed to obtain optical identifications for a large sample of hard (2 – 10 keV) X-ray sources detected in extragalactic *Chandra* fields in the flux range 10^{-13} – 10^{-15} erg cm^{-2} s^{-1}. This range contains sources which are the dominant contributors to the 2 – 10 keV extragalactic background, filling the gap between wide-area, shallow surveys (e.g., HELLAS – La Franca et al. 2002; ASCA Large Sky Survey – Akiyama et al. 2000; ASCA Medium Sensitivity Survey – Akiyama et al. 2003) and the deep, pencil-beam surveys (e.g., CDF-N – Alexander et al. 2003; Barger et al. 2003; CDF-S – Rosati et al. 2002; Szokoly et al. 2004).

Covering this phase space requires surveying 1 – 2 deg^2 with $\sim$ 50 ksec exposures. SEXSI selected 27 archival, high Galactic latitude fields ($|b| > 20°$), covering a total survey area of more than 2 deg^2 at $f_{2-10\ \rm keV} \geq 3 \times 10^{-14}$ erg cm^{-2} s^{-1} and more than 1 deg^2 for $f_{2-10\ \rm keV} \geq 1 \times 10^{-14}$ erg cm^{-2} s^{-1}. To maximize sensitivity in the hard band, we selected archival observations taken taken with the Advanced Camera for Imaging Spectroscopy (ACIS I- and S-modes; Bautz et al. 1998). The exposure times range from 18 to 186 ks, with three quarters of the fields having good-time integrations of between 40 and 100 ks.

Paper I provides details of the X-ray source extraction and analysis; we provide a brief summary here. In each field we initially used `wavdetect` to identify sources in soft (0.3 – 2.1

keV) and hard (2.1 – 7 keV) band images. In a subsequent step, we tested the significance of each source and eliminated sources with nominal chance occurrence probability $P > 10^{-6}$, which led to an average expected rate of ≤ 1 false detections per field. We extracted photons from each source, and used energy-weighted exposure maps to convert background-subtracted source counts to fluxes in the standard soft (0.5 – 2 keV) and hard (2 – 10 keV) bands, adopting a power-law spectral model with photon index $\Gamma = 1.5$. In addition, we corrected the source fluxes for Galactic absorption. We eliminated all *Chandra* target objects from the sample, with the exception of possible galaxy cluster members which we include in the catalog but flag accordingly. The X-ray catalog contains 1034 hard-band-selected sources. An additional catalog of 879 sources which have soft-band detections but which lack hard-band detections is presented in the Appendix of Paper I.

The SEXSI optical followup program is designed to maximize the fraction of spectroscopically identified sources in the survey area. We primarily used the MDM 2.4 m and the Palomar 60-inch and 200-inch telescopes for imaging, and the Keck telescopes for spectroscopy. We image each field in the R-band to minimum limiting magnitudes $R_{\rm limit} \sim 23$, a depth chosen to match the typical limit where classifiable optical spectra can be obtained in 1-hour integrations with Keck. Since the majority of sources in our X-ray flux range have optical counterparts at this limit, this is a good trade-off between areal coverage and depth.

Paper II describes the optical imaging and counterpart identification in detail. We iteratively matched the optical images to the X-ray catalog, utilizing optical astrometry to correct the *Chandra* pointing error for each field (typically these corrections are $\lesssim 1''$). For the 262 sources with imaging depths $22 < R_{\rm limit} < 23$, 160 (61%) have identified counterparts, while for the 434 sources with $23 < R_{\rm limit} < 24$, 291 (67%) have identified counterparts, and for the 167 sources with $R_{\rm limit} > 24$, 124 (74%) have identified counterparts. Our total sample of 947 sources with unambiguous photometry (e.g., no contamination from nearby bright stars, etc.) identifies 603 counterparts (64%).

Optical spectra of X-ray counterparts were primarily obtained using multi-slit spectrographs at the W.M. Keck Observatory: the Low Resolution Imaging Spectrometer (LRIS; Oke et al. 1995) on Keck I and the Deep Extragalactic Imaging Multi-Object Spectrograph (DEIMOS; Faber et al. 2003) on Keck II. Our basic slit mask design strategy was to place slits on all identified 2 – 10 keV SEXSI sources with counterpart magnitudes $R \lesssim 23$ (or, occasionally, from imaging in other bands when R-band images were not yet available). For

Table 5.1. Summary of spectroscopic follow-up of each of the SEXSI Fields

Name	R.A (J2000)	Decl (J2000)	Exp [ks]	# 2–10 keV srcs in X-ray area[a]	# 2–10 keV srcs in opt area[b]	# with phot. ID $R < 22$	# with phot. ID $R < 23$	# with phot. ID $R < 24$[c]	# with z	# with cont.[d]
NGC 891	02 22 33	+42 20 57	51	21	19	10	13	14	6	3
AWM 7	02 54 28	+41 34 47	48	28	24	11	14	16	14	2
XRF 011130	03 05 28	+03 49 59	30	33	33	17	21	24	20	2
NGC 1569	04 30 49	+64 50 54	97	33	31	18	19	19	16	3
3C 123	04 37 55	+29 40 14	47	26	25	13	15	15	7	3
CL 0442+0202	04 42 26	+02 00 07	44	45	37	2[e]	2[e]	2[e]	7	0
CL 0848+4454	08 48 32	+44 53 56	186	81	72	25	37	49	47	4
RX J0910	09 10 39	+54 19 57	171	92	89	25	43	55	40	4
1156+295	11 59 32	+29 14 44	49	44	42	20	24	29	7	0
NGC 4244	12 17 30	+37 48 32	49	31	28	9	17	19	8	0
NGC 4631	12 42 07	+32 32 30	59	23	23	7	11	12	0	0
HCG 62	12 53 08	−09 13 27	49	39	37	22	27	30	20	2
RX J1317	13 17 12	+29 11 17	111	62	60	17	29	31	27	1
BD 1338	13 38 25	+29 31 05	38	45	43	20	26	29	23	0
RX J1350	13 50 55	+60 05 09	58	35	33	12	15	15	0	0
3C 295	14 11 20	+52 12 21	23	8	8	3	5	5	4	0
GRB 010222	14 52 12	+43 01 44	18	23	23	14	18	18	12	0
QSO 1508	15 09 58	+57 02 32	89	47	39	11	15	17	18	0
MKW 3S	15 21 52	+07 42 32	57	36	33	16	20	21	8	1
MS 1621	16 23 36	+26 33 50	30	25	24	11	13	15	11	2
GRB 000926	17 04 10	+51 47 11	32	30	29	19	21	23	20	1
RX J1716	17 16 52	+67 08 31	52	46	45	13	22	28	29	0
NGC 6543	17 58 29	+66 38 29	46	21	21	9	10	11	6	1
XRF 011030	20 43 32	+77 16 43	47	27	23	8	12	12	5	2
MS 2053	20 56 22	−04 37 44	44	48	44	23	27	31	23	2
RX J2247	22 47 29	+03 37 13	49	50	50	19	26	32	27	4
Q2345	23 48 20	+00 57 21	74	35	34	16	21	23	22	2
TOTAL			1648	1034	969	390	523	595	438	39

[a]This column gives numbers from the entire X-ray catalog from Paper I

[b]This column gives numbers from the portion of the X-ray catalog that has adequate imaging coverage. This column excludes sources from the X-ray catalog that lack imaging coverage (optflag=0; Paper II) or fall near a bright source such that the optical counterpart is not identified and the $R_{\rm limit}$ cannot be determined (optflag=6; Paper II)

[c]This column gives the number of *confirmed* sources with $R < 24$. Additional sources may have $R < 24$ in cases where $R_{\rm limit} < 24$

[d]Sources with spectra that show continuum-only—no emission lines or absorption features—and thus no redshift or classification was determined

[e]Field CL 0442+0202 has shallow R-band imaging ($R_{\rm limit} = 21.1$). Since the numbers listed in this table are *confirmed* optical counterparts, this row indicates few R-band identifications

the majority of the masks made for LRIS, these sources received the highest priority; we then filled any extra space on the mask with sources from our soft-band-only catalog, and then with fainter optical counterparts. The soft-band-only spectra are not included in this paper. For DEIMOS masks we followed basically the same procedure. However, DEIMOS's large field-of-view affords space to place "blind" slits at the X-ray positions of hard-band sources which lack optical identifications.

Table 5.1 provides a summary of the SEXSI fields and our spectroscopic completeness for each. Note that the optical photometric identification completeness should be taken into account when gauging spectroscopic completeness—most sources for which we have found either very faint optical counterparts or only a limiting magnitude were not pursued spectroscopically.

5.3 Optical Spectroscopy: Data Collection and Reduction

Although the majority of the SEXSI spectroscopy was obtained using LRIS on Keck I and DEIMOS on Keck II, a small fraction ($\sim 2\%$) of the spectra were collected with Doublespec (Oke & Gunn 1982) at the Palomar 200 inch (5 m) telescope. Below we describe the data collection and reduction techniques for each of the three instruments. A small subset (19 sources) of the spectra were previously published in Stern et al. (2002b), Stern et al. (2002a), and Stern et al. (2003). Section 5.8 addresses the composition of the sample obtained from each instrument and possible sample biases that might occur as a consequence of the differing capabilities of the spectrographs; we show any such effects are small in our final sample.

5.3.1 LRIS Data

The 293 LRIS spectra included in our catalog were collected between September 2000 and June 2002. LRIS has a $5.5' \times 8.0'$ field of view that we typically filled with 5 – 20 slitlets. Our aim was followup of $R \lesssim 23$ SEXSI sources. Exposures of 1 – 2 hours provided sufficient signal to determine redshifts and perform classifications for most such objects (see § 5.4). The SEXSI source density varies with *Chandra* exposure time and off-axis angle, leading to a large range in slitlets per mask. The masks were machined with $1.4''$ wide slitlets.

LRIS is a dual-beam spectrograph, with simultaneous blue (LRIS-B) and red (LRIS-R) arms. LRIS-R has a 2048×2048 detector with $0.212''$ pixel^{-1}. From September 2000 to early June 2002, LRIS-B had a 2048×2048 pixel engineering-grade CCD with a similar platescale to the red side. In June 2002, prior to our final LRIS observing run, the CCD was replaced by a science-grade mosaic of two 2048×4096 CCDs with $0.135''$ pixel^{-1}. The new CCDs were selected to have high near-UV and blue quantum efficiency. Steidel et al. (2004) provides a more detailed description of the new LRIS-B.

We used the 300 lines mm^{-1} ($\lambda_{\rm blaze} = 5000$ Å) grism for blue-side observations providing a dispersion of 2.64 Å pixel^{-1} pre-upgrade and 1.43 Å pixel^{-1} post-upgrade. For red-side observations we employed either the 150 lines mm^{-1} ($\lambda_{\rm blaze} = 7500$ Å) grating providing a dispersion of 4.8 Å pixel^{-1} or the 400 lines mm^{-1} ($\lambda_{\rm blaze} = 8500$) grating providing 1.86 Å pixel^{-1}. In cases where only LRIS-R was available, we used the 150 lines mm^{-1} grating. The 400 lines mm^{-1} grating was only employed when we were using both arms

of the spectrograph. We typically split the red and blue channels at 5600 Å, although occasionally the 6800 Å dichroic was used. These spectrometer configurations provide wavelength coverage across most of the optical window. The wavelength window for each individual spectrum is included in the catalog (§ 5.5), since coverage depends on the source position on the slitmask and the particular setup parameters.

The majority of the LRIS observations (227 sources) used both arms of the spectrograph with the 400 lines mm^{-1} grating, while 51 of the earliest LRIS spectra used only LRIS-R. A final 19 spectra used a dichroic, but have only blue-side (4 sources) or red-side (15 sources) coverage due to technical problems during the observations.

Most of our LRIS masks were observed for a total integration time of 1 – 1.5 hr, usually consisting of three consecutive exposures. Between exposures we dithered $\sim 3''$ along the slit in order to facilitate removal of fringing at long wavelengths ($\lambda \gtrsim 7200$ Å). The LRIS data reductions were performed using IRAF[1] and followed standard slit-spectroscopy procedures. Some aspects of treating the slit mask data were facilitated by a home-grown software package, BOGUS,[2] created by D. Stern, A.J. Bunker, and S.A. Stanford. We calculated the pixel-to-wavelength transformation using Hg, Ne, Ar, and Kr arc lamps and employed telluric emission lines to adjust the wavelength zero point. The spectra on photometric nights were flux calibrated using long-slit observations of standard stars from Massey et al. (1990) taken with the same configuration as the multislit observations.

5.3.2 DEIMOS Data

Our 163 DEIMOS spectra were collected over three nights in August 2003.[3] The DEIMOS field of view is $4' \times 16'$, approximately four times that of LRIS, allowing more slitlets per mask. Observations used the 600 lines mm^{-1} grating blazed at 7500 Å with the GG455 order-blocking filter, eliminating flux below 4550 Å. With this setup, the spectrograph afforded spectral coverage from roughly 4600 Å to 1 μm, covering most of the optical window, though the blue-side sensitivity does not extend as far into the near-UV as does

[1] IRAF is distributed by the National Optical Astronomy Observatory, which is operated by the Association of the Universities for Research in Astronomy, Inc., under cooperative agreement with the National Science Foundation

[2] BOGUS is available online at http://zwolfkinder.jpl.nasa.gov/~stern/homepage/bogus.html

[3] A serendipitous galaxy at $z = 6.545$ in SEXSI field MS 1621 was also identified during the DEIMOS observing run. This was the third most distant object known at the time of the discovery, and had interesting implications for the ionization history of the Universe (Stern et al. 2005b)

LRIS-B. The observations of each mask were broken into three exposures of 1200 s to allow rejection of cosmic rays; no dithering was performed between exposures to allow for easy adoption of the pipeline reduction software (see below).

Calibration data consisting of three internal quartz flats and an arc lamp spectrum (Xe, Hg, Ne, Cd, and Zn) were obtained for each mask during the afternoon. The DEIMOS flexure compensation system ensures that the calibration images match the science data to better than ± 0.25 pixels.

The DEIMOS data reduction was performed using the automated pipeline developed by the DEEP2 Redshift Survey Team (Newman et al. 2005). Minor adjustments to the code were needed to process data from slit masks with too few slitlets or a slitlet that was too long for the original code. These changes were performed by both the authors and DEEP2 team members M. Cooper and J. Newman. The pipeline follows standard slit spectroscopy reduction procedures, performing all steps up to and including extraction and wavelength calibration.

5.3.3 Doublespec Data

While it is impractical to use the Palomar 200 inch (5 m) telescope for spectroscopy of sources fainter than $R = 21$, Doublespec was used in long slit mode for brighter sources that did not fit well onto Keck slit masks. Doublespec is a dual-beam spectrograph; we used the 600 lines mm^{-1} ($\lambda_{\rm blaze} = 3780$ Å) grating for blue-side observations (1.07 Å pixel^{-1}), the 158 lines mm^{-1} ($\lambda_{\rm blaze} = 7560$ Å) grating for red-side observations (4.8 Å pixel^{-1}), and the 5200 Å dichroic, which provided coverage of most of the optical window. Most of our Doublspec observations were performed for a total integration time of 30 min, usually consisting of three consecutive exposures. Between exposures we dithered along the slit in order to facilitate removal of fringing at long wavelengths. Our small number of Doublespec spectra (ten) were reduced using standard IRAF slit-spectroscopy procedures.

5.4 Redshift Determination and Source Classification

From the 477 spectra collected, we have obtained spectroscopic redshifts for 438 of the 1034 2 – 10 keV sources from Paper I. We do not include spectroscopic followup of any of the soft-only sources presented in the Appendix of Paper I, as the goal of our program has

always been to focus our telescope and analysis time on the hard-band populations.

To obtain source redshifts, we measure the observed line centers and average the corresponding redshifts. When possible, we avoid using broad lines in determining source redshifts; in particular, we exclude lines such as C IV λ1549 that are known to be systematically blueshifted from the object's systemic redshift (Vanden Berk et al. 2001). When possible we measure the narrow oxygen lines, [O II] λ3727 or [O III] λ5007, although determining source redshifts to $< 1\%$ is not essential for our scientific goals. When our emission or absorption line identification is tentative, we flag the source in the catalog. This occurs in $\sim 5\%$ of the cases—typically faint sources which lack bright, high-ionization lines.

When a source has a reasonable signal yet lacks identifiable spectral features, we include it in the source catalog and document the wavelength range observed. These sources mainly show faint, power-law-like continua, although in a few cases the signal to noise is quite high. Sources so faint that the continuum is not clearly detected are excluded from the catalog.

In addition to determining redshifts, our spectroscopic data allow us to group the sources into broad classes based on their spectral features. This classification is independent of the sources' X-ray properties. The broad goal of this classification is to separate sources that *appear* to have normal galaxy spectra from those that exhibit features characteristic of an active nucleus—high-ionization lines that are either broad or narrow. In detail, our spectral classification is as follows:

- **Broad-Lined AGN (BLAGN):** We classify sources as BLAGN if they have broad (FWHM $\gtrsim$ 2000 km s^{-1}) emission lines such as Lyα, C IV λ1549, C III] λ1909, Mg II λ2800, [Ne V] $\lambda\lambda$3346, 3426, Hβ, Hα. These sources include Type 1 Seyferts and QSOs, which in the unified theory (Antonucci 1993) are objects viewed with the obscuring torus face on and the central nuclear region unobscured. An example of a typical BLAGN optical spectrum is shown in Figure 5.2.

- **Narrow-Lined AGN (NLAGN):** We classify sources as NLAGN if they have high-ionization emission lines similar to those seen in BLAGN, but with FWHM $\lesssim$ 2000 km s^{-1}. Typical high-ionization lines indicating the presence of an AGN are C IV λ1549, C III] λ1909, and [Ne V] λ3426. Low-ionization lines such as Lyα, Mg II λ2800, Hβ, Hα, etc., will usually also be present given appropriate wavelength coverage, but are not alone sufficient to classify a source as a NLAGN. Figure 5.3 provides three

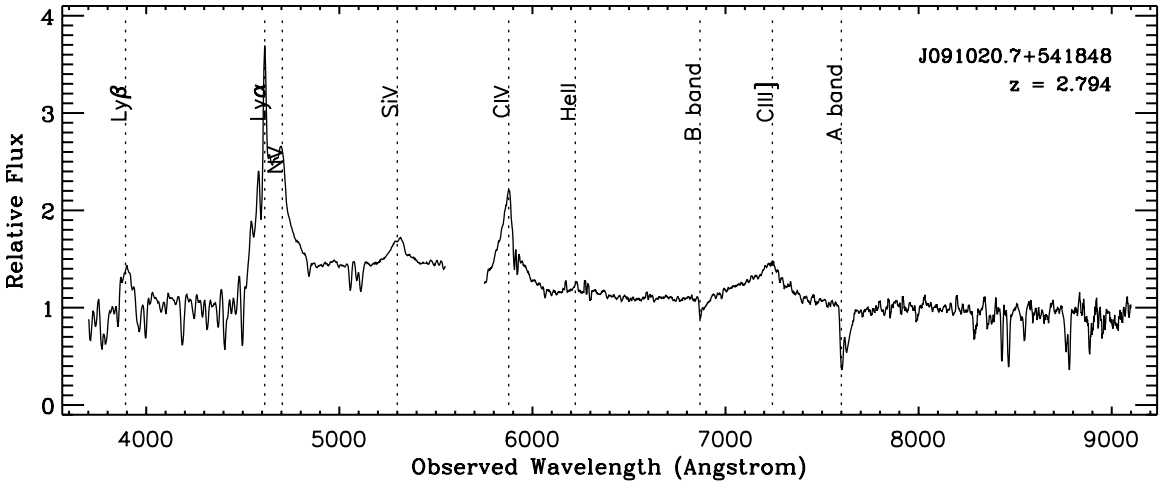

Figure 5.2 Example of one of the 212 SEXSI BLAGN. This source has $z = 2.794$. Note the broad, high-ionization emission lines typical of Type 1 Seyferts and quasars. This spectrum was obtained with LRIS, using a 5600 Å dichroic. The absorptions at 7600 Å (A-band) and 6850 Å (B-band) are telluric in nature

examples. These sources are the obscured AGN in the unified model (Antonucci 1993), viewed edge-on with an obscured view of the nucleus. In earlier studies of the lower-z universe, line ratios such as [O III] λ5007/Hβ, [N II] λ6583/Hα, etc., have been used to differentiate spectra that show narrow lines due to ionization by hot stars from spectra that show narrow lines due to an active nucleus (e.g., Veilleux & Osterbrock 1987). We do not measure such line ratios or apply them in our classification. Our sources span a large range in redshift and most are faint in the optical. Thus the emitted-frame spectral coverage varies greatly from source to source, and our spectral and spatial resolutions are too low to deblend and measure ratios accurately. There may be a handful of sources classifed as ELG (see below) that could be reclassifed as AGN-dominated based solely on their line ratios in our data, but this number of sources is expected to be small (< 10).

- **Emission-Line Galaxies (ELG):** Extragalactic sources with narrow emission lines, but with no obvious AGN features in their optical spectra (e.g., high-ionization and/or broad lines) are classified as ELG. The emission lines in these spectra indicate that the ionization mechanism dominating the *optical* light we receive is from hot stars, not from a hard, power-law source. This classification does not rule out the presence of an underlying active nucleus; indeed, we believe the X-ray emission from the vast

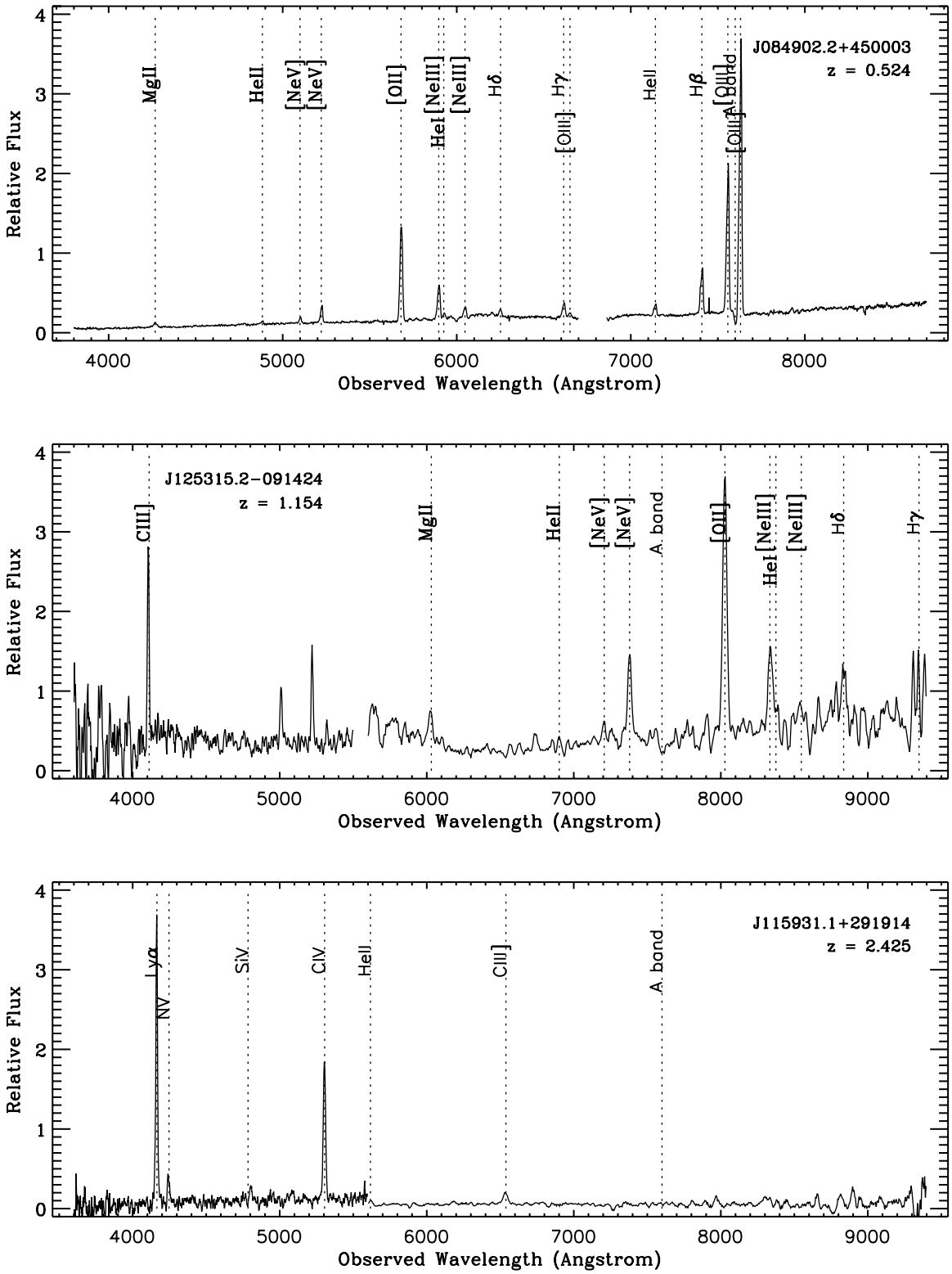

Figure 5.3 Example spectra of NLAGN at $z = 0.5$, $z = 1.2$, and $z = 2.4$. Note the narrow, high-ionization lines. For the lowest-z source (top panel) the classification depends on the [Ne V] λ3426 detection, while the higher-z sources have narrow, high-ionization, UV emission lines

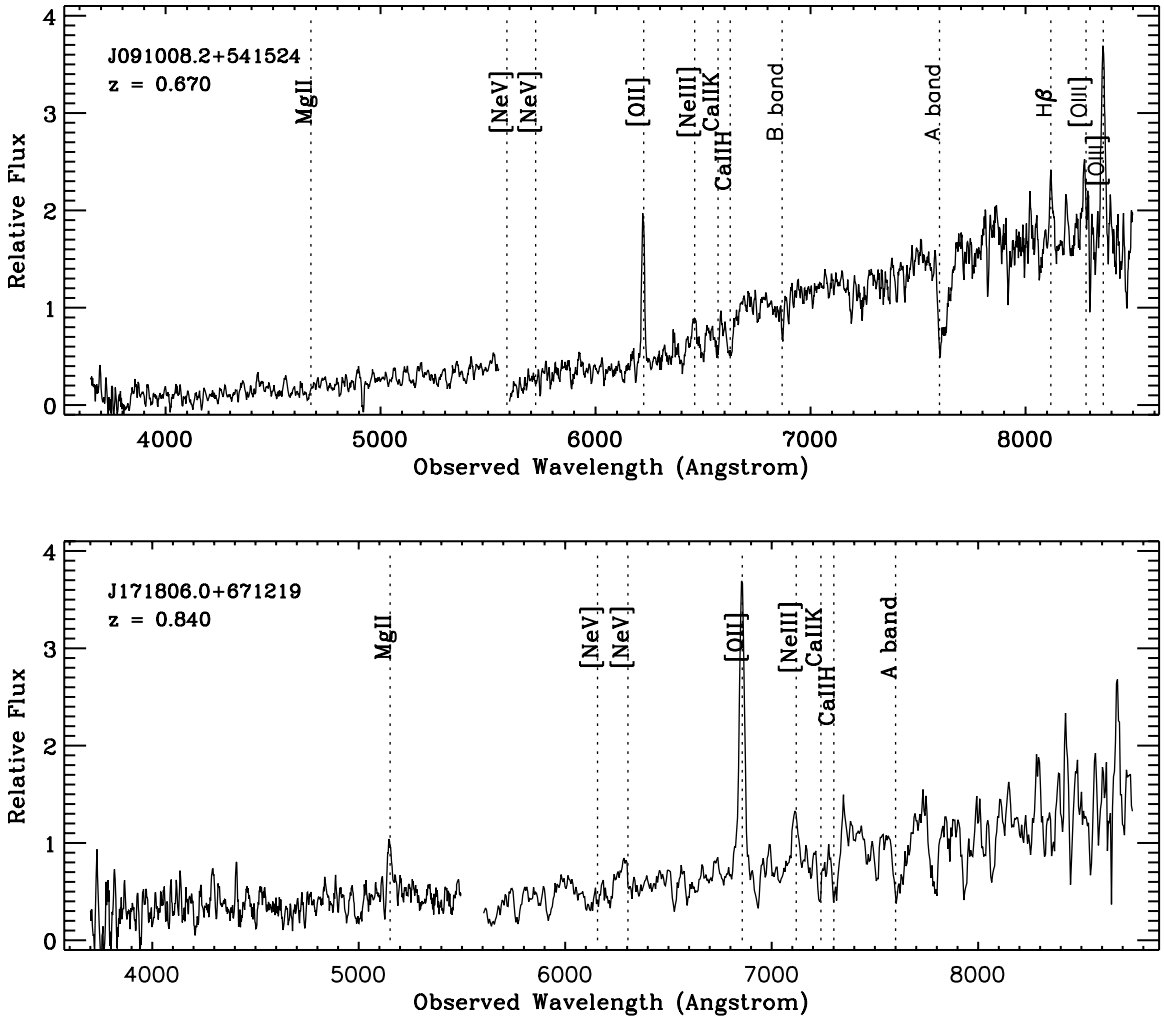

Figure 5.4 Example spectra for two of the 168 SEXSI ELG. The sources show narrow emission and absorption lines typical of normal galaxies and lack [Ne V] λ3426

majority of this subsample does arise from AGN activity. Figure 5.4 shows two example ELG spectra. These objects typically exhibit narrow lines such as [O II] λ3727, Hβ, and [O III] $\lambda\lambda$4959,5007, and often have narrow [Ne III] λ3869 emission, CaHK $\lambda\lambda$3934, 3968 absorption, and the continuum break at 4000 Å (D4000). Narrow [Ne V] λ3426 and other high ionization lines are not detected in our ELG spectra—sources with such lines are classified as NLAGN.

- **Absorption-Line Galaxies (ALG):** We distinguish between galaxies showing emission lines (ELG) and early-type galaxies (ALG), where the latter have continua marked only by absorption features, notably the D4000 continuum break and the CaHK $\lambda\lambda$3934, 3968 absorption lines. Figure 5.5 shows an example spectrum.

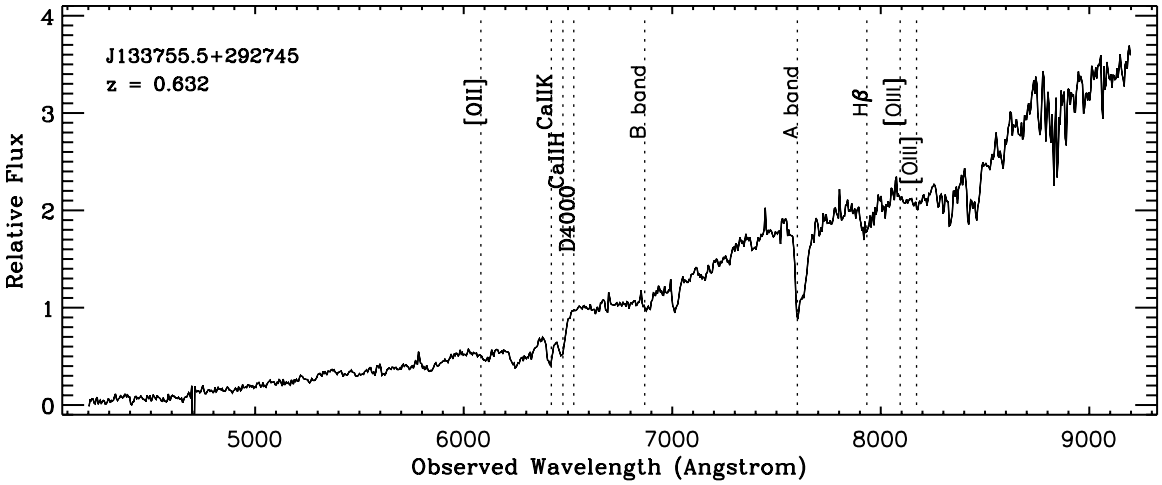

Figure 5.5 Example of one of the eight SEXSI ALG. The ALG are identified by CaHK $\lambda\lambda$3934, 3968 absorption and the break at 4000 Å, typical of early-type galaxies. No emission features are detected

- **Stars:** SEXSI fields are selected to be at high Galactic latitude to avoid contaminating our extragalactic sample with 2 – 10 keV emitting stars, but we do identify a small number of Galactic stars as optical counterparts (at $z = 0$). Seven of the optically bright SEXSI sources are identified in the literature as stars (Paper II); the other sources so identified are from our spectroscopy of fainter sources. Section 5.7.6 discusses the bright stars in more detail and assesses the possibility that the optically fainter objects are chance coincidences.

As mentioned above, these classifications depend only on the optical spectroscopic appearance, not on X-ray properties such as luminosity or intrinsic obscuring column density. With the exception of only a few sources, the identified extragalactic SEXSI sources have X-ray luminosities which suggest the presence of an accreting supermassive black hole. The emission-line galaxies, which are prevalent in our sample, do not show any optical indication of emission lines from atoms ionized by an X-ray source with copious hard X-ray emission. Instead, the ELG lines are typical of normal galaxies with lines from atoms excited by at best moderately energetic photons that can be produced thermally by the hottest stars. This apparent discrepancy in the optical and X-ray source properties is discussed further in § 5.10.

5.5 The Catalog

In Table 5.2 we present the catalog of 477 hard-band SEXSI sources with optical spectroscopic data; the catalog is also available in machine-readable format in the online version of the *Astrophysical Journal*. Complete X-ray data and optical photometry for these sources are presented in Papers I and II, respectively. The remaining ~ 550 unidentified sources from the complete sample of 1034 hard-band SEXSI sources do not have optical spectroscopic data and are omitted from this catalog. The first six columns present the X-ray source data, while the following columns present optical counterpart information – photometric data followed by spectroscopic data. The final columns describe the X-ray luminosity and the column density – quantities determined by combining the X-ray data with the redshift.

Column 1 presents source names, designated by "CXOSEXSI" followed by standard truncated source coordinates. X-ray source positions, $\alpha_{\rm x}$ and $\delta_{\rm x}$, corrected for the mean X-ray-to-optical offsets to eliminate *Chandra* pointing errors, are shown in columns 2 – 3. Column 4 lists the off-axis angle (OAA, the angular distance in arcmin of the source position from the telescope aim point). The 2 – 10 keV flux (in units of 10^{-15} erg cm^{-2} s^{-1}), converted from counts assuming $\Gamma = 1.5$ and corrected for Galactic absorption, is presented in column 5, while column 6 gives the source hardness ratio, $HR = (H-S)/(H+S)$, where H and S are photons cm^{-2} s^{-1} in the 2 – 10 keV and 0.5 – 2 keV bands, respectively. Here, as in Paper II, we quote hardness ratios derived from the net soft X-ray counts recorded at the hard-band source position when there was not a significant soft-band source detected (as distinct from Paper I, in which these cases were reported as $HR = 1$). In addition, for a subset of these cases, when the soft-band counts recorded at the hard-band position were less than twice the soft-band background counts, the HR is considered a lower limit, is flagged as such in the catalog, and is set to $HR = (H - S_{\rm limit})/(H + S_{\rm limit})$, where $S_{\rm limit} = 2 \times$ soft-band background counts corrected by the exposure map.

Table 5.2. SEXSI optical spectroscopy catalog (SEXSI III catalog)

	X-ray Data					Optical Counterpart Data											
CXOSEXSI_	α_x (J2000)	δ_x (J2000)	OAA	$S_{2-10}^{(-15)}$	HR	Flag	R	R_{limit}	$\log \frac{f_x}{f_o}$	z	Class	Notes	$\Delta\lambda_{rest}$	$\log L_x^{(2-10)}$	$\log N_H$	$\log N_H^-$	$\log N_H^+$
(1)	(2)[a]	(3)[a]	(4)	(5)	(6)[b]	(7)[c]	(8)	(9)	(10)	(11)	(12)[d]	(13)[e]	(14)[f]	(15)	(16)[g]	(17)[g]	(18)[g]
J022142.6+422654	02 21 42.75	+42 26 53.5	9.49	23.10	−0.33	1	18.73	24.3	−0.64	0.310	BLAGN	···	3553−7500	42.9	21.6[j]	···	···
J022205.0+422338	02 22 05.08	+42 23 37.7	4.24	8.73	0.84[h]	1	20.37	24.3	−0.41	0.622	ELG	···	2953−6165	43.1	23.7	23.5	23.9
J022210.8+422016	02 22 10.93	+42 20 16.1	2.17	3.63	−0.46	1	21.57	24.3	−0.31	3.563	BLAGN	···	1174−2321	44.3	22.1	<	22.7
J022215.0+422341	02 22 15.12	+42 23 41.0	3.15	15.40	−0.41	1	22.52	24.3	0.70	···	···	···	4515−9740[i]	···	···	···	···
J022215.1+422045	02 22 15.19	+42 20 44.5	1.32	42.90	−0.42	1	17.33	24.3	−0.94	0.155	ELG	···	4454−8982	42.5	<	<	20.0
J022215.5+421842	02 22 15.63	+42 18 41.7	2.46	6.79	0.28	1	20.33	24.3	−0.54	1.063	ELG	K	2695−5225	43.5	21.8	21.3	22.1
J022219.3+422052	02 22 19.40	+42 20 51.6	0.54	6.38	0.37	1	23.82	24.3	0.83	···	···	···	5000−10225[i]	···	···	···	···
J022224.3+422139	02 22 24.45	+42 21 38.4	0.91	64.60	−0.44	1	17.41	24.3	−0.73	1.181	BLAGN	···	2152−4539	44.6	20.8	20.3	21.1
J022236.3+421730	02 22 36.45	+42 17 30.2	4.23	12.00	0.01	1	22.38	24.3	0.53	···	···	···	5765−9700[i]	···	···	···	···
J025400.3+414006	02 54 00.28	+41 40 06.2	7.34	230.00	−0.41	1	19.56	24.2	0.69	0.420	BLAGN	···	4056−6651	44.1	20.8	20.3	21.0
J025416.8+414142	02 54 16.78	+41 41 42.7	4.65	14.30	−0.44	1	22.36	24.2	0.60	2.635	BLAGN	···	1337−2751	44.6	22.8	22.5	22.9
J025420.9+414032	02 54 20.92	+41 40 32.1	3.55	6.65	−0.18	2	24.20	24.2	1.00	···	···	···	4510−9700[i]	···	···	···	···
J025430.5+414213	02 54 30.51	+41 42 13.2	2.91	10.50	−0.18	1	20.96	24.2	−0.09	0.000	star	···	4520−9740	···	···	···	···
J025435.6+414100	02 54 35.60	+41 41 00.3	1.37	27.90	−0.21	2	24.20	24.2	1.63	1.194	ELG	···	2431−4785	44.2	22.4	22.2	22.5
J025437.0+414100	02 54 36.98	+41 41 00.7	1.26	24.60	−0.34	1	22.38	24.2	0.84	0.842	BLAGN	···	2874−5700	43.8	21.6	21.3	21.8
J025438.5+414529	02 54 38.53	+41 45 29.2	5.64	16.70	−0.29	2	24.20	24.2	1.40	0.438	ELG	K	3376−6954	43.0	21.1	<	21.5
J025440.6+414414	02 54 40.57	+41 44 14.5	4.39	6.04	−0.27	1	23.81	24.2	0.81	1.306	ELG	···	1960−4243	43.6	22.3	21.8	22.6
J025443.4+414505	02 54 43.37	+41 45 05.1	5.28	9.01	−0.16	2	24.20	24.2	1.13	···	···	···	4605−9850[i]	···	···	···	···
J025445.5+414156	02 54 45.51	+41 41 56.3	2.36	6.10	0.30[h]	4	22.57	24.2	0.31	0.763	ELG	···	2904−5870	43.1	23.3	22.9	23.6
J025446.3+414757	02 54 46.32	+41 47 57.6	8.20	71.70	−0.37	1	18.12	24.2	−0.40	2.351	BLAGN	···	1507−3058	45.2	21.6	<	22.0
J025446.3+414021	02 54 46.34	+41 40 21.1	1.36	13.50	−0.55	1	19.74	24.2	−0.47	1.516	BLAGN	···	1919−3974	44.1	21.9	21.5	22.1
J025449.5+414550	02 54 49.51	+41 45 50.4	6.27	10.00	−0.43	1	22.67	24.2	0.57	2.458	BLAGN	···	1314−2826	44.4	22.4	21.7	22.7
J025449.7+414530	02 54 49.68	+41 45 30.0	5.95	64.90	−0.46	1	19.62	24.2	0.16	1.370	BLAGN	···	1883−4092	44.7	20.7	<	21.4
J025454.3+414006	02 54 54.32	+41 40 06.5	2.76	8.92	0.00	1	23.38	24.2	0.80	2.587	NLAGN	···	1239−2705	44.4	23.6	23.3	23.7
J025509.9+415000	02 55 09.90	+41 50 00.5	11.62	39.10	−0.47	1	19.15	24.2	−0.25	0.730	BLAGN	···	3023−5179	43.9	<	<	20.8
J030446.2+034948	03 04 46.26	+03 49 48.7	10.29	32.30	−0.51	1	20.17	23.2	0.08	0.778	BLAGN	···	3143−5340	43.9	20.3	<	21.4
J030509.6+035027	03 05 09.64	+03 50 27.7	4.48	7.49	−0.00	1	20.72	23.2	−0.34	2.114	BLAGN	···	1518−3195	44.2	22.9	22.5	23.2
J030512.8+034935	03 05 12.85	+03 49 36.0	3.68	8.61	−0.22	1	21.71	23.2	0.12	3.035	BLAGN	···	1220−2519	44.5	23.0	22.6	23.3
J030514.2+034853	03 05 14.17	+03 48 53.9	3.50	25.40	0.45	1	21.84	23.2	0.64	0.913	NLAGN	···	2665−5397	43.9	23.0	22.9	23.1
J030517.9+035046	03 05 17.91	+03 50 47.2	2.52	8.20	−0.62	1	20.12	23.2	−0.54	1.579	BLAGN	···	1773−3801	43.9	<	<	21.5
J030522.3+035354	03 05 22.31	+03 53 55.0	4.13	6.54	−0.24	1	21.99	23.2	0.11	0.768	ELG	N	2519−5605	43.2	22.1	21.3	22.5
J030522.7+034934	03 05 22.69	+03 49 35.4	1.27	5.13	0.63[h]	1	23.08	23.2	0.44	1.089	ELG	···	2324−4786	43.4	23.8	23.5	24.0
J030525.3+035211	03 05 25.35	+03 52 11.9	2.27	5.16	0.68[h]	1	16.57	23.2	−2.16	0.090	ELG	···	4193−9010	41.1	23.6	23.3	23.8
J030527.0+035528	03 05 26.97	+03 55 29.3	5.49	9.01	0.06	1	17.61	23.2	−1.50	0.000	star	A	5165−10380	···	···	···	···
J030527.8+034656	03 05 27.84	+03 46 56.9	3.05	48.80	−0.25	1	19.90	23.2	0.15	0.351	ELG	···	4067−7772	43.3	21.3	21.0	21.5
J030529.3+034115	03 05 29.30	+03 41 16.4	8.73	15.60	0.64[h]	1	22.18	23.2	0.57	···	···	···	5250−10400[i]	···	···	···	···
J030532.4+035139	03 05 32.46	+03 51 40.2	2.08	27.90	−0.50	1	19.90	23.2	−0.09	1.183	BLAGN	···	2242−4635	44.2	21.4	<	21.8
J030532.6+034301	03 05 32.58	+03 43 02.0	7.08	16.20	0.49	4	19.12	23.2	−0.64	0.241	ELG	···	3867−8058	42.5	23.2	23.1	23.4
J030533.0+034927	03 05 32.99	+03 49 28.4	1.46	6.38	0.07	1	23.03	23.2	0.52	1.128	ELG	···	2255−4699	43.5	22.7	22.4	23.0
J030534.2+034958	03 05 34.21	+03 49 58.9	1.67	10.40	−0.43	1	20.53	23.2	−0.27	1.495	BLAGN	···	1887−3987	44.0	22.0	21.0	22.3
J030534.8+035147	03 05 34.82	+03 51 48.3	2.57	15.30	0.62	1	22.95	23.2	0.86	1.483	ELG	K	2027−4138	44.2	23.7	23.6	23.9
J030535.8+034639	03 05 35.82	+03 46 40.4	3.92	10.10	−0.37	1	22.33	23.2	0.44	1.564	ELG	K	2145−4167	44.0	22.8	22.5	23.1
J030537.0+034125	03 05 37.01	+03 41 26.0	8.88	81.80	−0.25	1	23.26	23.2	1.72	1.276	ELG	···	2311−4613	44.7	22.1	21.9	22.2
J030538.1+034816	03 05 38.10	+03 48 17.4	3.15	7.88	0.82[h]	2	23.20	23.2	0.69	···	···	···	4795−10000[i]	···	···	···	···
J030539.9+034148	03 05 39.92	+03 41 49.3	8.74	39.20	−0.49	1	20.84	23.2	0.43	1.137	BLAGN	···	2423−4859	44.3	<	<	21.2
J030541.4+034806	03 05 41.42	+03 48 07.3	3.94	10.50	−0.37	1	22.77	23.2	0.63	0.710	ELG	···	2807−5847	43.3	21.7	<	22.2
J030550.0+035008	03 05 50.06	+03 50 08.9	5.63	10.40	−0.35	1	21.67	23.2	0.19	1.104	BLAGN	···	2654−5123	43.7	21.6	<	22.1
J042900.3+644608	04 29 00.36	+64 46 08.2	12.76	32.60	−0.81	3	13.80	21.5	−2.47	0.000	star	B	···	···	···	···	···
J042941.6+644834	04 29 41.70	+64 48 33.9	7.91	17.20	0.79[h]	1	21.02	21.5	0.14	0.767	ELG	···	2119−5660	43.6	23.2[k]	···	···
J042952.4+644253	04 29 52.54	+64 42 52.8	9.59	23.90	−0.25	1	21.75	21.5	0.58	2.049	BLAGN	···	1534−3279	44.6	22.7[j]	···	···

Table 5.2 (cont'd)

	X-ray Data					Optical Counterpart Data											
CXOSEXSI_	α_x (J2000)	δ_x (J2000)	OAA	$S_{2-10}^{(-15)}$	HR	Flag	R	R_{limit}	$\log \frac{f_x}{f_o}$	z	Class	Notes	$\Delta\lambda_{rest}$	$\log L_x^{(2-10)}$	$\log N_H$	$\log N_H^-$	$\log N_H^+$
(1)	(2)[a]	(3)[a]	(4)	(5)	(6)[b]	(7)[c]	(8)	(9)	(10)	(11)	(12)[d]	(13)[e]	(14)[f]	(15)	(16)[g]	(17)[g]	(18)[g]
J042958.2+643938	04 29 58.33	+64 39 37.7	11.82	45.80	−0.36	2	21.00	21.0	0.56	···	···	···	4200−9500[i]	···	···	···	···
J043000.2+644525	04 30 00.29	+64 45 25.0	7.29	8.84	0.60[h]	5	22.53	21.5	0.46	0.753	ALG	···	2852−5704	43.3	23.0[k]	···	···
J043016.8+644317	04 30 16.90	+64 43 17.3	7.66	14.20	−0.29	1	19.92	21.5	−0.38	2.953	BLAGN	···	1328−2648	44.7	22.9[j]	···	···
J043025.2+645035	04 30 25.28	+64 50 35.0	3.29	8.71	−0.26	1	21.11	23.0	−0.12	1.573	BLAGN	···	2020−3886	44.0	22.7	22.5	22.8
J043030.9+645205	04 30 30.98	+64 52 04.8	3.46	17.30	−0.35	1	18.71	23.0	−0.78	0.547	BLAGN	···	2585−5946	43.3	21.4	21.2	21.6
J043032.6+644025	04 30 32.74	+64 40 24.7	9.66	29.20	−0.13	1	20.70	21.0	0.25	0.768	ELG	···	2319−5429	43.8	22.3[j]	···	···
J043034.3+644740	04 30 34.37	+64 47 40.0	3.06	44.20	−0.26	1	18.68	23.0	−0.38	···	···	···	4910−10000[i]	···	···	···	···
J043111.5+644947	04 31 11.60	+64 49 46.4	1.74	3.60	−0.12	1	21.21	22.5	−0.46	0.662	ELG	N	3206−6317	42.8	22.1	21.7	22.3
J043113.2+645229	04 31 13.26	+64 52 29.0	3.32	29.70	−0.46	1	19.76	22.5	−0.12	1.579	BLAGN	···	1527−3450	44.5	21.4	20.9	21.6
J043114.0+645107	04 31 14.08	+64 51 07.3	2.42	5.10	−0.95	3	12.41	22.5	−3.83	0.000	star	···	5140−10150	···	···	···	···
J043114.5+645024	04 31 14.58	+64 50 24.3	2.15	9.22	0.03	1	22.28	22.5	0.38	···	···	···	5285−10450[i]	···	···	···	···
J043116.8+644950	04 31 16.90	+64 49 49.5	2.30	98.50	−0.84	3	12.29	22.5	−2.59	0.000	star	···	5425−10620	···	···	···	···
J043120.5+645122	04 31 20.57	+64 51 21.9	3.13	20.40	−0.23	1	19.73	22.5	−0.30	0.638	ELG	···	3302−6150	43.5	21.4	21.3	21.6
J043124.3+645121	04 31 24.42	+64 51 20.7	3.48	6.11	0.41	1	20.25	22.5	−0.61	0.521	ELG	···	3668−6574	42.8	22.6	22.4	22.7
J043125.1+645154	04 31 25.22	+64 51 53.6	3.83	119.00	0.86	4	15.66	22.5	−1.16	0.279	ELG	···	4413−7689	43.5	23.2	23.1	23.2
J043129.2+645052	04 31 29.34	+64 50 52.1	3.79	11.60	−0.08	1	18.55	22.5	−1.02	2.074	BLAGN	···	1219−3253	44.3	22.5	22.3	22.6
J043641.6+295126	04 36 41.65	+29 51 26.7	12.83	526.00	−0.78	3	12.72	21.9	−1.69	0.000	star	B	···	···	···	···	···
J043646.8+293832	04 36 46.84	+29 38 32.3	3.94	87.70	−0.13	1	18.81	21.9	−0.03	0.970	BLAGN	···	2286−4934	44.5	22.2	22.1	22.3
J043650.1+293515	04 36 50.15	+29 35 15.9	5.31	6.49	−0.39	1	20.79	21.9	−0.37	···	···	···	4860−10000[i]	···	···	···	···
J043654.8+294018	04 36 54.89	+29 40 18.1	2.17	16.70	−0.12	1	20.06	21.9	−0.25	0.891	BLAGN	···	2562−5288	43.7	21.9	21.6	22.1
J043656.2+293959	04 36 56.22	+29 39 59.9	1.80	8.91	0.25	1	20.53	21.9	−0.34	0.755	ELG	···	2809−5754	43.3	22.5	22.3	22.6
J043657.4+294234	04 36 57.41	+29 42 34.8	3.34	6.39	0.10	2	21.90	21.9	0.06	···	···	···	4840−10000[i]	···	···	···	···
J043700.3+293525	04 37 00.33	+29 35 25.5	4.25	22.30	0.01	1	21.15	21.9	0.31	1.503	BLAGN	K	2161−4194	44.3	22.8	22.6	22.9
J043701.1+294148	04 37 01.18	+29 41 48.5	2.32	12.50	0.75[h]	1	20.41	21.9	−0.24	0.726	ELG	···	2954−5967	43.4	23.1	22.9	23.2
J043712.4+294331	04 37 12.44	+29 43 31.0	4.30	35.70	−0.14	1	20.61	21.9	0.30	···	···	···	5595−10500[i]	···	···	···	···
J043712.5+294631	04 37 12.56	+29 46 31.5	7.16	25.10	−0.16	1	18.81	21.9	−0.58	2.533	BLAGN	···	1553−2915	44.8	22.8	22.7	22.9
J044213.1+020437	04 42 13.18	+02 04 38.9	5.48	22.50	−0.13	2	21.10	21.1	0.29	1.380	BLAGN	···	1512−3235	44.3	22.2	21.9	22.4
J044223.1+020208	04 42 23.13	+02 02 09.5	2.12	13.70	−0.56	1	20.39	21.1	−0.21	0.886	BLAGN	···	1908−4984	43.6	20.5	<	21.5
J044223.1+020219	04 42 23.15	+02 02 20.5	2.29	25.50	−0.22	2	21.10	21.1	0.34	0.835	BLAGN	···	1961−4795	43.8	21.7	21.2	21.9
J044223.5+020231	04 42 23.54	+02 02 32.7	2.47	4.16	−0.49	2	21.10	21.1	−0.44	2.749	BLAGN	···	960−2507	44.1	22.7	21.7	23.0
J044223.7+020219	04 42 23.73	+02 02 20.6	2.26	66.60	−0.29	2	21.10	21.1	0.76	1.110	BLAGN	H	2654−4407	44.5	21.5	21.0	21.8
J044224.1+020310	04 42 24.16	+02 03 12.0	3.09	9.06	0.33	0	···	···	···	1.133	ELG	···	2766−4453	43.7	22.1	21.9	22.3
J044234.2+020510	04 42 34.21	+02 05 11.4	5.50	8.28	−0.31	2	21.10	21.1	−0.15	0.772	ELG	···	3047−4401	43.3	22.2	21.5	22.4
J044236.1+020325	04 42 36.19	+02 03 26.9	4.25	15.10	−0.10	2	21.10	21.1	0.11	1.863	NLAGN	···	1257−1955	44.4	23.0	22.8	23.1
J084811.7+445302	08 48 11.77	+44 53 03.3	7.77	8.01	0.44	1	23.46	24.4	0.79	···	···	···	3900−9000[i]	···	···	···	···
J084818.4+444844	08 48 18.52	+44 48 45.5	8.67	9.18	−0.40	1	20.66	24.4	−0.27	0.405	ELG	···	3380−6690	42.7	<	<	20.5
J084822.2+445223	08 48 22.28	+44 52 25.0	6.15	3.54	−0.04	1	23.32	24.4	0.38	2.187	BLAGN	J	1317−2949	43.9	20.8	<	22.0
J084822.5+445854	08 48 22.62	+44 58 55.9	7.17	3.67	−0.14	1	21.08	24.4	−0.50	0.413	NLAGN	A	2830−6475	42.3	21.7	<	22.1
J084823.9+445852	08 48 23.94	+44 58 53.8	6.96	6.62	−0.46	1	22.01	24.4	0.12	1.342	BLAGN	A	1793−3970	43.7	21.9	21.6	22.1
J084824.6+445355	08 48 24.70	+44 53 56.3	5.36	2.61	0.03	1	22.21	24.4	−0.20	0.747	ELG	···	2518−5294	42.7	22.4	22.2	22.6
J084824.8+445740	08 48 24.83	+44 57 41.3	6.15	3.18	0.25	1	20.52	24.4	−0.79	0.337	ELG	A	2991−7068	42.1	22.5	22.3	22.6
J084825.1+444808	08 48 25.14	+44 48 09.5	8.29	7.61	−0.55	1	20.73	24.4	−0.33	1.320	BLAGN	···	2327−4051	43.7	<	<	20.7
J084827.2+445433	08 48 27.29	+44 54 35.1	4.87	9.98	−0.40	1	20.33	24.4	−0.37	0.899	BLAGN	J	2227−4939	43.5	<	<	20.5
J084827.4+445604	08 48 27.51	+44 56 06.0	5.06	4.56	0.31	1	23.67	24.4	0.63	1.528	ELG	···	1424−3716	43.7	22.7	22.5	22.9
J084830.2+445604	08 48 30.23	+44 56 06.0	4.60	2.55	−0.18	2	24.40	24.4	0.67	···	···	···	4800−9000[i]	···	···	···	···
J084831.6+445442	08 48 31.71	+44 54 43.6	4.09	2.44	−0.15	1	25.42	24.4	1.06	1.267	ELG	KN	1588−4146	43.2	22.0	21.6	22.3
J084832.7+445711	08 48 32.75	+44 57 12.2	4.70	2.62	0.57	1	22.01	24.4	−0.28	0.749	ELG	···	2172−5431	42.7	23.0	22.9	23.1
J084836.9+444818	08 48 37.02	+44 48 19.9	6.99	22.50	−0.49	1	20.67	24.4	0.12	0.646	BLAGN	···	2551−5443	43.5	<	<	20.0
J084837.5+445710	08 48 37.60	+44 57 12.1	4.02	7.47	0.23	6	···	···	···	0.569	BLAGN	···	2421−6054	42.9	21.9	21.8	22.0
J084837.9+445352	08 48 37.94	+44 53 53.2	3.06	4.62	0.15	1	24.22	24.4	0.85	3.287	NLAGN	···	979−2169	44.3	23.6	23.4	23.7

Table 5.2 (cont'd)

	X-ray Data					Optical Counterpart Data											
CXOSEXSI_	α_x (J2000)	δ_x (J2000)	OAA	$S_{2-10}^{(-15)}$	HR	Flag	R	R_{limit}	$\log \frac{f_x}{f_o}$	z	Class	Notes	$\Delta\lambda_{rest}$	$\log L_x^{(2-10)}$	$\log N_H$	$\log N_H^-$	$\log N_H^+$
(1)	(2)[a]	(3)[a]	(4)	(5)	(6)[b]	(7)[c]	(8)	(9)	(10)	(11)	(12)[d]	(13)[e]	(14)[f]	(15)	(16)[g]	(17)[g]	(18)[g]
J084840.3+445800	08 48 40.37	+44 58 01.3	4.29	49.20	−0.34	1	21.23	24.4	0.68	0.716	BLAGN	···	2447−5477	44.0	21.3	21.2	21.4
J084840.5+445732	08 48 40.62	+44 57 33.3	3.89	9.72	−0.20	1	20.46	24.4	−0.33	3.093	BLAGN	J	934−2443	44.6	23.0	22.9	23.1
J084843.2+445806	08 48 43.25	+44 58 07.2	4.09	3.74	0.69	1	21.54	24.4	−0.31	0.566	ELG	···	2426−6002	42.6	23.4	23.2	23.5
J084845.1+445453	08 48 45.18	+44 54 54.6	1.73	1.84	0.05	1	23.42	24.4	0.13	1.015	ELG	···	2084−4665	42.9	22.3	22.0	22.5
J084845.4+445651	08 48 45.45	+44 56 52.8	2.83	1.55	0.20[h]	1	24.93	24.4	0.66	1.329	ELG	···	3112−4036	43.1	23.4	23.2	23.5
J084846.0+445945	08 48 46.11	+44 59 46.3	5.42	11.80	0.72	1	21.45	24.4	0.15	0.567	ELG	···	3012−5998	43.1	23.0	23.0	23.1
J084846.4+444830	08 48 46.46	+44 48 32.0	6.22	7.07	0.47	1	20.55	24.4	−0.43	0.432	ELG	A	2932−6564	42.7	22.6	22.5	22.7
J084846.5+445358	08 48 46.61	+44 53 59.8	1.56	2.98	−0.19	2	24.40	24.4	0.74	1.083	ELG	···	2016−4488	43.2	22.5	22.4	22.6
J084853.8+445351	08 48 53.85	+44 53 52.7	0.71	4.93	0.26	1	21.68	24.4	−0.14	0.725	ELG	···	···	43.0	22.5	22.4	22.7
J084854.4+445149	08 48 54.46	+44 51 50.4	2.73	14.90	−0.19	1	20.57	24.4	−0.10	1.035	BLAGN	···	2068−4486	43.8	21.7	21.5	21.8
J084855.3+445009	08 48 55.33	+44 50 10.7	4.40	2.86	0.78[h]	1	22.74	24.4	0.05	1.000	ELG	N	1800−4650	43.1	23.4	23.3	23.6
J084856.6+445225	08 48 56.70	+44 52 26.8	2.16	6.60	−0.24	1	22.04	24.4	0.14	1.329	BLAGN	···	2361−3993	43.7	21.7	20.8	22.0
J084857.7+445608	08 48 57.73	+44 56 09.5	1.67	2.50	−0.29	1	22.30	24.4	−0.18	0.621	ELG	···	2344−5675	42.5	21.8	21.5	22.0
J084858.0+445434	08 48 58.11	+44 54 35.4	0.59	57.50	−0.56	1	19.58	24.4	0.09	0.573	BLAGN	···	2670−5975	43.8	<	<	<
J084902.2+450003	08 49 02.27	+45 00 05.1	5.67	35.90	0.61	1	19.62	24.4	−0.10	0.524	NLAGN	···	2493−6069	43.5	22.8	22.8	22.9
J084902.4+445705	08 49 02.49	+44 57 06.3	2.88	15.70	0.02	1	22.57	24.4	0.72	1.780	BLAGN	···	1366−3417	44.3	23.0	23.0	23.1
J084902.5+450039	08 49 02.53	+45 00 40.5	6.25	12.60	−0.52	1	20.23	24.4	−0.31	0.523	BLAGN	···	2790−6106	43.1	<	<	20.0
J084903.9+445023	08 49 04.02	+44 50 24.8	4.47	2.21	0.43	1	23.92	24.4	0.41	1.276	ELG	H	1845−4130	43.2	23.0	22.8	23.2
J084904.0+445646	08 49 04.09	+44 56 47.1	2.76	2.19	0.38	1	25.12	24.4	0.89	1.263	ELG	···	2960−4197	43.2	23.1	22.9	23.2
J084905.0+445714	08 49 05.06	+44 57 15.2	3.24	33.10	−0.47	1	19.54	24.4	−0.16	1.263	BLAGN	···	1869−4131	44.3	<	<	20.3
J084905.3+445203	08 49 05.32	+44 52 04.3	3.12	9.62	0.64	1	24.61	24.4	1.33	1.266	ELG	H	2956−4148	43.8	23.4	23.3	23.5
J084905.9+445037	08 49 06.02	+44 50 38.6	4.41	2.22	0.72[h]	1	23.99	24.4	0.44	···	···	···	6700−9200[i]	···	···	···	···
J084906.3+450107	08 49 06.36	+45 01 08.9	6.89	15.40	−0.27	1	21.98	24.4	0.48	1.272	BLAGN	···	1672−4159	44.0	22.0	21.8	22.1
J084907.2+445813	08 49 07.24	+44 58 14.8	4.29	3.51	−0.15	1	22.59	24.4	0.08	0.860	BLAGN	···	2043−5107	43.0	21.8	21.5	22.1
J084907.5+450151	08 49 07.54	+45 01 52.3	7.64	5.01	0.01	1	22.36	24.4	0.14	0.091	ELG	···	3483−8661	41.1	22.1	21.9	22.2
J084908.2+445810	08 49 08.29	+44 58 11.2	4.33	3.13	−0.40	1	23.97	24.4	0.58	2.320	BLAGN	···	1265−2831	43.9	21.6	<	22.1
J084908.6+445842	08 49 08.65	+44 58 43.4	4.82	4.87	−0.04	1	25.16	24.4	1.25	1.333	ELG	···	2871−3986	43.6	22.4	22.2	22.6
J084911.3+445008	08 49 11.33	+44 50 09.2	5.31	10.40	0.14	1	23.28	24.4	0.83	1.515	BLAGN	···	1669−3737	44.0	22.5	22.2	22.6
J084913.6+445238	08 49 13.67	+44 52 39.1	3.86	2.95	0.81[h]	1	24.06	24.4	0.59	1.201	ELG	···	3225−4270	43.2	23.8	23.6	23.9
J084916.2+445954	08 49 16.23	+44 59 55.6	6.56	4.38	0.25	1	25.62	24.4	1.39	···	···	···	3900−9400[i]	···	···	···	···
J084918.0+450114	08 49 18.05	+45 01 15.2	7.85	10.20	0.86[h]	1	23.25	24.4	0.81	1.021	ELG	···	1929−4700	43.6	23.7	23.6	23.8
J084919.5+445707	08 49 19.57	+44 57 08.1	5.08	4.59	−0.34	6	···	···	···	1.259	ELG	···	1593−4161	43.5	20.7	<	21.0
J084922.5+445356	08 49 22.54	+44 53 57.4	4.95	15.50	−0.44	1	18.88	24.4	−0.76	0.510	BLAGN	J	2384−6225	43.2	21.1	20.8	21.2
J084923.2+445249	08 49 23.27	+44 52 51.0	5.33	9.85	−0.35	4	19.20	24.4	−0.83	2.177	BLAGN	···	1133−2958	44.3	22.4	22.2	22.5
J084927.7+445456	08 49 27.76	+44 54 58.1	5.85	142.00	0.53	1	20.76	24.4	0.96	0.884	BLAGN	···	2016−5042	44.6	23.0	23.0	23.0
J084930.4+445224	08 49 30.49	+44 52 25.6	6.68	5.48	−0.22	1	22.34	24.4	0.17	1.108	ELG	···	3178−4459	43.4	21.1	20.7	21.3
J084931.3+445549	08 49 31.38	+44 55 50.5	6.60	6.26	−0.09	1	21.20	24.4	−0.22	0.567	ALG	A	2425−6062	42.9	21.7	21.3	21.8
J084934.6+445448	08 49 34.69	+44 54 49.6	7.07	4.28	0.71[h]	1	22.18	24.4	0.00	0.716	ELG	···	2214−5477	42.9	23.3	23.3	23.5
J090954.0+541752	09 09 54.10	+54 17 55.0	6.89	5.67	0.71	1	22.07	23.9	0.08	1.101	ELG	I	1665−4188	43.4	23.5	23.5	23.7
J090955.5+541813	09 09 55.55	+54 18 15.4	6.59	5.13	0.42	1	22.21	23.9	0.09	1.102	ELG	AI	1665−4281	43.4	23.1	23.0	23.2
J090955.9+542915	09 09 55.98	+54 29 17.7	11.23	1570.00	−0.75	3	9.62	23.9	−2.46	0.000	star	B	···	···	···	···	···
J091008.0+541401	09 10 08.11	+54 14 04.1	7.45	3.73	−0.20	1	22.58	23.9	0.10	0.811	ELG	···	1932−4969	43.0	20.8	<	21.5
J091008.2+541524	09 10 08.25	+54 15 26.5	6.40	14.40	0.56	1	21.94	23.9	0.43	0.670	ELG	···	2095−5089	43.4	22.9	22.8	23.0
J091011.0+542721	09 10 11.13	+54 27 24.0	8.46	614.00	−0.43	1	17.05	23.9	0.11	0.622	BLAGN	N	2157−5024	44.9	<	<	<
J091012.7+541205	09 10 12.74	+54 12 07.8	8.75	15.20	0.40	1	22.49	23.9	0.68	0.792	ALG	AN	2416−5161	43.6	22.5	22.4	22.7
J091017.4+541757	09 10 17.46	+54 17 59.3	3.74	4.80	−0.73	3	12.79	23.9	−3.70	0.000	star	B	···	···	···	···	···
J091020.7+541848	09 10 20.81	+54 18 51.1	2.91	5.65	−0.33	1	19.64	23.9	−0.89	2.794	BLAGN	···	922−2424	44.3	22.4	22.3	22.6
J091021.9+541529	09 10 21.98	+54 15 31.9	5.11	2.89	0.35	1	23.44	23.9	0.34	0.482	ELG	···	2361−5566	42.4	22.2	21.8	22.4
J091022.2+542007	09 10 22.32	+54 20 09.8	2.46	5.69	0.28	1	22.37	23.9	0.20	0.898	ELG	N	2223−4952	43.3	22.8	22.7	22.9
J091023.3+541358	09 10 23.41	+54 14 01.2	6.40	14.40	−0.53	1	20.68	23.9	−0.07	0.499	NLAGN	···	2401−5803	43.1	<	<	<

Table 5.2 (cont'd)

CXOSEXSI_	X-ray Data					Optical Counterpart Data											
	α_x (J2000)	δ_x (J2000)	OAA	$S_{2-10}^{(-15)}$	HR	Flag	R	R_{limit}	$\log \frac{f_x}{f_o}$	z	Class	Notes	$\Delta\lambda_{rest}$	$\log L_x^{(2-10)}$	$\log N_H$	$\log N_H^-$	$\log N_H^+$
(1)	(2)[a]	(3)[a]	(4)	(5)	(6)[b]	(7)[c]	(8)	(9)	(10)	(11)	(12)[d]	(13)[e]	(14)[f]	(15)	(16)[g]	(17)[g]	(18)[g]
J091026.8+541241	09 10 26.90	+54 12 43.7	7.48	60.50	0.04	1	18.78	23.9	−0.21	0.373	NLAGN	···	2694−6991	43.4	21.9	21.9	21.9
J091027.0+542054	09 10 27.05	+54 20 56.5	2.00	17.50	−0.32	1	21.58	23.9	0.38	1.638	BLAGN	···	1364−3184	44.3	21.4	20.8	21.7
J091028.5+542320	09 10 28.59	+54 23 23.1	3.73	1.91	0.13	1	23.68	23.9	0.25	1.960	BLAGN	J	1182−2635	43.5	23.3	23.1	23.4
J091028.6+541634	09 10 28.69	+54 16 37.0	3.70	1.73	0.73[h]	1	22.91	23.9	−0.10	0.907	ELG	···	1835−4273	42.7	24.0	23.7	24.1
J091028.9+541523	09 10 29.03	+54 15 26.1	4.79	24.60	−0.38	1	22.03	23.9	0.70	0.647	BLAGN	···	2125−4918	43.6	20.0	<	20.8
J091029.0+542717	09 10 29.05	+54 27 19.3	7.48	234.00	−0.43	1	18.48	23.9	0.26	0.526	BLAGN	N	2522−6061	44.4	<	<	<
J091029.8+542746	09 10 29.84	+54 27 48.8	7.94	12.40	−0.40	1	20.30	23.9	−0.29	2.327	BLAGN	N	1202−2810	44.5	<	<	21.4
J091030.9+541914	09 10 30.99	+54 19 16.7	1.39	7.79	−0.35	1	23.88	23.9	0.94	···	···	···	4000−9500[i]	···	···	···	···
J091031.9+542342	09 10 31.94	+54 23 45.0	3.90	3.27	0.28	1	25.37	23.9	1.16	···	···	···	3900−7900[i]	···	···	···	···
J091032.9+541246	09 10 33.00	+54 12 48.4	7.24	5.47	−0.17	1	19.63	23.9	−0.91	0.595	ELG	···	2194−5793	42.8	20.3	<	21.3
J091034.2+542408	09 10 34.25	+54 24 10.7	4.25	2.41	−0.13	1	21.24	23.9	−0.62	0.340	ELG	AN	2835−6716	42.0	21.6	21.0	21.9
J091037.8+541543	09 10 37.89	+54 15 46.1	4.23	6.65	−0.36	1	23.59	23.9	0.76	···	···	···	3700−7800[i]	···	···	···	···
J091037.9+541608	09 10 37.98	+54 16 10.4	3.82	5.48	−0.26	1	22.42	23.9	0.21	1.102	ELG	···	1665−3758	43.4	21.2	<	21.6
J091039.8+542032	09 10 39.86	+54 20 34.7	0.60	8.90	−0.29	1	21.93	23.9	0.22	2.450	BLAGN	J	1043−2666	44.4	22.4	22.2	22.6
J091040.0+542259	09 10 40.12	+54 23 01.5	3.04	4.37	0.01	1	20.76	23.9	−0.56	0.252	ELG	N	2875−7188	41.9	21.7	21.5	21.9
J091040.8+542006	09 10 40.89	+54 20 08.6	0.30	2.42	0.74[h]	1	22.38	23.9	−0.16	1.097	ELG	···	1812−4434	43.1	23.7	23.5	23.9
J091041.4+541945	09 10 41.52	+54 19 47.9	0.40	26.30	−0.40	1	21.38	23.9	0.47	0.786	BLAGN	N	2239−5240	43.8	21.4	21.2	21.5
J091041.9+542127	09 10 41.97	+54 21 29.6	1.56	2.75	−0.26	1	21.13	23.9	−0.61	0.598	BLAGN	···	2190−5632	42.6	21.7	21.3	22.0
J091041.9+542340	09 10 42.02	+54 23 42.8	3.75	10.50	−0.35	1	23.02	23.9	0.73	1.638	BLAGN	···	1326−3184	44.1	21.8	21.5	22.0
J091042.7+542034	09 10 42.81	+54 20 37.1	0.83	1.46	0.05	1	22.59	23.9	−0.30	1.108	ELG	H	1802−4411	42.9	22.6	22.3	22.9
J091047.6+542211	09 10 47.66	+54 22 13.5	2.56	1.82	−0.34	1	23.99	23.9	0.36	1.341	ELG	···	1495−3908	43.1	21.3	<	21.9
J091049.7+541330	09 10 49.80	+54 13 33.2	6.62	9.45	0.71	1	23.52	23.9	0.88	1.008	ELG	···	1743−4731	43.6	23.3	23.1	23.4
J091053.3+541819	09 10 53.42	+54 18 21.6	2.64	1.98	−0.29	1	22.93	23.9	−0.03	1.850	BLAGN	···	1228−2842	43.5	21.1	<	22.1
J091057.0+542340	09 10 57.11	+54 23 43.2	4.56	5.61	−0.39	1	22.53	23.9	0.26	1.935	BLAGN	···	1192−2555	44.0	<	<	21.6
J091059.4+541715	09 10 59.44	+54 17 17.5	4.01	20.00	−0.21	1	22.46	23.9	0.79	1.860	BLAGN	···	1223−3041	44.5	22.1	21.9	22.2
J091059.8+542335	09 10 59.85	+54 23 37.9	4.73	2.69	0.58	1	19.79	23.9	−1.15	0.333	NLAGN	···	2850−7051	42.0	22.9	22.7	23.1
J091100.2+542540	09 11 00.31	+54 25 43.2	6.51	23.80	−0.23	1	21.41	23.9	0.44	1.890	BLAGN	···	1211−3044	44.6	22.1	21.8	22.2
J091107.8+541822	09 11 07.92	+54 18 24.9	4.48	698.00	0.62	1	21.66	23.9	2.01	0.761	NLAGN	···	2157−5139	45.2	23.1	23.0	23.2
J091108.5+541752	09 11 08.59	+54 17 54.7	4.77	8.69	−0.34	1	22.38	23.9	0.39	3.234	BLAGN	···	909−2170	44.6	22.6	22.4	22.8
J091112.8+542306	09 11 12.86	+54 23 08.4	5.84	17.80	0.11	1	23.65	23.9	1.21	0.754	ELG	···	2166−4917	43.6	22.5	22.4	22.5
J091115.4+541919	09 11 15.51	+54 19 21.3	5.34	4.34	−0.17	1	23.30	23.9	0.46	···	···	···	4100−9400[i]	···	···	···	···
J091129.6+541308	09 11 29.69	+54 13 11.2	10.04	34.30	−0.36	1	21.68	23.9	0.71	0.899	BLAGN	···	1895−5050	44.0	21.2	21.1	21.4
J091135.9+540814	09 11 36.03	+54 08 17.1	14.36	27.90	−0.38	0	···	···	···	1.435	BLAGN	···	1437−3696	44.4	<	<	20.5
J115917.7+291647	11 59 17.79	+29 16 48.6	3.67	3.67	0.67	1	22.05	24.4	−0.12	0.662	ELG	···	2166−5595	42.8	23.5	23.2	23.8
J115924.1+291512	11 59 24.19	+29 15 13.7	1.62	9.74	0.88[h]	1	21.25	24.4	−0.01	0.625	NLAGN	···	2215−5692	43.1	23.3	23.2	23.5
J115927.2+291849	11 59 27.26	+29 18 51.0	4.43	4.28	0.19	1	18.57	24.4	−1.44	0.256	ELG	···	2866−7484	41.9	22.4	22.1	22.6
J115929.7+291428	11 59 29.76	+29 14 29.9	0.23	15.40	−0.45	1	22.63	24.4	0.74	2.280	BLAGN	···	1067−2850	44.5	22.3	22.0	22.5
J115930.1+291744	11 59 30.16	+29 17 45.2	3.27	6.48	−0.13	1	23.04	24.4	0.53	0.988	ELG	A	1760−4728	43.4	21.9	21.3	22.3
J115931.1+291914	11 59 31.20	+29 19 15.4	4.77	5.94	0.39	1	23.89	24.4	0.83	2.425	NLAGN	···	1080−2627	44.2	22.6	22.0	23.0
J115938.5+292055	11 59 38.54	+29 20 56.7	6.68	14.00	−0.45	1	21.36	24.4	0.19	0.922	BLAGN	J	1925−4838	43.7	21.5	20.3	21.8
J121651.9+375438	12 16 51.91	+37 54 38.8	9.82	624.00	−0.51	3	12.96	22.9	−1.52	0.062	BLAGN	C	···	42.8	20.4[j]	···	···
J121726.9+374402	12 17 27.00	+37 44 02.9	2.96	25.10	0.52	1	22.15	23.4	0.76	0.727	ELG	···	2084−5500	43.7	22.8	22.7	22.9
J121727.5+374412	12 17 27.55	+37 44 12.3	2.85	5.12	−0.36	1	22.21	23.4	0.09	0.679	ELG	···	2144−5866	42.9	21.9	21.7	22.0
J121732.9+374644	12 17 32.96	+37 46 44.2	2.14	11.30	−0.34	1	20.90	23.4	−0.09	2.138	BLAGN	···	1115−3027	44.4	<	<	21.3
J121733.0+375047	12 17 33.11	+37 50 47.3	4.50	4.98	−0.49	1	22.30	23.4	0.12	0.287	ELG	···	2719−7614	42.1	20.5	<	20.9
J121739.5+374655	12 17 39.54	+37 46 55.1	3.44	5.38	0.86[h]	1	23.04	23.4	0.45	0.000	star	A	3700−9900	···	···	···	···
J121739.6+374646	12 17 39.68	+37 46 46.3	3.47	5.36	−0.51	2	23.40	23.4	0.61	2.987	NLAGN	···	928−2483	44.3	22.2	21.8	22.4
J121740.1+374749	12 17 40.17	+37 47 49.3	3.70	20.80	−0.44	1	19.24	23.4	−0.49	1.795	BLAGN	J	1323−3398	44.5	<	<	20.6
J125247.0-091637	12 52 47.01	−09 16 37.1	8.69	115.00	−0.53	1	18.24	23.4	−0.14	0.264	BLAGN	···	3058−7929	43.4	<	<	20.0
J125252.8-091921	12 52 52.88	−09 19 21.5	10.20	76.30	−0.49	1	17.99	22.4	−0.42	1.111	BLAGN	···	1828−4737	44.6	<	<	20.8

Table 5.2 (cont'd)

	X-ray Data					Optical Counterpart Data											
CXOSEXSI_	α_x (J2000)	δ_x (J2000)	OAA	$S_{2-10}^{(-15)}$	HR	Flag	R	R_{limit}	$\log \frac{f_x}{f_o}$	z	Class	Notes	$\Delta\lambda_{rest}$	$\log L_x^{(2-10)}$	$\log N_H$	$\log N_H^-$	$\log N_H^+$
(1)	(2)[a]	(3)[a]	(4)	(5)	(6)[b]	(7)[c]	(8)	(9)	(10)	(11)	(12)[d]	(13)[e]	(14)[f]	(15)	(16)[g]	(17)[g]	(18)[g]
J125300.3-091104	12 53 00.37	−09 11 04.2	2.63	6.23	0.61[h]	1	21.99	23.4	0.09	0.625	ELG	···	2154−6093	42.9	23.4	23.2	23.6
J125301.9-091134	12 53 01.90	−09 11 34.0	2.54	6.90	−0.36	1	21.80	23.4	0.06	0.713	ELG	···	2159−5662	43.1	21.3	21.0	21.5
J125302.4-091311	12 53 02.39	−09 13 11.7	3.65	106.00	−0.33	1	20.17	23.4	0.59	1.132	BLAGN	···	1512−4474	44.7	<	<	20.5
J125302.9-091057	12 53 02.93	−09 10 57.5	2.01	6.97	0.65[h]	1	20.86	23.4	−0.31	0.381	BLAGN	···	2535−7315	42.5	24.0	23.8	24.2
J125303.0-091241	12 53 03.01	−09 12 41.7	3.15	15.80	−0.52	1	20.62	23.4	−0.05	0.983	ELG	···	1765−4992	43.8	21.0	20.6	21.2
J125303.8-090809	12 53 03.84	−09 08 09.6	2.52	29.30	−0.16	1	17.96	23.4	−0.85	0.000	star	···	3865−9500	···	···	···	···
J125304.7-090442	12 53 04.75	−09 04 42.3	5.57	17.50	−0.50	1	19.14	23.4	−0.60	1.706	BLAGN	···	1428−3695	44.3	<	<	20.9
J125305.3-090823	12 53 05.33	−09 08 23.5	2.11	31.60	−0.46	1	19.58	23.4	−0.17	0.499	NLAGN	···	2828−6671	43.4	<	<	20.0
J125306.0-091316	12 53 05.99	−09 13 16.2	3.34	22.30	−0.08	1	21.84	23.4	0.58	···	···	···	3800−9400[i]	···	···	···	···
J125309.6-090323	12 53 09.64	−09 03 23.0	6.73	14.60	0.55	1	22.83	23.4	0.80	···	···	···	3800−9400[i]	···	···	···	···
J125310.4-091023	12 53 10.40	−09 10 23.4	0.28	12.80	−0.29	1	21.58	22.9	0.24	0.558	BLAGN	···	2458−6482	43.2	20.8	20.0	21.0
J125310.4-091442	12 53 10.40	−09 14 41.9	4.59	5.58	0.05	1	21.60	23.4	−0.11	1.134	NLAGN	···	1686−4311	43.5	<	<	21.9
J125311.1-091117	12 53 11.11	−09 11 17.5	1.20	11.80	0.55[h]	1	20.28	23.4	−0.32	0.478	ELG	···	2571−6698	43.0	23.6	23.4	23.7
J125312.6-090644	12 53 12.68	−09 06 44.0	3.42	6.02	−0.49	1	21.10	23.4	−0.28	0.000	star	···	3600−9500	···	···	···	···
J125314.8-091300	12 53 14.83	−09 13 00.8	3.11	38.20	0.63	1	21.62	23.4	0.73	0.716	ELG	···	2097−5535	43.9	22.8	22.7	22.9
J125315.2-091424	12 53 15.20	−09 14 24.3	4.47	30.20	0.66	1	23.82	23.4	1.51	1.154	NLAGN	···	1578−4178	44.2	23.2	23.1	23.2
J125319.1-091116	12 53 19.13	−09 11 15.9	2.47	4.77	0.65[h]	1	20.05	23.4	−0.80	0.478	ELG	···	2943−6292	42.6	22.9	22.7	23.1
J125322.6-090246	12 53 22.64	−09 02 46.5	7.94	24.90	−0.22	1	16.69	23.4	−1.43	0.000	star	A	3870−10000	···	···	···	···
J125323.2-090827	12 53 23.28	−09 08 27.3	3.60	18.90	0.44	1	21.93	23.4	0.55	0.503	ELG	···	2395−3759	43.2	22.7	22.6	22.8
J125323.6-090429	12 53 23.63	−09 04 29.8	6.50	27.20	0.42	1	21.08	23.4	0.37	0.519	ELG	···	2601−6189	43.4	22.6	22.5	22.8
J131653.0+291703	13 16 53.15	+29 17 04.7	7.94	16.40	−0.44	2	23.50	23.5	1.10	1.637	BLAGN	···	1338−3412	44.3	<	<	21.2
J131654.1+291320	13 16 54.28	+29 13 22.5	4.98	15.60	−0.49	1	22.16	23.5	0.56	1.756	BLAGN	···	1415−3265	44.3	<	<	21.2
J131654.6+291004	13 16 54.72	+29 10 06.2	3.85	31.00	0.06	1	22.15	23.5	0.85	0.908	ELG	···	2044−4848	44.0	22.4	22.3	22.4
J131655.4+290753	13 16 55.58	+29 07 54.7	4.38	3.88	0.20	1	19.12	23.5	−1.26	0.262	ELG	···	2773−6537	41.9	21.5	20.8	21.8
J131658.1+291017	13 16 58.29	+29 10 18.8	3.06	2.18	0.20	1	23.69	23.5	0.31	0.951	ELG	A	2075−4818	42.9	22.6	22.3	23.0
J131700.2+291307	13 17 00.37	+29 13 08.6	3.84	4.12	−0.15	1	22.45	23.5	0.09	0.580	ELG	I	2215−5031	42.7	21.4	20.0	21.8
J131701.2+290657	13 17 01.37	+29 06 58.6	4.12	8.85	−0.30	1	20.48	23.5	−0.36	0.491	BLAGN	J	2347−5264	42.9	20.9	<	21.3
J131701.3+291432	13 17 01.51	+29 14 34.5	4.86	17.50	0.01	2	23.50	23.5	1.13	1.169	ELG	···	1613−3964	44.0	22.4	22.3	22.5
J131706.0+290916	13 17 06.17	+29 09 18.2	1.69	40.00	−0.42	1	19.94	23.5	0.08	1.020	BLAGN	···	1881−4455	44.2	21.0	20.5	21.3
J131706.2+291058	13 17 06.35	+29 10 59.8	1.46	2.29	0.50	1	20.51	23.5	−0.94	0.579	ELG	I	2216−5668	42.4	22.9	22.7	23.1
J131708.6+291117	13 17 08.78	+29 11 19.0	1.25	6.62	0.49	1	19.80	23.5	−0.76	1.680	BLAGN	J	1380−3414	43.9	23.4	23.2	23.6
J131713.8+291519	13 17 14.01	+29 15 21.2	5.04	3.94	0.64	1	19.36	23.5	−1.16	0.367	ELG	N	3108−6858	42.2	22.8	22.7	23.0
J131714.5+291041	13 17 14.66	+29 10 42.7	0.64	3.80	−0.43	1	20.64	23.5	−0.66	2.702	BLAGN	J	945−2431	44.1	21.9	<	22.4
J131714.7+290636	13 17 14.82	+29 06 37.8	3.74	4.60	−0.18	1	18.39	23.5	−1.48	0.181	ELG	···	2963−6591	41.6	20.3	<	21.1
J131717.1+290639	13 17 17.26	+29 06 40.7	3.81	10.70	−0.15	1	19.57	23.5	−0.64	2.701	BLAGN	···	945−2107	44.5	22.6	22.3	22.8
J131718.8+291111	13 17 19.01	+29 11 12.8	1.71	7.49	−0.30	1	21.98	23.5	0.17	0.803	BLAGN	H	2107−4991	43.3	<	<	21.2
J131722.0+291124	13 17 22.12	+29 11 25.8	2.40	5.78	0.59	1	24.15	23.5	0.92	0.793	ELG	H	2230−5242	43.1	22.9	22.8	23.0
J131727.4+290930	13 17 27.59	+29 09 32.0	3.43	4.63	0.87[h]	1	22.05	23.5	−0.01	0.847	ELG	···	1894−4656	43.1	23.6	23.4	23.8
J131729.7+290730	13 17 29.82	+29 07 32.0	4.74	15.50	−0.15	1	22.17	23.5	0.56	2.540	BLAGN	···	988−2175	44.6	22.5	22.3	22.7
J131730.7+291055	13 17 30.86	+29 10 57.0	4.09	5.09	−0.46	1	21.74	23.5	−0.10	1.748	BLAGN	J	1410−3347	43.8	20.8	<	21.8
J131730.8+291217	13 17 30.94	+29 12 19.4	4.53	3.60	0.45	1	22.56	23.5	0.08	0.830	ELG	···	1912−4453	43.0	22.9	22.8	23.1
J131732.9+291055	13 17 33.06	+29 10 57.3	4.57	2.98	−0.19	1	21.61	23.5	−0.38	1.034	ELG	A	1769−3947	43.1	21.1	<	21.8
J131733.4+290810	13 17 33.59	+29 08 12.2	5.11	8.84	−0.03	1	22.53	23.5	0.46	1.690	BLAGN	···	1301−2992	44.0	22.2	21.9	22.4
J131736.5+291114	13 17 36.71	+29 11 15.7	5.40	8.44	−0.45	1	19.88	23.5	−0.62	1.958	BLAGN	···	1419−3177	44.1	21.8	20.8	22.1
J131737.3+291524	13 17 37.50	+29 15 26.4	7.50	4.56	−0.43	1	22.81	23.5	0.28	···	···	···	5710−9400[i]	···	···	···	···
J131742.5+290911	13 17 42.67	+29 09 12.7	6.72	5.29	0.75[h]	1	24.23	23.5	0.92	1.019	ELG	···	1733−4160	43.3	24.3	24.1	24.4
J131745.2+291201	13 17 45.40	+29 12 02.7	7.42	4.56	0.70[h]	1	22.34	23.5	0.09	0.715	ELG	···	2623−5481	42.9	24.0	23.7	24.1
J131746.0+290912	13 17 46.16	+29 09 13.7	7.47	15.40	−0.32	1	19.64	23.5	−0.46	2.040	BLAGN	···	1151−2861	44.4	<	<	21.0
J133730.8+292747	13 37 30.95	+29 27 48.4	6.56	8.62	−0.62	1	21.06	22.5	−0.14	1.428	BLAGN	···	1729−3871	43.9	<	<	20.9
J133734.7+292830	13 37 34.85	+29 28 31.2	5.57	16.50	−0.30	1	21.53	22.5	0.33	0.830	BLAGN	···	2295−5136	43.6	20.6	<	21.4

Table 5.2 (cont'd)

	X-ray Data					Optical Counterpart Data											
CXOSEXSI_	α_x (J2000)	δ_x (J2000)	OAA	$S_{2-10}^{(-15)}$	HR	Flag	R	R_{limit}	$\log \frac{f_x}{f_o}$	z	Class	Notes	$\Delta\lambda_{rest}$	$\log L_x^{(2-10)}$	$\log N_H$	$\log N_H^-$	$\log N_H^+$
(1)	(2)[a]	(3)[a]	(4)	(5)	(6)[b]	(7)[c]	(8)	(9)	(10)	(11)	(12)[d]	(13)[e]	(14)[f]	(15)	(16)[g]	(17)[g]	(18)[g]
J133739.0+292712	13 37 39.17	+29 27 13.3	5.11	5.47	−0.37	1	20.76	22.5	−0.46	1.551	BLAGN	···	1646−3684	43.7	21.0	<	22.0
J133741.8+292623	13 37 41.98	+29 26 24.1	5.05	53.20	−0.48	1	20.79	22.5	0.54	0.675	BLAGN	···	2507−5611	44.0	<	<	20.3
J133744.1+292605	13 37 44.24	+29 26 06.5	4.89	12.10	−0.24	1	21.89	22.5	0.34	1.064	ELG	···	2034−4554	43.7	21.4	<	21.9
J133744.2+293511	13 37 44.32	+29 35 12.9	6.56	22.70	−0.32	1	20.57	22.5	0.08	1.207	BLAGN	···	1585−4259	44.1	21.7	21.3	21.9
J133753.0+293452	13 37 53.11	+29 34 53.2	5.49	9.28	−0.55	1	20.62	22.5	−0.28	1.610	BLAGN	···	1340−3601	44.0	<	<	21.4
J133753.2+292433	13 37 53.35	+29 24 34.4	5.23	16.50	−0.49	1	19.90	22.5	−0.32	2.738	BLAGN	···	1123−2514	44.7	21.4	<	22.1
J133755.4+293502	13 37 55.50	+29 35 03.7	5.54	29.90	0.22	1	22.25	22.5	0.88	0.426	ELG	L	3927−6591	43.3	22.5	22.4	22.6
J133755.5+292745	13 37 55.65	+29 27 46.8	2.05	10.60	−0.66	1	19.52	22.5	−0.67	0.632	ALG	···	2573−5637	43.2	<	<	20.3
J133757.9+292608	13 37 58.04	+29 26 10.0	3.46	11.30	−0.17	1	18.30	23.0	−1.13	0.304	ELG	···	3220−7131	42.5	21.4	20.9	21.5
J133800.7+292927	13 38 00.82	+29 29 29.0	0.23	5.82	−0.05	2	23.00	23.0	0.45	0.853	ELG	···	2293−5072	43.2	22.3	22.0	22.5
J133803.0+292825	13 38 03.11	+29 28 26.9	1.35	8.18	0.80	1	21.86	23.0	0.16	0.717	ELG	···	3261−5474	43.2	23.0	22.8	23.1
J133803.6+292915	13 38 03.75	+29 29 16.7	0.89	10.10	0.76	1	22.46	23.0	0.49	1.001	NLAGN	···	2123−4622	43.6	23.0	22.8	23.2
J133805.1+292422	13 38 05.22	+29 24 23.3	5.34	9.98	−0.59	1	20.38	23.0	−0.35	1.100	BLAGN	···	1809−4476	43.7	<	<	20.8
J133807.0+292852	13 38 07.16	+29 28 53.9	1.72	4.31	0.70[h]	2	23.00	23.0	0.32	0.375	ELG	···	2545−6836	42.3	23.0	22.7	23.2
J133807.2+292734	13 38 07.39	+29 27 35.7	2.58	4.86	0.21	1	23.42	23.0	0.55	2.140	BLAGN	···	1114−2993	44.0	22.9	22.4	23.2
J133808.8+293128	13 38 08.98	+29 31 29.6	2.73	13.50	0.48	1	22.95	22.5	0.81	1.322	ELG	···	1851−4026	44.0	23.3	23.2	23.4
J133808.9+292412	13 38 09.06	+29 24 13.4	5.74	12.90	−0.50	1	19.64	23.0	−0.53	2.384	BLAGN	···	1241−2777	44.5	22.1	20.0	22.4
J133810.9+293119	13 38 11.06	+29 31 20.1	2.98	25.70	−0.33	1	19.81	22.5	−0.17	2.032	BLAGN	···	1418−3100	44.7	20.3	<	21.6
J133816.8+292350	13 38 16.98	+29 23 51.5	6.84	15.70	0.43	1	22.89	23.0	0.85	0.755	ELG	A	2905−5356	43.5	22.7	22.5	22.9
J133825.7+292956	13 38 25.83	+29 29 57.9	5.65	13.70	0.85[h]	1	23.18	23.0	0.91	0.983	NLAGN	···	2874−4538	43.7	23.4	23.2	23.7
J133833.0+292908	13 38 33.15	+29 29 09.1	7.24	32.50	−0.18	1	20.12	23.0	0.06	0.000	star	D	3700−9000	···	···	···	···
J133836.0+292940	13 38 36.15	+29 29 41.4	7.88	35.30	−0.14	1	20.42	23.0	0.22	0.469	ELG	···	3097−6296	43.4	21.6	21.4	21.8
J141114.2+520630	14 11 14.26	+52 06 30.6	6.54	22.60	−0.38	1	19.76	21.9	−0.24	1.524	BLAGN	···	1545−3763	44.3	<	<	20.7
J141119.4+521400	14 11 19.43	+52 14 00.5	1.56	30.90	−0.40	4	19.14	21.4	−0.35	1.279	BLAGN	···	1711−4168	44.3	<	<	20.0
J141123.4+521331	14 11 23.40	+52 13 31.6	1.89	90.70	−0.51	1	19.05	21.4	0.08	0.472	BLAGN	H	2625−6793	43.8	<	<	<
J141127.4+521131	14 11 27.38	+52 11 31.4	2.87	33.10	0.09	1	19.78	21.9	−0.07	0.451	ALG	HK	2412−6374	43.4	21.9	21.8	22.0
J145143.6+430600	14 51 43.70	+43 06 00.4	6.73	38.50	−0.21	1	20.47	22.9	0.27	0.558	BLAGN	···	2278−5969	43.6	<	<	21.0
J145149.0+430125	14 51 49.14	+43 01 25.2	4.23	86.90	0.09	1	20.38	22.9	0.59	1.150	BLAGN	···	1488−4418	44.7	20.9	<	21.3
J145150.2+430801	14 51 50.25	+43 08 01.5	7.45	14.80	0.03	1	22.98	21.9	0.86	1.785	BLAGN	···	1256−3231	44.3	22.0	<	22.3
J145151.2+430256	14 51 51.33	+43 02 56.6	4.00	25.90	−0.05	1	20.57	22.9	0.14	0.963	BLAGN	N	1782−4583	44.0	<	<	21.2
J145156.1+431008	14 51 56.22	+43 10 08.7	8.90	65.10	−0.14	1	21.34	21.9	0.85	0.744	ELG	···	2379−5676	44.1	22.0	21.8	22.1
J145200.2+430349	14 52 00.33	+43 03 49.3	3.01	10.80	0.09	1	21.64	22.9	0.19	1.548	BLAGN	N	1373−3649	44.0	21.9	<	22.4
J145201.7+430640	14 52 01.75	+43 06 40.1	5.29	43.10	0.73	1	19.25	22.9	−0.17	0.279	BLAGN	N	2873−7427	43.0	22.8	22.7	23.0
J145203.0+430542	14 52 03.13	+43 05 42.3	4.30	42.90	−0.44	1	20.67	22.9	0.40	1.609	BLAGN	···	1379−3641	44.7	21.6	20.8	21.9
J145209.4+430101	14 52 09.48	+43 01 00.9	0.88	23.30	−0.15	1	21.76	22.9	0.57	1.340	BLAGN	···	1769−4102	44.2	21.7	21.3	21.9
J145210.3+430525	14 52 10.35	+43 05 25.8	3.71	20.20	−0.44	1	20.51	22.9	0.01	1.385	BLAGN	···	1740−3983	44.2	21.9	21.4	22.1
J145215.0+430439	14 52 15.07	+43 04 39.1	2.96	8.59	0.48	1	19.95	22.9	−0.59	0.346	ELG	···	2749−7431	42.5	22.7	22.4	23.0
J145215.6+430448	14 52 15.66	+43 04 48.7	3.14	180.00	−0.41	1	17.91	22.9	−0.08	0.297	BLAGN	M	2853−7711	43.7	<	<	20.5
J150925.5+565729	15 09 25.64	+56 57 29.3	6.75	18.00	−0.13	1	21.27	24.0	0.26	1.607	BLAGN	···	1814−3807	44.3	22.0	21.7	22.2
J150929.9+570413	15 09 30.07	+57 04 13.6	4.21	13.90	−0.20	6	···	···	···	0.000	star	···	3500−5700	···	···	···	···
J150934.1+570314	15 09 34.25	+57 03 14.5	3.37	3.47	−0.36	1	22.91	24.0	0.20	2.826	BLAGN	···	914−2404	44.1	22.7	22.4	22.9
J150934.2+571006	15 09 34.33	+57 10 07.0	8.26	9.40	−0.24	1	20.54	24.0	−0.31	1.938	BLAGN	J	1242−3063	44.2	22.7[j]	···	···
J150935.7+570324	15 09 35.87	+57 03 25.1	3.20	8.60	−0.14	1	20.18	24.0	−0.49	0.310	BLAGN	···	2671−7099	42.4	21.7	21.5	21.8
J150935.8+565922	15 09 35.91	+56 59 22.7	4.41	43.50	−0.02	1	21.48	24.0	0.73	0.681	BLAGN	···	2769−5883	43.9	21.7	21.5	21.8
J150937.2+570507	15 09 37.28	+57 05 07.9	3.88	6.90	0.90[h]	6	···	···	···	1.093	ELG	···	2675−4300	43.5	22.7	22.5	22.9
J150941.1+565856	15 09 41.22	+56 58 56.2	4.30	4.64	−0.39	1	23.16	24.0	0.43	1.500	BLAGN	···	1954−4040	43.6	21.4	<	21.8
J150945.8+570100	15 09 45.91	+57 01 00.4	2.30	8.36	−0.31	6	···	···	···	0.003	ELG	E	4596−9825	38.3	···	···	···
J150946.6+565946	15 09 46.71	+56 59 46.9	3.19	4.89	0.04	6	···	···	···	0.002	ELG	E	4850−10079	37.7	···	···	···
J150949.5+570000	15 09 49.65	+57 00 00.4	2.80	54.50	−0.31	6	···	···	···	1.458	ELG	K	1989−4119	44.7	21.5	21.4	21.7
J150951.4+565928	15 09 51.50	+56 59 28.2	3.21	8.23	−0.03	1	21.37	24.0	−0.04	0.003	star	E	5029−10249	38.3	···	···	···

Table 5.2 (cont'd)

	X-ray Data					Optical Counterpart Data											
CXOSEXSI_	α_x (J2000)	δ_x (J2000)	OAA	$S_{2-10}^{(-15)}$	HR	Flag	R	R_{limit}	$\log \frac{f_x}{f_o}$	z	Class	Notes	$\Delta\lambda_{rest}$	$\log L_x^{(2-10)}$	$\log N_H$	$\log N_H^-$	$\log N_H^+$
(1)	(2)[a]	(3)[a]	(4)	(5)	(6)[b]	(7)[c]	(8)	(9)	(10)	(11)	(12)[d]	(13)[e]	(14)[f]	(15)	(16)[g]	(17)[g]	(18)[g]
J150953.2+570547	15 09 53.34	+57 05 48.1	3.33	3.66	−0.67	1	21.09	24.0	−0.50	0.806	BLAGN	···	1937−5121	43.0	<	<	20.0
J150953.7+570048	15 09 53.80	+57 00 48.2	1.85	17.70	−0.32	1	22.35	24.0	0.69	1.973	BLAGN	···	1633−3393	44.5	21.4	20.9	21.6
J150956.0+570534	15 09 56.14	+57 05 34.6	3.05	3.71	0.73	1	20.46	24.0	−0.75	0.150	ELG	A	3130−8173	41.4	22.6	22.3	22.7
J151004.7+570038	15 10 04.83	+57 00 38.6	2.08	8.90	0.09	2	24.00	24.0	1.04	1.215	ELG	···	2334−4695	43.7	22.5	22.3	22.6
J151008.4+570537	15 10 08.51	+57 05 37.6	3.37	21.10	0.92	1	20.62	24.0	0.07	0.272	ELG	···	2830−7272	42.7	23.0	23.0	23.1
J151010.3+570609	15 10 10.44	+57 06 09.6	3.97	33.90	0.54	1	20.34	24.0	0.17	0.546	NLAGN	···	2328−6015	43.6	22.7	22.6	22.7
J151013.3+570155	15 10 13.40	+57 01 56.1	2.12	3.35	0.35	2	24.00	24.0	0.61	0.101	ELG	···	3269−8628	41.0	22.2	22.1	22.4
J151015.1+570341	15 10 15.26	+57 03 41.7	2.56	6.00	−0.37	1	23.23	24.0	0.57	1.303	BLAGN	···	2103−4363	43.6	<	<	20.5
J151029.9+570513	15 10 30.03	+57 05 13.3	5.06	10.70	0.11	1	20.30	24.0	−0.35	0.536	ELG	···	3193−6484	43.0	22.3	22.2	22.4
J151030.9+570014	15 10 30.99	+57 00 14.8	4.98	5.26	−0.25	1	22.93	24.0	0.39	1.943	BLAGN	N	1427−3160	43.9	20.7	<	21.7
J151044.8+570340	15 10 44.89	+57 03 40.6	6.41	23.00	0.78	1	24.26	24.0	1.57	1.531	NLAGN	···	1422−3318	44.4	23.7	23.6	23.8
J152132.9+074856	15 21 33.02	+07 48 56.1	6.95	9.78	−0.47	1	21.29	23.4	0.01	1.539	BLAGN	···	1963−3938	44.0	20.8	<	21.7
J152135.0+074836	15 21 35.08	+07 48 36.7	6.35	9.41	−0.52	1	20.93	23.4	−0.15	1.513	BLAGN	···	2001−4058	44.0	<	<	21.3
J152151.4+074826	15 21 51.50	+07 48 26.3	3.34	14.70	−0.44	1	18.88	23.4	−0.78	2.049	BLAGN	···	1626−3345	44.4	21.7	20.5	22.0
J152151.6+074651	15 21 51.72	+07 46 51.8	1.99	10.20	−0.51	1	17.63	23.4	−1.44	0.000	star	···	5365−10500	···	···	···	···
J152156.3+074809	15 21 56.41	+07 48 09.1	2.75	10.50	0.07	1	17.73	23.4	−1.39	0.267	ALG	···	3946−7892	42.4	22.1	21.9	22.2
J152158.2+074832	15 21 58.29	+07 48 32.2	3.14	3.73	−0.19	1	21.92	23.4	−0.16	0.632	ALG	K	2993−6188	42.7	22.4	22.2	22.6
J152207.5+074528	15 22 07.56	+07 45 28.1	2.57	12.50	−0.39	1	21.30	22.9	0.12	···	···	···	5580−10500[i]	···	···	···	···
J152218.4+074916	15 22 18.48	+07 49 16.8	6.54	14.10	−0.41	1	21.49	22.9	0.25	1.027	BLAGN	···	2217−4686	43.8	21.3	<	21.7
J152227.2+074833	15 22 27.32	+07 48 33.1	8.10	38.40	0.04	1	21.90	22.9	0.84	0.998	BLAGN	···	2489−4604	44.2	22.2	22.0	22.3
J162252.1+263852	16 22 52.28	+26 38 52.3	7.89	19.00	−0.38	1	20.83	22.4	0.11	0.815	NLAGN	···	2947−5757	43.7	21.2	<	21.6
J162255.0+263720	16 22 55.12	+26 37 20.4	6.89	18.30	−0.01	1	21.41	22.4	0.33	1.017	BLAGN	A	2456−4923	43.9	21.8	<	22.1
J162256.7+264103	16 22 56.83	+26 41 02.9	8.03	18.50	0.43	4	21.70	22.4	0.45	0.690	ELG	···	3340−6213	43.5	22.8	22.6	23.0
J162300.1+263755	16 23 00.22	+26 37 55.2	5.91	35.20	−0.42	4	17.36	22.4	−1.01	0.091	ELG	···	4472−9165	41.9	<	<	20.3
J162305.6+263918	16 23 05.71	+26 39 18.2	5.40	9.07	0.62	1	22.09	23.9	0.29	0.929	ELG	···	2584−5287	43.5	23.1	22.9	23.3
J162315.4+263506	16 23 15.56	+26 35 06.3	2.48	5.14	−0.43	1	20.96	23.9	−0.41	0.425	ELG	···	3185−6866	42.5	21.6	20.9	21.9
J162327.2+263207	16 23 27.30	+26 32 07.3	4.10	19.90	−0.23	4	19.38	24.4	−0.45	1.438	BLAGN	K	2255−4388	44.2	21.5	<	21.9
J162328.0+264034	16 23 28.15	+26 40 33.7	4.39	16.20	0.61	1	23.92	23.9	1.28	0.951	ELG	···	2275−4971	43.8	23.2	23.0	23.3
J162331.9+264125	16 23 31.99	+26 41 25.6	5.42	8.60	0.07	1	21.96	23.9	0.22	1.575	BLAGN	···	1759−3782	44.0	22.9	22.6	23.1
J162333.9+263525	16 23 34.01	+26 35 25.0	2.06	7.06	−0.09	1	21.88	23.9	0.10	···	···	···	4805−9500[i]	···	···	···	···
J162335.9+263652	16 23 36.07	+26 36 52.5	2.45	11.40	−0.30	1	22.81	23.9	0.68	···	···	···	4450−9570[i]	···	···	···	···
J162343.7+263244	16 23 43.79	+26 32 44.6	5.36	122.00	−0.35	1	19.15	23.9	0.25	0.659	BLAGN	···	3408−6389	44.3	20.7	<	21.0
J162345.7+263335	16 23 45.88	+26 33 34.9	5.26	16.70	0.47	1	21.63	23.9	0.37	1.283	ELG	K	2492−4485	44.1	23.4	23.2	23.5
J170318.8+514319	17 03 18.96	+51 43 20.3	8.64	14.40	−0.55	1	20.52	22.9	−0.13	0.305	ELG	···	2681−7662	42.6	<[j]	···	···
J170320.5+514602	17 03 20.62	+51 46 02.9	7.77	11.70	−0.23	1	21.06	22.9	−0.01	0.957	ELG	···	1788−5033	43.6	22.2[j]	···	···
J170321.8+514526	17 03 21.88	+51 45 27.3	7.64	20.00	−0.23	1	18.39	22.9	−0.84	0.259	ELG	···	2779−7942	42.6	21.7[j]	···	···
J170323.2+514240	17 03 23.31	+51 42 40.8	8.31	23.00	0.75[h]	1	18.28	22.9	−0.83	0.297	ELG	···	2698−7710	42.8	22.8[k]	···	···
J170334.5+514207	17 03 34.66	+51 42 08.3	7.13	9.86	0.23	2	22.90	22.9	0.66	···	···	···	4000−9400[i]	···	···	···	···
J170342.4+514847	17 03 42.49	+51 48 48.5	4.90	27.40	−0.47	1	20.13	22.9	−0.01	1.476	BLAGN	N	1413−3634	44.4	<	<	20.3
J170343.8+514707	17 03 43.94	+51 47 08.1	4.18	18.50	−0.49	1	21.83	22.9	0.50	0.967	BLAGN	···	1779−5083	43.8	<	<	20.7
J170348.8+514454	17 03 48.94	+51 44 55.3	3.76	26.50	−0.53	1	19.99	22.9	−0.08	1.091	BLAGN	N	2068−4782	44.1	<	<	20.0
J170352.5+515340	17 03 52.65	+51 53 40.9	7.63	14.70	0.73[h]	1	18.59	22.9	−0.90	0.297	ELG	···	3084−7710	42.6	24.7	24.1	26.3
J170355.1+514935	17 03 55.17	+51 49 36.5	3.87	10.40	−0.16	1	21.24	22.9	0.01	0.631	BLAGN	···	2145−6131	43.2	21.8	21.6	22.0
J170355.8+514949	17 03 55.89	+51 49 49.7	3.98	29.40	−0.23	1	20.66	22.9	0.23	0.670	BLAGN	···	2095−5988	43.7	<	<	20.6
J170400.9+515515	17 04 01.03	+51 55 15.6	8.81	21.60	−0.27	1	20.64	22.9	0.09	1.974	BLAGN	···	1176−3093	44.6	22.5	22.2	22.6
J170402.8+514247	17 04 02.92	+51 42 48.4	3.96	6.93	−0.49	1	21.76	22.9	0.04	1.426	BLAGN	A	1236−3998	43.8	21.4	<	21.9
J170403.3+514756	17 04 03.44	+51 47 57.1	1.78	12.60	−0.26	1	19.74	22.9	−0.50	4.270	BLAGN	···	721−1802	45.0	<	<	22.0
J170403.3+514854	17 04 03.46	+51 48 54.9	2.60	13.30	−0.08	1	22.85	22.9	0.76	1.806	BLAGN	···	1318−3385	44.3	<	<	21.1
J170407.4+514957	17 04 07.47	+51 49 57.6	3.42	8.03	0.11	1	22.56	22.9	0.43	0.693	ELG	···	2362−5906	43.2	22.7	22.5	22.8
J170416.4+514306	17 04 16.55	+51 43 07.2	3.57	6.83	−0.44	1	21.02	22.9	−0.26	1.962	BLAGN	···	1114−3207	44.1	<	<	21.7

Table 5.2 (cont'd)

	X-ray Data					Optical Counterpart Data											
CXOSEXSI_	α_x (J2000)	δ_x (J2000)	OAA	$S_{2-10}^{(-15)}$	HR	Flag	R	R_{limit}	$\log \frac{f_x}{f_o}$	z	Class	Notes	$\Delta\lambda_{rest}$	$\log L_x^{(2-10)}$	$\log N_H$	$\log N_H^-$	$\log N_H^+$
(1)	(2)[a]	(3)[a]	(4)	(5)	(6)[b]	(7)[c]	(8)	(9)	(10)	(11)	(12)[d]	(13)[e]	(14)[f]	(15)	(16)[g]	(17)[g]	(18)[g]
J170419.1+514233	17 04 19.24	+51 42 33.9	4.22	11.00	0.03	1	23.59	22.9	0.98	1.049	ALG	···	1781−4880	43.7	22.5	22.3	22.7
J170421.9+514403	17 04 21.99	+51 44 03.6	3.06	15.90	−0.27	1	20.76	22.9	0.01	1.915	BLAGN	N	1166−3327	44.4	22.2	22.0	22.4
J170423.0+514321	17 04 23.14	+51 43 22.2	3.74	8.82	−0.05	1	19.83	22.9	−0.62	0.325	ELG	···	2792−7547	42.5	21.9	21.6	22.1
J170425.1+514716	17 04 25.22	+51 47 16.7	2.35	11.50	−0.07	2	22.90	22.9	0.73	2.220	BLAGN	···	1086−2950	44.4	21.6	<	22.0
J171600.9+670807	17 16 01.02	+67 08 06.7	6.85	8.68	−0.36	1	22.46	24.4	0.42	1.714	BLAGN	···	1470−3316	44.0	22.1	21.6	22.4
J171613.3+671133	17 16 13.40	+67 11 32.2	4.62	14.40	−0.31	1	22.99	23.9	0.85	1.584	BLAGN	J	1393−3482	44.2	22.5	22.4	22.7
J171614.4+671344	17 16 14.52	+67 13 43.5	4.94	12.90	−0.00	1	23.07	23.9	0.84	1.133	BLAGN	···	2625−4406	43.8	22.2	21.9	22.4
J171621.3+671312	17 16 21.39	+67 13 11.3	4.12	4.92	−0.43	1	21.13	23.9	−0.36	1.081	BLAGN	···	1729−4469	43.4	22.3	21.9	22.4
J171624.7+671239	17 16 24.81	+67 12 38.2	3.63	6.65	0.08	1	23.99	23.9	0.92	3.417	NLAGN	···	837−1924	44.5	23.5	23.1	23.8
J171635.5+671626	17 16 35.62	+67 16 24.9	5.31	21.30	−0.19	1	20.19	23.9	−0.10	0.501	BLAGN	···	2331−6195	43.3	20.9	<	21.3
J171636.9+670829	17 16 36.99	+67 08 28.5	3.99	38.60	0.72	1	22.00	24.4	0.89	0.795	ELG	H	2005−5236	44.0	23.3	23.2	23.4
J171637.9+671307	17 16 38.03	+67 13 06.4	2.63	18.00	0.38	1	23.27	23.9	1.06	1.272	NLAGN	···	1716−3807	44.1	23.2	23.0	23.2
J171638.0+671155	17 16 38.17	+67 11 54.7	2.23	9.85	−0.43	1	22.92	23.9	0.66	1.326	BLAGN	J	1590−3869	43.9	21.5	<	21.8
J171639.7+671640	17 16 39.88	+67 16 39.2	5.35	12.10	0.87[h]	1	23.36	23.9	0.93	1.275	NLAGN	···	1604−3846	43.9	24.0	23.9	24.2
J171651.7+670855	17 16 51.81	+67 08 53.8	2.95	30.80	0.03	2	23.90	23.9	1.55	2.067	NLAGN	···	1206−2771	44.8	23.1	23.0	23.2
J171652.0+671508	17 16 52.12	+67 15 07.7	3.52	4.22	−0.33	1	22.84	23.9	0.26	1.800	BLAGN	J	1367−2857	43.8	21.7	<	22.2
J171700.6+670520	17 17 00.77	+67 05 18.9	6.40	24.70	−0.40	1	20.68	24.4	0.16	1.147	BLAGN	···	1630−4191	44.1	<	<	21.1
J171703.8+670900	17 17 03.90	+67 08 58.8	2.75	4.32	0.58	4	21.79	23.9	−0.15	0.812	ELG	H	2378−5118	43.0	23.2	22.5	24.1
J171713.4+671433	17 17 13.50	+67 14 32.7	3.08	104.00	0.03	1	21.66	23.9	1.18	1.811	BLAGN	···	1316−3201	45.2	23.0	23.0	23.1
J171714.5+671136	17 17 14.65	+67 11 35.0	1.32	5.77	0.62	1	22.68	23.9	0.33	0.815	ELG	···	1983−5509	43.2	23.0	22.8	23.2
J171715.1+671217	17 17 15.23	+67 12 15.8	1.48	3.37	0.67[h]	2	23.90	23.9	0.59	1.340	ELG	···	1623−4017	43.4	23.8	23.5	24.1
J171724.7+670913	17 17 24.81	+67 09 11.9	3.41	3.65	0.16	1	17.16	23.9	−2.07	0.138	ELG	···	3075−8347	41.3	21.5	20.6	21.8
J171725.3+670616	17 17 25.39	+67 06 15.6	5.94	16.30	−0.29	1	21.30	24.4	0.23	1.814	BLAGN	···	1279−3020	44.4	<	<	21.2
J171731.9+670934	17 17 32.01	+67 09 33.7	3.69	6.03	0.48	1	23.36	23.9	0.62	2.850	NLAGN	···	935−2337	44.3	23.5	23.2	23.7
J171740.6+671147	17 17 40.76	+67 11 46.1	3.85	6.10	−0.56	1	21.83	23.9	0.02	2.313	BLAGN	A	1109−2867	44.2	22.6	22.3	22.9
J171747.4+671449	17 17 47.58	+67 14 48.3	5.46	7.63	0.10	1	22.91	22.9	0.55	0.846	ELG	A	2166−5146	43.3	22.8	22.7	23.0
J171748.5+670545	17 17 48.59	+67 05 43.9	7.55	26.50	−0.48	1	19.74	24.4	−0.18	0.480	BLAGN	···	2364−6081	43.3	<	<	20.8
J171758.4+671203	17 17 58.56	+67 12 01.9	5.58	37.20	−0.38	1	20.87	23.9	0.42	1.808	BLAGN	···	1246−3205	44.7	21.5	20.3	21.8
J171806.0+671219	17 18 06.11	+67 12 18.1	6.33	6.71	−0.38	1	22.56	23.9	0.35	0.840	ELG	···	1956−5027	43.3	21.2	<	21.7
J171807.6+670647	17 18 07.73	+67 06 45.9	8.15	45.40	−0.38	1	21.75	23.9	0.86	0.797	BLAGN	···	2114−4730	44.0	<	<	20.8
J171837.5+671351	17 18 37.62	+67 13 50.1	9.59	13.80	−0.44	1	20.56	22.9	−0.14	1.540	BLAGN	J	1417−3346	44.1	20.3	<	21.8
J171838.3+671309	17 18 38.42	+67 13 08.6	9.54	17.80	0.16	1	22.14	23.9	0.61	0.000	star	···	5600−9200	···	···	···	···
J171859.5+671443	17 18 59.67	+67 14 42.7	11.87	52.70	−0.37	1	20.40	22.4	0.38	1.147	BLAGN	···	1676−3959	44.5	<	<	20.8
J175745.4+664112	17 57 45.50	+66 41 12.2	5.12	14.70	0.68	1	20.32	22.9	−0.20	0.680	ELG	K	3133−5636	43.4	23.1	23.0	23.2
J175812.1+664252	17 58 12.20	+66 42 52.7	4.71	12.50	0.12	2	22.90	22.9	0.75	2.750	NLAGN	···	1488−2800	44.6	23.5	23.4	23.7
J175823.5+663950	17 58 23.65	+66 39 50.7	1.47	14.00	−0.45	1	19.66	22.9	−0.49	0.995	BLAGN	K	2513−5130	43.7	21.0	20.3	21.3
J175859.6+663729	17 58 59.69	+66 37 29.8	3.17	3.78	0.81[h]	2	22.90	22.9	0.23	···	···	···	4870−10100[i]	···	···	···	···
J175911.9+663512	17 59 12.04	+66 35 12.3	5.36	45.90	−0.29	1	20.46	22.9	0.35	1.922	BLAGN	···	1519−3319	44.9	21.6	21.4	21.7
J175928.1+663851	17 59 28.21	+66 38 51.5	5.84	20.70	−0.33	1	20.22	22.9	−0.10	4.328	BLAGN	A	1036−2016	45.2	<	<	21.9
J175947.3+663552	17 59 47.42	+66 35 53.0	8.17	14.70	0.08	1	23.08	22.9	0.90	0.838	ELG	···	2725−5505	43.6	22.6[l]	···	···
J204359.5+771417	20 43 59.58	+77 14 17.6	2.87	5.58	0.71[h]	1	22.15	21.4	0.11	0.807	ELG	···	2855−5755	43.1	23.6	23.3	23.8
J204411.3+771427	20 44 11.43	+77 14 27.6	3.15	10.30	−0.26	1	22.75	21.4	0.61	1.023	ELG	···	2469−5042	43.6	21.9	21.4	22.1
J204412.5+771927	20 44 12.65	+77 19 28.1	3.54	12.70	0.31	1	18.30	21.4	−1.08	0.366	ELG	···	3715−7503	42.7	22.2	22.0	22.3
J204420.5+772039	20 44 20.65	+77 20 39.7	4.76	11.10	0.59	2	21.40	21.4	0.11	···	···	···	5230−9750[i]	···	···	···	···
J204430.7+771215	20 44 30.81	+77 12 15.4	5.53	9.68	−0.63	1	20.77	21.4	−0.21	0.768	ELG	A	2641−5599	43.3	<	<	20.7
J204433.8+772049	20 44 33.93	+77 20 50.0	5.33	50.70	−0.08	1	20.16	21.4	0.27	0.816	BLAGN	···	2813−5214	44.1	21.8	21.7	21.9
J204441.1+771146	20 44 41.26	+77 11 46.4	6.26	8.62	0.69[h]	1	22.95	21.4	0.62	···	···	···	4510−9735[i]	···	···	···	···
J205531.8-043101	20 55 31.94	−04 31 02.3	12.18	36.70	−0.94	3	10.74	22.8	−3.64	0.000	star	B	···	···	···	···	···
J205558.2-043340	20 55 58.27	−04 33 40.7	5.18	13.30	−0.23	1	19.27	23.8	−0.67	1.676	BLAGN	···	1765−3714	44.2	22.2	21.8	22.4
J205601.1-042955	20 56 01.25	−04 29 55.5	6.36	9.60	0.75[h]	1	20.68	22.8	−0.25	···	···	···	5435−10000[i]	···	···	···	···

Table 5.2 (cont'd)

	X-ray Data					Optical Counterpart Data											
CXOSEXSI_	α_x (J2000)	δ_x (J2000)	OAA	$S_{2-10}^{(-15)}$	HR	Flag	R	R_{limit}	$\log \frac{f_x}{f_o}$	z	Class	Notes	$\Delta\lambda_{rest}$	$\log L_x^{(2-10)}$	$\log N_H$	$\log N_H^-$	$\log N_H^+$
(1)	(2)[a]	(3)[a]	(4)	(5)	(6)[b]	(7)[c]	(8)	(9)	(10)	(11)	(12)[d]	(13)[e]	(14)[f]	(15)	(16)[g]	(17)[g]	(18)[g]
J205602.0-043644	20 56 02.08	−04 36 45.2	4.70	12.10	0.79	1	21.21	23.8	0.07	0.467	NLAGN	···	2215−6816	43.0	23.7	23.5	23.9
J205603.0-043613	20 56 03.14	−04 36 14.0	4.24	11.40	0.25	1	20.32	23.8	−0.32	0.469	ELG	···	2314−6398	42.9	22.5	22.3	22.6
J205603.1-043848	20 56 03.24	−04 38 48.8	5.75	11.60	0.72	1	23.66	23.8	1.03	1.395	ELG	···	1908−4085	44.0	23.7	23.5	23.8
J205603.6-043117	20 56 03.68	−04 31 17.5	4.98	11.00	−0.60	1	20.57	23.8	−0.23	1.477	BLAGN	···	1251−5248	44.0	<	<	21.1
J205604.1-043149	20 56 04.26	−04 31 49.4	4.53	8.60	−0.12	1	23.98	23.8	1.03	1.902	BLAGN	K	1309−3273	44.1	21.8	<	22.7
J205605.5-044058	20 56 05.57	−04 40 58.4	7.21	33.30	−0.28	1	20.80	23.8	0.34	0.801	BLAGN	···	2501−5391	43.9	20.9	<	21.4
J205606.1-043329	20 56 06.17	−04 33 29.6	3.31	6.62	−0.43	1	22.55	23.8	0.34	···	···	···	5225−10400[i]	···	···	···	···
J205606.6-043725	20 56 06.75	−04 37 25.7	4.15	16.80	−0.55	1	19.56	23.8	−0.45	1.190	BLAGN	···	2239−4611	44.0	<	<	21.3
J205608.1-043210	20 56 08.21	−04 32 11.0	3.54	7.32	0.42	1	22.24	23.8	0.26	0.731	ELG	A	2108−5488	43.2	22.3	21.9	22.7
J205608.9-043539	20 56 08.99	−04 35 39.4	2.67	7.95	0.51	1	20.75	23.8	−0.30	1.435	BLAGN	···	2141−4271	43.8	22.3	21.0	23.1
J205609.3-043832	20 56 09.46	−04 38 32.8	4.62	10.40	−0.12	1	20.44	23.8	−0.31	0.398	BLAGN	···	3551−7296	42.7	21.6	21.1	21.8
J205609.5-043728	20 56 09.62	−04 37 29.1	3.71	23.60	−0.27	1	17.86	23.8	−0.98	0.000	star	···	5075−10300	···	···	···	···
J205614.9-044135	20 56 14.99	−04 41 35.9	7.11	9.51	−0.53	1	21.33	23.8	0.01	2.478	BLAGN	···	1434−2903	44.4	22.2	<	22.5
J205618.6-043429	20 56 18.74	−04 34 29.5	0.06	28.90	0.78	1	21.52	22.3	0.57	0.529	NLAGN	···	2288−6212	43.5	23.0	22.9	23.1
J205622.2-044005	20 56 22.29	−04 40 06.2	5.62	28.60	−0.35	1	20.67	23.8	0.22	0.641	ELG	···	3397−6398	43.6	<	<	20.9
J205624.7-043533	20 56 24.84	−04 35 34.2	1.83	32.20	0.89	1	19.40	23.8	−0.23	0.260	ELG	···	2777−7936	42.8	23.3	23.1	23.4
J205628.8-043521	20 56 28.87	−04 35 22.1	2.65	4.84	−0.27	1	19.83	22.3	−0.88	0.262	ELG	···	2694−7450	42.0	21.2	<	21.6
J205629.1-043415	20 56 29.23	−04 34 16.2	2.63	7.82	−0.62	1	21.29	22.3	−0.09	1.035	BLAGN	···	1769−4422	43.5	20.5	<	21.4
J205631.3-043614	20 56 31.46	−04 36 14.7	3.59	21.10	−0.23	1	21.92	23.8	0.59	0.953	BLAGN	···	1740−4608	43.9	21.3	<	21.6
J205635.1-043944	20 56 35.27	−04 39 45.2	6.63	23.00	0.89[h]	1	22.35	23.8	0.80	0.732	ELG	···	2020−5773	43.7	23.4	23.3	23.6
J205636.7-043950	20 56 36.84	−04 39 50.5	6.95	9.54	−0.31	1	23.10	23.8	0.72	1.536	BLAGN	···	1380−3667	44.0	22.3	22.1	22.5
J205638.1-043753	20 56 38.18	−04 37 53.7	5.88	18.90	−0.48	1	19.21	23.8	−0.54	2.974	BLAGN	···	962−2491	44.9	22.4	22.0	22.6
J224638.3+034124	22 46 38.37	+03 41 23.2	12.02	36.60	−0.44	1	20.65	23.4	0.32	1.110	BLAGN	K	2665−4976	44.3	21.6	21.4	21.8
J224649.9+033937	22 46 50.02	+03 39 36.2	9.03	15.60	0.55	1	20.44	23.4	−0.13	0.533	ELG	K	3496−6849	43.2	22.8[l]	···	···
J224703.1+034350	22 47 03.17	+03 43 49.6	6.95	9.98	0.74[h]	1	19.78	23.4	−0.59	0.367	ELG	N	3785−7534	42.6	23.6	23.2	23.9
J224706.0+033951	22 47 06.09	+03 39 50.8	5.02	77.10	0.62	1	20.01	23.4	0.39	0.452	BLAGN	···	3133−6749	43.7	22.9	22.8	22.9
J224707.5+034629	22 47 07.62	+03 46 28.1	8.02	9.87	0.31	1	22.02	23.4	0.30	0.840	ELG	···	2491−5095	43.4	23.0	22.8	23.1
J224708.7+033619	22 47 08.80	+03 36 18.8	5.65	14.40	−0.19	2	23.40	23.4	1.00	···	···	···	5090−10300[i]	···	···	···	···
J224710.2+033657	22 47 10.34	+03 36 56.4	4.96	11.70	−0.24	2	23.40	23.4	0.91	0.972	ELG	K	2487−5121	43.6	22.2	21.9	22.3
J224710.5+033738	22 47 10.64	+03 37 37.3	4.51	4.57	0.54	2	23.40	23.4	0.50	3.335	NLAGN	···	1098−2306	44.3	24.1	23.9	24.3
J224712.0+034124	22 47 12.10	+03 41 23.7	3.81	18.80	0.49	2	23.40	23.4	1.11	1.248	ELG	K	2355−4679	44.1	23.3	23.2	23.4
J224716.7+034127	22 47 16.75	+03 41 26.5	2.80	31.90	−0.32	1	19.27	23.4	−0.29	0.264	BLAGN	···	4022−8164	42.8	20.9	<	21.2
J224716.9+033432	22 47 17.02	+03 34 31.2	5.87	58.90	−0.37	1	21.32	23.4	0.80	3.818	BLAGN	···	1040−2117	45.6	22.1	21.3	22.4
J224717.4+033230	22 47 17.45	+03 32 29.1	7.75	19.30	0.10	1	23.53	23.4	1.20	1.046	ELG	···	2727−4936	43.9	22.8	22.6	22.9
J224718.7+033651	22 47 18.81	+03 36 50.5	3.59	18.50	0.93[h]	1	23.00	23.4	0.97	1.288	NLAGN	···	1975−4254	44.1	23.7	23.6	23.8
J224720.5+033249	22 47 20.61	+03 32 48.6	7.25	11.70	0.41	1	23.17	23.4	0.84	0.608	ELG	···	3420−6082	43.2	22.6	22.4	22.8
J224722.2+034319	22 47 22.33	+03 43 18.0	3.51	12.70	−0.22	1	22.48	23.4	0.60	1.251	ELG	···	1974−4309	43.9	21.9	21.6	22.2
J224729.5+033916	22 47 29.57	+03 39 15.5	1.07	5.62	0.09	1	22.85	23.4	0.39	1.065	ELG	···	2397−4891	43.4	22.7	22.4	22.9
J224729.8+034559	22 47 29.86	+03 45 58.4	6.12	38.00	−0.53	1	18.73	23.4	−0.43	1.315	BLAGN	···	2051−4241	44.4	21.0	<	21.5
J224729.8+034232	22 47 29.93	+03 42 31.1	2.76	11.50	0.40	2	23.40	23.4	0.90	···	···	···	5515−8095[i]	···	···	···	···
J224731.1+034709	22 47 31.22	+03 47 08.0	7.32	32.50	0.77	1	21.16	23.4	0.48	0.540	ELG	K	2938−6090	43.5	23.1	23.1	23.2
J224731.6+033550	22 47 31.74	+03 35 49.1	4.33	17.00	−0.46	1	20.85	23.4	0.07	0.997	BLAGN	···	2759−5307	43.8	21.3	20.3	21.6
J224732.0+033859	22 47 32.09	+03 38 58.1	1.75	4.97	−0.14	1	21.78	23.4	−0.09	2.154	BLAGN	···	1141−2694	44.0	22.3	21.2	22.7
J224732.2+033818	22 47 32.26	+03 38 17.6	2.22	5.53	−0.12	1	21.05	23.4	−0.34	0.708	ELG	···	2936−5971	43.0	21.6	<	22.3
J224734.1+033510	22 47 34.15	+03 35 09.3	5.16	22.00	0.23	1	22.23	23.4	0.73	0.711	ELG	···	3226−6136	43.6	22.5	22.4	22.6
J224734.2+033608	22 47 34.28	+03 36 07.7	4.30	24.40	0.86	1	22.04	23.4	0.70	0.647	ELG	···	3242−6376	43.6	23.3	23.2	23.5
J224735.4+034005	22 47 35.52	+03 40 04.6	2.33	8.94	0.11	1	22.62	23.4	0.50	···	···	···	4535−9755[i]	···	···	···	···
J224737.6+033645	22 47 37.68	+03 36 44.7	4.28	5.82	−0.47	1	23.51	23.4	0.67	1.775	BLAGN	···	1261−3063	43.9	21.8	<	22.2
J224739.0+034129	22 47 39.13	+03 41 28.8	3.58	24.50	−0.19	1	23.23	23.4	1.18	0.767	ELG	···	3084−5998	43.7	22.1	21.9	22.3
J224739.1+034416	22 47 39.19	+03 44 15.2	5.41	42.60	−0.56	1	19.18	23.4	−0.20	0.962	BLAGN	···	2464−5096	44.2	<	<	20.3

Table 5.2 (cont'd)

	X-ray Data					Optical Counterpart Data											
CXOSEXSI_	α_x (J2000)	δ_x (J2000)	OAA	$S_{2-10}^{(-15)}$	HR	Flag	R	R_{limit}	$\log \frac{f_x}{f_o}$	z	Class	Notes	$\Delta\lambda_{rest}$	$\log L_x^{(2-10)}$	$\log N_H$	$\log N_H^-$	$\log N_H^+$
(1)	(2)[a]	(3)[a]	(4)	(5)	(6)[b]	(7)[c]	(8)	(9)	(10)	(11)	(12)[d]	(13)[e]	(14)[f]	(15)	(16)[g]	(17)[g]	(18)[g]
J224744.5+034314	22 47 44.55	+03 43 13.9	5.65	7.86	−0.15	1	21.80	23.4	0.12	1.319	BLAGN	K	2104−4355	43.8	22.7	22.5	22.9
J224745.3+033740	22 47 45.40	+03 37 39.7	5.30	10.10	−0.46	1	21.63	23.4	0.16	1.427	BLAGN	···	1918−3887	43.9	<	<	21.5
J224745.9+033630	22 47 46.04	+03 36 29.8	6.02	6.42	−0.07	1	24.83	23.4	1.24	···	···	···	5145−9340[i]	···	···	···	···
J234757.9+010328	23 47 57.95	+01 03 28.9	7.01	8.82	−0.02	1	19.91	23.4	−0.59	0.248	ELG	···	4046−8213	42.2	21.9	21.6	22.2
J234759.5+010122	23 47 59.53	+01 01 22.9	5.41	11.30	−0.02	1	24.19	23.4	1.23	1.325	BLAGN	G	1952−4204	43.9	22.2	22.0	22.4
J234806.5+010351	23 48 06.57	+01 03 51.5	5.99	14.80	−0.27	2	23.40	23.4	1.04	···	···	···	5300−10500[i]	···	···	···	···
J234806.6+010043	23 48 06.61	+01 00 44.1	3.58	7.95	−0.24	1	20.70	23.4	−0.32	0.768	BLAGN	···	1979−5260	43.3	<	<	21.2
J234808.0+005812	23 48 08.00	+00 58 13.1	2.56	6.69	0.17	1	22.37	23.4	0.27	2.792	BLAGN	J	949−2241	44.4	23.2	22.9	23.4
J234808.4+010111	23 48 08.40	+01 01 12.1	3.56	16.80	−0.10	1	22.96	23.4	0.91	1.425	BLAGN	K	1917−4082	44.2	20.0	<	21.5
J234811.5+005700	23 48 11.55	+00 57 00.7	2.29	12.30	−0.59	1	21.45	23.4	0.17	1.820	BLAGN	···	1241−3191	44.2	<	<	20.3
J234812.7+005750	23 48 12.73	+00 57 50.6	1.55	16.40	−0.37	1	23.36	23.4	1.06	1.040	BLAGN	···	1789−4166	43.9	20.6	<	21.0
J234812.8+010022	23 48 12.89	+01 00 22.7	2.20	26.40	−0.44	1	20.92	23.4	0.29	0.718	BLAGN	···	2639−5681	43.7	20.8	<	21.2
J234813.2+005611	23 48 13.27	+00 56 11.9	2.69	14.30	0.81	1	21.24	23.4	0.15	0.550	NLAGN	···	2322−5806	43.2	23.1	23.0	23.2
J234813.7+005639	23 48 13.78	+00 56 40.2	2.22	7.24	0.60	1	20.48	23.4	−0.45	1.031	BLAGN	···	1723−4529	43.5	23.0	22.8	23.4
J234814.4+010312	23 48 14.46	+01 03 12.8	4.70	13.60	−0.47	1	23.06	23.4	0.86	1.388	BLAGN	···	2206−4396	44.0	22.1	21.9	22.3
J234815.3+010139	23 48 15.33	+01 01 39.8	3.14	10.60	0.93[h]	1	25.94	23.4	1.90	···	···	···	4900−10100[i]	···	···	···	···
J234818.4+005520	23 48 18.47	+00 55 21.0	3.26	3.93	0.04	1	22.96	23.4	0.28	0.957	ELG	···	1839−4726	43.2	22.6	22.4	22.6
J234818.9+005950	23 48 18.94	+00 59 50.4	1.25	15.10	−0.45	1	21.80	23.4	0.40	1.930	BLAGN	···	1194−2901	44.4	<	<	20.5
J234820.2+005437	23 48 20.21	+00 54 37.9	4.01	17.80	0.57	1	19.31	23.4	−0.53	0.279	ELG	···	2814−7271	42.6	22.6	22.5	22.7
J234820.8+010024	23 48 20.83	+01 00 24.5	1.93	29.90	−0.38	1	21.19	23.4	0.45	1.208	BLAGN	···	2117−4479	44.3	20.0	<	20.8
J234823.2+010358	23 48 23.23	+01 03 58.7	5.52	8.21	−0.59	1	21.47	23.4	0.00	2.223	BLAGN	···	1739−3350	44.2	21.9	21.6	22.2
J234825.5+010425	23 48 25.58	+01 04 25.6	6.11	21.60	−0.03	1	21.53	23.4	0.45	1.281	BLAGN	···	2452−4603	44.2	21.8	20.9	22.1
J234826.2+010330	23 48 26.28	+01 03 31.0	5.32	52.90	−0.41	1	20.96	23.4	0.61	1.153	BLAGN	···	2575−3771	44.5	21.1	20.0	21.4
J234835.3+005832	23 48 35.32	+00 58 32.9	4.30	54.30	−0.39	1	20.59	23.4	0.47	0.948	BLAGN	···	2512−4594	44.3	<	<	20.0
J234835.5+005836	23 48 35.58	+00 58 36.6	4.37	35.30	−0.10	1	22.66	23.4	1.11	0.948	ELG	···	2733−5390	44.1	22.1	22.0	22.2
J234839.5+010828	23 48 39.58	+01 08 28.7	11.24	49.10	−0.35	1	22.13	23.4	1.04	1.021	ELG	FK	2770−4453	44.3	22.0[j]	···	···
J234840.1+010753	23 48 40.15	+01 07 53.3	10.80	139.00	−0.47	1	18.39	23.4	−0.00	0.717	BLAGN	···	2871−5241	44.4	21.3[j]	···	···

Table 5.2 Notes

[a] X-ray positions are corrected for average X-ray to optical offset (to correct *Chandra* pointing errors); see Paper II

[b] $HR = (H - S)/(H + S)$ where H is the corrected counts in the 2.0 – 10 keV band and S is the corrected counts in the 0.5 – 2.0 keV band. See § 5.5 for details

[c] See Paper II, § 4 for details of the flag code. Briefly: 0 = no optical coverage, 1 = solid optical ID, 2 = upper limit, 3 = saturated in SEXSI optical image; R-band magnitude taken from the Guide Star Catalog II (McLean et al. 2000), 4 = solid ID but R-band magnitude affected by nearby bright source, 5 = more than one optical source consistent with the X-ray source position, 6 = upper limit (no optical counterpart) but area contaminated by nearby bright source so limiting magnitude is unknown

[d] BLAGN = Broad-Lined AGN, NLAGN = Narrow-Lined AGN, ELG = Emission Line Galaxy, ALG = Absorption Line Galaxy. See § 5.4 for classification details

[e] Notes (Column 13):

- **A:** optical counterpart falls just outside the strict search area (see § 5.5 and Table 5.3).
- **B:** identification from the Guide Star Catalog II (McLean et al. 2000) or VIZIER database.
- **C:** identification from the Einstein Observatory Extended Medium-Sensitivity Survey (Stocke et al. 1991), object MS1214.3+3811.
- **D:** cataclysmic variable, spectrum shows 274 km s^{-1} blueshift.
- **E:** member of (non-target) nearby galaxy, NGC 5879. This galaxy happened to be in the *Chandra* pointing of SEXSI field QSO 1508. The three 2 – 10 keV sources spectroscopically confirmed to be associated with NGC 5879 are flagged.
- **F:** this object was identified using its 2-D spectrum as it could not easily be extracted to form a 1-D spectrum; the observable wavelength range is thus omitted.
- **G:** in Paper II this source had optflag=5 (> 1 optical source in the search area). Our spectrum shows a BLAGN, thus we have changed the source to optflag=1, a secure optical counterpart identification.
- **H:** confirmed target cluster member (spectroscopically confimred within 1 Mpc of target cluster center). In Papers I and II sources were flagged as being potentially within 1 Mpc of the target cluster center as determined by their position in the image. These sources were all ignored for the $\log N - \log S$ calculation in Paper I. Now that redshift information is available, only sources at the target cluster z remain flagged. See § 5.11 for details on these sources.
- **I:** confirmed (non-target) cluster/group detected in Holden et al. (2002) — see § 5.11.
- **J:** possible BALQSO.
- **K:** line identification or redshift tentative.
- **L:** this source spectrum shows two ELG, one at z=0.426, one at z=1.432. The nearer source matches the R=22.25 in our photometry (Paper II), but the fainter z=1.432 source, undetected in our photometry, also appears in the error circle. This source is thus eliminated from our analysis.
- **M:** J145215.6+430448: low-ionization, broad absorption line quasar.
- **N:** spectrum has gap of > 100 Å between red and blue side.

[f] Optical spectroscopic wavelenth coverage in angstroms

[g] Columns 16-18 present the logarithm of the best-fit N_H value, as well as 1σ low and 1σ high values from the fit. When a N_H measurement is zero we report '<' in the table

[h] HR is lower limit

[i] $\Delta\lambda$ is in the observed frame — no z was measured, only continuum

[j] Source detected on an off-axis ACIS-S chip (2-3) and thus N_H is calculated from HR, not spectral fit. See § 5.5

[k] N_H is lower limit

[l] Bad XSPEC fit. N_H is calculated from HR, not spectral fit

The data describing the optical counterparts begin in column 7, with the photometric optical counterpart flag (optflag), a code essential for interpreting the optical photometric data (see Table 5.2 footnote). Note that in this spectroscopic catalog the majority of entries in this column are optflag = 1, indicating a solid optical identification, since a successful spectroscopic identification depends on having a counterpart bright enough that emission lines or absorption features are detectable. In a handful of cases the optical flag is a 2, indicating a limiting magnitude. These cases occur either when we placed a slitlet on an optical counterpart identified in a band other than R, or when a slitlet was placed 'blindly' at the X-ray source position even though no optical counterpart was present to the depth of our imaging data.

Column 8 is the R-band magnitude of the optical counterpart; in the next column we show the limiting R magnitude for the image from which the optical counterpart, or a limit thereto, was derived. Next we present the logarithmic X-ray-to-optical flux ratio (column 10), given by the relation

$$\log\left(f_{\rm x}/f_{\rm o}\right) = \log f_{2-10\ \rm keV} + (R/2.5) + 5.50, \tag{5.1}$$

derived using the Kron-Cousins R-band filter transmission function (see Paper II and references therein). Note that special attention must be paid to the optical flag when interpreting the data of columns 8 – 10. For example, if the code is a 2 (optical counterpart not detected), then columns 8 and 10 describe limits on each quantity.

The optical spectroscopic data begins with the redshift in column 11, followed by the classification in column 12 (see § 5.4 for details of the redshift and classification determinations). Column 13 provides notes on individual sources where necessary.

The rest-frame wavelength range in angstroms for each optical spectrum is recorded in column 14; when a source spectrum shows continuum only and no redshift has been

determined, we present the observed-frame wavelength range. This column is essential for determining which spectral features are accessible for a given source. It is important to know, for example, whether the absence of high-ionization lines (typical of AGN and necessary for an AGN classification) is a consequence of non-detection in the measured spectrum or as the result of inadequate spectral coverage. In most cases both the blue and red sides of the spectrographs were employed; if this is the case and there is a significant spectral coverage gap (> 100 Å) between the red and blue sides, a note is added in column 13.

Column 15 presents the log of the absorbed rest-frame 2 – 10 keV X-ray luminosity in erg s^{-1}, calculated from the hard-band flux (column 5) and the redshift assuming an X-ray photon index of $\Gamma = 1.5$.

The final three columns (16–18) present the log of the neutral hydrogen column density (N_H) in cm^{-2} and the associated 1 σ lower- and upper-limit to the value. These values are determined by X-ray spectral fitting of each source using XSPEC,[4] a spectral fitting program. Since many SEXSI sources have a low number of counts in the X-ray we did not allow a many-free-parameter fit; instead, we performed the fits assuming an intrinsic power-law spectrum with photon index $\Gamma = 1.9$ typical of AGN continua. We fixed Γ and the Galactic N_H at $z = 0$ and allowed only the intrinsic column density at the source redshift to vary. The Galactic N_H value used for each field is given in Paper I, Table 2. The photoelectric absorption was determined using Wisconsin cross sections (Morrison & McCammon 1983). The fitting was performed using C-statistic minimization instead of chi-squared minimization since the observed data bins have few counts (Cash 1979, and the XSPEC Manual, Appendix B). The fits use data from 0.3 – 7.0 keV, to match the energy range we used to extract counts in Paper I. The X-ray spectral data analysis was aided greatly by `acis_extract`[5] Version 3.91 (Broos et al. 2002), software written in IDL that assists in performing the many CIAO and XSPEC tasks involved in analyzing the spectra of large numbers of sources observed with ACIS. For the spectral analysis presented here we use CIAO Version 3.2 and CALDB Version 3.1.

Spectra were extracted for each source with a spectroscopic redshift (excluding stellar sources at $z = 0$). We choose 1.4967 keV as the primary PSF energy at which the PSF

[4]Available at http://heasarc.gsfc.nasa.gov/webspec/webspec.html
[5]Available at http://www.astro.psu.edu/xray/docs/TARA/ae_users_guide.html

fraction is to be computed, and a PSF fraction of 0.8. Individual auxiliary response files (ARFs) and redistribution matrix files (RMFs) were calculated for each source.

We extracted a background spectrum for each source from a local circular background region that includes at least 100 counts and an exposure ratio between background and source region of at least four, taking care to mask out all X-ray sources (SEXSI sources, including soft-only sources, target point sources, and extended cluster emission). The background spectra were scaled based on the ratio of total exposure in the source extraction region to that of the background region.

For ACIS-I observations, all sources on all chips were fit; for ACIS-S observations, only sources on chips 6-8 were fit since PSF libraries do not exist for chips 2-3 given an ACIS-S pointing. Fourteen SEXSI sources fall in this category and are marked in catalog; the N_H values reported for them are derived instead using hardness ratios: we determine what column density is necessary, given the source redshift, to produce the measured hardness ratio assuming an underlying intrinsic power-law spectrum with photon index $\Gamma = 1.9$. We use WebPIMMS[6] for this calculation.

Throughout the paper, the luminosities we refer to are the obscured (observed) luminosities presented in column 15, unless we specifically indicate that we are using intrinsic, unobscured luminosities, corrected for absorption by the obscuring column density at the source redshift. To calculate the unobscured luminosity we multiply L_x in column 15 by an approximate correction factor calculated using WebPIMMS, assuming an intrinsic $\Gamma = 1.9$, the best-fit N_H value, and the source redshift.

We now discuss the 23 sources flagged with an 'A': sources whose optical spectra are from potential counterparts which lie just outside the formal matching area. In the photometry catalog from Paper II, these sources were listed as having limiting R-magnitudes (optflag=2) since there were no optical counterparts in the search area. We include the spectroscopic information for these sources in the main catalog here (Table 5.2) and present the new photometric and astrometric information in Table 5.3. This Table lists the X-ray source position as well as the new R-magnitude and its error and the offset between the X-ray and optical position (in R.A. ($\Delta\alpha = \alpha_x - \alpha_o$), Dec. ($\Delta\delta = \delta_x - \delta_o$), and total position error ($\Delta r = \sqrt{\Delta\alpha^2 + \Delta\delta^2}$)). Column (9) gives the original X-ray search radius (which depends on *Chandra* OAA), and the final column presents $\log(f_{\rm x}/f_{\rm o})$.

[6] Available at http://heasarc.gsfc.nasa.gov/Tools/w3pimms.html

Table 5.3. Photometry for sources with spectral ID outside the formal match area

CXOSEXSI_ (1)	α_x (J2000) (2)[a]	δ_x (J2000) (3)[a]	R (4)	σ_R (5)	$\Delta\alpha$ (6)	$\Delta\delta$ (7)	Δr (8)	Rad (9)[b]	$\log \frac{f_x}{f_o}$ (10)
J030527.0+035528	03 05 26.97	+03 55 29.3	17.61	0.17	2.5	0.1	2.5	1.5	−1.50
J084822.5+445854	08 48 22.62	+44 58 55.9	21.08	0.13	−2.3	−0.4	2.3	1.9	−0.50
J084823.9+445852	08 48 23.94	+44 58 53.8	22.01	0.13	−1.8	−0.6	1.9	1.8	0.12
J084824.8+445740	08 48 24.83	+44 57 41.3	20.52	0.13	2.2	−0.5	2.3	1.5	−0.79
J084846.4+444830	08 48 46.46	+44 48 32.0	20.55	0.13	2.2	0.8	2.4	1.5	−0.43
J084931.3+445549	08 49 31.38	+44 55 50.5	21.20	0.13	2.3	1.3	2.7	1.7	−0.22
J090955.5+541813	09 09 55.55	+54 18 15.4	22.21	0.13	−2.7	0.4	2.8	1.7	0.09
J091012.7+541205	09 10 12.74	+54 12 07.8	22.49	0.13	−1.1	3.5	3.6	2.8	0.68
J091034.2+542408	09 10 34.25	+54 24 10.7	21.24	0.12	−2.5	0.1	2.5	1.5	−0.62
J115930.1+291744	11 59 30.16	+29 17 45.2	23.04	0.24	0.4	−1.7	1.8	1.5	0.53
J121739.5+374655	12 17 39.54	+37 46 55.1	23.04	0.27	−1.1	−1.1	1.5	1.5	0.45
J125322.6-090246	12 53 22.64	−09 02 46.5	16.69	0.37	2.1	−2.0	3.0	2.3	−1.43
J131658.1+291017	13 16 58.29	+29 10 18.8	23.69	0.28	−1.3	1.8	2.2	1.5	0.31
J131732.9+291055	13 17 33.06	+29 10 57.3	21.61	0.26	−1.3	0.6	1.5	1.5	−0.38
J133816.8+292350	13 38 16.98	+29 23 51.5	22.89	0.16	1.8	0.3	1.9	1.8	0.85
J150956.0+570534	15 09 56.14	+57 05 34.6	20.46	0.10	0.1	2.9	2.9	1.5	−0.75
J162255.0+263720	16 22 55.12	+26 37 20.4	21.41	0.12	−0.5	−2.7	2.7	1.8	0.33
J170402.8+514247	17 04 02.92	+51 42 48.4	21.76	0.17	−0.2	−1.7	1.7	1.5	0.04
J171740.6+671147	17 17 40.76	+67 11 46.1	21.83	0.05	1.8	−0.8	2.0	1.5	0.02
J171747.4+671449	17 17 47.58	+67 14 48.3	22.91	0.20	1.4	0.4	1.5	1.5	0.55
J175928.1+663851	17 59 28.21	+66 38 51.5	20.22	0.07	−0.2	−2.2	2.3	1.5	−0.10
J204430.7+771215	20 44 30.81	+77 12 15.4	20.77	0.28	−0.8	−1.6	1.8	1.5	−0.21
J205608.1-043210	20 56 08.21	−04 32 11.0	22.24	0.04	−1.1	−1.6	1.9	1.5	0.26

[a]X-ray positions are corrected for average X-ray to optical offset (to correct *Chandra* astrometry)

[b]The search radius, in arcsec, used for X-ray-to-optical source matching (Paper II). This radius may be compared with the value in Column (8), the offset from the X-ray source to the optical source in the spectroscopy catalog (Table 5.2)

Of these 23 sources, 5 are BLAGN, 1 is a NLAGN, 12 are ELGs, 2 are ALGs, and 3 are stars. Given the low surface density of AGN on the sky, we assume that all of the six sources with with spectra indicative of AGN activity are true counterparts. Comparing the BLAGN and NLAGN to the ELGs, we see that $6/212 = 3\%$ of the active galaxies are outside the search radius (as expected for radii defined as approximately 2σ error radii), while $12/168 = 7\%$ of the ELG are outside. The surface density of ELGs is also much higher than that of AGN, and thus it is likely that some of the 12 ELG are chance coincidences. The numbers for stars ($3/19 = 16\%$) and ALG ($2/8 = 25\%$) are even higher; these objects are even more likely to be chance coincidences (see also § 5.7).

The number of false matches due to an optical source randomly overlapping the matching search area depends on the depth of both the X-ray and optical images as well as the size of the match area, which is determined by the X-ray source off-axis angle. In Paper II, Section 3 we estimated the number of false matches considering the probability that an optical source would overlap the X-ray match area; now that we have our set of identifications, we can estimate the number of false matches on a source-by source basis, taking into account the particular match areas and optical magnitudes of the identified sources in each class as well as the optical source density of that class.

The optical sources that dominate in our high-Galactic latitude fields are normal galaxies, sources that would be classified spectroscopically as ELG or ALG. The false match rate will be lower than that estimated in Paper II for several reasons, most importantly that the R-magnitude of many of the spectroscopically identified sources are considerably brighter than the limiting magnitudes of the optical images. In addition, since *Chandra* is more sensitive closer to the aim point, the source density is highest for low-OAA sources with the smaller match areas, and spectroscopic observing efficiency favors these high-space-density sources. Taking into account each ELG and ALG match area and R-magnitude, we calculate the false match probability for each source. Considering the 176 ELG and ALG we estimate a total of $\lesssim 4$ false ELG or ALG matches. The surface density of (optically identifiable) active galaxies is $\sim 100\times$ lower than the normal-galaxy surface density for $R \lesssim 23$ in optical surveys (e.g., Wolf et al. 2003), thus we estimate that there will be < 1 false NLAGN or BLAGN match. These estimates support our assertion that all of the BLAGN and NLAGN from Table 5.3 are true counterparts.

5.6 Hard X-ray Source Population Statistics

5.6.1 Redshift Distribution

Figure 5.6 shows the redshift distribution for the 419 spectroscopically identified extragalactic sources (the 19 stars are excluded). The top panel (a) presents the entire distribution with the optical spectroscopic classifications indicated in different shades. Panels (b) – (e) present the same z-distribution with a different source class shaded in each panel to highlight their very different redshift distributions.

These plots show that the 2 – 10 keV sources are dominated by two classes: BLAGN which show the typical broad, high-ionization-line signature indicative of gas near a source emitting copious hard X-rays, and ELGs, a class of sources that show only emission lines typical of normal galaxies.

The BLAGN population (shaded in panel (b)) exhibits a broad redshift distribution; it includes 50% of the identified sources and has a mean redshift $\langle z \rangle_{\rm BLAGN} = 1.46 \pm 0.75$, with objects ranging from $z = 0.06$ to our highest redshift source at $z = 4.33$.

The next panel (c) shows the emission-line galaxies, which comprise 40% of the identified sources. This redshift distribution is distinct from that of the BLAGN, with a much lower average redshift as well as a much tighter distribution about the average: $\langle z \rangle_{\rm ELG} = 0.75 \pm 0.36$. Note that there are no ELGs found above $z = 1.56$, and only three are above $z = 1.4$ (two of which are flagged as tentative identifications). There are two essential facts to keep in mind when discussing the ELG redshift distribution. First, although the optical spectra of these sources are identified as a result of emission from the host galaxy, the 2 – 10 keV X-ray luminosities are, with the exception of eleven sources, above 10^{42} erg s^{-1}, which is too high to be produced purely from stars and stellar remnants in a star-forming galaxy (see § 5.10.1). Second, the decline in sources above $z \sim 0.8$ does not necessarily represent the underlying distribution of hard X-ray emitting ELG in the universe, but is more likely a result of observational biases. There are several strong selection effects that dominate at higher redshift, most importantly the fact that as a typical galaxy is seen at greater distances, it gets too faint for us to identify optically (see § 5.8); the redshift desert—the absence of strong emission lines within the typical wavelength regime covered—also militates against finding ELGs above $z \approx 1.4$. Figure 5.7 presents a scatter plot of R-magnitude versus redshift, showing the rapid rise in ELG (triangles) R-magnitude as z increases as compared

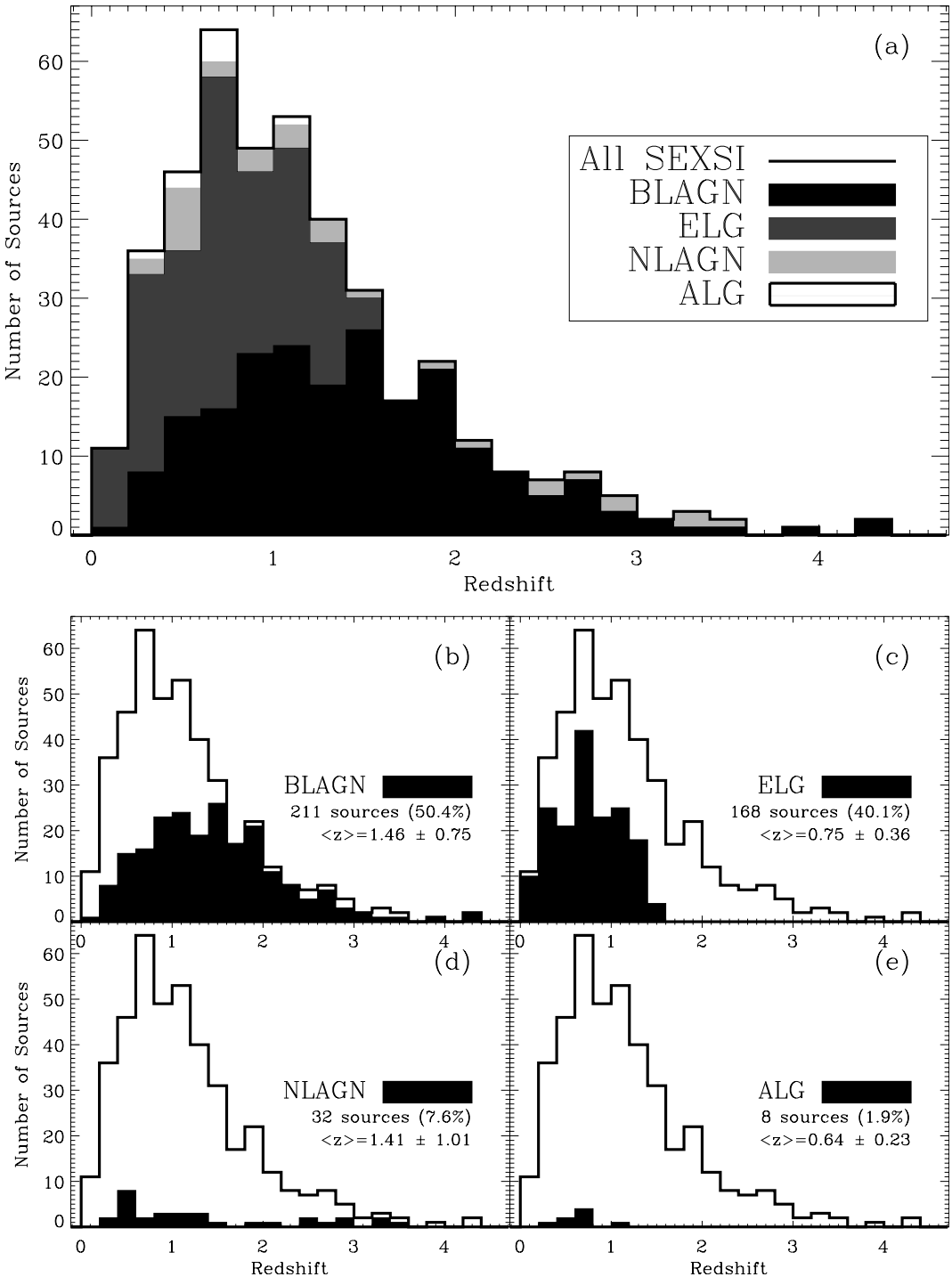

Figure 5.6 Redshift histogram for the 419 sources with spectroscopic redshifts presented in Table 5.2, excluding the stars (at $z = 0$). Panel (a) shows the entire histogram with shading according to class. Panels (b) – (e) show the same histogram with each individual source class highlighted in black. These plots emphasize that the sample is dominated by the BLAGN, with a broad redshift distribution, and the ELG, dominant at lower z. The NLAGN have a z-distribution most similar to the BLAGN; the NLAGN are the only narrow-lined sources with $z > 1.5$

to, for example, the broad spread in R over a large z range exhibited by the BLAGN (black crosses).

Panel (d) of Figure 5.6 displays the redshift range for the 32 NLAGN, sources that show narrow high-ionization lines indicative of an obscured active nucleus. These sources comprise only $\sim 8\%$ of the total identified sources. The redshift distribution is broad, with $\langle z \rangle_{\rm NLAGN} = 1.41 \pm 1.01$, similar to the BLAGN distribution.

The final category of sources are the absorption line galaxies (ALG) that make up only a very small fraction of our sample. These, like the ELG, are found primarily at $z < 1$ ($\langle z \rangle_{\rm ALG} = 0.64 \pm 0.23$), with none at $z > 1.2$. Selection effects similar to those that affect the identification of ELGs also constrain this distribution.

5.6.2 X-ray Flux and X-ray-to-Optical Flux Ratio Distributions

Figure 5.8 shows the 2 – 10 keV flux distribution for spectroscopically-identified extragalactic sources with $R < 22$ (top panel) and $R > 22$ (bottom panel); source classes are indicated by shading. Not surprisingly, the distribution of optically fainter sources has a lower average $f_{2-10\ \rm keV}$ than does the distribution of $R < 22$ sources. This effect has been seen previously in many of the *Chandra* and *XMM-Newton* surveys (e.g., Hornschemeier et al. 2001). At all but the faintest fluxes the optically brighter distribution is dominated by BLAGN (black), while the optically-fainter distribution is dominated by ELG (dark gray). The relationship between R-magnitude distribution, redshift, and source class will be explored in detail in § 5.10.2.

A related distribution is the $\log(f_{\rm x}/f_{\rm o})$ distribution for identified extragalactic SEXSI sources presented in Figure 5.9. Again, source classes are indicated by shading. The large majority of SEXSI sources are found with $-1 < \log(f_{\rm x}/f_{\rm o}) < 1$, typical values for AGN. The higher values of $\log(f_{\rm x}/f_{\rm o})$ generally indicate more obscuration – the 2 – 10 keV light is relatively unaffected by the obscuring material while the AGN optical light is absorbed. The highest $\log(f_{\rm x}/f_{\rm o})$ sources in the identified sample are dominated by ELG.

5.6.3 X-ray Luminosity Distribution

The majority of the spectroscopically-identified SEXSI sources have 2 – 10 keV luminosities between 10^{43} and $10^{45}\,{\rm erg\ s^{-1}}$; all but twelve sources (eleven ELGs, one NLAGN) have $L_{\rm x} > 10^{42}\,{\rm erg\ s^{-1}}$. Figure 5.10 shows the (a) 2 – 10 keV and (b) 0.5 – 2 keV luminosity

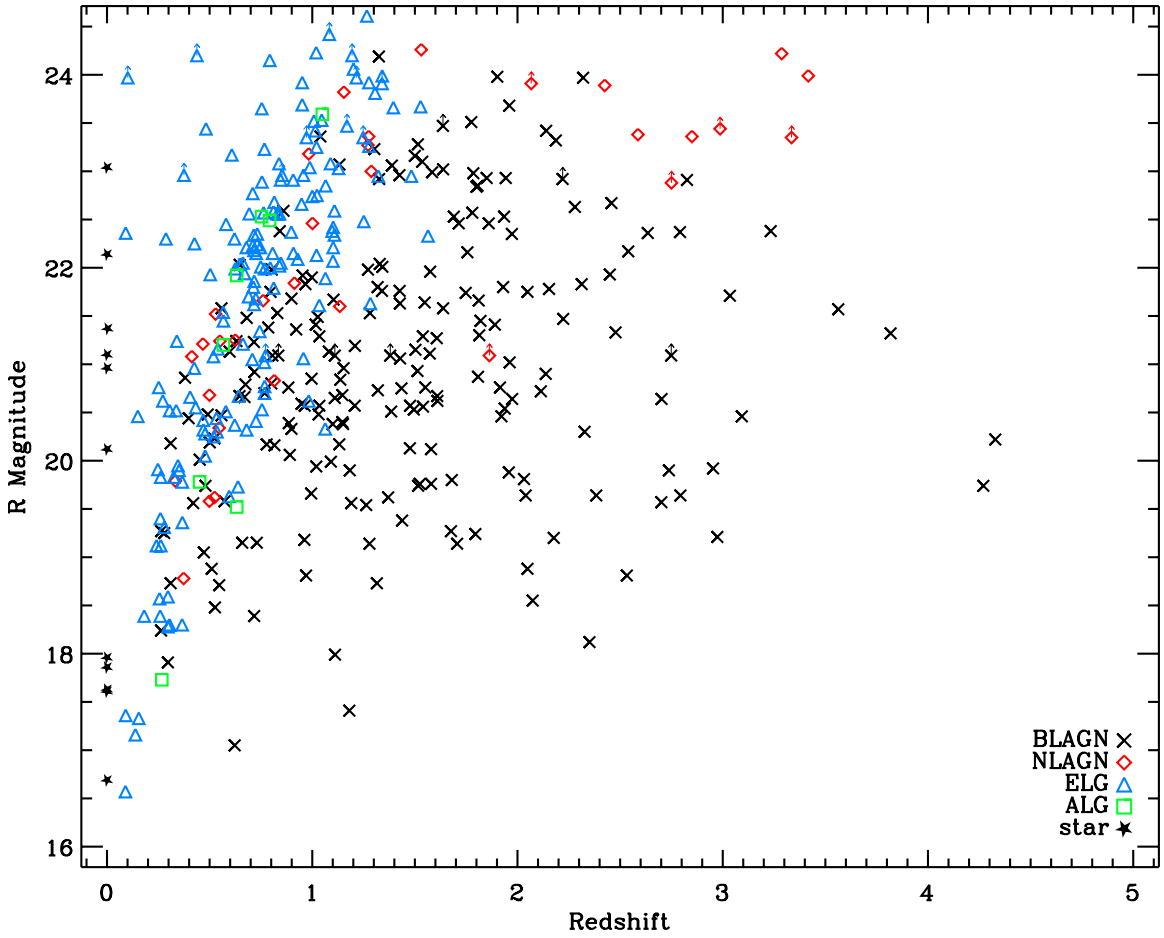

Figure 5.7 R-magnitude versus redshift for spectroscopically identified sources. The distinct regions in $R - z$ parameter space covered by each class type is illustrated. The BLAGN have the largest spread in z and also occupy a large spread R, though they are not found in as great number at the faintest R fluxes. The NLAGN are also spread widely in z, but tend to be the nearer the faint end of the R distribution. The ELG appear with $z \lesssim 1.5$ and are mainly found to have $R > 20$. The few ALG have a distribution similar to the ELG. Stars with $R > 18$ are most likely chance coincidences, and not real X-ray counterparts

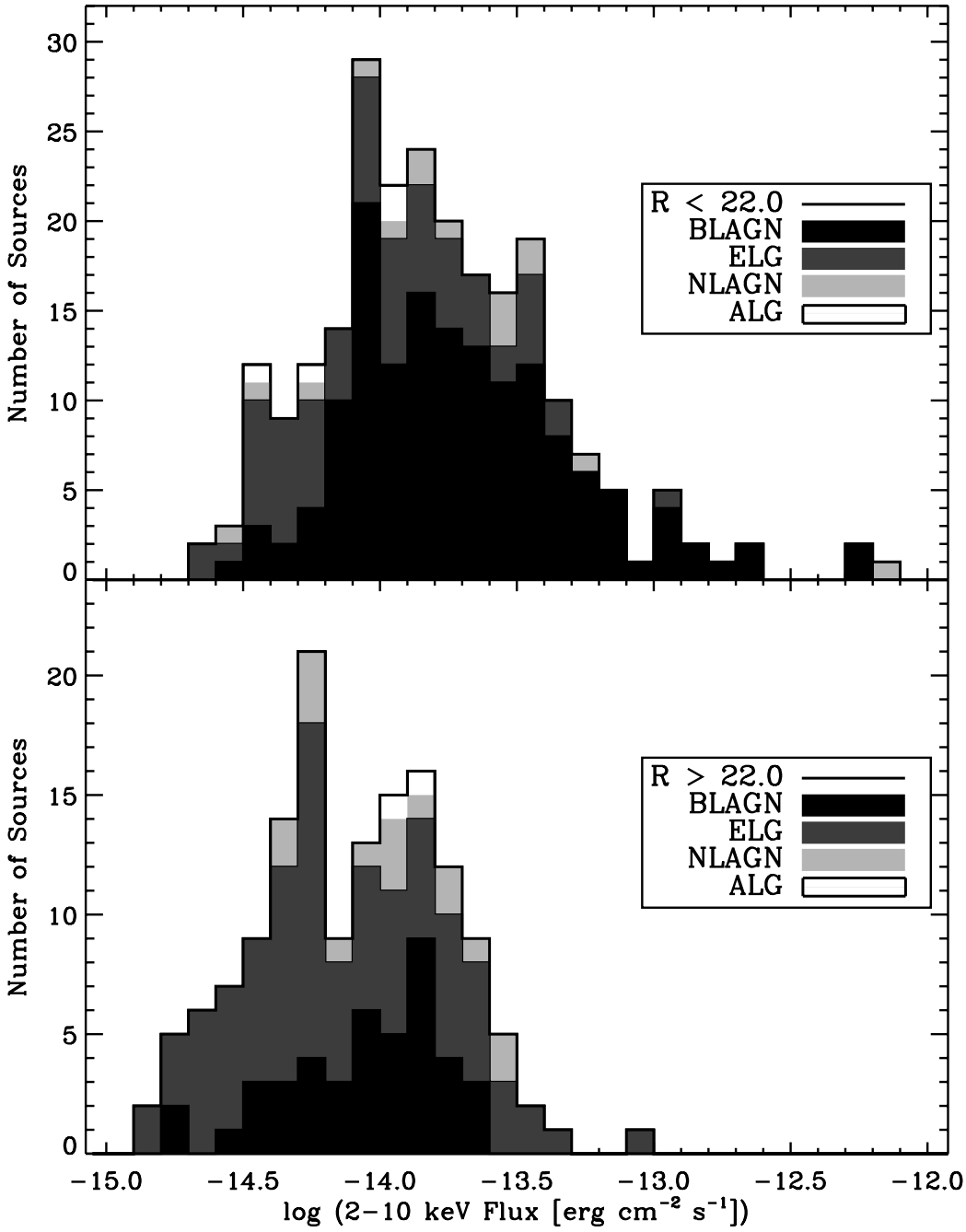

Figure 5.8 The 2 – 10 keV flux histogram of spectroscopically-identified sources, excluding stars, split at $R = 22$. The optically-brighter sources ($R < 22$), presented in the top panel, show a broad peak between $f_{2-10\ \mathrm{keV}} \sim 10^{-14}$ erg cm^{-2} s^{-1} and $f_{2-10\ \mathrm{keV}} \sim 10^{-13.5}$ erg cm^{-2} s^{-1}. These $R < 22$ sources are dominated by BLAGN. The bottom panel shows the optically-fainter sources ($R > 22$). The hard-flux histogram is shifted to lower fluxes and includes many ELG as well as BLAGN, ALG, and NLAGN. (Only sources with $R_{\mathrm{limit}} > 22$ are included in this plot. This cut eliminates few sources since most SEXSI imaging has $23 < R_{\mathrm{limit}} < 24$.)

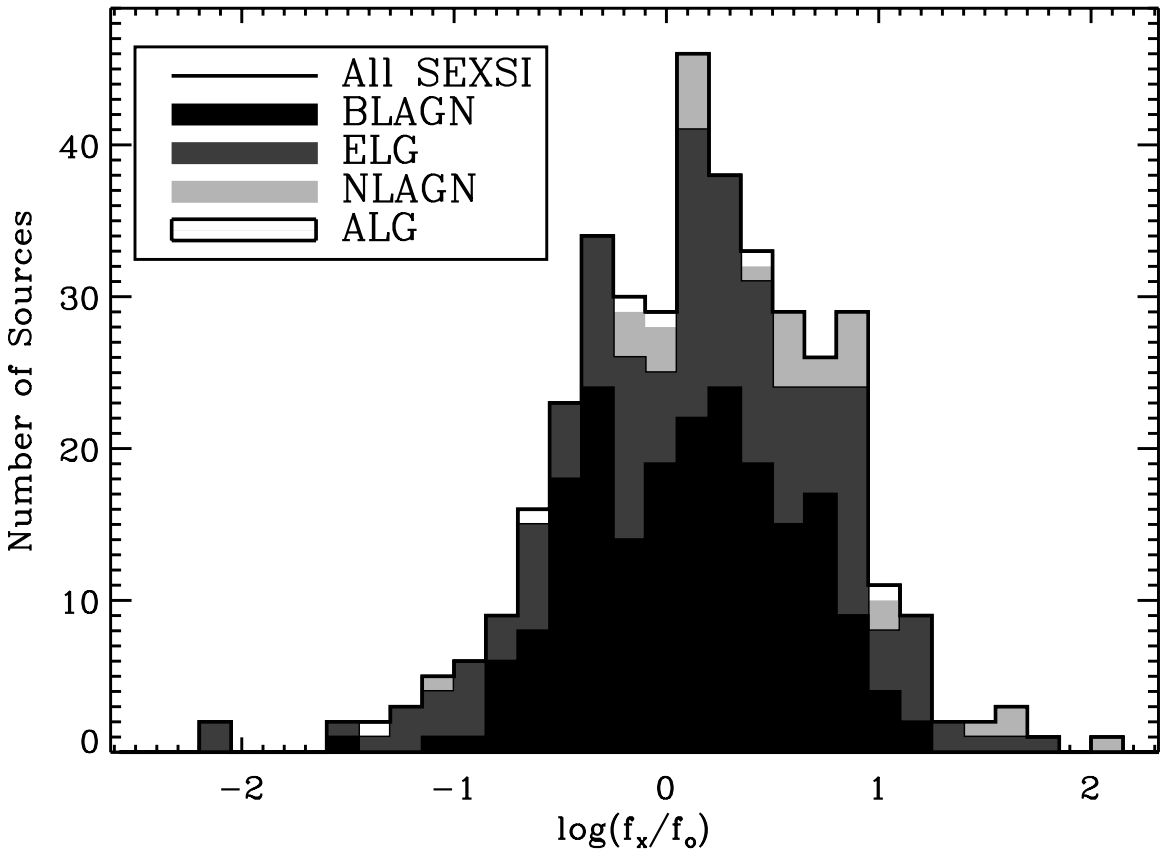

Figure 5.9 Histogram of $\log(f_{\rm x}/f_{\rm o})$ distribution of spectroscopically-identified sources ($f_{\rm x} = f_{2-10\ {\rm keV}}$). Most sources are found between $-1 < \log(f_{\rm x}/f_{\rm o}) < 1$, while the NLAGN tend towards higher values of $\log(f_{\rm x}/f_{\rm o})$. At $\log(f_{\rm x}/f_{\rm o}) > 1$, all but five of the twenty-six sources lack broad lines

distributions. Since SEXSI is a purely hard-band-selected sample, the top panel includes all identified sources, while the bottom panel displays the subset of these sources having significant soft-band *Chandra* detections as well as a dashed histogram showing upper limits to sources undetected below 2 keV. In addition, Figure 5.11 shows a scatter plot of HR versus 2 – 10 keV luminosity.

The BLAGN tend to be softer sources—they mainly fall below $HR \sim 0.2$ in Figure 5.11—and thus most have significant soft detections and are included in black in both panels of Figure 5.10. The BLAGN dominate the higher-luminosity end of the 2 – 10 keV distribution, while they comprise almost the entirety of the high-luminosity end of the 0.5 – 2 keV distribution. The other contribution to the high-luminosity hard-band sources is from the NLAGN. These tend to be harder (probably obscured) sources; thus, their corresponding 0.5 – 2 keV luminosities are lower (four have no soft-band detections).

The ELG dominate the 2 – 10 keV luminosity distribution below $\sim 10^{43.5}$ erg s^{-1} where the BLAGN distribution falls away and the ELG numbers rise. The ELGs have a broad range of HRs; thus, there are many ELG (26) without significant soft detections. The limit to these detections are shown in the dashed histogram.

Although they are few in number, the ALG we do detect all have 2 – 10 keV luminosities between $10^{42.5}$ and 10^{44} erg s^{-1}, indicating all likely host hidden AGN. A subset of our ELG plus all of our ALG represent the population of sources dubbed X-ray Bright, Optically Normal Galaxies (XBONGs; see Comastri et al. 2002, and references within), sources that show X-ray luminosities indicative of AGN activity but which lack optical spectroscopic indication of the underlying AGN.[7]

5.6.4 Absorbing Column Density Distribution

Figure 5.12 presents the N_H distribution for BLAGN, ELG, and NLAGN. ALG are omitted from this plot owing to their small number (see § 5.7.4). The BLAGN (top panel) are distributed broadly in N_H, with many more unobscured ($N_H < 10^{22}$ cm^{-2}) sources than for either the ELG or NLAGN populations. A total of 60 (29%) of the BLAGN have $N_H > 10^{22}$ cm^{-2}, while 149 (71%) have $N_H < 10^{22}$ cm^{-2}. Note that inclusion in our sample requires a significant hard-band X-ray detection – we expect that many of the 879 soft-only

[7]We refrain from using the term "XBONG" further in this paper because it lacks a clear definition; e.g., does XBONG refer to all X-ray luminous sources that lack optical AGN lines or *only* such sources that have optical spectra dominated by stellar absorption features?

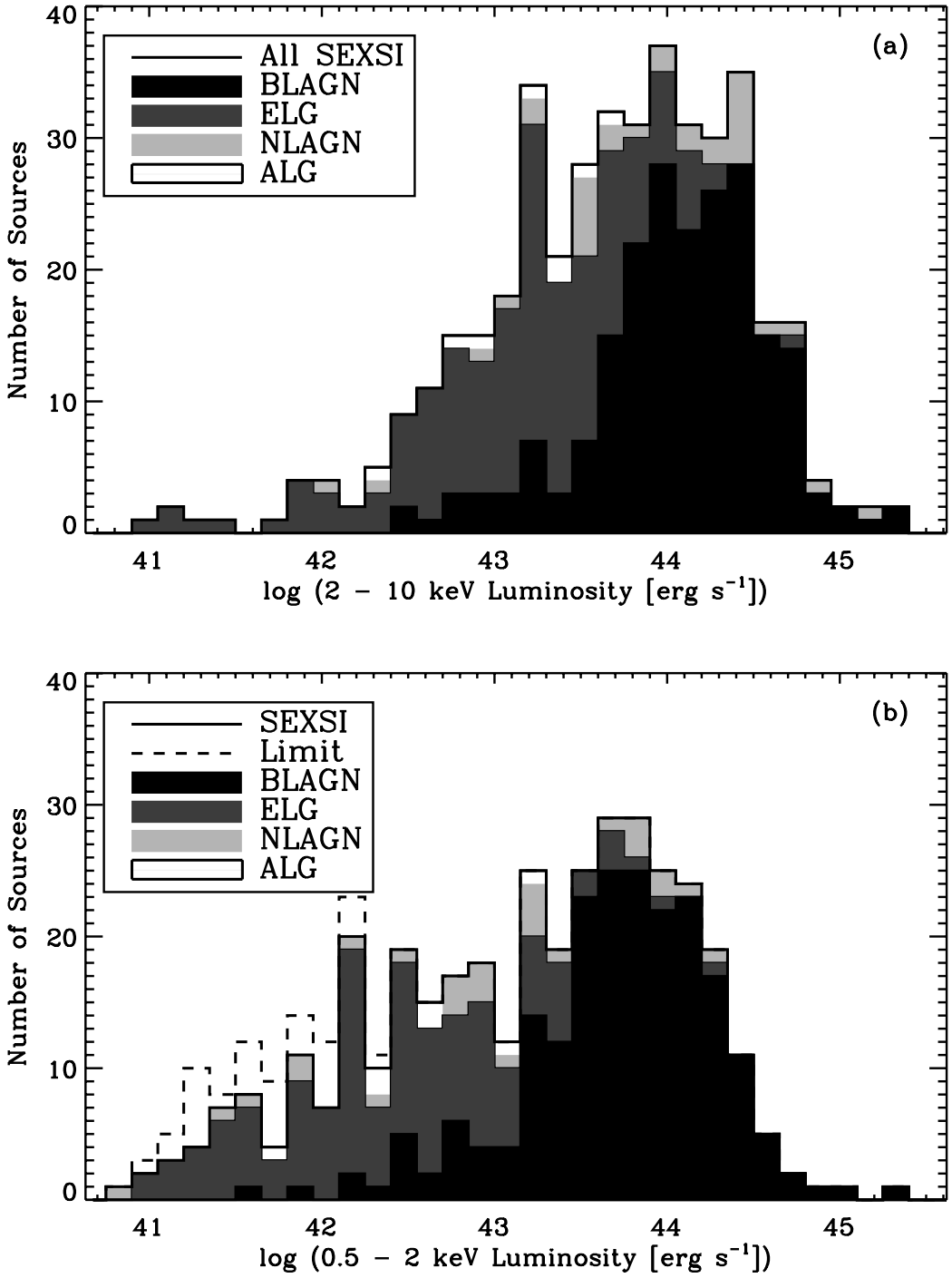

Figure 5.10 X-ray luminosity histograms, uncorrected for intrinsic absorption at the source. The top panel shows the 2 – 10 keV luminosity distribution, while the bottom panel shows the 0.5 – 2 keV distribution. The dashed histogram in the bottom panel indicates the 32 sources with upper limits to $L_{0.5-2.0\ \mathrm{keV}}$; the majority of these sources (26/32) are ELG while 4 are NLAGN

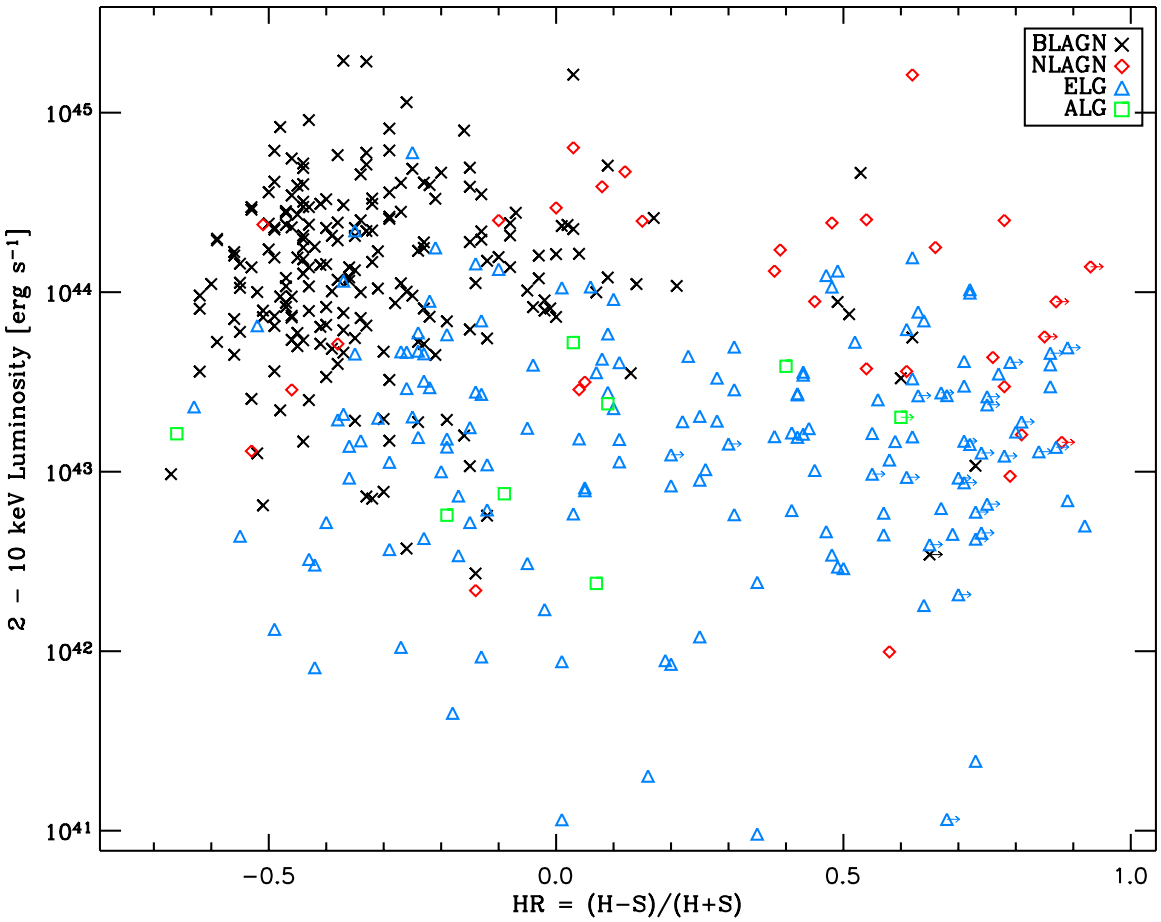

Figure 5.11 2 – 10 keV luminosity vs. HR. Crosses indicate BLAGN – note that they mainly fall at high luminosity and $HR < 0$. NLAGN are shown in diamonds; most have $HR > 0$, consistent with the notion that obscuration at the source is involved. Emission-line galaxies (triangles) have a wide spread in HR, as do the absorption-line galaxies (squares)

sources presented in Table 6 of Paper I will be unobscured BLAGN, and thus the population statistics and N_H distributions will be very different for a sample selected in the full-band (0.5 – 8 keV). The middle panel of Figure 5.12 presents the ELG. The majority of these sources have $N_H > 10^{22}$ cm^{-2} – only 27% (43 sources) have $N_H < 10^{22}$ cm^{-2}. The NLAGN sources appear even more obscured than the ELG. Of the 32 NLAGN only six (19%) have $N_H < 10^{22}$ cm^{-2}, with more than half the sample having $N_H > 10^{23}$ cm^{-2}.

5.7 Source Classes

5.7.1 Broad-Lined AGN

The BLAGN are the most common source type in our spectroscopically identified sample, comprising over half of all sources; they are by far the dominant source type above $z \gtrsim 1.4$. At the highest luminosities, these are (type 1) quasars; the lower luminosity sources are Seyfert 1 galaxies. They are also the easiest type of source to identify over a broad redshift range; their optical counterparts tend to be bright and they have easily detectable broad emission lines. Table 5.4 gives a list of commonly detected lines and the percentage of time each is detected. Figure 5.13 shows the hardness ratio distribution split by R-band magnitude, with the top panel including sources with $R < 22$ and the bottom panel showing the optically fainter sources. At $R < 22$ the BLAGN, shown in black, dominate the distribution, with a sharp peak at $HR \sim -0.5$. In Paper II we speculated that this HR peak near -0.5 was due to unobscured Seyferts and quasars, since that HR corresponds to a power-law photon index (Γ) between 1.8 and 1.9, a typical value for unobscured broad-line AGNs; the spectroscopy presented here confirms that conjecture.

Figure 5.12 shows the N_H distribution of the BLAGN in the top panel. In the unified AGN model, the existence of broad lines indicates a relatively unobstructed view to the central regions of the nucleus with low obscuring column densities ($N_H < 10^{22}$ cm^{-2}). While our BLAGN do have the lowest mean HR among our four source classes, we still find that 29% $\pm$ 4% have $N_H > 10^{22}$ cm^{-2}, indicating significant X-ray absorption. However, a significant fraction of these sources are at a high enough redshift that their N_H values are less-well constrained due to the absorption edges shifting out of the *Chandra* bandpass (see lower right panel of Figure 5.14 and § 5.8). To quantify this effect, we consider the 114 BLAGN at $z < 1.5$; only 12% of this subset have $N_H < 10^{22}$ cm^{-2}, compared to 29% for

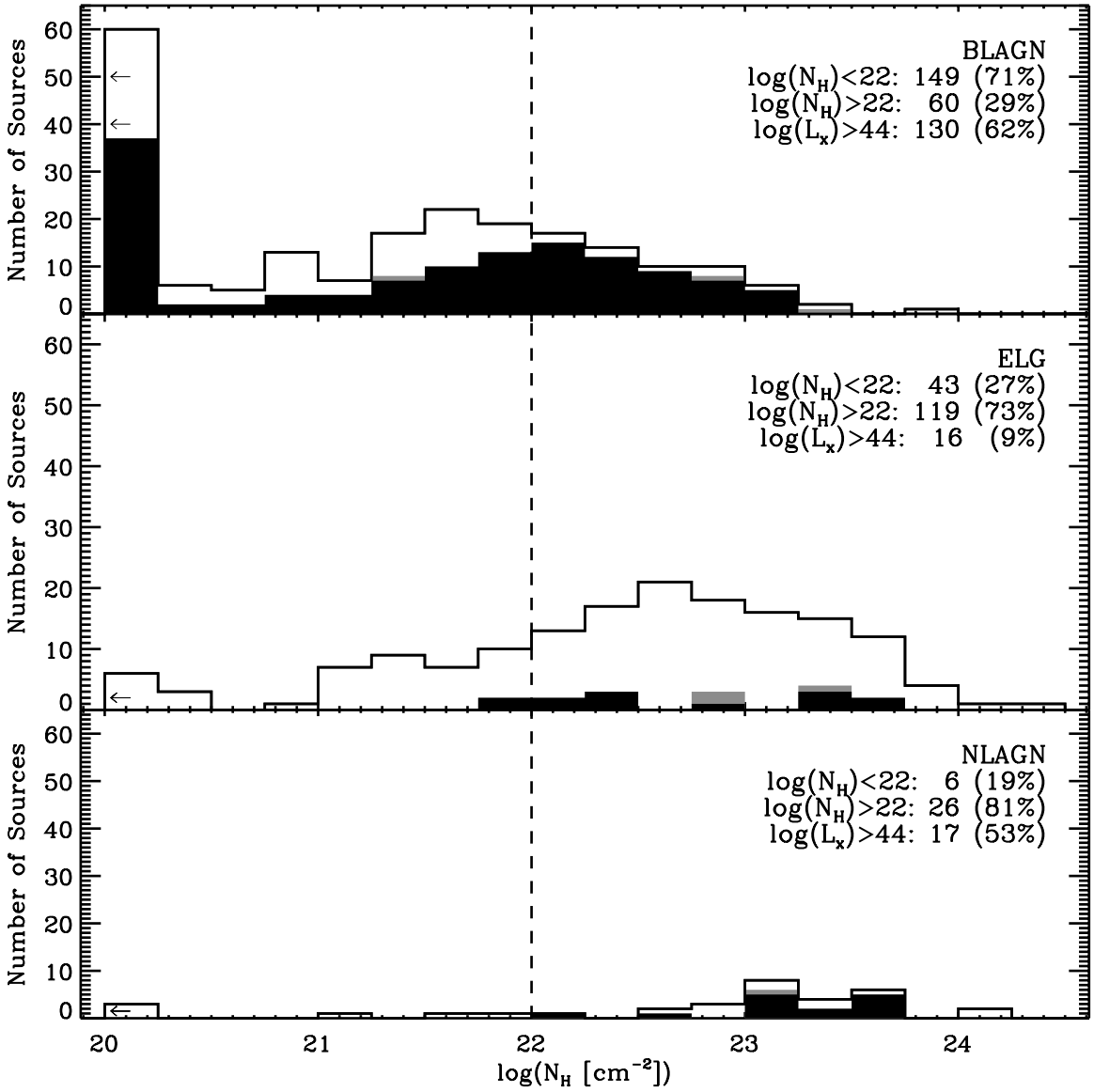

Figure 5.12 N_H histogram for BLAGN, ELG, and NLAGN. The small number of ALG are omitted. Sources with a best-fit N_H value below $\log N_H = 20$ are placed in the bin at 20. The black fill indicates sources with obscured 2 – 10 keV rest-frame luminosities above 10^{44} erg s^{-1}, wile gray indicates sources with unobscured luminosities above 10^{44} erg s^{-1}. The dashed line shows our adopted break, at $\log N_H = 22$, between obscured sources and unobscured sources. Note that while about half of the SEXSI sources have $N_H > 10^{22}$ cm^{-2}, it is the BLAGN that dominate the unobscured distribution. The majority of the ELG are obscured as are the NLAGN to an even greater extent

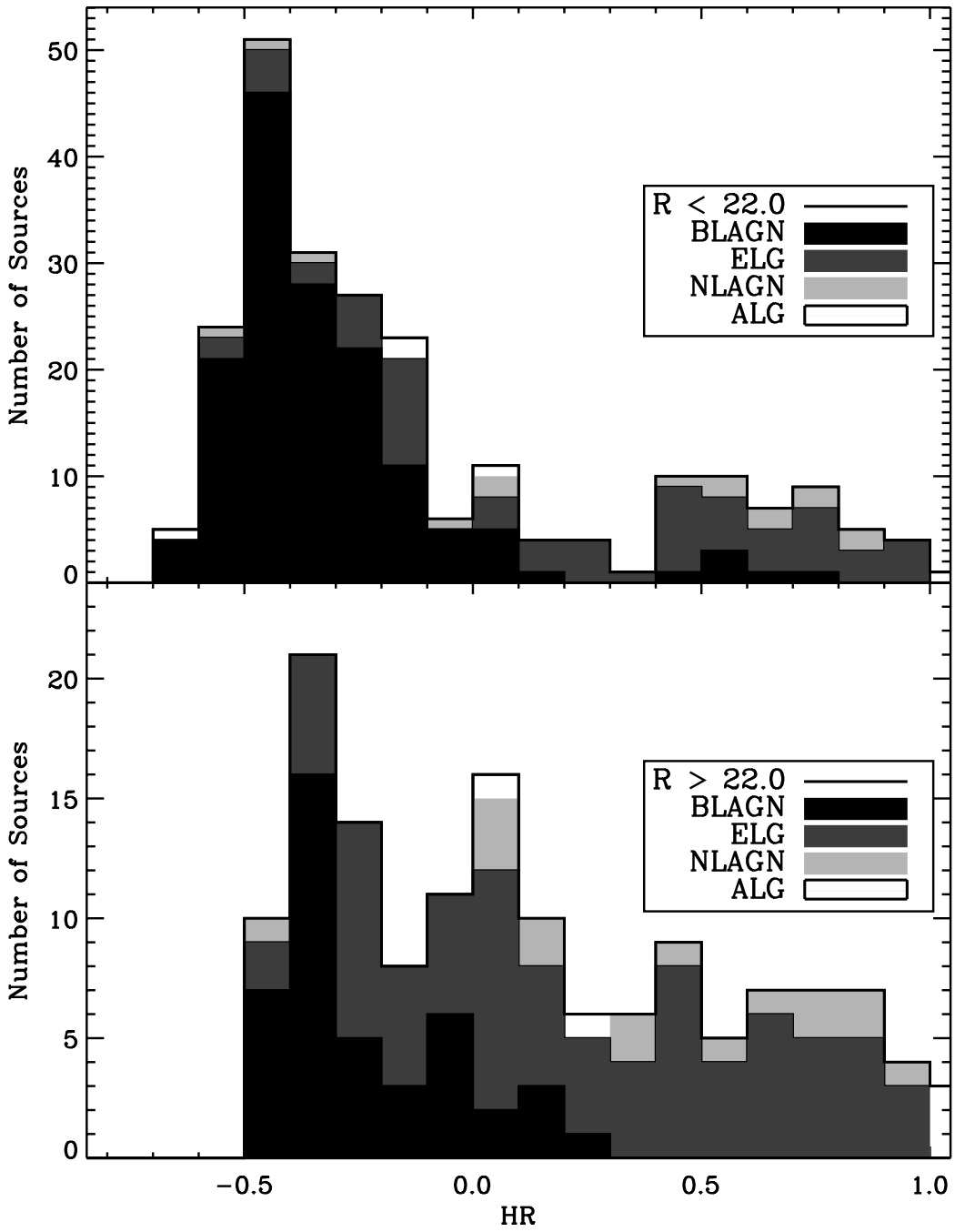

Figure 5.13 Hardness ratio histogram of spectroscopically identified sources, excluding stars, split at $R = 22$. The top panel shows the optically brighter sources ($R < 22$). The black-filled peak near $HR = -0.4$ represents the broad-lined sources, which dominate the optically brighter population of 2 – 10 keV SEXSI sources. The lower panel shows the optically fainter ($R > 22$) sources which are, on average, much harder and have a broader HR distribution. This group of sources is a mix of spectral classes: there are BLAGN, but in addition there are many ELG, ALG, and NLAGN

Table 5.4. Optical spectroscopic line detections

Feature	BLAGN			NLAGN			ELG		
	# w/ $\Delta\lambda$[a]	# w/ Det	% Det	# w/ $\Delta\lambda$[a]	# w/ Det	% Det	# w/ $\Delta\lambda$[a]	# w/ Det	% Det
C IV λ1549	105	66	62%	13	10	76%	0	···	···
C III] λ1909	129	83	64%	16	10	62%	0	···	···
Mg II λ2800	169	151	89%	18	4	22%	112	13	11%
[Ne V] λ3426	126	26	20%	21	17	80%	147	0	0%
[O II] λ3727	119	54	45%	21	21	100%	151	115	76%
[Ne III] λ3869	110	19	17%	19	12	63%	151	10	6%
CaHK $\lambda\lambda$3934, 3968	103	20	19%	19	7	36%	148	67	45%
D4000 break	102	10	9%	19	8	42%	146	59	40%
Hβ	58	26	44%	14	7	50%	113	24	21%
[O III] λ5007	50	41	82%	14	13	92%	103	68	66%

[a]These columns (# w/ $\Delta\lambda$) indicate the number of sources with spectral coverage of the given spectral feature

BLAGN at all redshifts. For the 62 BLAGN with $z < 1$, the fraction is even lower (9%). This systematic trend also likely explains the tendency for many of the most luminous BLAGN in Figure 5.12 to be the most obscured. SEXSI, as with any flux-limited survey, has a redshift-luminosity relation (Figure 5.1): our most distant sources are the most luminous sources, and this systematic effect makes them also appear most obscured.

Furthermore, the column density measurements can be affected by changes in the Galactic N_H (which is fixed during the spectral fitting): small underestimates in the true Galactic N_H can give rise to overestimates of the intrinsic column density. We note that, for consistency with all previous work, we have used for Galactic absorption column density the N_{HI} derived from 21 cm observations (Dickey & Lockman 1990). This common practice is incorrect, however; the X-ray absorption column density is two to three times the N_{HI} value, since it is the heavy elements, rather than hydrogen, that absorb X-rays, and they are present in the molecular and ionized phases of the ISM as well as in the atomic phase (e.g., Iyengar et al. 1975). Doubling or tripling the Galactic N_H value can reduce the inferred intrinsic column density by a large factor, particularly for high-redshift sources, and particularly for sources from fields with relatively large Galactic column densities. Indeed, we find the fraction of high-N_H BLAGN monotonically increases as the Galactic column density increases, from 25% for the 10 fields with $N_H < 2 \times 10^{20}$ cm^{-2}, to 28% for the eleven fields with $2 < N_H < 7 \times 10^{20}$ cm^{-2}, to 32% for the four fields with $N_H \sim 9 \times 10^{20}$

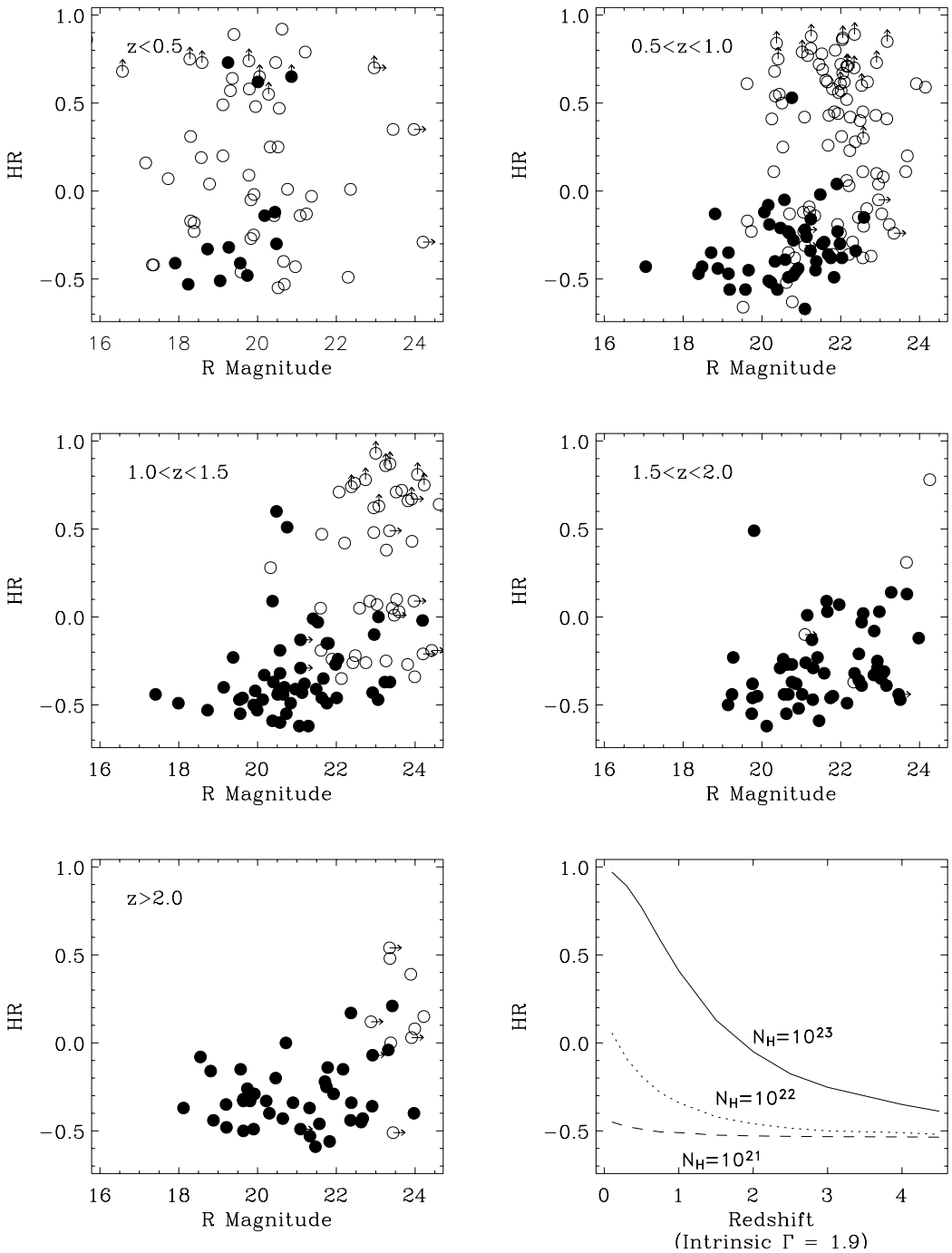

Figure 5.14 HR versus R-magnitude for five redshift ranges. Broad-lined sources (BLAGN) are shown with filled circles, while non-BL sources (NLAGN, ELG, ALG) are open. Arrows indicate limits to the HR (upward pointing) and R-magnitude (right pointing). The abrupt drop in the number of non-BL sources in the highest-z panels ($z > 1.5$) is apparent, and caused both by [O II] λ3727 shifting out of the optical band, and the inability to spectroscopically identify faint sources. The bottom right panel shows HR versus z for three typical values of intrinsic obscuring column density given a source power-law index $\Gamma = 1.9$, for reference. The column densities indicated on the plot are in units of cm^{-2}

cm^{-2}, to 70% for the two fields with $N_H \sim 20 \times 10^{20}$ cm^{-2}. Any use of the N_H distribution in this, and all other, survey paper(s) for quantitative purposes must take the uncertainty in Galactic column density and the insensitivity of measurements for high-redshift sources into account.

The Doppler-broadened emission lines exhibit a distribution of widths; for the purposes of consistency, SEXSI puts a strict cutoff between narrow- and broad-lined sources at 2000 km s^{-1}, following Veilleux & Osterbrock (1987). Some sources have a line or lines that are just above this width cut and thus are classified as BLAGN, although their other properties may be more similar to a typical NLAGN. Our BLAGN classification includes sources with broad-absorption lines blueshifted with respect to the object redshift (BALQSO) or broad-absorption at the source redshift. Of the nine sources with $N_H > 10^{23}$ cm^{-2}, four of the sources are noted as possible BALQSO's, a type of quasar associated with high N_H values (e.g., Gallagher et al. 2002).

5.7.2 Narrow-Lined AGN

The NLAGN, comprising 8% of our sample, tend to be both the most obscured objects and highly luminous. Of our 32 NLAGN, five had no optical counterpart in our imaging — four of these were blind pointings at the X-ray positions in fields with $R_{\rm limit} = 23 - 24$, while the fifth was from our shallowest field with $R_{\rm limit} = 21.1$. The 27 NLAGN with optical counterpart photometry have $\langle R \rangle = 22.0 \pm 1.6$, while the BLAGN have $\langle R \rangle = 20.9$.

As mentioned in § 5.4, the redshift distribution of the NLAGN is broad, extending over the redshift range $z = 0 - 4$. The NLAGN are the only narrow-lined sources in the sample with $z > 1.5$. This fact is largely a consequence of a two-part selection effect: (1) bright, high-ionization UV emission lines are availably only for objects at higher z, while we reach the redshift desert for typical galaxy emission lines found in ELG at $z > 1.5$, and (2) for redshifts sufficiently high that Lyα moves into the optical window, normal galaxies would be too faint both optically and at X-ray energies in our moderate-depth, wide-area survey. In addition, the higher mean luminosity of the NLAGN makes them visible to higher redshift.

For the NLAGN, we find an average (obscured) luminosity near 10^{44} erg s^{-1}: $\langle \log L_{2-10\ \rm keV} \rangle = 43.8 \pm 0.6$. Fifteen sources have obscured quasar luminosities, with $L_{2-10\ \rm keV} > 10^{44}$ erg s^{-1} and, of these, 73% are found at $z > 1.5$. Twelve out of these fifteen galaxies have $R > 23$, while two have limiting R magnitudes of 21.1 and 22.9, and one has $R = 21.7$. Of the

sources with lower luminosities, two have luminosities near 10^{42} erg s^{-1}. The other fifteen have $43.0 < \log L_{2-10\ \mathrm{keV}} < 44.0$. The non-quasar luminosity ($L_{\mathrm{x}} < 10^{44}$ erg s^{-1}) sources are all found at redshifts below $z = 1.5$, with $0.3 < z < 1.3$. The luminosities presented in the catalog and referred to in this paragraph are all *obscured* 2 – 10 keV rest-frame luminosities, uncorrected for the intrinsic obscuring column. Since the majority of the NLAGN are obscured, their intrinsic luminosities are larger. At $z = 0$ and $N_H < 10^{23}$ cm^{-2} unobscured luminosity will be increased by a factor of $\lesssim 2$, while at $N_H = 10^{24}$ cm^{-2} the unobscured X-ray luminosity increases by a factor of ~ 10. At higher redshifts this increase is not as large since the lower energy X-rays that are most subject to absorption shift out of the observed frame; at $z = 1$ ($z = 2$) the $N_H < 10^{23}$ cm^{-2} unobscured luminosity is increased by a factor of ~ 1.2 (~ 1.04) and the $N_H = 10^{24}$ cm^{-2} unobscured luminosity increases by ~ 2.6 (~ 1.36). Using unobscured luminosites, 17 (53%) of NLAGN have quasar luminosities.

5.7.3 Emission-Line Galaxies

One of the surprising discoveries made by the various *Chandra* and *XMM-Newton* surveys conducted to date is the large population of X-ray sources that lack AGN signatures in their optical spectra, and yet have X-ray luminosities too high to be powered by stellar emission alone. In § 5.10 we discuss the nature of these sources; here we explore the properties of the ELG found in our sample. Table 5.4 shows the typical emission lines detected in our ELG spectra (eg., [O II] λ3727, [O III] λ5007, etc.). In addition, it shows that 45% of the 148 ELG with the requisite wavelength coverage show CaHK $\lambda\lambda$3934, 3968 absorption and 42% of the 146 ELG with requisite wavelength coverage show the D4000 break.

Of the 168 ELG, we find an average (obscured) luminosity nearly an order of magnitude lower than for the NLAGN: $\langle \log L_{2-10\ \mathrm{keV}} \rangle = 43.14 \pm 0.05$ (this rises to $\log L_{\mathrm{x}} = 43.25 \pm 0.04$ if we exclude the eleven sources with $L_{\mathrm{x}} < 10^{42}$ erg s^{-1} which, in principle, could be starburst galaxies – but see § 5.10). Thirteen sources (8%) have (obscured) quasar luminosities, $> 10^{44}$ erg s^{-1}. The majority of the ELG tend to be obscured and, thus, their intrinsic luminosities are larger; considering unobscured luminosities, 16 (9%) ELG have quasar luminosities.

Twelve identified extragalactic SEXSI sources have $L_{2-10\ \mathrm{keV}} < 10^{42}$ erg s^{-1}; eleven of the twelve are classifed as ELG with $0.09 < z < 0.34$. In § 5.10.1 we discuss these sources and the possibility that their X-ray emission is starburst dominated instead of AGN-dominated.

5.7.4 Absorption-Line Galaxies

Absorption-line galaxies are not found in great numbers in our survey. Although nearly half of our ELG spectra show absorption features, such as CaHK absorption and/or the D4000 break, those sources also have emission lines, most frequently [O II] λ3727. With 98% of our spectroscopy from the Keck 10 m telescopes, our ability to detect faint lines is greater than in surveys that use smaller telescopes and thus our identification statistics may be skewed towards ELG. In addition, some surveys (e.g., ChaMP – Silverman et al. 2005) classify sources as ALG even if emission lines are detected.

Of the 438 sources with redshift and classification information, only eight ($< 2\%$) are identified as ALGs. Of these eight, two are flagged as having only a tentative line identification, meaning their redshift and class identification is likely but not secure. In addition, two other ALGs are flagged as falling just outside the X-ray-to-optical counterpart search area (see Table 5.3). The distances of these two objects from the edges of their respective search areas are $\sim 1''$, among the larger offsets found in Table 5.3. One more source identified in the catalog is flagged as an ALG that is identified using the spectrum of one of two optical sources within the X-ray-to-optical search area — we would need additional data (e.g., a spectrum of the other source or an on-axis *Chandra* observation) to determine the true counterpart identification.

Setting aside these special cases, we find that there are are only three sources with a secure identification as an ALG — less than 1% of the identified sources. This fraction is lower than in some other surveys, as deiscussed further in § 5.9.1.

5.7.5 Line-Free Spectra

Of the 477 spectra we collected, 39 exhibit roughly power-law continuum emission with no detectable line emission. Here we explore the possibility that the sources are BL Lac objects – AGN that have X-ray and radio emission but show no emission lines in their optical spectra – and the alternative notion that they are the higher-redshift end of the ELG distribution.

5.7.5.1 BL Lac Contribution

Prominent among the serendipitous sources found in the first wide-area X-ray imaging survey – the *Einstein Medium Sensitivity Survey* (*EMSS*: Gioia et al. 1990; Stocke et al. 1991) – were BL Lac objects which comprised $\sim 6\%$ of the point sources detected. Subsequent radio and X-ray surveys for BL Lacs have left the population statistics of this relatively rare AGN class somewhat uncertain owing to the non-Euclidean $\log N - \log S$ relation for X-ray-selected objects, and the debate over the relative proportions of the X-ray-bright and radio-bright segments of the population. The two recent X-ray surveys using, respectively, the whole *ROSAT All-Sky Survey (RASS)* and the Greenbank radio catalog (Laurent-Muehleisen et al. 1999), and the *ROSAT*/VLA North Ecliptic Pole survey (Henry et al. 2001) define the $\log N - \log S$ relation for X-ray-selected objects down to a flux of $1 - 3 \times 10^{-13}$ erg cm^{-2} s^{-1} in the 0.5 – 2 keV band. Thus, reaching the SEXSI flux limit of 10^{-15} erg cm^{-2} s^{-1} requires an extrapolation of nearly two orders of magnitude and a shift from soft X-rays to hard X-rays. Our detection of BL Lacs, or a lack thereof, could be constraining.

Adopting the mean power law slope of $\Gamma = 2.2$ derived from a large collection of RASS-detected BL Lacs by Brinkmann et al. (1997) and assuming only Galactic absorption, the 2 – 10 keV flux should be 95% of the 0.5 – 2 keV band flux. Using the SEXSI coverage of 1 deg^2 at 10^{-14} erg cm^{-2} s^{-1} and 0.1 deg^2 at 2.5×10^{-15} erg cm^{-2} s^{-1} (Figure 1 in Paper I) with this flux correction factor, and extrapolating the $\log N - \log S$ for X-ray-detected BL Lacs from Figure 5 of Henry et al. (2001) ($\alpha \sim 0.7$), we expect between 0.5 and 1 BL Lacs to appear in SEXSI. Increasing the $\log N - \log S$ slope by 0.1 (well within the uncertainties) more than doubles this number. Furthermore, if we use the radio number counts for BL Lacs at 1.0 mJy from Figure 5 of Giommi et al. (1999), we would also expect roughly one source in our survey area (although, again, the extrapolation required is nearly two orders of magnitude in radio flux density). Note that while the extreme, high-energy-peaked BL Lacs discussed in Giommi et al. (1999) make up only $\sim 2\%$ of this expected radio population, the fact that our survey goes nearly three orders of magnitude deeper in X-ray flux means that essentially all of the radio-selected objects should be detected.

Using large-area, public radio surveys we checked for radio emission from our 39 sources that exhibit line-free spectra. FIRST (15) and NVSS (24) radio images were examined

for each of these sources; no sources were detected in the FIRST images to a 3σ limit of 0.75 mJy. Of the NVSS images, 19 had upper limits of ~ 1.4 mJy, while three were in a single noisy field with upper limits closer to 5 mJy. One source (J125306.0-091316) is within the contours of an extended NVSS source, but the low resolution of that survey ($\sim 50''$) makes it difficult to establish an association. The final source, J022215.0+422341, has a 2.8 mJy NVSS source within $10''$ (1.5σ), and may represent the expected ~ 1 radio-loud BL Lac source in our survey area. This general lack of radio counterparts leads us to conclude that most of these 39 line-free SEXSI sources are not BL Lacs.

5.7.5.2 ELGs in the Redshift Desert?

Since it is highly likely that the majority of these line-free objects are not BL Lacs, what are they? In Figure 5.15, we examine the notion that these objects are predominantly ELGs in which the [O II] λ3727 line has slipped beyond the wavelength coverage of our spectra. We estimate a redshift for each continuum-only source by assuming that [O II] λ3727 falls just longward of the optical spectral range for each source. Six of the objects have spectra with limited wavelength coverage, and could fall within the redshift distribution of the other ELGs at $z < 1.5$; the remaining 34 objects would have to be at higher redshifts (see lower left panel of Figure 5.15).

As would be expected if their mean redshift is higher, their magnitude distribution is shifted toward fainter values: 85% are fainter than $R = 22$ while only 57% of the ELGs are this faint (comparing only sources with $R_{\rm limit} > 22$). The median R-magnitude for the ELG is 22.2, while for the continuum-only sources, $R_{\rm median} > 23$ – the measurement is limited by our imaging depths. The $f_{\rm x}$ distributions of the two samples are statistically indistinguishable, while the HR distribution of the lineless objects is slightly softer, consistent with the fact that we can more easily detect unobscured objects at higher redshift. The values of $L_{\rm x}$ derived using the estimated redshifts are consistent with the rest of the ELG distribution, although, again, since the sources are by definition at higher redshift but have similar 2 – 10 keV fluxes, the median value of $L_{\rm x}$ is higher (see lower panel in Figure 5.15). We determine that these continuum-only sources are *consistent* with being the high-redshift end of the ELG population.

Treister et al. (2004) combine X-ray luminosity functions with spectral energy distributions of AGN to model the X-ray and optical distributions of X-ray sources from the GOODS

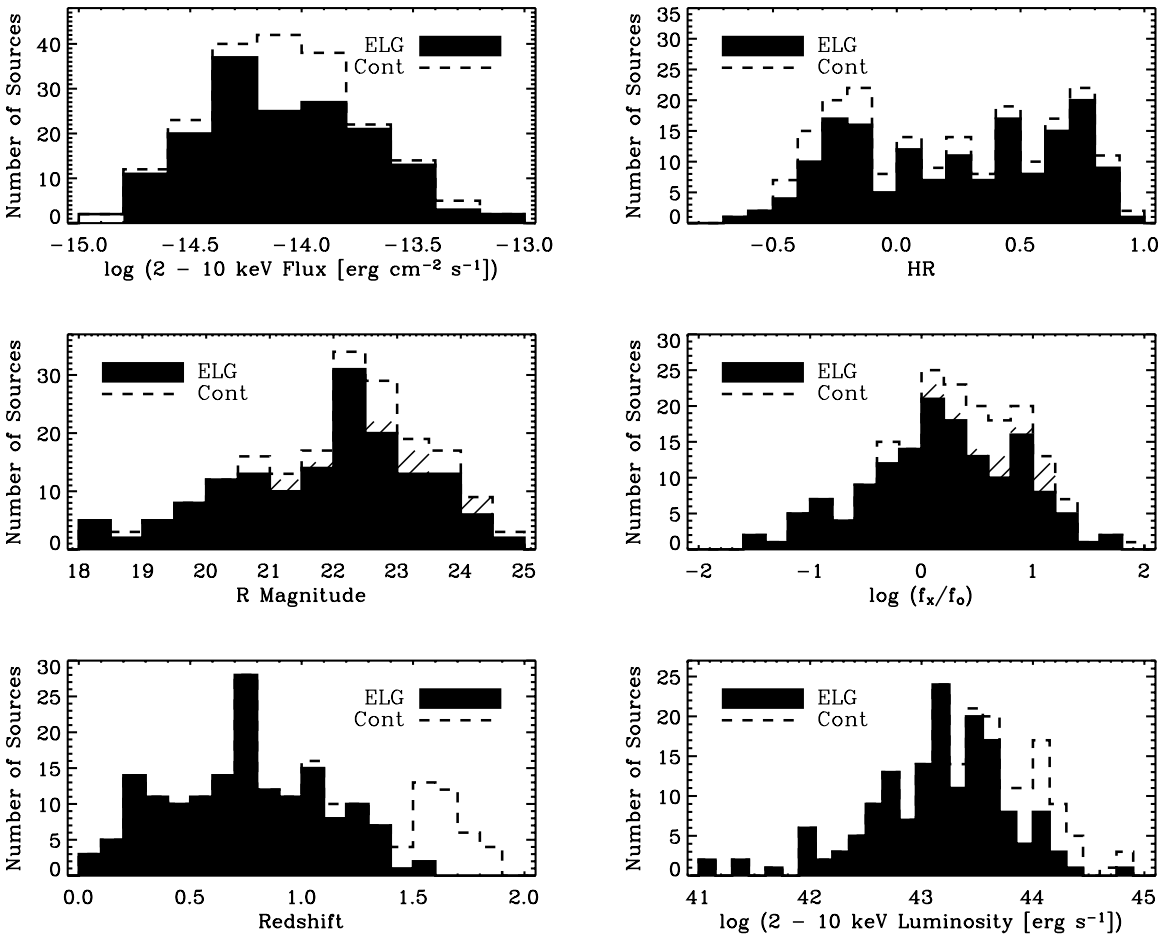

Figure 5.15 The ELG population compared to sources that have spectra with a continuum lacking detected emission or absoprtion features. The top panels show the 2 – 10 keV flux, HR, R-magnitude, and $\log(f_{\rm x}/f_{\rm o})$ distributions of the ELG (filled black) and the continuum-only sources (dashed line). The hatched regions show the continuum-only sources that have $R = R_{\rm limit}$. The bottom two panels show the spectroscopic redshift distribution and corresponding $L_{\rm x}$ distribution for the ELG (filled black). These distributions are compared to distributions of the continuum-only sources whose assigned "redshift limits" were calculated assuming that [O II] λ3727 falls just longward of the optical spectral range for each source

survey and find that the predicted distribution for $R < 24$ sources is consistent with the GOODS spectroscopically identified redshift distribution. The sources that remain spectroscopically unidentified are predicted to be either optically faint, obscured sources nearby or in the redshift desert, consistent with our notion that the SEXSI line-free sources are part of the redshift-desert ELG population.

The population statistics of the SEXSI sample change if we include these 39 line-free spectra with the ELG sample: 44.8% ± 3.1% BLAGN, 42.7% ± 3.0% ELG, 6.9% ± 1.2% NLAGN, and 1.7% ± 0.6% ALG. Adopting this assumption, the BLAGN and ELG fractions are the same within 1 σ, at $\sim$ 43%–44% each.

5.7.6 Stars

Of the 969 X-ray sources covered by our optical images, seven are associated with bright ($8.5 < R < 14$) stars, all of which were previously detected by ROSAT (although several are apparently identified here for the first time); these seven sources are labeled as 'star' in Table 5.2. All have colors of spectral types G to M and hardness ratios at the softest end of the distribution ($-0.73 < HR < -0.95$); six out of seven have hard-band X-ray-to-optical flux ratios in the range $10^{-2.5}$ to 10^{-4}, typical of the upper end of the stellar $L_{\rm x}/L_{\rm o}$ distribution (cf. Pizzolato et al. 2003; Feigelson et al. 2004). The seventh source has $\log(f_{\rm x}/f_{\rm o}) \sim -1.8$ which is extraordinarily high; however, since it is one of the five brightest sources in our entire survey, the identification with a 12^{th} magnitude star is likely correct. The very small fraction of stars ($< 1\%$) we detect is simply a consequence of our hard-band selection criterion.

Of the 468 spectra we obtained for the fainter optical counterparts, an additional eleven objects have stellar spectra at zero redshift. One of these is a 20^{th} magnitude object with strong H and He emission lines superposed on TiO bands, characteristic of a cataclysmic variable. The spectrum for this source is shown in Figure 5.16. The observed velocity is -274 km s^{-1} marking it as a candidate for a rare halo CV, although the high velocity may simply mean the system was at an extremum in orbital phase at the time of our observation. The remaining stellar objects are likely to all be chance coincidences. Five are fainter than 20^{th} magnitude, have hardness ratios $HR > -0.5$, and have $\log(f_{\rm x}/f_{\rm o}) > -0.3$, e.g., values quite atypical of stellar X-ray sources. In order to eliminate the possibility that a giant hard X-ray flare was responsible for the detected source, we examined the light curves for

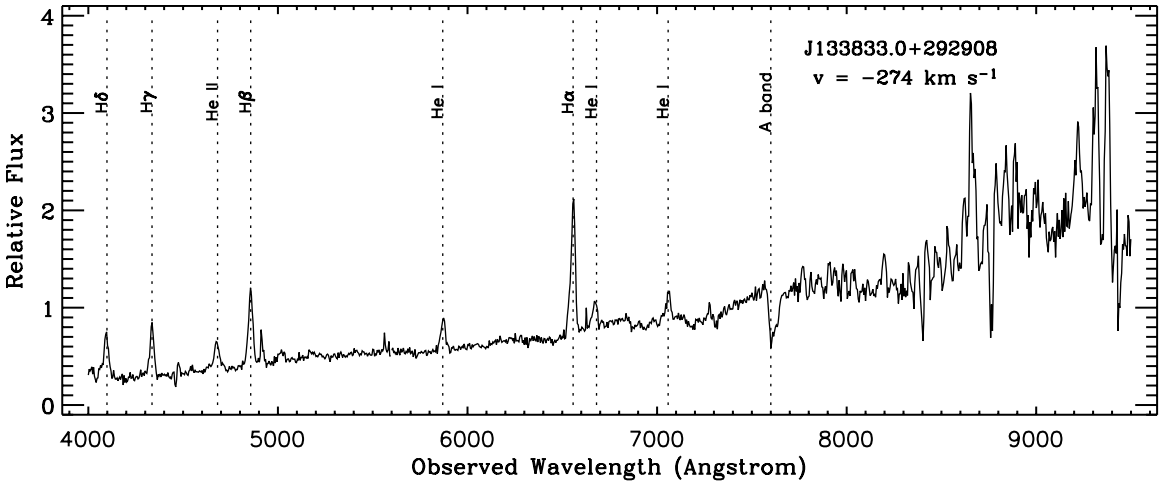

Figure 5.16 A cataclysmic variable (CV) that shows a blueshift of 274 km s^{-1}. This source has $f_{2-10\ \mathrm{keV}} = 3.25 \times 10^{-14}$ erg cm^{-2} s^{-1}, $HR = -0.18$, and $R = 20.1$. The measured velocity indicates either that the star is at an extremum in its orbit or that it is a rare halo CV

all five sources and found no evidence of dramatic variability. We calculated the probability of chance coincidence for each source using stellar and X-ray number counts and error radii for each field, and found that all had probabilities of $\gtrsim 10\%$; in a survey with 27 fields, all are comfortably consistent with being chance alignments of a foreground star with a faint background source that is the true origin of the X-ray emission.

The remaining five stellar spectra are for counterparts with magnitudes $16.7 < R < 18$. CXOSEXSI J152151.6+074651, the softest of the five stars, showed evidence of variability, with a rapidly declining count rate in the first 5% of the observation. Two of the others lie outside the formal error circles (see Table 5.3), making it likely they are chance coincidences. The remaining two sources have extreme $\log(f_\mathrm{x}/f_\mathrm{o})$ values (> -1, using a hard-band f_x) and $HR > -0.3$; it is unlikely that these stars are the true counterparts.

5.8 Selection Effects and Sample Completion

Like all surveys with *Chandra*, the steep roll off in effective area above ~ 5 keV limits the range of column densities that can be probed by SEXSI. Our sample includes only sources detected in the 2 – 7 keV band, limiting our ability to identify sources with $\log N_H \gtrsim 23.4$ at $z \lesssim 1$. In addition, we become less able to constrain N_H for high-redshift sources, where the absorption cutoff for typical columns shifts out of the soft band (to $E \lesssim 0.3$ keV). For

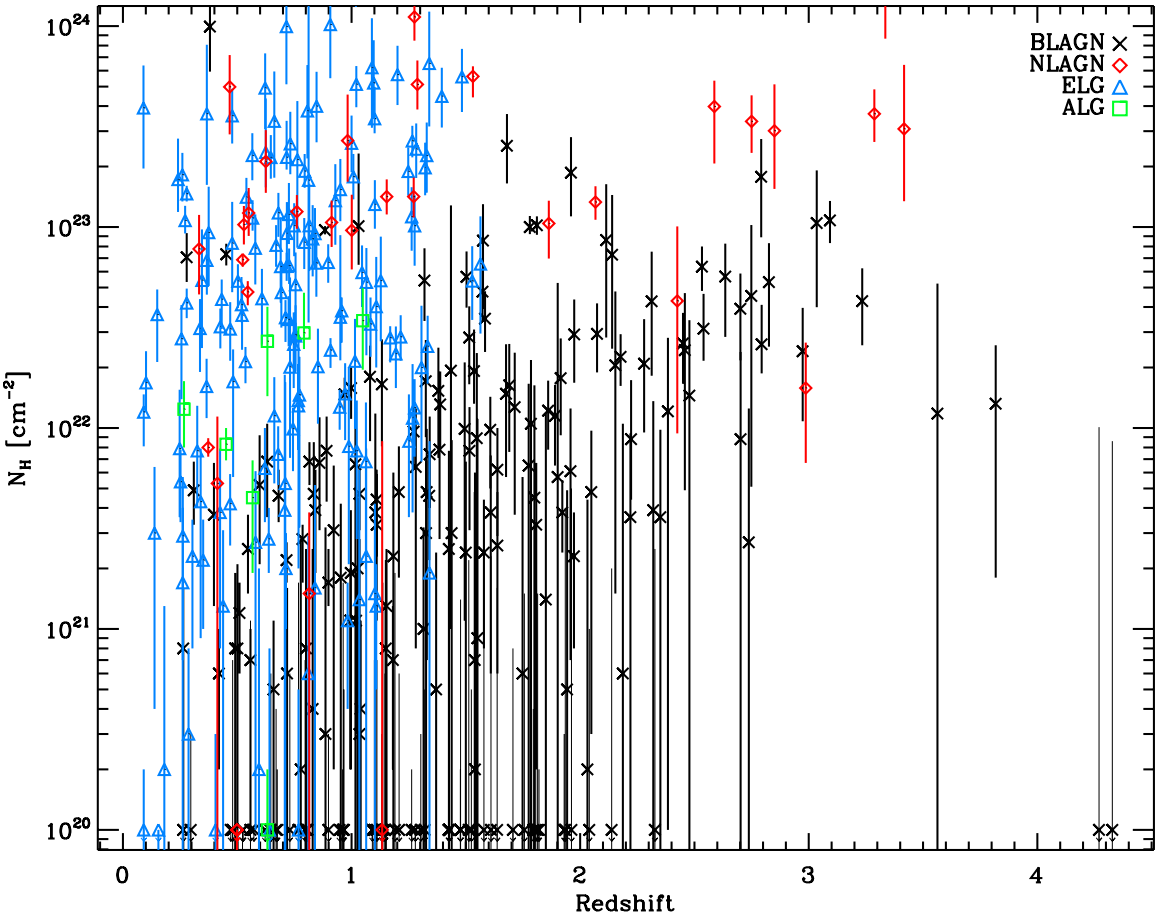

Figure 5.17 N_H versus redshift. 1 σ error bars from the XSPEC fits are presented; the 14 sources with N_H values determined from the HR (see § 5.5) are omitted. Sources with a best-fit N_H value below 10^{20} cm^{-2} are placed at 10^{20} cm^{-2} with a downwards pointing arrow. If the 1 σ upper bound to the N_H is above 10^{20} cm^{-2} then the error bar shows on the plot; conversely if the upper bound is also below 10^{20} cm^{-2} no error bar is present

a $z = 2$ source this happens for columns $N_H \lesssim 10^{22}$ cm^{-2}. This effect can be seen in Figure 5.14, which shows the hardness ratio distribution in different redshift bins. In the highest bin ($z > 2$), the hardness ratios tend toward -0.5. Figure 5.17 shows N_H versus z and illustrates the inability to constrain well the N_H measurement of high-z, low-column density sources.

Compared to some "hard-selected" surveys, we are somewhat biased against steep-spectrum X-ray sources. We have focused our followup effort on sources with independent hard-band detections. By comparison, some surveys compile source lists by searching full-band images and then count a source as a hard-detection if it has positive counts in the hard-band image (e.g., Stern et al. 2002b; Yang et al. 2004); this will happen $\sim 50\%$ of

the time due to statistical fluctuations in the background when no hard-band counts are recorded. These catalogs will therefore include a higher fraction of steep-spectrum sources.

Completeness at our followup magnitude limits varies with source class and redshift range. The procedures we use to classify sources depend on specific lines, so that the redshift and R magnitude ranges over which we can properly identify sources depend on the source type. BLAGN are relatively easy to identify even at our typical followup limit of $R = 23 - 24$, since their broad lines constitute a significant fraction of the total R band luminosity. NLAGN, ELG, and ALG are all more challenging to identify at the faint end, since their typical line-to-continuum ratios are smaller. The ELG, which are identified only from nebular lines such as [O II] λ3727, [O III] λ5007, etc., have a large "redshift desert" from $z \sim 1.4 - 2.2$, where the [O II] λ3727 has shifted into the IR and Lyα has yet to shift into the optical from the UV. Our 39 sources with continuum-only emission have X-ray and optical properties consistent with the notion that they are ELG in the redshift desert (§ 5.7.5.2). For most ELG, the optical counterparts are roughly consistent with L* host galaxies and thus their R-band magnitude increases predictably with redshift (see § 5.10.2), unlike BLAGN, for example, where the optical luminosity is dominated by AGN emission and thus R is related to $L_{\rm x}$. Thus, there are likely many more ELGs at higher redshifts that we have not spectroscopically followed up due to faint R-band counterparts; the ELG we do identify at $z \gtrsim 1$ typically have little continuum emission.

Since we use two different instruments for spectroscopy, we have investigated the extent to which their different quantum efficiencies as a function of wavelength may have affected source identification. The blue arm of LRIS (LRIS-B) has good sensitivity further into the near-UV than does the blue side of DEIMOS. There was one case where we had both a DEIMOS spectrum and an LRIS spectrum of a source which suggested different classifications: the DEIMOS spectrum showed only ELG lines, while the LRIS spectrum had a broad Mg II λ2800 line on the blue side which led to the final classification as a BLAGN. This seems to be an isolated case in our sample, although there are few sources for which we have both LRIS and DEIMOS coverage.

We checked the statistics of the sources we identified with these two instruments, ignoring the Doublespec data from the Palomar 200 inch (5 m) since it only comprises 2% of the sample and includes only bright sources. We find no significant difference in classification statistics between the 137 sources classified by DEIMOS and the 280 sources classifed

by LRIS. With DEIMOS, we find $48.9 \pm 6.0\%$ (67) BLAGN while in the LRIS spectra, $48.2 \pm 4.1\%$ (135) are BLAGN; DEIMOS and LRIS identify $40.1 \pm 5.4\%$ (55 sources) and $37.5 \pm 3.7\%$ (105) ELGs, respectively. Both instruments classify a small number of targets as ALG (both $< 2\%$), and find a small number of stars ($\sim 3\%$–5%).

The only marginal difference we find is in the rate of identifying NLAGN. Using LRIS, we identify 26/280 such sources ($9.3 \pm 1.8\%$), while with DEIMOS we find only only 6/137 sources ($4.4 \pm 1.8\%$). The NLAGN DEIMOS may be missing would be classified as ELG. This difference probably results from the superior LRIS-B sensitivity, which allows faint, narrow, high-ionization UV-lines such as C III] λ1909 or C IV λ1549 to be detected at observed wavelengths below $\simeq 5000$ Å enabling LRIS to properly identify NLAGN in the redshift range $1 \lesssim z \lesssim 2$. Also, the [Ne V] λ3426 line does not shift into the band covered by DEIMOS until $z \sim 0.3 - 0.4$ and, as a consequence, we should also expect more low-z NLAGN with LRIS. These trends are seen in the data – of the six NLAGN identified with DEIMOS, only one has $1 < z < 2$, a source identified by its [Ne V] λ3426 line at $z = 1.28$. There are no DEIMOS-identified NLAGN below $z = 0.8$ and half of the sources are found at $z > 2$. LRIS, on the other hand, identifies eight (31% of its) NLAGN at $1 < z < 2$ and another eight at $z \lesssim 0.5$.

Figure 5.18 gives an indication of our spectroscopic completeness (defined as the fraction of spectroscopically identified sources as compared to the number of 2 – 10 keV SEXSI sources) as a function of several quantities: 2 – 10 keV flux, R-magnitude, $\log(f_{\rm x}/f_{\rm o})$, and HR. *Chandra* targets that were eliminated from the X-ray catalog (e.g., nearby galaxies, quasars, extended target cluster emission - see Paper I) are not considered SEXSI sources, while X-ray point sources near target clusters are included in the catalog. To best illustrate the selection effects, separate from incompleteness due to lack of follow-up, we plot data only from the seventeen fields where we have a substantial fraction of spectroscopically identified sources (see Table 5.1). All fields were included in this subset if they had 50% completeness; we added six fields that have <50% completeness when a high fraction of $R < 24$ sources are identified. When considering only photometrically identified $R < 24$ sources the fraction of spectroscopically-identified sources ranges from 67% to 100%. These $R < 24$ completeness numbers depend on the particular $R_{\rm limit}$ of each field since some imaging does not reach $R = 24$ (see Paper II). These seventeen fields contain 725 2 – 10 keV SEXSI sources and 375 (52%) spectroscopically identified sources (86% of all spectroscopic IDs presented in this

article). The fields contain 445 photometrically identified $R < 24$ counterparts (84% of the photometrically identified $R < 24$ sources in these fields have spectroscopic IDs). Figure 5.18 shows histograms of all 725 X-ray sources from these fields (open histogram), sources with optical spectroscopic z and class (shaded black), and sources with optical follow-up but continuum only – no z or class (shaded gray). The hatched histogram shows sources with $R > R_{\rm limit}$.

The first plot of Figure 5.18 shows that the spectroscopic completeness in 2 – 10 keV flux is relatively even, 45% – 70% complete for $10^{-13.5} < f_{2-10\ \rm keV} < 10^{-15}$ erg cm^{-2} s^{-1}, where the majority of the sources lie. The last plot shows that the distribution of spectroscopic identifications in HR is ∼40% – 65% for the majority of sources, with 80% – 100% identification rates for the softest bins. The middle two plots show that, as expected, the fraction classified decreases towards fainter R-magnitudes, from 80% near $19 \lesssim R \lesssim 22$, to ∼30% at $23 < R < 24$ (note that this bin has the highest number of sources). The third plot illustrates the distribution in $\log(f_{\rm x}/f_{\rm o})$. The identification rate again is near 80% for low $\log(f_{\rm x}/f_{\rm o})$ and then falls to <40% for $\log(f_{\rm x}/f_{\rm o}) > 0.5$, which is expected due to the difficulty identifying sources at faint optical fluxes.

Figure 5.14 shows scatter plots of HR versus R-magnitude for five redshift bins. As discussed above, the average HR becomes smaller as redshift increases since at higher redshift the HR is less sensitive to changes in N_H. The first three boxes ($z < 1.5$) contain the majority of the open circles (non-BL sources) due to the large ELG population. The correlation between ELG R-magnitude and z is apparent – for $z < 0.5$ the majority of non-BL sources are spread from $16 \lesssim R \lesssim 22$, while for $0.5 < z < 1$ the spread shifts to $20 \lesssim R \lesssim 24$, and for $1 < z < 1.5$ the sources are almost all found at $R > 22$. The non-BL sources at $z > 1.5$ (all NLAGN) on average have $R > 22$. The BLAGN (filled circles) lie predominantly at low HRs with a spread in R-magnitude; some are optically bright even at high z (typical of unobscured quasars/AGN).

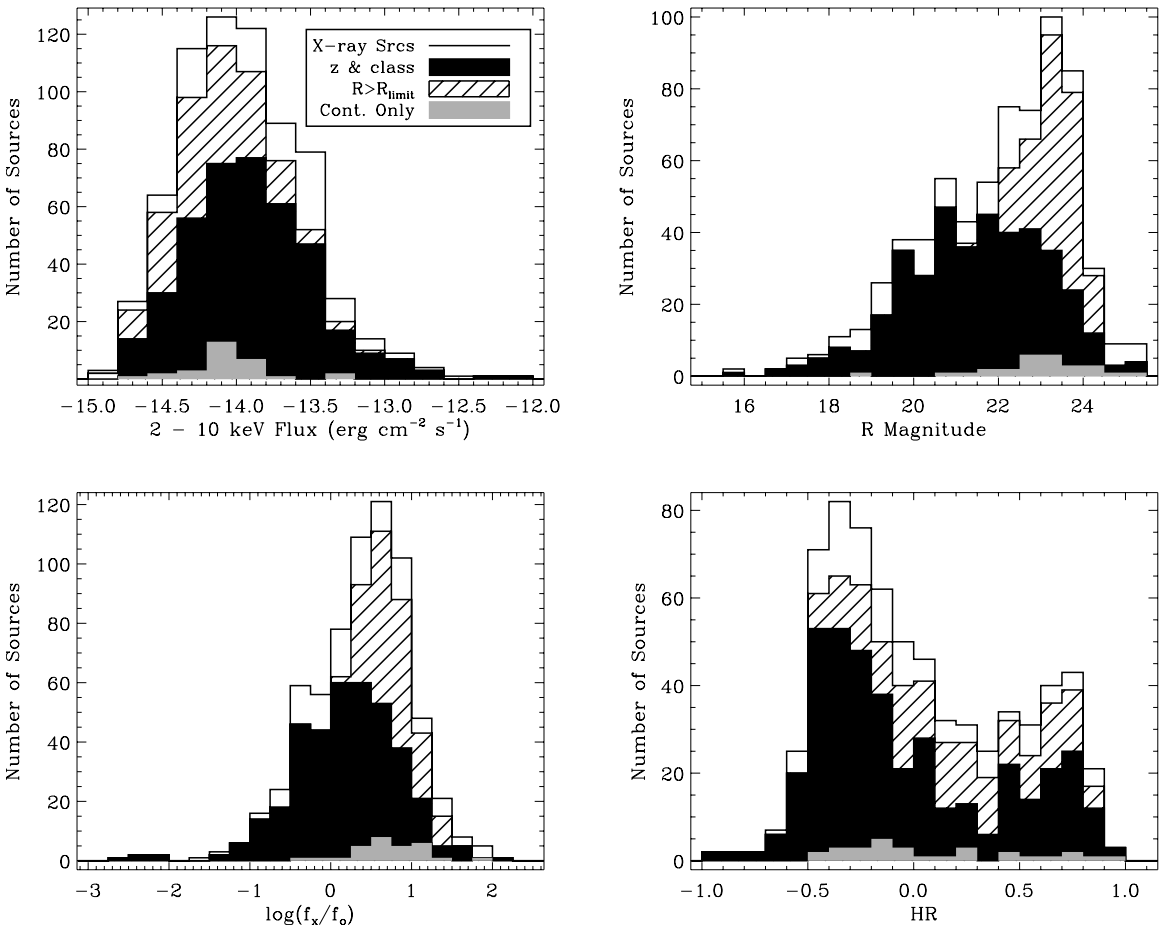

Figure 5.18 Histograms of $f_{2-10\ \mathrm{keV}}$, R, $\log(f_\mathrm{x}/f_\mathrm{o})$, and HR from seventeen fields where we have extensive spectral coverage. Each panel shows a histogram of all SEXSI 2 – 10 keV sources from these fields. Sources with a spectroscopic redshift and classification are filled with black and sources with a spectra that show continuum only are shaded in gray. The hatched part of each histogram indicates sources with no photometrically identified optical counterpart ($R > R_\mathrm{limit}$). For the R-magnitude and $f_\mathrm{x}/f_\mathrm{o}$ plot the R-magnitude plotted is R_limit. Sources with no shading or hatch marks have optical photometric IDs but no spectroscopic followup

5.9 Global Characteristics of the Sample and Comparison with Other Surveys

5.9.1 Redshift Distribution

The SEXSI sample confirms several of the basic conclusions of other survey work. First, as can be seen in Figure 5.1, very few low-redshift AGN have high rest-frame X-ray luminosities. Only 22/203 (11%) of sources with $z < 1$, and 1/65 (1.5%) with $z < 0.5$ have unobscured $L_{\rm x} \geq 10^{44}$ erg s^{-1}. The difference in survey volume cannot alone explain this trend. Of the high-luminosity $z < 1$ sources, the majority (65%) are BLAGN. Even accounting for the smaller volume surveyed at low redshift, if the X-ray to bolometric luminosity of this sample is typical of AGN (if there is not an uncharacteristically high fraction of the accretion luminosity emitted at longer wavelengths), then this reflects a dearth of high-mass, high-accretion-rate sources at low redshift. This was hinted at in the deep surveys (Barger et al. 2001a), albeit from small survey volumes. Steffen et al. (2004) found this effect in the 0.4 deg^2 CLASXS survey, and we confirm it here with SEXSI, which samples the high-luminosity, low-z population with a high degree of completeness over ~ 2 deg^2.

Figure 5.19 shows the source redshift distributions found by SEXSI, ChaMP (Silverman et al. 2005), CLASXS (Steffen et al. 2004), CYDER (Treister et al. 2005), and HELLAS2XMM (Fiore et al. 2003). Broad-lined AGN are shown by filled histograms, while non-broad-lined sources are left unshaded. To provide the best comparison to our sample of hard-band-selected sources, we have eliminated sources from CLASXS and CYDER which have significant soft or broad-band detections, but where the hard flux is determined from a small number of counts (S/N < 2), and should therefore be considered an upper limit. To obtain similar hard-band detection significance to SEXSI, we impose a cut at $f_{2-10\ \rm keV} < 2 \times 10^{-15}$ erg cm^{-2} s^{-1}, removing approximately 50 sources from the CLASXS sample. CLASXS reaches a similar magnitude limit for spectroscopy as SEXSI. We adopt the ChaMP hard sample from Silverman et al. (2005) that includes *Chandra* sources selected to have S/N > 2 in the 2.5 – 8 keV band. ChaMP obtained optical spectroscopic classifications for 44% (220 sources) of their sample of 497 hard-band *Chandra* sources, primarily for sources with counterparts having $R < 22$.

All the surveys demonstrate that the BLAGN population peaks at higher redshift than

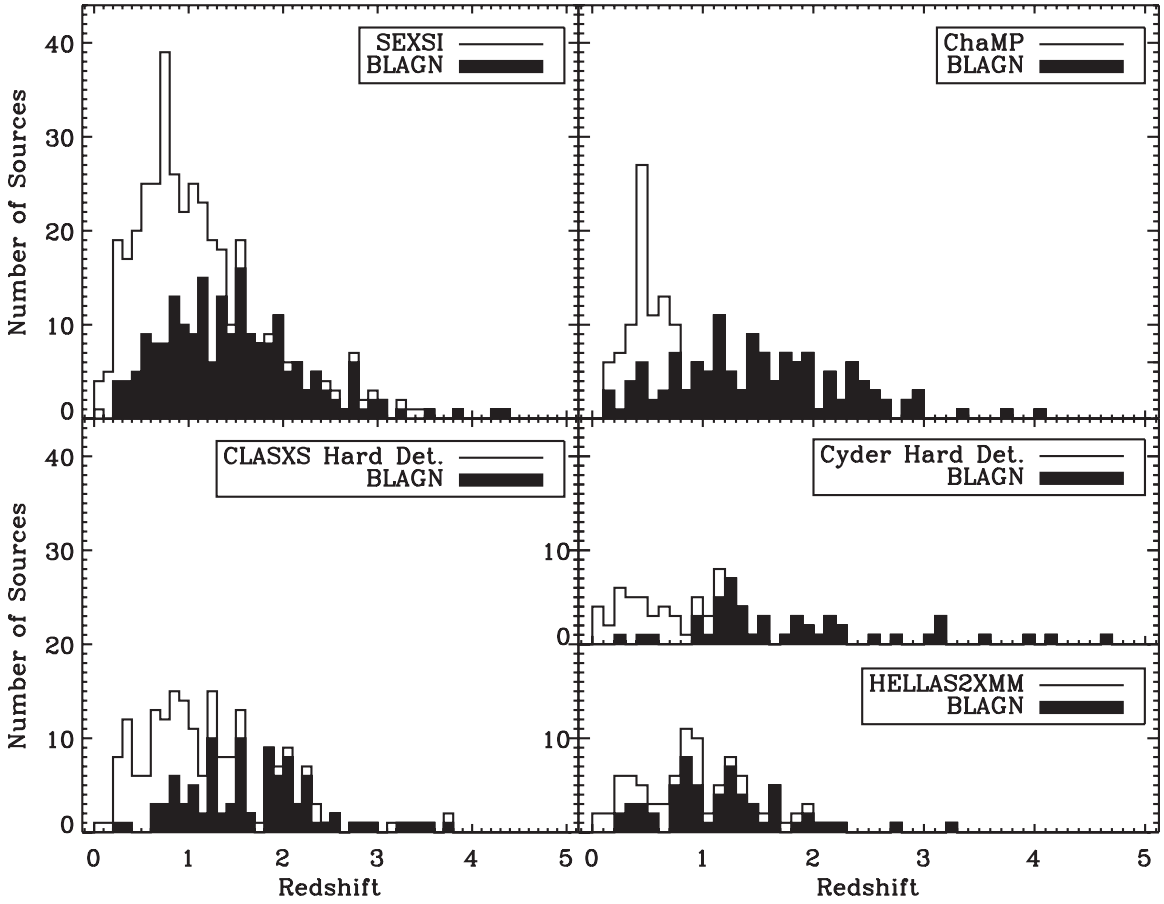

Figure 5.19 Redshift distribution of SEXSI, ChaMP (Silverman et al. 2005), CLASXS (Steffen et al. 2004), CYDER (Treister et al. 2005), and HELLAS2XMM (Fiore et al. 2003). Broad-lined AGN are represented by filled histograms, while non-broad-lined sources are left unshaded. We plot only *hard-band-selected* sources; to this end we have eliminated sources with $f_{2-10\ \mathrm{keV}} < 2 \times 10^{-15}$ erg cm^{-2} s^{-1}. See §5.9.1 for details

the sample as a whole. NLAGN and ELG peak at $z < 1$ in all samples, and show rapid evolution up to $z \sim 0.7$. It should be noted that for $z \gtrsim 1$, incompleteness due to the faintness of optical counterparts is a significant factor, so the decline in source density above this redshift is likely an artifact of the spectroscopic survey depth. As can be seen from the second panel of Figure 5.14, almost all SEXSI non-BLAGN sources above $z = 1$ have $20 < R < 24$, with half above $R = 22$, so that our survey limit of $R = 23-24$ implies we are increasingly incomplete above this redshift. ChaMP's shallower spectroscopic magnitude cutoff ($R \lesssim 22$) results in the sharper redshift cutoff of the ChaMP non-BLAGN population compared to SEXSI (ChaMP finds no non-BLAGN above $z = 0.8$, whereas the SEXSI NLAGN spread to above $z = 3$ and ELG/ALG to $z \approx 1.5$). SEXSI, CYDER and CLASXS, with similar survey depths for spectroscopy, find similar redshift distributions.

The ChaMP BLAGN z-distribution is broader and flatter than that of SEXSI, with a larger fraction of broad-lined sources at $z > 2$. Again, this is largely a result of selection effects. The ChaMP X-ray source population is on average softer than ours, due to the fact that they select sources from full-band images and include any source with a hard-band S/N ≥ 2. Combined with the predominance of BLAGN in the $z > 1$, $R < 21$ sample (see Figure 5.7), this results in a larger relative fraction of BLAGN.

In addition, we note that ChaMP finds a significantly larger fraction of ALG (7%). This is simply a matter of nomenclature. They classify as ALG sources with absorption lines and a D4000 break whether or not they exhibit weak emission lines. Our ALG are strictly sources in which only absorption features are detected. Since 50% of our 168 ELG do show absorption features, our sample would contain *more* ALG than ChaMP if we adopted their definition; our greater ability to detect weak lines explains any discrepancy.

5.9.2 Obscured Sources

To explore the fraction of obscured sources, we split our sample at $\log N_H = 22$. Figure 5.20 shows the fraction of obscured sources ($\log N_H > 22$) as a function of *unobscured* 2 – 10 keV flux (fluxes corrected for intrinsic N_H obscuration) for spectroscopically identified sources from SEXSI (filled circles), GOODS CDFN (triangles; E. Treister, private communication), and ChaMP (diamonds; Silverman et al. 2005). The data points are calculated using the survey catalogs, binned into flux ranges shown by the vertical dashed lines at the bottom of the plot. Each SEXSI, ChaMP, and GOODS CDFN data point is offset slightly

along the x-axis for clarity and the number of sources in each bin is indicated at the bottom.

Both SEXSI and ChaMP N_H values are calculated using X-ray spectral fitting, which also provides individual (asymmetric) errors for each column density. We would like to calculate a fraction of obscured sources and its associated error taking into account both the individual N_H errors from the spectral fits and Poisson counting statistics. To calculate the fraction of obscured sources for each flux bin we first generate, for each individual source in that flux bin, a Monte Carlo distribution of 1000 N_H values. To account for the asymmetric error bars provided by the spectral fitting, we generate two Gaussian distributions, one with a standard deviation equal to σ^+ and one with a standard deviation equal to σ^-. The two distributions are then patched together to make a single, asymmetric Gaussian distribution. ChaMP reports 90% confidence error bars instead of 1 σ, as SEXSI does, so we estimate that the ChaMP σ is equal to 1/1.65 times the 90% confidence limit. Because the purpose of this exercise is to calculate a fraction of sources above and below $\log N_H = 22$, we do not need to take into account N_H values in these distributions that, for example, fall below 0 or are otherwise unphysical. By construction, each distribution has 500 N_H values above and below the best-fit value.

We then use the Monte Carlo N_H values to calculate the mean and standard deviation of obscured fractions ($\log N_H > 22$) in each flux bin. These are plotted in Figures 5.20 and 5.21. The plotted error bars are the 1 σ errors that result from adding the standard deviation described above in quadrature with Poisson counting error ($\frac{\sqrt{N}}{N}$, where N is the number of sources in each bin). For many sources, the column density and associated errors constrain the source to lie either solidly above or below $\log N_H = 22$; thus the individual N_H errors contribute negligibly to the uncertainty in the fraction of obscured sources; the errors from the Poisson counting statistics strongly dominate the overall error bars.

The GOODS CDFN sources are calculated from hardness ratios and thus do not have similar errors from the fits. For these sources we simply calculate a fraction of obscured sources by counting the number with $\log N_H > 22$ in each bin and dividing by the number of sources in that bin. The errors presented are solely from Poisson counting statistics, which provide an adequate comparison since the counting errors dominate in the SEXSI and ChaMP calculation.

In Figure 5.20 the SEXSI data shows an obscured fraction consistent with ~ 0.5 for all flux ranges, with a marginally significant decrease with increasing flux. In the second

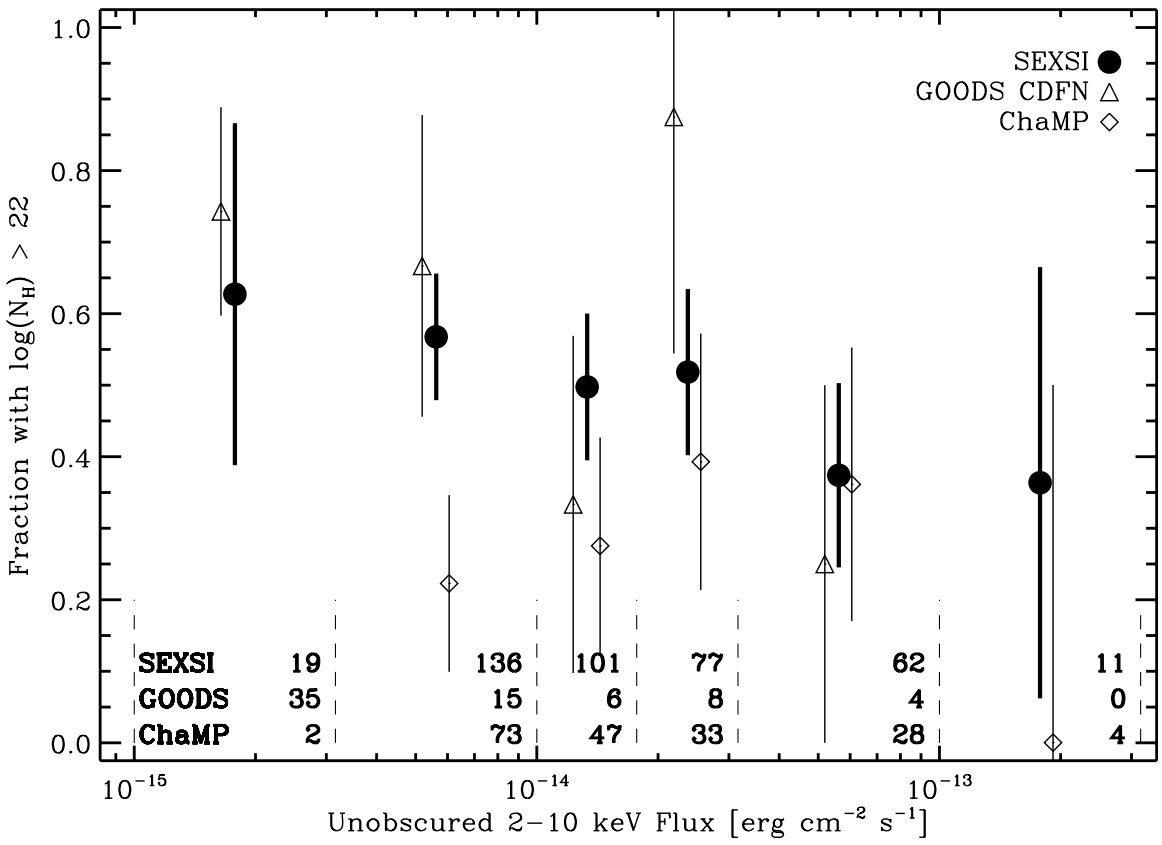

Figure 5.20 Fraction of obscured ($\log N_H > 22$) sources as a function of *unobscured* 2 – 10 keV flux for the spectroscopically identified samples from SEXSI (filled circles), GOODS CDFN (triangles; E. Treister, private communication), and ChaMP (diamonds; Silverman et al. 2005). The data points are calculated using the available catalogs, binned into flux ranges shown by the vertical dashed lines at the bottom of the plot. The errors on the GOODS CDFN fractions are 1 σ, calculated from Poisson counting statistics, while the SEXSI and ChaMP error bars incorporate the individual N_H error bars from the spectral fits in addition (see § 5.9.2 for details). The numbers printed near the bottom of each bin show the number of sources in each bin for each survey. Data points are offset slightly along the x-axis for clarity. The GOODS CDFN data lacks sources in the highest flux bin so we omit the data point at $\sim 2 \times 10^{-13}$ erg cm^{-2} s^{-1}. Conversely, ChaMP has only two sources below $\sim 3 \times 10^{-15}$ erg cm^{-2} s^{-1} and we omit the lowest flux data point

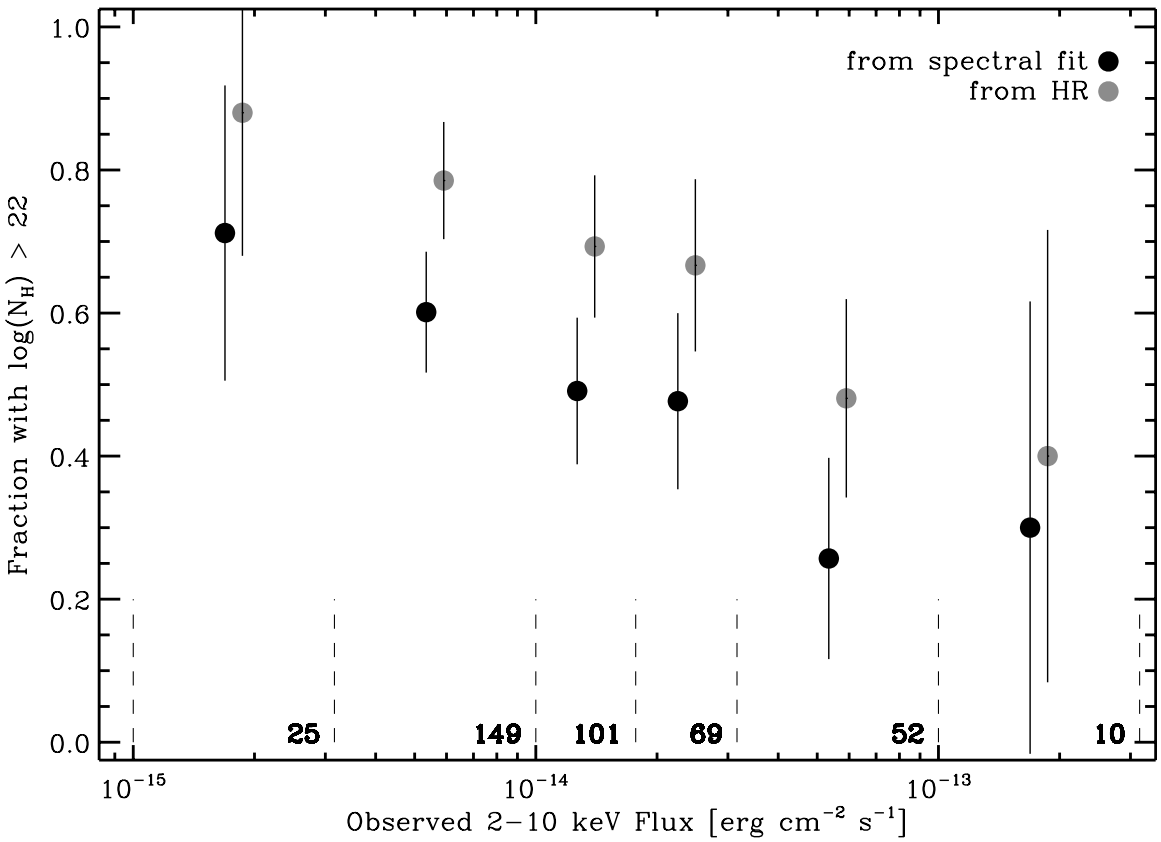

Figure 5.21 Comparison of N_H calculation methods. The fraction of obscured sources as a function of observed (absorbed) 2 – 10 keV flux for SEXSI sources with N_H calculated by X-ray spectral fitting (black), as presented in the source catalog and throughout this article, and from hardness ratios (gray). The HR derived obscured fractions tend to be significantly higher. See § 5.9.2 for discussion. The number of sources in each bin are shown in text along the bottom

through fourth bins, which include sources from $3 \times 10^{-15} - 3 \times 10^{-14}$ erg cm^{-2} s^{-1}, the range over which the 2 – 10 keV $\log N - \log S$ changes slope, there are 314 SEXSI sources, providing a tight constraint on the obscured fraction. All three of these fractions fall between 0.5 and 0.6.

The GOODS CDFN data shows a higher fraction of obscured sources, though most of the flux bins contain few sources (since the majority of GOODS sources fall below our flux limit) and thus have large errors. Since GOODS uses hardness ratios to calculate their N_H values we explored the difference between the SEXSI N_H values when calculated as described using the XSPEC fits, and when using the HR. Both methods are described in more detail in § 5.5. Figure 5.21 shows the fraction of obscured SEXSI sources calculated using absorbed (observed) 2 – 10 keV fluxes. The black filled circles are calculated using the method described above, with the N_H values from the spectral fits. The lighter gray points show the fraction of obscured sources when we use N_H values calculated from HRs. There is an obvious difference: the HR-calculated fractions of obscured sources are consistently higher, across the entire flux range. In the bin from $\sim 3 \times 10^{-15} - 1 \times 10^{-14}$ erg cm^{-2} s^{-1}, where we have 149 sources, the two values are not even consistent to within 1 σ. This discrepancy arises mainly from sources with the lowest column densities. For sources with a significant ($\gtrsim 5 \times 10^{21}$ cm^{-2}) column density from the X-ray spectral fit, the N_H values from the two methods are typically consistent within errors. The large discrepancy arises from sources where the XSPEC fit finds no significant obscuration ('<' in the catalog), though the 1 σ^+ high value does include significant obscuration (even $\log N_H > 22$) in some cases — see Figure 5.17. For such sources, the HR-calculated value is often $> 10^{22}$ cm^{-2}. This difference seems to result from details of the calculation. For example, a source with many counts near 0.3 keV will affect the XSPEC fit differently than the HR-based N_H calculation. To calculate HR, as described in more detail in Paper I, we extract counts from 0.3–2.1 keV and from 2.1–7 keV and transform each value using the appropriate exposure map into the standard band (0.5 – 2 keV and 2 – 10 keV) fluxes. Our exposure maps correction assumes $\Gamma = 1.5$. We then use these fluxes to calculate the N_H values. Thus, a source with many counts near 0.3 keV but fewer at 2 keV will result in an increased flux for the entire 0.5 – 2 keV band, while in the X-ray spectral fit we know that those counts are actually at 0.3 keV. The HR based N_H values will have large individual errors, and these are not taken into account on the plots. Thus, the discrepancy of the fraction of obscured sources

in Figure 5.20 is not wholly unexpected.

The ChaMP data show consistently smaller fractions of obscured sources in all flux ranges, although the discrepancy is highly significant only for the flux bin from $\sim 3 \times 10^{-15} - 1 \times 10^{-14}$ erg cm^{-2} s^{-1}. The lower obscured fractions in ChaMP results from the predominance of BLAGN, which, as described above, arises from the brighter magnitude limit of their spectroscopic followup. As a population, the BLAGN have lower obscuration than the NLAGN and ELG. This selection effect is illustrated in Figures 5.8 and 5.13. From our sample, 79% of BLAGN have $R < 22$ and 52% have $R < 21$. Combining these with the N_H histogram split by source type, one can see that a brighter optical spectroscopic followup limit will cause an N_H distribution with fewer obscured sources. Not only will there be more BLAGN compared to other source types, but of the BLAGN found, a higher fraction are unobscured sources brighter in R.

Figure 5.22 shows the fraction of obscured sources as a function of unobscured luminosity for sources with spectroscopic redshifts. The luminosities are calculated using unobscured fluxes and the calculation of each fraction and associated error are determined as described for Figure 5.20. The SEXSI sample (filled circles) shows a constant fraction of obscured sources of ~ 0.5. The difference with ChaMP can once again be explained by the difference in spectroscopic followup depth. SEXSI's most obscured sources tend to be NLAGN and ELG (see Figure 5.12).

Of the total sample of NLAGN, 26/32 (81%) are obscured ($N_H > 10^{22}$ cm^{-2}) and of those with the highest luminosities ($L_{\rm x} > 10^{44}$ erg s^{-1}) all fifteen (100%) are obscured. Of the more numerous ELG, 119/162 (73% $\pm$ 7%) are obscured. For the quasar-luminosity ELG, 11/13 (85%) are obscured. These numbers are both consistent with the obscured fraction of NLAGN. These sources make up about half of the total SEXSI AGN sample, and thus they contribute heavily to the obscured fractions seen in Figure 5.22. They have median magnitudes of $R \gtrsim 22$; following up brighter sources only misses most of these low-luminosity, obscured AGN.

5.9.3 Obscured Sources with Quasar Luminosities

According to unified AGN models (Antonucci 1993), hard X-ray surveys should find significant numbers of type-2 quasars (e.g., quasars viewed edge on, through significant amounts of absorbing material). These will be identified as X-ray sources with large N_H, $L_x \gtrsim$

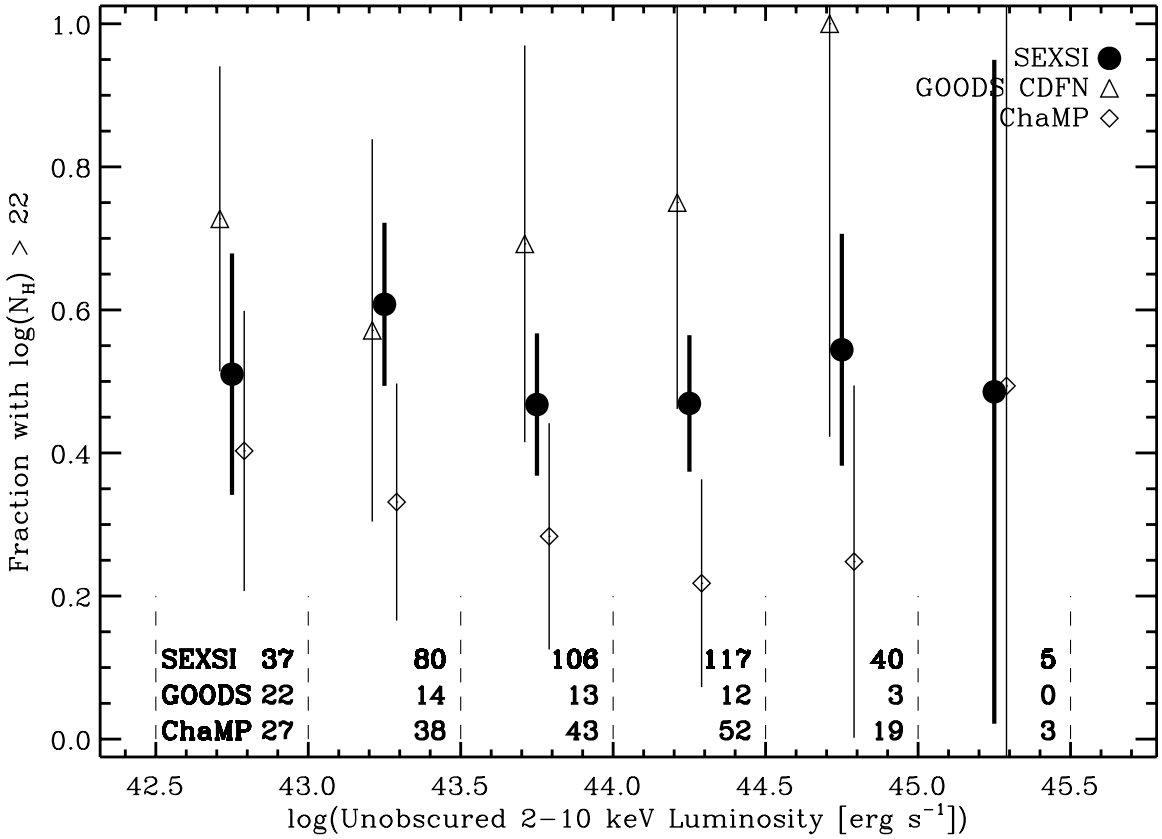

Figure 5.22 Fraction of obscured sources as a function of *unobscured* luminosity for spectroscopically identified sources. The luminosities are calculated based on the observed luminosity corrected for intrinsic N_H. Figure 5.20 gives references to the catalogs used to calculate the non-SEXSI points. The luminosity bins are shown by the vertical dashed lines at the bottom of the plot; the errors are 1 σ, calculated using Poisson counting statistics and the N_H errors when available (for ChaMP and SEXSI). The numbers printed near the bottom of each bin show the number of sources in each bin for each survey. Each data point is offset slightly along the x-axis for clarity

10^{44} erg s^{-1}, and with narrow-lined optical counterparts. Confirming candidate type-2 quasars is, however, difficult. The two *Chandra* deep fields have found fourteen narrow-lined sources with quasar X-ray luminosities (Norman et al. 2002; Barger et al. 2003; Dawson et al. 2003; Szokoly et al. 2004). Of these, only Dawson et al. (2003) has published an infrared spectrum confirming that lines, such as Hα, that are redshifted out of the optical, are narrow.

In the SEXSI survey we find 17 sources with *unobscured* rest-frame luminosities above 10^{44} erg s^{-1} which we classify as NLAGN, and 16 which we classify as ELG. Of these 33 sources, 32 (97%) have $N_H > 10^{22}$ cm^{-2}. Nine of these, all NLAGN, have $z > 2$. This $z > 2$ type-2 quasar density is roughly consistent with the 1 – 2 type-2 quasars per deep *Chandra* field predicted by Stern et al. (2002b), although it is unlikely that all of our candidates are true type-2 quasars (e.g., see Halpern et al. 1999; Stern et al. 2002a). We note that by comparison to our 33 narrow-lined quasars, ChaMP find no luminous, narrow-lined quasars. This difference is mainly attributable to their shallower spectroscopic coverage. Of our narrow-lined quasars, only five have $21 < R < 22$ while the rest have $R > 22$ – and, in fact, most NLAGN quasars have $R > 23$.

5.10 The Nature of the Emission-Line Galaxies

SEXSI has identified a substantial population of X-ray luminous ($10^{41} - 10^{44}$ erg s^{-1}) sources with optical spectra lacking both high-ionization lines and evidence for a non-stellar continuum. Such sources, with typical redshifts $z < 1$, are found in most *Chandra* and *XMM* surveys, in particular in the deep fields (see Brandt & Hasinger 2005, and references therein). The nature of this population is somewhat uncertain. Moran et al. (2002) suggest that most are akin to Seyfert galaxies where dilution by the host-galaxy light hinders detection of the high-ionization lines. In some cases, these high-ionization lines may also be weak due to partial obscuration. Some ELG, however, have optical spectra of high signal to noise, implying the AGN signatures are extremely weak or absent (Comastri et al. 2002). A number of suggestions as to the nature of these sources have been made. At the low-luminosity end of the distribution, some may be powered by starburst activity; Yuan & Narayan (2004) suggest that some may be AGN with radiatively inefficient accretion flows. Alternatively, they may be AGN that are entirely obscured (over 4π sr) so that ionizing

photons cannot escape the nuclear region (Matt 2002). A few may also be BL Lac objects (Brusa et al. 2003).

In this section we discuss constraints that we can place on the SEXSI sample of ELG.

5.10.1 Low-Luminosity ELG; Powered by Star Formation?

Starburst galaxies exhibit low-ionization, narrow emission lines and produce significant hard X-ray fluxes, and so must be considered as potential contributors to the low-luminosity end of our ELG population. Their X-ray emission arises from a combination of hot gas heated in supernova remnant shocks and the population of high-mass X-ray binaries whose compact components are produced in these supernovae. Starburst galaxy radio emission is predominantly synchroton emission from cosmic rays accelerated in these same remnants; since the galaxy residence time for the cosmic rays is comparable to the lifetime of the X-ray binary population, the X-ray and radio luminosities are correlated (Ranalli et al. 2003). The most luminous local starburst is NGC 3256; detailed spectral analysis by Moran et al. (1999) of this galaxy showed that it has a 2 – 10 keV X-ray luminosity of 2.5×10^{41} erg s^{-1}, produced by a star formation rate of $\sim 40\ M_{\odot}$ yr^{-1}. Helfand & Moran (2001) use the radio source $\log N - \log S$ relation in conjunction with the specific X-ray luminosity per O-star and the ratio of radio to X-ray luminosities in starbursts to predict a surface density for 2 – 10 keV X-ray sources attributable to starburst galaxies of 2.2 deg^{-2} at the SEXSI flux threshold of 2×10^{-15} erg cm^{-2} s^{-1}.

More recent work by Ranalli et al. (2003), Grimm et al. (2003), and Gilfanov et al. (2004) explicitly use 2 – 10 keV luminosity as a star-formation rate indicator and reach similar conclusions. With a total sample of 37 local star-forming galaxies, NGC 3256 remains the most luminous, although two of six candidate star-forming galaxies selected by Ranalli et al. (2003) from the *Chandra/Hubble* Deep Field have inferred luminosities of $\sim 3 \times 10^{42}$ erg s^{-1}, implying star formation rates of several hundred solar masses per year. These authors predict higher surface densities of $10 - 20$ deg^{-2} at 2×10^{-15} erg cm^{-2} s^{-1} and $1 - 2.5$ deg^{-2} at 1×10^{-14} erg cm^{-2} s^{-1}. Folding these higher predicted densities with our areal coverage curve from Paper I predicts that we should have $1 - 3$ such objects in our 2 deg^2 sample of hard X-ray sources.

A total of 11 ELGs in our sample have hard X-ray luminosities $L_{\rm x} < 10^{42}$ erg s^{-1}, and another 11 have $10^{42} < L_{\rm x} < 10^{42.5}$ erg s^{-1} (this upper limit would imply a star formation

rate of $\sim 600\ M_\odot\ \mathrm{yr}^{-1}$ according to the Ranalli et al. (2003) calibration). We examined radio images for all 22 galaxies from the FIRST (Becker et al. 1995) and NVSS (Condon et al. 1998) surveys. Of the 17 sources that fell within the FIRST survey limits, 15 have upper limits of $f_{20\ \mathrm{cm}} < 0.75$ mJy and one (in a slightly noisy field) has a limit of ~ 1 mJy. The final source, J170423.0+514321, is coincident with a bright (17 mJy) barely resolved double (or core-jet) source, clearly marking it as an AGN. For the five sources appearing only in the NVSS, four have upper limits of $1.5-2$ mJy, while the fifth, J030532.6+034301, is coincident with a subthreshold source with a flux density of a little over 2 mJy (although a slight positional offset suggests the possibility of a chance coincidence).

When plotted on the $L_\mathrm{x} - L_r$ correlation plot of Ranalli et al. (2003), both the two possible detections described above and the upper limits place galaxies factors of $3-10$ above the correlation (i.e., they are too X-ray bright for their radio luminosities – or upper limits thereon – to be starburst galaxies). A few of the ELG with $L_\mathrm{x} > 10^{42.5}\,\mathrm{erg\ s}^{-1}$ are also coincident with weak radio sources. However, their X-ray luminosities fall more than an order of magnitude above the Ranalli et al. (2003) L_x/L_r correlation for starbursts. Thus, consistent with the expectations of the starburst surface density described above, we conclude that few if any of the ELGs in our sample have X-ray luminosities dominated by star formation – essentially all must be powered by accretion.

5.10.2 Non-Stellar Emission

The hypothesis that ELG are dominated in the optical by galaxy light rather than non-stellar emission can be tested to some degree by plotting $\log(f_\mathrm{x}/f_\mathrm{o})$ as a function of $\log(L_{2-10\ \mathrm{keV}})$ (Fiore et al. 2003). Figure 5.23 shows this for BLAGN (top panel), and sources which lack broad emission lines (bottom panel) for the SEXSI sample, together with sources from HELLAS2XMM and CDFN. The BLAGN, clearly dominated by accretion luminosity, are clustered at high luminosity, whereas the non-BLAGN sources show a correlation between $\log(f_\mathrm{x}/f_\mathrm{o})$ and $\log(L_{2-10\ \mathrm{keV}})$. Fiore et al. (2003) argue that the correlation between the two quantities indicates that the optical light is largely dominated by $\sim$L* host galaxy light in the non-broad-lined sources, approximately independent of AGN luminosity. This is seen by the relatively small (one decade) scatter in optical flux seen over a large range (four decades) in X-ray flux. This correlation is due to a relationship in $R-z$ that is independent of L_x; Figure 5.7, the $R-z$ plot, shows that the R-magnitude of the

ELG (triangles) varies predictably with z (with some scatter). Bauer et al. (2004) show that this $\log(f_{\rm x}/f_{\rm o}) - L_{\rm x}$ relationship does not hold for $R \gtrsim 24$, the optical brightness at which the $R-z$ track of Fiore et al. (2003) and simple galactic evolution tracks begin to differ noticeably.

Figure 5.24 plots the Fiore et al. (2003) correlation for NLAGN and ELG separately. The ELG generally fall on the best-fit line from Fiore et al. (2003), but the NLAGN tend to fall below the line. This suggests that NLAGN have brighter X-ray-luminosity-normalized-optical magnitudes than do ELG. This would be consistent with NLAGN having a smaller fraction of their AGN optical emission obscured from view. Again, this result is not unexpected, as Figure 5.7 shows that NLAGN do not have the same $R-z$ relationship as ELG; instead many of the NLAGN have redshifts much higher than would be expected if their R-magnitude were simply dominated by L* galaxy light. Figure 5.24 also suggests that searching only the highest $\log(f_{\rm x}/f_{\rm o})$ sources for type 2 quasars, as suggested by Fiore et al. (2003), will miss some of the highest-luminosity NLAGN accessible via optical spectroscopy with current telescopes.

5.10.3 Search for Faint High-Ionization Lines

In this section we discuss difficulties in detecting weak high-ionization lines over the SEXSI redshift range, and investigate to what extent narrow-line AGN signatures may be present, but not detected in individual spectra. In addition, we ask if significant numbers of BLAGN could be identified as ELG due to host-galaxy dilution.

Dilution of AGN light by emission from the host galaxy, and the resulting difficulty in detecting weak high-ionization lines, is certainly an important factor in optically classifying the population of ELG. Moran et al. (2002) obtained wide-slit integrated spectra (including both the nuclear region and the galaxy) of well-studied, nearby Seyfert 2 galaxies to mimic observations of distant sources and found that eleven of eighteen galaxies would not be considered Seyfert 2s based on their integrated spectra: the nuclear emission lines had diminished flux compared to the stellar lines, so that the line-flux ratios (e.g., [N II] λ6583/Hα, [O III] λ5007/Hβ) were consistent with the values observed in H II regions or starburst galaxies, not with those of Seyfert 2s. These sources were all at low redshift, so that optical spectroscopy covers a different observed wavelength range than is the case for the large majority of our objects; these line-flux ratio diagnostics are not available for most

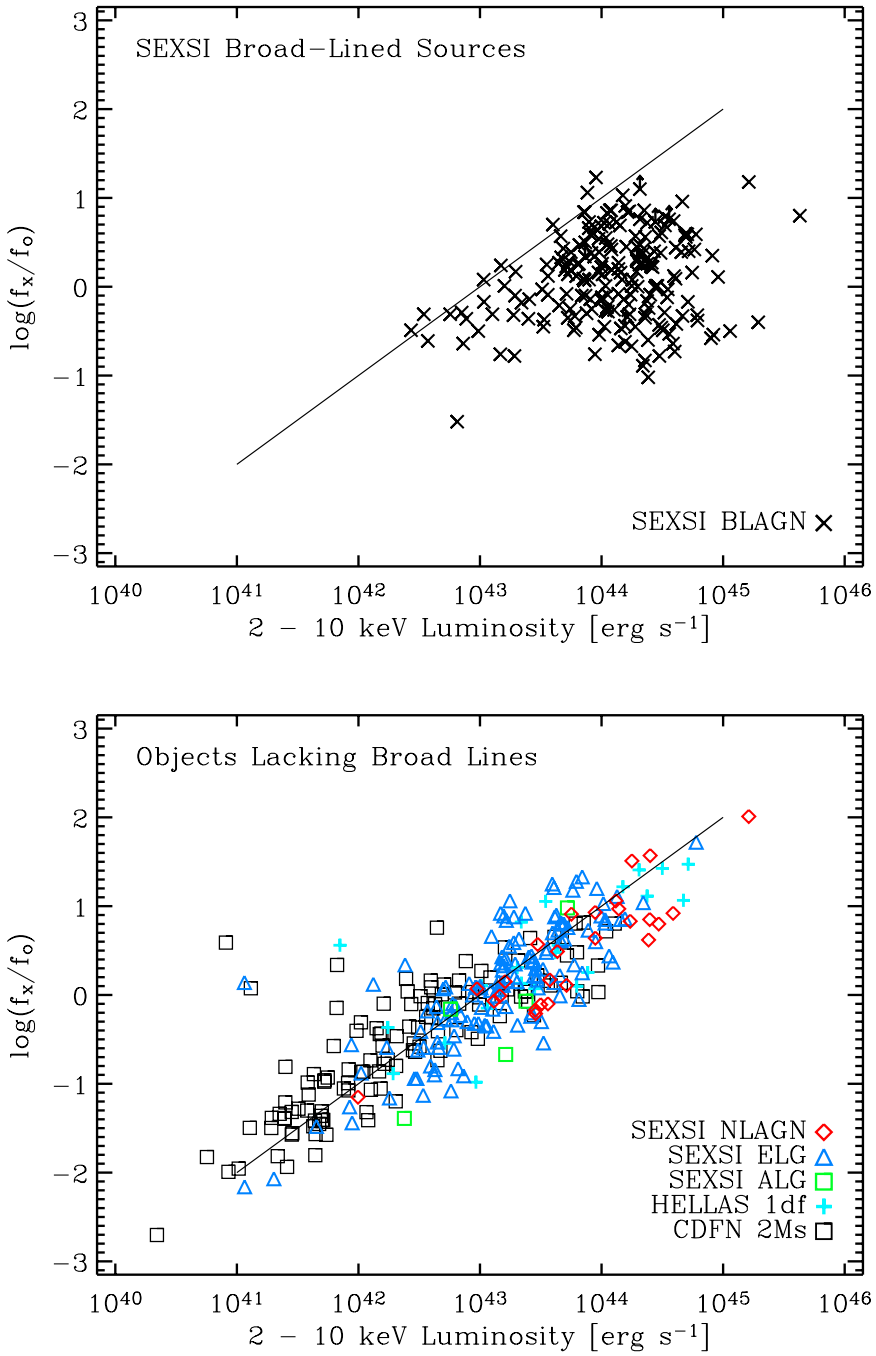

Figure 5.23 These plots show the relationship between $\log(f_x/f_o)$ versus $\log(L_{2-10\ \mathrm{keV}})$ for SEXSI BLAGN (top panel) and sources that lack broad emission lines in their optical spectrum including SEXSI NLAGN, ELG, and ALG as well as the HELLAS2XMM 1-degree field (Fiore et al. 2003) and the CDFN 2 Ms sample (Barger et al. 2003). The objects that lack broad lines show a correlation between $\log(f_x/f_o)$ and $\log(L_{2-10\ \mathrm{keV}})$, which would be expected were the optical photometry dominated by galactic light (see §5.7.3) as opposed to emission from the AGN. The BLAGN do not show the correlation. The line shown in both panels is a linear regression to the data of Fiore et al. (2003)

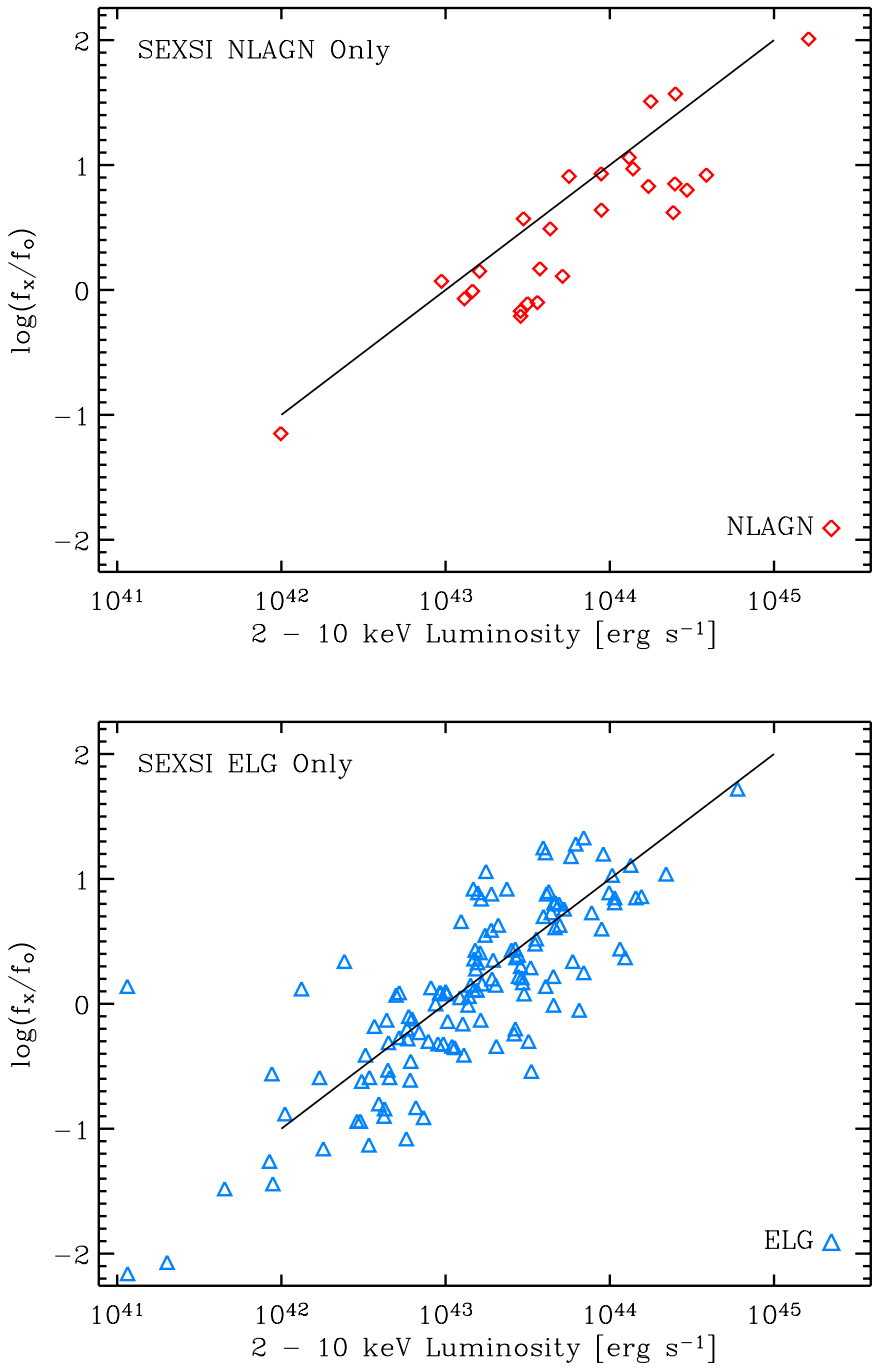

Figure 5.24 Here we again plot the relationship between $\log(f_{\rm x}/f_{\rm o})$ and $\log\left(L_{2-10\ {\rm keV}}\right)$ for the NLAGN and ELG separately. The identified ELG may well be fit by the line (again, from Fiore et al. 2003), but the NLAGN tend to fall below the line

of our sources.

SEXSI classifies ELG based on failure to detect broad or narrow high-ionization lines, rather than on quantitative line-flux ratio measurements. Here we explore the line-detection statistics as a qualitative indicator of line-flux ratios and source class diagnostic. The relatively broad redshift range and significant stellar continuum makes Hβ difficult to detect; we identify it in only 21% of 113 ELG with appropriate wavelength coverage (Table 5.4). In two-thirds of the 103 lower-z ELG we do detect [O III] λ5007. High [O III] λ5007/Hβ ratios are found in Sy2 spectra but also in H II region-like galaxy spectra; without another line ratio such as [N II] λ6583/Hα or S II (λ6716 + λ6731)/Hα we are unable to securely classifiy the optical spectrum as a NLAGN. 151 ELG spectra include [Ne III] λ3869 coverage, but only 6% show the emission line. Strong [Ne III] λ3869 is also found in Sy2 spectra, but again multiple line ratios are needed to secure the Sy2 classification. [Ne III] λ3869 is a weaker line in Seyfert 2 spectra, and was shown to be easily erased by dilution by Moran et al. (2002); thus, the low detection rate of [Ne III] λ3869 is not constraining.

The line that primarily allows us to identify a source as a NLAGN rather than an ELG over much of our redshift range is [Ne V] λ3426. This line is redshifted into the optical window over the redshift range $0.1 \lesssim z \lesssim 1.8$, the range within which most of the ELG in our sample lie. The other typical high-ionization UV lines do not shift into the optical until $z \sim 1.1$ (C III] λ1909) and $z \sim 1.6$ (C IV λ1549). Thus, it is detection of [Ne V] λ3426, or the lack thereof, that most often places a source in the NLAGN or ELG subsample.

As shown in Table 5.4, 80% of the NLAGN with [Ne V] λ3426 access have [Ne V] λ3426, while only 20% of our BLAGN exhibit this line. The fraction of the NLAGN in which [Ne V] λ3426 is present should be treated as an upper bound, since in the range $z < 1-2$ we cannot identify the source *unless* [Ne V] λ3426 is present. Thus there are many instances where a NLAGN has no [Ne V] λ3426 detection in its spectrum, consistent with the idea that [Ne V] λ3426 may be hidden, and, due to wavelength coverage, a significant fraction of NLAGN will be classified as ELG since only [Ne V] λ3426 is useful for making the distinction.

In contrast, we conclude that few BLAGN are classified as ELG due to finite wavelength coverage. 89% of our BLAGN with wavelength coverage of the Mg II λ2800 line do show broad Mg II λ2800 emission. Mg II λ2800 shifts into the optical near $z \sim 0.4$, thus the Mg II λ2800 line is accessible in the majority of the ELG spectra but broad emission is not

detected. Since the Mg II λ2800 detection rate is so high, we conclude that BLAGN are not easily misclassified as ELG, even at $z \lesssim 1$, when the broad, high-ionization lines farther in the UV (eg., C III] λ1909, C IV λ1549) do not lie in our spectral range. A note of caution is in order, however; Glikman et al. (2004) have shown that dust-reddened quasars which exhibit only narrow lines in their optical spectra, can have broad Paschen lines in the near IR.

Our basic conclusion is that many of the ELG may be classified as NLAGN in higher S/N spectra and/or with wider wavelength coverage, but that few are broad-lined sources we have misclassified. This conclusion is consistent with the N_H distribution of the ELG (85% of which have $N_H > 10^{22}$ cm^{-2}). To further test this hypothesis we have stacked a group of ELG optical spectra to increase the signal to noise, searching for [Ne V] λ3426 emission that is the hallmark of NLAGN over much of our redshift range.

Figure 5.25 presents the spectrum created by stacking 21 ELG spectra obtained with LRIS on the Keck I Telescope. Sources from our March and June 2002 observations were used such that the spectra were obtained with the same spectrometer configuration. Of these spectra, we chose 21 sources with $0.7 < z < 1.2$. This redshift range ensures that the [Ne V] λ3426 emission line will fall on LRIS-R from $5800 - 7500$ Å (observed frame). The stacking procedure used standard stacking commands in IRAF. First each spectrum is shifted to its rest frame using `dopcor` and then these spectra are combined with `scombine` using median weighting. The weights of each spectrum were close to 0.05 as would be expected for equal weighting: no single individual bright spectrum dominated the stacked spectrum.

The stacked spectrum shows the features typical in individual ELG at these wavelengths: the strong [O II] λ3727 emission line, the CaHK $\lambda\lambda$3934, 3968 absorption lines and the D4000 continuum break. The stacked spectrum also shows additional absorption features such as H10 λ 3798, H9 λ 3835, and Hζ λ 3889. [Ne III] λ3869 emission, which is seen in only 6% of the ELG spectra, is well detected in the stacked spectrum. Most importantly, however, is the detection of [Ne V] λ3426. This emission is produced by highly ionized Ne, confirming the presence of a strong AGN X-ray ionizing continuum and consistent with the idea that our ELG population contains a significant fraction of NLAGN.

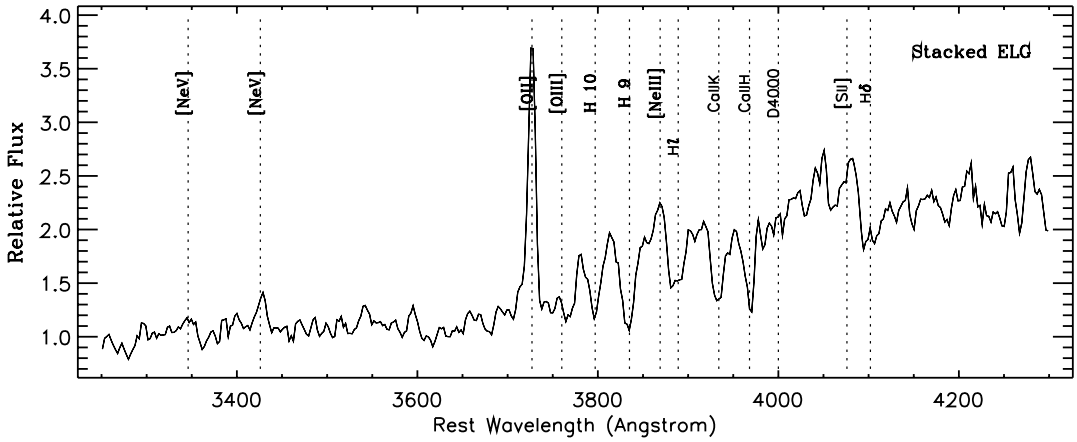

Figure 5.25 Stacked spectrum of 21 ELG all obtained with LRIS on the Keck I Telescope (individual ELG example spectra are shown in Figure 5.4, for reference). See § 5.10.3 for further details of the stacking procedure. Note that the individual ELG spectra do not show evidence of the [Ne V] λ3426 high-ionization emission line indicative of underlying AGN activity, while the increased S/N of the stacked spectrum does show the [Ne V] λ3426 emission. In addition, [Ne III] λ3869 emission and several absorption features from $\sim 3800 - 4000$ Å are well detected

5.11 Sources Associated with Target and Non-Target Galaxy Clusters

Few cluster galaxies have been determined to have obvious AGN signatures; in this section we explore the population of spectroscopically identified SEXSI AGN associated with known galaxy clusters. The pre-*Chandra* best estimate was that 1% of cluster galaxies host AGN (Dressler & Gunn 1983). This estimate came from laborious optical spectroscopic studies of galaxies. *Chandra's* unprecedented angular resolution in the 2 – 10 keV band allows identification of X-ray emitting galaxies that appear in images near the cluster center. While some of these sources will be unassociated AGN, searching these sources for cluster-member AGN is much more efficient than searching in the optical for AGN signatures, since the optical source density is high compared to the X-ray source density; furthermore, as we have discussed throughout this paper, many of the X-ray sources assumed to be AGN from their high X-ray luminosities will have no obvious optical indication of nuclear activity.

Martini et al. (2002) obtained spectra of the optically-bright ($R < 20$) counterparts to 2 – 10 keV *Chandra* sources near A2104, a well studied $z = 0.154$ cluster, and found that at least 5% of the cluster galaxies (6 sources) had X-ray fluxes consistent with AGN activity,

Table 5.5. Cluster fields: SEXSI sources associated with known clusters

Field Name	cluster z	# flagged total[a] (# with spectra)	confirmed cluster members	additional cluster members[b]	Notes
AWM 7	0.017	28 (14)			
3C 123	0.218	10 (3)			
CL 0442+0202	1.11	8 (4)	BLAGN[c]		
CL 0848+4454	1.27	7 (5)	ELG, ELG		
RX J0910	1.11	13 (6)	ELG	ELG (∼1.1 Mpc)	cluster at $z \sim 1.10$, 2 AGN ID'd[d]
HCG 62	0.014	39 (20)			
RX J1317	0.805	6 (4)	ELG, BLAGN		cluster at $z \sim 0.58$, 2 AGN ID'd[e]
BD 1338	0.640	5 (1)			
RX J1350	0.804	4 (0)			
3C 295	0.46	3 (3)	ALG, BLAGN		
MKW 3S	0.045	36 (8)			
MS 1621	0.428	6 (3)		ELG (∼1.9 Mpc)	
RX J1716	0.81	7 (3)	ELG, ELG	ELG (∼2.1 Mpc)	
MS 2053	0.583	0 (0)			
RX J2247	0.18	17 (9)			
TOTAL		189 (83)	10	3	4

[a]A source was flagged in Paper I when it fell within an area potentially less than 1 Mpc from the target cluster center, and excluded from the $\log N - \log S$ calculation to avoid including target cluster members. With the addition of redshift data (# of flagged sources with spectroscopic redshifts are indicated in parenthesis), we can definitively identify or exclude cluster membership. Confirmed cluster members are flagged in the spectroscopic catalog, Table 5.2

[b]This column inicates sources within $\sim$ 2 Mpc of the cluster center – the particular distances are noted in parenthesis. These sources are not cluster flagged in the Catalog. Their IDs are CXOSEXSI_J091040.8+542006, _J162315.4+263506, and _J171714.5+671136

[c]Cluster member is target radio galaxy, MG1 J04426+0202 (MG 0442+0202), a borderline NLAGN from our spectrum. See Stern et al. (2003)

[d]Apendix A of Holden et al. (2002) (paper on RX J1317+2911, RX J1350+6007) notes that there is an X-ray group, CXOU_J091008.6+541856, at $z = 0.68 \pm 0.06$ or $z = 1.18^{+0.08}_{-0.07}$ (T, z degeneracy). We find two ELG (CXOSEXSI_J090954.0+541752 and _J091008.6+541806) at $z = 1.101$ and $z = 1.102$, 1.2 Mpc and 1.0 Mpc away from their reported position, respectively. See § 5.11.2

[e]Appendix A of Holden et al. (2002) notes that there is a cluster/group, CXOU_J131654.2+291415, at $z = 0.42^{+0.14}_{-0.10}$. We find two ELG (CXOSEXSI_J131700.2+291307 and _J131706.2+291058) at $z \sim 0.58$, 0.8 MPc and 2.0 Mpc from the reported position. See § 5.11.2

while only ∼1% showed AGN activity in the optical in agreement with the earlier estimates derived via optical surveys. We explore this finidng further here using our larger sample of cluster X-ray sources.

5.11.1 Target Clusters

Of the SEXSI fields, fifteen (56%) have galaxy clusters as targets. Three of these are nearby clusters ($z = 0.014 - 0.045$), two are at $0.18 < z < 0.22$, and the rest are at $z > 0.43$. In Paper I we flagged sources when they fell within 1 comoving Mpc of the cluster center as projected on the sky. The area associated with this 1 Mpc radius region and the sources within the area (the flagged sources) were excluded from our $\log N - \log S$ calculation to avoid biasing our background sample. The SEXSI spectroscopic followup, however, establishes source redshifts, enabling the determination of cluster membership. Table 5.5 lists the SEXSI cluster fields and details the spectroscopic completeness among cluster-flagged sources and the spectroscopically identified X-ray emitting cluster members.

Of the three nearby clusters for which the 1 Mpc radius covered more than the entire *Chandra* field of view, we have spectra for 43 of the 103 sources, and none are at the cluster redshift. This result is likely a consequence our spectroscopic followup strategy which skipped the brightest sources (likely cluster members) to focus on background sources.

Of the twelve higher-z cluster fields, we have taken 41 spectra of sources that fall near the cluster in our image and have discovered that ten of the flagged sources are at the target cluster redshift (see Table 5.5). Of these ten, only three show high-ionization optical emission lines characteristic of active galaxies, although all ten have 2 – 10 keV luminosities of $L_{\rm x} \gtrsim 10^{43}$ erg s^{-1}, suggesting an active nucleus. Of the ten confirmed members, the BLAGN have luminosities of $\log L_{\rm x} = 43.3,\ 43.8,$ and 44.5 with obscuring column densities of $N_H < 10^{21.2}, 0,$ and $10^{21.5}$ cm^{-2}, respectively. The ELG have $42.9 < \log L_{\rm x} < 44.0$ and $22.6 < \log N_H < 23.4$. The ALG has $\log L_{\rm x} = 43.4$ and $\log N_H = 21.9$. All of the non-broad-lined sources are considered obscured ($\log N_H > 22$), save the ALG just below the $\log N_H = 22$ cutoff. In addition to the ten sources within 1 Mpc (projected), we identify three additional sources at the target cluster redshift lying from $1-2$ Mpc (projected) from the cluster center. These three sources are all ELG with $L_{\rm x} > 10^{43}$ erg s^{-1}.

Of the thirteen sources listed in Table 5.5 within ~ 2 Mpc of the target clusters we find that only 23% ± 13% are BLAGN (3 sources). One of these BLAGN has broad lines barely over our 2000 km s^{-1} cut; this radio source, MG1 J04426+0202, was the target of the CL 0442+0202 *Chandra* exposure (see Stern et al. 2003); thus, we exclude this field from the analysis. We then find that only 17% ± 12% (two of twelve sources) of the confirmed cluster AGN have broad lines. The target clusters for which we have identified member AGN have redshifts in the range $0.46 < z < 1.27$, where ELG's are still readily detectable. If we naively look at the SEXSI 2 – 10 keV source class statistics including only sources in that z range, we find 37% ± 4% (82 sources) BLAGN and 52% ± 4% (114 sources) ELG. Though our cluster member AGN sample is relatively small, they hint that the fraction of BLAGN is lower in cluster AGN than in the SEXSI background sample.

5.11.2 Non-Target Clusters Identified in Holden et al. (2002)

In addition to the thirteen target cluster member AGN we also report on two additional clusters from Holden et al. (2002); we have identified two cluster member AGN (ELG) in each cluster. The "Notes" column and associated footnotes of Table 5.5 references these

serendipitous clusters, with redshift determinations from spectroscopic followup of our 2 – 10 keV sources. Appendix A of Holden et al. (2002) reports two new X-ray emitting groups or low-mass clusters of galaxies, discovered as extended sources, in SEXSI fields RX J0910 and RX J1317; their study included no optical spectroscopic followup. We have spectra of 2 – 10 keV SEXSI sources nearby these non-target clusters.

For SEXSI field RX J0910, we have identified two ELG at $z \simeq 1.1$, $\sim 2'$ from the position of CXOU_J091008.6+541856. The X-ray analysis of Holden et al. (2002) suggests two redshift possibilities due to a T, z degeneracy: $z = 0.68 \pm 0.06$ or $z = 1.18^{+0.08}_{-0.07}$. The two SEXSI ELG, CXOSEXSI_J090954.0+541752 and J090955.5+541813, are at $z = 1.101$ and $z = 1.102$ and $2.4'$ and $2.0'$ away (projected 1.2 Mpc and 1.1 Mpc) from the position of CXOU_J091008.6+541856. These sources are 3.2 Mpc projected ($6.17'$) from the target-cluster of the field, RX J0910+5244 ($z = 1.11$). Our spectroscopic redshifts at $z \sim 1.1$ agree within 1 σ of the higher-z prediction of Holden et al. (2002).

The other serendipitous cluster is in SEXSI field RX J1317, which had a target of cluster RX J1317+2911 ($z = 0.805$). The *Chandra* data analysis of CXOU_J131654.2+291415 by Holden et al. (2002) suggests a cluster with $T = 2.9^{+3.1}_{-2.1}$ keV and $z = 0.42^{+0.14}_{-0.10}$. We have identified two 2 – 10 keV sources that fall from $1.7'-4.2'$ of the reported position and have redshifts around $z \sim 0.58$. The sources, CXOSEXSI_J131700.2+291307 and J131706.2+291058 at $z = 0.580$ and 0.579, fall $\sim$0.8 Mpc and 2.0 Mpc (projected) from the CXOU_J131654.2+291415, an indication of a cluster at $z \sim 0.58$. This redshift agrees within ~ 1 σ of the prediction in Holden et al. (2002).

Including these four additional cluster AGN in our comparison of cluster member class statistics to those of the SEXSI background sample, we find a fraction of cluster BLAGN to be even lower: 12% ± 8%. This fraction again is calculated excluding SEXSI field CL 0442+0202. Comparing to the SEXSI background sample from $0.46 < z < 1.27$ which contains 37% ± 4% BLAGN, we find a stronger indication (albeit still short of 3 σ) that the AGN cluster-member sample has fewer BLAGN than does the background sample.

5.12 Summary

We have presented a sample of 477 spectra of 2 – 10 keV *Chandra* sources. Of our 438 spectroscopically identified sources with counterpart magnitudes $R \lesssim 24$, we confirm with

high significance a number of results found in other surveys. We find that few AGN at $z < 1$ have high rest-frame X-ray luminosities, reflecting a dearth of high-mass, high-accretion-rate sources at low redshift. In addition, our sample of broad-lined AGN peaks at significantly higher redshift ($z > 1$) than do sources we identify as emission-line galaxies. We find that 50% of our sources show significant obscuration, with $N_H > 10^{22}$ cm^{-2}, independent of intrinsic luminosity. We have identified nine narrow-lined AGN with $z > 2$ having quasar luminosities ($L_{\rm x} > 10^{44}$ erg s^{-1}). This is consistent with predictions based on unified AGN models.

We have investigated in some detail the nature of the large sample of 168 sources which we classify as emission-line galaxies. These X-ray luminous objects (most with $L_{\rm x} > 10^{42}$ erg s^{-1}) have optical spectra lacking both high-ionization lines and evidence for non-stellar continuum. We conclude that few of these sources, even at the low-luminosity end, can be powered by starburst activity. By stacking 21 spectra for sources in a similar redshift range in order to increase the signal to noise, we are able to identify [Ne V] λ3426 emission, a clear signature of AGN activity. This demonstrates that the majority of these sources are Seyfert 2 galaxies, where the high-ionization lines are diluted by stellar emission and/or extincted by dust.

Acknowledgments

We are grateful to Michael Cooper and Jeffrey Newman of UC Berkeley for their help with the DEIMOS data reduction pipeline. The analysis pipeline was developed at UC Berkeley with support from NSF grant AST-0071048. We thank Patrick Broos of Penn State for his generous help with `acis_extract` and *Chandra* Fellow Franz Bauer for a careful reading of the manuscript and many helpful suggestions. We also thank Ed Moran, Mark Davis, and Alison Coil for collaboration on the CL 0848+4454 spectroscopy. We wish to recognize and acknowledge the significant cultural role that the summit of Mauna Kea plays within the indigenous Hawaiian community. We are fortunate to have the opportunity to conduct observations from this mountain. In addition, this research has made use of NASA's Astrophysics Data System Abstract Service and the NASA/IPAC Extragalactic Database (NED) which is operated by the Jet Propulsion Laboratory, California Institute of Technology, under contract with NASA. This work has been supported by NASA NAG5-6035 (DJH), as well as by a small *Chandra* archival grant. MEE gratefully acknowledges

support from the NASA Graduate Student Research Program. The work of DS was carried out at the Jet Propulsion Laboratory, California Institute of Technology, under a contract with NASA.

Chapter 6

Obscured AGN: Comparing X-ray and Mid-Infrared Selection

6.1 Introduction

Both the hard X-ray and mid-infrared wave bands provide powerful and complementary methods for identifying and studying active galactic nuclei (AGN). Most radiation seen from active galaxies in the X-ray range is due to direct radiation from accretion processes near the central supermassive black hole, while the near- to far-infrared light at $\lambda \gtrsim 2$ μm is typically dominated by radiation from dusty obscuring material surrounding the AGN central engine. Hard X-ray and mid-IR surveys of AGN will be less biased and more complete than surveys in the optical (e.g., Richards et al. 2006) and soft X-ray at $E \lesssim 2.4$ keV (e.g., Hasinger et al. 1998; Schmidt et al. 1998), as the optical and soft X-ray bands are highly susceptible to the effects of dusty, obscuring material. However, AGN samples selected in the X-ray or the infrared will both likely suffer incompleteness, just as a some AGN identified by optical spectroscopy are X-ray undetected even in the deepest X-ray images ever obtained (e.g., Steidel et al. 2002). Conversely, X-ray missions have identified likely AGN whose optical spectra are devoid of AGN signatures (e.g., "X-ray bright, optically normal galaxies," or XBONGs, Comastri et al. 2002; and the ELGs and ALGs presented in Chapter 5).

The 2003 launch of the *Spitzer Space Telescope* (Werner et al. 2004) opened a new era in mid-infrared observations, providing orders of magnitude improvement in sensitivity at $3.6 - 160$ μm. The increased sensitivity, combined with the large FOV, allows, for the first time, efficient survey capabilities in these wave bands to probe large volumes of space.

6.1.1 *Spitzer* "Wedge" Selection of AGN

Several selection methods have been developed to select AGN based on their *Spitzer* colors. These methods exploit the difference in the typical spectral energy distribution (SED) of AGN as compared to the SEDs of 'normal' galaxies. While the near-infrared emission of typical galaxies is primarily produced by a thermal stellar population, resulting in SEDs peaked near 1.6 μm, AGN-dominated SEDs have a non-thermal, roughly power-law shape (for $\lambda \lesssim 10$ μm). At longer wavelengths ($\lambda \gtrsim 20$ μm) contributions from stellar blackbody emission is low, while radiation from obscuring dust near the central engine of an AGN provides strong, isotropic emission. Stern et al. (2005a), for example, suggested a selection technique exploiting the fact that, for AGN, the long-wavelength side of the 1.6 μm stellar peak does not decline; the technique uses an empirically-determined 'wedge' in IRAC color-color space ([3.6 μm]−[4.5 μm] versus [5.8 μm]−[8.0 μm]) that preferentially contains AGN as compared to normal galaxies or Galactic stars. Combining a sample of 10,000 $R < 21.5$ spectroscopically identified sources from the AGN and Galaxy Evolution Survey (AGES; Kochanek et al., in prep.) and mid-IR observations from the IRAC Shallow Survey (Eisenhardt et al. 2004), Stern et al. (2005a) defined mid-IR AGN selection criteria which robustly identify broad- and narrow-lined AGN, with only 18% sample contamination from galaxies (17%) and stars (1%). The sample contamination is likely lower, since many of the optically selected galaxies will be AGN as well (e.g., ELGs, XBONGs). Working from the full spectroscopically defined AGES sample, the wedge selects 91% of the broad-lined AGN, 40% of the narrow-lined AGN, and less than 3% of the normal galaxies.

Lacy et al. (2004) define a 'wedge' based in [4.5 μm]−[8.0 μm] and [3.6 μm]−[5.8 μm] color space. Other groups have pursued selection techniques using IRAC and MIPS data, selecting AGN based on adherence to power-law SED shapes (e.g., Alonso-Herrero et al. 2006). For the purposes of this section we primarily work from the Stern et al. (2005a) criteria.

We present here an exploration of the relative strengths of *Chandra* and *Spitzer* as black-hole finders. In general, *Chandra* is good at identifying low-luminosity AGN, which at other wavelengths are often left unidentified, since stellar light can outshine the AGN from the ultraviolet through the infrared. Although *Chandra* is good at finding AGN with significant obscuring column densities, it is still unable to detect the most heavily obscured

sources with $N_H \gtrsim 10^{24}$ cm^{-2}, where most of the light at $E \lesssim 10$ keV is absorbed. *Spitzer*, on the other hand, is well suited to detect luminous sources, as the mid-IR radiation from the obscuring material outshines other radiation sources regardless of the viewing angle. We present IRAC and MIPS observations of selected areas covered by the SEXSI program. The *Spitzer* data is targeted to provide mid-infrared imaging of the sample of ~ 250 hard X-ray-selected AGN, most of which have published optical photometric and spectroscopic followup (Chapters 3–5). In addition, selecting AGN based on IRAC colors allows us to examine the X-ray and mid-IR-selected samples and to comment on the effectiveness of the IR selection technique. We discuss first the IR properties of the sample of SEXSI sources and then explore the X-ray-undetected *Spitzer* AGN sample.

We organize the section as follows: § 6.2 presents the mid-IR observations and data reduction; § 6.3 presents the catalog; § 6.4 discusses the mid-IR properties of the 2 – 10 keV SEXSI sources; § 6.5 presents the mean X-ray properties of X-ray-non-detected *Spitzer* sources; § 6.6 describes future directions.

6.2 *Spitzer* Imaging with IRAC and MIPS

The data used for this work are drawn from published catalogs from the SEXSI program as well as from archival and targeted *Spitzer* observations. The X-ray and optical SEXSI datasets are presented in Chapters 3–5; here we describe the complementary mid-IR observations and data reduction.

The *Spitzer* data analyzed here covers six SEXSI fields and comes from five separate programs (see Table 6.1). Program ID 20808 is designed specifically for the SEXSI follow-up, with typical exposure times of 600 s for IRAC observations and 840 s for MIPS observations. Because the SEXSI data are drawn from the *Chandra* public archive, the fields are not 'blank': the target sources in the SEXSI *Spitzer* fields are all $z > 0.18$ galaxy clusters (5 of the 6 fields are $0.64 < z < 1.3$ clusters). Data reduction and SExtractor catalogs were produced as described in Seymour et al. (2007), and matching to X-ray and optical data was performed using a $2.5''$ search radius.

Table 6.1. *Spitzer* data

Cluster Field	z	Instrument	PID[a]	notes
CL0848+44	1.27	IRAC	00017	
		IRAC	00064	
		IRAC	20694	wider FOV
		MIPS	00083	
		MIPS	20694	wider FOV
RXJ0910+54	1.11	IRAC	00017	
		IRAC	**20808**	wider FOV
		MIPS	00083	
		MIPS	**20808**	wider FOV
RXJ1317+29	0.81	IRAC	00017	
		MIPS	00083	
BD1338+29	0.64	IRAC	**20808**	
		MIPS	**20808**	
RXJ1716+67	0.81	IRAC	00017	
		IRAC	**20808**	wider FOV
		MIPS	**20808**	
RXJ2247+03	0.18	IRAC	**20808**	
		MIPS	**20808**	

[a]PID 00017: distant X-ray galaxy clusters (Fazio et al. GTO); PID 00064: combined program (Fazio et al. GTO); PID 00083: use of massive clusters (Rieke et al. GTO); PID 20694: IRAC and MIPS maps (Stanford et al. GO2); **PID 20808:** SEXSI (Stern et al. GO2)

6.3 Source Catalog

Here we present a catalog of mid-IR photometry of SEXSI sources. An example page of the catalog is shown in Table 6.2; the full machine-readable catalog that includes 250 SEXSI sources will be presented in the online version of Eckart et al. (in preparation).

Column 1 presents the source ID, followed by $\Delta\alpha$ and $\Delta\delta$, the difference in RA and declination, respectively, between the X-ray position and the *Spitzer* counterpart. Columns 4–10 present X-ray and optical followup data for reference, and columns 11–15 present the IRAC and MIPS photometric data.

Column 4 presents the 2 – 10 keV flux in units of 10^{-15} erg cm^{-2} s^{-1}, while Column 5 presents the X-ray hardness ratio, described in Chapter 5. The optical-counterpart R-band magnitude is presented in Column 6, and the following columns provide the optical-spectroscopic classification and the source redshift. Sources marked 'unid' have no spectroscopic classification. The observed X-ray luminosity is presented in Column 9 and the N_H value determined from the X-ray data is presented in Column 10. Columns 11–14 provide the flux in each of the IRAC bands with associated errors. The errors are typically $\sim 10\%$ of the source flux owing to the systematic zero-point uncertainty. The MIPS data are presented in the final column. Entries in Columns 11–15 that are left blank indicate that a source was not observed in that band.

6.4 X-ray Selected SEXSI Sources Viewed in the Infrared

Our *Spitzer* data covers 250 hard-X-ray-selected SEXSI sources; 140 of these have spectroscopic redshifts. A significant fraction of the sources in the catalog do not have coverage in all of the IRAC bands; our preliminary analysis here will focus on the sources with detection in all four IRAC bands. Because of the relative depths of the IR data compared to the X-ray data, close to all of the SEXSI sources have IR counterparts in one or more of the bands. 170 SEXSI sources were observed in all four IRAC bands, and of those 146 have MIPS coverage. Of the 4-band IRAC-observed sources 60% have optical spectroscopic redshifts, and of those 91% are detected in all four IRAC bands, with a corresponding MIPS detection rate of 70%. Overall, over 97% of SEXSI sources observed at 3.6 μm are detected, and the detection rate for the other IRAC bands are all above 90%, while the overall MIPS detection rate is 75%.

Table 6.2. SEXSI-*Spitzer* Catalog

CXOSEXSI	$\Delta\alpha$	$\Delta\delta$	S_{2-10}	HR	R	class	z	$\log(L_x)$	$\log(N_H)$	$f_{3.6}$	$f_{4.5}$	$f_{5.8}$	$f_{8.0}$	f_{24}
	[']	[']	[10^{-15}]							[μJy]	[μJy]	[μJy]	[μJy]	[μJy]
(1)	(2)	(3)	(4)	(5)	(6)	(7)	(8)	(9)	(10)	(11)	(12)	(13)	(14)	(15)
J090954.0+541752	-0.5	-0.8	5.67	0.71	22.07	ELG	1.101	43.4	23.5					139.2± 93.2
J090955.5+541813	1.7	-1.2	5.13	0.42	>23.90	ELG	1.102	43.4	23.1					215.6± 103.8
J090959.6+542458	0.5	0.5	4.66	0.71	22.93	unid								178.2± 301.0
J091004.7+542050	1.0	-1.3	3.60	-0.39	21.25	unid								210.4± 88.5
J091008.0+541401	0.1	1.5	3.73	-0.20	22.58	ELG	0.811	43.0	20.8	16.6 ± 1.7	17.4± 1.8	9.9 ± 2.4	<15.8	<158.5
J091008.2+541524	-1.1	1.4	14.40	0.56	21.94	ELG	0.670	43.4	22.9	50.6± 5.1		43.6 ± 5.1		143.0± 75.2
J091009.7+541507	0.0	0.0	4.75	-0.06	>23.90	unid				<10.0	<15.8	<10.0	<15.8	<158.5
J091012.7+541205	1.1	0.2	15.20	0.40	>23.90	ALG	0.792	43.6	22.5	15.6± 1.6	23.2± 2.4	25.8 ± 3.5	54.0± 6.2	
J091014.3+541255	-1.1	-0.2	60.80	-0.35	19.24	unid				149.2± 14.9	245.7± 24.6	365.8 ± 36.8	639.0± 64.1	<158.5
J091017.4+541757	0.6	2.1	4.80	-0.73	12.79	star	0.000	0.0	0.0	5096.1± 509.7	±	1996.6 ± 200.4		812.7± 125.2
J091018.6+541316	-2.4	-0.1	6.46	-0.32	>23.90	unid				<10.0	<15.8	<10.0	<15.8	341.1± 155.9
J091020.7+541848	-0.9	-0.9	5.65	-0.33	19.64	BLAGN	2.794	44.3	22.4	43.1± 4.3		77.5 ± 8.1		503.3± 88.0
J091021.9+541529	0.3	0.1	2.89	0.35	23.44	ELG	0.482	42.4	22.2	18.6± 1.9	26.3± 2.7	38.3 ± 4.3	39.1± 4.9	<158.5
J091022.2+542007	-0.3	-0.5	5.69	0.28	22.37	ELG	0.898	43.3	22.8					259.7± 62.4
J091023.3+541358	-0.4	-0.5	14.40	-0.53	20.68	NLAGN	0.499	43.1	0.0	82.9± 8.3	112.4± 11.3	128.5 ± 13.1	184.5± 18.7	444.7± 133.1
J091023.7+541514	-1.0	-1.1	7.92	0.32	25.34	unid				16.1± 1.6	19.9± 2.1	20.8 ± 2.8	16.9± 3.3	<158.5
J091026.8+541241	-0.1	-0.1	60.50	0.04	18.78	NLAGN	0.373	43.4	21.9	558.2± 55.9	620.8± 62.2	570.7 ± 57.3	773.4± 77.5	
J091027.0+542054	-0.2	-0.2	17.50	-0.32	21.58	BLAGN	1.638	44.3	21.4	19.4± 2.0	32.2± 3.3	52.8 ± 5.9	88.7± 9.3	268.6± 49.9
J091028.5+542320	-0.8	1.4	1.91	0.13	23.68	BLAGN	1.960	43.5	23.3	17.9± 1.9	15.8± 15.8	29.5 ± 5.0	33.8± 5.5	69.2± 53.6
J091028.6+541634	0.1	-0.1	1.73	>0.73	22.91	ELG	0.907	42.7	24.0	40.7± 4.1		16.5 ± 3.1		97.0± 54.8
J091028.9+541523	-0.4	0.0	24.60	-0.38	22.03	BLAGN	0.647	43.6	20.0	41.5± 4.2	51.2± 5.2	63.5 ± 6.6	78.0± 8.4	351.5± 88.1
J091030.9+541914	-0.3	-1.0	7.79	-0.35	23.88	unid				54.7± 5.5		122.0 ± 12.5		888.8± 120.5
J091031.4+542157	-0.1	-1.1	1.59	0.01	23.61	unid				27.2± 2.7	25.3± 2.6	21.9 ± 2.9	17.8± 2.9	75.2± 40.0
J091031.7+542024	0.1	-0.1	2.78	-0.20	25.61	unid				10.0± 1.0	13.6± 1.5	11.9 ± 2.1	12.8± 2.9	79.3± 34.8
J091031.9+542342	0.4	-1.3	3.27	0.28	25.37	unid				68.9± 6.9	58.3± 5.9	52.8 ± 6.1	47.7± 5.5	<158.5
J091032.9+541246	0.1	0.3	5.47	-0.17	19.63	ELG	0.595	42.8	20.3	175.3± 17.6	116.8± 11.7	93.0 ± 9.8	109.8± 11.2	478.6± 263.9
J091033.2+541526	-0.2	0.4	3.02	0.60	>23.90	unid				47.2± 4.7	59.2± 6.0	41.5 ± 4.5	15.8± 3.5	<158.5
J091034.2+542408	-2.2	-0.7	2.41	-0.13	>23.90	ELG	0.340	42.0	21.6	17.9± 1.8	16.3± 1.7	22.4 ± 3.7	<15.8	110.5± 39.7
J091034.5+541918	0.5	0.5	5.31	0.45	>23.90	unid				35.5± 3.6		<10.0		<158.5
J091037.8+541543	2.3	2.1	6.65	-0.36	23.59	unid				7.2± 0.9				134.3± 44.2
J091037.9+541608	-0.3	-0.2	5.48	-0.26	22.42	ELG	1.102	43.4	21.2	49.9± 5.0		37.5 ± 4.9		289.6± 67.7
J091038.5+542025	-0.1	-0.2	4.45	-0.32	21.12	unid				60.9± 6.1	55.3± 5.6	69.9 ± 7.3	88.3± 9.1	454.0± 70.5
J091039.2+541320	-1.2	-2.1	7.27	-0.09	>23.90	unid				<10.0	<15.8	<10.0	<15.8	218.8± 83.0
J091039.8+542032	-0.5	-1.4	8.90	-0.29	21.93	BLAGN	2.450	44.4	22.4	<10.0	<15.8	<10.0	<15.8	643.8± 92.0
J091040.0+542259	0.3	0.1	4.37	0.01	20.76	ELG	0.252	41.9	21.7	33.8± 3.4	35.1± 3.6	22.5 ± 3.4	50.4± 5.5	81.0± 41.4
J091040.5+542033	-0.2	-0.9	1.65	0.14	>23.90	unid				11.6± 1.2	16.0± 1.7	25.0 ± 3.1	<15.8	<158.5
J091040.8+542006	-0.2	-0.4	2.42	>0.74	22.38	ELG	1.097	43.1	23.7	67.1± 6.7	68.4± 6.9	57.7 ± 6.1	87.6± 9.1	639.5± 86.2
J091041.4+541945	-0.1	-0.4	26.30	-0.40	21.38	BLAGN	0.786	43.8	21.4	94.0± 9.4	69.3± 7.0	74.5 ± 7.8	83.3± 8.7	362.4± 61.4
J091041.9+542127	1.0	-0.5	2.75	-0.26	21.13	BLAGN	0.598	42.6	21.7	49.4± 5.0	36.3± 3.7	46.3 ± 5.0	37.1± 4.4	113.0± 45.6
J091041.9+542340	-0.2	-0.6	10.50	-0.35	23.02	BLAGN	1.638	44.1	21.8	11.9± 1.2	14.8± 1.6	<10.0	25.9± 3.4	<158.5
J091042.6+541618	-0.7	-0.8	2.19	0.40	>23.90	unid				4.6± 0.8				253.2± 60.9
J091042.7+542008	0.1	0.1	1.67	0.31	>23.90	unid				41.0± 4.1	35.9± 3.7	21.9 ± 2.9	29.2± 3.7	<158.5
J091042.7+542034	-0.3	-0.4	1.46	0.05	22.59	ELG	1.108	42.9	22.6	53.3± 5.3	51.9± 5.2	39.9 ± 4.4	67.8± 7.2	234.5± 43.8
J091043.8+541724	-0.4	-0.4	4.61	0.52	>23.90	unid				20.2± 2.0	20.2± 2.1	14.5 ± 2.3	24.3± 3.9	49.6± 34.8

Figure 6.1 shows a color-color diagram of all *Spitzer* 4-band detected IRAC sources (small black dots) with larger symbols indicating the SEXSI 2 – 10 keV sources. SEXSI sources with optical-spectroscopic classification or continuum-only spectra have symbols indicated by the legend; sources with no optical spectroscopic information are marked with a blue square. The dotted lines indicate the Stern et al. (2005a) AGN selection wedge.

The majority (62%, or 68/109) of the X-ray selected AGN lie in the Stern et al. (2005a) selection wedge. Considering the spectroscopic sample, the AGN wedge contains 86% (30/35) of the BLAGN, 67% (8/12) of NLAGN, and 28% (8/28) of the ELG, as shown in Figure 6.1. Considering the errors on the IRAC fluxes, all but two of the BLAGN are consistent with the wedge (one of these is the lowest-luminosity BLAGN in the sample, with $\log(L_x) = 42.6$) and all of the NLAGN are consistent with the wedge selection.

6.4.1 X-ray Luminosity Dependence

Figure 6.2 illustrates the wedge selection for four 2 – 10 keV luminosity ranges, showing that X-ray luminosity strongly affects the fraction of sources which appear as AGN in the mid-IR. The entire lowest luminosity subsample ($L_x < 10^{43}$ erg s^{-1}) lie either outside of the wedge or near the outskirts of the wedge, while the fraction within the wedge increases monotonically with X-ray luminosity. At the highest X-ray luminosities ($L_x > 10^{43.5}$ erg s^{-1}), all but two of the sources are consistent with the wedge. Table 6.3 tabulates the fraction of X-ray sources in the wedge for the four plotted X-ray luminosity ranges. The X-ray luminosities used for binning the sources are the intrinsic, absorption-corrected luminosities described in § 5.5; the results are not significantly different if we use observed luminosities.

These results are consistent with the notion that for low-luminosity (unobscured) AGN, 2 – 10 keV X-ray surveys will find sources missed by infrared selection techniques: for lower-luminosity AGN the mid-IR is less likely to be energetically dominated by the AGN-component than for higher-luminosity AGN. Our results are consistent with those of Donley et al. (2007), who use deeper X-ray data over a smaller field of view from the *Chandra* Deep Field North and find that a small fraction of low-L_x sources fit their mid-IR power-law AGN selection criterion.

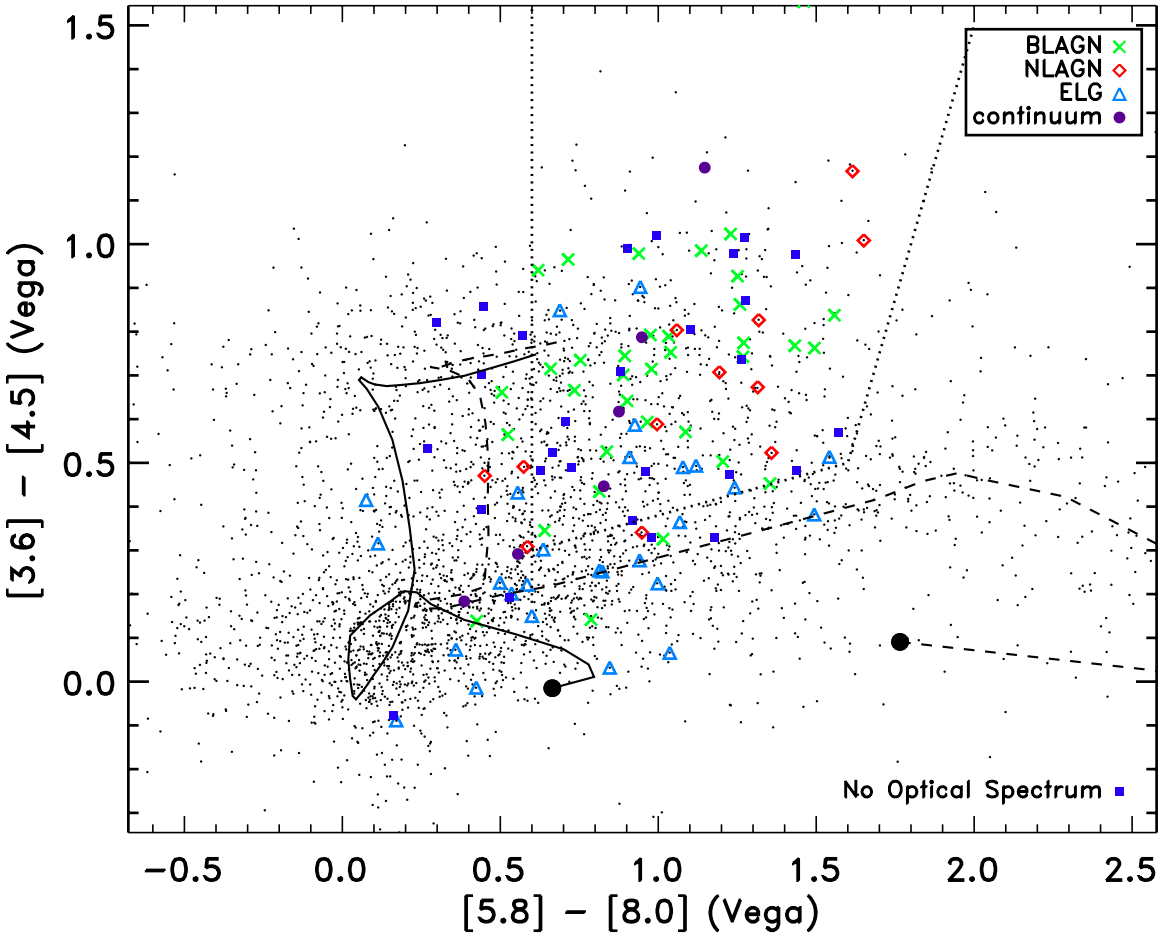

Figure 6.1 Color-color diagram of sources with IR-detections in all four IRAC bands. All 4-band *Spitzer* sources are indicated by small black dots. Sources with a 2 – 10 keV X-ray detection have a larger symbol overlaid; the specific symbol indicates the optical-spectroscopic classification. The dotted lines demarcate the AGN selection wedge introduced by Stern et al. (2005a). The $0 \leq z \leq 3$ color tracks for two non-evolving galaxy templates from Devriendt et al. (1999) are illustrated; the large filled circles indicate $z = 0$. A starburst galaxy is illustrated with the track of M82 (dashed line) and NGC 4429, an S0/Sa galaxy with a star-formation rate $\sim 4000\times$ lower, is indicated with a solid line

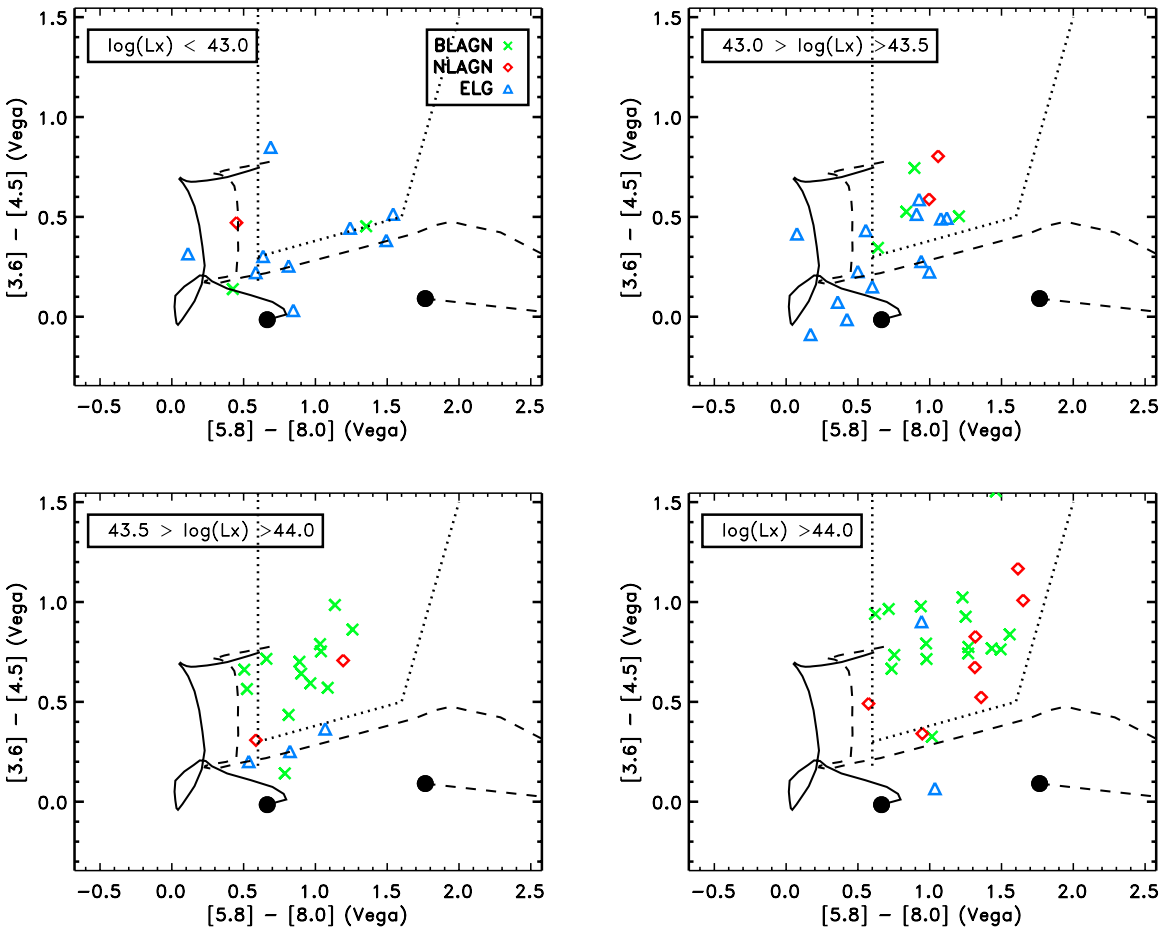

Figure 6.2 IRAC color-color diagram of SEXSI 2 – 10 keV sources, split by absorption-corrected intrinsic X-ray luminosity. As the X-ray luminosity grows, a higher fraction of sources fall solidly into the Stern et al. (2005a) infrared-AGN selection wedge

Table 6.3. Wedge selection of SEXSI X-ray sources for several luminosity ranges

Sample	$\log(L_{\rm min})$	$\log(L_{\rm max})$	$L_{\rm min} < L_x < L_{\rm max}$ Wedge	Total	%
All classes	—	43.0	4	13	31%
BLAGN			1	2	50%
NLAGN			0	1	0%
ELG			3	10	30%
All classes	43.0	43.5	10	19	53%
BLAGN		.	4	4	100%
NLAGN			2	2	100%
ELG			4	13	31%
All classes	43.5	44.0	11	18	61%
BLAGN			10	13	77%
NLAGN			1	2	50%
ELG			0	3	0%
All classes	44.0	—	21	25	84%
BLAGN			15	16	94%
NLAGN			5	7	71%
ELG			1	2	50%

6.4.2 Dependence on R-band Magnitude

Figures 6.3 and 6.4 show this same color-color diagram but split at $R_{\rm cut} = 22$; Figure 6.3 shows *Spitzer* and SEXSI sources with bright optical counterparts and Figure 6.4 shows those fainter than $R_{\rm cut} = 22$.[1] Tabulated results comparing the wedge selection shown in these plots are presented in Table 6.4; the results are similar using $R_{\rm cut} = 22.5$.

These data show a few strong trends. Only 5% of optically bright 4-band IRAC sources lie in the wedge area, while 20% of the optically fainter 4-band IRAC sources do. If we consider the subset of these sources that have 2 – 10 keV detections, we see that the 67% of the optically bright X-ray sources lie in the wedge and 59% of the optically faint X-ray sources are in the wedge. The X-ray sources in general are more likely to fall in the wedge than a typical IRAC source, consistent with the notion that the wedge preferentially identifies AGN. An interesting trend evident from this sample is the small fraction of $R < 22$ X-ray non-detected wedge sources: of the 40 IRAC sources in the wedge with $R < 22$, 31 (78%) are X-ray detected. In contrast, the corresponding optically faint ($R > 22$) sample are only detected by *Chandra* 31% (37/121) of the time. This trend is consistent with

[1]Note that the total number of *Spitzer*-only sources (small black dots) from Figures 6.3 and 6.4 is smaller than the number of sources shown in Figure 6.1. This is because Figures 6.3 and 6.4 require an R-band detection, while Figure 6.1 includes optically undetected sources as well as IRAC sources outside of the optical FOV

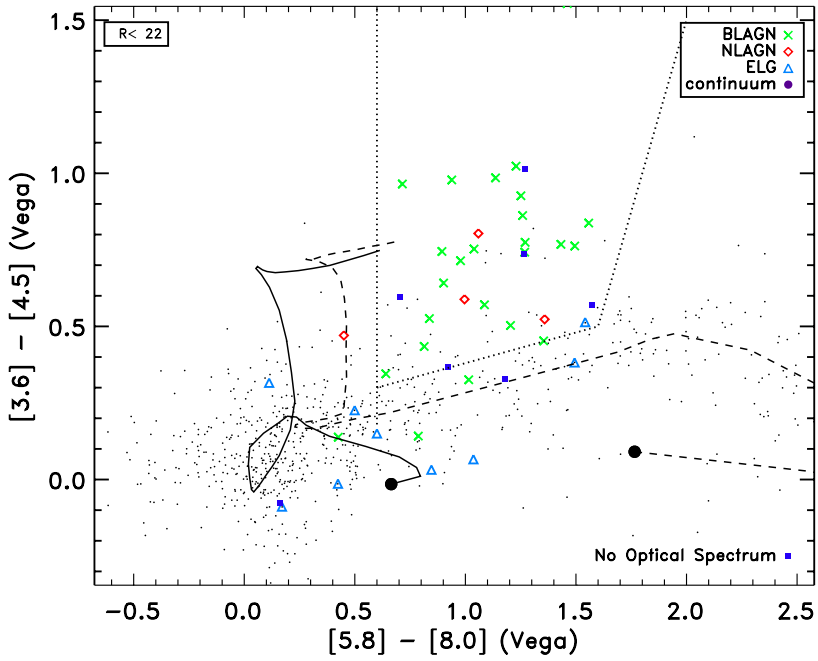

Figure 6.3 IRAC color-color diagram of sources with optical counterparts brighter than $R = 22$. The symbols and galaxy tracks are the same as in Figure 6.1

.

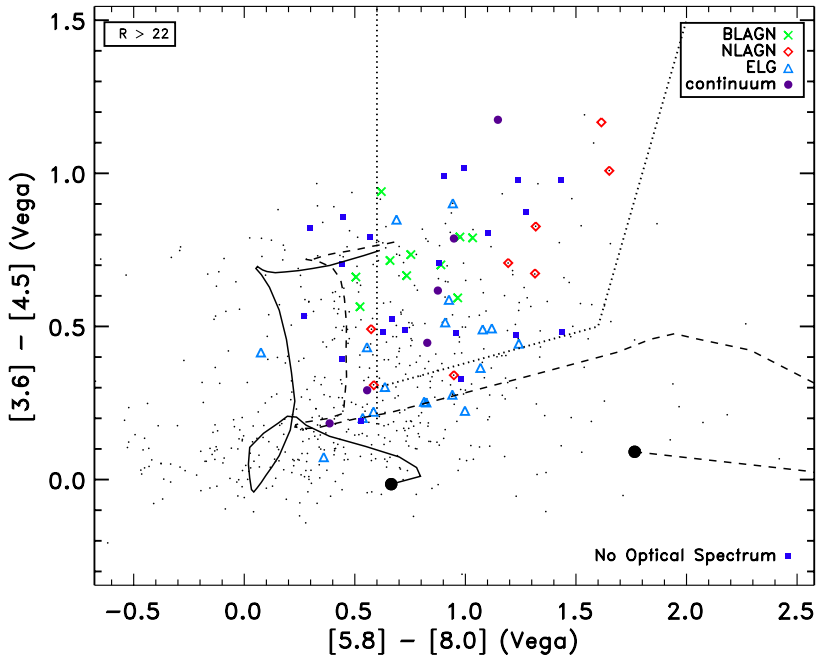

Figure 6.4 IRAC color-color diagram of sources with optical counterparts fainter than $R = 22$. The symbols and galaxy tracks are the same as in Figure 6.1

Table 6.4. Wedge selection of IRAC sources and SEXSI X-ray sources split at $R_{\rm cut} = 22$

		Bright: $R < R_{\rm cut}$						Faint: $R > R_{\rm cut}$					
		All 4-band IRAC			SEXSI X-ray			All 4-band IRAC			SEXSI X-ray		
Sample	$R_{\rm cut}$	Wedge	Total	%	Wedge	Total	%	Wedge	Total	%	Wedge	Total	%
All	22.0	40	759	5%	31	46	67%	121	596	20%	37	63	59%
BLAGN	22.0				22	25	88%				8	10	80%
NLAGN	22.0				3	4	75%				5	8	71%
ELG	22.0				1	10	10%				7	18	39%

the idea that many of the X-ray non-detected *Spitzer* AGN are obscured, resulting in faint optical counterparts and X-ray non-detections.

The final three lines of Table 6.4 split the population by spectroscopic source type; the columns for *Spitzer* sources are blank here because we do not have spectroscopic followup of the non-X-ray-detected *Spitzer* AGN candidates. The final line of Table 6.4 shows the population of emission-line galaxies, which do not show optical spectroscopic emission lines typical of AGN, but have X-ray luminosities that indicate that a strong active nucleus is present. Of the optically bright ELG, only one of ten sources lie within the wedge (and that one is near the boundary), while closer to 40% of the eighteen $R > 22$ ELG lie in the wedge. This trend is different from that seen with the BLAGN and NLAGN, where a similar (e.g., similarly high) fraction of sources lie in the wedge, independent of R magnitude. This may indicate that for optically bright ELG the starburst component of the SED is brighter than the AGN component pushing the source away from the AGN-defined wedge, while for some of the optically fainter sources the AGN component is strong in the infrared leading to wedge selection. This trend is explained by the trend that higher X-ray luminosity sources tend to fall in the wedge: as ELG are identified at higher redshift they will be fainter in R and also have higher average L_x due to selection effects, and thus preferentially fall in the wedge as compared to low-luminosity, low-z sources. Splitting the wedge sources by redshift confirms this assertion. Overall, regardless of R-magnitude, the ELG tend to fall outside of the wedge.

6.5 Mean X-ray Properties of Infrared Selected Active Galaxies

We now perform an X-ray stacking analysis to explore the mean X-ray properties of mid-IR-selected sources that lack significant *Chandra* detections. The following section describes the stacking methodology, while § 6.5.2 presents the results.

6.5.1 X-ray Stacking Methodology

The X-ray stacking analysis used tools provided by CIAO and was aided greatly by `acis_extract`[2] Version 3.91 (Broos et al. 2002). We use CIAO Version 3.2 and CALDB Version 3.1 for the analysis presented here. The basic X-ray data preparation and observations are described in Harrison et al. (2003).

Source lists for X-ray spectral extraction were assembled using SExtractor catalogs of 4-band-detected IRAC sources that fall on *Chandra* images, excluding sources very near the edge of an ACIS chip. Care was taken to avoid including regions near the original *Chandra* targets. IRAC sources that fell within 1 Mpc of the target-cluster center were eliminated from the stacking analysis to reduce contamination from cluster galaxies.

The mid-IR-derived positions were then 'uncorrected:' IRAC 3.6 μm source positions were shifted to the uncorrected SEXSI X-ray frame by adding to each mid-IR position the average X-ray-to-optical offset correction. These average X-ray-to-optical offsets were calculated for each *Chandra* field in the SEXSI survey to correct the early *Chandra* pointing errors (see § 3 and Table 2 of Eckart et al. 2005). The magnitude of these errors was typically less than an arc-second, but that is large enough to skew X-ray source extraction if the 'corrected' positions are used in the 'uncorrected' frame of the X-ray images.

Spectra were extracted for each source in the resulting catalog. We choose 1.5 keV as the primary PSF energy at which the PSF fraction is to be computed, and a PSF fraction of 0.8. Individual auxiliary response files (ARFs) and redistribution matrix files (RMFs) were calculated for each source. We extracted a background spectrum for each source from a local circular background region that includes at least 100 counts, taking care to mask out all detected X-ray sources (SEXSI sources, including soft-only sources, target point sources, and extended cluster emission). The background spectra were scaled based on the ratio of

[2]Available at http://www.astro.psu.edu/xray/docs/TARA/ae_users_guide.html

total area in the source extraction region to that of the background region.

Source counts and scaled background counts were tabulated for each source in several energy bands: the standard $0.5-8$ keV (full band), $2-8$ keV (hard band), and $0.5-2$ keV (soft band), as well as $2-4$ keV, $4-6$ keV, and $6-8$ keV. Estimates of individual source significance are calculated for each band. Following Laird et al. (2005) we define detection significance as $S/\sqrt{B}$ and signal-to-noise ratio as $S/\sqrt{S+B}$, where S and B are the net source counts and background counts, respectively. The average exposure per pixel (in each energy band) is calculated for each source by averaging the ARF over the given energy band and then over the source extraction cell. In addition to the IRAC sources, we also followed this procedure using a catalog with randomly shifted source positions.

After calculating individual source statistics for all of the sources we are able to stack the sources. The average signal in each band is calculated by summing the net counts. To calculate an average flux we divide the summed signal by the sum of the average exposure per pixel in each extraction cell to convert from counts to ph cm^{-2} s^{-1}. To convert from ph cm^{-2} s^{-1} to erg cm^{-2} s^{-1} we assume a power-law spectrum with photon index $\Gamma = 1.5$. To ensure that the stacks are not dominated by a handful of sources with significant X-ray counts (sub-SEXSI-threshold X-ray sources) we eliminate all sources with an individual source significance of 10 or greater. The choice of sig=10 is slightly arbitrary; the exact significance cut does not affect the stack, it just acts to eliminate the ~ 10 sources with significant (yet sub-SEXSI) X-ray detections.

6.5.2 Stacking Results

Stacking the emission from the undetected IRAC 4-band detected sources produced significant detections.[3] We stacked three basic samples: all X-ray undetected sources (1788 sources), the wedge-selected sources (288 sources), and those that fall outside of the wedge (1500 sources). Table 6.5 presents a summary of the results of these stacks, where N is the number of sources in the particular stack, Cts provides the number of net counts in the stack, Sig provides an estimate of the source significance, and f_x is the X-ray flux in units of 10^{-17} erg cm^{-2} s^{-1}. The stacks of the sources created by the randomly-shifted source catalog showed no significant detection in any band.

[3] Only 5 of the 6 fields are included in this preliminary stacking analysis. The sources from field CL 0848+44 will be added at a later date

Table 6.5. Average properties of X-ray undetected IRAC sources

Sample	N	0.5 – 8 keV			0.5 – 2 keV			2 – 8 keV		
		Cts	Sig	f_x $[10^{-17}]$	Cts	Sig	f_x $[10^{-17}]$	Cts	Sig	f_x $[10^{-17}]$
All	1788	683	16.8	10.0	473.8	20	2.3	209.5	6.4	6.9
Inside Wedge	288	257	14.3	21.2	135.7	13	3.8	121.0	8.3	22.7
Outside Wedge	1500	427	11.7	7.6	338.0	16	2.0	88.5	3.0	3.6
Inside Extended Wedge	475	379	16.4	18.6	210.5	16	3.5	168.7	9.0	18.9
Outside Extended Wedge	1313	304	9.0	6.3	263.2	13	1.8	40.7	1.5	1.9

For the IRAC sources as a whole, the stacked emission produces a total of 683 net counts with a detection significance of 16.8 in the full band, 473.8 net counts in the soft band with a source significance of 20, and a hard-band detection of 209.5 net counts with a source significance of 6.4. These detections correspond to mean fluxes of 1×10^{-16} erg cm^{-2} s^{-1} (full band), 2×10^{-17} erg cm^{-2} s^{-1} (soft band), and 7×10^{-17} erg cm^{-2} s^{-1} (hard band).

Stacking only the wedge-selected sources, we again find significant detections in all three X-ray bands. The wedge-selected sample contains over six times fewer sources than the full sample, while the stacked signals from the wedge contribute $\sim 1/3 - 1/2$ of the total counts of the full sample. This trend is most significant in the hard band, where the average flux of the wedge-selected sample is over three times that of the total sample. The stack of sources outside the wedge show only a marginal detection in the hard band, with detection significance of 3, and source flux over six times lower than that of the wedge-sources. These findings are consistent with the idea that AGN preferentially lie inside the wedge.

To allow for errors in the IRAC photometry, we also stacked based on an extended wedge defined by:

$$\begin{aligned} ([5.8]-[8.0]) > 0.5 \quad &\wedge \quad ([3.6]-[4.5]) > 0.2 \cdot ([5.8]-[8.0]) + 0.078 \\ &\wedge \quad ([3.6]-[4.5]) > 2.5 \cdot ([5.8]-[8.0]) - 3.77 \ , \end{aligned} \tag{6.1}$$

where $\wedge$ is the logical AND operator. This extended wedge is constructed by taking the original Stern et al. (2005a) wedge and adding a swath of width 0.1 at each edge. The stacks for inside and outside the extended wedge are also presented in Table 6.5; the extended wedge swath includes 187 sources. Removing these 187 sources from the 1500 sources not

Table 6.6. Wedge stack: implied N_H

z	$\log(N_H)$
0.0	8.5×10^{21}
0.5	2.3×10^{22}
1.0	4.8×10^{22}
1.5	8.9×10^{22}
2.0	1.5×10^{23}
3.0	3.2×10^{23}

selected by the original wedge removes about half of the counts in the hard-band stack, leaving a source significance of only 1.5 in the extended-wedge hard-band stack. This suggests that the hard-X-ray radiation that is easily produced by AGN but less so by star formation comes from sources in or just outside the wedge, at our detection sensitivity.

Although the wedge-selected sources are harder than those outside the wedge, the column density implied by the hardness ratio of is not extreme, as compared to *Chandra*-detected samples. Table 6.5 provides estimated N_H values based on the HR of the wedge-selected stack for assumed source redshifts ranging from 0.0 to 3.0. The N_H values are calculated assuming an underlying power-law spectrum with $\Gamma = 1.9$ and a Galactic column density of 10^{20} cm^{-2}. The calculated N_H estimates range from $\sim 9 \times 10^{21}$ cm^{-2} -3×10^{23} cm^{-2}, suggesting that the sources are intrinsically obscured, but are not, on average, Compton thick.

6.6 Conclusions and Future Work

In this Chapter we have presented an exploration of the relative merits of AGN selection in the X-ray with *Chandra* and in the infrared with *Spitzer*, along the path toward the ultimate goal of composing a complete, unbiased census of supermassive black hole growth and evolution in the Universe.

While many of the X-ray-selected AGN are also selected by the Stern et al. (2005a) *Spitzer* AGN selection criteria, we find that a large fraction of the low-L_x AGN ($L_x < 10^{43.5}$ erg s^{-1}) identified by *Chandra* will be missed by *Spitzer*. In addition, we find that while $\sim 80\%$ of the optically bright ($R < 22$) wedge selected *Spitzer* AGN are also identified

by *Chandra*, many of the optically faint ($R > 22$) wedge sources are X-ray undetected. To explore the mean X-ray properties of the X-ray undetected wedge AGN, we stacked the corresponding X-ray data. The stacked wedge sources show significant X-ray signals in the full, soft, and hard X-ray bands.

The hardness ratio of the wedge-selected stack is consistent with moderate intrinsic obscuration, but is not suggestive of a highly obscured, Compton-thick source population. It is possible that the stack is missing a population of sources, such that the stacked counts are dominated by a subset of the wedge-selected sources. For instance, perhaps the stack is dominated by fewer than half of the sources, which fall below the SEXSI detection threshold, but have a much higher flux than the other half of the X-ray-undetected sources. In that case the average X-ray fluxes and hardness ratios will not be indicative of the overall source population, and may miss flux from truly highly obscured sources with $N_H \gtrsim 10^{25}$ cm^{-2}. Another possibility is that the simple assumption of an intrinsic $\Gamma = 1.9$ power-law component plus photoelectric absorption is too simple, so that the estimated N_H values are not representative of the sample. The soft X-ray emission may originate in a different location than the hard, power-law component, skewing the N_H estimates to lower values. In reality, it is likely some combination of these and other effects.

In the short term, we plan to study the distribution of counts in our stack to determine if we can suggest whether the stack is dominated by a subset of the stacked sources. In addition we plan to calculate the implied contribution of the *Spitzer*-selected AGN to the X-ray background using the SEXSI data combined with public data from the deep, pencil-beam fields included in the Great Observatories Origins Deep Survey (GOODS).[4]

In the long-term, an X-ray mission sensitive at higher energies will be important to study the *Spitzer*-selected AGN and their contribution to the X-ray background. For example, the Nuclear Spectroscopic Telescope Array (NuSTAR)[5] is a proposed focusing telescope designed to image the hard ($\lesssim 80$ keV) X-ray sky. In addition, future X-ray survey missions at $E \lesssim 10$ keV that have orders-of-magnitude gains in effective area and non-dispersive spectroscopic resolution will allow detailed spectral studies of sources that are only faint detections with *Chandra*.

[4]GOODS: http://www.stsci.edu/science/goods/
[5]http://www.nustar.caltech.edu

Part II

Microwave Kinetic Inductance Detectors for X-ray Astrophysics

Chapter 7

Focal-Plane Arrays for Next-Generation Missions

7.1 Scientific Motivation for Next-Generation X-ray Survey Missions

7.1.1 Overview

Large-FOV imagers with high spectral resolution will enable advances in many areas of astrophysics and cosmology. Here I introduce two key areas: the accretion history of the Universe, through X-ray surveys of active galactic nuclei, and the nature of dark energy and dark matter, via X-ray surveys of galaxy clusters.

Many square degrees of sky have been surveyed with the current generation *Chandra* and *XMM-Newton* X-ray telescopes, studying the intermediate-redshift ($z \lesssim 2$) 0.5 – 10 keV X-ray Universe with unprecedented depth. However, these are CCD-grade low spectral resolution surveys with limited photon counts. There is great scientific potential if these surveys can extend a decade in sensitivity and sample tens of square degrees with a factor of ~ 30 improvement in spectroscopic resolution.

7.1.2 Next-Generation AGN Surveys

The accretion history of the Universe provides a fundamental key to understanding the formation and evolution of our Universe. Supermassive black holes reside at the center of every galaxy, and the formation and growth of each central black hole and host galaxy are intimately linked (Magorrian et al. 1998; Tremaine et al. 2002). X-ray surveys efficiently

select AGN, and current X-ray telescopes have pinpointed statistical samples of accreting extragalactic sources, probing AGN demographics across a diverse array of AGN types to $z \sim 1$. For example, Chapter 5 discusses the identified sample of AGN from the SEXSI survey and compares to other *Chandra* and *XMM-Newton* surveys. Our current understanding begins to fall short at higher redshifts; one primary goal for future surveys is to push to higher redshifts to find the first black holes as they are forming. Future surveys should also allow detailed X-ray spectral modeling of large samples of AGN at cosmic distances; this is currently unavailable for all but the brightest sources in the X-ray sky. The current surveys rely heavily on optical spectroscopic followup or many-band optical and IR photometry to determine source redshifts. This severely limits the surveys to lower redshift sources or to sources with intrinsically bright or unobscured optical counterparts. High resolution X-ray spectral information will not only allow redshift determination via the Fe Kα line at 6.4 keV in many cases but allow studies of the detailed X-ray spectral shape of faint sources that currently only have rough estimates of spectral shape from broad band hardness ratios. These future survey goals require large, multiplexed detector arrays to ensure sufficient survey area to find the rare, high-z sources, and non-dispersive spectrometers with excellent energy resolution and high efficiency for spectral study.

7.2 Basic Design Requirements for Future X-ray Survey Missions

The science goals of future survey missions guide the proposed design requirements for future X-ray survey missions, such as *XEUS*, a proposed European mission, and *Generation-X,* the working name for a future NASA X-ray mission after *Constellation-X* These telescopes will combine a large effective area — a current proposed number for *Generation-X* is ~ 150 m^2, more than 3000 times the effective area of *Chandra* — with sub-arcsecond angular imaging over a large FOV. Spectral imagers with excellent energy resolution will be required, and, due to the large FOVs and small PSFs, the detector will need tens or hundreds of thousands of pixels. The required pixel size will be chosen to match the focal length and angular imaging performance of the telescope. A suggested goal for a *Generation-X* imaging spectrometer is ~ 30000 pixels of size 100 μm $\times$100 μm, although because it is likely that the mission FOV will be limited by the detector array sizes, a larger array will facilitate a

larger FOV and thus more efficient and fruitful science.

Constellation-X, a (nearer-term) proposed X-ray mission, in comparison to *Chandra, XEUS,* or *Generation-X,* will have a small FOV. This mission will have $\sim 5''$ angular resolution combined with a comparatively small 1000-element detector array, but will have a collecting area over 10 times that of *Chandra* and $\Delta E \sim 5$ eV at 6 keV, providing unprecedented spectroscopic opportunities for targeted observations. This focal length is not set, but the current design calls for 240 μm pixels to sufficiently oversample the PSF. Efforts are underway to extend current detector technologies to achieve the array size and energy resolution required for *Constellation-X*; here I focus on applications and motivations for missions that require a much larger FOV.

7.3 Superconducting Detectors for X-ray Astrophysics

Low temperature detectors are the detectors of choice for applications in non-dispersive X-ray spectroscopy. Superconductors have an energy gap in their electronic density of states of order milli-eV, in contrast to semiconductor band gaps that are a thousand times larger, which provides great advantages in spectroscopy owing to the large number of excitations produced by a given X-ray absoprtion. Debye energies of superconductors — a measure of the maximum allowed phonon energy — are typically two orders of magnitude larger than the superconducting gap energy. This energy mismatch means that phonons created by the photon absorption and subsequent energy downconversion process can break further Cooper pairs, adding to the number of quasiparticle excitations (see § 8.5.1.1 for more detail); this feature is another advantage of superconductors over semiconductors for photon detection.

To provide background and motivation for MKID development I review other detector technologies being pursued for large arrays. MKIDs are in an early stage of development, but, theoretically, they should be able to achieve similar energy resolution to the other detectors. The real advantage of MKIDs is the ease with which they are multiplexed. Therefore, in the rest of this chapter I will describe the status of the field and where the various technologies are in regard to to energy resolution and multiplexing performance to provide context for our detector development.

Several types of superconducting sensors have been pursued and will be introduced in this section: superconducting tunnel junctions (STJs) measure changes in the tunneling

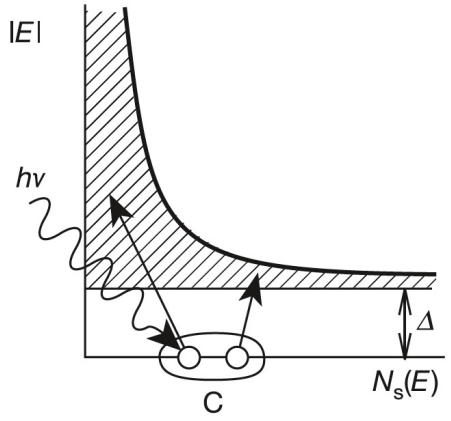

Figure 7.1 A superconductor cooled to $T \ll T_c$ has a finite energy gap Δ. A photon of energy $h\nu > 2\Delta$ absorbed into the superconductor will break Cooper pairs (C) and create quasiparticles. This plot is from Day et al. (2003), Figure 1a

current through a thin oxide barrier fabricated between two superconducting layers, while changes in the superconductor impedance are measured by transition-edge sensor (TES) based microcalorimeters and microwave kinetic inductance detectors (MKIDs). STJs and MKIDs are non-equilibrium quasiparticle sensors with an 'operational' stage defined by the lifetime of the photon-generated quasiparticles (because it is these excited quasiparticles that are sensed), while TESs sensitively measure the resistance change in the superconductor at its superconducting transition due to a thermalized increase in energy.

In the following sub-sections I introduce the basic operational principles of STJs and TES-based microcalorimeters, two promising technologies that existed prior to the development of MKIDs. I highlight the challenges faced in building large arrays of these detectors and briefly present innovations in multiplexing schemes that are being pursued to overcome these challenges, with mention of the remaining technical difficulties. Finally, I give a brief introduction to the easily multiplexed MKIDs.

7.3.1 Pair-Breaking Detectors: Analogy to Photoconductors

Superconducting pair-breaking detectors are in many ways analogous to photoconductors. Within a superconductor, pairs of electrons are bound together by the electron-phonon interaction with a binding energy of $2\Delta \simeq 3.5 k_B T_c$. Figure 7.1 shows the finite gap, Δ, in the electronic density of states. The states below the gap represent the bound electron pairs, called Cooper pairs, while states above the gap represent single-electron quasipar-

ticle excitations. Figure 7.1 also includes a drawing of an incoming photon of energy $h\nu$. Photons with energy $h\nu > 2\Delta$ can break Cooper pairs, each producing of order $\sim h\nu/\Delta$ quasiparticles. These broken Cooper pairs will recombine on timescales of $\tau_{\rm qp} \approx 10^{-3} - 10^{-6}$ s. The goal of both STJs and MKIDs is to measure with high precision these quasiparticles produced by incoming photons. Because the superconducting gap is of order a thousand times smaller than the band-gap energy of semiconductors, using superconductors provides a major advantage over CCDs.

In principle, the random generation and recombination of thermal quasiparticles limits the detector performance. These processes create fluctuations in the mean number N of quasiparticles in the detector of order $\sqrt{2N}$. However, the thermal quasiparticles obey a Boltzmann distribution proportional to $e^{-\Delta/kT}$, and the resulting sensitivity limit, given by the noise equivalent power (NEP), is NEP $= (2\Delta/\eta)\sqrt{N/\tau_{\rm qp}}$, where η is the quantum efficiency (Sergeev et al. 2002). Thus, by operating the detector at $T \ll T_c$ where the quasiparticle density is very low, it is, in principle, possible to build a sensitive detector with excellent energy resolution if the photons can be absorbed efficiently and if the quasiparticles produced by the photons can be measured.

7.3.2 Superconducting Tunnel Junctions

Superconducting tunnel junctions are superconducting pair-breaking detectors. STJs sensitively measure changes in the quasiparticle tunneling current across a thin oxide barrier between two superconducting electrodes, called a Josephson junction. At currents below the critical current ($I_c = 2\Delta/e$) in a Josephson junction, a supercurrent of Cooper pairs will flow across the oxide barrier. At currents equal to or above I_c a voltage builds up across the barrier (see Figure 7.2).

In STJs the Cooper pair tunnel current is suppressed by applying a magnetic field parallel to the plane of the junction. A bias voltage is applied to the junction and the current across the barrier due to thermally excited quasiparticles can be measured. When a photon is absorbed in one of the electrodes and excess quasiparticles are generated there is a pulse of excess quasiparticle current across the barrier. This current pulse is integrated to determine the number of excess quasiparticles, and thus the incident photon energy.

Superconducting tunnel junctions were first demonstrated for efficient X-ray detection over two decades ago (Twerenbold & Zehnder 1986) using a single STJ connected to a strip

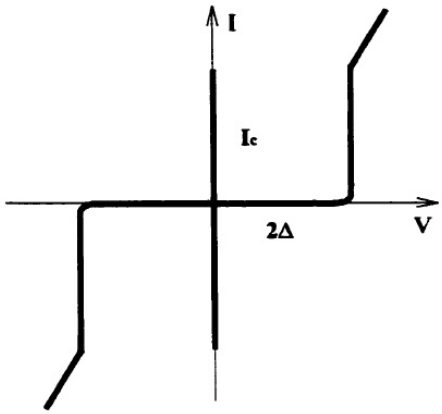

Figure 7.2 The I-V curve of a superconducting tunnel junction with no applied magnetic suppression. The dc-Josephson supercurrent is the current at $V = 0$. This drawing was originally presented at Figure 2.1 in Li (2002)

of absorbing material. Kraus et al. (1989) first demonstrated a imaging detector with a strip of virtual pixels using a strip-detector architecture with a STJ attached at each end. The current best energy resolution using this double-junction scheme is 13 eV at 6 keV (Li 2002). Section 7.4.3.2 describes this architecture and the STJ results in more detail.

7.3.3 Microcalorimeters

Microcalorimeters are not pair-breaking detectors but thermal detectors; also, they do not operate strictly in the superconducting regime, but at the transition region between the superconducting and normal states. Instead of measuring non-equilibrium quasiparticle populations, microcalorimeters sensitively measure the increase in temperature caused by the absorption of a photon. The three basic components of a microcalorimeter are an absorber, a thermometer, and a weak thermal link to a bath, as depicted in Figure 7.3. When a photon hits the absorber its energy is quickly converted into heat. This increase in temperature is measured by a sensitive thermometer and then the device quickly cools back to its equilibrium via the weak thermal link to the bath. The signal from an ideal microcalorimeter is a pulse with height proportional to the photon energy divided by the absorber heat capacity ($h\nu/C$) and an exponential decay with cooling time constant $\tau = C/G$ (in the absence of electrothermal feedback in the thermometer). STJs (and MKIDs) measure deposited energy while it resides in the electronic system; microcalorimeters instead measure thermal energy in the phonon system.

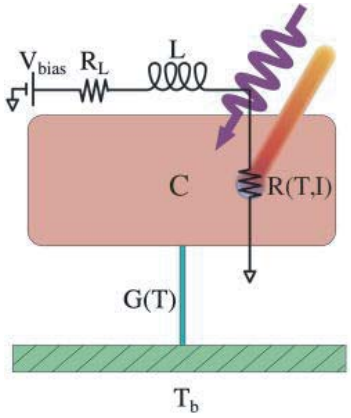

Figure 7.3 From Figueroa-Feliciano (2006), this cartoon illustrates an ideal microcalorimeter with an absorber of heat capacity C, a thermometer and an example circuit to read out the thermometer, and a weak thermal link of conductance G(T) to a thermal bath at T_b. The incident photon is thermalized in the absorber and causes an increase in temperature that is sensitively measured by the thermometer

The best X-ray microcalorimeter performance to date has been achieved by coupling an absorber made of gold (Au) or bismuth (Bi) to a voltage biased thermometer. In this scheme the absorber is chosen for its high X-ray absorption efficiency, as well as for a swift and complete thermalization of the absorbed energy. The TES thermometer is made of a superconductor voltage biased to sit in its transition between the superconducting and normal states, near its critical temperature (T_c). Figure 7.4 shows the resistance versus temperature curve for a superconductor. In transition the slope is very steep, indicating that a small change in temperature will provide a large change in resistance, which translates to a sensitive measure of the change in temperature. The electrothermal feedback employed in the TES readout circuit is also critical to the performance of the microcalorimeter, significantly speeding up the pulse decay time from the initial $\tau = C/G$, to allow higher count rates (Irwin 1995). As the TES registers an increase in temperature its bias voltage stays constant, resulting in a decreased power dissipation ($P = V^2/R$). This drop in power dissipation causes the TES to cool rapidly and stay in its transition. This fast electrothermal feedback significantly decreases the pulse decay time. Using this scheme a group at Goddard Space Flight Center (GSFC) and a group at NIST, Boulder (Ullom et al. 2005), have achieved the world's best microcalorimeter energy resolution: $\Delta E = 2.5$ eV at 6 keV, meeting spectral resolution requirements for upcoming space missions such as *Constellation-X*

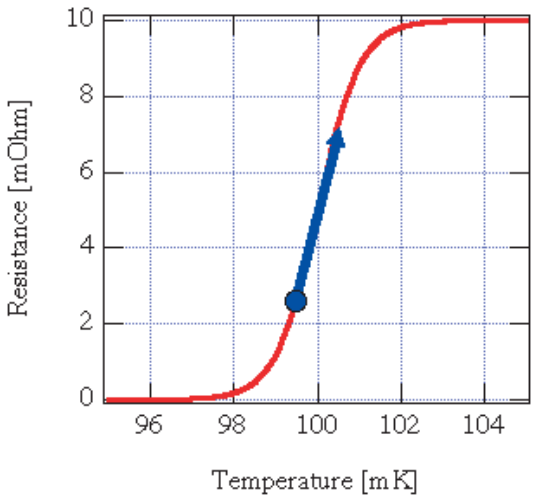

Figure 7.4 The resistance as a function of temperature for a superconductor with a critical temperature of $T_c \sim 100$ mK. In transition edge sensors the superconductor is voltage biased to sit in its transition (dot); energy absorption causes the temperature to rise on this steep part of the $R - T$ curve, causing a large resistance change for a small temperature change, and thus a sensitive thermometer. *Diagram credit: http://web.mit.edu/figueroagroup/*

7.4 The Push for Large Arrays

These excellent results using single-pixel or small-arrays of detectors must be extended to large pixel count for future X-ray survey missions. Building the large arrays required for X-ray astrophysics is a formidable technical challenge.

7.4.1 Brute Force: Scaling Up Current Detector Arrays

In the small arrays of microcalorimeters each TES, and thus each pixel, is read out with a Superconducting QUantum Interference Device (SQUID), devices that, in typical X-ray detector designs, operate within a cryostat at $\lesssim 100$ mK and require complex cryogenic wiring. The complexity and associated heat load prohibit easy fabrication of larger arrays and allow only large individual pixels ($\gtrsim 0.25$ mm $\times$ 0.25 mm); the material that follows will describe some of the approaches to reducing the wiring complexity and heat load via multiplexing techniques.

7.4.2 TES Multiplexing Approaches

For *Constellation-X,* part of NASA's Beyond Einstein program to study the structure and evolution of the universe, a 32 $\times$ 32-pixel microcalorimeter array is under development for

use in the soft X-ray telescopes. This spectrometer consists of a kilopixel array of transition-edge sensors and will be used to achieve $\lesssim 5$ eV spectral resolution from 0.6 to 10 keV. The pixels are expected to be read out using several stages of multiplexed SQUID amplifiers before being coupled to external electronics.

For such arrays, SQUID multiplexing is required to reduce the wiring and circuit complexity; in parallel with detector development efforts there are significant efforts underway to develop SQUID multiplexers for large arrays.

7.4.2.1 Time-Division and Frequency-Division Multiplexing

The two most common TES-multiplexing approaches, time-division multiplexing (TDM) and (low) frequency-division multiplexing (FDM), involve arranging the TESs into an $M \times N$–pixel array (for a review, see Irwin 2002).

In TDM the array contains $M * N$ first-stage SQUIDs (one per TES) and N second-stage SQUIDs (one per column). By arranging the SQUIDs in this manner, signal and bias wiring from the array to room-temperature electronics is reduced since the first-stage SQUID signals are combined at each second-stage SQUID and only second-stage SQUID signals leave the cryostat. Figure 7.5 presents a 'series-address' TDM multiplexer. In this scheme each row is turned on sequentially by applying currents $I_1(t)$, $I_2(t)$, ..., $I_M(t)$ in sequence. The current from each first-stage SQUID is inductively coupled to a second-stage SQUID that is shared by an entire column.

In FDM schemes it is the TESs themselves that are multiplexed, unlike TDM in which first-stage SQUIDs are multiplexed. In FDM, instead of sequentially addressing each row of detectors, the rows are concurrently addressed with sinusoidal currents at various frequencies and thus each TES signal is upshifted to a frequency band around this carrier frequency. The TES signals from a column are combined into the common SQUID and demultiplexed at room temperature.

Care must be taken in both TDM and FDM schemes to avoid increasing the noise so that the energy resolution is not degraded. It is this requirement that contributes heavily to the technical difficulty of developing and fabricating practical multiplexers. While TES noise is wide band and close to white noise, the bandwidth of TES signals themselves is determined by the thermal response of the detectors: at frequencies above the thermal-response frequency the TES signal rolls off. To attain a maximal signal-to-noise ratio

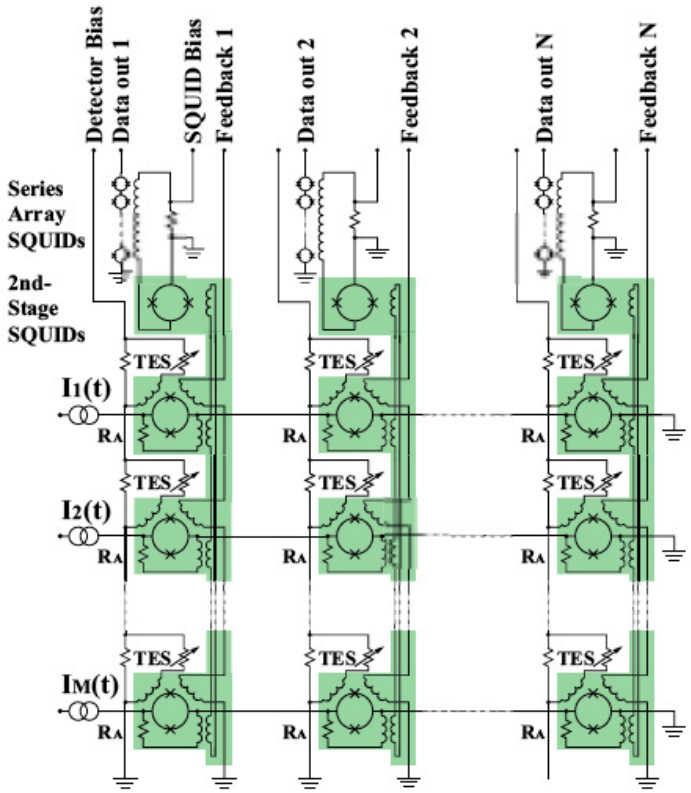

Figure 7.5 This diagram shows a scheme for time-division multiplexing of TES-based microcalorimeters (Irwin 2002). In this scheme each TES signal is amplified by a first-stage SQUID and the resulting signal is combined, along with the signal from other first-stage SQUIDs in the same column, at a second-stage SQUID. Each row of TESs is sequentially addressed by applying currents $I_1(t)$, $I_2(t)$, ..., $I_M(t)$ in sequence

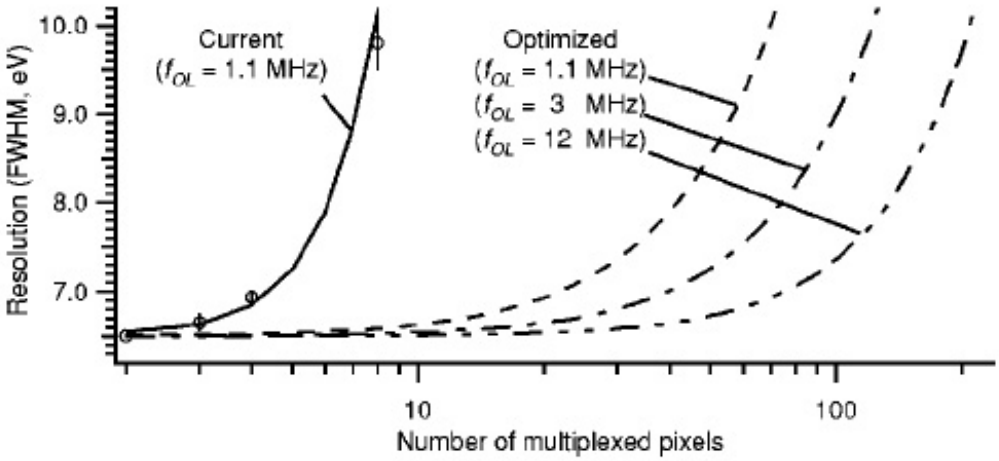

Figure 7.6 This plot shows TES resolution as a function of number of multiplexed pixels using a time-division multiplexer (Doriese et al. 2004). The experimental results are shown in a solid line, while the dashed lines represent the results expected with improvements to the multiplexer and TES-multiplexer coupling including slowing the TES pulse risetimes, reducing multiplexer SQUID amplifier noise, and optimizing the coupling between the TESs and the first-stage SQUIDs

each TES signal must be filtered; multiplexing unfiltered signals will degrade the SNR. In addition, TES detectors have significant dark-current noise so multiplexing schemes must avoid adding noise from different detectors to maintain the SNR.

Both TDM and FDM have significant technical challenges, and currently only small arrays of multiplexers have been demonstrated for X-ray applications; because of the fast pulses and required energy resolution of X-ray detectors, the development of TES multiplexers for X-ray applications lags that of multiplexers for arrays of sub-millimeter bolometers, for example. Doriese et al. (2004) present results of a four-pixel columnar array read out through a single amplifier channel by using a TDM SQUID multiplexer. These pixels showed a 6.94 eV FWHM energy resolution at 6 keV with a 0.44 eV degradation in energy resolution from non-multiplexed operation. Figure 7.6 shows the energy resolution measured by Doriese et al. (2004) as a function of number of columnar pixels read out by the experimentally tested multiplexer (solid) and the expected resolution given various improvements in multiplexer and device design. The improvements include slowing the TES pulse rise times by altering the TES circuitry, reducing multiplexer SQUID amplifier noise, and optimizing the coupling between the TESs and the first-stage SQUIDs. The energy degradation occurs when the time between measurements of a pixel is either too long or too short. At the

longer timescales the pulse rise is not sampled well enough, causing degradation, and at short timescales there is contamination from switching transients that have not fully decayed. These authors predict that straightforward improvements of this multiplexer scheme will allow multiplexing of 32-pixel linear arrays, allowing a square kilopixel readout, with only 0.1 eV energy-resolution degradation to the $\sim$ 6 eV-resolution TESs; they also estimate that with substantial upgrades the TDM architecture can multiplex kilopixel arrays with 100 μs response times and 2 eV energy resolution at 6 keV.

In FDM the implementation of LC filters with the required frequencies ($f = \frac{1}{\sqrt{LC}}$) involve large capacitors ($\gtrsim$ 10 nF) that are difficult to fabricate. Other challenges involve developing SQUIDs that can handle the combined carrier signals from all multiplexed pixels and attaining high SQUID slew rates so that the SQUIDs are able to respond effectively to high bias frequencies, which will be required to ensure the requisite bandwidth needed to preserve interesting fast-time information. Lanting et al. (2005) demonstrate an eight-channel frequency-domain readout multiplexer and provide a discussion of associated challenges.

This discussion of the TES multiplexer development shows that arrays of large, close-packed arrays of these complex detectors is difficult. Promising efforts are underway to build the kilopixel scale multiplexing capabilities needed for *Constellation-X* with TDM architectures, but there is no guarantee that this technology will improve to meet mission requirements for coming X-ray survey missions. Since the TDM technology is being pushed to attain the 32-pixel columnar multiplexing, it is easy to imagine that increasing this number by an order of magnitude (or two) will be prohibitive.

7.4.2.2 Microwave Frequency-Domain Multiplexing

SQUID multiplexing via microwave frequency readout electronics is a novel multiplexing technique being pursued to increase microcalorimeter pixel count to the 100 $\times$ 100 level and eventually the 1000 $\times$ 1000 level (Irwin & Lehnert 2004; Lehnert et al. 2006). These schemes employ thin-film superconducting microwave resonators, similar to those employed in MKIDs (see § 8.2), as SQUID readouts. The resonators are coupled to a transmission line, and the reflected or transmitted signal at the resonance frequency of each resonator is monitored via microwave signals on the transmission line. The amplitude and phase shifts associated with each resonator are a function of the magnetic flux in the SQUID, or the

current through its input coil. In these microwave SQUID multiplexer schemes each TES has its own power-efficient SQUID that is coupled to a microwave resonator. A low-pass filter is fabricated between the TES and the SQUID so that the low-frequency detector signal can pass from the TES to the SQUID, while the microwave carrier signal from the resonator cannot pass to the TES.

These multiplexers are in an early stage of development and currently a simple 32-pixel SQUID multiplexer (without TESs) has been demonstrated. To avoid energy-resolution degradation there must be either a reduction in the phase noise of the microwave resonators or an implementation of a flux modulation scheme (Lehnert et al. 2006). Current estimates predict that microwave SQUID multiplexers will have the ability to multiplex 10000 SQUIDs. We note that, like in time-division multiplexing, this approach still requires one SQUID per TES.

7.4.3 Distributed Pixel Approaches

7.4.3.1 Position Sensitive TES (PoST) Microcalorimeter Arrays

One approach that is being pursued to extend the field of view of upcoming missions is through Position Sensitive TES (PoST) microcalorimeter arrays. PoSTs contain the same general microcalorimeter components discussed in § 7.3.3, but in this case a chain of absorbers is measured by two TESs. A temperature increase in an absorber causes heat flow towards both ends of the chain, where the TESs sense the signal. The incident photon position along the absorber chain is determined by the pulse-height ratio between the signals measured in the two TESs while the total energy of the photon is given by the sum of the pulse heights.

PoST arrays hold promise to increase microcalorimeter array sizes and to push to smaller pixel size ($\lesssim$ 0.25 mm), but there are several potential drawbacks to this method. For example, by employing a chain of absorbers the total absorber heat capacity has increased. The whole sensitivity of the detector depends on keeping a low heat capacity in the absorber so that the deposited photon energy will produce a large signal. Measuring a chain of absorbers with $C_{\rm tot} = N_{\rm abs}C_{\rm abs}$ will degrade the energy resolution. If large, distributed arrays of TES-based microcalorimeters are achieved, there is still a significant challenge in the SQUID readout electronics, although it will be easier than if each absorber required its

own TES.

7.4.3.2 STJ-Based Strip Detectors

STJs are arranged in a strip-detector architecture to provide arrays of distributed X-ray pixels. A strip detector employs a long strip of superconducting material as the photon absorber with quasiparticle sensors attached at either end. This scheme allows precise position determination by measuring the ratio of number of quasiparticles sensed at each end and energy determination from the sum of the two signals. Strip detectors with two STJs as the sensing elements were first demonstrated by Kraus et al. (1989) using a Sn absorber. Subsequent experiments at Yale using Ta absorbers and Al STJs have resulted in an energy resolution of 13 eV at 6 keV. Using these distributed strips as the sensing element increases array sizes but there are still challenges in the STJ readout of many strips. Each strip itself is limited in length to $\lesssim 1$ mm due to constraints placed by the diffusion length of the absorber.

7.5 Motivation for MKIDs Development

Microwave kinetic inductance detectors are a relatively novel superconducting detector technology that hold promise to fulfill the design requirements for future X-ray space missions due to the ease in which they are multiplexed. MKIDs have a wide variety of applications in photon and particle detection: MKID schemes are currently being developed for submillimeter, optical/UV, X-ray, and dark matter (WIMP) detection. By using high quality factor resonant circuits, MKIDs are able to employ passive frequency-domain multiplexing through a single pair of coaxial cables and a single HEMT (high electron mobility transistor). Instead of requiring cryogenic preamplifiers and individual wiring at each detector element, MKIDs are capacitively coupled to a single microwave transmission line allowing hundreds or more detectors to be simultaneously monitored using a single input and single output coaxial cable. Each detector is both excited and read out with a sine wave at its unique microwave frequency. Room-temperature readout electronics both generate the comb of microwave frequencies necessary to excite each detector and separate the output signals from the individual resonators. Array readouts comprised of synthesizers and quadrature receivers at room temperature are readily implemented using miniature, low-

cost, low-power integrated circuits developed for wireless communication (Day et al. 2003) and prototype array readouts have already been demonstrated in the laboratory (Mazin et al. 2006b). A single HEMT is capable of amplifying the output signatures for as many as $10^3 - 10^4$ detectors, depending on the amplifier bandwidth and the frequency spacing of the detectors. The limit to the detector frequency spacing will depend on lithographic tolerances, which will affect the uncertainty in the resonance frequencies with-respect-to the design resonance frequencies, and the resonator quality factors.

In summary, all of the other multiplexing techniques described earlier in this chapter have limitations. In contrast, MKID multiplexing is easily achievable using room-temperature electronics that have been developed for the wireless communications industry. By leveraging off of this huge industrial technology effort, these readout electronics will continue to improve, completely independent of MKID development. The electronics and multiplexing technologies for the other detectors are being developed specifically for these astronomical applications, instead of having the complementary commercial drivers.

This thesis focuses on the demonstration of MKIDs in an architecture suitable for efficient coupling to X-rays. These results should allow the development of large-format X-ray imaging spectrometers. This work is also a precursor to both optical/UV photon-counting imaging spectrometers — by using a similar detector architecture with increased MKID responsivity (e.g., thinner films) the detector results presented here can be extended to detect the lower-energy UV and optical photons — and large-area WIMP detectors.

Chapter 8

Microwave Kinetic Inductance Detectors and the Strip Detector Architecture

8.1 Basic Electrodynamics of Superconductors

For a superconducting metal below a critical temperature, T_c, electrons with opposite wavevectors (**k, -k**) and opposite spins ($\uparrow$, $\downarrow$) are bound into pairs called Cooper pairs, with binding energy $2\Delta(T)$:

$$2\Delta(0) \approx 3.5 k_B T_c \ , \tag{8.1}$$

where $\Delta(T) \approx \Delta(0)$ for $T \ll T_c$. At $T = 0$ the superconductor will be in its Bardeen-Cooper-Schrieffer (BCS) groundstate (Bardeen et al. 1957), with all free electrons bound in Cooper pairs. For finite temperatures ($0 < T < T_c$), some fraction of the Cooper pairs will be broken into single-electron quasiparticles. According to BCS theory the number density of thermally excited quasiparticles for $T \ll T_c$ is given by:

$$n_{th}(T) = 2N_o\sqrt{2\pi k_B T \Delta(0)}\ e^{-\frac{\Delta(0)}{k_B T}} \ , \tag{8.2}$$

where N_o is the single-spin density of electron states at the Fermi energy of the superconductor. The value of N_o for aluminum is 1.72×10^{10} μm^{-3} eV^{-1} (McMillan 1968). Energy deposited by photons with $h\nu > 2\Delta$ can also generate quasiparticles: it is this population of $N_{qp} \sim h\nu/\Delta$ excess quasiparticles that we detect using MKIDs. Details of photon-induced quasiparticle generation are described in more detail in § 8.5.1.1. Note that I refer to the

number density of excess quasiparticles as n_{qp} and the number of excess quasiparticles as N_{qp}.

The presence of bound electron pairs causes a supercondcutor to have zero DC resistance; however, the behavior is not the same with AC currents. Because the Cooper pairs can be accelerated by an electric field applied close to the superconductor's surface, energy storage in the form of kinetic energy is allowed. Magnetic fields can penetrate a superconductor a short distance ($\sim$ 50 nm), and energy can similarly be stored in the magnetic field of the superconductor. These combined effects cause a superconductor to have a surface inductance $L_s = \mu_o \lambda$, where λ is the penetration depth. This surface inductance caused by accelerated Cooper pairs gives rise to the phrase "kinetic inductance." The total surface impedance Z_s is

$$Z_s = R_s + i\omega L_s \ , \tag{8.3}$$

where R_s is the frequency-dependent surface resistance caused by the presence of quasiparticles. When T is far below T_c the magnitude of the surface impedance is dominated by the surface inductance, since the number of thermally excited quasiparticles is small and thus $R_s \ll \omega L_s$.

MKIDs operate by sensitively measuring changes in the surface impedance of thin superconducting films due to photon-excited excess quasiparticles. To understand MKID operation we must first understand how the surface impedance depends on the number density of excited quasiparticles.

Theory developed by Mattis & Bardeen (1958) provides analytical expressions for the complex conductivity, $\sigma = \sigma_1 - i\sigma_2$, of superconductors. Approximations to the Mattis-Bardeen equations for the real (σ_1) and imaginary (σ_2) parts of the complex conductivity are presented in (Mazin 2004):

$$\frac{\sigma_2}{\sigma_n} \approx \frac{\pi \Delta(T)}{\hbar\omega}[1 - 2e^{-\frac{\Delta(0)}{k_B T}} e^{-\frac{\hbar\omega}{2k_B T}} I_o(\hbar\omega/2k_B T)] \ , \tag{8.4}$$

$$\frac{\sigma_1}{\sigma_n} \approx \frac{2\Delta(T)}{\hbar\omega} e^{-\frac{\Delta(0)}{k_B T}} K_o(\hbar\omega/2k_B T)[2\sinh(\hbar\omega/2k_B T)] \ , \tag{8.5}$$

where $I_o(x)$ and $K_o(x)$ are modified Bessel functions of the first and second kind, respec-

tively. These approximations are valid in the limit $k_B T \ll \Delta(0),\ \hbar\omega \ll \Delta(0)$.

A common approximation in which we can relate the surface impedance to the equations for σ_1 and σ_2 is called the extreme anomalous limit.[1] This approximation is valid when the London penetration depth $\lambda_L = (mc^2/4\pi ne^2)^{1/2}$ is much smaller than the coherence length, ξ_o, where $\xi_o = \hbar v_f/\pi\Delta(0)$, v_f is the Fermi velocity of the electrons, m is the electron mass, e is the electron charge, and n is the density of conduction electrons. The devices explored in this thesis are firmly in this limit: we use aluminum films that are several hundred nanometers thick (see § 8.5.1.4), in which the coherence length, $\xi_o \approx 1600$ nm, is of order a hundred times larger than the London penetration depth, $\lambda_L = 16$ nm. Z_s is approximated by:

$$Z_s = i\frac{\sqrt{3}\omega\mu_o}{2}\left(\frac{3\pi\omega}{4v_f\lambda_L^2}\frac{\sigma_1 - i\sigma_2}{\sigma_n}\right)^{-\frac{1}{3}} . \tag{8.6}$$

For small changes in n_{qp} at low temperature, the change in Z_s can be approximated as $\delta Z_s/Z_s = -\delta\sigma/3\sigma$. Day et al. (2003) provide an equation for the change in Z_s in terms of a change in the number of quasiparticles, which is derived using the fact that for small changes in n_{qp} the additional quasiparticles can be related to a change in temperature.

$$\frac{\delta Z_s}{Z_s} \approx \delta n_{qp}\frac{\partial Z_s}{\partial n_{qp}} , \tag{8.7}$$

$$\frac{\delta L_s}{L_s} \approx \frac{\delta N_{qp}}{2N_o\Delta} , \tag{8.8}$$

where the quantity $N_o\Delta$ can be thought of as the fraction of Cooper pairs within $1\cdot\Delta$ of the Fermi surface, such that the fractional change in surface inductance is proportional to the fraction of these Cooper pairs that are broken. Although the changes in the surface impedance caused by single-photon absorption will be small, they can be sensitively measured by a resonant circuit.

[1] The other common limit is the 'dirty' or local limit. In the 'dirty' limit the electron mean free path is much less than the magnetic penetration depth and the coherence length

8.2 MKIDs with Quarter-Wave Resonators

The resonant circuit we use to monitor the change in surface impedance consists of a planar quarter-wavelength transmission-line resonator. The MKID resonators are made of a thin film of superconducting material deposited on top of a crystalline substrate and patterned with microfabrication techniques (see Figure 8.2.2). Section 8.2.2 addresses the practical implementation of the resonators; here we first present the basic theory of quarter-wave transmission-line resonators and describe their response to excess quasiparticles.

A quarter-wave transmission-line resonator consists of a quarter-wavelength length of a transmission line, with one end capacitively coupled to a feed line and the other end shorted to ground. Figure 8.1b shows the approximate equivalent electrical circuit for the quarter-wavelength resonator. In reality, there will also be a small surface-resistance component to account for the resistive loss due to the excited quasiparticles. Changes in L_s affect the resonance frequency and changes in R_s affects the width and depth of the resonance, which can be measured as changes of the complex phase and amplitude of a microwave signal transmitted through the circuit. These effects are shown in Figure 8.1c-d.

8.2.1 Response to Quasiparticles

As depicted in Figure 8.1, an incoming photon will change the surface impedance of the resonator because of the increase in the number of quasiparticles, resulting in a change in the frequency and width of the resonance, denoted by f_o and Q^{-1}. The quality factor, Q, is defined as $Q = f_o\tau_{1/e}/2\pi$, where $\tau_{1/e}$ is the time it takes for the energy in the resonator to decay to $1/e$ of its initial value. For small signals the fraction of broken Cooper pairs is small so we regard $\partial Z_s/\partial n_{qp}$ as a constant. The frequency as a function of the number density of quasiparticles can be expressed as follows:

$$f(t) = f_{\mathrm{o}} + \frac{\partial f}{\partial n_{qp}}\, n_{qp}(t)\ , \tag{8.9}$$

$$\frac{\partial f}{\partial n_{qp}} \approx -f_{\mathrm{o}}\,\frac{0.5\alpha}{2N_o\Delta}\ , \tag{8.10}$$

where α is the kinetic inductance fraction given by L_{kin}/L_{total} (Day et al. 2003). This equation for $f(t)$ assumes that the resonator responds instantaneously with respect to the

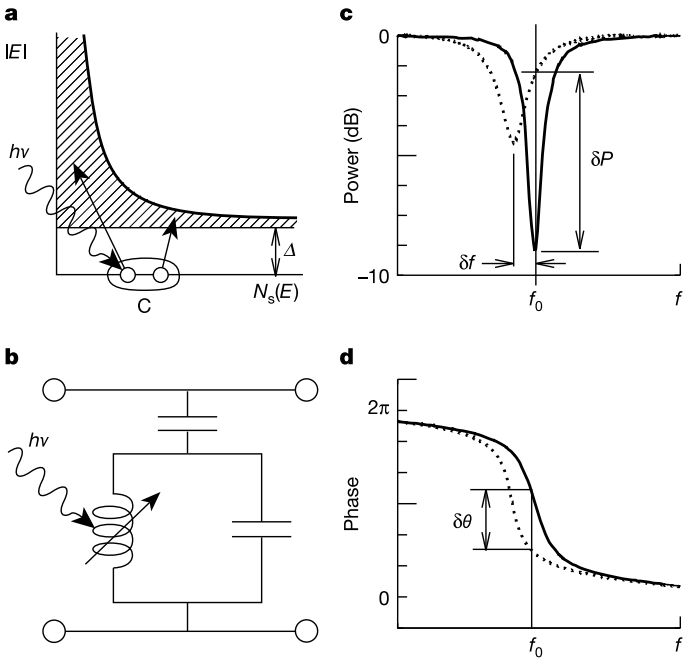

Figure 8.1 These diagrams, from Day et al. (2003), illustrate the MKID detection scheme. **a**, A superconductor cooled to $T \ll T_c$ has a finite energy gap Δ. A photon of energy $h\nu > 2\Delta$ absorbed into the superconductor will break Cooper pairs and create quasiparticles. **b**, Equivalent resonator circuit, depicted as parallel LC circuit capacitively coupled to a through line. The incoming photon will produce quasiparticles and increase the (mainly inductive) surface impedance of the film. **c**, On resonance the LC circuit loads the through line and produces a dip in the transmission. The increase in quasiparticles causes the resonance frequency to down-shift and the shape of the resonance to broaden. Thus the microwave probe signal's amplitude changes, producing a change in power δP, as does the phase (**d**)

characteristic time it take for the quasiparticle density to change. The formula will thus be valid for the slow decay of the quasiparticle pulse, since the lifetime of the quasiparticles is of order 100 μs and the ring-down time of the resonator itself is of order 1 μs. Let $A \equiv 0.5\alpha/2N_o\Delta$ and define the frequency change, $\delta f(t) = f(t) - f_o$. Using these definitions, the frequency shift is described by the simple relation:

$$\frac{\delta f(t)}{f_o} = -A\, n_{qp}(t) \qquad (A > 0)\ . \tag{8.11}$$

In addition to the shift to lower frequency that accompanies the creation of excess quasiparticles, there is also a shift to lower quality factor (or larger resonance width). The resonator starts with an initial total quality factor (Q_o) determined by the coupling strength (Q_c) and the internal Q at the base temperature with no excess quasiparticles (Q_{i_o}).

$$Q_o = \frac{Q_{i_o} Q_c}{Q_{i_o} + Q_c} \tag{8.12}$$

The quality factor responds to excess quasiparticles as follows:

$$\frac{1}{Q(t)} = \frac{1}{Q_o} + \frac{\partial Q^{-1}}{\partial n_{qp}}\, n_{qp}(t)\ , \tag{8.13}$$

$$\frac{\partial Q^{-1}}{\partial n_{qp}} \approx \frac{\alpha}{2\pi\, N_o \sqrt{\hbar f_o \Delta}}\ . \tag{8.14}$$

Using the definitions $B \equiv \partial Q^{-1}/\partial n_{qp}$ and $\delta Q^{-1} = Q^{-1}(t) - Q_o^{-1}$ we find that:

$$\delta Q^{-1} = B\, n_{qp}(t) \qquad (B > 0)\ . \tag{8.15}$$

Combining this expression for δQ^{-1} with Equation 8.11 for the fractional frequency change and eliminating $n_{qp}(t)$ we are able to compare the relative change in f_o to the change in Q:

$$\left| \frac{\frac{\delta f(t)}{f_o}}{\delta Q^{-1}} \right| = \frac{A}{B}\ . \tag{8.16}$$

For thick ($\sim 200 - 300$ nm) aluminum the relevant parameters are:

$$\alpha \approx 0.06\ , \qquad N_o = 1.72 \times 10^{10} \mathrm{eV}^{-1} \mu\mathrm{m}^{-3}\ , \qquad \Delta = 0.171 \times 10^{-3} \mathrm{eV},$$

which gives $A = 5.1 \times 10^{-9}$ μm^{-3}, $B = 8.5 \times 10^{-9}$ μm^{-3}, and $\frac{A}{B} \sim 0.6$. For a 6 keV photon absorbed directly into the sensitive end of a 300 nm aluminum MKID with design resonance frequency $f_o = 6$ GHz and $Q_o = 10^5$, the fractional frequency change will be $\sim 5 \times 10^{-6}$ and the change in Q^{-1} will be $\sim 9 \times 10^{-6}$. The fractional frequency change can be compared to the resonance width, $Q^{-1} = 10^{-5}$, which shows that the frequency signal is significant as compared to the resonance width, and the photon will be easily detected.

Measurement of the resonator parameters is performed by monitoring the forward scattering matrix of the microwave-frequency transmission through the feedline, denoted S_{21}. See § 9.3 for details on the readout. Starting with the equations of Day (2002), a portion of which is presented in Mazin (2004), we relate the behavior of $S_{21}(t)$ to the change in Q and f_o. At $f = f_o$ the transmission magnitude past the resonator is at the minimum of the resonance dip:

$$S_{21}^{min}(t=0) = \frac{Q_c}{Q_i(0) + Q_c} \ , \tag{8.17}$$

where Q_c is the coupling Q and Q_i is the internal Q ($Q_o = 1/(Q_c^{-1} + Q_i(0)^{-1})$ is the initial total loaded Q). After energy deposition, the transmission minimum changes as the internal Q changes:

$$S_{21}^{min}(t) = \frac{Q_c}{Q_i(t) + Q_c} \ . \tag{8.18}$$

When driving the resonator at f_o, the original resonance frequency, the transmission as a function of time is described as:

$$S_{21}(t) = \frac{S_{21}^{min}(t) + 2iQ_o\frac{\delta f(t)}{f_o}}{1 + 2iQ_o\frac{\delta f(t)}{f_o}} \ , \tag{8.19}$$

$$S_{21}(t) = \frac{S_{21}^{min}(t) - 1}{1 + 2iQ_o\frac{\delta f(t)}{f_o}} + 1 \ , \tag{8.20}$$

$$S_{21}(t) - 1 = \frac{S_{21}^{min}(t) - 1}{1 + 2iQ_o\frac{\delta f(t)}{f_o}} \ . \tag{8.21}$$

This expression for $(S_{21}(t) - 1)$ may be written:

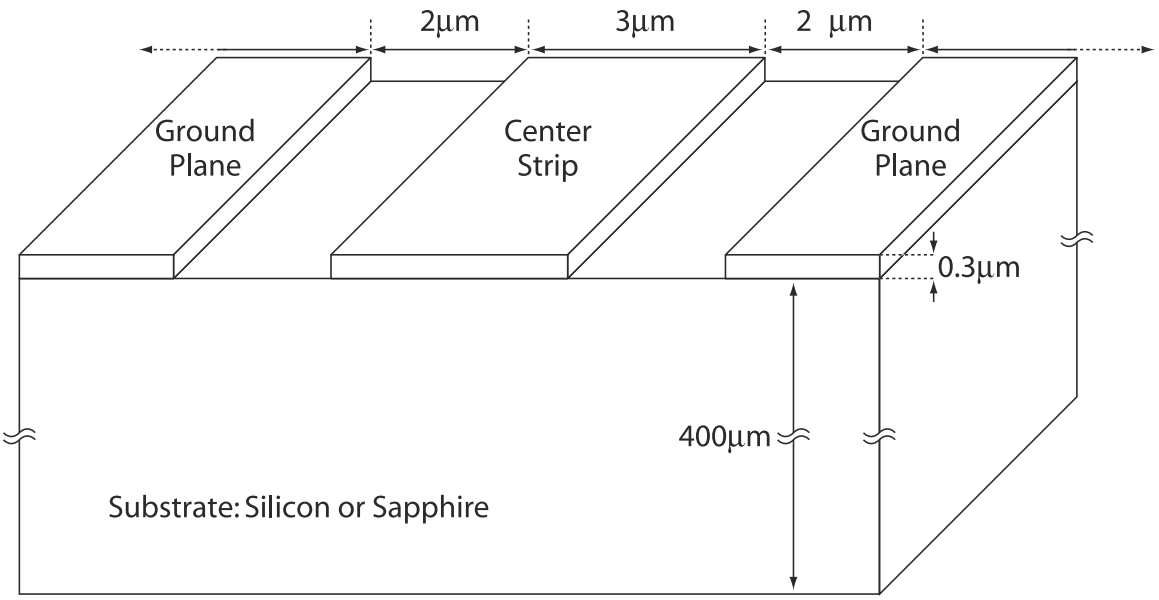

Figure 8.2 Cross-section of a coplanar-waveguide resonator. The widths and thickness drawn here are typical of those used in the X-ray strip detectors. The length of the CPW will be of order 1000-times longer than the section shown here (~ 5000 μm long)

$$S_{21}(t) - 1 = -\frac{Q(t)}{Q_c}\left[1 + \left(\frac{2\delta f Q_o}{f_o}\right)^2\right]^{-\frac{1}{2}} e^{i\phi} \ , \tag{8.22}$$

where

$$\phi = \arctan\left(\frac{2\delta f(t) Q_o}{f_o}\right) \ , \tag{8.23}$$

and $1/Q(t) = (1/Q_c + 1/Q_i(t))$.

The phase change as a function of number of excess quasiparticles is given by $\partial\theta/\partial N_{qp}$, which is calculated using the Mattis-Bardeen equations for the complex conductivity, and approximations thereof. Mazin (2004) provides the approximate, empirically determined formula that holds for small phase changes:

$$\frac{\partial\theta}{\partial N_{qp}} = 1.63 \times 10^{-7} \ \frac{\alpha Q}{V} \ , \tag{8.24}$$

where $\partial\theta/\partial N_{qp}$ is in units of radians per quasiparticle and V is in μm^3.

8.2.2 Practical Implementation and Design

For practical implementation of both the feedline and the resonators we use coplanar waveguides (CPWs), illustrated in Figure 8.2.2. Mazin (2004) includes a lengthy discussion of resonator design; here I highlight a few key points.

- The length of the CPW will determine the resonance frequency of the resonator. Mazin (2004) presents this approximate equation for a quarter-wavelength resonator:

$$l = \frac{c}{4 f_o} \sqrt{\frac{2}{1+\epsilon}} \,, \tag{8.25}$$

  where l is the length of the resonator and ϵ is the dielectric constant of the substrate. For our typical substrates of silicon or sapphire, $\epsilon \sim 10$. To design a resonator for $f_o = 6$ GHz the length will be ~ 5000 μm.

- The geometry of the CPW can be changed. We chose resonators with a 3 μm center strip and a 2 μm gap between the center strip and the ground plane (a '3-2' resonator), which gives a $Z_o \sim 50$ Ω transmission line when fabricated on silicon or sapphire. This geometry is easily attained: the minimum feature size is large compared to the current fabrication capabilities. See Figure 8.2.2.

- The volume of the resonator must be chosen with care. Given a particular CPW geometry, e.g., a 3-2 resonator, it is the thickness of the film that can be adjusted to change the response. The volume of the resonator affects the surface impedance of the resonator in two dominant ways. First, the Z_s depends on the number density of quasiparticles so that for a given deposited photon energy the number density of quasiparticles scales inversely with the volume. The volume must be such that the photon pulse is detectable with a high SNR, but not so large that the pulse saturates the resonator. In addition, the film thickness will affect α, the kinetic inductance fraction, since for a thinner film $L_{\rm kin}/L_{\rm tot}$ will increase. Measurements of α as a function of film thickness are given in Gao et al. (2006).

- We must ensure that the radiation loss from the resonator is not apprecable. Vayonakis (2001) calculates the radiation loss analytically. For a $f_o = 6$ GHz, 3-2 resonator, the radiation Q is $Q_{\rm rad} \sim 6 \times 10^6$, which is sufficiently high for our purposes (radiation

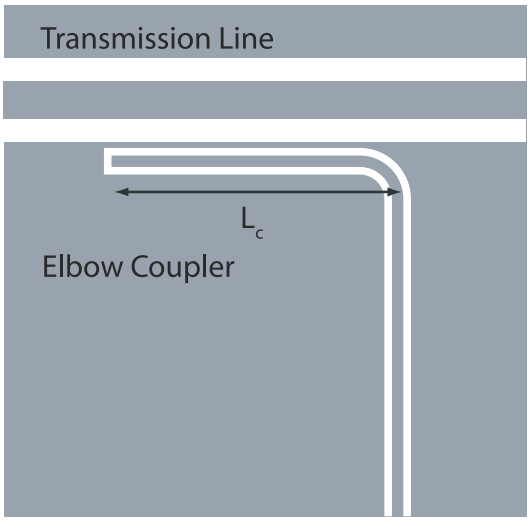

Figure 8.3 An illustration of an elbow coupler. The long arm parallel to the transmission line provides capacative coupling between the transmission line and the MKID, which extends off the bottom of the diagram. The longer the arm of the elbow coupler, the lower the Q_c

losses will not degrade our resonator Qs).

- To couple the resonator to the CPW feedline, the group designed the 'elbow coupler,' as described in Mazin (2004), § 3.3.2. Figure 8.3 shows the layout. With this design the coupling Q can be computed from $|S_{13}|$, the transmission from the feed line through the coupler: $Q_c = \frac{\pi}{2|S_{13}|^2}$. Mazin (2004) presents the equation for $|S_{13}|$ as a function of resonance frequency and elbow-coupler length: $|S_{13}| = AfL_c + BL_c + Cf + D$, where $A = 4.01 \times 10^{-6}$, $B = -3.35 \times 10^{-8}$ μm^{-1}, $C = 2.60 \times 10^{-5}$ GHz^{-1}, and $D = 4.55 \times 10^{-8}$.

8.2.2.1 Resonator Fabrication

MKIDs are fabricated using optical lithographic techniques. The devices are fabricated at the Microdevices Laboratory at JPL. For one-layer, CPW-based MKIDs a superconducting film is deposited onto a 3″- or 4″-diameter wafer. The wafer substrate is typically high-resistivity silicon or sapphire. MKIDs may be made from a variety of superconductors, but the resonator materials most often used at Caltech/JPL are aluminum and niobium. All resonators presented in this thesis are aluminum CPWs with 3 μm center strip and 2 μm gap to the ground plane ('3-2'). The on-chip transmission line is also a CPW that typically has a 10 μm center strip and a 6 μm gap. The aluminum films are deposited by

DC magnetron sputtering in a ultrahigh vacuum deposition system and the CPW gaps are etched in a parallel plate reactive ion etcher (RIE) using trichloride and chlorine gas.

8.3 Basic Quasiparticle Generation and Decay in MKIDs

The MKID signal we measure is related to the number density of excess quasiparticles as a function of time. When a photon is absorbed with $E_{photon} > 2\Delta$ and excess quasiparticles are created, the quasiparticles decay almost exponentially back to the equilibrium level set by the detector's operating temperature. The time constant for this decay is of order $\tau \sim 100$ μs in aluminum, for example. Self recombination also plays a role in the process; § 8.5.1.1 examines this process in more detail. The differential equation that controls the decay of the excess quasiparticles is given by:

$$\frac{\partial n_{qp}}{\partial t} = -\frac{n_{qp}}{\tau_{qp}} - R n_{qp}^2, \tag{8.26}$$

where n_{qp} is the number of excess quasiparticles, τ_{qp} is the time constant for the exponential decay, and R is the recombination constant.

To solve this equation analytically we make the substitution $n_{qp} = 1/X$, such that

$$\frac{\partial n_{qp}}{\partial t} = -\frac{1}{X^2}\frac{\partial X}{\partial t} \ . \tag{8.27}$$

The differential equation then looks like:

$$\frac{\partial X}{\partial t} - \frac{X}{\tau_{qp}} = R \ , \tag{8.28}$$

and the solution is: $X = C \ \exp(+\frac{t}{\tau_{qp}}) - R\tau_{qp}$, where C is the constant of integration. Substituting back ($X = 1/n_{qp}$):

$$n_{qp}(t) = \frac{1}{C\, e^{\frac{t}{\tau_{qp}}} - R\tau_{qp}} \ . \tag{8.29}$$

The initial condition ($t = 0$) is set by the incoming photon energy, the superconductor parameter, and the volume: $n_{qp}(0) = \eta h\nu/\Delta V$. These parameters determine the integration constant, C:

$$C = \frac{V\Delta}{\eta h\nu} + R\,\tau_{qp}\ , \tag{8.30}$$

and finally,

$$n_{qp}(t) = \frac{1}{\left(\frac{V\Delta}{\eta h\nu} + R\,\tau_{qp}\right) e^{\frac{t}{\tau_{qp}}} - R\,\tau_{qp}}\ . \tag{8.31}$$

This equation (8.31) assumes an infinitely fast resonator response time (and no diffusion). If we want to include a finite response time (pulse rise time $\tau_{\rm rise}$) then we have:

$$n_{qp}(t) = \left(\frac{1}{\left(\frac{V\Delta}{\eta h\nu} + R\,\tau_{qp}\right) e^{\frac{t}{\tau_{qp}}} - R\,\tau_{qp}}\right)\left(1 - e^{-\frac{t}{\tau_{\rm rise}}}\right)\ . \tag{8.32}$$

For our detectors the response time of the resonator is fast compared to other timescales.

Longer quasiparticle lifetimes will give a lower noise equivalent power (NEP; see § 8.4.1). Kaplan et al. (1976) gives an expression for the quasiparticle lifetime, τ_{qp}:

$$\frac{1}{\tau_{qp}} = \frac{\pi^{\frac{1}{2}}}{\tau_o}\left(\frac{2\Delta}{k_B T_c}\right)^{\frac{5}{2}}\left(\frac{T}{T_c}\right)^{\frac{1}{2}}\ e^{-\frac{\Delta}{k_B T}}\ , \tag{8.33}$$

where τ_o relates to the electron–phonon coupling strength and is material dependent. For aluminum $\tau_o = 4.38 \times 10^{-7}$ s (Kaplan et al. 1976).

8.4 Noise Processes in MKIDs

Here we explore the processes that impact the noise floor of MKIDs in the absence of photon-produced excess quasiparticles. We focus on generation-recombination noise ("g-r noise") and the excess phase noise related to two-level-system fluctuations in (or around) the substrate. Fano noise and other noise processes associated with statistical fluctuations of excess-quasiparticle generation are discussed in § 8.5.1.3.

8.4.1 Generation-Recombination Noise

Fluctuations in the random generation and recombination of thermal quasiparticles are a fundamental noise source for MKIDs. These processes create fluctuations in the mean number N of quasiparticles in the detector of order $\sqrt{2N_{qp}}$. However, the thermal quasiparticles obey a distribution proportional to $e^{-\Delta/kT}$. The resulting sensitivity limit, given by the

noise equivalent power (NEP), is NEP $= (2\Delta/\eta)\sqrt{N_{qp}/\tau_{qp}}$, where η is the quantum efficiency and τ_{qp} is the quasiparticle lifetime (Sergeev et al. 2002). By operating the detector at $T \ll T_c$ where the quasiparticle density is very low, it should be possible to build a sensitive detector with excellent energy resolution. Also, choosing a superconductor with a long recombination time will lower the g-r noise. Considering only the g-r noise, aluminum MKIDs at $T \lesssim 100$ mK will have a NEP of 10^{-20} W Hz$^{-1/2}$ (Mazin 2004).

8.4.2 Excess Phase Noise

Experimental results from many MKIDs, made primarily of either Al ($T_c \approx 1.2$ K) or Nb ($T_c \approx 9.2$ K) show a large excess noise that is entirely in the phase direction, equivalent to a jitter in the resonance frequency; excess amplitude fluctuations are not observed at the sensitivity of the measurements (Gao et al. 2007). The excess phase noise exhibits a strong dependence on the microwave drive power inside the resonator, $P_{\rm int}$, as well as a material dependence (the noise seems to depend on both superconductor material and substrate material or at least the superconductor-substrate combination). For all of the superconductor-substrate combinations that have been tested $S_{\delta f}/f_o^2 \propto P_{\rm int}^{-1/2}$, where $S_{\delta f}/f_o^2 \propto P_{\rm int}^{-1/2}$ is the power spectral density (PSD) of the frequency noise, normalized by the resonance frequency. Figure 8.4 shows this $P_{\rm int}^{-1/2}$ scaling for various material combinations. The behavior of this excess noise is indicative of fluctuating two-level systems (TLS) in the dielectric material, although the exact location of the TLSs have not been determined (e.g., are the TLSs in the bulk substrate, its exposed surface, the interface between the superconductor and the substrate, or in an oxide layer on the surface of the superconductor?). Gao et al. (2007) and Kumar et al. (2007, in preparation) contain detailed discussions of the phase noise. The impact of this noise on our experimental results will be discussed in more detail in Chapter 11.

8.5 Coupling to X-ray Photons

For X-ray astrophysics applications our detectors must have both an efficient way to absorb X-rays and a sensitive method for measuring the energy deposited by the photon. These two requirements can place contradictory constraints on the design of the detector: for high X-ray stopping power a thick film is required, but the MKID responsivity decreases as the

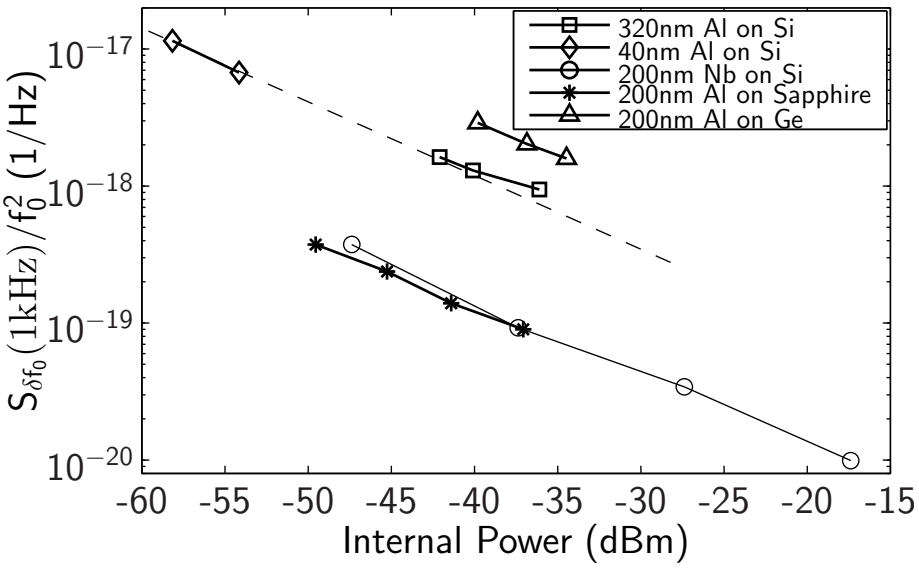

Figure 8.4 Fractional frequency noise at $\nu = 1$ kHz, illustrating the power and material dependence of MKID excess phase noise, from Gao et al. (2007). The phase noise PSD is converted to fractional frequency noise so that resonators with different f_o and Qs can be compared: $S_{\delta f}(\nu)/f_o^2 = S_{\mathrm{ph}}/4Q^2$, where S_{ph} is the PSD of the phase noise

volume increases. For example, an aluminum film would need to be 50 μm thick to stop 75% of 6 keV photons. Not only is this thickness not readily achievable with standard thin-film deposition and lithography techniques, but it would be an extremely low-responsivity quasiparticle sensor, unable to sensitively measure the energy deposited into the aluminum.

Another constraint on practical MKID-based photon-counting detectors derives from the position-dependent response to a localized population of excess quasiparticles along the length of the resonator. The voltage and current distributions of a quarter-wave resonator vary along the length of the resonator, which result in changes in kinetic inductance that depend upon where along the resonator the quasiparticles are created (Zmuidzinas 2002; Mazin 2004). The MKID response to a localized injection of quasiparticles ends up being weighted by the square of the current distribution in the resonator for resonators with lengths longer than the diffusion length of quasiparticles. For aluminum MKIDs there is thus degeneracy between the absorption location and deposited energy for direct photon absorptions in the MKID itself; a simple method for avoiding this degeneracy is to constrain incident quasiparticles to enter the MKID at the sensitive, high current end of the resonator.

As discussed in the previous chapter, the X-ray astrophysical applications also require a design that is readily scalable to large array sizes.

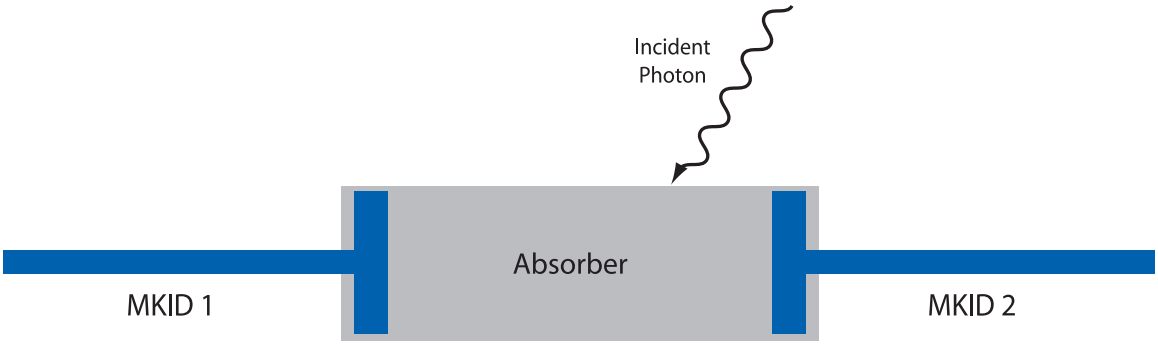

Figure 8.5 A cartoon of a strip detector, as viewed from above. Incoming photons are incident upon the superconducting absorber, where they break Cooper pairs and excite quasiparticles. MKIDs attached at each end of the strip sense the quasiparticles created by the photon absorption

8.5.1 The Strip Detector Architecture

Strip detectors have a design architecture that enables efficient coupling of photon energy to the MKID for optical, UV, and X-ray applications. This approach employs a long strip of superconducting material as the photon absorber with MKIDs attached at either end as quasiparticle sensors; Figure 8.5 illustrates the basic layout of a strip detector. A major driver for this architecture is the ability to separate the absorbing and sensing elements so that the device can attain a high absorption efficiency and also have the ability to sensitively measure the quasiparticle excitations. Quasiparticles generated by an incident photon diffuse to the ends of the strip absorber and into the shorted, sensitive end of each MKID, circumventing the position-dependent response of the resonator.

In the following sections we introduce the device physics relevant to strip detectors. Similar strip-detector designs have been successfully employed for imaging X-ray detectors with STJs as the quasiparticle sensing elements (e.g., Kraus et al. 1989; Li 2002); much of the strip-detector discussion builds on this previous work.

8.5.1.1 Quasiparticle Generation and Dynamics in the Absorber

Photon Absorption and Energy Down-Conversion The detection process begins when a photon is absorbed in the superconducting strip, ionizing an atom and releasing an inner-shell electron. Rapid energy down-conversion proceeds, dominated by electron–electron interactions that consist of secondary ionization and cascade plasmon emission. Kozorezov et al. (2000) calculate that the energy down-conversion from a 10 keV photoelectron

to a thermal population of electrons and holes at a characteristic energy of $E_1 \sim 1$ eV takes less than 0.1 ps. This first stage of energy down-conversion ends when the electron–phonon inelastic scattering rate becomes larger than that of the electron–electron interactions.

Following the initial cascade, a second stage of down-conversion begins as the electrons at $E \sim E_1$ emit a large number of Debye-energy phonons (Ω_D). The end state of the cascade is a narrow phonon distribution peaked at the Debye energy (the "phonon bubble"). At this point the energy of the phonon distribution exceeds that of the electron distribution by a large factor because the Debye-phonon lifetime, the time it takes for a Debye-energy phonon to break a Cooper pair, is much longer than the duration of this $E_1 \rightarrow \Omega_D$ cascade.

Since the Debye energy of superconductors is higher than the superconducting gap energy, phonons with $\Omega > 2\Delta$ can break quasiparticles; it is this stage of energy down-conversion that controls the quasiparticle generation. Kozorezov et al. (2000) study this stage of energy down-conversion in detail to better understand the quasiparticle signals sensed by STJs. Following the emission of the phonon bubble, a phonon down-conversion process follows, with the kinetics of the system of interacting quasiparticles and phonons fully controlled by the slowly varying phonon distribution. Electronic excitations act as mediating agents, modifying the phonon spectral distribution and leaving the energy of the phonon system approximately unchanged. Once the characteristic energy of the phonons falls below a characteristic energy Ω_1, the temporal variations are controlled by the slower electronic transitions, while on this time scale the phonons break Cooper pairs instantly. This passage across the Ω_1 threshold results predominantly in a population of long-lived electronic excitations, while the phonons act as the mediators for quasiparticle energy down-conversion. As long as $\Omega_1 \gg \Delta$, intensive generation of lower energy quasiparticles take place. Quasiparticles of $E > 3\Delta$ can emit phonons of $\Omega > 2\Delta$; this second down-conversion stage ends when the quasiparticle population enters the spectral range below 3Δ, at which point the generation of excess quasiparticles stops since the mean quasiparticle energy has reached the threshold for producing 2Δ phonons and there are no more 2Δ phonons left in the system to break extra Cooper pairs.

Combined, the first two stages of energy down-conversion last only a few nanoseconds, while the third and final stage lasts much longer, of order $1 - 1000$ μs for superconducting materials considered for MKIDs. This final stage is the 'operational' stage for MKIDs, where there is a mixed distribution of quasiparticles and phonons that remains strongly non-

equilibrium; the quasiparticles reside near the the superconducting gap edge with $E \sim \Delta$. It is this final stage that determines the output of the MKIDs.

The number of quasiparticles produced by a photon absorption is of order E_{photon}/Δ. The actual number is scaled down due to the fact that a large percentage of the photon energy stays in the phonon system. Kurakado (1982) finds that $\sim 60\%$ of the photon energy deposited in Ta eventually resides in the quasiparticle system, while $\sim 40\%$ stays in the phonon system, indicating an efficiency of $\eta = 0.6$ and number of quasiparticles N_{qp}:

$$N_{qp} = \frac{\eta h\nu}{\Delta} = \frac{h\nu}{\varepsilon\Delta} \ . \tag{8.34}$$

For a 6 keV photon incident upon Ta, with $\Delta_{Ta} \sim 0.67$ meV, there will be 5.1 million quasiparticles. The average effective energy required for creation of one quasiparticle is thus $\varepsilon = 1.67\Delta$. Kozorezov et al. (2000) also calculate that for small gap superconductors, including Al, $\varepsilon = 1.67$.

Quasiparticle Dynamics and Recombination At this stage, recombination into Cooper pairs is the dominant quasiparticle loss process. At cases close to equilibrium, the excess quasiparticle population adds a small perturbation on the thermal quasiparticle population, given in Equation 8.2. In this case the excess quasiparticles recombine with thermal quasiparticles, and the recombination can be described by:

$$\frac{\partial n_{qp}}{\partial t} = -\frac{n_{qp}}{\tau_{qp}} \ , \tag{8.35}$$

where τ_{qp} is the recombination time in the absorber material; the theoretical value for τ_{qp} is given in Equation 8.33. This τ_{qp} depends on $n_{th}(T)$ and was calculated by Kaplan et al. (1976) for many of the low-temperature superconductors. When the number of excess quasiparticles is comparable or large compared to $n_{th}(T)$, then the quasiparticle recombination is also affected by self recombination. The number of ways to pair-wise combine N quasiparticles is $N(N-1)/2$, which is approximately $N^2/2$ for large N. This decay can be described by this non-linear differential equation:

$$\frac{\partial n_{qp}}{\partial t} = -\frac{n_{qp}}{\tau} - R n_{qp}^2 \ , \tag{8.36}$$

where R is the recombination rate. The Rn_{qp}^2 term does not include the factor of 1/2 from

the combinatorics since each self-recombination event removes two excess quasiparticles. With the addition of diffusion in the absorber strip the equation becomes

$$\frac{\partial n_{qp}}{\partial t} = D\nabla^2 n_{qp} - \frac{n_{qp}}{\tau_{qp}} - R n_{qp}^2 \ , \tag{8.37}$$

where D is the diffusion constant in the absorber. The values of D, τ_{qp}, and R will affect the design requirements of a practical strip detector. The length of the absorber will be limited to $l \sim \sqrt{D\tau_{qp}}$, the quasiparticle mean free path, so that the quasiparticle losses in the strip are minimal.

Phonon Trapping As the quasiparticles diffuse some are lost to recombination. However, the effective quasiparticle lifetime is lengthened by phonon trapping. Since the Debye energy of superconductors is higher than the the superconducting gap energy, phonons with $\Omega > 2\Delta$ emitted by the quasiparticle recombination can break another Cooper pair. Rothwarf & Taylor (1967) first identified that these recombination phonons cannot be ignored when calculating quasiparticle lifetimes. For the near-equilibrium case where $n_{\rm excess}/n_{th} \ll 1$ Rothwarf & Taylor (1967) find that the experimental recombination time, τ_{exp} is enhanced by a factor of $\tau_\gamma\beta/2$:

$$\tau_{exp} = \tau_R(1 + \frac{\tau_\gamma\beta}{2}) \ . \tag{8.38}$$

Here τ_R is the intrinsic recombination time if phonon trapping is not considered while β is the transition probability for pair breaking by $\Omega > 2\Delta$ phonons and τ_γ^{-1} is the net transition probability for the productive phonons to be lost by processes other than pair production. The dominant phonon loss mechanism for Ta and Al will be loss to the substrate, as anharmonic decay of phonons will be slow compared to the pair-breaking time (e.g., Gaidis 1994, and references therein). Gray (1971) finds an expression for f, the fraction of productive phonons that escape from the superconductor into the substrate, where $f \equiv (1 + \frac{1}{2}\beta\tau_\gamma)^{-1}$ is the factor that acts to enhance the observed recombination time:[2] $\tau_{exp} = \tau_R/f$. The fraction of escaping phonons depends on the acoustic match between the superconductor and the substrate.

[2] In Gray (1971) there is a typo in the definition of f just after equation 13; the sentence should read "and make the obvious identification $f \equiv (1 + \frac{1}{2}\beta\tau_\gamma)$." The equation given in the text is missing the factor of 1/2

$$f = \frac{\alpha\Lambda}{4d}[1 - \alpha\sum_{n=1}^{\infty}(1-\alpha)^n \Xi\{(n+1)\frac{2d}{\Lambda}\}] \ , \tag{8.39}$$

where

$$\Xi(\xi) = (1-\xi)e^{-\xi} - \xi^2 E_i(-\xi) \ . \tag{8.40}$$

Here α is the average phonon transmission coefficient (see Little 1959), Λ is the phonon mean free path against pair breaking, and d is the thickness of the film. E_i is the exponential integral. The expression for f is complicated, but the leading term that dominates[3] f, $\alpha\Lambda/4d$, can be qualitatively examined. In this case the effective recombination time will increase as the film thickness increases or the phonon mean-free path decreases, since either of these changes will result in more of a chance for a phonon to break a Cooper pair before escaping to the substrate. Similarly, the lifetime will be enhanced as α decreases and it becomes more likely that a phonon will be reflected off of the absorber-substrate interface and back into the superconductor.

8.5.1.2 Quasiparticle Trapping

When a quasiparticle reaches an end of the strip it can diffuse into the MKID. By choosing the MKID material such that $\Delta_{\mathrm{MKID}} < \Delta_{\mathrm{absorber}}$ we can trap the quasiparticles in the MKID material so that they stay in the MKID, where they are sensed, instead of diffusing back into the absorber, where they may recombine before being sensed. Figure 8.6 presents a cartoon showing the trapping scheme. Quasiparticles at the gap edge of the absorber ($S_1,\ \Delta_1$) diffuse into the MKID ($S_2,\ \Delta_2$; $\Delta_2 < \Delta_1$), where they emit a phonon and fall in energy to the gap edge of the trap, creating an energy barrier that keeps the quasiparticle from diffusing back into the absorber. To design an effective quasiparticle trap we must consider that the quasiparticle scattering time depends on the difference in the gap energies of the two superconductors.

Booth (1987) first proposed the use of quasiparticle trapping for STJ-based applications. The author points out that the trapping time depends on the scattering time τ_s for a quasiparticle of energy $E > \Delta_2$ in S_2 to relax close to the gap edge. Kaplan et al. (1976) cal-

[3] In experiments using Ta (600 nm) and Al (200 nm) films on SiO_2, Gaidis (1994) finds that the corrections to this leading term are less than 10%

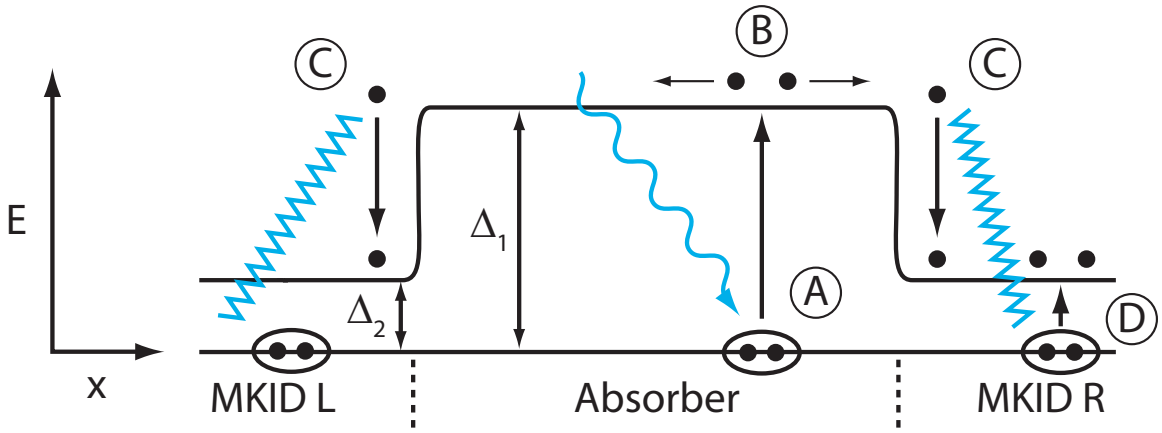

Figure 8.6 An illustration of quasiparticle dynamics and trapping in a strip detector, with a superconducting absorber of gap Δ_1 and MKIDs with a lower gap energy, Δ_2. The incoming photon is shown as a blue sinusoidal line, while the relaxation phonons are represented with blue triangle waves. **A:** Energy deposited by an incoming photon breaks Cooper pairs in the absorber. **B:** The resulting quasiparticles reside at $E \approx \Delta_1$, where they diffuse toward the ends of the strip. **C:** When a quasiparticle diffuses into the MKID it emits a phonon and drops in energy to near Δ_2, where it is trapped in the lower-gap superconductor. **D:** If $\Delta_1 > 3\Delta_2$ some relaxation phonons are able to break a Cooper pair in the MKID, causing quasiparticle multiplication

culates the scattering time: $\tau_s \propto \tau_o \left(\frac{\Delta_2}{E-\Delta_2}\right)^3$; in this case the incoming quasiparticle energy E is approximately equal to the energy gap of the absorber (Δ_1) so that:

$$\tau_s \propto \tau_o \left(\frac{\Delta_2}{\Delta_1 - \Delta_2}\right)^3 . \tag{8.41}$$

Additionally, Booth (1987) points out that for cases where $\Delta_1 > 3\Delta_2$, the relaxation scattering process can cause quasiparticle multiplication in the trap, as the relaxation phonons have the energy to break Cooper pairs in the trap. Approximating the relaxation-phonon energy distribution as flat from 0 to $(\Delta_1 - \Delta_2)$, Booth (1987) estimates that the multiplication factor per relaxation stage is $1 + 2\eta$, where

$$\eta = [1 - \left(\frac{2\Delta_2}{\Delta_1 - \Delta_2}\right)]. \tag{8.42}$$

For superconductor combinations with large Δ_1/Δ_2 there will be several stages in the down-conversion process. The quasiparticle multiplication factor will also be affected by the thickness of the trapping film with respect to the phonon mean free path for pair breaking.

8.5.1.3 Energy Resolution

The fundamental energy-resolution limit of a strip detector is set by the statistical fluctuations in the initial number of quasiparticles. For incident photon energy E the variance in the energy measurement is:

$$\sigma_E^2 = FN_{qp} = F\varepsilon E \ . \tag{8.43}$$

The Fano factor, $F \simeq 0.2$ (Fano 1947), describes the deviation from Poissonian statistics in the case of a complete energy absorption in the superconductor owing to the strong interaction between phonons and quasiparticles during the energy down-conversion process. The Fano factor was found to be 0.2 for both Sn (Kurakado 1982) and Nb (Rando et al. 1992). The FWHM uncertainty in the energy will be $2.355 \times \sigma_E$:

$$R = \frac{E_{photon}}{\Delta E_{FWHM}} = \frac{1}{2.355}\sqrt{\frac{E_{photon}}{F\varepsilon}} \ . \tag{8.44}$$

Additional statistical fluctuations on the number of quasiparticles gained by trapping multiplication will add to the overall energy uncertainty. Segall (2000) derives an expression for this additional energy uncertainty, ΔE_{multi}, assuming that every quasiparticle in the absorber has the same probability to break a Cooper pair and create two additional quasiparticles in the trap.

$$\Delta E_{multi} = 2.355\sqrt{\varepsilon E\frac{(\kappa-1)(3-\kappa)}{\kappa^2}} \ , \tag{8.45}$$

where $\kappa = 2 + 2N_{multi}/N_{qp}$, N_{multi} is the average number of quasiparticles that will break Cooper pairs in the trap, and N_{qp} is the initial number of quasiparticles created in the absorber. Friedrich (1997), for example, finds a quasiparticle multiplication factor of ≈ 1.6, implying that $\kappa \approx 2.6$.

Beyond these fundamental limits, the energy resolution can be degraded by noise in the MKIDs, like the excess phase noise described in § 8.4. Also, in Appendix B we discuss potential degradation because of statistical fluctuations on the number of productive phonons lost into the substrate during the initial energy down-conversion.

8.5.1.4 Materials Choices

For our strip detectors we use a tantalum absorber and aluminum MKIDs, typically on epitaxial sapphire substrates. In the conclusion, Chapter 12, we address the relative merits of other superconducting materials as well as practical array architectures.

Tantalum ($Z = 73$) is a dense material that provides a high X-ray stopping power: 1 μm (2 μm) of tantalum will stop 44% (69%) of 6 keV photons. Tantalum is also known to hold up well under thermal cycling. Beyond the high stopping power, Ta is an attractive material because it efficiently converts the absorbed energy into quasiparticles, with $\eta = 0.6$, and, theoretically, has low quasiparticle recombination losses (the theoretical lifetime at 300 mK is $\tau > 1$ ms) and significant quasiparticle lifetime enhancement due to phonon trapping. In addition the Ta gap is such that the energy-resolution limit due to Fano noise is ~ 2 eV at 6 keV: sufficient to meet design requirements for next-generation X-ray missions. The Ta gap is ~ 4 times that of Al, providing efficient quasiparticle trapping and quasiparticle multiplication. Ta is also a good choice for optical/UV applications because it has a $\sim 60\%$ quantum efficiency at those wavelengths. To make large, imaging spectrometers we would like these absorbing strips to be long, but we also need the majority of quasiparticles to reach the sensors before recombining. The length of the absorbing strip must be limited to less than the diffusion length of the material, thus using epitaxial Ta (see § 9.4) with a long recombination time and a high diffusion constant will increase the achievable strip length.

Aluminum is a widely used material for microdevidces that is relatively easy to work with. The Al transition temperature is $T_c \approx 1.2$ K, so operating at $T/T_c \lesssim 10$ is possible using a standard dilution refrigerator. Aluminum has a long recombination time that can lead to devices with lower NEPs. Also, using Al MKIDs, we are able to leverage off of the large effort using Al MKIDs at Caltech/JPL. In addition, Ta/Al strip detectors have been experimentally verified by groups using STJs.

The Yale group that has made X-ray detectors with Ta strips and STJs has made a concerted effort to use a substrate with a poor acoustic match to Ta. This ensures that phonons incident on the interface will tend to be reflected back into the Ta instead of escaping to the substrate. They choose passivated silicon substrates for this reason.[4] At this stage of our development we are continuing with the crystalline sapphire wafers while we

[4]The Yale group (e.g., Gaidis 1994; Li 2002) uses passivated silicon substrates. A typical substrate of this sort is a silicon wafer with a thin layer (300 nm) of SiO_2 deposited on the surface

first establish basic experimental goals. At a later stage we can explore different substrates or fabrication on a membrane to improve the phonon trapping.

Chapter 9

Experimental Setup and Strip Detector Device Fabrication

Both the MKID testing setup and fabrication processes are interesting and involved subjects in their own right. Appendix A reviews the basics of dilution-refrigerator operational principles; here we describe generally the dilution refrigerator used for strip detector testing. Section 9.2 details microwave-wiring changes and other recent refrigerator upgrades we made to allow efficient MKID-based strip-detector testing. The room-temperature and 4 K electronics are described briefly in § 9.3, while the fabrication procedure for strip detectors is reported in § 9.4. Descriptions of the strip-detector mask sets are given in § 9.4.1. and a list of fabrication parameters of key strip-detector wafers is included in § 9.4.2.

9.1 Cryogenics: Achieving $T \lesssim 100$ mK

Liquid helium is commonly used to achieve low temperatures for cryogenic experiments. ^{4}He, the common isotope of helium has a boiling point of 4.2 K. By pumping on a bath of liquid ^{4}He its vapor pressure will be decreased and the temperature will drop accordingly. Temperatures down to ~ 1 K can be achieved easily by pumping on ^{4}He.

At a given temperature, ^{3}He, a helium isotope that naturally occurs at an abundance of only 10^{-4} times that of ^{4}He, has a higher vapor pressure than that of ^{4}He. By pumping on a bath of ^{3}He, rather than ^{4}He, temperatures of ~ 300 mK can be achieved. Many low-temperature experiments that require base temperatures near ~ 300 mK rely on refrigerators that operate upon simple ^{3}He pumping schemes.

For experiments that need even lower base temperatures, ^{3}He refrigerators are not suf-

ficient. The most common refrigerator used for achieving low base temperatures is the dilution refrigerator. Common dilution refrigerators reach base temperatures of 10–100 mK. These refrigerators rely not on liquid ^{4}He or ^{3}He alone, but on a mixture of the two liquids. A discussion of the phase behavior of ^{3}He – ^{4}He mixtures and of general dilution refrigerator design is presented in Appendix A.

9.1.1 The Oxford 25 MKIDs Testbed

The dilution refrigerator used for MKIDs testing is an Oxford 25, acquired in 2001. This refrigerator has a cooling power of 25 μW at 100 mK. Upon installation in the MKIDs laboratory in Bridge, the refrigerator reached a base temperature of 23 mK during its trial cooldown — this was before any additional wiring, etc., was installed.

9.2 Testbed and Wiring Upgrades

For initial MKID testing the refrigerator was outfitted with coaxial cables; a low-temperature, high electron mobility (HEMT) amplifier; precise low-temperature thermometry; and a gold-plated copper attachment to the mixing chamber for sample-box mounting. These installations were performed primarily by Ben Mazin and Peter Mason and are described in Mazin (2004).

This initial setup allowed measurement of one MKID chip per cooldown, since it included one input and one output coaxial line that was used to bring microwave signals to and from the device's transmission line, respectively. In this section we describe testbed upgrades that were implemented to increase the testing efficiency by allowing testing of two device chips per cooldown. In addition, we lowered the base temperature of the refrigerator by $\gtrsim 30$ mK and eliminated heating from the HEMTs. These upgrades also added fiber-optic cables from room temperature to the cold stage to allow the strip detectors to be illuminated with UV or IR photons.

In early 2006 we performed the following upgrades:

- Removed all coaxial wiring from room temperature to the sample stage.
- Installed new mount at the top of the refrigerator that contains four male SMA connectors on the top and a fiber-optic vacuum feed through on either side.

- Added an additional HEMT amplifier, provided by Sandy Weintraub's group in the Electrical Engineering Department.

- Installed four stainless steel, semirigid, 0.085″ coaxial cables. One end of each cable was attached to the K-connectors at the top of the refrigerator while the other end was connected to either a SMA bulkhead installed in a gold-coated copper block at 4 K (input cables) or to the output of a HEMT amplifier (output cables).

- Installed four 0.86 mm niobium coax to take the input signal for each channel from the 4-K bulkhead to the mixing-chamber stage and to take the output signal for each channel from the mixing-chamber stage to the input of each HEMT amplifier. The dielectric in this coax is polytetrafluoroethylene (PTFE, commonly known by its DuPont brand name, Teflon).

- Installed a UV fiber from room temperature to the cold stage as well as an IR fiber. The IR fiber broke shortly after installation and was not replaced.

These upgrades doubled the testing efficiency by allowing us to test two device chips per cooldown. However, after these upgrades there was significant unwanted heating that prevented the refrigerator from reaching its base temperature ($T \gtrsim 270$ mK). To test the origin of the heating we removed the four niobium coaxial cables that connect the 4-K stage to the mixing-chamber stage. With these cables removed the refrigerator reached $T \lesssim 90$ mK,[1] indicating that heat had been traveling down the niobium coaxial cables and loading the cold stage. On this run we did note heating at the mixing chamber when either HEMT amplifier was powered, indicating that we were suffering from some radiative heating from the amplifiers.

To address these heat-load issues we made several additional changes, completed on $\sim$ 4/24/2006:

- **Heatsinking Clamps on Nb Coax:** We made copper clamps to heat sink the Nb coax to the still and 1K pot, which have enormous cooling powers compared to the cooling power at the mixing chamber. Gold leaf (thin sheets of gold) was added

[1] The $T \lesssim 90$ mK was measured with the Oxford-installed mixing chamber thermometer, which is less reliable and less well calibrated as compared to the Lakeshore thermometer. The mixing chamber thermometer typically shows a temperature ~ 20 mK higher than the actual temperature (at low temperature) but because the Lakeshore thermometer was broken during this run we only had the mixing-chamber-thermometer reading

between the clamps and Nb coax to make sure the fit was snug, ensuring a good thermal link. We used high quality copper speaker wire to connect the clamps to the still and 1K pot stages.

- **HEMT Radiative Shield:** We soldered together a copper scrim stop box and painted the inside of the box with blackened epoxy (by weight: Sycast 2850 = 1, catalyst = 0.07, lamp black = 0.07). The box was placed over the HEMTs and screwed to the brass plate at the top of the inner vacuum chamber to provide proper heat sinking to 4 K.

- **Better Strap from 4-K Bulkhead to 4-K Plate:** We added a new gold-plated copper strap that connects the brass 4 K plate (top of vacuum can) to the bulkhead where the four stainless steel coax from room temperature attach to the two Nb coax to the cold stage and two copper cables to the HEMT outputs. The new strap is much heftier — thicker and wider metal, and better attached at the 4 K brass plate and the bulkhead. This change was an effort to ensure that the heat from room temperature was dumped to the 4 K stage.

- **Grease Beneath HEMT** We added a small amount of grease between the HEMTs and the gold-plated copper plate they screw to, and between that plate and the 4K brass plate. Ensuring that the HEMTs are well sunk to 4 K is important to limit the heat transmitted between the HEMT and mixing chamber stage.

- **New Lakeshore Thermometer** Finally, we added a new Lakeshore thermometer at the device stage, replacing an identical one that was broken. We ran the thermometer wire up from the M/C through the heat exchanger, heat sunk it at the still and then soldered to the 25-pin crimp connector for connection to room temperature.

With these changes in place our base temperature was 69 mK — much improved from the previous performance. It is likely that the heatsinking of the Nb coax with the clamps made the primary difference. Although the base temperature was lower than required for our testing purposes there was still significant heating when a HEMT was powered on. For example, on our first cooldown with the new setup, the temperature rose from 69 mK to 87 mK with the Channel 1 HEMT drain current (I_{d1}) at 10 mA and from 69 mK to $\gtrsim$ 100 mK at $I_{d2} = 10$ mA. This HEMT power level is sufficient for making measurements,

but the HEMT gain would be improved by operating at levels closer to $I_d = 20$ mA. At this higher end of the HEMT power range the heating was unsatisfactory. Additionally, over the handful of cooldowns that followed, the amp heating not only became worse overall, but it also was unpredictable. For example, on one run Channel 2 would rise to ~ 200 mK with even low HEMT powers ($I_{d2} \sim 4$ mA) and Channel 1 would be much better, and then the following run Channel 1 would be more affected by HEMT-caused heating and Channel 2 would be better. In an effort to combat this amp heating we changed the way that the HEMTs were attached to the 4K plate, in an effort to ensure that the HEMTs were not self heating to much more that ~ 10 K. This change did not have any noticeable effect on the amp-heating problem, although since the amp heating effects had been unpredictable, we were not able to say definitively if the change in HEMT mounting had any effect on the problem. The behavior limited us to measuring devices at minimum temperatures that varied between ~ 120 and 250 mK from late April 2006 until early September 2006 (Run 86).

During late summer of 2006 we became concerned that we needed to be more careful with the magnetic shielding in our experimental setup. This caused us to consider different locations for the magnetic shielding; we settled on adding a still shield made of Cryoperm. Not only would this capped, cylindrical compartment reduce the Earth's magnetic field by a factor of ~ 500, but it would act to shield the mixing chamber stage from seeing 4K surfaces, instead seeing only the still shield surface at $T \sim 700$ mK. Most dilution refrigerators that frequently reach $\lesssim 50$ mK have a still shield to reduce any heat load incident upon the cold stage due to 4 K radiation. In mid-October, 2006 we made the following changes to the testbed:

- **Cryoperm Still Shield:** Added a Cryoperm still shield.
- **Replaced Nb Coax with NbTi Coax:** Removed the thin (0.86 mm diameter) niobium coax from the experiment. Replaced all wiring from 4 K to the mixing chamber with $0.085''$ niobium-titanium coax.
- **Broke Coax at Still Stage:** Instead of having a continuous cable from the 4K stage to the mixing chamber stage for each of the input and output microwave signals, we instead broke each of the four wires at the bulkhead attached to the still stage. By breaking these wires we were more certain that any heat from 4 K (or residual

$T > 4$ K) was dumped to the still, with its large cooling power, instead of being dumped at the cold stage.

These changes had an immediate positive impact upon the experiment. After installing the still shield and the new NbTi coaxial cables, the base temperature is now always near 50 mK and there is no heating from the HEMT amplifiers, even at high powers ($I_d \sim 20$ mA).

Twice during the lifetime of our dilution refrigerator we have experienced first an unrecognized partial block of the dilution system and then, on the following cooldown, a full block of the system. When the dilution unit is blocked the ^{3}He -^{4}He mixture is unable to circulate, and thus the refrigerator cannot reach temperatures below about 1 K. Throughput tests at 4 K, 77 K, and room temperature all indicated a full blockage of the circulation system. Each time the refrigerator experienced a full block, it seems, in retrospect, to have been partially blocked on the previous run, experiencing a higher-than-normal base temperature.

The obvious place in our system that would have a block is the thermal impedance between the heat exchanger and the mixing chamber. At this part of the circulation system there is a thin capillary inside a slightly larger-diameter tube. The capillary acts to increase the thermal impedance of the line. To clear the blockage we split the impedance line. The first time, in late August 2006, prior to Run 85, we split it, checked for a block using the leak detector, and found that it was no longer blocked. We assumed that by splitting the impedance we had allowed the impeding particle to escape. We then closed the impedance using a new indium seal. In this case we used 0.040″-diameter indium for the seal, as is used to seal the inner vacuum chamber. On 1/5/2007 the refrigerator blocked again. Because the refrigerator blocked only four months after the first blockage we were more careful to pull out the entire capillary and clean the entire region as best we could. We then resealed using our smaller-gauge indium. Additionally, on 1/17/2007 we changed the ^{3}He-pump oil, to ensure that we were running with clean oil and oil filter that would not allow dirt into the circulation system. This was the first time that the ^{3}He pump oil had been changed since its delivery to Caltech. The refrigerator has been working fine since then.

A custom-designed ^{3}He -pump silencer was purchased from Great Southern Insulation, Corp., Fort Lauderdale, FL, and installed on 8/30/2006. The pump-box silencer includes a 120V AC exhaust fan with 230 cubic-feet-per-minute (CFM) capacity and an intake opening.

A similar intake fan can be installed in the intake opening if additional airflow is desired.

9.3 Electronics

The readout of MKIDs is performed by monitoring the feedline transmission using homodyne detection. The basic readout circuit diagram is shown in Figure 9.1. A microwave signal is generated by a synthesizer and then split in two: one copy is sent into the cryostat and onto the transmission line of the device chip, through a HEMT amplifier, and back out of the cryostat to an IQ mixer, where it is mixed with the original microwave signal. The IQ mixer actually contains a quadrature coupler (a 90-degree hybrid (3 dB) coupler), a splitter, and two mixers so that a copy of the incoming signal is mixed with the original microwave signal (producing output I) and another copy of the incoming signal is mixed with a 90-degree phase-shifted copy of the synthesized signal (producing output Q). The outputs I and Q represent the real and imaginary parts of the transmitted signal, and are easily converted to describe the the phase and amplitude of the signal transmitted past the resonator. Detailed descriptions of the readout components are described in Chapter 5 of Mazin (2004); the current readout electronics are nearly unchanged from those covered in that thesis.

Each resonator is carefully characterized by stepping the synthesized microwave frequency so that we probe several line widths around the resonance frequency while recording I and Q. These frequency sweeps are used to carefully fit for resonance frequencies and quality factors. Resonator noise is measured by driving a resonator at a given frequency (typically we are interested in the noise at the resonance frequency) and recording the output I and Q. The typical time-stream length for noise data is 10 s.

To monitor a resonator for response due to a transient event such as X-ray absorption, we drive the resonator at the resonance frequency and monitory I and Q. In practice our readout system includes two synthesizers and two IQ mixers to allow simultaneous monitoring of two resonators, as required for strip detector testing.

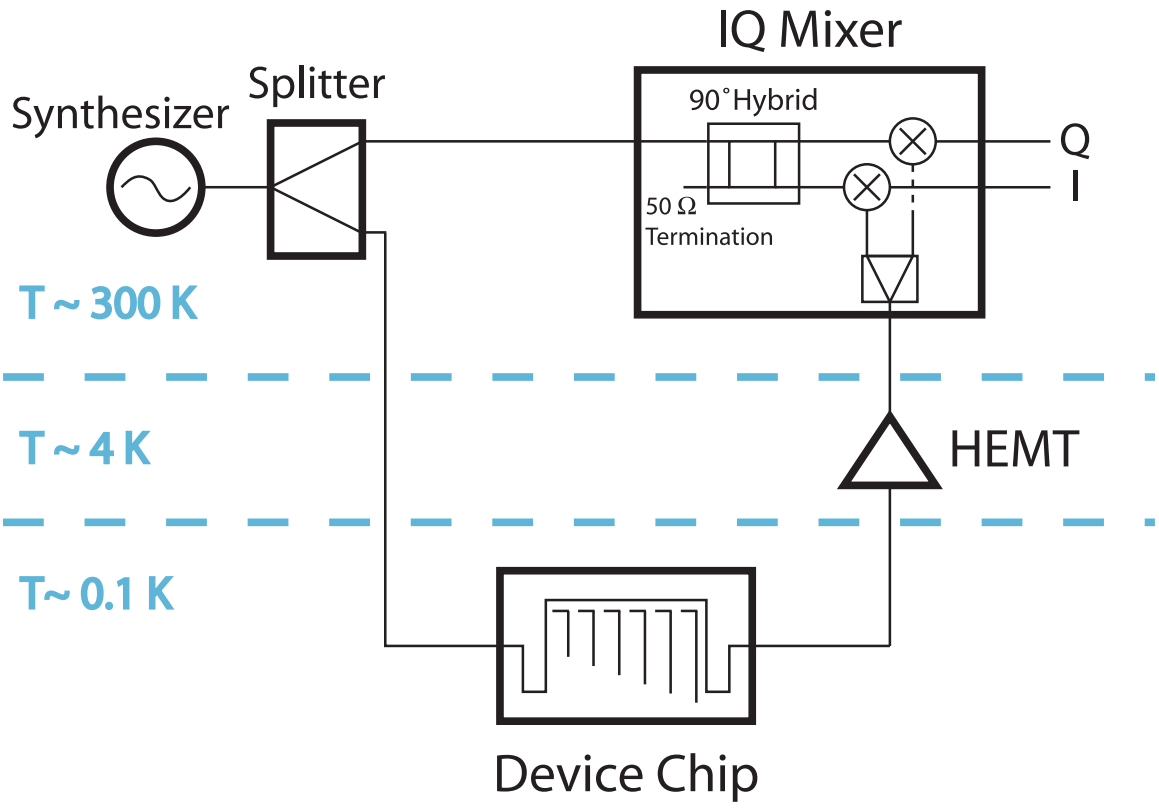

Figure 9.1 The homodyne detection scheme employed for MKID readout

9.4 Strip Detector Fabrication

Our current sample of strip detectors is almost entirely comprised of devices with aluminum MKIDs and tantalum absorbing strips fabricated by Bruce Bumble (JPL). Most of the devices are fabricated on R-plane sapphire substrates to allow epitaxial growth of α-phase (bcc) tantalum; bcc Ta is essential for achieving long diffusion lengths. Epitaxial Ta growth requires deposition at high temperature ($\sim 700B$ C), above the melting temperature of Al. In practice, this means that the Ta absorber must be deposited and etched before the aluminum layer for the resonator is deposited.

A typical strip-detector fabrication process is as follows. All metal depositions are carried out in a load-locked ultra high vacuum (UHV) sputtering system with a base pressure of 10^{-7} Pa. Epitaxial Ta films are typically deposited at 60 angstroms per minute with substrate temperature 700 C. The structures are patterned using a Canon 3000 stepping mask aligner with a Cymer 250 nm laser. The Ta film is reactive ion etched (RIE) and then the surface is solvent cleaned. The wafer is then argon ion cleaned in the Al deposition

system before the aluminum for the MKID blanket is deposited. RIE of aluminum is done with a mixture of 2:1, BCl_3:Cl_2 at a pressure of 4 Pa. A water rinse to remove chlorine compounds is followed by cleaning with acetone or isopropyl alcohol and NMP (N-methylpyrrolidone). After all processing is complete, a 3 μm layer of photoresist is applied to protect the devices during diamond-saw dicing of the sapphire. This resist remains until it is removed with acetone shortly before the chip is mounted in a sample box and wire bonded for installation in the dilution refrigerator.

We employ several variations on this typical procedure; two key additions that were implemented during the course of this work are:

1. **Sloping of Ta Edges:** After the tantalum is deposited, the photoresist is patterned, and the exposed areas of the resist are removed, the remaining photoresist is reflowed for 5 minutes at 130 C. The reflow is followed by RIE using a gas mixture of 30% O_2 in CF_4 at a pressure of 27 Pa. The resist is eroded back as the tantalum is removed, leaving nicely sloped Ta edges instead of the straight-walled edges that would be achieved without the resist reflow.

2. **Al Patch Layer:** After the Al is deposited and etched a lift-off Al patch layer is added at the Ta strip edge to ensure Al continuity as the Al climbs over the edge. The patch layer is made with a negative tone stencil of $\sim$ 600 nm photoresist. The patch areas are Ar ion cleaned *in situ* prior to sputter deposit of $\sim 200 - 400$ nm of Al. The excess aluminum is lifted off in solvents with the aid of ultrasonic scrubbing.

9.4.1 Masks for Strip Detector Testing

The strip detector mask sets, which are used as stencils for the patterning of structures during fabrication, were designed at Caltech using the Ledit software and made by an external company. Below we summarize relevant details of the three strip-detector masks used in fabricating the devices tested in this thesis. All of these masks employ quarter-wavelength resonators using a '3-2' CPW geometry and a '10-6' CPW feedline. The coupling between resonator and feedline was achieved with 'elbow' couplers unless otherwise noted.

9.4.1.1 Original Optical Mask (2003)

- An old mask, designed by Mazin and detailed in Chapter 3.7 of Mazin (2004).

- Some chips have only a single absorber strip (and two attached resonators).
- Mask contains 50 μm wide strips of length 600 μm, 1.0 mm, and 1.6 mm.
- Naming convention: S(center strip width in micron).(pixel size in micron)(T,H,B)-(Resonator 0 f_0 in GHz).(Resonator spacing in MHz)-(Design Q)-(Strip length in pixels)x(Number of strips)

9.4.1.2 X-Ray Test Mask (2005)

Here I summarize the seven chip designs on this mask, with label prefix 'J' for JPL.

- J-A: Ten 400 μm strips with resonators of various quality factors.
- J-AP: J-A design with Ta plugs for the ground connection between the Al and Ta to keep quasiparticles from diffusing from the Ta strip to the Al ground plane rather than into the center strip of the resonator.
- J-B: Various length strips ranging from 200 μm to 3200 μm.
- J-BP: J-B with Ta plugs for ground connection.
- J-C: Huge square pixel of dimensions 1000 μm $\times$ 1000 μm (never tested).
- J-D: Sixteen single pixel devices in which a single resonator is attached to a square absorber. Absorber sizes were 20 μm $\times$ 20 μm, 100 μm $\times$ 100μm, 240 μm $\times$ 240 μm. Additionally two grounded resonators (no absorber) were included for comparison. J-E: Test chip: 400 μm strips with distinct frequency spacing and two grounded resonators.

9.4.1.3 Lateral Trapping Mask (2006)

This final mask set has devices with label prefix 'LT' for 'lateral trapping.'

- Trapping bars that fan out for better lateral trapping.
- A test devices chip that includes RRR test structures and interface junction test structures (no MKIDs).

Table 9.1. Fabrication Parameters of Selected Wafers

Wafer ID	Al MKID			Al Plug	Ta Absorber					Sapphire
	thk [nm]	RRR	ρ ($T > T_c$) [$\mu\Omega$ cm]	thk [nm]	thk [nm]	T [C]	sloped? [y/n]	RRR	ρ ($T \gtrsim T_c$)[a] [$\mu\Omega$ cm]	Substrate
(1)	(2)	(3)	(4)	(5)	(6)	(7)	(8)	(9)	(10)	(11)
B060530.1	200	9.5	0.29	400	600	700	y	22.6	0.762	U. Carbide
B060816(A)	300	17.0	0.17	300	1000	700	y	53.0	0.533	U. Carbide
B060816(B)	300	17.0	0.17	···	1000	700	y	53.0	0.533	U. Carbide
B061003	200	11.0	0.25	···	600	700	y	32.7	0.764	Cryopolis

[a]The Ta resistivities we present are measured at ~ 5 K. The resistivity values are affected by the Ta edge sloping. The cross sections of the Ta test structures used for resistance measurement change shape with Ta thickness and thus direct comparisons of Ta resistivities from different wafers must be made with caution

- The LT-A device is the chip we tested the most often (and the device that the analysis presented in Chapter 11 is based on):
  - 35 μm wide strips with lengths 100, 200, 400, 800 μm, 35 μm $\times$35 μm single pixel, grounded resonator.
  - Two of each of the above, one with a low-Q_c resonator, one with a high-Q_c resonator. Design Q_cs were 25000 and 50000.
- Absorber-layer feedline and resonators on LT-B (e.g., Ta feedline and resonators), which is otherwise similar to the LT-A design.
- Strap couplers rather than elbow couplers on LT-B.
- The mask includes an array device that was never tested.

9.4.2 Fabrication parameters of selected wafers

Table 9.1 details the fabrication parameters and film resistances for three of the wafers that show promising results. Detector performance of devices from these wafers are analyzed in Chapter 11.

Chapter 10

Detector Testing: From Working Resonators to Working Strip Detectors

The path from a working resonator to a working strip detector was laced with unexpected challenges. At the start of this thesis project, the fabrication of simple single-layer aluminum MKIDs on silicon or sapphire substrates was becoming increasingly routine, at least given the talent and expertise of our colleagues at the JPL microdevices laboratory. For the X-ray/UV/optical-detector effort, the pressing challenge lay in developing strip detectors that would serve as an appropriate scheme to couple the incident photon energy to the MKIDs. Similar schemes had been developed for use with STJs (see § 7.4.3.2) but had not been successfully tested with MKIDs serving as the quasiparticle sensing element. An early strip detector design was pursued previous to my involvement in the project, which showed resonators that functioned as expected, but that had no quasiparticle connection between the absorber and the MKID[1] (for example, see Chapter 10 of Mazin 2004). In this Chapter we discuss the device testing during our exploration of MKID-based strip detectors.

10.1 Questions Addressed During Strip-Detector Testing

Before introducing our tests in detail, I highlight some of the question we sought to answer during the tests. First, we explored the quasiparticle connection between the absorber and MKIDS:

- **Al Step Coverage at the Edge of the Ta ('Step Coverage')**

[1] aside from one very early and unreproducible result; see § 10.3.1

  - **Thin Absorber:** If we make the Ta absorber thinner than the Al resonator layer will we avoid a step and thus have uninhibited quasiparticle transmission from Ta to Al?
  - **Liftoff Plug:** Will the addition of a liftoff plug of resonator material over the step help quasiparticle transmission?
  - **Sloped Edge of Absorber:** Will sloping the tantalum-absorber edges help with a quasiparticle connection?
  - **Layered Structure:** Can we put the resonator layer under the absorber, thus eliminating the step, and rely upon the gap difference between proximitized and unproximitized Al for quasiparticle trapping?

- **Quasiparticle Trapping**
  - **Vertical versus Lateral Trapping:** Will the quasiparticles trap in the resonator vertically or is lateral trapping necessary?

- **Physical Barrier at Interface**
  - **Oxide Tunnel Barrier:** Is there a tunnel barrier between the tantalum absorber and aluminum MKID, formed during the time that the fabrication setup requires a break in vacuum?

- **Bad Tantalum:** Is the tantalum diffusion so poor that the quasiparticles generated in the Ta recombine before they reach the resonators? Can we see coincident pulses from a strip if we have much shorter strips?

How do we improve the diffusion parameters of the strip detectors?

- **Higher RRR:** If we increase the residual resistivity ratio of the Ta will the diffusion length increase?

- **Thicker Tantalum:** Does the diffusion length increase as the absorber thickness increases?

- **Protect Ta During Al Etch:** Is the Ta getting damaged during the subsequent Al etching? If we protect the Ta with SiO_2 during Al etching will the diffusion parameters change?

- **Introduce an Acoustic Mismatch between Ta and Substrate:** Since the Ta and sapphire have a good acoustic match is the diffusion length suffering due to productive phonon loss into the substrate? Can we increase the diffusion length by introducing an acoustic mismatch at the interface?

- **Straight-walled Ta Along the Length of the Strip:** Does sloping of the Ta-strip edges cause enhanced quasiparticle recombination and thus a reduced diffusion length? Will straight-walled Ta strips exhibit better diffusion performance?

The following are tests performed to explore the noise performance of the detectors:

- **Single-Layer Resonator Noise versus Strip-Detector Resonator Noise:** Do the extra fabrication steps required to produce a strip detector cause an increase in phase noise as compared to a device from a wafer that has only undergone simple, single-layer fabrication steps (given fabrication on similar sapphire substrates)?

- **Sapphire versus Sapphire:** Have we been using 'bad' sapphire? Will switching brands improve our energy resolution by decreasing the resonator phase noise?

- **Chlorine in Etch:** Is the chlorine that is used in the resonator slot etching causing increased phase noise? If we ion mill instead of Cl-plasma etch the slots does the resonator noise improve?

10.2 Record of Testing

Tables 10.1 and 10.2 present a summary of the detector testing that we performed. In the subsequent section (§ 10.3) we discuss the tests in detail.

10.2.1 Calibration Sources for Detector Testing

The following list details the sources used for device illumination, as referenced in Table 10.1.

- **None:** resonator testing only, not pulse testing.

- **^{55}Fe 1:** Emission at 5.89 keV and 6.4 keV; Fe decay to Mn; 2.7-year half-life. Source was $\lesssim 10$ μCi during tests.

Table 10.1. Log of strip detector tests

Run ID (1)	Date (2)	Ch (3)	Wafer ID (4)	Device ID (5)	Resonator [nm] (6)	Step Plug[a] [nm] (7)	Absorber [nm] (8)	Substrate[b] Note (9)	Source[c] (10)
51	2005-06-01	-	GSFCarr	···	Al		In		
59	2005-09-14	-	L030218	10-20-1Q5-12x1	275 Al	···	300 Ta (300 sloped SiO_2)	sapphire	^{55}Fe 1
61	2005-09-30	-	B050921	J-BP	150 Al	···	80 Ta	500 μm sapphire	^{55}Fe 1
66	2005-12-13	-	L030502.1	2.5Q5, 12x1	450 Al	···	450 Ta (SiO_2)	sapphire	^{55}Fe 1
68	2006-01-03	-	B051215	J-AP	150 Al	···	75 Ta	sapphire	^{55}Fe 1
69	2006-01-10	-	B051215	J-D	150 Al	···	75 Ta	sapphire	^{55}Fe 1
72	2006-03-13	1	B060306	J-AP	400 Al	···	200 Ta	sapphire	^{55}Fe 1
		2	LeDuc	D0	20 Al	···	···	high-ρ Si	···
73	2006-03-20	1	B060324	J-AP	30 Al	···	200 Nb (layered)	high-ρ Si	^{55}Fe 1
		2	B060327	J-AP	30 Al	···	200 Ta (layered; Nb seed)	high-ρ Si	UV
74	2006-04-06	-	fridgetest	···	···	···	···	···	···
75	2006-04-25	1	B060411.2	LT-A	400 Al	···	200 Ta	sapphire	^{55}Fe 1
		2	B060411.1	LT-A	20 Al	···	100 Ta (layered; Nb seed)	sapphire	UV
76	2006-05-06	1	B060413	LT-A	200 Al	300	300 Ta (Nb seed)	high-ρ Si	^{55}Fe 1; SS Mask
		2	LeDuc	hybrid	Nb/20 Al	···	···	···	UV
77	2006-05-16	1	B060510	LT-A	25 Al	···	100 Ta (layered; Nb seed)	C-plane	^{55}Fe 1; SS Mask
		2	B060510	LT-A	25 Al	···	100 Ta (layered; Nb seed)	C-plane	UV
78	2006-05-28	1	B060413	LT-A	200 Al	300	300 Ta (Nb seed)	high-ρ Si	^{55}Fe 1
		2	B060510	LT-A	25 Al	···	100 Ta (layered; Nb seed)	C-plane	reflection
79	2006-06-12	1	B060530.1	LT-A	200 Al	400	600 Ta (hot); sloped	Valley D.	^{55}Fe 1
		2	B060530.1	LT-A	200 Al	400	600 Ta (hot); sloped	Valley D.	reflection
81	2006-07-06	1	KID0605a	G-BP	100 Al	···	500 In	sapphire	^{55}Fe 1
		2	B060615	LT-A	20 Al	200	580 Ta (hot); sloped	Valley D.	UV
82	2006-07-18	1	B060530.1	LT-A	200 Al	400	600 Ta (hot); sloped	Valley D.	^{55}Fe 1
		2	B060615	LT-A	18 Al	200	580 Ta (hot); sloped	Valley D.	UV
85	2006-08-30	1	Daal200608	HH_0.5_400	200 Nb	···	···	sapphire	···
		2	B060816.2	Alpha2	300 Al	···	···	Valley D.[d]	···
86	2006-09-11	1	B060816	LT-A	300 Al	300	1000 Ta (hot); sloped	Valley D.[d]	^{55}Fe 1
		2	B060816	LT-A	300 Al	···	1000 Ta (hot); sloped	Valley D.[d]	Si refl
87	2006-10-20	1	B060921	LT-A	25 Al	225	300 Ta (hot); sloped	Cryopolis	UV
		2	B061003	LT-A	200 Al	···	600 Ta (hot); sloped	Cryopolis	^{55}Fe 1
88	2006-11-13	1	B061031	LT-A	20 Al	···	300 Ta (hot); sloped	Cryopolis	UV
		2	B061002	LT-B	250 Al	300	600 Ta (hot); sloped	Cryopolis	Si refl.
89	2006-12-01	1	B061120	LT-A	250 Al	···	600 Ta (hot); sl, SiO_2 on top	Cryopolis	^{55}Fe 1
		2	B061120	LT-A	250 Al	···	600 Ta (hot); sl, SiO_2 on top	Cryopolis	reflection
90	2007-01-03	1	B061215	LT-A	250 Al	···	600 Ta (hot); sl, 50 SiO_2 under; SiO_2 on top	sapphire (old)	^{55}Fe 2
		2	B061120	LT-A	250 Al	···	600 Ta (hot); sl, SiO_2 on top	Cryopolis	^{55}Fe 1
91	2007-01-17	1	B061215	LT-A	250 Al	···	600 Ta (hot); sl, 50 SiO_2 under; SiO_2 on top	sapphire (old)	^{55}Fe 2
		2	B061120	LT-A	250 Al	···	600 Ta (hot); sl, SiO_2 on top	Cryopolis	^{55}Fe 1
92	2007-02-22	1	B070207	LT-A	250 Al	350	600 Ta (hot); NOT sloped	Cryopolis	^{55}Fe 3
		2	B070207	LT-A	250 Al	350	600 Ta (hot); NOT sloped	Cryopolis	^{55}Fe 2

[a] The liftoff plug material is aluminum for all devices listed here

[b] Unless noted as high-ρ Si or C-plane (sapphire), all substrates are R-plane sapphire and the entry in this column denotes the sapphire brand, if known

[c] The particular sources used for device illumination are explained in § 10.2.1

[d] Sapphire was oxygen annealed at high T before fabrication

Table 10.2. Strip detector test notes

Run ID (1)	Date (2)	Ch (3)	Purpose (4)	Summary/Notes (5)
51	2005-06-01	-	GSFC collaboration; test alternate material (In absorber)	some resonances; no coincident pulses
59	2005-09-14	-	retest older device with SiO_2 over step (600 μm single strip)	
61	2005-09-30	-	thinner absorber, thicker Al; device has Ta plugs, 200 μm strips	resonances, no coincidences
66	2005-12-13	-	test device from old wafer that showed a working strip detector	no coincidences
68	2006-01-03	-	thinner absorber, thicker Al	
69	2006-01-10	-	single-pixel device; thinner absorber, thicker Al	pulse count rates & shapes independent of absorber size (no Ta-Al connection)
72	2006-03-13	1	thinner Ta than Al but Ta is 2× thicker than previous tests; try for lateral trapping with J-AP	no coincidences
		2	...	HEMT on Ch 2 not working
73	2006-03-20	1	test layered structure with Al under Nb absorber	$T > 300$mK; fridge problems
		2	same layered structure with Al under room-temperature Ta	$T > 300$mK; fridge problems
74	2006-04-06	...	Fridge Test with Nb Coax Removed	T_{base} <90 mK
75	2006-04-25	1	new LT-A device; try again thin abs; thick Al with lateral trapping	$T_{base} \sim 60$ mK; no coincidences
		2	layered structure with LT-A design	no coincidences
76	2006-05-06	1	new LT-A device with 300 nm Ta and 300 nm Al plug layer for step coverage	no resonances due to SS mask
		2	test Nb hybrid device with Al section at the end	short Al recombo time; noisy UV pulses from Al hybrid section
77	2006-05-16	1	retest layered structure with thin Al and better sapphire; no Cl in etch (and test whether SS mask kills resonances again)	no resonances due to SS mask
		2	retest layered structure with thin Al and better sapphire; no Cl in etch	resonances, very noisy; no coincidences
78	2006-05-28	1	retest device from Run 76, Ch 1 without SS mask	100 μm low-Q strip shows banana !
		2	retest device from Run 77, Ch 1 without SS mask; no Cl in etch	significant heating from HEMT
79	2006-06-12	1	sloped Ta edges, plug layer, on sapphire	coincidences on $100 - 800$ μm strips; $\Delta E \sim 87$ eV at 5.9 keV on 200 μm strip
		2	copy of Ch 1 device; reflection X-ray illumination	bananas on $100 - 400$ μm strips
81	2006-07-06	1	GSFC collaboration; test In absorber	some resonances; no coincidences
		2	thin Al (optical device) with 580 nm Ta with sloped edges	resonances extremely shallow - gunk in CPW slots?; no useful data
82	2006-07-18	1	same device as Run 79 Ch 1; acquired data with lower powers	better R: $\Delta E \sim 65$ eV @ 5.89 keV on 200 μm strip
		2	similar to Run 81, Ch 2; aggressive cleaning to get gunk from CPW slots	saw improvement, but resonances still too shallow to get pulse data
85	2006-08-30	1	unrelated device	fixed fridge blockage
		2	testing single-layer Al MKID sapphire (Valley D.) noise	noise consistent with strip-detector Al MKIDs on Valley D.; extra processing steps do not increase resonator noise
86	2006-09-11	1	thicker Ta (1 μm) for better diffusion performance - with liftoff plug	bananas on $100 - 400$ μm strips; diffusion performance unchanged or worse than the 600 μm-thick device
		2	same as Ch 1, but no liftoff plug	resonances and bananas; Si refl source energy made comparisons difficult
87	2006-10-20	1	optical device; new Cryopolis sapphire	$T < 50$ mK, no amp heating; coincidences
		2	repeat of 600 nm Ta device with sloped edges (but no plug) on new sapphire	bananas on 100 & 200 μm strips; 400 hi-Q strip had banana buried in noise
88	2006-11-13	1		high-Q resonances; no coincident pulses;
		2	test LT-B device with strap couplers (150 nm SiO_2)	high-Q resonances; no coincident pulses; low X-ray count rate: Si refl. chip slipped during testing
89	2006-12-01	1	Ta protected with SiO_2 to improve diffusion length	
		2	Ta protected with SiO_2 to improve diffusion length	no coincidences; very long Al recombination constant
90	2007-01-03	1	SiO_2 under Ta to simulate oxidized Si of Yale, etc.	FRIDGE BLOCKED
		2	retest Ta protected with SiO_2; same device as Run 89 Ch 2	FRIDGE BLOCKED
91	2007-01-17	1	SiO_2 under Ta to simulate oxidized Si of Yale, etc., same device from Run 90 Ch 1	some coincidences; 100 μm hi-Q strip shows possible banana buried in noise
		2	retest Ta strip protected with SiO_2, same device from Runs 89, 90 Ch 2	banana on 100 & 200 μm hi-Q strips; low diffusion length; long Al $\tau \sim 0.5 - 1$ ms; resonators can be driven v. hard; low noise
92	2007-02-22	1	straight-walled Ta	no Ta-Al qp connection
		2	straight-walled Ta	no Ta-Al qp connection; dataset for pulse τ vs. P_{int} vs. T

- **^{55}Fe 2:** Emission at 5.89 keV and 6.4 keV borrowed from 2nd floor Space Radiation Laboratory; ~ 10 μ Ci during tests.

- **^{55}Fe 3:** Emission at 5.89 keV and 6.4 keV purchased in 2007. Source was 92 μCi in February 2007.

- **reflection:** X-ray source with line emission from $\sim 1-6.4$ keV. This source consists of a strong ^{55}Fe source (50 mCi in $\sim$2003) that reflects off of a special glass (NIST K3670) that contains Si, Fe, Mg, Al, Ca, Ni, Zn, Pb, Ti. Figure 10.1 shows the spectrum of the reflection source, obtained with a standard room-temperature Si X-ray detector with 200 eV energy resolution.[2] The lines identified in the spectrum are:

  - Ca Kα_1, Kβ_1 at 3.69, 4.01 keV
  - Ti Kα_1, Kβ_1 at 4.51, 4.93 keV
  - ^{55}Fe decay at 5.89, 6.40 keV

  See Figure 10.1 caption for further details.

- **Si refl.:** Similar to the reflection source described above, but the reflecting (fluorescing) material is a 400 μm thick Si chip instead of the NIST glass. Figure 10.2 presents the source spectrum. The lines identified in this spectrum consist of a strong silicon line at 1.74 keV and the ^{55}Fe decay lines at 5.89 and 6.40 keV.

- **UV:** UV fiber.

10.2.2 Stainless-Steel Masking Experiment

Prior to the devices tested in Runs 78 and 79, which exhibited coincident pulses with our new design and fabrication, our X-ray datasets were dominated by pulses created by X-ray absorption directly in the Al CPW center-strip or ground plane, or by substrate events (X-ray absorptions in the substrate that cause phonons in the substrate to break Cooper pairs in the MKID). We worried that these events, particularly the numerous substrate events with small phase changes, were potentially hiding the desired absorber events. To this end, we machined a thin X-ray mask from stainless-steel shim stock designed for use with LT-A

[2] http://www.amptek.com/xr100cr.html

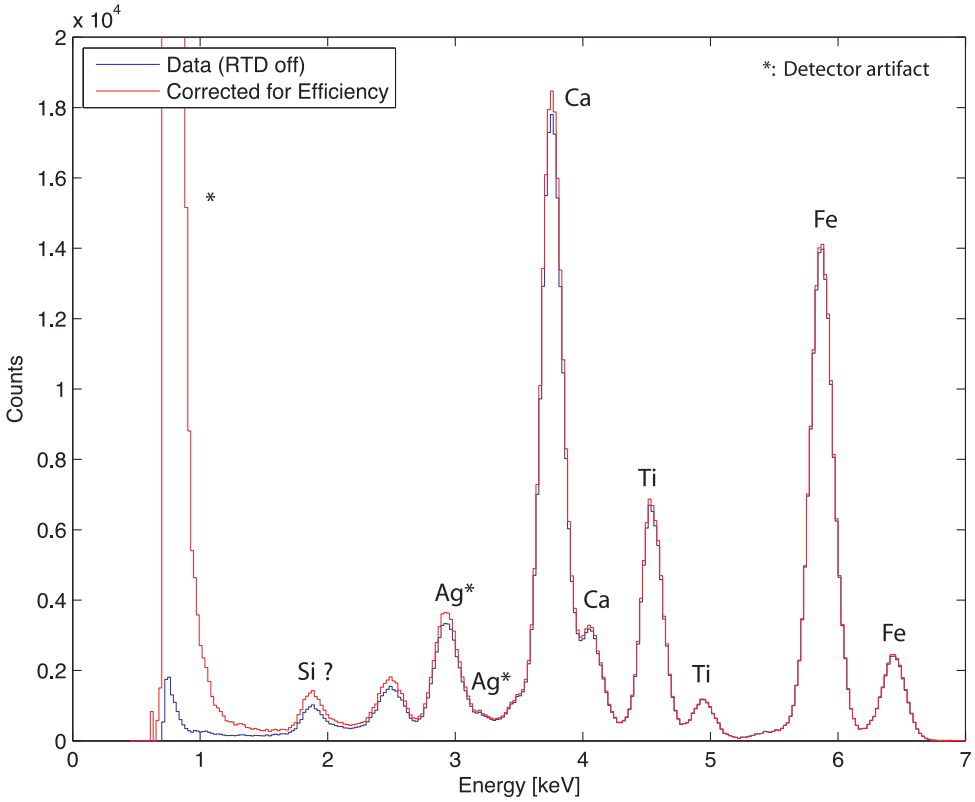

Figure 10.1 Spectrum of the "reflection" X-ray source. "Reflection" X-ray illumination indicates that we used the K3670 NIST glass reflection source, which is comprised of a strong, 50 mCi ^{55}Fe source shining onto the NIST glass. The reflected line radiation and some ^{55}Fe radiation ($\sim 0.5 - 6$ keV) is incident upon the detector. The K3670 NIST glass contains (percent weight): SiO_2 (38), FeO (10), MgO (10), Al_2O_3 (9), CaO (9), NiO (4), ZnO (8), PbO (10), TiO_2 (2). NIST contact: D. Newbury, 301-975-3921, dale.newbury@nist.gov. This spectrum was obtained with a 200 eV resolution Amptek XR100 silicon detector. The XR100 has a 300 μm Si detector with an 0.5 mil Be window. This spectrum was energy calibrated with the ^{155}Eu line at 6.058 keV. The calibration may be off at the lowest energies. This spectrum has the rise-time discriminator off for better low-energy sensitivity. The lines identified in the spectrum are presented in § 10.2.1

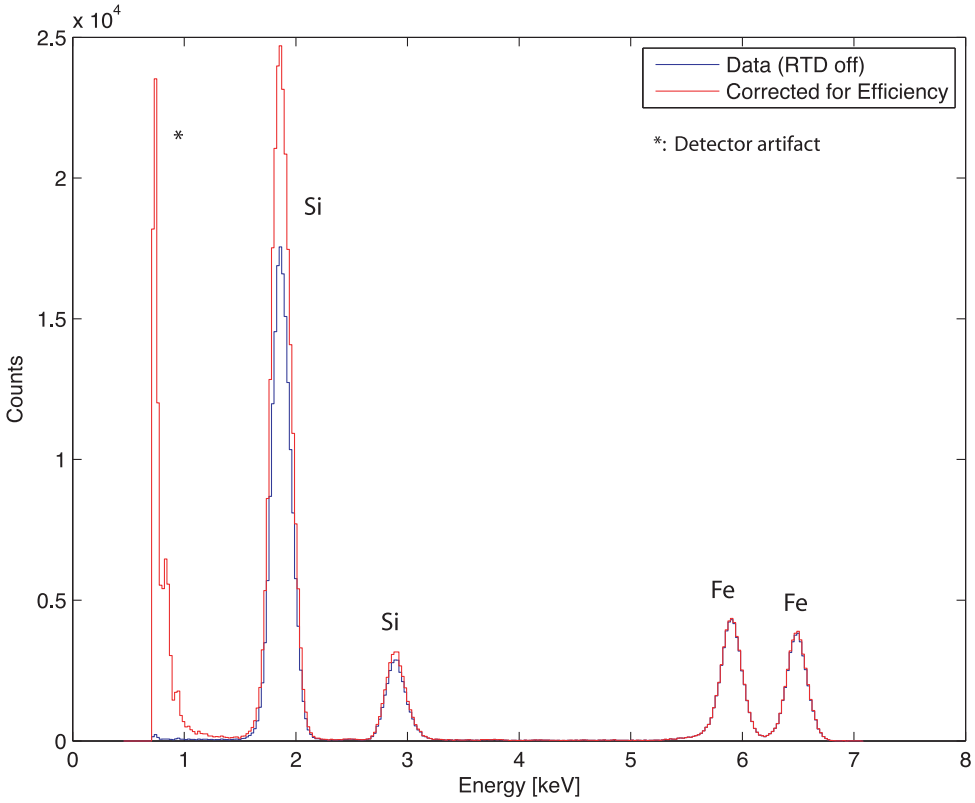

Figure 10.2 Spectrum of a strong ^{55}Fe source reflecting off of a silicon chip. The same setup is employed as for Figure 10.1, but instead of the NIST glass, the reflecting element is a piece of a 400 μm thick silicon wafer. This spectrum was acquired using the Amptex XR 100 with the rise-time discriminator off. The energy calibration was performed using the ^{155}Eu line at 6.058 keV. The raw data (blue) and detector efficiency-corrected (red) spectra are shown. The real features are a strong silicon fluorescence line at 1.74 keV and the ^{55}Fe lines at 5.89 keV and 6.4 keV

devices. The stainless steel absorbs all 6 keV photons so that the device illumination is limited to the particular areas under the openings in the mask: the center of the Ta strips and the Ta single pixels — see Figure 10.3. The mask was placed sufficiently far above the device (and secured with brass screws to the sample box) to ensure that the mask would not touch the device and that this addition of a metal ground plane would not change the fields of the resonator.

This mask was tested with two different devices on Runs 76 and 77 and no resonances were observed either time: the microwave transmission looked fine aside from this lack of resonances. The device tested in Run 76 was tested again on Run 78 without the mask and all resonances were present. The working theory is that magnetic fields associated with the stainless-steel mask are responsible for killing the resonances, as we know that magnetic fields can strongly affect the resonator characteristics in this manner. Although stainless steel is non-magnetic, it is possible that the material used here is slightly magnetized, especially since the shim stock is rolled. We tested the mask at room temperature with a Hall probe, and the magnetic field was non-negligible compared to the Earth's magnetic field. MKIDs will resonate in the Earth's magnetic field, but it is possible that small areas of the mask have a non-negligible magnetic field, causing the resonances to disappear. The stainless steel was originally chosen because it will be sturdy and durable even when using such a thin sheet. The easiest way to test this theory is to make the mask out of a hard, non-magnetic material, such as BeCu. Because these failed tests with the mask occured just before the strip detectors started showing much-improved performance, we did not make another mask.

10.3 Observations

In this section I will present observations and conclusions we draw from the various strip-detector tests.

10.3.1 Quasiparticle Connection Between Absorber and MKID

The first and primary concern in our testing was to achieve a quasiparticle connection between the absorber and the MKID. There was an electrical connection between the absorber and the MKIDs: if this were not the case then the quarter-wave resonators would not be

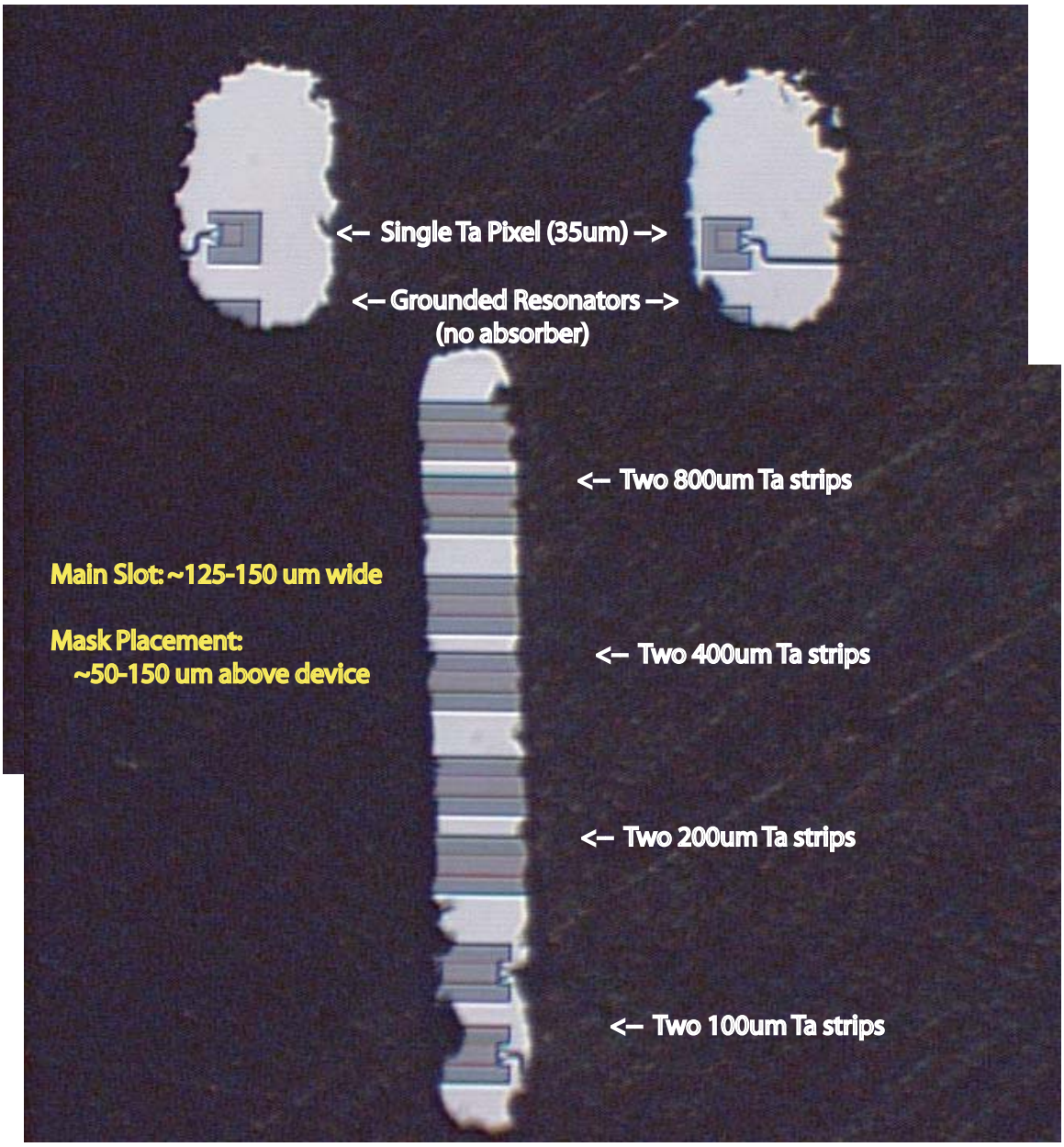

Figure 10.3 This figure presents an optical microscope image of the stainless-steel mask placed on top of an LT-A Ta-Al strip detector. This masking allows us to only illuminate the unmasked areas with X-rays, since the mask will absorb all X-rays incident on it. The masked region appears black, while the three slots in the mask are bright, and the underlying device can be seen. The brightest areas are the Al ground plane, while the darker gray areas contain Ta absorbers surrounded by bare Si substrate. This mask was placed $\sim 50-100$ μm above the device

grounded at their ends (because the path from the end of the MKID to the ground plane is through the Ta strip) and the observed resonance frequencies would be far from the design frequencies, which was not the case. However, we were not seeing any coincident pulses between resonators attached to the same strip, indicating that the quasiparticles created in the absorber strip were not getting into the MKIDs at each end. In addition, the pulse shapes of the X-ray events we observed had sharp rise times, indicative of direct hits into the Al, not events that occured in the Ta with subsequent quasiparticle diffusion to the absorber. We initially had confidence in our design because of one long-ago (circa 2003) test that showed quasiparticle trapping from a Ta absorber into an Al MKID, relying on vertical trapping bars similar to those in our design; however these results were not reproducible. The following sections review the testing and designs as we work to achieve Ta-Al quasiparticle connections.

10.3.1.1 Thinner Absorber to Reduce the Step

The first approach we took to eliminating a step-coverage problem was to use a simple fabrication approach and a Ta absorber thinner than the Al MKID. For example, Figure 10.4 shows a scanning-electron microscope (SEM) image of such a device. Although this device would not be a practical X-ray detector because the absorber is far from thick enough to exhibit near unity X-ray stopping power and the Al-MKID volumes are too large to provide sensitive quasiparticle sensors, our goal with this test was to achieve a quasiparticle connection. However, we never did achieve the desired quasiparticle connection. We tested devices with thin absorbers and thick MKIDs on Runs 61, 68, 69, 72, and 75, and each time we did not observe events from X-rays absorbed in the Ta. It is possible that the 'flag' at the edge of the Ta was causing a problem with the Al continuity over the edge, or simply the thinner edge may still have been too sharp for the Al.

10.3.1.2 Physical Barrier

Another consideration was that there was a physical barrier at the Al-Ta interface. The fabrication procedure for the strip detectors involves a break in vacuum between the Ta deposition/etch and the Al deposition. During the time that the wafer is in air it is possible for an oxide to grow on the surface of the Ta, thus forming an oxide barrier at the interface. To ensure that there is not an oxide barrier we used an aggressive argon ion-mill procedure

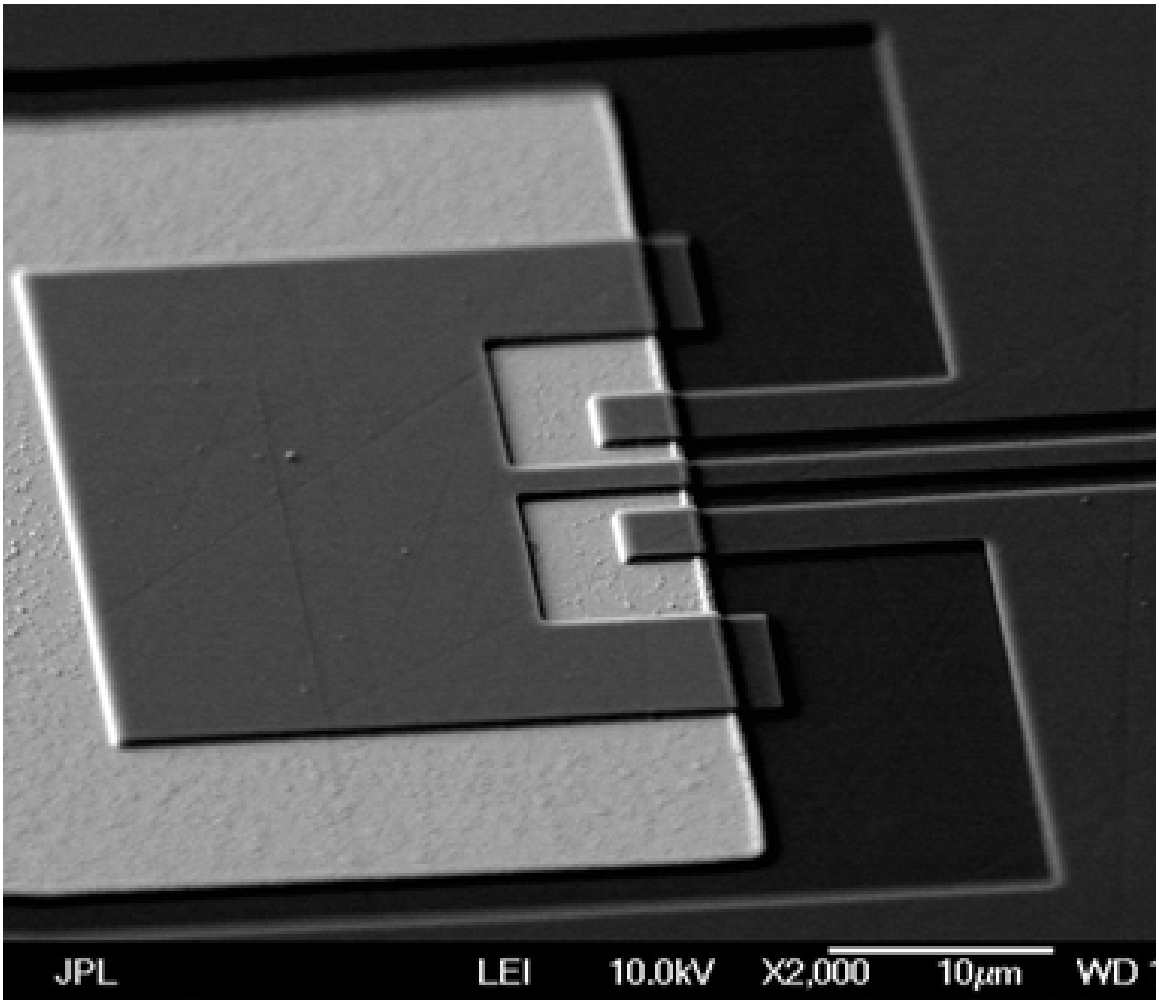

Figure 10.4 This SEM shows the trapping-bar region of a device from wafer B060306. The light colored metal is the end of the 200 nm thick Ta strip, while the darker gray is the 400 nm thick Al; the absorber was designed to be thinner than the MKIDs to eliminate step coverage problems. The wafer was patterned using the X-ray test mask (§ 9.4.1.2), and employs vertical trapping. A device from this wafer was tested during Run 72 and there were no observed Ta-absorption events that produced a signal in the MKIDs. Note that along the edge of the Ta, where the Al climbs onto the Ta, there is a 'flag.' The edge of the Ta seems rough; this may hinder the flow of the quasiparticles from the Ta to the Al. SEM credit: Bruce Bumble

to clean the surface in the Al vacuum system before Al deposition. This procedure will remove oxides on the surface.

10.3.1.3 Bad Tantalum

The Original Optical Mask (§ 9.4.1.1) had several strip lengths, but the shortest one was 600 nm. We were concerned that instead of a quasiparticle connection problem the real problem was that the diffusion length of the Ta was so poor that the quasiparticles created in the absorber were recombining before they could be sensed by the MKIDs. Although this explanation could explain the lack of coincident pulses, we would expect that the MKIDs would sense quasiparticles from X-ray absorptions in the Ta that occured close to the end of the strip; these pulses would be look different from other pulses owing to their slow rise-times. On the X-ray Test Mask we designed some shorter strips, and in the LT-A device for the Lateral Trapping Mask we designed multiple devices with 100 μm and 200 μm long strips. The decrease in strip-length alone did not show an immediate quasiparticle connection.

10.3.1.4 Sloped Edge of Absorber

X-ray detectors with sloped Ta edges have been showing consistent quasiparticle connections over devices from multiple wafers; we note that all of the wafers with sloped Ta edges also have lateral trapping bars. Figure 10.5 shows a device with a 600 nm thick device with well-sloped edges. The Al MKID climbs smoothly over the absorber and it is appears that there is no break in the aluminum layer. This device functions as expected, and coincident pulses are observed from even the longest strips on the device. This device, and several from other wafers that employ this sloping technique, will be analyzed in detail in Chapter 11. The photo-resist reflow technique for edge sloping is discussed in § 9.4.

10.3.1.5 Liftoff Plug

The Lateral Trapping Mask allows inclusion of an additional liftoff plug layer at the step (see Figure 10.5). The addition of this patch should ensure that there is Al covering the step onto the Ta. The role of this patch layer is still unclear. Several of the working strip detectors have this patch layer, but those devices also have sloped Ta edges, and several working detectors with sloped edges do not have a patch layer.

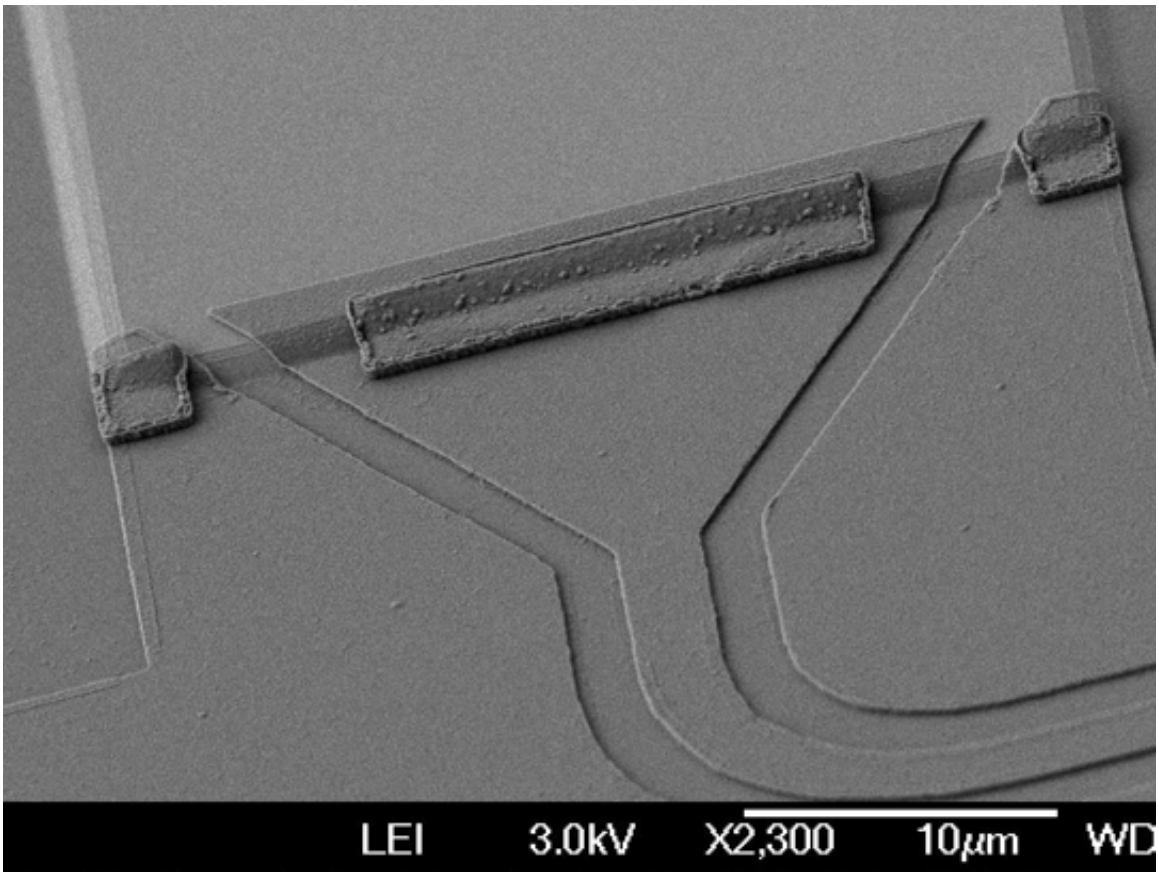

Figure 10.5 SEM of device from wafer B060530.1. This device is patterned with the Lateral Trapping Mask (§ 9.4.1.3) and exhibits the triangle-shaped lateral trapping bar. The edge of the 600 nm thick Ta is nicely sloped and the 200 nm thick Al MKID climbs smoothly over the Ta edge. The extra bars of material on top of the Al at the Ta edge are liftoff plugs of Al to ensure Al coverage over the edge at both the trapping bar and at the ground contacts on the left and the right edges of the strip. SEM credit: Bruce Bumble

In Run 86 we tested two devices from the wafer B060816 that has 1 μm Ta with sloped edges and 300 nm Al MKIDs; half of the wafer had a 300 nm liftoff patch, while the other half had no liftoff patches. We tested one device from each half of the wafer. Both the patched and unpatched devices showed a quasiparticle connection; a careful comparison of the devices was not performed because the unpatched device was illuminated with the Si reflection sources, causing noisy, low-phase-shift pulses. However, the fact that the un-patched strips have a Ta-Al quasiparticle connection, suggests that the patch is not necessary as long as the Ta edges are sloped.

The tests conducted in Run 92 argue against the plug's efficacy, although all that can be said definitively is that the plug did not ensure a quasiparticle connection given the relative thicknesses involved (the Ta is almost twice as thick as that of the plug layer). Both of the testing channels of Run 92 held devices from B070207, a wafer with 600 nm straight-walled Ta, 250 nm Al, and 350 nm Al plugs on sapphire. The Ta walls were left sharp, as opposed to the previous example where the edges were sloped. Figure 10.6 shows a close-up of the Ta-Al interface region. Neither device showed coincident pulses or any pulses that appeared to originate in the absorber and the implication is that there is not a good connection at this interface. The production of $\gtrsim$ 300 nm liftoff patches is difficult with the standard lithography technique we have been using, and thus the patch was made only 350 nm in this case. Additional tests with a thinner Ta absorber or a thicker patch layer are necessary to fully understand this behavior; these tests have not yet been completed due to lack of time.

Alternately, an earlier test of a device on a silicon substrate may argue that the plug is effective in some cases, although these results are also inconclusive. During Run 78, Channel 1 contained an LT-A device from B060413, a wafer with 300 nm of room-temperature Ta fabricated on a silicon substrate using a thin Nb seed layer. The wafer had a 200 nm Al MKID layer and a 300 nm Al plug. The Ta edge was not sloped, however the device did exhibit a quasiparticle connection. The Ta had a very low diffusion length, as expected since the Ta was deposited at room temperature, but the shortest (100 μm) strip did exhibit coincident pulses. This is thus far the only quasiparticle connection achieved without sloped Ta edges. However, because the majority of our tests were performed on sapphire substrates, it is unclear how similar devices on Si that lack a plug layer will behave.

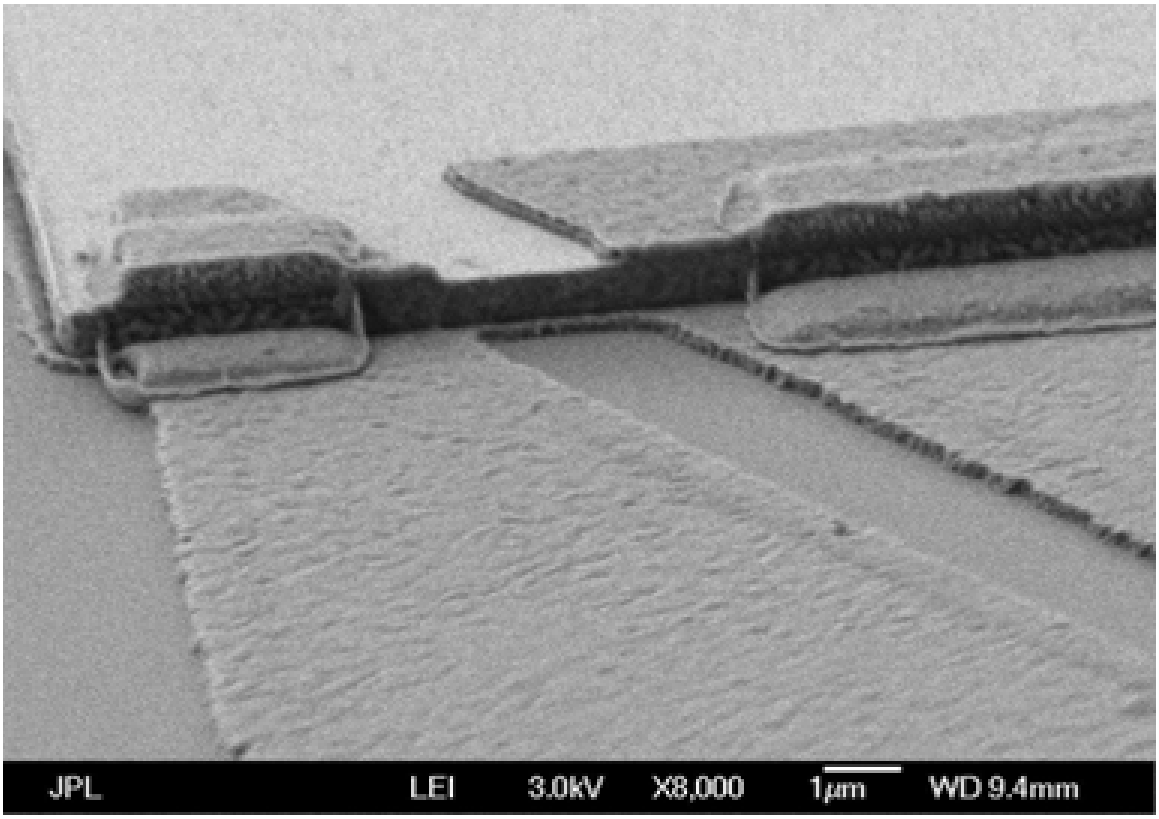

Figure 10.6 SEM of device from wafer B070207; 8000× magnification of the Ta edge. As opposed to the device in Figure 10.5, this device does not have sloped Ta edges, instead there is a sharp edge at the end of the 600 nm thick Ta strip. The 250 nm-thick Al MKID and 350 nm thick Al patch layer do not climb smoothly over the edge, and it is unclear whether or not the Al plug is sufficiently thick to serve its design purpose. This device did not exhibit a Ta-Al quasiparticle connection during testing (Run 92). SEM credit: Bruce Bumble

10.3.2 Quasiparticle Trapping: Vertical versus Lateral

We employ several different trapping bar designs; some are designed to use vertical trapping, some for lateral trapping. Figure 10.4 shows a typical vertical trapping bar. The bar is designed so that quasiparticles enter the Al from the Ta below and relax in energy, becoming trapped in the large square of Al that resides on top of the Ta strip, before diffusing into the resonator center strip and off of the Ta. The device in Figure 10.5 is designed for lateral trapping. The Al trapping bar stays wide over the edge of the Ta, before smoothly narrowing into the 3 μm wide center strip. This design allows quasiparticles that are incident on the edge of the Ta strip to diffuse laterally into the Al and away from the Al-Ta interface.

It is important to ensure that the quasiparticles from the Ta are trapped into the Al in a sufficiently short time so that they are forced to stay in the MKID instead of diffusing back into the absorber. Equation 8.41 shows that the trapping time is proportional to $(\Delta_1 - \Delta_2)^{-3}$. Near the Ta-Al interface the Al gap will be proximitized, so that its gap is above its nominal value (see Golubov et al. 1995, plus Gaidis 1994 and Friedrich 1997 for a discussion of Ta-Al proximitization). The worry, for vertical trapping schemes, is that the Al will be too thin so that a significant fraction of the film thickness will have $\Delta > \Delta_{\rm Al}$, slowing the trapping time and allowing quasiparticles to diffuse back into the Ta before they can be trapped and sensed. For this reason our bars were designed large enough (see, e.g., Mazin 2004) and the Al films we use are thick enough ($t \gtrsim 50$ nm, see Friedrich 1997) so that we should achieve the desired quasiparticle trapping.

While we were testing devices with the vertical trapping bars and seeing no quasiparticle connection, we decided to redesign the bars so that we could test devices with lateral trapping bars. Although it is with devices from the Lateral Trapping Mask that we finally saw the Ta-Al quasiparticle connection, it is still unclear at this point whether the vertical trapping was ineffective. The positive results we have obtained are with lateral trapping bars, but since we have never tested vertical trapping bars with sloped Ta edges and/or a liftoff plug, it is unclear as to what results we would obtain. Another potential issue with the vertical trapping bar design is that it relies on a very narrow connection between the trapping bar and the MKID itself: Figure 10.4 shows the large square trapping bar that is in direct contact with the narrow, 3 μm wide center strip of the CPW, while, in contrast, the Lateral Trapping Mask's triangular trap regions narrow gradually from the trapping region

to the CPW center strip. It is possible that quasiparticles were successfully trapped in the Al trapping bar, but that once trapped, the quasiparticles were unable to diffuse into the sensitive part of the CPW center strip. Both vertical trapping and lateral trapping schemes have been employed effectively by groups using STJs in strip-detector architecture (e.g., Kraus et al. 1989; Gaidis 1994). The circa-2003 early MKID strip detector also employed vertical trapping, although we note that the old design was slightly different in that it employed an insulating layer of SiO_2 between the Ta and Al everywhere except at the trapping bar (i.e., the SiO_2 layer insulated the Al CPW from the Ta as it climbed over the step, and it was only in the vertical trapping bar region that the Al dropped into a hole in the SiO_2 to make contact with the Ta), whereas devices from the more recent masks do not have this SiO_2 layer.

10.3.3 Diffusion Parameters of Ta Absorber

Once we had quasiparticle connections such that we were able to measure the quasiparticle diffusion parameters of the absorbers, we began to focus on improving the Ta diffusion length. The diffusion results from key devices will be examined quantitatively in the following chapter; here I discuss the approaches qualitatively.

10.3.3.1 Higher RRR or Thicker Tantalum

The residual resistivity ratio (RRR) is a measure of the ratio of the resistivity at room-temperature to that at low temperature, e.g., $RRR = \rho_{\mathrm{Ta\ 300\ K}}/\rho_{\mathrm{Ta\ 5\ K}}$. The RRR of our Ta films increases as the films get thicker: see Figure 10.7. We naively expect that the quasiparticle diffusion length will increase as the RRR increases, since the higher RRR is indicative of a cleaner film with fewer defects. Table 9.1 provides the RRR of the Ta used in several of our devices: the RRR of the 600 nm devices tested in Run 79 was 26.2, while the 1 μm thick devices of Run 86 had RRR of 53. However, the increase in RRR did not increase the Ta diffusion length. Some of our other tests are in agreement that the Ta diffusion length is not strictly related to the RRR. This notion is consistent with results published by STJ groups. For example, the Yale group achieved a diffusion length of 250 μm with Ta RRR of 17 (Li et al. 2003), while Kirk et al. (2000) tested a Ta strip with RRR of 53 and measured a much shorter (33 μm) diffusion length.

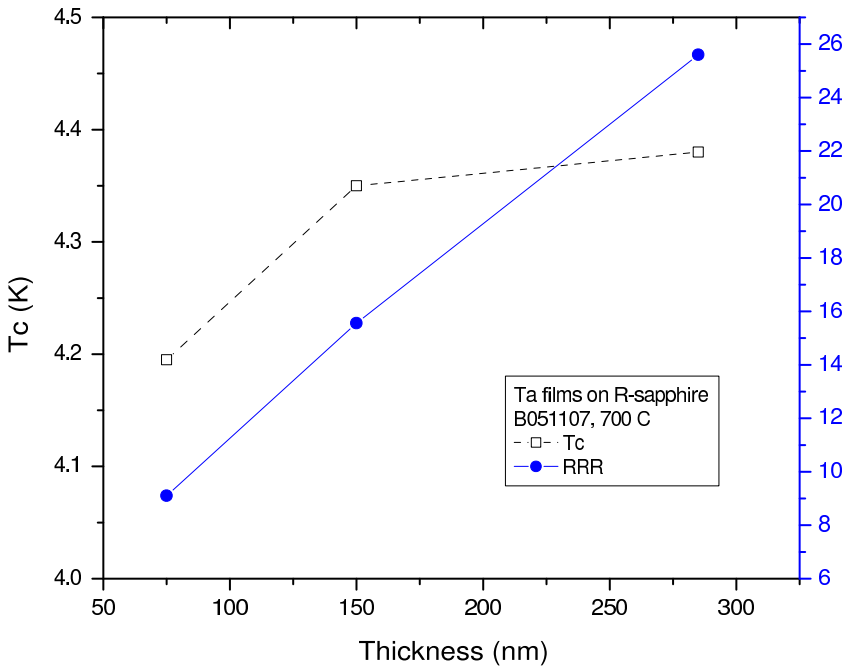

Figure 10.7 Ta T_c and RRR as a function of film thickness

10.3.3.2 Protect Ta During Al Etch

SEM images of some devices show Ta surfaces that appear grainy or rough; see, e.g., Figure 10.8. In Runs 89 and 91 we tested devices that had a layer of SiO_2 on top of the Ta absorber to protect the Ta surface during the Al etching. If the Ta surface were damaged during the etching then there might be extra quasiparticle recombination sites along the top surface of the strip, which would act to decrease the absorption length. The tests performed during Runs 89 and 91 did not show such improvement.

10.3.3.3 Absorber–Substrate Acoustic Match

In the introduction to the strip detector architecture (§ 8.5.1.1), I discussed the idea of an enhanced effective quasiparticle lifetime due to phonon trapping. The effective lifetime will be increased if productive phonons incident on the absorber-substrate interface are reflected back into the absorber; this preferentially occurs if the acoustic match between the absorber and substrate is poor. As Ta and sapphire have a good acoustic match, we deposited 50 nm of SiO_2 on sapphire substrates to mimic the passivated silicon substrates used by other groups (e.g., Gaidis 1994) for this purpose. In Run 91 we measured such a device and the

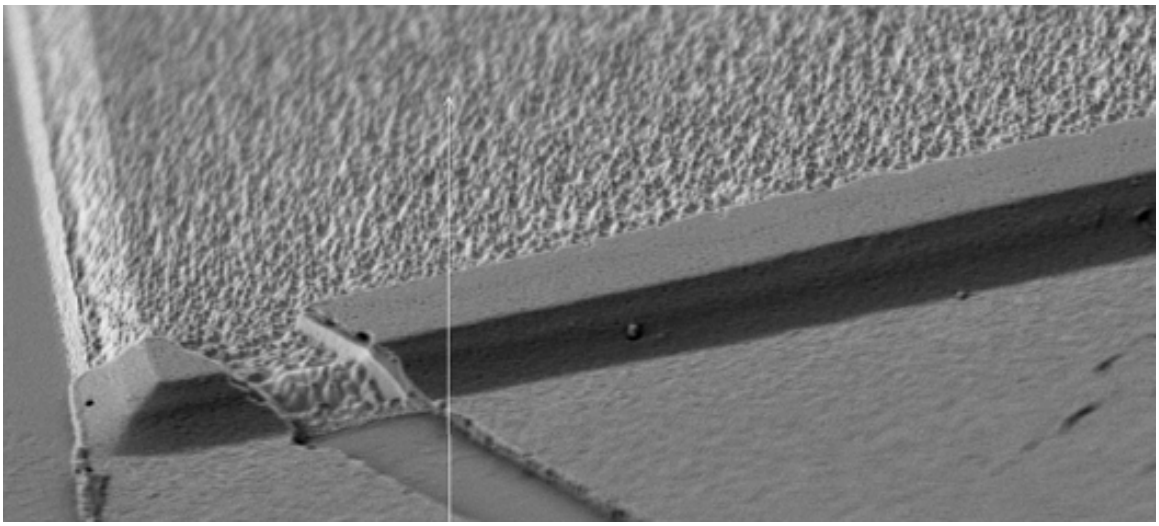

Figure 10.8 SEM image of device from wafer B061002; 5000× magnification shows a grainy surface. SEM credit: Bruce Bumble

performance was poor. The 100 μm high-Q strip showed a 'banana,' but it was buried in noise, and none of the other strips showed coincident pulses.

10.3.3.4 Straight-Walled Strips versus Sloped-Wall Stri

Since the information we have about the diffusion parameters stems from Ta with sloped edges, it is possible that the sloped walls along the length of the strip are causing loss in the strip. The edge of the strips will be thinner and may exhibit a reduced gap energy. If this is the case, quasiparticles that diffuse to this edge region might get trapped there and recombine instead of diffusing to the MKID. During Run 92 we tested an LT-A device with straight walls to check this idea, but the test was inconclusive since there was no quasiparticle connection (see § 10.3.1.5 and Figure 10.6). Future tests are planned with devices that have straight walls along the length of the strip but sloped walls on the ends to ensure quasiparticle transmission from the absorber to the MKIDs. This test will require a new mask set which has not yet been acquired.

10.3.4 Noise Properties in Strip-Detector MKIDs

During the strip detector testing we had a parallel focus on achieving the best possible resonator noise performance, so that the energy resolution degradation from the resonator noise is as small as possible.

10.3.4.1 Single-Layer Resonator Noise versus Strip-Detector Resonator Noise

Figure 10.9 presents a comparison of the frequency noise as a function of internal power for Al MKIDs on several substrates. The green symbols represent the best noise performance on sapphire. The noise performance, circa mid-2006, of the Al MKIDs on Valley Design sapphire in the strip-detector architecture is shown with black circles. This noise level is significantly higher than the best sapphire level. When we first noticed this discrepancy we hypothesized that the sapphire surface or surrounds might be damaged or changed during the additional processing steps (Ta deposition, Ta etch, and especially argon ion milling), causing the degraded noise performance. To test this idea we fabricated single-layer Al devices on a sapphire wafer from the same batch that had been used for the strip detector fabrication. This test was performed using an Alpha2 test device during Run 85. The noise performance of this single-layer device (blue filled circles in Figure 10.9) matched that of the strip-detector resonators that were fabricated on the same sapphire, thus arguing that the extra processing steps will not degrade the MKID energy resolution.

10.3.4.2 One Sapphire is Better than Another

As discussed in the previous subsection, Figure 10.9 shows that the sapphire we were using had higher resonator noise than the best performance of Al MKIDs on sapphire (green dots). We concluded from this that the batch of sapphire wafers that we were using were somehow non-ideal. We purchased new sapphire wafers from a different company, and fabricated similar strip-detector devices for comparison (e.g., see Run 87, Channel 2). The most recent sapphire (labeled Cryopolis) has a better noise performance than the earlier Valley Design sapphire, with noise performance consistently on par with the best Al on sapphire. The sapphire wafers purchased from Valley Design were refurbished wafers that had previously been used for growing epitaxial Si on the sapphire surface. It is possible that this previous use affected the sapphire noise performance.

10.3.4.3 Chlorine in Etch

Another concern was whether the chlorine in the aluminum etch was causing additional phase noise. Noise performance with Nb MKIDs on Si had much better noise performance than did Al MKIDs on Si (Gao et al. 2007). Because there is no chlorine in the Nb etch

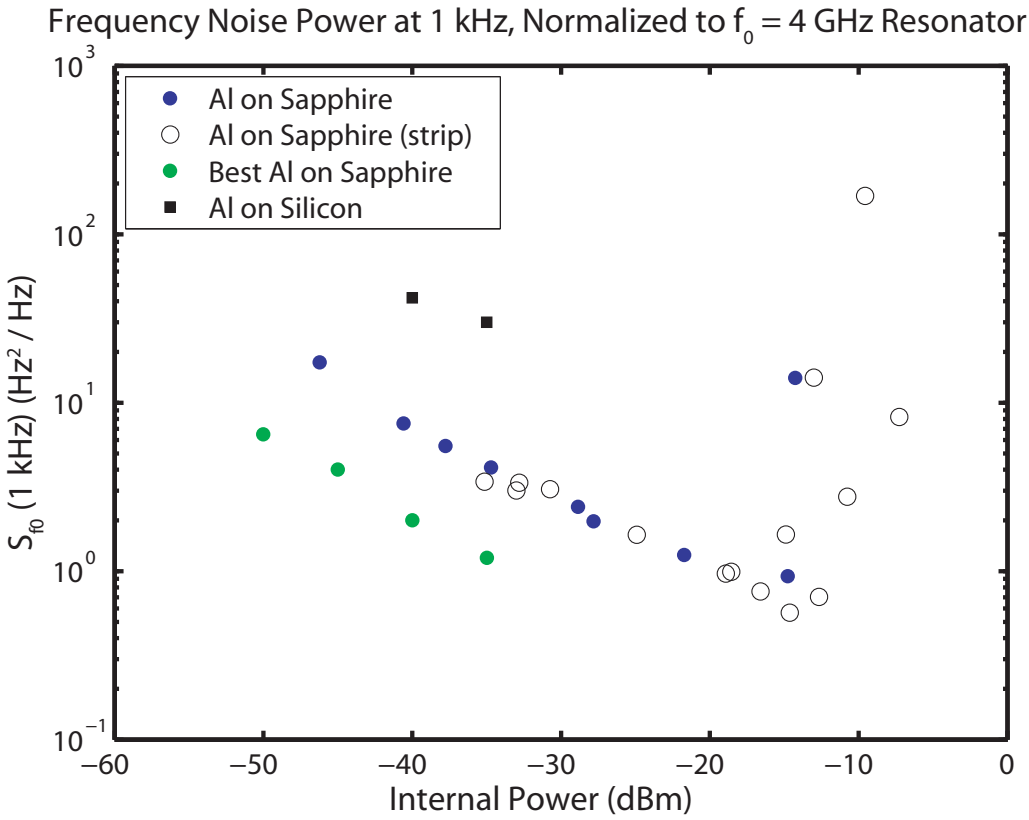

Figure 10.9 Frequency noise power-spectrum at 1 kHz as a function of the internal power in the resonator. The frequency noise is normalized to a $f_o = 4$ GHz resonator so that fair comparisons between resonators with different resonance frequencies may be made. The green points show the to-date best noise performance of Al MKIDs on sapphire, while the black squares show the typical performance of Al MKIDs on silicon substrates; both exhibit the $P_{\rm int}^{-1/2}$ power scaling law presented in Gao et al. (2007). The noise performance of Al MKIDs in the strip-detector architecture are shown with black circles. These data are taken from resonators on the Valley Design sapphire, and the noise performance falls significantly above that of the 'best' sapphire. The blue dots indicate the noise level of single-layer MKIDs on the same sapphire substrate (Run 85, Channel 2). The behavior at high internal powers ($P \gtrsim -15$ dBm) that rise off of the $P_{\rm int}^{-1/2}$ slope is due to resonator saturation effects as the microwave drive power begins to saturate the MKID

we decided to explore the possibility that the particular chemistry of the Cl etch with the Al MKIDs or surrounds was contributing to the excess phase noise. To test this we used thin Al resonators and argon ion milled away the Al instead of using the Cl RIE. The phase noise was not improved.

10.4 Testing Conclusions

During strip-detector testing over the past couple of years, we have gathered data on a variety of devices. Many of our observations have been mentioned in this chapter and a quantitative analysis of key devices will follow in Chapter 11. The most obvious qualitative results from the tests can be summarized briefly:

- Step Coverage
  - Every device we tested that has sloped Ta edges has shown a Ta-Al quasiparticle connection. This implies that the sloped edges ensure a quasiparticle connection, at least for the devices that are designed with lateral trapping bars
  - The only device with straight Ta walls and a quasiparticle connection was fabricated on a high-ρ Si substrate and had a 300 nm liftoff plug at the step to the 300 nm Ta
- Absorber RRR
  - The RRR of the Ta does not seem to directly correlate with quasiparticle diffusion length; higher-RRR strips have not demonstrated better diffusion performance.
- Noise
  - Different sapphire substrate brands provide different noise performance for Al MKIDs
  - The extra processing steps used in this strip-detector fabrication do not increase the resonator noise, as compared to the single-layer MKID fabrication processes

Chapter 11

Experimental Results

In this chapter we present data and analyses from three of the devices that showed Ta-Al quasiparticle connections. The majority of the discussion will focus on the device tested in both Run 79 and Run 82 (from B060530.1), which provide our best strip-detector results to date. we briefly compare these results to devices measured during Runs 86 and 87. In Section 11.1 we describe general routines for determining resonator parameters, detector energy resolution, and absorber diffusion characteristics, followed by the discussion of the strip-detector data in the following sections.

11.1 Data Analysis Procedures

11.1.1 Fitting the Resonance Data

First, to understand the MKID resonator parameters we measure S_{21} as a function of frequency and fit the data to determine the resonance parameters. Before fitting the data, we first remove an $e^{i\phi}$ cable delay term imparted on S_{21} by the experimental setup and correct for the power and frequency dependent gain and zeropoint in the IQ mixers. Next, we fit a circle to the data to find the circle radius and center. The data are then translated so that the circle center lies at the origin. The resonator parameters Q, f_o, and θ_o are determined by fitting the translated data to the model for the phase of S_{21} as a function of frequency:

$$\theta(f) = \theta_0 + 2\arctan\left[2Q\left(1 - \frac{f}{f_0}\right)\right] , \tag{11.1}$$

using a procedure similar to that described in Petersan & Anlage (1998) (and Gao 2005).

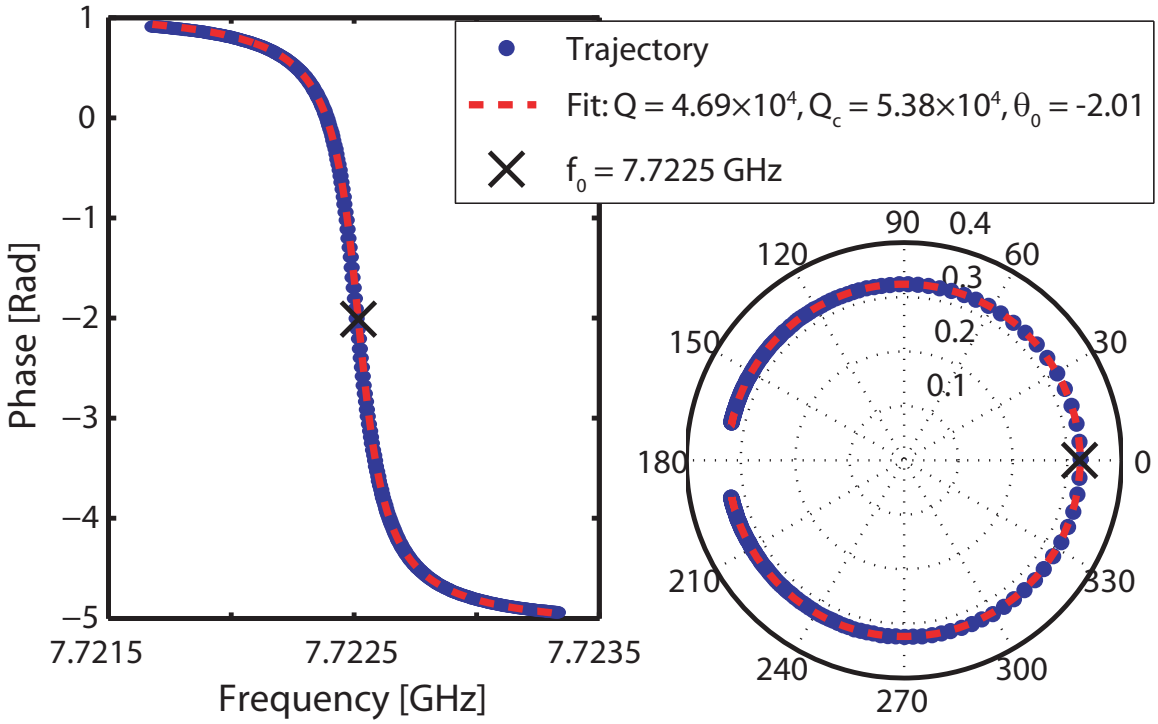

Figure 11.1 Resonance data of a $Q \approx 47000$ resonator with $f_o \approx 7.7$ GHz at 60 mK (from B070207). The right panel shows the transmission as a function of frequency in the complex plane; the data has been corrected and translated to the origin as described in § 11.1.1, with arbitrary normalization. The blue dots are the data and the circle fit is overlaid in red; the resonance frequency is marked with an **x**. The left panel shows the phase a function of frequency, with the model fit overlaid in red.

The fit to the model is performed using a nonlinear least squares minimization. Figure 11.1.1 shows the resonator data in I, Q space (note that in this context I and Q refer to the real and imaginary parts of S_{21}, respectively) and as a phase versus frequency with the fitting model overlaid. Finally, we determine the coupling Q_c using the relationship $Q_c = Q \cdot 2r/l$, where r is the radius of the circle and l is the length from the origin to the off-resonance point on the resonance circle (using the untranslated data), following Gao (2005).

11.1.2 Optimal Pulse-Height Estimator

A pulse we detect has the form:

$$v(t) = Ap(t) + n(t) \ , \tag{11.2}$$

where $v(t)$ is the measured pulse, A is the amplitude of the pulse (to be estimated), $p(t)$ is

the expected pulse shape (normalized to have a peak height of 1), and $n(t)$ describes the noise. For strip-detector analysis we would like to determine the best estimate of A for each pulse instead of simply reporting the maximum pulse height of the measured pulse, which will be affected by noise. To determine the best estimate of A we apply an optimal filter, $\phi(\nu)$ to each pulse in frequency space:

$$\phi(\nu) = \frac{p^*(\nu)}{C(\nu)} \ , \tag{11.3}$$

where $C(\nu)$ is the power spectral density of the resonator noise. Following Golwala (2000), the best estimator for the amplitude is given by:

$$\hat{A} = \frac{\int_{-\infty}^{\infty} d\nu \frac{e^{i\omega\hat{t}} p^*(\nu) v(\nu)}{C(\nu)}}{\int_{-\infty}^{\infty} d\nu \frac{|p(\nu)|^2}{C(\nu)}} \ , \tag{11.4}$$

where the $\exp(i\omega\hat{t})$ term allows for a time offset in the pulse data.

11.1.3 Energy Resolution Limit Set By Resonators

To calculate the energy-resolution limit for our strip detectors set by the resonator (MKID) noise, we use a similar formalism. In this context, the energy resolution can be written as:

$$\sigma_E^2 = \left(\frac{E}{A}\right)^2 \sigma_A^2 \tag{11.5}$$

$$\sigma_E^2 = \left(\frac{E}{A}\right)^2 \left[\int_{-\infty}^{\infty} d\nu \ \frac{|p(\nu)|^2}{C(\nu)} \right]^{-1} , \tag{11.6}$$

This equation indicates the best possible resolution achievable given a particular pulse shape ($p(\nu)$) and noise power spectral density ($C(\nu)$). Changing to the full width at half max (FWHM) we pick up a factor of 2.355: $\Delta E_{\mathrm{FWHM}} = 2.355 \, \sigma_E$, and if we then use a single sided Fourier transform we end up with:

$$\Delta E_{\mathrm{FWHM}} = 2.355 \left|\frac{E}{A}\right| \left[\int_0^{\infty} d\nu \, 2 \frac{|p(\nu)|^2}{C(\nu)} \right]^{-\frac{1}{2}} . \tag{11.7}$$

This calculation can also be expressed as an integral of the noise-equivalent power (NEP), which is defined as:

$$\mathrm{NEP}^2(\nu) = \left(\frac{E}{A}\right)^2 \frac{2C(\nu)}{|p(\nu)|^2} \ , \tag{11.8}$$

so that the expression for energy resolution is:

$$\Delta E_{\mathrm{FWHM}} = 2.355 \left[\int_{-\infty}^{\infty} d\nu \frac{4}{\mathrm{NEP}^2(\nu)}\right]^{-\frac{1}{2}} \ . \tag{11.9}$$

To calculate for the discrete case we use the following transformations (see, e.g., Golwala 2000):

$$p(\nu) \longrightarrow \frac{p_n}{\Delta\nu} \tag{11.10}$$

$$C(\nu) \longrightarrow C_n \tag{11.11}$$

$$\int_{-\infty}^{\infty} d\nu \longrightarrow \sum_{n=-N/2}^{N/2-1} \Delta\nu \ . \tag{11.12}$$

Using these relations we have the expression for the energy resolution limit due to the resonator noise that we use in the data analysis:

$$\Delta E_{\mathrm{FWHM}} = 2.355 \left|\frac{E}{A}\right| \left[\sum_{n=0}^{N/2-1} 2\Delta\nu \frac{|p_n|^2}{(\Delta\nu)^2} \frac{1}{C_n}\right]^{-\frac{1}{2}} \tag{11.13}$$

$$= 2.355 \left|\frac{E}{A}\right| \left[\sum_{n=0}^{N/2-1} 2 \frac{|p_n|^2}{\Delta\nu} \frac{1}{C_n}\right]^{-\frac{1}{2}} \ . \tag{11.14}$$

11.1.4 Fitting for Absorber Diffusion Parameters

We determine the absorber diffusion constant (D) and recombination time τ_{Ta}, and accordingly determining the diffusion length $l_{Ta} = \sqrt{D\tau_{Ta}}$, by fitting the detailed pulse shapes from a set of measured pulses to a diffusion-recombination model. The set of measured pulses will include two pulse traces, one from each MKID, per X-ray absorption event. The fitting procedure allows each individual X-ray event to have a unique absorption location and time offset, but the entire set of pulses (generally we use $\sim$ 10 X-ray events per set) will be fit with a single Ta diffusion constant, Ta quasiparticle lifetime, Al quasiparticle

lifetime in MKID 1, Al quasiparticle lifetime in MKID 2 (the Al quasiparticle lifetimes are known to vary significantly from resonator to resonator and chip to chip; this is not fully understood at this time), and Al self-recombination constant.

The model starts by placing a Gaussian distribution of $N_{qp} = \eta h\nu/\Delta$ quasiparticles with a FWHM of 10 μm in in a tantalum strip, which is divided into 100 bins. The initial distribution is propagated forward in time with a time step of 2 ns using the Euler method, a standard numerical technique that acts do discretize the derivatives needed to calculate the quasiparticle dynamics given by Equation 8.37. Here we do not include the self-recombination term (Rn_{qp}^2) because the quasiparticle densities are not high enough in the Ta to be significantly affected by this term. When a quasiparticle reaches the end of the strip it diffuses into the Al MKID. Perfect trapping is assumed at the ends of the strip, so that any quasiparticles incident on the Ta/Al interface will diffuse into the Al and stay there. The quasiparticle populations in the Al MKIDs evolve based upon the incoming flux from the absorber and the quasiparticle recombination in the Al. In the case of the Al we do include the quasiparticle self-recombination term.

Measured pulses in phase are translated into quasiparticle pulses using the linear model for MKID responsivity given in Equation 8.24, using the Qs from the resonance fit and volume $V \sim 5000 \cdot 3 \cdot t$ in μm^3 where t is the thickness of the resonator in μm. This measured pulse data is then compared to the simulated data. The comparison of the data and the simulated pulses is performed with Matlab function `nlinfit`, which performs a nonlinear least squares regression given the measured data and the model function and returns the best fit coefficients. The nonlinear fitting is performed in time space. The following section presents results using this prescription; Figure 11.2 shows example pulses with the best-fit model simulations overlaid. Future work will involve combining an analytical model for the diffusion with the numerical model for the Al quasiparticle density and phase excursion (see, e.g., Kraus et al. 1989; Jochum et al. 1993).

11.1.5 Energy Resolution of a Strip Detector

Kraus et al. (1989) derives an expression for the number of quasiparticles that reach the ends of an absorber strip:

$$J(x_0) = J_0 \frac{\sinh(\beta x_0 L)}{\sinh(\beta)} \ , \tag{11.15}$$

where x_0 is the photon hit position, L is the length of the strip, and $\beta = L/\sqrt{D\tau}$. Using the value of β estimated with our diffusion fits, we compute the total energy of the photon J_0 using the expression:

$$J_0 = \sqrt{J_1^2 + J_2^2 + 2J_1 J_2 \cosh \beta} \ , \tag{11.16}$$

where J_1 and J_2 are the signals detected in MKIDs 1 and 2, respectively. By calculating J_0 for events of known energy (e.g, Mn Kα events) we are able to determine the energy resolution of the strip detector by fitting the distribution of J_0 values.

11.2 Data Analysis of Device Tested During Runs 79 and 82

Our to-date best strip-detector performance comes from an LT-A device from wafer B060530.1 that we measured during Run 79 and again in Run 82. The device has a 600 nm-thick Ta absorber with sloped edges, 200 nm-thick Al MKIDs with lateral trapping bars, and 400 nm-thick Al liftoff plugs. Table 9.1 presents further fabrication details. A short Letter (Mazin et al. 2006a) was published by our group on this device; the analyses here use the some of the same data sets but have been analyzed independently.

The 200 μm low-Q strip provided an excellent dataset from which to measure the strip-detector energy resolution. The data we present were measured during Run 82 at $T = 200$ mK[1] and microwave drive power of ~ -72 dBm. The resonators attached to this strip have $Q_1 \approx 20450$ and $Q_2 \approx 20840$ and resonance frequencies of $f_{0_1} \approx 6.845$ GHz and $f_{0_2} \approx 6.851$ GHz. Figure 11.2 gives an example of our X-ray pulse data. The signals measured in MKID 1 and MKID 2 are illustrated for a given X-ray absorption event in the Ta strip.

To understand the expected energy resolution limit from the MKIDs we measure the resonator noise by driving each resonator at f_0 for 10 s while recording the output. The power spectrum of the noise for the 200 μm long resonators is presented in the top left panel of Figure 11.2. This plot presents the frequency noise corrected to a resonator with

[1] This temperature was high due to amplifier heating issues described in § 9.2

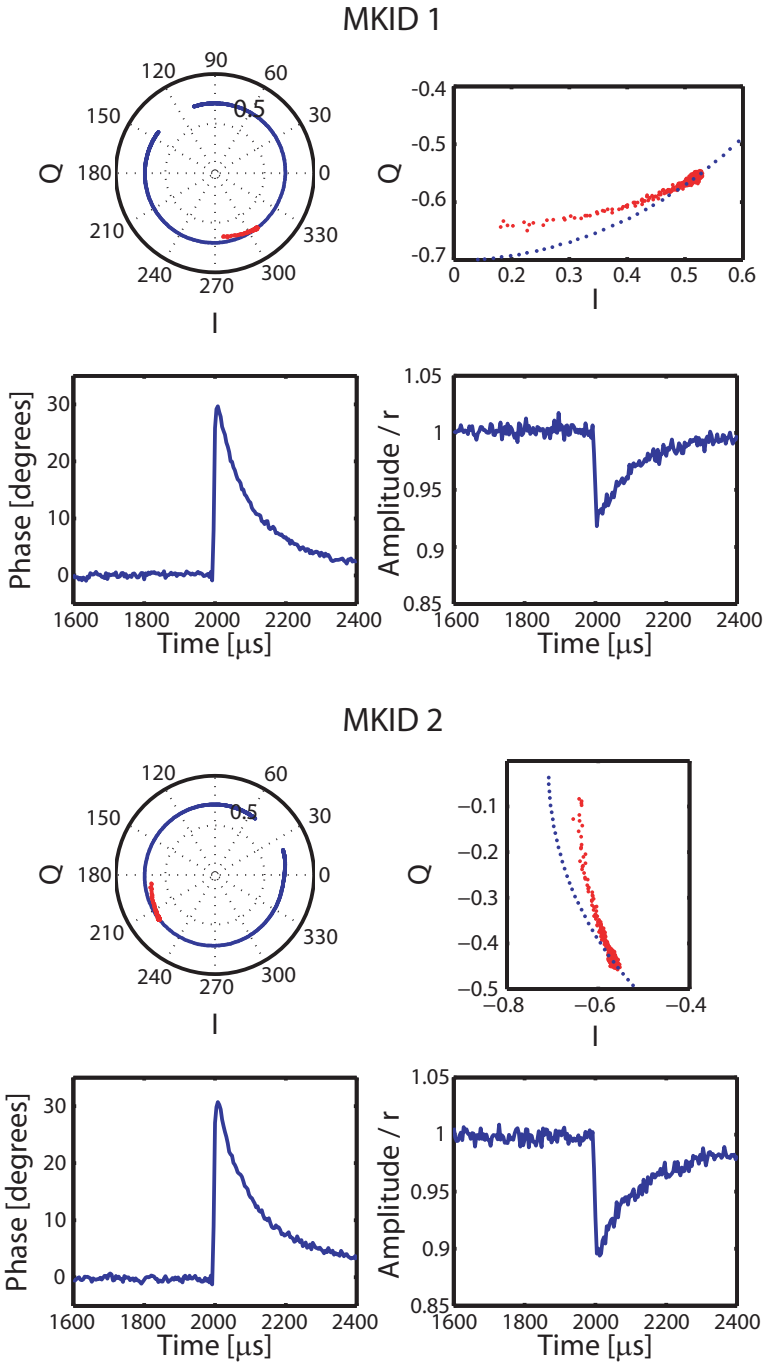

Figure 11.2 These plots show the response to a ^{55}Fe Kα X-ray absorption event in the Ta absorber from the 200 μm-long strip tested during Run 82. The top four panels show the response in MKID 1, while the bottom four panels show the response in MKID 2. In each set of plots the top left panel shows the resonance curve in I-Q space in blue (where each point represents the complex transmission at a given frequency) with the X-ray pulse overlaid in red. The pulse data points are drawn from the 4000 μs-long pulse time-stream where the microwave drive frequency is constant at f_0 and the X-ray absorption event occurs near $t = 2000$ μs. When the X-ray is absorbed, a shift in phase and amplitude is observed. The top right panel zooms in on the pulse, and the bottom two panels show the phase and amplitude as a function of time for this same X-ray pulse. The amplitude pulse is normalized by the radius of the resonance circle (r)

$f_0 = 4$ GHz, allowing comparisons between resonators of different Qs and f_0s. The frequency noise is calculated by calculating the power spectrum of the phase noise, S_θ and converting to $S_{f_0} = S_\theta/(4Q/f_0)^2$. To normalize to a resonator at 4 GHz, the frequency power spectral density is multiplied by $(4\text{ GHz}/f_0)^2$. Restricting ourselves to Mn Kα X-ray pulses from near the center of the Ta strip, we calculate a template pulse for each resonator by averaging the events with a phase change of $\geq 25°$ in both resonators. The template pulses are shown in both time-space and frequency-space in Figure 11.2. Using the noise spectra and the pulse templates we calculate the NEP for each resonator, and display the NEPs for MKID 1 in the final panel of Figure 11.2. Using Equation 11.14 we calculate the best expected energy resolution from each MKID. We find a FWHM energy uncertainty of 47 eV at 5.9 keV in MKID 1 using only the phase data, 109 eV at 5.9 keV using only the amplitude data, and 43 eV at 5.9 keV if we use both the amplitude and phase data. In MKID 2 we similarly find FWHM energy uncertainties of 48 eV (phase), 89 eV (amplitude), and 42 eV (2-D). For the purposes of this section we use only the phase data. Adding these uncertainties in quadrature we find $\Delta E_{FWHM} \approx 67$ eV at 5.9 keV, when using only the phase data. This measurement provides an estimate of the best energy resolution achievable given the resonator noise. Here we have assumed that the pulses are all the same shape, in reality the pulse shapes will vary although by restricting our analysis to only events with phase changes of $\geq 25°$ in both resonators we eliminate the more extreme pulse-shape deviations. This calculation also does not take into account quasiparticle losses. The effect of the losses will be minor for this 200 μm long strip (as evidenced by the straightness of the 6 keV lines in Figure 11.2), but will be more important for longer strips or on a device with a lower Ta diffusion length.

We also need to understand the losses in the strip. To this end we use the data from the 800 μm-long strip tested during Run 79. We use the 800 μm strip because it is the longest strip on the chip and will provide the most accurate determination of the diffusion parameters. Using the fitting code and multiple sets of ten pulses we find best-fit parameters of the tantalum diffusion constant, D, that range from $9-12$ cm^2 s^{-1} and best fit parameters for the Ta recombination that range from 25 μs to 32 μs. For the Al recombination times we find $\tau_{\text{Al }1} \approx 280 - 310$ μs and $\tau_{\text{Al }2} \approx 130 - 160$ μs. These values for the the Al recombination times are consistent with the values derived by fitting the tail of template pulses. Figure 11.2 shows two pulses with the pulse fit overlaid.

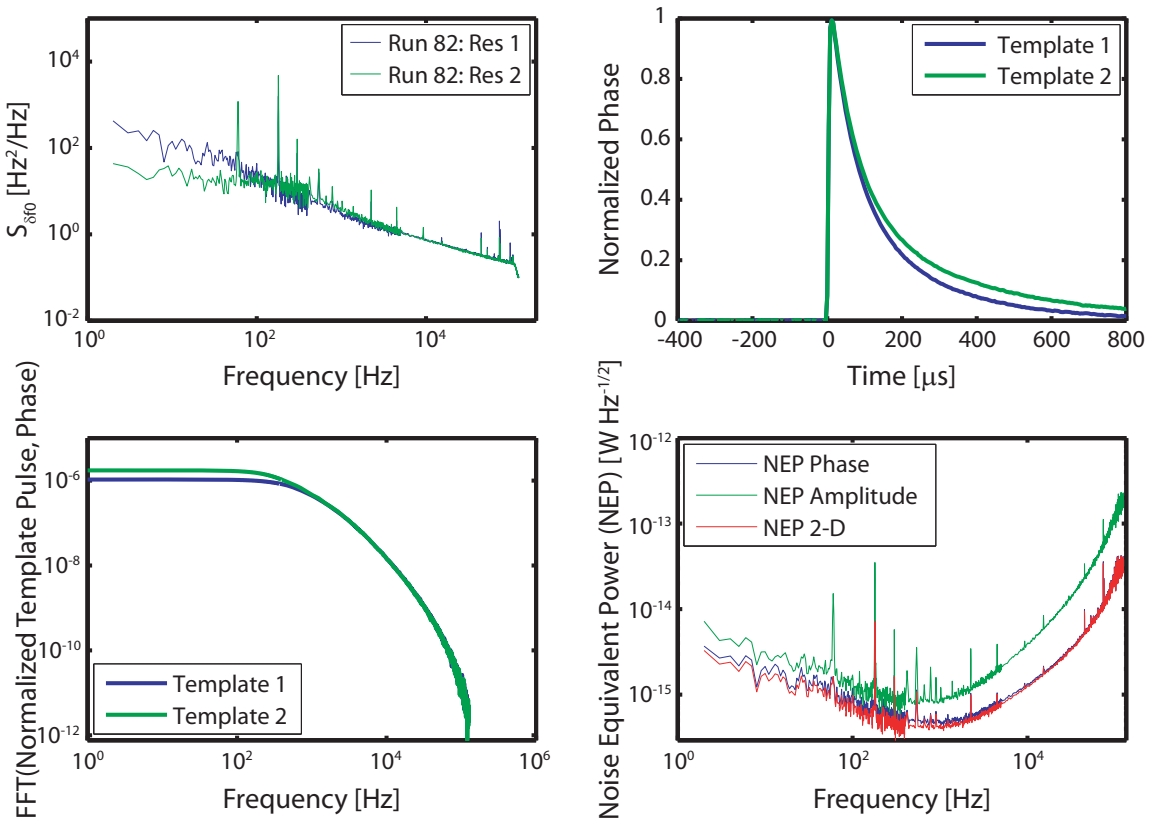

Figure 11.3 These data are derived from the 200 μm strip tested in Run 82. The top left panel shows the power spectra of the frequency noise measured in each resonator. The spectra have been converted to $f_0 = 4$ GHz. The top right panel shows the template pulse in each resonator, determined from Mn Kα events that occured near the center of the strip (restricted to pulses that show greater than 25° phase shift in each MKID). The bottom left panel shows these pulse templates in frequency space. The final panel shows the NEPs of MKID 1 calculated separately using the phase data and the amplitude data. The 2-D curve shows the NEP if we simultaneously use the phase and amplitude data. All three NEPs are calculated using the pulse templates (shown) from near the center of the absorber

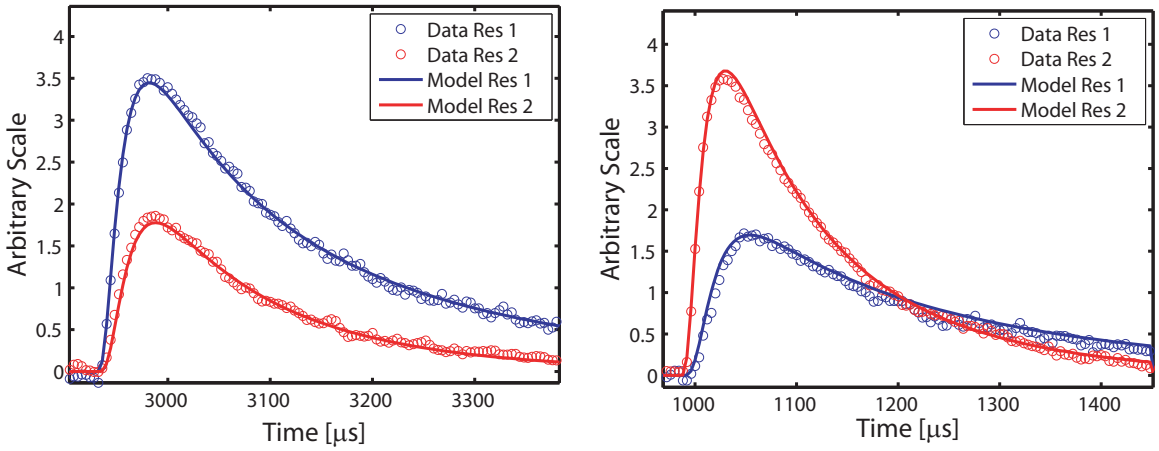

Figure 11.4 These plots show pulses from the 800 μm-long Ta strip tested in Run 79 at 160 mK (from the same chip that was also measured in Run 82), that were created by 5.9 keV absorptions that occured near the center of the strip. The circles present the measured phase shift in each resonator (with an arbitrary overall scale) as a function of time, while the solid lines show the fits provided by the diffusion model. The model was calculated by simultaneously fitting 10 pulses.

In Mazin et al. (2006a) we report a $D = 13.5 \pm 1.8$ cm^2 s^{-1} and a Ta quasiparticle lifetime of 34.5 ± 5.7 μs, which provide a tantalum diffusion length of 216 ± 30 μm; and Al recombination lifetimes of 186 ± 13 μs and $115 \pm 8.3 \mu$s. These parameters were generated by B. Mazin with a separate fitting procedure; future work entails reconciling the differences between these parameters and those derived using the fitting procedure described here.

The value of the diffusion constant we calculate is similar to or slightly higher than many presented in the literature, while the Ta recombination lifetime is lower. For example, Li et al. (2003) test a 600 nm-thick Ta absorber on an passivated Si substrate and find a diffusion constant of 8.3 cm^2 s^{-1} and a Ta recombination lifetime of 83 μs. It is possible that the recombinaton lifetime on our sapphire devices is lower than that on the passivated Si substrate because of phonon losses to the substrate, as Ta-sapphire interfaces have a better acoustic match than that of the interfaces of Ta and passivated Si. We also explored the idea that the diffusion length was being degraded by trapped magnetic fluxons in the strips, however after the installation of a a still shield made of Cryoperm magnetic shielding we did not observe an improvement in the difussion length. In addition, we are concerned that the sloped edges of the Ta strips are providing sites for excess quasiparticle recombination and plan to test a strip detector with straight walls along the length of the strip in the near future.

Switching back to the 200 μm-long strip measured in Run 82, Figure 11.2 shows the 'banana' plot of X-ray pulses. Each point on this plot represents a unique X-ray absorption event, with the phase shift in MKID 1 plotted against the phase shift in MKID 2. The pulse data has been optimally filtered and the heights we present are the optimal pulse-height estimates (see Equation 11.4). The left panel of the plot shows the pulses from the entire dataset of 20000 X-ray absorptions. A few features are readily noticeable: the two lines diagonally down the middle of the plot represent Mn Kα and Kβ absorptions in the Ta strip, where the pulse locations along the line are determined by the absorption location along the Ta strip. The line of pulses that lies along the x-axis and extends off the edge of the graph represent the pulses that were direct absorptions in MKID 1 (or the nearby ground plane) and accordingly the line of data along the y-axis represents direct hits in MKID 2. The scatter of data concentrated near the origin and extending toward the Mn Kα line represent absorptions in the substrate, either below the Ta strip or below the MKIDs. These pulses are not easily calibrated since the energy deposited into the system depends both on the X-ray absorption location on the chip and the absorption depth, but are easily eliminated using some combination of physical masking (e.g., see § 10.2.2), a thicker absorber with a higher X-ray stopping power, or post-experiment pulse analysis (the pulse shapes of many of the substrate events will be different from the events from X-rays that are absorbed in the Ta absorber).

We find that there is a very slight drift in our pulse-height data over time (the X-ray datasets often take of order half-a-day to acquire). For example, if we examine the Mn Kα line presented in the left panel of Figure 11.2 in detail, we find that the beginning of the dataset produces a curve nearer the origin, on average, than the data taken later in the run. This effect is likely caused by a drift in the center of the IQ plane which changes the pulse normalization; our newer array readout schemes (Mazin et al. 2006b) should eliminate this problem. This normalization change will degrade the energy resolution we measure; to this end we examine in detail the dataset that includes only the first 3000 X-ray absorptions in the total sample.

The right panel of Figure 11.2 presents the banana plot of these first 3000 data points. Using these optimally filtered phase pulse heights and the estimate of the diffusion length in the Ta strip, we calculate the total energy in each pulse using Equation 11.16, and again restrict our analysis to data from near the center of the strip (with a phase shift of $> 25^\circ$ in

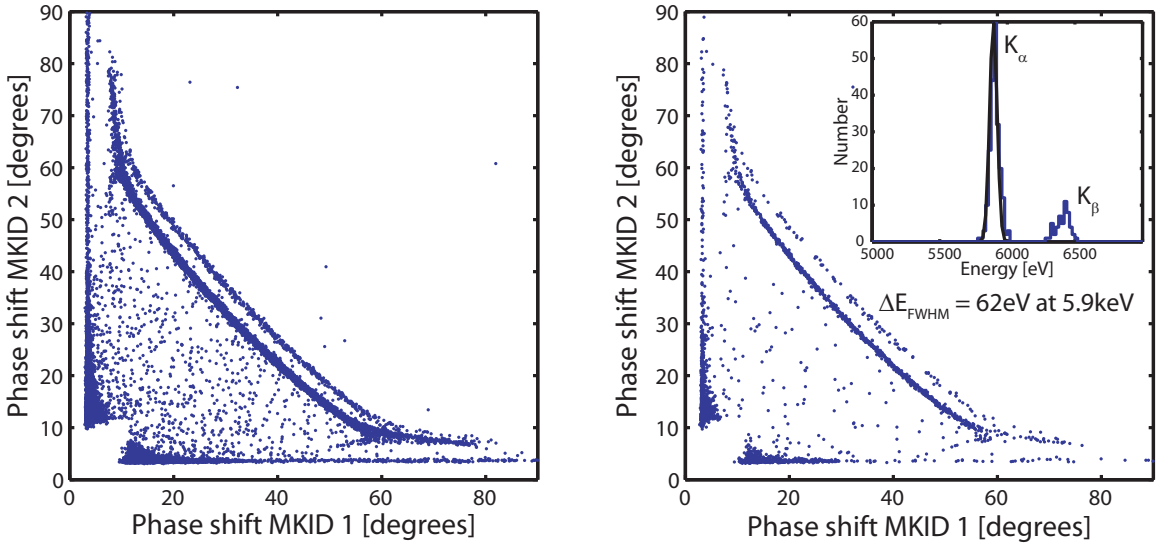

Figure 11.5 These plots show the optimally filtered maximum phase height in degrees observed in the MKIDs attached to the 200 μm-long Ta strip from Run 82 (a 'banana' plot). The left panel presents the data from 20000 X-ray events. Large pulses along each axis represent direct hits along the length of each Al resonator and the two diagonal strips near the center of the plot represent Mn Kα and Kβ absorptions in the Ta strip, respectively. X-ray absorptions in the substrate account for the pulses that fall below the Mn Kα line. The right panel presents the same data, but only the first 3000 X-ray events are shown. Using these data and restricting our analysis to points with phase shift greater than 25 degrees in both resonators (the center of the banana) we calculate a FWHM energy width of $\Delta E_{FWHM} = 65$ eV at 5.9 keV

both resonators). The histogram of the resulting energy distribution is presented in the top right panel of Figure 11.2, and a Gaussian fit to the Mn Kα line at 5.899 keV is overlaid. The histogram fit indicates a FWHM energy resolution of $\Delta E_{\mathrm{FWHM}} = 65$ eV. This energy resolution is consistent with the estimate of the energy resolution limit calculated using the resonator data and pulse template, where we estimated a combined energy resolution limit of 67 eV. This result indicates that, at the level of the phase noise measured in these particular resonators, the resonator phase noise provides the dominant limit to the strip-detector noise (the energy resolution does not appear to be limited by other loss processes in the strip, for example).

11.2.1 Brief Comparison to Run 86

The device tested in Run 86, Ch 1 is similar to that of Run 79/82, but with thicker films: 1 μm of Ta with sloped edges and 300 nm of Al for the MKIDs. The Al liftoff patch is

thinner than that of the Run 79/82 device, with a 300 nm Al liftoff patch over the Ta step. The RRR of the film is high, with RRR $\approx$ 53; however the increased Ta thickness and RRR did not act to increase the diffusion length. The 800 μm strips on this device did not produce useful datasets for modeling purposes (the bananas were buried in noise), so we had to rely on data from the 400 μm long strip. Using the nonlinear fitting technique with the diffusion-recombination model returned low values of the diffusion parameters ($D \lesssim 5$ cm^2 s^{-1} and $\tau_{Ta} \lesssim 10$ μs), but because of the losses in the strip the banana was strongly curved toward the origin and the pulses were noisy. The fit parameters reported here should only be used considered rough estimates of the best-fit values. Changes in the fitting procedure described in the previous section may aid in constraining these diffusion parameters.

11.2.2 Comparison to Run 87

In Run 87 we tested a device with similar fabrication parameters to the device tested in Runs 79 and 82, but with new sapphire and no Al liftoff patch over the edge of the Ta (both are fabricated with the Lateral Trapping Mask). Because we found that the energy resolution of the device from Run 79/82 was limited by the phase noise of the MKIDs, and because the sapphire (Valley Design) used for that device was known to cause a higher phase noise than our best results on sapphire, we thought that this new sapphire (Cryopolis) would provide a strip detector with improved energy resolution. The left panel of Figure 11.2.2 shows a comparison of the frequency noise between the Run 82 200 μm-long strip discussed previously, and the resonator noise of the 200 μm strip from Run 87. The MKIDs fabricated on the Cryopolis sapphire do show a lower frequency noise than the Run 82 MKIDs. However, the NEPs, plotted on the right panel, show the opposite trend. This effect is almost entirely due to the relative magnitudes of the phase shifts recorded in each dataset, which are likely the result of a short diffusion length in the Ta strip of the Run 87 device. Figure 11.2.2 illustrates the difference in maximum phase shifts: the banana of blue points is produced by ^{55}Fe-decay photons detected in Run 82, while the banana of red points is produced by ^{55}Fe-decay photons detected in the Run 87 device. The middle of the Run 82 banana has much higher pulse heights as compared to that in Run 87, while the opposite trend is expected, based on the relative quality factors. While both MKIDs in Run 82 have $Q \sim 20000$, both MKIDs in the Run 87 device have $Q \sim 37000$ (and the MKID responsivity is directly proportional to Q). For comparison, the banana with green points,

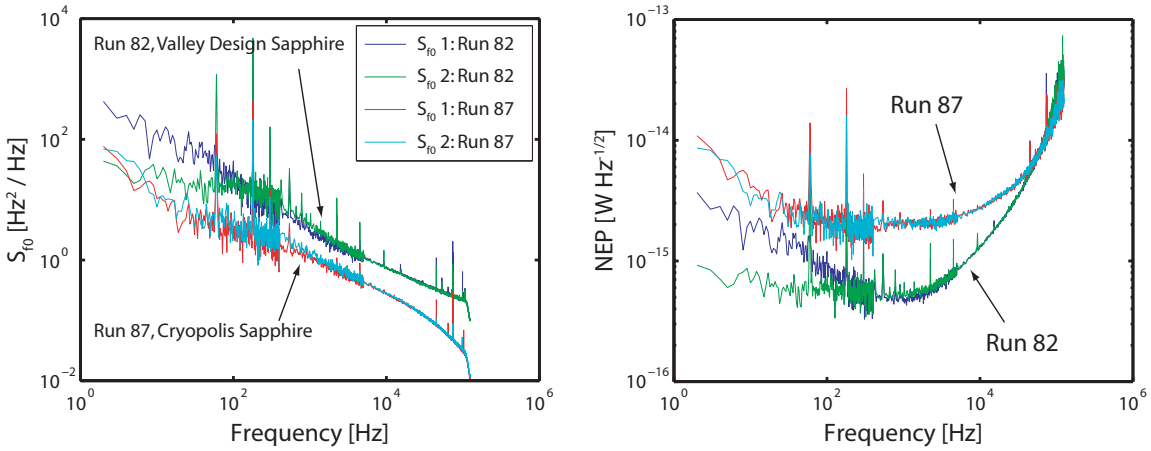

Figure 11.6 This plot shows a comparison of the frequency noise, normalized to $f_0 = 4$ GHz, between the 200 μm strip detectors tested in Runs 82 and 87, respectively. The fractional frequency noise is significantly lower on the Run 87 device with Cryopolis sapphire. The right panel shows the NEPs considering the phase noise and pulse templates. Again the pulse templates are calculated considering only X-ray absorption events near the center of each strip. The Run 82 NEP is significantly lower than the Run 87 NEP

closest to the origin, shows the Run 87 data corrected by the ratio of the Qs, calculated by multiplying each pulse height by 20000/37000. The Run 87 banana is also much more curved than that of the Run 82 banana, also indicative of losses in the strip.

The MKID responsivity itself behaves generally as expected, as the direct X-ray absorptions in either MKID, shown along the x- and y-axes, stretch to larger phase shifts in the Run 87 device as do those in the Run 82 device. (Note that in the Q-normalized green points the direct Al absorption points do not stretch as far as those from the Run 82 plot because the original Run 87 data (red) saturates at phase shifts of $\sim 160°$.) This also suggests that losses in the strip cause the depressed banana of Run 87.

In summary, although we were able to test a strip detector that exhibited lower resonator noise than the Run 82 device described earlier, the overall performance of the strip detector was poorer due to quasiparticle losses in the strip. The energy resolution limit calculated with Equation 11.14 is 130 eV (considering only the phase data).

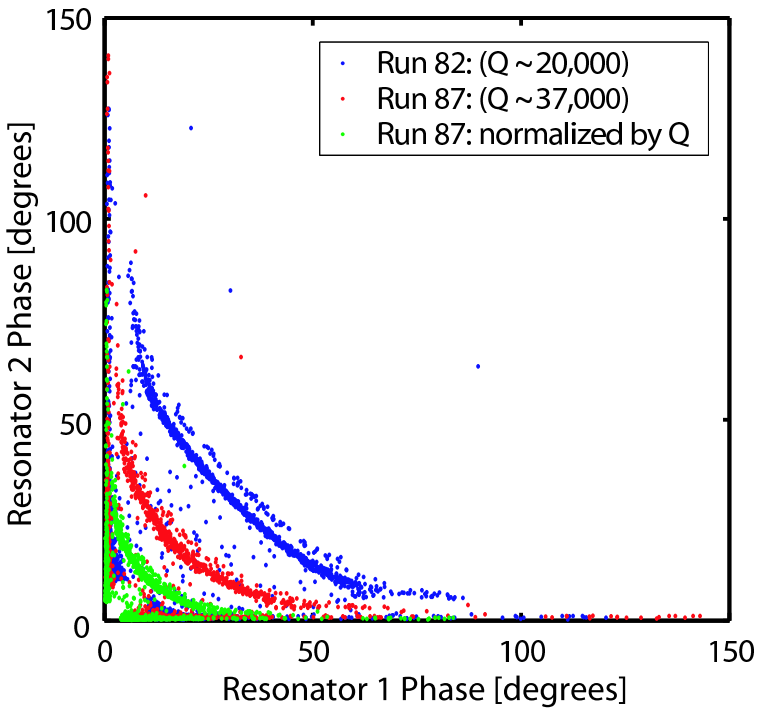

Figure 11.7 Maximum phase pulse height in resonator 1 versus resonator 2 for the 200 μm-long Ta strip detectors measured in Runs 82 and 87, respectively. Both MKIDs attached to the strip in Run 82 have $Q \sim 20000$, while the MKIDs attached to the strip in Run 87 have $Q \sim 37000$. The blue dots show the pulses measured in the Run 82 device, while the red dots show the pulses measured in the Run 87 device. The green dots show the pulses of the Run 87 device if we normalize to the Q of the Run 82 device (by multiplying each pulse height by $\sim 20000/37000$). This plot suggests that the quasiparticle losses during diffusion in the strip are much greater in the Run 87 device as compared to the Run 82 device (the volumes of the resonators are the same).

Chapter 12

MKIDs Conclusion

We explore novel photon-counting superconducting X-ray detectors that hold promise to fulfill the design requirements of next-generation X-ray astrophysics missions. By using high quality factor resonant circuits, MKIDs are able to employ passive frequency-domain multiplexing. Instead of requiring cryogenic preamplifiers and individual wiring at each detector element, MKIDs are capacitively coupled to a single microwave transmission line allowing hundreds or more detectors to be simultaneously monitored using a single input and single output coaxial cable. Each detector is both excited and read out with a sine wave at its unique microwave frequency. Array readouts comprised of synthesizers and quadrature receivers at room temperature are readily implemented using miniature, low-cost, low-power integrated circuits developed for wireless communication.

The practical application of MKIDs for photon detection requires a method of efficiently coupling the photon energy to the MKID. To this end we have been studying MKIDs in a strip-detector architecture for X-ray detection; the devices we present in this thesis use Ta absorbers and Al MKIDs. We have explored different detector designs and fabrication procedures, and the best energy resolution achieved to date is ≈ 65 eV (FWHM) at 6 keV. Although MKIDs are still in an early stage of development, the ease with which they can be multiplexed into large-format arrays is a key advantage over other cryogenic detectors, as progress in multiplexing TES microcalorimeters and other low-temperature detectors for X-ray detection has been slow.

Appendix A

Dilution Refrigerators

Common dilution refrigerators reach base temperatures of 10-100 mK. These refrigerators rely on ^{3}He – ^{4}He mixtures. This appendix describes the phase behavior of ^{3}He and ^{4}He mixtures and the general design of dilution refrigerators.

A.1 ^{3}He-^{4}He Mixtures

The detailed phase behavior of ^{3}He and ^{4}He mixtures provide dilution-refrigerator cooling power. Here we review the basic thermodynamics of these fluids.

Figure A.1 displays the phase diagram of liquid ^{3}He – ^{4}He mixtures, showing the normal, superfluid, and two-phase regions, plotted with temperature as a function of X_3, the fractional ^{3}He concentration. The mixtures exist in two configurations: a normal fluid and a superfluid. The separation between the two states occurs at the line marked 'lambda line.' At $T = 872$ mK and $X_3 = 0.669$ there exists a 'tricritical point.' At temperatures below the tricritical point there is a coexistence curve that encloses a region where the liquid separates into two phases: a ^{4}He-rich phase and a ^{3}He-rich phase. In this region only points that lie on the curves represent real states of the mixture. The phase diagram shows that a ^{3}He – ^{4}He mixture will always separate into these two phases below $T \sim 870$ mK if there is at least 6% ^{3}He present.

The vertical dashed line in Figure A.1 demarcates the 'dilute' region, where $X_3 \leq 0.15$. In this region the ^{3}He portion of the mixture can be considered a gaslike solute. In this 'dilute' region, at low temperatures ($T \lesssim 500$ mK) the ^{4}He is non-interactive and can be approximated as a vacuum; the ^{3}He in the ^{4}He -rich phase behaves as a perfect gas with effective mass $m_3^* = 2.4 m_3$ (Betts 1989).

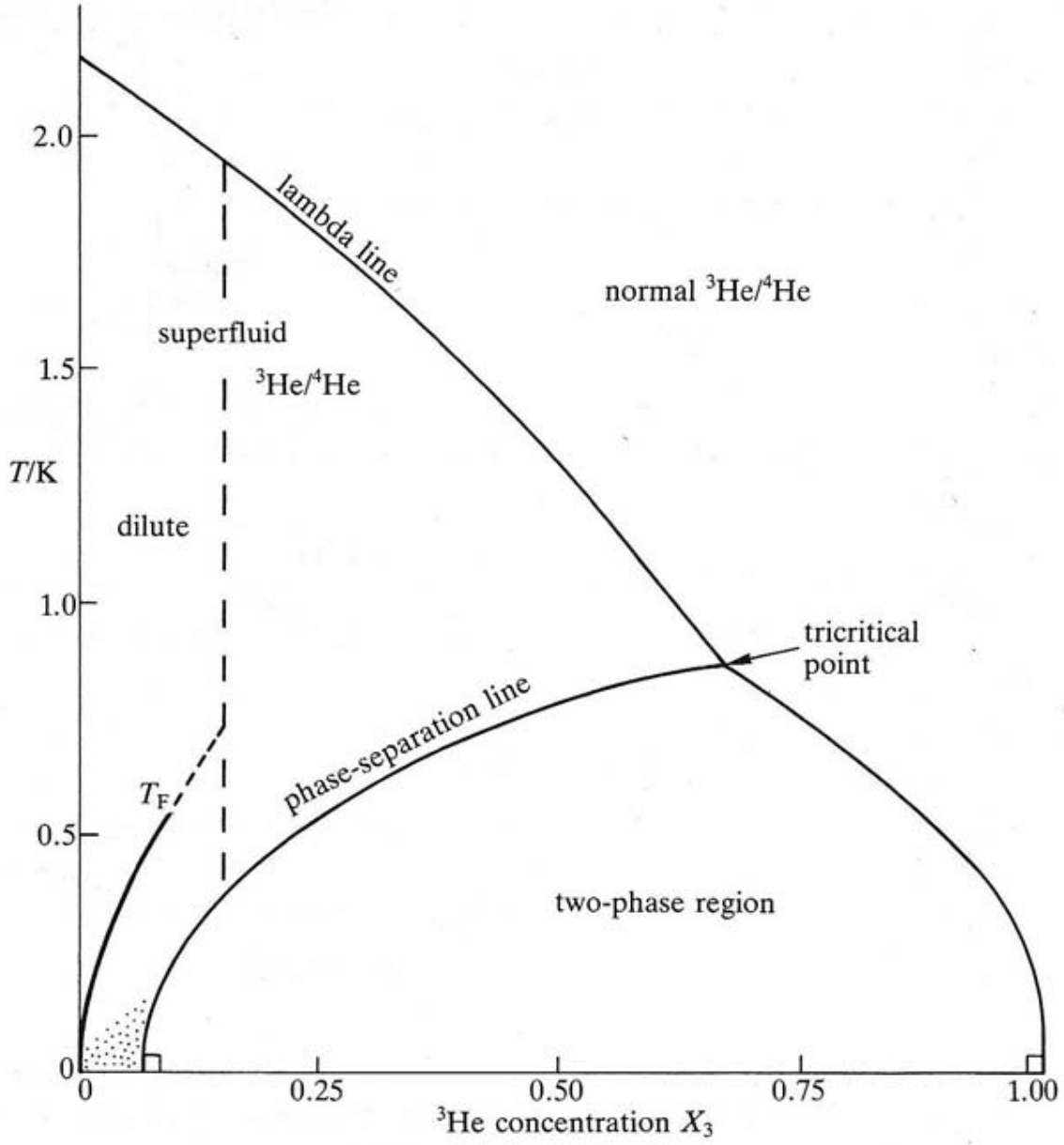

Figure A.1 Phase diagram of liquid ^{3}He -^{4}He mixtures at zero pressure, with temperature in Kelvin versus ^{3}He concentration. The diagram is from (Wilks & Betts 1987) and references therein

A.2 Design of a Dilution Refrigerator

It is the two-phase region below the tricritical point that is exploited in dilution refrigerators. In particular, the fact that the ^{4}He-rich phase will always contain a finite amount of ^{3}He, even as $T \to 0$ K, is critical for reaching the lowest temperatures. As a consequence of the phase separation, combined with the differing masses of ^{4}He and ^{3}He, the two-phase region always involves a physical separation of the phases, with the ^{3}He-rich phase floating on top of the ^{4}He-rich phase.

Figure A.2 illustrates a simple example of the concept of dilutive cooling, as compared to evaporative cooling. In this cartoon the left diagram shows evaporative cooling, where the cooling occurs due to lowering of the vapor pressure, as discussed for ^{3}He refrigerators, while the right diagram illustrates dilutive cooling. The dilutive cooling can be though of as an inverted example of evaporative cooling. In this case pot at the bottom is filled with a liquid phase on top of a dilute gaseous phase: for mixtures of ^{3}He and ^{4}He the liquid would be the ^{3}He-rich phase of the mixture while the gas would be the dilute ^{3}He in the 'vacuum' of superfluid ^{4}He. The cooling would occur as the gaslike ^{3}He is pumped away and ^{3}He atoms from the ^{3}He-rich phase are forced to move across the phase boundary and into the lower ^{4}He-rich phase. The problem with this simple cartoon of dilutive cooling (Figure A.2) is that the vapor pressure of the ^{4}He-rich phase is nearly zero, and any real-world pump will not be able to lower the vapor pressure of the dilute ^{3}He. However, this setup can be modified to provide practical cooling schemes.

Figure A.3 diagrams a common layout for dilution refrigerators. The bottom pot, or mixing chamber, serves the same purpose as the pot in the simplified example of dilution cooling: the mixing chamber, with $T < 870$ mK, is the area where the phase boundary exists and thus where the dilution occurs. The mixing chamber achieves the lowest temperature in the system and is where the refrigeration occurs – in experiments the low-T sample stage is affixed to the mixing chamber wall (typically to the bottom surface of the mixing chamber). The base temperature of the refrigerator is established by a balance between the heat load on this cold stage and the cooling power of the refrigerator.

Instead of pumping directly on the dilute mixture at the cold stage, the pumping occurs at the still. The goal of the still stage is to pump nearly pure ^{3}He out of the ^{4}He-rich phase, leaving all of the ^{4}He in the superfluid. This goal is well achieved by having a chamber that

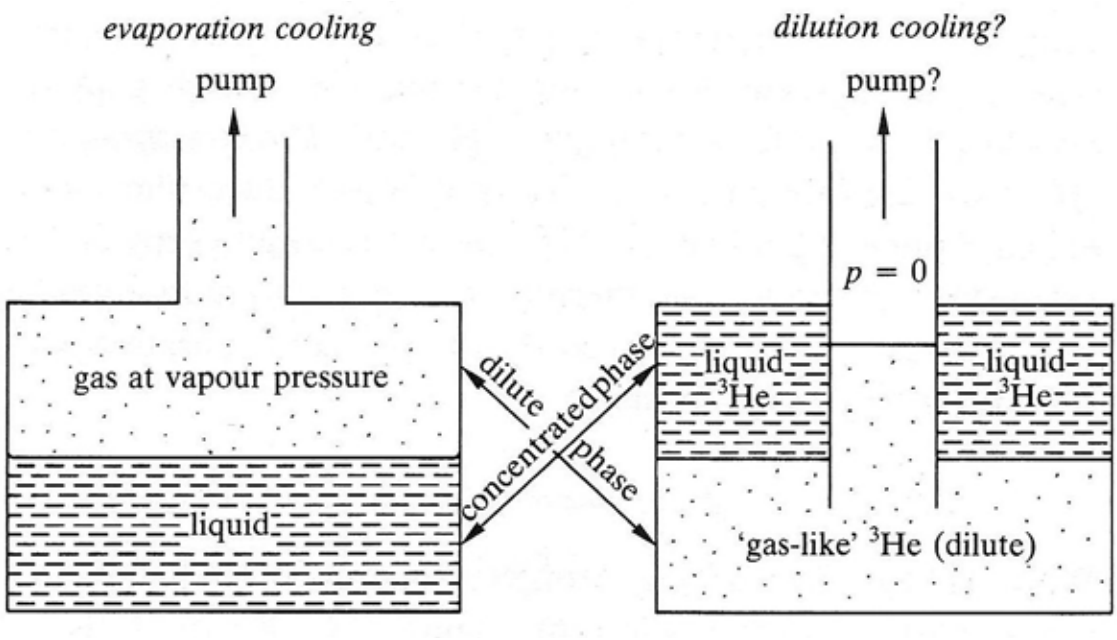

Figure A.2 This cartoon illustrates the idea of dilution cooling as compared to evaporative cooling. Digram credit: Betts (1989)

is maintained at $\sim$ 0.7 K. A tube from the lower ^{4}He-rich phase in the mixing chamber brings the mixture through a heat exchanger and into the still. The concentration of ^{3}He in the still depends on balancing the osmotic pressure between the ^{3}He in the still and the ^{3}He in the mixing chamber – this balance will be affected by the temperatures of each stage. Also affected by temperature is the ratio of ^{3}He to ^{4}He that is pumped away when the still mixture is pumped on by an external pump.

A heater is applied to the walls of the still chamber so that the mixture inside the still remains at $\sim 0.65 - 0.7$ K. This temperature will cause the ^{3}He-vapor pressure to be a maximal $\sim$ 1000 times larger than that of the ^{4}He, meaning that the system will attain its goal of pumping nearly pure ^{3}He from the mixture. The imbalance in osmotic pressure between the ^{3}He in the still and the mixing chamber will cause atoms to pass from the upper layer in the mixing chamber to the lower layer, thus providing the cooling.

The tube from the room-temperature pump back to the mixing chamber contains almost pure ^{3}He. The ^{3}He gas from room temperature is condensed to a liquid in the condenser, which is kept at $T \sim 1.5$ K. The condenser temperature is maintained by the '1 K pot,' a pot of liquid ^{4}He with its vapor pressure lowered such that its temperature remains at 1.5 K. The condensed ^{3}He gas flows down through a heat exchanger and into the ^{3}He-rich

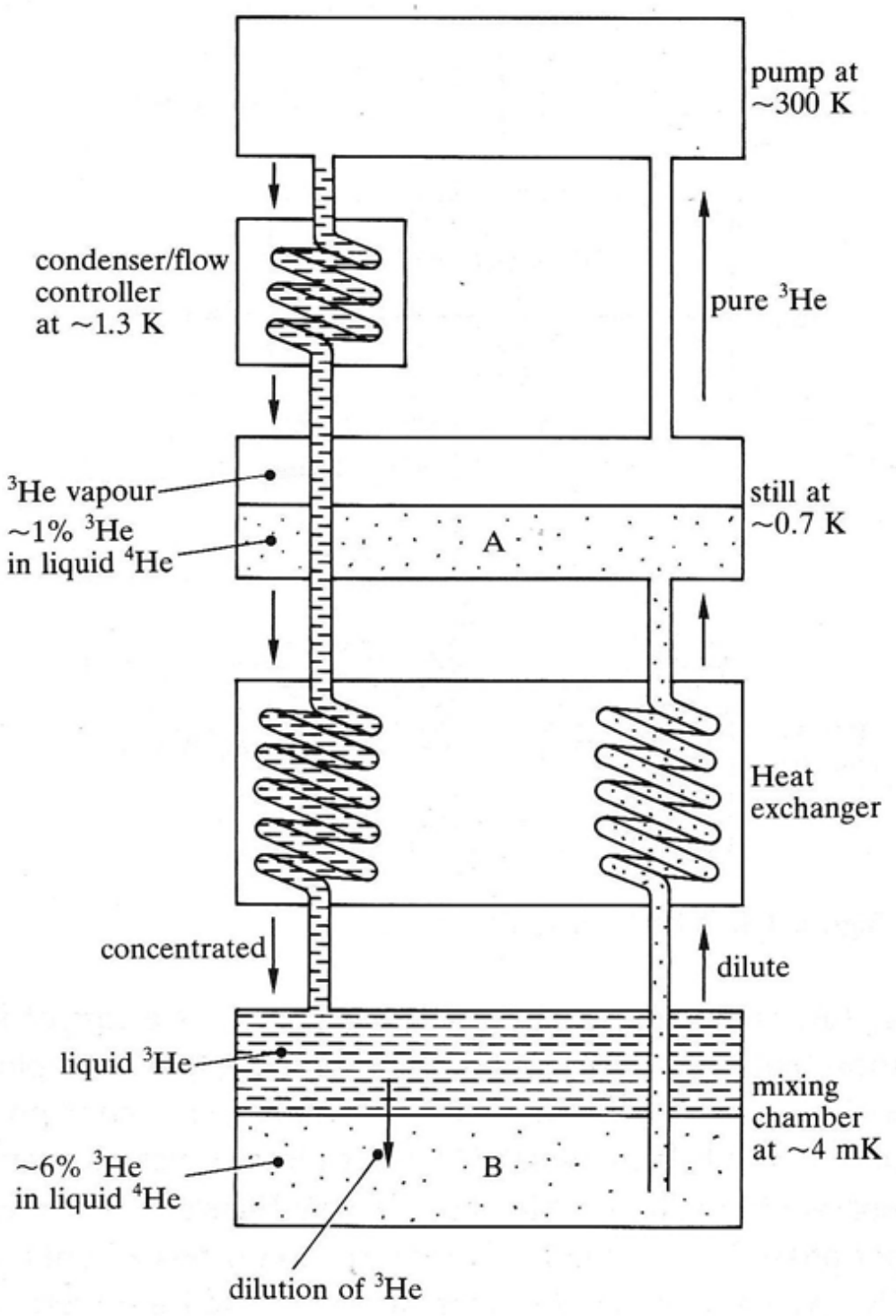

Figure A.3 This diagram shows the main components of a dilution refrigerator with continuous circulation. The mixing chamber is at the bottom, where the liquid ^{3}He phase floats on top of the ^{4}He-rich phase. ^{3}He is forced down across the phase boundary into the ^{4}He-rich phase providing cooling power. Diagram Credit: Betts (1989)

layer of the mixing chamber, replenishing the supply of ^{3}He.

Much of the internals of a refrigerator are contained within a vacuum chamber. For example, in Figure A.3, all components aside from the ~ 300 K pump lie physically inside an inner vacuum chamber. The vacuum chamber is surrounded by the liquid-^{4}He bath. Being surrounded by vacuum allows these components to stay at $T < 1$ K instead of being immediately heated to 4 K if in direct contact with a liquid-^{4}He bath.

Appendix B

Phonon Loss to Substrate During Initial Energy Downconversion

When we consider the initial quasiparticle generation after the absorption of an X-ray in our strip absorber, we typically assume that, during the initial energy downconversion, all the phonons stay in the Ta and create quasiparticles. In this case the phonon energy stays in the system until it is sensed by the MKIDs. However, in the thin films used in our devices, the phonon mean free path may be longer than the distance from the photon absorption site to the substrate. Productive phonons may be lost to the substrate during the initial energy downconversion cascade, with the magnitude of the loss dependent on the depth of the photon absorption. This process will act to degrade the energy resolution of the device. Since the X-ray absorption depth is a strong function of the photon energy, this means that this phonon loss will be energy dependent. Martin et al. (2006) study optical Al/Ta STJs and find a degradation in resolving power that they attribute to phonon noise generated during energy down-conversion in the superconducting electrodes; the degradation is energy dependent and is seen to correlate with changes in the Ta absorption depth.

The physics of the energy downconversion in the absorber is described in Section 8.5.1.1, which relies heavily on Kozorezov et al. (2000). In this section we derive an expression for the magnitude of the energy resolution degradation at 6 keV in Ta films with thicknesses of $\sim 500 - 1000$ nm.

Photon absorption is described by:

$$I(x) = I_0 \ \exp\left(-\frac{x}{l_x}\right) \ , \tag{B.1}$$

where I_0 is the flux incident on the surface, I is the flux at distance x from the surface, with

the surface at $x = 0$ and the substrate at $x = d$. At 6 keV the cross-section for absorption in tantalum is $\sigma_{\rm Ta} = 355$ cm^2 g^{-1} and the density is $\rho_{\rm Ta} = 16.6$ g cm^{-3}. The absorption depth of Ta is thus $l_x = (\sigma\ \rho)^{-1} = 1.7$ μm. At 6 keV a 1 μm-thick film will absorb 44% of the photons; a 0.5 μm-thick film will absorb 25%. The photon flux is equally described by the photon number:

$$N(x) = N_0\ \exp\left(-\frac{x}{l_x}\right)\ , \tag{B.2}$$

and the photon energy at x may be described as:

$$E_\gamma(x) = N_0\gamma_0\ \exp\left(-\frac{x}{l_x}\right)\ , \tag{B.3}$$

where γ_0 is the incident photon energy.

$$\frac{dN}{dx} = -\frac{N}{l_x}\ , \tag{B.4}$$

and the probability of being absorbed in dx at x is dx/l_x.
The number absorbed in dx at x is given by:

$$\frac{N(x)}{l_x}\ dx = \frac{N_0}{l_x}\ \exp\left(-\frac{x}{l_x}\right)\ dx\ . \tag{B.5}$$

Table B.1 provides relevant parameters for Ta, taken from the literature (e.g., Kaplan 1979; Goldie et al. 1994; Kozorezov et al. 2000; Martin et al. 2006).
With $\tau_{\rm ph} \sim 80$ ps the phonon mean free path against pair breaking for Ω_1 phonons (Kozorezov et al. 2000) is $l_{\rm ph} \approx \tau_{\rm ph}\ c \approx 0.2$ μm.

Acoustic mismatch theory (Kaplan 1979) provides that a critical cone for transmission of phonons incident from Ta to sapphire. For Ta/sapphire interfaces the critical angle to the normal of the surface is $\theta_{\rm critical} = 19°$, and the probability for a phonon to be traveling within the cone is given by $p_{\rm escape} = \sin^2(\theta_{\rm critical}/2) = 0.027$.

A photon is deposited at $0 \leq x \leq d$ (0.5 μm $\leq d \leq$ 1 μm) and excites electrons and then a phonon production cascade of $E_{\rm phonon} = \Omega_D$ in $\tau_1 \simeq 1.6$ ps, where τ_1 is the time it takes for the downconversion from hot electrons to the Debye-energy phonon "bubble" (Kozorezov et al. 2000), while traveling less than 1 nm. These Debye phonons start to break Cooper pairs at a rate of $\tau_{\rm ph,D}^{-1}$ and downconvert toward Ω_1 in a few $\tau_{\rm ph,D}$ cycles (it takes

Table B.1. Important Ta parameters

v_e	$5-10$ cm^2 s^{-1}	electron velocity
D_e	$\sim 10^{-4}$ m^2 s^{-1}	diffusion constant of electrons
l_e	0.1 nm	electron mean free path
ϵ_F	9.5 eV	Fermi energy
Δ	0.7 meV	Superconducting gap energy
ε	$1.7 \times \Delta = 1.19$ meV	average energy to break Cooper pair
Ω_D	20.7 meV	Debye phonon energy
$\tau_{\rm ph,D}$	2.4	pair-breaking time for Debye energy phonon
Ω_1	3.3 meV	phonon energy below which phonon control ends
$\tau_{\rm ph}$	$22-80$	phonon lifetime (for Ω_1 phonons)
c	2.5×10^5 cm s^{-1} = 2.5 nm $^{-1}$	low-frequency phonon sound velocity
$\theta_{\rm critical}$	19°	critical angle to normal of surface
$p_{\rm escape}$	0.027	probability of being inside critical cone

26 ps to get to $\Omega \sim 2\Delta$). The phonons near Ω_1 travel at c in Ta toward the interface, where some will be lost (Ω_1 is the phonon energy below which the phonon control gives way to electronic control).

For a given photon deposition at x the probability of losing $N_{\rm lost}$ phonons is[1]

$$p_{N_{\rm lost}} = \frac{1}{\sqrt{2\pi}\sigma(x)} \exp\left[-\frac{(N_{\rm lost} - N_0(x)p_{\rm escape})^2}{2\sigma^2(x)}\right] , \tag{B.6}$$

where $N_0(x) = N_{\Omega_1}\ \exp\left(-\frac{d-x}{l_{\rm ph}}\right)$ and

$$\sigma^2(x) = N_{\Omega_1}\ \exp\left(-\frac{d-x}{l_{\rm ph}}\right)\ p_{\rm escape}\ . \tag{B.7}$$

We transform the equation for $p_{N_{\rm lost}}$ to a probability of loss that depends on energy, $p_x(E_{\rm lost} = E_0 - E)$, by making the substitution:

$$N_{\rm lost} = \left(\frac{E_0 - E}{E_B}\right) , \tag{B.8}$$

[1]Here we are simplifying the calculation by assuming a near normal phonon-travel length of $d-x$, when in reality phonons will travel $(d-x)/\cos(\theta)$

$$p_x(E_{\rm lost} = E - E_0) = \frac{1}{\sqrt{2\pi}\sigma(x)} \exp\left(-\frac{\left[\left(\frac{E_0 - E}{E_B}\right) - N_0(x) p_{\rm escape}\right]^2}{2\sigma^2(x)} \right) , \tag{B.9}$$

where E_B is the (average) energy of the lost phonon. Now we need to average over the photon absorption location x:

$$\langle o_{E_{\rm lost}} \rangle = \int_0^d \frac{dx}{l_x} \exp\left(-\frac{x}{l_x}\right) p_x(E_{\rm lost} = E_0 - E) \tag{B.10}$$

$$\begin{aligned} =& \frac{1}{\sqrt{2\pi}} \int_0^d \frac{dx}{l_x} \left[\frac{1}{N_{\Omega_1} p_{\rm escape} \exp\left(-\frac{d-x}{l_{\rm ph}}\right)} \right]^{1/2} \\ & \times \exp\left[-\frac{x}{l_x} - \frac{\left(\frac{E_0 - E}{E_B} - N_{\Omega_1} \exp\left(-\frac{d-x}{l_{\rm ph}}\right) p_{\rm escape}\right)^2}{2 N_{\Omega_1} \exp\left(-\frac{d-x}{l_{\rm ph}}\right) p_{\rm escape}} \right] \end{aligned} \tag{B.11}$$

This expression allows us to calculate the spread in energy due to phonon loss. The parameters in this equation will typically lie in the following ranges (e.g., see Kaplan 1979; Goldie et al. 1994; Kozorezov et al. 2000; Martin et al. 2006):

$$\tilde{n} = N_{\Omega_1} p_{\rm escape} \approx 5.5 \times 10^4 \tag{B.12}$$

$$\beta = \frac{l_{\rm ph}}{l_x} \approx 0.2 - 0.1 \tag{B.13}$$

$$\bar{d} = \frac{d}{l_{\rm ph}} \approx 3 - 5 \tag{B.14}$$

We calculate the value of this integral using Mathematica for a 600 nm-thick Ta film with the following choice of parameters: $\tilde{n} = 5 \times 10^4$, $\bar{d} = 3$, and $\beta = 0.1$. Figure B.1 presents the result of the integration, which shows that a 6 keV line will be spread by about 10 eV (FWHM) due to the phonon energy lost to the substrate during the initial energy downconversion. Going to thicker Ta films will greatly reduce this effect.

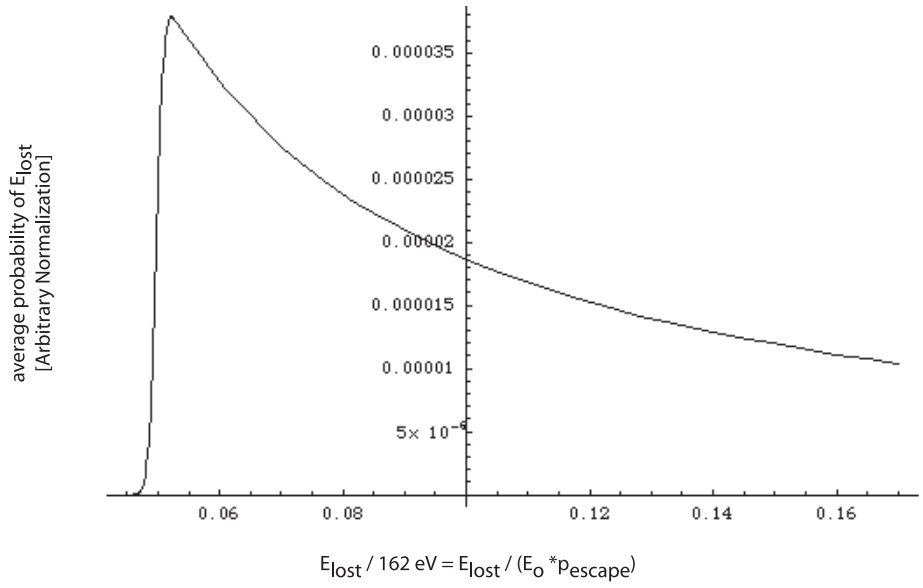

Figure B.1 This figure presents the average probability of phonon energy loss E_{lost} to the substrate as a function of E_{lost} normalized by 162 eV (162 eV is the quantity $E_0 \times p_{\text{escape}}$, where $E_0 = 6$ keV is the incident photon energy). The curve is calculated using Equation B.11 and the parameters $\tilde{n} = 5 \times 10^4$, $\bar{d} = 3$, and $\beta = 0.1$

Bibliography

Abazajian, K. *et al.* 2003, Astron. J., 126, 2081 57

Akiyama, M., Ueda, Y., and Ohta, K. 2002, IAU Colloquium 184 'AGN Surveys'; astro-ph/0201495 23

Akiyama, M., Ueda, Y., Ohta, K., Takahashi, T., and Yamada, T. 2003, Astrophys. J. Suppl., 148, 275 3, 81, 82

Akiyama, M. *et al.* 2000, Astrophys. J., 532, 700 3, 23, 25, 67, 82

Alexander, D. M. *et al.* 2001, Astron. J., 122, 2156 72

—. 2003, Astron. J., 126, 539 3, 53, 70, 71, 81, 82

Alonso-Herrero, A. *et al.* 2006, Astrophys. J., 640, 167 161

Antonucci, R. 1993, Annu. Rev. Astron. Astrophys., 31, 473 14, 88, 89, 144

Antonucci, R. R. J. 1982, Nature, 299, 605 14

Antonucci, R. R. J. and Miller, J. S. 1985, Astrophys. J., 297, 621 14

Baldi, A., Molendi, S., Comastri, A., Fiore, F., Matt, G., and Vignali, C. 2002, Astrophys. J., 564, 190 24, 54, 80

Bardeen, J., Cooper, L. N., and Schrieffer, J. R. 1957, Phys. Rev., 108, 1175 193

Barger, A. *et al.* 2003, Astron. J., 126, 632 3, 70, 71, 81, 82, 146, 150

Barger, A. J., Cowie, L. L., Bautz, M. W., Brandt, W. N., Garmire, G. P., Hornschemeier, A. E., Ivison, R. J., and Owen, F. N. 2001a, Astron. J., 122, 2177 24, 137

Barger, A. J., Cowie, L. L., Brandt, W. N., Capak, P., Garmire, G. P., Hornschemeier, A. E., Steffen, A. T., and Wehner, E. H. 2002, Astron. J., 124, 1839 23, 73

Barger, A. J., Cowie, L. L., Mushotzky, R. F., and Richards, E. A. 2001b, Astron. J., 121, 662 24

Bauer, F. E., Alexander, D. M., Brandt, W. N., Schneider, D. P., Treister, E., Hornschemeier, A. E., and Garmire, G. P. 2004, Astron. J., 128, 2048 149

Bautz, M. W. *et al.* 1998, in Proc. SPIE Vol. 3444, p. 210-224, X-Ray Optics, Instruments, and Missions, Richard B. Hoover; Arthur B. Walker; Eds., 210–224 17, 27, 82

Becker, R. H., White, R. L., and Helfand, D. J. 1995, Astrophys. J., 450, 559 148

Bertin, E. and Arnouts, S. 1996, Astron. & Astrophys., 117, 393 37, 57, 67

Betts, D. S. 1989, An Introduction to Millikelvin Technology (Cambridge University Press) 266, 269, 270

Booth, N. E. 1987, Appl. Phys. Lett., 50, 295+ 211, 212

Boyle, B. J., Griffiths, R. E., Shanks, T., Stewart, G. C., and Georgantopoulos, I. 1993, Mon. Not. R. Astron. Soc., 260, 49 14

Brandt, W. N., Alexander, D. M., Bauer, F. E., and Vignali, C. 2004, in Physics of Active Galactic Nuclei at All Scales, Eds. Alloin D., Johnson R., Lira P. (Springer-Verlag, Berlin), astro-ph/0403646 54

Brandt, W. N. *et al.* 2001, Astron. J., 122, 2810 23, 25, 26, 29

Brandt, W. N. and Hasinger, G. 2005, Annu. Rev. Astron. Astrophys., 43, 827 3, 20, 79, 146

Brinkmann, W. *et al.* 1997, Astron. & Astrophys., 323, 739 127

Broos, P., Townsley, L., Getman, K., and Bauer, F. 2002, ACIS Extract, An ACIS Point Source Extraction Package, Pennsylvania State University 106, 172

Brusa, M. *et al.* 2003, Astron. & Astrophys., 409, 65 54, 147

Cagnoni, I., della Ceca, R., and Maccacaro, T. 1998, Astrophys. J., 493, 54 25

Canizares, C. R. *et al.* 2005, Proc. Astron. Soc. Pacific, 117, 1144 17

Capak, P. *et al.* 2004, Astron. J., 127, 180 58, 59

Cash, W. 1979, Astrophys. J., 228, 939 106

Comastri, A. *et al.* 2002, Astrophys. J., 571, 771 116, 146, 160

Comastri, A., Setti, G., Zamorani, G., and Hasinger, G. 1995, Astron. & Astrophys., 296, 1 14

Condon, J. J., Cotton, W. D., Greisen, E. W., Yin, Q. F., Perley, R. A., Taylor, G. B., and Broderick, J. J. 1998, Astron. J., 115, 1693 148

Cowie, L. L., Garmire, G. P., Bautz, M. W., Barger, A. J., Brandt, W. N., and Hornschemeier, A. E. 2002, Astrophys. J., 566, L5 3, 20, 24, 25, 34, 37, 38, 42, 71, 79

Crotts, A. P. S. 2001, BAAS, 33, 792 55, 56

Dawson, S., McCrady, N., Stern, D., Eckart, M. E., Spinrad, H., Liu, M. C., and Graham, J. R. 2003, Astron. J., 125, 1236 70, 146

Day, P. K. 2002, Quarterwave transmission line resonators, unpublished 199

Day, P. K., LeDuc, H. G., Mazin, B. A., Vayonakis, A., and Zmuidzinas, J. 2003, Nature, 425, 817 5, 181, 192, 195, 196, 197

Devriendt, J. E. G., Guiderdoni, B., and Sadat, R. 1999, Astron. & Astrophys., 350, 381 167

Dickey, J. M. and Lockman, F. J. 1990, Annu. Rev. Astron. Astrophys., 28, 215 27, 122

Donley, J. L., Rieke, G. H., Pérez-González, P. G., Rigby, J. R., and Alonso-Herrero, A. 2007, Astrophys. J., 660, 167 166

Doriese, W. B. *et al.* 2004, Appl. Phys. Lett., 85, 4762 188

Dressler, A. and Gunn, J. E. 1983, Astrophys. J., 270, 7 154

Eckart, M. E., Laird, E. S., Stern, D., Mao, P. H., Helfand, D. J., and Harrison, F. A. 2005, Astrophys. J. Suppl., 156, 35 6, 16, 24, 53, 64, 80, 172

Eckart, M. E., Stern, D., Helfand, D. J., Harrison, F. A., Mao, P. H., and Yost, S. A. 2006, Astrophys. J. Suppl., 165, 19 6, 24, 78

Eisenhardt, P. R. *et al.* 2004, Astrophys. J. Suppl., 154, 48 161

Faber, S. M. *et al.* 2003, in Instrument Design and Performance for Optical/Infrared Ground-based Telescopes. Proceedings of the SPIE., ed. M. Iye & A. F. M. Moorwood, 1657–1669 83

Fano, U. 1947, Phys. Rev., 72, 26 213

Feigelson, E. D. *et al.* 2004, Astrophys. J., 611, 1107 130

Field, G. B. and Perrenod, S. C. 1977, Astrophys. J., 215, 717 12

Figueroa-Feliciano, E. 2006, J. Appl. Phys., 99, 114513 184

Fiore, F. *et al.* 2003, Astron. & Astrophys., 409, 79 70, 73, 80, 137, 138, 148, 149, 150, 151

—. 2001, Mon. Not. R. Astron. Soc., 327, 771 26

Friedrich, S. 1997, PhD thesis, Yale University 213, 243

Fukugita, M., Ichikawa, T., Gunn, J. E., Doi, M., Shimasaku, K., and Schneider, D. P. 1996, Astron. J., 111, 1748 55

Gaidis, M. C. 1994, PhD thesis, Yale University 210, 211, 214, 243, 244, 245

Gallagher, S. C., Brandt, W. N., Chartas, G., and Garmire, G. P. 2002, Astrophys. J., 567, 37 124

Gao, J. 2005, Fitting the resonance data from network analyzer, unpublished 250, 251

Gao, J., Zmuidzinas, J., Mazin, B. A., Day, P. K., and Leduc, H. G. 2006, Nucl. Instr. and Meth. A, 559, 585 201

Gao, J., Zmuidzinas, J., Mazin, B. A., Leduc, H. G., and Day, P. K. 2007, Appl. Phys. Lett., 90, 2507 205, 206, 247, 248

Gehrels, N. 1986, Astrophys. J., 303, 336 35

Giacconi, R., Gursky, H., Paolini, F., and Rossi, B. 1962, Phys. Rev. Lett., 9, 439 1, 10

Giacconi, R. *et al.* 2002, Astrophys. J. Suppl., 139, 369 23, 25, 26, 37, 38, 47, 53

Giavalisco, M. *et al.* 2004, Astrophys. J., 600, L93 70

Gilfanov, M., Grimm, H.-J., and Sunyaev, R. 2004, Mon. Not. R. Astron. Soc., 347, L57 147

Gioia, I. M., Maccacaro, T., Schild, R. E., Wolter, A., Stocke, J. T., Morris, S. L., and Henry, J. P. 1990, Astrophys. J. Suppl., 72, 567 127

Giommi, P., Menna, M. T., and Padovani, P. 1999, Mon. Not. R. Astron. Soc., 310, 465 127

Giommi, P., Perri, M., and Fiore, F. 2000, Astron. & Astrophys., 362, 799 25

Glikman, E., Gregg, M. D., Lacy, M., Helfand, D. J., Becker, R. H., and White, R. L. 2004, Astrophys. J., 607, 60 153

Goldie, D. J., Brink, P. L., Patel, C., Booth, N. E., and Salmon, G. L. 1994, Appl. Phys. Lett., 64, 3169 273, 275

Golubov, A. A., Houwman, E. P., Gijsbertsen, J. G., Krasnov, V. M., Flokstra, J., Rogalla, H., and Kupriyanov, M. Y. 1995, Phys. Rev. B, 51, 1073 243

Golwala, S. R. 2000, PhD thesis, University of California, Berkeley 252, 253

Gray, K. E. 1971, Journal of Physics F, 1, 290 210

Green, P. J. *et al.* 2004, Astrophys. J. Suppl., 150, 43 54, 80

Grimm, H.-J., Gilfanov, M., and Sunyaev, R. 2003, Mon. Not. R. Astron. Soc., 339, 793 147

Gruber, D. E., Matteson, J. L., Peterson, L. E., and Jung, G. V. 1999, Astrophys. J., 520, 124 10, 11

Guilbert, P. W. and Fabian, A. C. 1986, Mon. Not. R. Astron. Soc., 220, 439 12

Halpern, J. P., Turner, T. J., and George, I. M. 1999, Mon. Not. R. Astron. Soc., 307, L47 146

Hamilton, T. T. and Helfand, D. J. 1987, Astrophys. J., 318, 93 40

Harrison, F. A., Eckart, M. E., Mao, P. H., Helfand, D. J., and Stern, D. 2003, Astrophys. J., 596, 944 3, 6, 20, 22, 54, 71, 79, 80, 172

Hasinger, G., Burg, R., Giacconi, R., Schmidt, M., Trumper, J., and Zamorani, G. 1998, Astron. & Astrophys., 329, 482 2, 13, 160

Helfand, D. J. and Moran, E. C. 2001, Astrophys. J., 554, 27 147

Henry, J. P., Gioia, I. M., Mullis, C. R., Voges, W., Briel, U. G., Böhringer, H., and Huchra, J. P. 2001, Astrophys. J., 553, L109 127

Holden, B. P., Stanford, S. A., Squires, G. K., Rosati, P., Tozzi, P., Eisenhardt, P., and Spinrad, H. 2002, Astron. J., 124, 33 104, 155, 156, 157

Hooper, E. J. and ChaMP Collaboration. 2002, BAAS, 200, #13.12 24

Hornschemeier, A. E. *et al.* 2001, Astrophys. J., 554, 742 50, 67, 70, 112

Irwin, K. D. 1995, Appl. Phys. Lett., 66, 1998 184

—. 2002, Physica C Superconductivity, 368, 203 186, 187

Irwin, K. D. and Lehnert, K. W. 2004, Appl. Phys. Lett., 85, 2107 189

Iyengar, V. S., Naranan, S., and Sreekantan, B. V. 1975, Astrophys. & Space Sci., 32, 431 122

Jaffe, W., Ford, H. C., Ferrarese, L., van den Bosch, F., and O'Connell, R. W. 1993, Nature, 364, 213 14

Jansen, F. *et al.* 2001, Astron. & Astrophys., 365, L1 15

Jochum, J., Kraus, H., Gutsche, M., Kemmather, B., Feilitzsch, F. V., and Mössbauer, R. L. 1993, Annalen der Physik, 505, 611 254

Kaplan, S. B. 1979, Journal of Low Temperature Physics, 37, 343 273, 275

Kaplan, S. B., Chi, C. C., Langenberg, D. N., Chang, J. J., Jafarey, S., and Scalapino, D. J. 1976, Phys. Rev. B, 14, 4854 204, 209, 211

Kells, W., Dressler, A., Sivaramakrishnan, A., Carr, D., Koch, E., Epps, H., Hilyard, D., and Pardeilhan, G. 1998, Proc. Astron. Soc. Pacific, 110, 1487 56

Kim, D.-W. *et al.* 2004, Astrophys. J. Suppl., 150, 19 54, 79

Kinney, A. L., Calzetti, D., Bohlin, R. C., McQuade, K., Storchi-Bergman , T., and Henrique, R. 1996, Astrophys. J., 467, 38 57

Kirk, E. C., Lerch, P., Olsen, J., Zehnder, A., and Ott, H. R. 2000, Nucl. Instr. and Meth. A, 444, 201 244

Koekemoer, A. M. *et al.* 2004, Astrophys. J., 600, L123 70

Kozorezov, A. G., Volkov, A. F., Wigmore, J. K., Peacock, A., Poelaert, A., and den Hartog, R. 2000, Phys. Rev. B, 61, 11807 207, 208, 209, 272, 273, 275

Kraus, H., von Feilitzsch, F., Jochum, J., Mössbauer, R. L., Peterreins, T., and Pröbst, F. 1989, Phys. Lett. B, 231, 195 183, 191, 207, 244, 254

Kron, R. G. 1980, Astrophys. J., 43, 305 58

Kurakado, M. 1982, Nucl. Instr. and Meth. A, 196, 275 209, 213

La Franca, F. *et al.* 2002, Astrophys. J., 570, 100 3, 23, 82

Lacy, M. *et al.* 2004, Astrophys. J. Suppl., 154, 166 161

Laird, E. S., Nandra, K., Adelberger, K. L., Steidel, C. C., and Reddy, N. A. 2005, Mon. Not. R. Astron. Soc., 359, 47 173

Landolt, A. U. 1992, Astron. J., 104, 340 57

Lanting, T. M. *et al.* 2005, Applied Physics Letters, 86, 2511 189

Laurent-Muehleisen, S. A., Kollgaard, R. I., Feigelson, E. D., Brinkmann, W., and Siebert, J. 1999, Astrophys. J., 525, 127 127

Lehnert, K. W., Irwin, K. D., Castellanos-Beltran, M. A., Mates, J. A. B., and Vale, L. R. 2006, submitted to Appl. Superconductivity Conference proceedings 189, 190

Li, L. 2002, PhD thesis, Yale University 183, 207, 214

Li, L., Frunzio, L., Wilson, C. M., and Prober, D. E. 2003, Journal of Applied Physics, 93, 1137 244, 259

Little, W. A. 1959, Canadian J. Phys., 37, 334 211

Magorrian, J. *et al.* 1998, Astron. J., 115, 2285 1, 178

Mainieri, V., Bergeron, J., Hasinger, G., Lehmann, I., Rosati, P., Schmidt, M., Szokoly, G., and Della Ceca, R. 2002, Astron. & Astrophys., 393, 425 73

Martin, D. D. E., Verhoeve, P., Peacock, A., Kozorezov, A. G., Wigmore, J. K., Rogalla, H., and Venn, R. 2006, Appl. Phys. Lett., 88, 3510 272, 273, 275

Martini, P., Kelson, D. D., Mulchaey, J. S., and Trager, S. C. 2002, Astrophys. J., 576, L109 154

Massey, P., Gronwall, C., and Pilachowski, C. A. 1990, Proc. Astron. Soc. Pacific, 102, 1046 86

Mather, J. C. *et al.* 1990, Astrophys. J., 354, L37 12

Matt, G. 2002, Royal Society of London Philosophical Transactions Series A, 360, 2045 147

Mattis, D. C. and Bardeen, J. 1958, Phys. Rev., 111, 412 194

Mazin, B. A. 2004, PhD thesis, California Institute of Technology 194, 199, 200, 201, 202, 205, 206, 217, 222, 224, 227, 243

Mazin, B. A., Bumble, B., Day, P. K., Eckart, M. E., Golwala, S., Zmuidzinas, J., and Harrison, F. A. 2006a, Appl. Phys. Lett., 89, 2507 255, 259

Mazin, B. A., Day, P. K., Irwin, K. D., Reintsema, C. D., and Zmuidzinas, J. 2006b, Nucl. Instr. and Meth. A, 559, 799 192, 260

McLean, B. J., Greene, G. R., Lattanzi, M. G., and Pirenne, B. 2000, in ASP Conf. Ser. 216: ADASS IX, 145 65, 66, 104

McMillan, W. L. 1968, Phys. Rev., 167, 331 193

Mignoli, M. *et al.* 2004, Astron. & Astrophys., 418, 827 70

Monet, D. G. 1998, BAAS, 30, 1427 56

Monet, D. G. *et al.* 2003, Astron. J., 125, 984 57

Moran, E. C., Filippenko, A. V., and Chornock, R. 2002, Astrophys. J., 579, L71 146, 149, 152

Moran, E. C., Lehnert, M. D., and Helfand, D. J. 1999, Astrophys. J., 526, 649 147

Morrison, R. and McCammon, D. 1983, Astrophys. J., 270, 119 106

Mushotzky, R. F., Cowie, L. L., Barger, A. J., and Arnaud, K. A. 2000, Nature, 404, 459 25

Nandra, K. and Pounds, K. A. 1994, Mon. Not. R. Astron. Soc., 268, 405 2, 13

Newman, J. A. *et al.* 2005, in preparation 87

Norman, C. *et al.* 2002, Astrophys. J., 571, 218 70, 146

Ohta, K. *et al.* 2003, Astrophys. J., 598, 210 16

Oke, J. B. and Gunn, J. E. 1982, Proc. Astron. Soc. Pacific, 94, 586 85

Oke, J. B. *et al.* 1995, Proc. Astron. Soc. Pacific, 107, 375 56, 83

Perola, G. C. *et al.* 2004, Astron. & Astrophys., 421, 491 80

Petersan, P. J. and Anlage, S. M. 1998, J. Appl. Phys., 84, 3392 250

Pizzolato, N., Maggio, A., Micela, G., Sciortino, S., and Ventura, P. 2003, Astron. & Astrophys., 397, 147 130

Ranalli, P., Comastri, A., and Setti, G. 2003, Astron. & Astrophys., 399, 39 147, 148

Rando, N. *et al.* 1992, Nucl. Instr. and Meth. A, 313, 173 213

Richards, G. T. *et al.* 2006, Astron. J., 131, 2766 2, 160

Rosati, P. *et al.* 2002, Astrophys. J., 566, 667 3, 23, 42, 47, 81, 82

Rothwarf, A. and Taylor, B. N. 1967, Phys. Rev. Lett., 19, 27 210

Schmidt, M. 1963, Nature, 197, 1040 1

Schmidt, M. *et al.* 1998, Astron. & Astrophys., 329, 495 2, 13, 160

Segall, K. 2000, PhD thesis, Yale University 213

Sergeev, A. V., Mitin, V. V., and Karasik, B. S. 2002, Applied Physics Letters, 80, 817 182, 205

Seymour, N. *et al.* 2007, astro-ph/0703224 162

Silverman, J. D. *et al.* 2005, Astrophys. J., 618, 123 80, 126, 137, 138, 139, 141

Simcoe, R. A., Metzger, M. R., Small, T. A., and Araya, G. 2000, BAAS, 32, 758 55, 56

Steffen, A. T., Barger, A. J., Capak, P., Cowie, L. L., Mushotzky, R. F., and Yang, Y. 2004, Astron. J., 128, 1483 79, 137, 138

Steidel, C. C., Hunt, M. P., Shapley, A. E., Adelberger, K. L., Pettini, M., Dickinson, M., and Giavalisco, M. 2002, Astrophys. J., 576, 653 160

Steidel, C. C., Shapley, A. E., Pettini, M., Adelberger, K. L., Erb, D. K., Reddy, N. A., and Hunt, M. P. 2004, Astrophys. J., 604, 534 85

Stern, D. *et al.* 2005a, Astrophys. J., 631, 163 161, 166, 167, 168, 174, 175

Stern, D., Holden, B., Stanford, S. A., and Spinrad, H. 2003, Astron. J., 125, 2759 85, 155, 156

Stern, D., Yost, S. A., Eckart, M. E., Harrison, F. A., Helfand, D. J., Djorgovski, S. G., Malhotra, S., and Rhoads, J. E. 2005b, Astrophys. J., 619, 12 86

Stern, D. *et al.* 2002a, Astrophys. J., 568, 71 23, 70, 85, 146

—. 2002b, Astron. J., 123, 2223 24, 25, 37, 39, 67, 70, 85, 132, 146

Stocke, J. T., Morris, S. L., Gioia, I. M., Maccacaro, T., Schild, R., Wolter, A., Fleming, T. A., and Henry, J. P. 1991, Astrophys. J. Suppl., 76, 813 104, 127

Szokoly, G. P. *et al.* 2004, Astrophys. J. Suppl., 155, 271 3, 81, 82, 146

Taylor, G. B. and Wright, E. L. 1989, Astrophys. J., 339, 619 12

Tozzi, P. *et al.* 2001, Astrophys. J., 562, 42 50, 73

Treister, E. *et al.* 2005, Astrophys. J., 621, 104 137, 138

Treister, E. *et al.* 2004, Astrophys. J., 616, 123 128

Tremaine, S. *et al.* 2002, Astrophys. J., 574, 740 1, 178

Twerenbold, D. and Zehnder, A. 1986, J. Appl. Phys., 61, 1 182

Ueda, Y., Ishisaki, Y., Takahashi, T., Makishima, K., and Ohashi, T. 2001, Astrophys. J. Suppl., 133, 1 25

Ullom, J. N. *et al.* 2005, Appl. Phys. Lett., 87, 194103 184

Vanden Berk, D. E. *et al.* 2001, Astron. J., 122, 549 57, 88

Vayonakis, A. 2001, Radiative losses from 2-d apertures, unpublished 201

Veilleux, S. and Osterbrock, D. E. 1987, Astrophys. J. Suppl., 63, 295 89, 124

Weisskopf, M. C., O'dell, S. L., and van Speybroeck, L. P. 1996, in Proc. SPIE Vol. 2805, p. 2-7, Multilayer and Grazing Incidence X-Ray/EUV Optics III, Richard B. Hoover; Arthur B. Walker; Eds., 2 2, 15, 23, 53

Werner, M. W. *et al.* 2004, Astrophys. J. Suppl., 154, 1 160

Wilks, J. and Betts, D. S. 1987, An Introduction to Liquid Helium, 2nd edn. (Oxford: Clarendon Press) 267

Wolf, C., Wisotzki, L., Borch, A., Dye, S., Kleinheinrich, M., and Meisenheimer, K. 2003, Astron. & Astrophys., 408, 499 109

Worsley, M. A. *et al.* 2005, Mon. Not. R. Astron. Soc., 357, 1281 3, 20, 79

Yang, Y., Mushotzky, R. F., Steffen, A. T., Barger, A. J., and Cowie, L. L. 2004, Astron. J., 128, 1501 79, 132

Yuan, F. and Narayan, R. 2004, Astrophys. J., 612, 724 146

Zmuidzinas, J. 2002, Modal Description of Kinetic Inductance Detectors, unpublished 206

Who cares? It's only a thesis.

—Fiona A. Harrison (1993)